TECHNISCHE UNIVERSITÄT MÜNCHEN
Lehrstuhl für elektrische Antriebssysteme und Leistungselektronik

On Control of Grid-Tied Back-to-Back Power Converters and Permanent Magnet Synchronous Generator Wind Turbine Systems

Zhenbin Zhang

Vollstaendiger Abdruck der von der Fakultät für Elektrotechnik und Informationstechnik der Technischen Universität München zur erlangung des Grades eines

Doktor-Ingenieur

genehmigten Dissertation.

Vorsitzender: Prof. Dr.-Ing. Andreas Jossen

Prüfer der Dissertation:

1. Prof. Dr.-Ing. Ralph Kennel
2. Prof. Dr.-Ing. José Rodríguez
   Universidad Andres Bello, Chile
3. Prof. Dr.-Ing. Marian Kazmierkowski
   Warsaw University of Technology, Polen

Die Dissertation wurde am 22.12.2015 bei der Technischen Universität München eingereicht und durch die Fakultät für Elektrotechnik und Informationstechnik am 19.10.2016 angenommen.

To my daughter: Yinan Zhang

Acknowledgment

This dissertation at hand is based on my research carried out at the *Institute for Electrical Drive Systems and Power Electronics*, **Technische Universität München (TUM)** supervised by *Prof. Dr.-Ing. Ralph Kennel*. My deep gratitude goes foremost to Prof. Ralph Kennel, who has walked me through all the stages of my projects. The trust he has in me has given me a lot of encouragements. The proper freedom and right entrusted from him equipped me with the capability of organizing certain research projects. The international atmosphere of the institute he has been cultivating brings me a cherish chance to learn from different cultures at an early age of my life, which also brings me colleagues and friends from different parts of the world. All of these made me feel lucky to have worked at this nice institute.

I would like to express my sincere gratitude to Prof. Dr.-Ing. José Rodríguez and Prof. Dr.-Ing. Marian Kazmierkoski, two of the most respectable specialists in the filed of power electronics and drives, for reviewing and co-examining my dissertation. With the guidance of Prof. Rodríguez, we have already published several IEEE transaction papers; some more are still under revision/review. Prof. Kazmierkoski's outstanding and remarkable publications have enlightened me even before my starting of Ph.D. program. It is my great honor to have both as my co-supervisors. I wish we may have more cooperation in my future career and life.

Parts of my Ph.D. projects were cooperated with two respectable companies: Infineon and National Instruments. Dr.-Ing. Martin Schulz (from Infineion), and Mr. Barc Backmeyer, Mr. Wolfgang Zwick and Mr. Jan Kniewasser (from National Instruments) have offered me tremendous help during my test-bench constructions. My deep gratitude will go to them. The cooperating experiences generated the most positive impression of how leading and responsible companies would behave and how education/research can cooperate with the industry. I believe our cooperation will go on in my later careers.

I am also greatly indebted to my colleagues. Dr.-Ing. Christoph Hackl is one of the most important partners. His help and guidance in particular on how to transfer ideas and results precisely into readable publications will benefit me forever. Dr.-Ing. Peter Landsmann and Dr. -Ing. Peter Stolze, these two team leaders, have also helped me. I also appreciate the co-working experiences with Dietmar Schuster, Ali Hafni, Felix Rojas, Reza Fotouhi, Daniel Glose, Julien Cordier, Dr. Esteban Fuentes, Florian Bauer, Mohamed Abdelrahem, Ayman Ayad, Darshan Manoharan, Dr. Petros Karamanakos, et al. I appreciate the cooperation with our Chinese group: Dr. Jianbo Gao, Dr.-Ing. Zhixun Ma, Dr.-Ing. Fengxiang Wang, Zhe Chen, Guangye Si, Xinbo Cai, Hui Fang, Wei Tian, et al. In particular, the cooperation with Dr. Wang has made us fruitful both in work and friendship. Master students that I have supervised (Ming Xue, He Xu, Congming Bao, Jochen Schenek, Yuanpeng Zhang, et al.), have also helped me. In particular, the co-working experiences with Mr. Xue, Xu, Bao and Schenek were quite pleasant ones.

Last but also the most sincere gratitude goes to my beloved family. It is my beloved wife, my parents and my brother who have always been backing me up, trusting and supporting me. Without them, I could hardly finish this work.

Munich, Germany in October, 2015
Zhenbin Zhang

Abstract

This dissertation has investigated both the "framework" level and certain "dedicated control techniques" for grid-connected two- and three-level neutral-point-clamped back-to-back power converters and permanent magnet synchronous generator wind turbine systems. Deeply investigated "framework" level control techniques include the classical vector oriented control, direct control with both modulator and switching table, deadbeat control and the modern predictive control classes, with computationally efficient and performance enhanced direct model predictive control techniques as the major emphasized ones. The closely investigated "dedicated control techniques" presented in this work include performance enhanced DC-link control, grid side voltage sensorless control with fast state estimation, generator side encoderless control using fundamental model, etc. The real-time verification of the electric control unit, particularly its functionality at abnormal situations (e.g., the low-voltage ride through (LVRT) capabilities of the underlying LVRT control unit), for grid-tied back-to-back power converter wind turbine systems, through the signal level hardware-in-the-loop technique, has also been closely discussed and investigated. The performances of the aforementioned control techniques are experimentally assessed at three self-designed test-benches. Digital controller realization via field programmable gate array for the aforementioned techniques has been comprehensively studied as well.

Kurzzusammenfassung

Diese Dissertation behandelt sowohl die „Strukturebene“ als auch bestimmte „dedizierte Regelungsmethoden“ für netzgebundene zwei- und drei-Level Neutral-Point-Clamped Back-to-Back Stromrichter zusammen mit Permanentmagnet-erregten Synchrongeneratoren für Windkraftanlagen. Zu den untersuchten Verfahren der „Strukturebene“ gehören die klassische Vektor-Orientierte Regelung, Direkte Regelung sowohl mit Modulator als auch mit Schalttabelle, Deadbeat-Regelung und die Klassen der modernen prädiktiven Regelungsmethoden, wobei die Direkten Modellprädiktiven Regelungsmethoden mit erhöhter Recheneffizienz und Leistung besonders hervorzuheben sind. Zu den im Detail untersuchten „dedizierten Regelungsmethoden“ gehören eine leistungsgesteigerte Zwischenkreisregelung, netzseitige spannungssensorlose Regelung mit schneller Zustandsbeobachtung und Generator-seitige geberlose Regelung u.a. mit dem Grundwellenmodell. Die Echtzeit-Verifikation der Verfahren, insbesondere auch in anormalen Situationen (z.B. Dynamische Netzstabilisierung/Low-Voltage Ride Through) wurde durch Signal-Level Hardware-in-the-Loop-Simulationen für netzgebundene Back-to-Back Stromrichter für Windkraftanlagen untersucht. Die Regelverfahren wurden an drei eigens gebauten Testständen experimentell getestet und bewertet. Zusätzlich wurden auch Möglichkeiten für die digitale Implementierung der Verfahren auf einem Field Programmable Gate Array im Detail untersucht.

Contents

1 Introduction **1**
- 1.1 Power electronics and control techniques for renewable energy systems . . . 1
- 1.2 Control techniques for back-to-back converter wind turbine systems 3
  - 1.2.1 Cascaded vector oriented control with modulators 4
  - 1.2.2 Direct control with look-up tables 5
  - 1.2.3 Direct control with modulator 6
  - 1.2.4 Model predictive control 6
  - 1.2.5 Special control objectives 7
- 1.3 Problem description, motivation and objectives 8
  - 1.3.1 Problem description 8
  - 1.3.2 Motivation and objectives 11
- 1.4 Contributions 12

2 System modeling and physical system description **14**
- 2.1 Mathematical basics for system modeling 15
  - 2.1.1 Three phase system coordinate transformation 15
  - 2.1.2 Linear time-invariant (LTI) state space model 16
  - 2.1.3 Discretization of LTI 16
  - 2.1.4 Explicit discretization and approximations of LTI 16
- 2.2 Two- and three-level back-to-back power converter system modeling 17
  - 2.2.1 Two-level back-to-back power converter 17
  - 2.2.2 Three-level NPC back-to-back power converter 19
- 2.3 RL load dynamics 21
- 2.4 PMSG wind turbine system with back-to-back power converter 21
  - 2.4.1 Aerodynamics and turbine model 21
  - 2.4.2 Permanent-magnet synchronous generator (PMSG) 25
  - 2.4.3 Grid side dynamics: grid and filter 27
- 2.5 Lab-constructed test-benches and real-time controller 29
  - 2.5.1 Two-level back-to-back power converter system 29
  - 2.5.2 Three-level back-to-back power converter system 30
  - 2.5.3 FPGA based HiL simulation system configuration 32
  - 2.5.4 Real-time system structure and utilization 32
- 2.6 Summary 34

3 Classical control techniques **35**
3.1 Introduction . . . 35
3.2 Field and voltage oriented control . . . 36
3.2.1 Field oriented control for MSC . . . 36
3.2.2 Voltage oriented control for GSC . . . 39
3.3 Direct torque and power control with SVM . . . 41
3.3.1 Direct torque control (with SVM) for MSC . . . 42
3.3.2 Direct power control with SVM for GSC . . . 45
3.4 Deadbeat control with SVM . . . 46
3.4.1 Deadbeat (torque) control for machine side . . . 47
3.4.2 Deadbeat (power) control for grid side . . . 48
3.5 Direct torque and power control with switching table . . . 50
3.5.1 Direct torque control for MSC . . . 50
3.5.2 Direct power control for GSC . . . 53
3.6 Performance evaluation with experimental data . . . 55
3.6.1 Control performances of FOC-VOC and DBC with SVM . . . 56
3.6.2 Control performances of DTC-DPC with SVM and switching table 58
3.6.3 Control performances of ST-DTC-DPC for the three-level system . 59
3.7 Summary . . . 61

4 Direct model predictive control **62**
4.1 Model predictive control: a brief introduction . . . 62
4.1.1 MPC for power electronics and electrical drives . . . 63
4.1.2 Concept of classical direct model predictive control . . . 65
4.2 DMPC for two-level back-to-back PMSG systems . . . 66
4.2.1 Direct model predictive torque and power control . . . 67
4.2.2 Direct model predictive current control . . . 69
4.3 DMPC for three-level back-to-back PMSG systems . . . 70
4.3.1 Direct model predictive torque and power control . . . 70
4.3.2 Direct model predictive current control . . . 71
4.4 Performance evaluations with experimental data . . . 74
4.4.1 FCS-DTC-DPC and FCS-DCC for two level PMSG systems . . . 75
4.4.2 FCS-DTC-DPC and FCS-DCC for three-level NPC PMSG systems 75
4.4.3 FCS-DTC-DPC and ST-DTC-DPC for back-to-back PMSG systems 79
4.5 Summary . . . 87

5 Advanced direct model predictive control **90**
5.1 Problems of classical DMPC . . . 90
5.2 Computationally efficient DMPC for three-level NPC power converters . . 93
5.2.1 Introduction . . . 93
5.2.2 Concept of the proposed computationally efficient DMPC . . . 96
5.2.3 CE-DMPC with hexagon candidate region . . . 98
5.2.4 CE-DMPC with triangle candidate region . . . 102
5.2.5 Evaluation and analysis . . . 104
5.3 Performance-enhanced DMPC with two switching vectors . . . 114

5.3.1 Concept of the proposed two-vector DMPC . . . 114
5.3.2 Realization of V2-DMPC . . . 115
5.3.3 Application of the V2-DMPC to grid side control . . . 118
5.3.4 Application of the V2-DMPC to machine side control . . . 122
5.4 Performance-enhanced DMPC with three switching vectors . . . 124
5.4.1 Concept of three-vector DMPC (V3-DMPC) . . . 124
5.4.2 Realization of the proposed V3-DMPC . . . 125
5.4.3 Application of V3-DMPC to grid side control . . . 127
5.4.4 Application of V3-DMPC to machine side control . . . 130
5.4.5 Evaluation and analysis . . . 131
5.5 Predictive control of back-to-back power converter under unbalanced grid . 137
5.5.1 Introduction . . . 137
5.5.2 Conventional unbalanced grid control . . . 139
5.5.3 Extended instantaneous power theory and its combination to DMPC 143
5.5.4 Evaluation and analysis . . . 143
5.6 Summary . . . 147

6 Quasi-centralized direct model predictive control 148
6.1 Background . . . 148
6.2 QC-DMPC for back-to-back power converter with RL load . . . 149
6.2.1 PI DC-link controller based DMPC scheme . . . 150
6.2.2 The proposed quasi-centralized DMPC scheme . . . 151
6.2.3 FPGA implementation comparison . . . 154
6.2.4 Evaluations and analysis . . . 156
6.3 A revised QC-DMPC for back-to-back power converter with PMSG . . . 164
6.3.1 Introduction . . . 164
6.3.2 Classical PI-DMPC and QC-DMPC controllers . . . 165
6.3.3 Revised QC-DMPC without DC-link voltage bias . . . 168
6.3.4 FPGA design and experimental evaluation . . . 170
6.4 Summary . . . 177

7 Grid side voltage sensorless control 179
7.1 Introduction . . . 179
7.2 Virtual flux concept and voltage sensorless control techniques . . . 181
7.2.1 Virtual flux concept . . . 181
7.2.2 Grid voltage estimation with filter based VF techniques . . . 182
7.2.3 Proposed initial bias compensation based VF estimation . . . 185
7.3 Deadbeat control of back-to-back power converter with IBC-VF . . . 187
7.3.1 Overall control strategy . . . 187
7.3.2 Simulative verification . . . 190
7.3.3 Experimental verification . . . 191
7.4 Summary . . . 199

8 Encoderless control of PMSG wind turbine system **200**
8.1 Introduction . . . 200
8.2 Encoderless control with EKF . . . 201
8.2.1 Nonlinear system state estimation with EKF . . . 202
8.2.2 Case-I: EKF estimation without turbine drive torque . . . 203
8.2.3 Case-II: EKF estimation with turbine drive torque . . . 204
8.2.4 FPGA design and experimental evaluations . . . 206
8.3 Encoderless control with sliding mode observer . . . 211
8.3.1 Sliding mode observer . . . 211
8.3.2 Design of the time-varying sliding mode observer . . . 211
8.3.3 Evaluation . . . 213
8.4 Summary . . . 215

9 FPGA HiL technique and low voltage ride through control **216**
9.1 Introduction . . . 216
9.2 FPGA based S-HiL technique for wind turbine ECU evaluations . . . 217
9.2.1 FPGA S-HiL realization for PMSG wind turbine systems . . . 218
9.2.2 Emulator refreshing rate effects and analysis . . . 220
9.3 LVRT and its FPGA based S-HiL evaluation . . . 222
9.3.1 State-of-the-art LVRT control techniques . . . 224
9.3.2 Proposed LVRT within DMPC scheme . . . 228
9.3.3 LVRT evaluations with FPGA S-HiL solution . . . 229
9.4 Summary . . . 232

10 Conclusions and future prospects **233**

Appendices **239**

A Symbols and abbreviations **241**

B Switching matrix **243**

C System per-unit model **246**

D Switching table for three-level NPC power converter **248**

E List of publications **251**

Bibliography **254**

Chapter 1

Introduction

This work focuses on control techniques of grid-tied two- and three-level neutral-point-clamped (3L-NPC) back-to-back power converters and permanent-magnet synchronous generator (PMSG) wind turbine systems. In this chapter the background, research focus, motivations and objectives of this dissertation are introduced. The contributions indexed to each of the following chapters have been summarized as well.

1.1 Power electronics and control techniques for renewable energy systems

In general, electricity has been generally utilized in two directions, which are *information transmission* and *energy conversion*. However, it is exactly these two directions that have changed and are still changing the whole world. One of the back-bone forces comes from the technology development driven by the entire group of electrical engineers. In 1831, the first DC generator (also named *Faraday Disk*) was invented by *Michael Faraday* applying *Faraday's Law*. Since then, each generation of the electrical engineers have been facing and fulfilling the requirements put-forward by their time. For the time being, issues such as, limited fossil fuel resources and undesired sub-productions from using the fuel resources force us to seek for more sustainable and cleaner solutions for a long-run development. Distributed energy generation/conversion systems, in particular, renewable energy applications (e.g., energy generations using hydro, wind, solar, biomass, geothermal, etc.) become therefore one of the promising solutions [1, 2]. For the last decades, energy generations using wind, solar and other renewable resources have been increasing extremely fast [3, 4], among which wind energy application[1] grows more significantly than any other kinds and is playing an important role in the modern energy supply system.

Power electronics and control techniques have already been playing one of the essential roles in distributed energy generations/conversion systems. Fig. 1.1 depicts an overview of

[1] Wind energy is the second mostly-utilized renewable energy, with hydro energy being the first. Humans have been harnessing this source of energy for centuries. However, only after the late 19th century, it was for the first time harnessed to generate electricity [5].

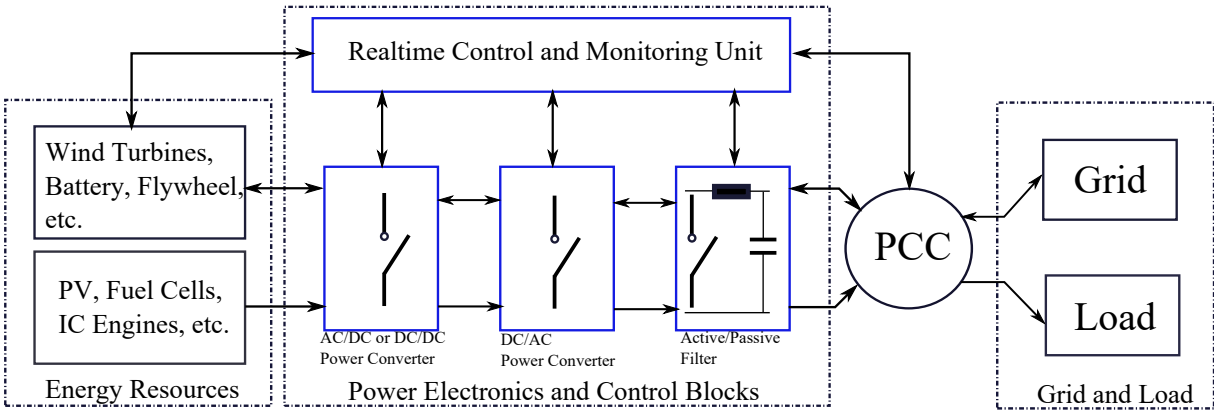

Fig. 1.1: Power electronics and control for distributed energy generation/conversion system [1]. For some applications one-direction energy flow is required (such as photovoltaic systems), while for certain situations a bi-directional energy flow is important (e.g., variable speed wind energy systems and energy conversion systems with re-generation functions).

how power electronics and control techniques contribute in distributed energy generation and energy conversion systems. They are widely used in four main aspects, namely, i) *converter interface to the original resource*, ii) *intermediate power conversion*, iii) *grid connection interface*, and iv) *control and monitoring units*. Within these four parts, power electronics and control techniques enhance the performances of (renewable) energy generation/conversion systems.

The fast development/utilization of renewable energy resources, on the other side, introduces even larger space for the evolution of power electronics and control techniques. In the early ages of 1980s, power electronics for wind turbines was just a soft starter to initially interconnect the squirrel-cage induction generator with the power grid [6]. Only *thyristors* were used and they were not required to carry the power continuously [5]. In the 1990s it was seen the applications of the power electronics for controlling the rotor resistance of the wound-rotor induction generator to reduce the mechanical stress and load especially at nominal power operation points; more advanced *diode bridges* with a chopper were used [7]. Since the beginning of this century, more advanced *back-to-back power converters* were introduced in the double fed induction generator (DFIG) with partial-scale power capacity of the system, which started to regulate the electrical power transferred from the wind turbines. Afterward, they were introduced in the full-scale power capacity for the asynchronous/synchronous generator systems [2, 5].

With voltage source back-to-back power converters, the direction of the active power flow is allowed to be reversed at any instant, i.e., true four-quadrant operations. Therefore, with a full-scale power capacity voltage source back-to-back power converter, it is possible to fully control the power extracted/supplied from/to the turbines/load. Ancillary services (frequency and voltage supports) to the grid can also be provided [8]. Together with the increasingly advanced control techniques, the whole power electronics based power conversion parts are therefore gradually playing an essential role not only to reduce the mechanical stress and increase the energy yield, but also to make the whole generation system a completely controllable energy conversion/generation unit [6]. Therefore, this

topology, despite having a slight lower energy efficiency, due to its switching losses, becomes an attractive topology for modern advanced variable speed drives, grid connected distributed energy applications and High Voltage AC/DC (HVAC/DC) transmission systems [9, 10].

As the penetration of wind energy generation goes on, the grid code requirements become stricter [11]. Compared with double-fed induction generator (DFIG) based wind turbine systems equipped with partial power rating power converters, direct-drive permanent-magnet synchronous generator (PMSG) wind turbine configuration shows many advantages [9, 12–14], such as, wider wind speed operating range, higher energy density and efficiency, better grid side support and fault ride through capabilities, and, more importantly, reduced maintenance requirements. These properties make PMSG wind turbine systems with back-to-back power converter and direct-drive train a more attractive solution in particular for off-shore wind energy systems.

Power rating increase is another important aspect in the wind energy application area. Since years, multi-megawatt (MW) wind turbines have already arrived. Currently, 7.5 MW systems are available in the market and numerous research activities aim at 10-12 MW level for offshore applications [15, 16]. This increase in the power rating will bring more requirements to the power electronics and control techniques, such as, lower switching frequencies to reduce switching losses, converter/inverter to stand higher voltage/current levels, power converter topologies and control techniques to guarantee low total harmonic distortions (THDs), etc. [2]. In particular, the three-level neutral-point (diode) clamped (3L-NPC) back-to-back converters seem promising. They allow higher power rating or power levels, but the required amount of components is drastically less than e.g. five-level topologies.

In this work both the two-level (2L) and 3L-NPC back-to-back power converters, PMSG wind turbine systems and their control techniques are closely investigated.

1.2 Control techniques for back-to-back converter wind turbine systems

A simplified direct-drive PMSG based grid-tied back-to-back wind turbine system consists of a generator/machine-side converter (MSC) and a grid side converter (GSC), which share a commonly connected DC-link (see Fig. 1.2). From the power electronics perspectives, the *general control objectives* (GCOs) for MSC and GSC are (see e.g. [10, 17, 18]):

(co_1) *Machine side torque (current) control:* The underlying torque (current) controller for the MSC must be fast and accurate to assure (a) maximum power point tracking (MPPT) of the wind turbine system or (b) nominal torque generation for wind speeds above the nominal speed. In addition, to achieve high efficiency and to reduce stresses on the mechanical components, small torque ripples shall be guaranteed;

(co_2) *Grid side power (current) control:* The GSC controller assures grid-side active and

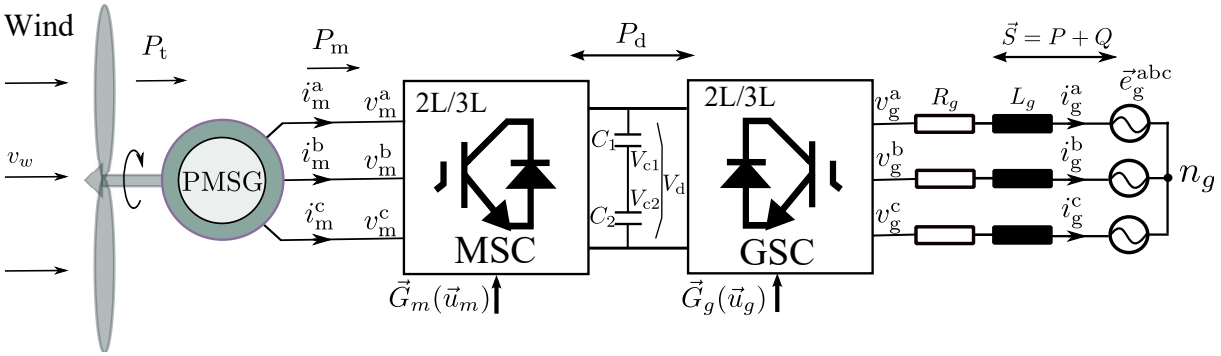

Fig. 1.2: Simplified structure of a voltage source back-to-back power converter PMSG wind turbine system.

reactive power (current) control[2]. Moreover, the underlying GSC current controller shall guarantee a certain power (current) quality to fulfill grid codes;

(co_3) *DC-link voltage control:* For both 2L- and 3L-NPC back-to-back power converters, a constant DC-link voltage is required. This can normally be realized by assigning certain references produced by a (extra outer-loop) DC-link voltage controller. For 3L-NPC back-to-back converters, (at least) one side (of the MSC and GSC) needs to assure voltage balancing in the upper and lower DC-link capacitors (see Fig. 1.2), i.e.

$$V_{c1} \stackrel{!}{=} V_{c2} > 0 \quad \Longrightarrow \quad V_d := V_{c1} + V_{c2} > 0, \tag{1.1}$$

is essential for maintaining a constant DC-link voltage and to allow for low-voltage ride through (LVRT) capabilities [19].

At "framework" level, control schemes, which achieve the control objectives mentioned above, can be divided into four groups (see e.g., [14,20–25]): (C_a) cascaded control schemes with modulators, (C_b) direct control with look-up table, (C_c) direct control with modulator, and (C_d) predictive controller for both the GSC and MSC sides.

Apart from these *general control objectives*, some *special control objectives* (SCOs), which are interesting for certain specific applications, are also closely investigated in my dissertation. These include *encoderless control* for the generator side, *advanced DC-link control* for the DC-Link control part, *voltage sensorless control* for the grid side converter control, *low-voltage ride through control* for grid fault situations, etc. The following sections introduce an overview of each technique of the aforementioned GCOs and SCOs.

1.2.1 Cascaded vector oriented control with modulators

This class refers to field-oriented control (FOC) for the MSC and voltage-oriented control (VOC) for GSC -both with modulators[3].

[2]During normal operations, the active power (current) is controlled indirectly by the DC-link voltage controller.

[3]Mainly space vector modulators (SVMs) are utilized due to their nice properties such as easy to implement, better DC-link utilization and lower THDs [25].

By decoupling the stator current into two separate components rotating with the rotor flux vector, FOC provides independent control of torque and flux, which is similar to controlling a separately excited DC machine. It was reported by Hasse and Blaschke in 1972 [25]. The so-called "field-orientation" is achieved by aligning the rotor flux linkage vector along the d-axis of the synchronous reference frame. The magnitude and phase of the stator currents are controlled in such a way that flux and torque components of current remain decoupled during transient and static conditions [26]. With such a solution, the control dynamics of the highly coupled nonlinear structure of the induction machine become (approximately) linearized and decoupled. Similarly, VOC decouples the grid side current into two independent (perpendicular to each other) components in the (synchronously) rotating reference frame of the *grid side voltage vector* [27]. The active power/current can be controlled directly by manipulating the one which aligns along the grid voltage vector; while the reactive power/current by the other.

In Sec. 3.2 the combination of FOC and VOC for the generator and grid side control, respectively, is revisited in detail. This is one of the most popular methods for wind turbine system control since their introduction [9, 28, 29]. With this combination, nice steady state performances are in general achievable. However, the dynamics are limited by the constrained controller bandwidth caused by the cascaded structure. The controller parameter tuning is also tedious and requires certain expertise. The required modulator, usually based on the time-averaged principle, is also complex in design (in particular for multilevel power converter) and problematic at low switching frequency operations. The coordinate transformation, for both VOC and FOC, requires both the angles of grid side voltage vector and the rotor flux. Since the flux/voltage angle cannot be directly measured from the terminals, it is necessary to implement voltage sensors and a shaft-mounted encoder, or estimator/observer to obtain these angles.

1.2.2 Direct control with look-up tables

This class refers to MSC with direct torque control (DTC) and GSC with direct power control (DPC)– both with offline designed switching tables. Instead of approximating the plant as a linear system, this class directly manipulates the switching states by an offline designed switching table in a non-linear manner, without a modulator.

The DTC technique was reported by Takahashi in [30] and Depenbrock in [31]. It was promoted by ABB. Different from vector oriented control, it does not require a synchronous coordinate transformation but replaces the linear PI controller with faster hysteresis controllers. Therefore the inner controller loop bandwidth is greatly enlarged, which leads to an excellent torque response. Additionally, much less information of the system parameters, even the flux position requirement, is almost un-required for AC machines[4].

DPC was derived from DTC and reported by Nouguchi in 1996 [32] using the in-

[4]For PMSM(G) to apply DTC technique, (only) the initial position of the permanent-magnet (rotor flux) is required; asynchronous induction motor does not have even this requirement.

stantaneous power theory (reported by Akagi[5] in [34]). Similar to DTC, no coordinate transformation is required, and no inner PI control loops exist. The switching sequence is selected directly based on the information produced by a hysteresis controller and the grid voltage vector location, which takes the instantaneous active and reactive power errors as input. Simple and direct in structure, but effective in dynamic response are the properties of this scheme. However, variable switching frequency and big control variable ripple problems are regarded as the disadvantages for the standard DTC and DPC methods [1, 25, 35]. The former makes the filter design a challenging task, and the latter requires much higher sampling frequency to achieve comparable steady state performances as (C_a). The design and implementation of the switching table is also not an easy task, especially for multilevel power converters. In Sec. 3.5 the combination of DTC and DPC scheme is revisited. Its principles and implementations are presented in detail.

1.2.3 Direct control with modulator

This class mainly refers to MSC with DTC and GSC with DPC – both with linear controllers and space vector modulator (SVM).

DTC-SVM incorporates the simplified vector orientation concept and reduces one of the inner PI control loops. It can be further divided into *flux closed-loop* and *torque closed-loop* (two sub-methods) [25, 35]. DPC-SVM [36] shares some similarities with DTC-SVM (both require vector orientation and frame transformation). However, DPC-SVM is more similar in structure with VOC, since still two inner PI control loops and the frame transformation are required. The difference is: DPC-SVM directly controls the active and reactive powers and is derived from the power dynamics, while VOC takes the direct and quadrature currents as the control variables and originates from the grid side current dynamics.

In general, direct control with modulator combines parts of the "direct" property of (C_b), and achieves a constant switching frequency, with a modulator. The tuning is also seen as easier, due to the reduction of parts of the inner control loops. A more detailed instruction to this combination can be found in Sec. 3.3

As a brief summary, all the aforementioned methods have already been comprehensively researched over the past decades. Deeper analysis and experimental evaluations of all these schemes are given in Chp. 3.

1.2.4 Model predictive control

Two of the common properties of the schemes introduced in the above sections (Sec. 1.2.1 to Sec. 1.2.3) are: (i) the available system models and the discrete (nonlinear) nature of the power converters, which may help to further improve the system control performances

[5]The first instantaneous (reactive) power theory was proposed in 1932 by Fryze in the time domain, only for single phase systems. In 1950, Buchholz extended this into multiphase systems, and in 1962 Depenbrock has extended Buchholz work into generic multiphase systems with neutral conductors. In 1983, the p-q theory was reported by Akagi with the contribution of a clear imaginary power definition (i.e., the instantaneous reactive power). In 1996, its modification to systems with zero sequence was reported by Peng and Lai. Then, in 2004 a generalized instantaneous power theory for multi-phase systems was presented by Dai in [33].

and ease the controller design, have not been fully considered; (ii) the actuating variables are calculated based on a "post-error" between the reference and the feedback signals (i.e., only after the error happens, the controller starts to modify its actuating variables).

On the contrary, model predictive control (MPC) (also referred to as receding horizon control) class, which was "discovered" in the petrochemical industrial in the early 1970s [21, 37, 38], takes the whole system model into consideration and can penalize the (multiple) system control targets with a flexible cost function. The optimum values of the actuating variables are not computed based on the "post-error" between the reference and the feedback signals, but through minimizing a flexibly designed cost function (which is also named as objective function) with penalized "predicted behaviors" of the system, fully using the system model and the past control actions over a receding prediction horizon [37, 39, 40]. Potentially it has more freedom to further improve the system control performances, since the "predicted behaviors" of the system are utilized within the control/decision process. Additionally, using a cost function to define the control targets makes it more straightforward (at least from a concept level) for more complicated systems with multiple control targets.

The main disadvantage of this class is its heavy online calculation efforts, especially with long horizons and multilevel & multiphase systems [37, 40, 41]. Therefore, although it has been successfully used since the 1970s in many long time-constant applications (e.g., petrochemical industry), only the introduction of fast digital signal processing (DSP) and the development of field programmable gate arrays (FPGAs) has made it possible to apply such techniques in fast dynamic process industries such as power electronics and drives [21, 40, 42]. Variable switching frequency, hence wide spread harmonic spectrum (although some work has proposed certain solution [43]), is still an issue. Robustness to system parameter variations is another concern, since it is a fully model based technique. In spite of that, this technique achieves promising control performances with much less design and tuning efforts for most systems and has further potential. Therefore, two separate chapters (Chp. 4 and Chp. 5) in this work are spent to exclusively discuss this technique, in particular the direct model predictive control (also named as finite-control-set model predictive control).

1.2.5 Special control objectives

Besides the above mentioned "framework level" *general control objectives*, the *special control objectives* considered in this thesis include:

(a) **High performance DC-link control.** This may not be a standard term fully recognized from all the research/contributions in this area. However, from the personal perspective of the author, DC-link control is one the key issues for any back-to-back power converter system. A sufficiently controlled DC-link will help to simplify a back-to-back converter system into two "independent" sub-systems, which would ease the controller design meanwhile greatly improve the system stability. Additionally, with certain solutions, it allows size and volume reduction of the bulky DC-link capacitors. Chp. 6 presents the proposed techniques, using quasi-centralized direct

model predictive control and aiming to improve the DC-link control performances of back-to-back power converter systems.

(b) **Grid side voltage sensorless control**, i.e., to reduce or eliminate the physical measurement hardware for obtaining the grid side voltages. Typically it is realized using the "virtual flux" (VF) concept, i.e., by assuming the grid side as a "virtual machine" to estimate the "virtual flux"/voltages. It brings the following benefits. (a) No or fewer voltage sensors are required. Therefore, robustness, to sensor failure or measurements inaccuracy, will be improved. (b) Cost reduction, which comes from both the sensor/circuit device reduction and the controller analog input channel reduction. (c) A virtual flux is potentially good in face of unbalanced or harmonic-polluted grid due to the "integration" relationship between the grid voltage and its flux. Chp. 7 presents a thorough discussion of such techniques invoking the VF concept.

(c) **Encoderless control of the generator**, i.e., to perform the control of the generator without using a shaft mounted encoder. The motivation is that the absence of the encoder reduces the cost and system complexity. More importantly, incorporating an encoderless controller into the system will help to make the system "backuped" in face of emergency situations, such as, encoder failure or position/speed feedback cable breakdown[6]. Chp. 8, will give a more detailed introduction.

(d) **Low voltage ride through control and hardware-in-the-loop (HiL) based electrical control unit (ECU) evaluations**, i.e., to perform a control technique for a generation unit to safely ride-through voltage dip fault situations, meanwhile to meet the local grid code (power/current profile). It allows to test the hardware controller in a real-time manner. Due to the (drastic) increase in installation of renewable energy systems, the grid code (required output profile of the generation unit during both normal and grid fault situations) has become much stricter than ever before to ensure the global stability of the power grid. Grid-tied wind turbine system has to have the so-called low-voltage-ride-through (LVRT) capability. On-site testing of such techniques (without assuring the controllers' functionality) may impose great risks on both the (expensive) system hardware and also the engineers, which makes the signal level HiL technique a desirable solution. With regard to this, an FPGA based HiL simulation technique is deeply investigated and more details are presented in Chp. 9.

1.3 Problem description, motivation and objectives

1.3.1 Problem description

This section formulates the problems of the state-of-the-art direct model predictive control (DMPC) techniques, DC-link control, generator side encoderless control, grid side voltage sensorless control, the ECU HiL verification methods, etc.

[6] In comparison with the whole system cost and the required controller development efforts to achieve encoderless control, the cost reduction by using endcoderless control techniques is less important for big wind turbine systems, however, the back-up function in face of certain potential failures is essential.

1.3.1.1 Problem formulation of the classical DMPC concept

Classical DMPC exploits the finite number of switching states of power converters to minimize a cost function and combines current/torque/flux or power control and modulation into one computational step. Conceptually it is very simple and direct. However, a cost enumeration concept is usually used for the optimization process, and only one switching vector can be selected and applied for a whole control interval. Therefore, two main problems are with such techniques, inherently.

1.3.1.1.1 Heavy computational efforts. The cost optimization problems are usually solved by a complete enumeration of all the possible solutions which directly depend on the admissible switching states and grow exponentially with the prediction horizon. This leads to extremely *heavy computational efforts*, in particular for multilevel power converters (e.g., for a three-level NPC power converter, the state prediction requires to consider *27* switching states for a single step prediction; the cost function shall also evaluate all of the *27* possibilities, to achieve the minimized cost and the optimal switching state). As a consequence, DMPC quickly becomes intractable for real-time applications in multilevel or long prediction horizon cases. Despite attempts to overcome the computational burden of these methods, the problem remains open to allow implementation of these algorithms on common embedded systems. In short,
(P_{r1}) : *the computational efficiency of DMPC schemes shall be improved to ease the real-time realization, in particular for multilevel converters.*

1.3.1.1.2 Relatively poor steady state control performances. Only one (optimal) voltage vector is applied for a whole control interval, i.e., *one-vector-per-control-interval*, which leads to big control variable ripples in comparison with the classical modulator based techniques with a similar sampling frequency, where typically three vectors (e.g., SVM based solutions) are applied for a whole control interval. Increasing the sampling frequency (i.e., controller refreshing rate) would help to reduce the ripples. However, it imposes an even higher requirement on the system hardware. Therefore,
(P_{r2}) : *how to reduce the control variable ripples (without increasing the sampling frequency) hence to enhance the steady static performances is one of the problems faced by the DMPC scheme*[7].

1.3.1.2 DC-link control issues

DC-link control represents one of the key parts of back-to-back power converter systems. A typical and most standard solution in the industry is to use a proportional-integration (PI) controller with anti-windup, which takes the tracking error of the DC-link voltage as input and generates a reference for the grid side inner controller to follow. Such solution works in general fine in steady state, but requires expertise and tedious tuning efforts to

[7]Within the same topic, other issues such as un-fixed switching frequency, wide-spread harmonics, and theoretical and systematical level weighting-factor design are also the questions still remaining open.

achieve good overall performances. The inevitable (heavy) over- and undershoot voltages appear, during the transient phases of the system operation, may potentially shorten the life span of the DC-capacitors or require big capacitors to smooth it down. Especially, when the energy/power flows from the grid to the machine side, a *non-minimum phase situation* will greatly retrain the stability region of the system [44], for which a tedious parameter tuning process or theoretical calculation is required. Therefore,
(P_{r3}) : *performance enhanced DC-link control techniques, which reduce/simplify the tuning processes, and minimize the under-and overshoot effects of the DC-link voltage, shall be further investigated.*

1.3.1.3 Fast dynamic voltage sensorless control techniques

A good voltage sensorless control scheme for grid-tied power converters will improve the system robustness against device failures and reduce the system setup complexity. As a state-of-the-art solution, the so-called "virtual flux" concept, with frequency-domain filters to extract the related component(s), achieves nice steady state accuracy. However, due to the inevitable transient time of the filter [45], relatively long delays occur at both the *initial* and the *transient* phases of the estimation, yielding inaccurate control during these phases. Therefore,
(P_{r4}) : *voltage sensorless control scheme with fast dynamics, and accurate estimation during both steady state and transient phases is still lacking.*

1.3.1.4 Efficient real-time electrical control unit (ECU) testing solution needs to be further researched

Installations of big wind turbines have been seen a huge increase in the last decades. The ECUs are required to be capable of dealing with multiple control objectives and able to deal with different situations, which makes the controller design rather complicated. The right actions of each functionality of the underlying controller is essential. In particular for the special situations (e.g., fault ride through ability of the system), a real-time verification process of the ECU through certain effective, safe and flexible testing process is greatly desired.

Hardware-in-the-Loop (HiL) testing is a viable concept [46], of which the signal level HiL is very helpful in this context to evaluate the functionality of the ECU. Fast refreshing-rate of the emulator, flexibility for adding different testing functions, high testing efficiency, and ease for constructing the testing environments are important. Field programmable gate array (FPGA) provides a feasible solution to achieve high refreshing-rate of the emulator, however,
(P_{r5}) : *highly efficient and flexible realizations of for the ECU evaluation systems using FPGA-HiL concept requires further research.*

1.3.1.5 Research on unbalanced grid control with MPC solutions

More than 75% of today's grid faults are asymmetric faults where the grid voltage is (temporarily) unbalanced[8]. A severely unbalanced grid has a heavy impact on the performance and safety of the wind turbine system and shall be considered and investigated carefully. To date, already many efforts have been spent in dealing with the control of unbalanced grids. Techniques with satisfying performances *and* simple structure rarely appeared. Therefore,
(P_{r6}) : *improved unbanned grid control methods incorporated into DMPC schemes, with effective performances but simple structure are required.*

1.3.1.6 FPGA realizations of advanced control/estimation algorithms

Many of the modern advanced control methods require high computational-power of the controller hardware. Even for the conventional control methods a fast calculation will reduce the calculation time delay, resulting in increased control performances. However, for most cases in both industrial and academic area, the real-time realization of the controller is still implemented on serially-computational targets. FPGA is of multiple benefits to deal with these issues but the controller realizations are usually quite tedious. Therefore,
(P_{r7}) : *efficient FPGA based real-time design solutions are desired for the power electronics and electrical drive areas.*

1.3.2 Motivation and objectives

The main motivations and objectives of this dissertation are to closely investigate (and trying to solve) the problems listed in Sec. 1.3.1, and a careful study of both the grid-tied two- and three-level back-to-back power converters and PMSG wind turbine systems. More specifically, the objectives of this dissertation are:

- A (thorough) mathematical modeling of both the two- and three-level NPC back-to-back power converters and PMSG wind turbine systems for theoretical analysis and controller design of the inner electrical power conversion parts;

- Realization and experimental evaluation of both the conventional and classical DMPC techniques for two- and 3L-NPC back-to-back power converter PMSG wind turbine systems, with an efficient FPGA based solution;

- Investigation of computationally efficient DMPC schemes for three-level NPC back-to-back power converter PMSG wind turbine system as (effective) alternatives for the classical "cost-enumeration" solution; also, to investigate their FPGA implementation issues;

[8] i.e. for some period of time, the sum of the grid voltage does not cancel: $e_g^a + e_g^b + e_g^c \neq 0$.

- Investigation of performance-enhanced DMPC schemes for two-level back-to-back power converter control, to conquer its big ripple problem resulting from the classical "one-vector-per-control-interval" [47] concept of the classical DMPC schemes;
- Investigation of DMPC based DC-link control methods for back-to-back power converter driven systems, aiming to achieve improved performances with reduced tuning efforts;
- Study on the virtual-flux based voltage sensorless control concept, to achieve improved dynamics and accuracy for both the initial and transient phases;
- Study on the FPGA based signal level HiL simulation concept; investigate the refreshing rate effects on the on-line (real-time) HiL simulation results and apply FPGA based HiL to the LVRT evaluation of the ECUs;
- Investigation of suitable observer based encoderless control techniques for PMSG wind turbine systems and its FPGA based realtime realization.
- A thorough application of an efficient solution to implement/realize *both* the classical *and* the newly proposed methods with a fully FPGA based control target.

1.4 Contributions

This dissertation focuses on (advanced) control techniques for both two- and three-level NPC back-to-back power converters and PMSG wind turbine systems. Within my work, *both* a two- *and* three-level NPC back-to-back power converter systems have been self-designed and constructed[9] using Infineon power switches and National Instruments FPGA based real-time systems, for experimentally verifying relevant control techniques. Through cooperation with National Instruments, a signal level hardware-in-the-loop system concept based on FPGA for testing the electrical control unit of a back-to-back power converter PMSG wind turbine system has also been constructed, to verify the refreshing rate effects of the emulator and the grid fault ride-through control methods. *More than 30 peer reviewed journal & conference papers* (See please at Appendix E) have been published, contributing in the fields of control of both the grid connected power converter (active front end) and AC-motor drives, wind energy applications, multilevel power converters and FPGA based digital control. More specifically, within my work the following have been achieved:

- A thorough modeling of both the two- and three-level NPC back-to-back power converters and PMSG wind turbine system are developed in detail. Three test-benches (two- and three-level NPC back-to-back power converter PMSG systems and an FPGA based HiL simulation system) have been designed and constructed (See Chp. 2);

[9] All the design for both the two- and three-level NPC power converters is totally based on my own efforts; Parts of the PCB and construction realizations for the three-level set-up were helped by my master students MSc. Ming Xue and He Xu, some mechanical construction was helped by Mr. Schuster. Here I want to acknowledge my gratitude to them.

- The actual control techniques (principles and digital realizations) are revisited in detail. Fully FPGA based experimental verifications of the classical/conventional control schemes including FOC-VOC with SVM, DTC-DPC with both witching table and SVM and deadbeat-like predictive (torque and power) control techniques are carried out at the self-designed test-benches (See Chp. 3 for details);

- State-of-the-art model predictive control concepts are revisited. DMPC methods including predictive torque, current and power control methods for both the two- and three-level grid-tied back-to-back power converter PMSG wind turbine systems are experimentally investigated using a fully FPGA based solution (See Chp. 4);

- Combining the deadbeat control and the DMPC concept, two computationally efficient DMPC schemes for three-level NPC back-to-back power converter control within the direct model predictive torque (DMPTC) and power control (DMPPC) frames are developed and realized using an FPGA based controller (See Sec. 5.2);

- Performance-enhanced multiple-vector model predictive control schemes, using synthesized switching vectors and the time optimal concept are proposed. Their applications for both the grid side and machine control of a back-to-back power converter PMSG wind turbine system are presented (See Sec. 5.3 and Sec. 5.4);

- A new time domain "initial bias compensation" (IBC) based voltage sensorless control method for grid-tied back-to-back power converter with fast dynamics (*one sampling interval*) is proposed and experimentally verified (See Chp. 7);

- By using a so-called "dynamic reference generation" concept, quasi-centralized DMPC schemes for both back-to-back power converter with RL load and back-to-back PMSG wind turbine system are proposed and experimentally evaluated using FPGA (See Chp. 6);

- A PMSG wind turbine system using FPGA based signal level HiL concept is constructed and the refreshing rate effects are investigated and verified through (*online*) real-time simulation data. A low voltage ride through control method is incorporated into the direct model predictive control framework and verified through the FPGA based HiL concept during grid voltage dips (See Chp. 9);

- Encoderless control methods for PMSG(M) are reviewed and observer based solutions (including both the *extended Kalman filter* and *sliding mode observer* based methods) and their combination to deadbeat control frame for PMS(M)G are investigated and verified. (See Chp. 8);

- An efficient FPGA controller realization method, invoking the single-cycle-timed-loop (SCTL) technique, has been extensively investigated and comprehensively applied in the power electronics and electrical drive areas, both for machine side and grid side control. All the experimental evaluations of the relevant control schemes presented in my dissertation are implemented on an NI-FPGA based platform, which may serve as a viable alternative for fast prototyping in industrial or academic domain.

Chapter 2

System modeling and physical system description

This chapter summarizes the symbols and abbreviations used in the following chapters. Following, the mathematical basics for the system modeling are revisited, which includes coordinate transformations, and continuous and discrete linear time-invariant system descriptions (see Sec. 2.1). Then mathematical models for both the two- and three-level back-to-back power converters (in Sec. 2.2), RL load (in Sec. 2.3) and PMSG wind turbine system (in Sec. 2.4) are explicitly developed. Afterward, the lab-constructed two- and three-level NPC back-to-back power converter test-benches for experimentally verifying the control algorithms discussed in the following chapters are depicted in Sec. 2.5.

Nomenclature

Table 2.1 lists all the nomenclatures used in this chapter.

$\mathbb{N}, \mathbb{R}, \mathbb{C}$	natural, real, and complex numbers
$\vec{x} \in \mathbb{R}^n, n \in \mathbb{N}, \vec{x}^\top, \vec{x}^\dagger$	column vector, its transpose and conjugate
$\mathrm{diag}\{a_1, \cdots, a_n\}$	diagonal matrix in $\mathbb{R}^{n\times n}$ with entries $a_1, \cdots, a_n \in \mathbb{R}$
$\mathbf{I}_n \in \mathbb{R}^{n\times n} := \mathrm{diag}\{1, \cdots, 1\}$	identity matrix
$\mathrm{C}, \mathrm{L}, \mathrm{R}$	capacitance [F], inductance [H], resistance [Ω]
$\mathrm{MSC}, \mathrm{GSC}$	machine-side, grid-side converter.
$\omega, \phi_{\mathrm{e,g}}$	frequency [rad/s], position of voltage or flux vectors
t, T_s, k	time [s], sampling time [s], sampling instant [1]
$\vec{x}^{\mathrm{dq}}, \vec{x}^{\alpha\beta}, \vec{x}^{\mathrm{abc}}$	vectors in dq-, $\alpha\beta$-, abc-reference frame
x_m, $x_{\mathrm{g/n}}$	machine-side, grid/(net)-side quantities
$\Re\{\vec{x}\}, \Im\{\vec{x}\}$	real and imaginary part of $\vec{x}$
$\vec{u}, \vec{G}$	switching state, gate signal vector
$\vec{S}$, P, Q	Appar. [VA], active [W], react. power [var]

Table 2.1: Symbols and abbreviations for this chapter.

2.1 Mathematical basics for system modeling

2.1.1 Three phase system coordinate transformation

Fig. 2.1 shows three coordinate systems, where abc (in red), $\alpha\beta$ (in blue) and dq (in green) are the *natural three-phase*, *stationary two-phase* and *rotational two-phase* coordinates, respectively. In the following of this dissertation, I will name these three coordinates as *abc*, $\alpha\beta$ and *dq* frames, respectively.

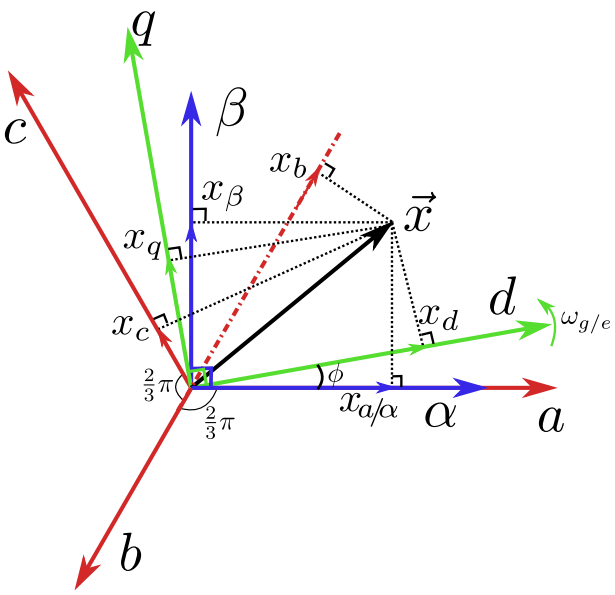

Fig. 2.1: Coordinate transformations.

As is illustrated in Fig. 2.1, aligning the α-axis of the $\alpha\beta$ frame with a-axis of the *abc* frame, and naming the angle between d-axis of the *dq* frame and α/a-axis as ϕ, all quantities $\vec{x}^{\alpha\beta}$ in the $\alpha\beta$ coordinate, and quantities $\vec{x}^{dq}$ in the *dq* coordinate can be derived by the corresponding quantities $\vec{x}^{abc}$ in the *abc* coordinate invoking (power invariable)[1] Clarke- and Park-Transformation, i.e. for angle $\phi \in \mathbb{R}\,[\text{rad}]$

$$\left.\begin{aligned} \vec{x}^{\alpha\beta} &= \underbrace{\sqrt{\tfrac{2}{3}}\begin{bmatrix} 1 & -\frac{1}{2} & -\frac{1}{2} \\ 0 & \frac{\sqrt{3}}{2} & -\frac{\sqrt{3}}{2} \end{bmatrix}}_{=:\mathbf{T}_{\mathrm{C}}\ \text{(Clarke transformation)}} \vec{x}^{\mathrm{abc}} \text{ and} \\ \vec{x}^{\mathrm{dq}} &= \underbrace{\begin{bmatrix} \cos(\phi) & \sin(\phi) \\ -\sin(\phi) & \cos(\phi) \end{bmatrix}}_{=:\mathbf{T}_{\mathrm{P}}(\phi)\ \text{(Park transformation)}} \vec{x}^{\alpha\beta}. \end{aligned}\right\} \tag{2.1}$$

[1] Infinite types of transformations can be built up by using different coefficients. However, typically two formats are usually used, namely, *magnitude-invariant* (i.e., before and after transformation, the vector magnitudes are kept as a constant as is shown in Fig. 2.1) and *power invariant transformations* (i.e., the "amount of power" before and after transformation remains constant). *Power-invariant transformation* requires no further coefficient in front of the power and torque calculations. Therefore, it is used for all the relevant processes within this dissertation.

2.1.2 Linear time-invariant (LTI) state space model

The continuous state space representation of a linear time-invariant system (LTI) can be written in form of

$$\frac{d}{dt}\vec{x}(t) = \mathbf{A}\vec{x}(t) + \mathbf{B}\vec{u}(t), \tag{2.2a}$$

$$\vec{y}(t) = \mathbf{C}\vec{x}(t) + \mathbf{D}\vec{u}(t), \tag{2.2b}$$

where $\mathbf{A, B, C}$ and $\mathbf{D}$ are the system (state), control (input), output and the feed-through matrices with proper dimensions, respectively. Equation (2.2a) is referred to as the *system function* which describes the system dynamics, and (2.2b) is the *output function*, mapping the system states and inputs to the system outputs.

The solution for this continuous linear Ordinary Differential Equation (ODE) of the *system function* with initial condition $\vec{x}_0 \triangleq \vec{x}(t_0)$ is

$$\vec{x}(t) = e^{\mathbf{A}(t-t_0)}\vec{x}_0 + \int_{t0}^{t} e^{\mathbf{A}(t-\tau)}\mathbf{B}\vec{u}(\tau)d\tau \tag{2.3}$$

where $e^{\mathbf{A}(t-t_0)} \triangleq \sum_{n=0}^{\infty} \frac{(\mathbf{A}(t-t_0))^n}{n!}$.

2.1.3 Discretization of LTI

The digital implementation of a model based control scheme requires the discrete format of a system model. Assuming $\vec{u}_{[\mathrm{k}]}$ keeps as a constant during the sampling/control interval $T_\mathrm{s}(<< 1[\mathrm{s}])$ of the digital system; the actual sampling interval is $k = \frac{t}{T_\mathrm{s}}$, then, one obtains $\forall t \in [t, t+T_\mathrm{s})$ the system state at $k+1$ as

$$\vec{x}_{[\mathrm{k+1}]} = e^{\mathbf{A}T_\mathrm{s}}\vec{x}_{[\mathrm{k}]} + \int_{t}^{t+T_\mathrm{s}} e^{\mathbf{A}\cdot(t+T_\mathrm{s}-\tau)}\mathbf{B}d\tau\vec{u}_{[\mathrm{k}]} = \underbrace{e^{\mathbf{A}\cdot T_\mathrm{s}}}_{\triangleq\mathbf{A_d}}\vec{x}_{[\mathrm{k}]} + \underbrace{\int_{0}^{T_\mathrm{s}} e^{\mathbf{A}\cdot(T_\mathrm{s}-\tau')}\mathbf{B}d\tau'}_{\triangleq\mathbf{B_d}}\vec{u}_{[\mathrm{k}]}$$

$$= \mathbf{A_d}\vec{x}_{[\mathrm{k}]} + \mathbf{B_d}\vec{u}_{[\mathrm{k}]}. \tag{2.4}$$

The discretization format of equations (2.2a) and (2.2b) can be put as

$$\vec{x}_{[\mathrm{k+1}]} = \mathbf{A_d}\vec{x}_{[\mathrm{k}]} + \mathbf{B_d}\vec{u}_{[\mathrm{k}]} \quad \text{and} \tag{2.5a}$$

$$\vec{y}_{[\mathrm{k}]} = \mathbf{C_d}\vec{x}_{[\mathrm{k}]} + \mathbf{D_d}\vec{u}_{[\mathrm{k}]}, \tag{2.5b}$$

respectively.

2.1.4 Explicit discretization and approximations of LTI

Highly depending on the sampling/control interval of the implementation process, there exists different ways to obtain an explicit discretization which (closely) approximates its

continuous format, among which, the *Euler-forward* discretization of

$$\frac{\mathrm{d}\vec{x}(t)}{\mathrm{d}t} \approx \frac{\vec{x}_{[\mathrm{k}+1]} - \vec{x}_{[\mathrm{k}]}}{T_\mathrm{s}} \tag{2.6}$$

is usually used for a small enough sampling interval ($T_\mathrm{s} \leq 100\mu\mathrm{s}$)[2] due to its simplicity and accurate approximations[3].

Applying (2.6) to equations (2.2a) and (2.2b) one obtains $\mathbf{A_d} = \mathbf{I} - \mathbf{A}T_\mathrm{s}$, $\mathbf{B_d} = \mathbf{B}T_\mathrm{s}$, $\mathbf{C_d} = \mathbf{C}$, and $\mathbf{D_d} = \mathbf{D}$, where $\mathbf{I}$ is the identity matrix with the dimension of $\mathbf{A_d}$.

2.2 Two- and three-level back-to-back power converter system modeling

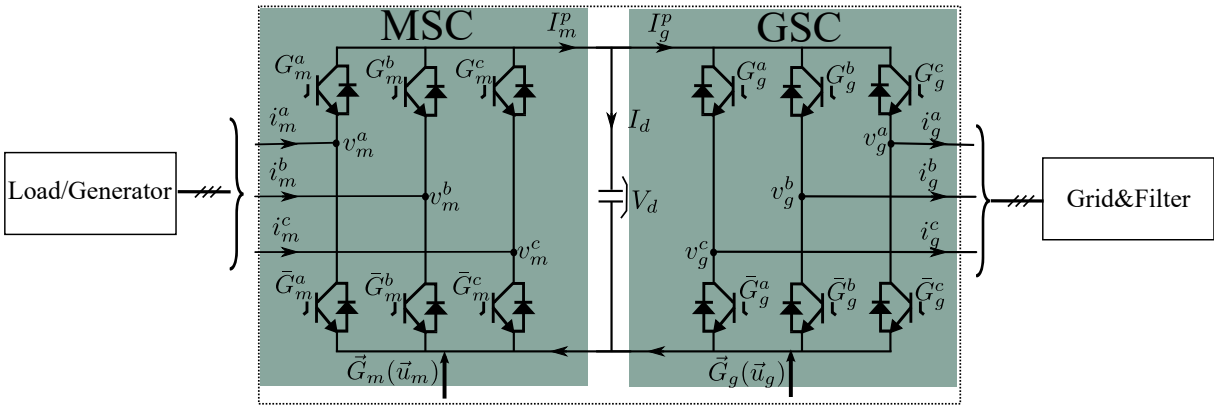

Fig. 2.2: Two level voltage source back-to-back power converter.

2.2.1 Two-level back-to-back power converter

Fig. 2.2 depicts the simplified circuit of a two level voltage source back-to-back power converter. It is not difficult to find, the gate signal of G_y^x has to be complementary[4] to $\bar{G}_\mathrm{y}^\mathrm{x}$, i.e., when $G_\mathrm{y}^\mathrm{x} = 1$ (switched on), $\bar{G}_\mathrm{y}^\mathrm{x}$ must be switched off ($= 0$), since no shoot-through operation is allowed for such a voltage source power converter, where, $\mathrm{x} \in \{\mathrm{a}, \mathrm{b}, \mathrm{c}\}$, representing the phases, and, $\mathrm{y} \in \{\mathrm{m}, \mathrm{g}\}$, indicating the load/machine (m) side or grid (g) side. In the following chapters, the switching state $\mathrm{u}_\mathrm{y}^\mathrm{x}$ is defined for the two-level voltage source power converter, as

$$\vec{u}_\mathrm{y}^\mathrm{x} := \mathcal{G}(G_\mathrm{y}^\mathrm{x}) = \begin{cases} 1\,(P) \text{ if} : G_\mathrm{y}^\mathrm{x} = 1 \wedge \bar{G}_\mathrm{y}^\mathrm{x} = 0, \\ 0\,(N) \text{ if} : G_\mathrm{y}^\mathrm{x} = 0 \wedge \bar{G}_\mathrm{y}^\mathrm{x} = 1. \end{cases} \tag{2.7}$$

[2] If longer time-interval is used, higher-order and more sophisticated methods (e.g., Runge-Kutta, higher order Taylor methods, etc.), shall be considered (See "Numerical Methods for Ordinary Differential Equations", 2nd ed. Wiley, J. C. Butcher, June 2008).

[3] Exact methods using Laplace transformations are too complex while approximations with high order power series do not lead to significant performance improvement when using predictive control solutions.

[4] Here the tail-time of the IGBT is not considered.

The switching vector of $\vec{u}_{\mathrm{y}}^{\mathrm{abc}} := \left(\mathrm{u}_{\mathrm{y}}^{\mathrm{a}}, \mathrm{u}_{\mathrm{y}}^{\mathrm{b}}, \mathrm{u}_{\mathrm{y}}^{\mathrm{c}}\right)^{\top}$ is therefore can only be chosen from $\mathcal{U}_8 := \{\mathrm{NNN}, \mathrm{NNP}, \ldots, \mathrm{PPN}, \mathrm{PPP}\}$ of 8 admissible switching states. The terminal voltage (to the neutral (n) of the load/source) vector $\vec{v}_{\mathrm{y}}^{\mathrm{abc}}$ can be modeled as a function of the DC-link voltage V_{d} and the corresponding switching vector $\vec{u}_{\mathrm{y}}^{\mathrm{abc}}$. For an ideal switching behavior of the power switches in Fig. 2.2, the following holds[5]

$$\vec{v}_{\mathrm{y}}^{\mathrm{abc}}(\mathrm{t}) = \begin{bmatrix} v_{\mathrm{y}}^{\mathrm{an}}(t) \\ v_{\mathrm{y}}^{\mathrm{bn}}(t) \\ v_{\mathrm{y}}^{\mathrm{cn}}(t) \end{bmatrix} = \underbrace{\frac{V_{\mathrm{d}}}{3}\begin{bmatrix} 2 & -1 & -1 \\ -1 & 2 & -1 \\ -1 & -1 & 2 \end{bmatrix}}_{=:\mathbf{T}_{\mathrm{SW}}} \vec{u}_{\mathrm{y}}^{\mathrm{abc}}(\mathrm{t}) \tag{2.8}$$

For simplicity, in the following of this dissertation, $v_{\mathrm{y}}^{\mathrm{xn}}$ is written as $v_{\mathrm{y}}^{\mathrm{x}}$. The line-to-line voltages are therefore[6]

$$\vec{v}_{\mathrm{y}}^{\mathrm{ltl}}(\vec{u}_{\mathrm{y}}) := \begin{bmatrix} v_{\mathrm{y}}^{\mathrm{a}} - v_{\mathrm{y}}^{\mathrm{b}} \\ v_{\mathrm{y}}^{\mathrm{b}} - v_{\mathrm{y}}^{\mathrm{c}} \\ v_{\mathrm{y}}^{\mathrm{c}} - v_{\mathrm{y}}^{\mathrm{a}} \end{bmatrix} = V_{\mathrm{d}} \begin{bmatrix} 1 & -1 & 0 \\ 0 & 1 & -1 \\ -1 & 0 & 1 \end{bmatrix} \vec{u}_{\mathrm{y}}^{\mathrm{abc}}. \tag{2.9}$$

The converter terminal voltage vectors in $\alpha\beta$ and dq frames can be computed by

$$\left.\begin{array}{rcl} \vec{v}_{\mathrm{y}}^{\alpha\beta}(\vec{u}_{\mathrm{y}}) & = & \mathbf{T}_{\mathrm{C}}\, \vec{v}_{\mathrm{y}}^{\mathrm{abc}}(\vec{u}_{\mathrm{y}}), \\ \vec{v}_{\mathrm{y}}^{\mathrm{dq}}(\vec{u}_{\mathrm{y}}) & = & \mathbf{T}_{\mathrm{P}}(\phi)\vec{v}_{\mathrm{y}}^{\alpha\beta}(\vec{u}_{\mathrm{y}}), \end{array}\right\} \tag{2.10}$$

or

$$\left.\begin{array}{rcl} \vec{v}_{\mathrm{y}}^{\alpha\beta}(\vec{u}_{\mathrm{y}}) & = & \sqrt{\frac{2}{3}}\begin{bmatrix} \frac{1}{2} & 0 & -\frac{1}{2} \\ 0 & \frac{\sqrt{3}}{3} & 0 \end{bmatrix} \vec{v}_{x}^{\mathrm{ltl}}(\vec{u}_{\mathrm{y}}), \\ \vec{v}_{\mathrm{y}}^{\mathrm{dq}}(\vec{u}_{\mathrm{y}}) & = & \mathbf{T}_{\mathrm{P}}(\phi)\vec{v}_{\mathrm{y}}^{\alpha\beta}(\vec{u}_{\mathrm{y}}), \end{array}\right\} \tag{2.11}$$

where ϕ is *either* the electrical angle of the rotor flux, i.e. $\phi_{\mathrm{e}} = \int \omega_{\mathrm{e}}(\tau)\,\mathrm{d}\tau + \phi_{\mathrm{e}}^{0}$, *or* the electrical angle of the grid voltage vector, i.e. $\phi_{\mathrm{g}} = \int \omega_{\mathrm{g}}(\tau)\,\mathrm{d}\tau + \phi_{\mathrm{g}}^{0}$; $\phi_{\mathrm{e}}^{0}, \phi_{\mathrm{g}}^{0}$ are the initial positions of the rotor flux and grid voltage vector, respectively.

2.2.1.1 DC-link of two-level back-to-back power converter

Considering the DC-link current flow of the two level back-to-back converter (see Fig. 2.2), the DC-link dynamics can be modeled as follows

$$\frac{\mathrm{d}V_{\mathrm{d}}(t)}{\mathrm{d}t} = \frac{1}{C} I_{\mathrm{d}}(t) = \frac{1}{C}\left[I_{\mathrm{m}}^{\mathrm{p}}(t) - I_{\mathrm{g}}^{\mathrm{p}}(t)\right], \tag{2.12}$$

where $I_{\mathrm{g}}^{\mathrm{p}}(t) = \vec{i}_{\mathrm{g}}^{\mathrm{abc}}(t) \cdot \vec{u}_{\mathrm{g}}^{\mathrm{abc}\top}(t)$ and $I_{\mathrm{m}}^{\mathrm{p}}(t) = \vec{i}_{\mathrm{m}}^{\mathrm{abc}}(t) \cdot \vec{u}_{\mathrm{m}}^{\mathrm{abc}\top}(t)$ are DC-link components of the grid and machine/load side currents, respectively. Applying the forward Euler approximation yields the discrete voltage equation, as

$$V_{\mathrm{d[k+1]}} = V_{\mathrm{d[k]}} + \tfrac{T_{\mathrm{s}}}{C}\left(I_{\mathrm{m[k]}}^{\mathrm{p}} - I_{\mathrm{g[k]}}^{\mathrm{p}}\right) = V_{\mathrm{d[k]}} + \tfrac{T_{\mathrm{s}}}{C}\left(\vec{i}_{\mathrm{m[k]}}^{\mathrm{abc}} \cdot \vec{u}_{\mathrm{m[k]}}^{\mathrm{abc}\top} - \vec{i}_{\mathrm{g[k]}}^{\mathrm{abc}} \cdot \vec{u}_{\mathrm{g[k]}}^{\mathrm{abc}\top}\right). \tag{2.13}$$

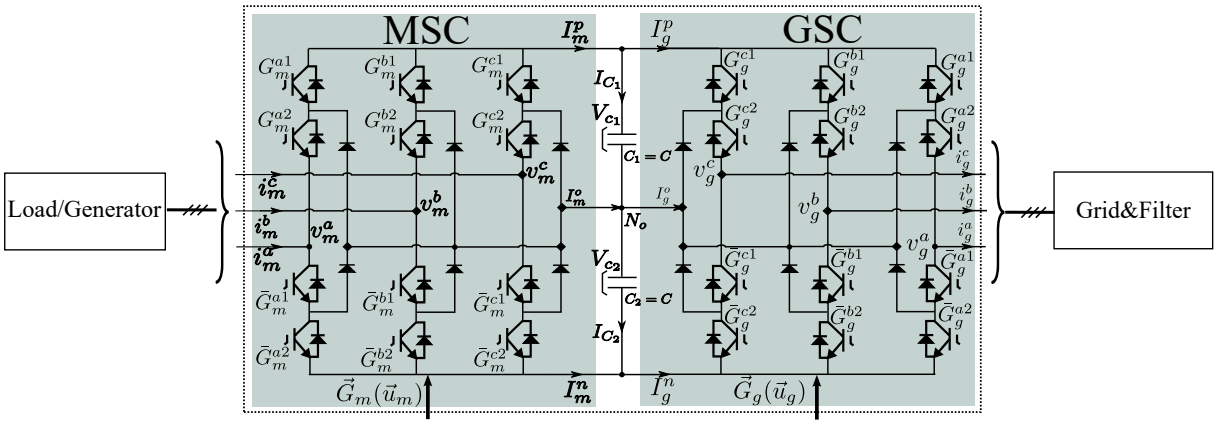

Fig. 2.3: Three level voltage source back-to-back power converter.

2.2.2 Three-level NPC back-to-back power converter

Considering the 3L-NPC back-to-back converter depicted in Fig. 2.3, the gate signal of the upper-most IGBT in the first leg (phase a) of the machine side converter is denoted by $G_{\mathrm{m}}^{\mathrm{a1}}$. In general, for $y \in \{\mathrm{m}, \mathrm{g}\}$, $x \in \{\mathrm{a}, \mathrm{b}, \mathrm{c}\}$ and $i \in \{1, 2\}$, the gate signal for the upper IGBTs is introduced as $G_{\mathrm{y}}^{\mathrm{xi}}$ and, for the lower IGBTs, the negated gate signal as $\bar{G}_{\mathrm{y}}^{\mathrm{xi}}$ (complementary to $G_{\mathrm{y}}^{\mathrm{xi}}$, see Fig. 2.3). In the following chapters, the switching state $\mathrm{u}_{\mathrm{y}}^{\mathrm{x}}$ for such three-level NPC power converter is defined in the following relationship with the gate signal, G_y^x

$$u_{\mathrm{y}}^{\mathrm{x}} := \mathcal{G}(G_{\mathrm{y}}^{\mathrm{x}}) = \begin{cases} P & \text{if}: G_{\mathrm{y}}^{\mathrm{x1}} = 1 \wedge G_{\mathrm{y}}^{\mathrm{x2}} = 1 \\ 0 & \text{if}: G_{\mathrm{y}}^{\mathrm{x1}} = 0 \wedge G_{\mathrm{y}}^{\mathrm{x2}} = 1 \\ N & \text{if}: G_{\mathrm{y}}^{\mathrm{x1}} = 0 \wedge G_{\mathrm{y}}^{\mathrm{x2}} = 0 \end{cases}. \tag{2.14}$$

The switching state vector has therefore the form of $\vec{u}_{\mathrm{y}} = (u_{\mathrm{y}}^{\mathrm{a}}, u_{\mathrm{y}}^{\mathrm{b}}, u_{\mathrm{y}}^{\mathrm{c}})^{\top} \in \mathcal{U}_{27} := \{\mathrm{NNN}, \mathrm{NN0}, \ldots, \mathrm{PP0}, \mathrm{PPP}\}$ of 27 admissible switching states. Hence, naming the DC-link capacitor voltages as voltages V_{c_1} and V_{c_2}, respectively (see Fig. 2.3), the phase voltages of the converter can be obtained as

$$\vec{v}_{\mathrm{y}}^{\mathrm{abc}} = \begin{bmatrix} v_{\mathrm{y}}^{\mathrm{a}} \\ v_{\mathrm{y}}^{\mathrm{b}} \\ v_{\mathrm{y}}^{\mathrm{c}} \end{bmatrix} = \frac{(V_{c1} + V_{c2})}{6} \begin{bmatrix} 2 & -1 & -1 \\ -1 & 2 & -1 \\ -1 & -1 & 2 \end{bmatrix} \vec{u}_{\mathrm{y}} + \frac{(V_{c1} - V_{c2})}{6} \begin{bmatrix} 2 & -1 & -1 \\ -1 & 2 & -1 \\ -1 & -1 & 2 \end{bmatrix} |\vec{u}_{\mathrm{y}}|. \tag{2.15}$$

where $|\vec{u}_{\mathrm{y}}| = (|u_{\mathrm{y}}^{\mathrm{a}}|, |u_{\mathrm{y}}^{\mathrm{b}}|, |u_{\mathrm{y}}^{\mathrm{c}}|)^{\top}$. The line-to-line voltages $\vec{v}_{\mathrm{y}}^{\mathrm{ltl}}$ can be calculated by[7]

$$\vec{v}_{\mathrm{y}}^{\mathrm{ltl}} := \begin{bmatrix} v_{\mathrm{y}}^{\mathrm{a}} - v_{\mathrm{y}}^{\mathrm{b}} \\ v_{\mathrm{y}}^{\mathrm{b}} - v_{\mathrm{y}}^{\mathrm{c}} \\ v_{\mathrm{y}}^{\mathrm{c}} - v_{\mathrm{y}}^{\mathrm{a}} \end{bmatrix} = V_{c1} \begin{bmatrix} 1 & -1 & 0 \\ 0 & 1 & -1 \\ -1 & 0 & 1 \end{bmatrix} \frac{|\vec{u}_{\mathrm{y}}| + \vec{u}_{\mathrm{y}}}{2} - V_{c2} \begin{bmatrix} 1 & -1 & 0 \\ 0 & 1 & -1 \\ -1 & 0 & 1 \end{bmatrix} \frac{|\vec{u}_{\mathrm{y}}| - \vec{u}_{\mathrm{y}}}{2} \tag{2.16}$$

[5] The detailed development of the switching matrix T_{sw} can be found at the Appendix B.1.
[6] Line-to-line voltages are useful in particular where phase voltages are not easy to measure.
[7] The detailed development of the switching matrix can be found at the Appendix B.1.

where $|\vec{u}_{\mathrm{y}}| := \left(|u_{\mathrm{y}}^{\mathrm{a}}|, |u_{\mathrm{y}}^{\mathrm{b}}|, |u_{\mathrm{y}}^{\mathrm{c}}|\right)^{\top}$ is the vector of the absolute values of the elements of $\vec{u}_{\mathrm{y}}$. In the analogy, the converter terminal voltage vectors in $\alpha\beta$ and dq frames can be computed by equations (2.10) or (2.11).

2.2.2.1 DC-link of three-level NPC back-to-back power converter

For a three-level NPC back-to-back power converter, the DC-link modeling includes both the DC-link charging/discharging equation and also the neutral point voltage equation.

2.2.2.1.1 DC-link (charging/discharging) equation: In analogy to the two level back-to-back power converter, the DC-link voltage equation, when considering the current flow of the converter (see Fig. 2.3), can be modeled as follows

$$\frac{\mathrm{d}V_{\mathrm{d}}(t)}{\mathrm{d}t} = \frac{1}{C} I_{\mathrm{d}}(t) = \frac{1}{C}\big[I_{\mathrm{g}}(t) - I_{\mathrm{m}}(t)\big], \tag{2.17}$$

where $I_{\mathrm{g}}(t) = \vec{i}_{\mathrm{g}}^{\,\mathrm{abc}}(t) \cdot \vec{u}_{\mathrm{g}}^{\,\mathrm{abc}}(t)$ and $I_{\mathrm{m}}(t) = \vec{i}_{\mathrm{m}}^{\,\mathrm{abc}}(t) \cdot \vec{u}_{\mathrm{m}}^{\,\mathrm{abc}}(t)$ are DC-link components of the net (grid) and load side currents, respectively. Applying the forward Euler approximation yields the discrete voltage equation

$$V_{\mathrm{d[k+1]}} = V_{\mathrm{d[k]}} + \tfrac{T_{\mathrm{s}}}{C}\Big(I_{\mathrm{g[k]}} - I_{\mathrm{m[k]}}\Big), \tag{2.18}$$

where $I_{\mathrm{g[k]}} = \vec{i}_{\mathrm{g[k]}}^{\,\mathrm{abc}} \cdot \vec{u}_{\mathrm{g}}^{\,\mathrm{abc}\top}$ and $I_{\mathrm{m[k]}} = \vec{i}_{\mathrm{m[k]}}^{\,\mathrm{abc}} \cdot \vec{u}_{\mathrm{m}}^{\,\mathrm{abc}\top}$.

2.2.2.1.2 DC-link capacitor voltage difference equation: To achieve voltage balancing, the difference voltage $V_o(t) := V_{\mathrm{c_1}}(t) - V_{\mathrm{c_2}}(t)$ shall be zero and it can be controlled through either the grid side or the machine side power converter (or through both sides). Known from Fig. 2.3, V_o depends on the charging state of the two DC-link capacitors C_1 and C_2 ($C_1 = C_2 = C$) and will only change when currents $I_{\mathrm{m,g}}^{o}$ are drawn from it (see Fig. 2.3), i.e., when $\vec{u}_{\mathrm{y}}$ contain "zero" elements (see Eq.(2.14)). For a given phase current vector $\vec{i}_{\mathrm{y}}^{\,\mathrm{abc}} := [i_{\mathrm{y}}^{\mathrm{a}}, i_{\mathrm{y}}^{\mathrm{b}}, i_{\mathrm{y}}^{\mathrm{c}}]^{\top}$, the positive and negative currents at the DC-link part can be computed as

$$I_{\mathrm{y}}^{\mathrm{p}} = \frac{1}{2}(|\vec{u}_{\mathrm{y}}| + \vec{u}_{\mathrm{y}})\,\vec{i}_{\mathrm{y}}^{\,\mathrm{abc}} = \frac{1}{2}\Big((|u_{\mathrm{y}}^{\mathrm{a}}| + u_{\mathrm{y}}^{\mathrm{a}}), (|u_{\mathrm{y}}^{\mathrm{b}}| + u_{\mathrm{y}}^{\mathrm{b}}), (|u_{\mathrm{y}}^{\mathrm{c}}| + u_{\mathrm{y}}^{\mathrm{c}})\Big) \cdot \vec{i}_{\mathrm{y}}^{\,\mathrm{abc}\top} \tag{2.19a}$$

$$I_{\mathrm{y}}^{\mathrm{n}} = \frac{1}{2}(|\vec{u}_{\mathrm{y}}| - \vec{u}_{\mathrm{y}})\,\vec{i}_{\mathrm{y}}^{\,\mathrm{abc}} = \frac{1}{2}\Big((|u_{\mathrm{y}}^{\mathrm{a}}| - u_{\mathrm{y}}^{\mathrm{a}}), (|u_{\mathrm{y}}^{\mathrm{b}}| - u_{\mathrm{y}}^{\mathrm{b}}), (|u_{\mathrm{y}}^{\mathrm{c}}| - u_{\mathrm{y}}^{\mathrm{c}})\Big) \cdot \vec{i}_{\mathrm{y}}^{\,\mathrm{abc}\top} \tag{2.19b}$$

Therefore, the dynamics of V_o are given by

$$\frac{\mathrm{d}V_o}{\mathrm{d}t} = \frac{\mathrm{d}V_{c_1}}{\mathrm{d}t} - \frac{\mathrm{d}V_{c_2}}{\mathrm{d}t} = \frac{1}{C}\Big\{(I_{\mathrm{m}}^{\mathrm{p}} + I_{\mathrm{m}}^{\mathrm{n}}) - (I_{\mathrm{g}}^{\mathrm{p}} + I_{\mathrm{g}}^{\mathrm{n}})\Big\} = \frac{1}{C}\left(|\vec{u}_{\mathrm{m}}^{\,\mathrm{abc}}|\,\vec{i}_{\mathrm{m}}^{\,\mathrm{abc}\top} - |\vec{u}_{\mathrm{g}}^{\,\mathrm{abc}}|\,\vec{i}_{\mathrm{g}}^{\,\mathrm{abc}\top}\right) \tag{2.20}$$

Applying the forward Euler approximation yields the discrete equation for the DC-link capacity voltage difference

$$V_{\mathrm{o[k+1]}} = V_{\mathrm{o[k]}} + \frac{T_{\mathrm{s}}}{C}\left(|\vec{u}_{\mathrm{m[k]}}^{\,\mathrm{abc}}|\,\vec{i}_{\mathrm{m[k]}}^{\,\mathrm{abc}\top} - |\vec{u}_{\mathrm{g[k]}}^{\,\mathrm{abc}}|\,\vec{i}_{\mathrm{g[k]}}^{\,\mathrm{abc}\top}\right). \tag{2.21}$$

2.3 RL load dynamics

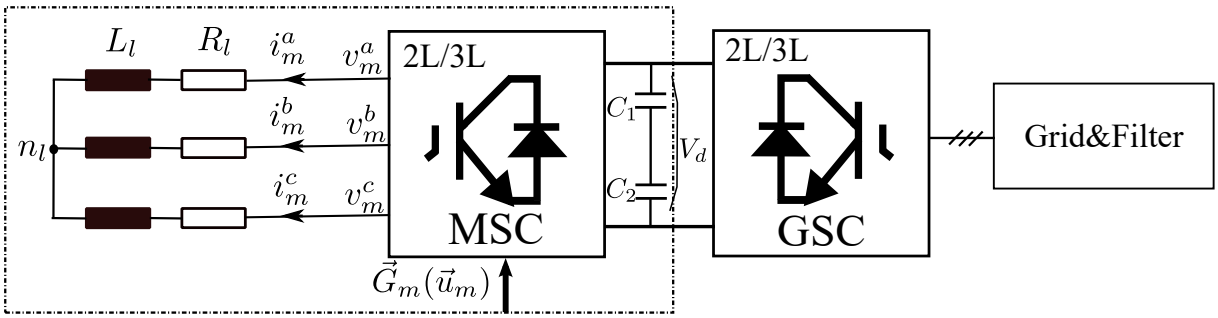

Fig. 2.4: Simplified circuit of a back-to-back power converter with RL-load.

As is shown in Fig. 2.4, the current dynamics of such a system (the part in the dashed brace) in $\alpha\beta$ frame can be modeled as (see e.g. [42]).

$$\frac{\mathrm{d}\vec{i}_{\mathrm{m}}^{\alpha\beta}(t)}{\mathrm{d}t} = \frac{1}{L_{\mathrm{l}}}\vec{v}_{\mathrm{m}}^{\alpha\beta}(t) - \frac{R_{\mathrm{l}}}{L_{\mathrm{l}}}\vec{i}_{\mathrm{m}}^{\alpha\beta}(t),\ \vec{i}_{\mathrm{m}}(0) = \vec{i}_{\mathrm{m}}^{0} \in \mathbb{R}^2 \tag{2.22}$$

where $\vec{i}_{\mathrm{m}}^{\alpha\beta} = (i_{\mathrm{m}}^{\alpha},\, i_{\mathrm{m}}^{\beta})^{\top}$ and $\vec{v}_{\mathrm{m}}^{\alpha\beta} = (v_{\mathrm{m}}^{\alpha},\, v_{\mathrm{m}}^{\beta})^{\top}$ are RL-load side current and MSC voltage vector, respectively; $\vec{i}_{\mathrm{m}}^{0}$ is the initial current vector, $\vec{v}_{\mathrm{m}}^{\alpha\beta}$ can be obtained through Equation (2.10), or (2.11). All quantities in the $\alpha\beta$ reference frame can be obtained from the corresponding quantities in the *abc* reference frame as follows

$$\vec{x}^{\,\alpha\beta}(t) = \mathbf{T}_{\mathrm{C}} \cdot \vec{x}^{\,\mathrm{abc}}(t),\ x \in \{i, v\},\ \mathbf{T}_{\mathrm{C}} \text{ is as in Eq. (2.1).} \tag{2.23}$$

Transferring (2.22) into the discrete format yields

$$\vec{i}_{\mathrm{l[k+1]}}^{\alpha\beta} = \big(1 - \tfrac{T_{\mathrm{s}}R_{\mathrm{l}}}{L_{\mathrm{l}}}\big)\vec{i}_{\mathrm{l[k]}}^{\alpha\beta} + \tfrac{T_{\mathrm{s}}}{L_{\mathrm{l}}}\vec{v}_{\mathrm{g[k]}}^{\alpha\beta}. \tag{2.24}$$

2.4 PMSG wind turbine system with back-to-back power converter

In this section the PMSG wind turbine system (as is shown in Fig. 2.5) with (both 2L and 3L) back-to-back power converter is modeled. As can be seen from Fig. 2.5, except the back-to-back power converter (which has already been described in Sec. 2.2.1 and Sec. 2.2.2), there are still three parts to describe, namely, the aerodynamic and turbine model, PMSG and the dynamics of grid side and filter.

2.4.1 Aerodynamics and turbine model

The mechanical power extracted by the wind turbine from the passing wind is given by (see [17, 48])

$$\forall\, t \geq 0, P_t(t) = \frac{1}{2}\rho A\, v_{\mathrm{w}}^3(t)\, C_p(t). \tag{2.25}$$

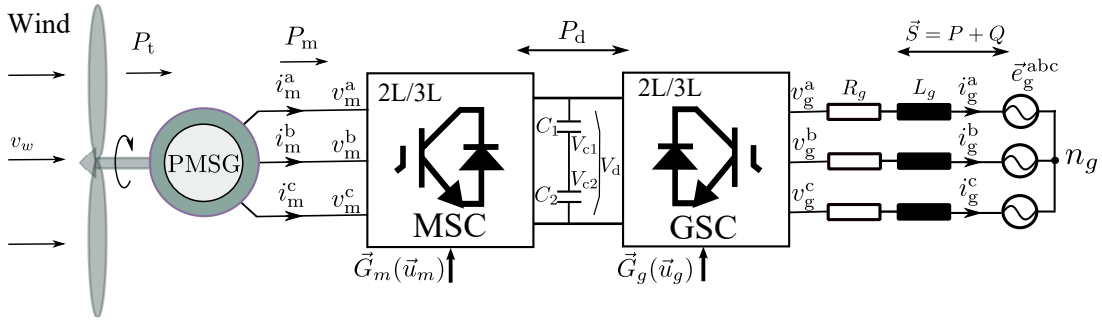

Fig. 2.5: Simplified structure of two- and three-level back-to-back power converter PMSG wind turbine system.

In discrete format (taking $\lambda = \frac{R_t \omega_m}{v_w}$ into consideration), the mechanical power extracted

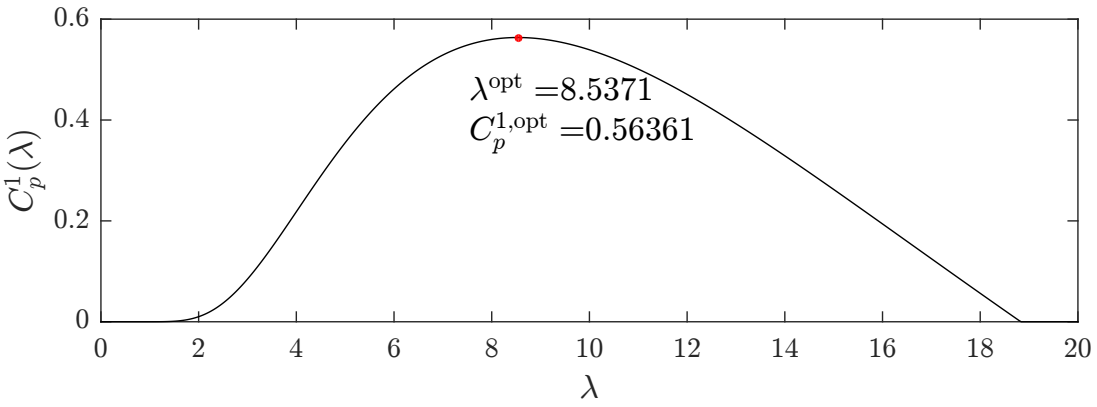

Fig. 2.6: Relationship of the power coefficient to tip ratio.

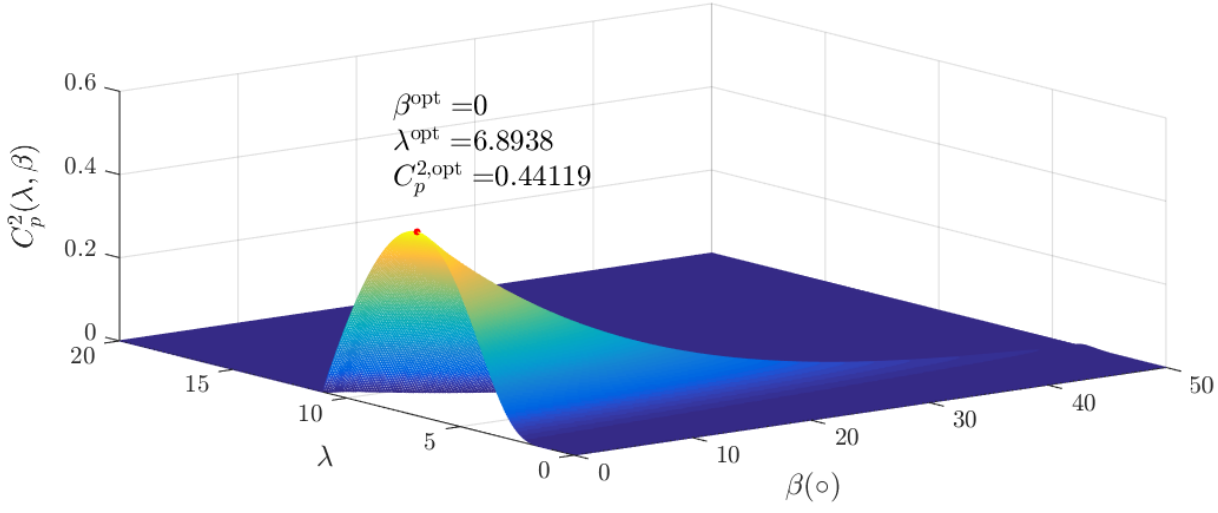

Fig. 2.7: Relationship of the power coefficient to tip ratio and pitch angle.

by the wind turbine from the wind is given by (see e.g., [17, 48])

$$\forall\, k \geq 0\colon\ P_{\mathrm{t[k]}} = 0.5\rho A\, v_{\mathrm{w[k]}}^3\, C_{\mathrm{p[k]}} = 0.5\rho A C_{\mathrm{p[k]}} (\tfrac{R_{\mathrm{t}}}{\lambda_{\mathrm{[k]}}})^3 \times \omega_{\mathrm{m[k]}}^3 \geq 0, \tag{2.26}$$

where $\rho\,[\mathrm{kg/m^3}]$ is the air density, $A\,[\mathrm{m^2}]$ is the rotor area, R_{t} [m] is the blade radius,

$$\lambda = \frac{R_{\mathrm{t}}\omega_m}{v_{\mathrm{w}}}, \tag{2.27}$$

is the tip speed ratio (TSP)[8], $C_p \leq C_{p,\mathrm{Betz}} = 16/27 \approx 0.5926$[9] is the power coefficient of the wind turbine, and is a function of λ and the pitch angle $\beta\,[^\circ]$.

Generally speaking, depending on whether the *blade pitch* is controllable or not, there are two kinds of turbines [49, 50], namely, (I) *wind turbine without pitch control*, and (II) *wind turbine with pitch control*. Accordingly, there are also two types of power coefficients of $C_{\mathrm{p}}^{\mathrm{I}}$ (for type (I)) and $C_{\mathrm{p}}^{\mathrm{II}}$ (for type (II)) due to the different system structures. Through *numerical approximations*[10] one can calculate the power coefficient of C_p^{I} and C_p^{II}. The following approximations of (2.28a) and (2.28b) are the ones used for C_p^{I} and for C_p^{II} [44], respectively.

$$C_{\mathrm{p}}^{\mathrm{I}}(\lambda) = \max\Big\{46.4(1/\lambda - 0.01) - 2) \cdot e^{(0.165-15.6/\lambda)}; 0\Big\} \tag{2.28a}$$

$$C_{\mathrm{p}}^{\mathrm{II}}(\lambda,\beta) = \max\Big\{0.73\big(151\gamma - 0.58\beta - 0.02\beta^2.14 - 13.2\big) \cdot e^{-18.4\gamma}; 0\Big\} \tag{2.28b}$$

where $C_{\mathrm{p}}^{\mathrm{I}}$ and $C_{\mathrm{p}}^{\mathrm{II}}$ are the energy conversion coefficients for fixed-pitch and controllable pitch wind turbine systems, respectively, and $\gamma = \frac{1}{\lambda - 0.02\beta} - \frac{0.003}{1+\beta^3}$. Fig. 2.6 and 2.7 illustrate the range and peek (optimal) values of $C_{\mathrm{p}}^{\mathrm{I}}$ and $C_{\mathrm{p}}^{\mathrm{II}}$, respectively.

For simplicity, it is assumed that the turbine power is transformed without losses to mechanical power in the generator (otherwise an adequate efficiency factor should be introduced). Hence,

$$\forall\, k \geq 0\colon \qquad T_{\mathrm{t[k]}} = \frac{P_{\mathrm{t[k]}}}{\omega_{\mathrm{m[k]}}} \geq 0, \tag{2.29}$$

where T_{t} [Nm] is the turbine (aerodynamic) torque.

Note that, no wind turbine system can work under all wind speed range [49–51]. Fig. 2.8 gives the speed ranges based on the operation stages of a variable speed wind turbine system in general. When the wind speed is lower than the cut-in speed of $v_w^{\mathrm{cut-in}}$, i.e., at

[8] The TSP is defined as the ratio of the speed of the rotor tip to the free stream wind speed. Easy to know, there exists an optimal TSP value related to the optimal power coefficients of C_p [49–51]: if a rotor rotates too slowly, i.e., TSP is too small, the turbine blades allows too much wind to pass through undisturbed, and thus does not extract the maximum energy it can. On the other hand, if the rotor rotates too fast, i.e., TSP is too big, it appears to the wind as a large flat disc, which creates a large amount of drag. The rotor TSR depends on the blade airfoil profile used, the number of blades, and the type of wind turbine. In general, three-bladed wind turbines operate at a TSR of between 6 and 8, with 7 being the most widely-reported value (See "Wind Turbines Theory - The Betz Equation and Optimal Rotor Tip Speed Ratio", by Magdi Ragheb and Adam M. Ragheb)

[9] This is the so-called *Betz Constant* developed by Albert Betz in 1919 and reported in his book "Wind Energie und ihre Ausnutzung durch Windmuehlen" in 1926 [49–51].

[10] Developed through minimizing the error between the power curves obtained from the equations of (2.28a) or (2.28b), and the ones obtained from manufacturer data sheets. There are many different approximations methods to develop an accurate coefficient curve on different wind turbines. But differences between the curves of wind turbine types are very small [49, 50]

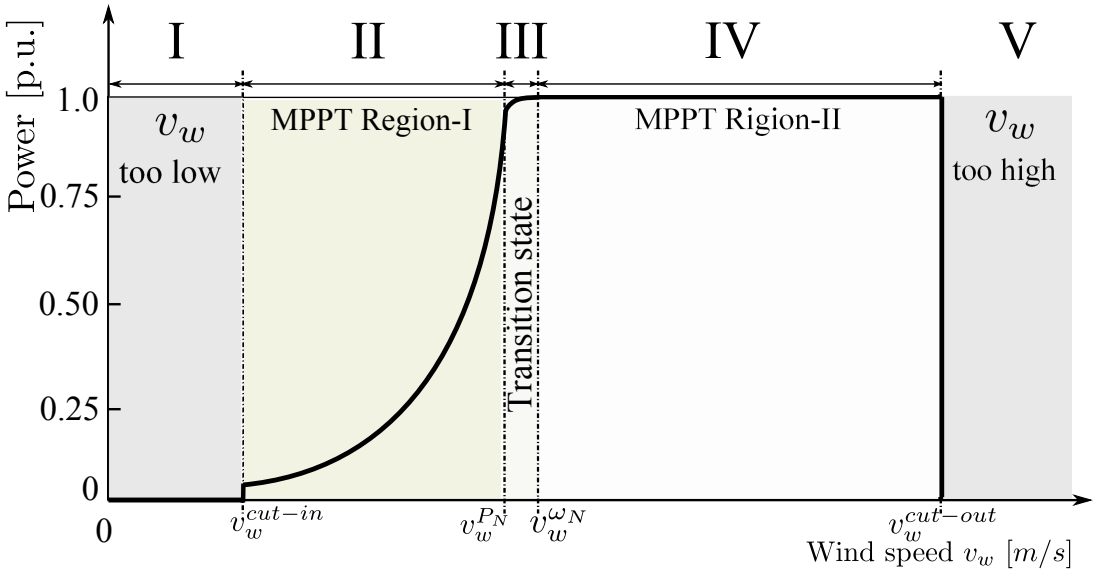

Fig. 2.8: Wind speed and operation regions [52].

stage-I, the wind turbine will stay still and no power is generated. During wind speed stage-II, i.e., the wind speed between the cut-in speed and rated speed, maximum power can be produced only when the turbine operates at a maximum C_p, i.e., at C_p^{opt}, which depends on a optimum tip-speed ratio of λ^{opt} (β is kept at zero). Therefore, the targeted optimum power at this stage is

$$P_{\text{m[k]}}^{\text{opt}} = \underbrace{0.5\rho A C_p^{\text{opt}} (\frac{R_t}{\lambda^{\text{opt}}})^3}_{K_1^{\text{opt}}} \times (\omega_{\text{m[k]}}^{\text{opt}})^3 \tag{2.30}$$

and the optimum generator torque is therefore

$$T_{\text{e[k]}}^{\text{opt}} = K^{\text{opt}} \times (\omega_{\text{m[k]}}^{\text{opt}})^2 = \underbrace{0.5\rho A C_p^{\text{opt}} \frac{R_t}{\lambda^{\text{opt}}}}_{K_2^{\text{opt}}} \times v_{\text{w[k]}}^2. \tag{2.31}$$

The reference torque to reach maximum power tracking can be obtained as:

$$T_{\text{e[k]}}^{*} = \begin{cases} K_1^{\text{opt}} \times \omega_{\text{m[k]}}^2 & \text{if } v_{\text{w}} \text{ unavailable} \;:\; \textit{Case-I} \\ K_2^{\text{opt}} \times v_{\text{w[k]}}^2 & \text{if } v_{\text{w}} \text{ available} \;:\; \textit{Case-II} \end{cases} \tag{2.32}$$

The stability analysis of using torque reference generation scheme as given by *Case-I* of (2.32) can be found in [53]. Note that, in practice, anemometer based torque reference generation scheme, i.e., *Case-II* in (2.32), increases cost and reduces the reliability of the overall system.

Another scheme, when knowing the wind speed (which can be obtained by using a anemometer sensor) and the optimal tip speed ratio λ^{opt} (which is usually available from

the manufacture data sheet for a specific wind turbine), the optimal rotating speed for the generator to follow under the given wind speed, invoking Eq. (2.27), can be expressed as:

$$\omega_{\mathrm{m}}^{*} = \omega_{\mathrm{m}}^{\mathrm{opt}} = \frac{\lambda^{\mathrm{opt}} \cdot v_{\mathrm{w}}}{R_{\mathrm{t}}}. \tag{2.33}$$

During stage-IV, i.e., the wind speed is higher than the rated value, the turbine will operate at the rated rotating speed and the control system should be able to reduce the input power (or torque) through changing (increasing) pitch angle β to maintain the overall generated power not goes beyond its safety range.

When the wind speed is higher than the cut-out speed $v_w^{\mathrm{cut-out}}$, i.e., in stage-V, the pitch angle control (to reduce the input power) is not enough to keep the system in safety mode, then the turbine will be shut-down.

From the above analysis, the MPPT control requires (the inner loop of) MSC to follow an optimal torque reference $T_{\mathrm{e[k]}}^{*}$ or speed reference ω_{m}^{*} command with fast dynamics.

2.4.2 Permanent-magnet synchronous generator (PMSG)

In most cases, for a direct-drive wind turbine system, a smooth surface multi-pole (pole-pair defined as N_{p}) PMSG is used [17]. Both the physical (structural) and saturation salience is in practice quite small and can be neglected, i.e., $L_{\mathrm{s}}^{\mathrm{d}} = L_{\mathrm{s}}^{\mathrm{q}}, \frac{\partial L_{\mathrm{s}}}{\partial \theta_{\mathrm{e}}} = 0$[11]. Moreover, the armature reaction affect is assumed to be negligible.

2.4.2.1 PMSG in $\alpha\beta$ frame

A smooth surface multi-pole PMSG can be modeled in $\alpha\beta$ reference frame. The dynamics in the current can be described with the following nonlinear model

$$\frac{\mathrm{d}\vec{i}_{\mathrm{m}}^{\alpha\beta}(t)}{\mathrm{d}t} = \frac{-R_{\mathrm{s}}}{L_{\mathrm{s}}}\vec{i}_{\mathrm{m}}^{\alpha\beta}(t) + \frac{1}{L_{\mathrm{s}}}\left(\vec{v}_{\mathrm{m}}^{\alpha\beta}(t) - \underbrace{\begin{pmatrix} -\psi_{\mathrm{pm}}\omega_{\mathrm{e}}(t)\sin\left(\theta_{\mathrm{e}}(t)\right) \\ \psi_{\mathrm{pm}}\omega_{\mathrm{e}}(t)\cos\left(\theta_{\mathrm{e}}(t)\right) \end{pmatrix}}_{=:\vec{e}_{\mathrm{m}}^{\alpha\beta}(t)}\right), \; \vec{i}_{\mathrm{m}}^{\alpha\beta}(0) = \vec{i}_{\mathrm{m}}^{0} \in \mathbb{R}^2 \tag{2.34}$$

where $R_{\mathrm{s}}\,[\Omega]$ is the stator resistance, $\vec{e}_{\mathrm{m}}^{\alpha\beta} = (e_{\mathrm{m}}^{\alpha}, e_{\mathrm{m}}^{\beta})^{\top}\,[\mathrm{V}]^2$ is the back-EMF vector, $\vec{v}_{\mathrm{m}}^{\alpha\beta} = (v_{\mathrm{m}}^{\alpha}, v_{\mathrm{m}}^{\beta})^{\top}\,[\mathrm{V}]^2$ is the output voltage vector of the generator side converter, $\vec{i}_{\mathrm{m}}^{\alpha\beta} = (i_{\mathrm{m}}^{\alpha}, i_{\mathrm{m}}^{\beta})^{\top}\,[\mathrm{A}]^2$ is the generator current vector: all in $\alpha\beta$ frame. $\omega_{\mathrm{e}}(t) = N_{\mathrm{p}}\omega_{\mathrm{m}}(t)\,[\mathrm{rad/s}]$ is the electrical frequency of the rotor (rotating with ω_{m}), $N_{\mathrm{p}}\,[1]$ is the pole pair number, $\psi_{\mathrm{pm}}\,[\mathrm{Wb}]$ is the permanent-magnet flux linkage, $\theta_{\mathrm{e}}\,[\mathrm{rad}]$ is the electrical position of the rotor flux.

[11] For salience based encolderless control, the true property of $\frac{\partial L_{\mathrm{s}}}{\partial \theta_{\mathrm{e}}} \neq 0$ is utilized.

The stator flux and electro-magnetic torque in the $\alpha\beta$ frame can be modeled as

$$\vec{\psi}_{\mathrm{s}}^{\alpha\beta}(t) = \int \left(\vec{v}_{\mathrm{m}}^{\alpha\beta}(t) - R_{\mathrm{s}}\vec{i}_{\mathrm{m}}^{\alpha\beta}(t)\right)dt,\ \vec{\psi}_{\mathrm{s}}^{\alpha\beta}(0) = \vec{\psi}_{\mathrm{s}}^{0} \in \mathbb{R}^2; \tag{2.35}$$

$$T_{\mathrm{e}}(t) = N_{\mathrm{p}}\left(\psi_{\mathrm{s}}^{\alpha} i_{\mathrm{m}}^{\alpha} - \psi_{\mathrm{s}}^{\beta} i_{\mathrm{m}}^{\beta}\right) \tag{2.36}$$

The dynamics of the mechanical wind turbine system are given by

$$\Theta_m \frac{\mathrm{d}\omega_{\mathrm{m}}(t)}{\mathrm{d}t} = T_{\mathrm{t}}(t) - T_{\mathrm{e}}(t) + \mathcal{F}(\omega_{\mathrm{m}})(t),\ \omega_{\mathrm{m}}(0) = \omega_{\mathrm{m}}^{0} \in \mathbb{R}; \tag{2.37}$$

where $T_{\mathrm{e}}(t)$, as in (2.36), is the electric torque of the generator, Θ_m [kgm^2] is the overall inertia (of turbine and generator), T_{e} [Nm] is the electro-magnetic (generator) torque, T_{t} [Nm] is the torque from the turbine, as in (2.29), and $\mathcal{F}(\omega_{\mathrm{m}})$ models nonlinear, dynamic friction effects; in this work, a constant coefficient B is used to model the friction effects.

Applying the Euler-forward method, the following discrete format of the generator in $\alpha\beta$ frame can be obtained:

$$\left.\begin{aligned}
\vec{i}_{\mathrm{m[k+1]}}^{\alpha\beta} &= \left(1 - \tfrac{T_{\mathrm{s}}R_{\mathrm{s}}}{L_{\mathrm{s}}}\right)\vec{i}_{\mathrm{m[k]}}^{\alpha\beta} + \tfrac{T_{\mathrm{s}}}{L_{\mathrm{s}}}\left(\vec{v}_{\mathrm{m[k]}}^{\alpha\beta} - \underbrace{\begin{pmatrix} -\psi_{\mathrm{pm}}\omega_{\mathrm{e[k]}}\sin\left(\theta_{\mathrm{e[k]}}\right) \\ \psi_{\mathrm{pm}}\omega_{\mathrm{e[k]}}\cos(\theta_{\mathrm{e[k]}}) \end{pmatrix}}_{=:\vec{e}_{\mathrm{m[k]}}^{\alpha\beta}}\right), \\
\vec{\psi}_{\mathrm{s[k+1]}}^{\alpha\beta} &= \vec{\psi}_{\mathrm{s[k]}}^{\alpha\beta} + \left(\vec{v}_{\mathrm{m[k]}}^{\alpha\beta} - R_{\mathrm{s}}\vec{i}_{\mathrm{m[k]}}^{\alpha\beta}\right)T_{\mathrm{s}}, \\
\omega_{\mathrm{e[k+1]}} &= \omega_{\mathrm{e[k]}} + \tfrac{T_{\mathrm{s}}}{\Theta_{\mathrm{m}}N_{\mathrm{p}}}\left(T_{\mathrm{t[k]}} - \underbrace{N_{\mathrm{p}}\left(\psi_{\mathrm{s[k]}}^{\alpha} i_{\mathrm{m[k]}}^{\alpha} - \psi_{\mathrm{s[k]}}^{\beta} i_{\mathrm{m[k]}}^{\beta}\right)}_{=:T_{\mathrm{e[k]}}} - B\cdot\omega_{\mathrm{m[k]}}\right).
\end{aligned}\right\} \tag{2.38}$$

2.4.2.2 PMSG in dq frame

The mathematical model of a PMSG in direct-quadrature (dq) reference frame (indicated by superscript ^{dq}) is given by

$$\vec{v}_{\mathrm{m}}^{\mathrm{dq}}(t) = R_{\mathrm{s}}\vec{i}_{\mathrm{s}}^{\mathrm{dq}}(t) + \frac{\mathrm{d}\vec{\psi}_{\mathrm{s}}^{\mathrm{dq}}(t)}{\mathrm{d}t} + \omega_{\mathrm{e}}(t)\underbrace{\left[\begin{smallmatrix} 0 & -1 \\ 1 & 0 \end{smallmatrix}\right]}_{:=\mathbf{J}}\vec{\psi}_{\mathrm{s}}^{\mathrm{dq}}(t),\ \ \vec{\psi}_{\mathrm{s}}^{\mathrm{dq}}(0) = \vec{\psi}_{\mathrm{s}}^{0} \in \mathbb{R}^2 \tag{2.39}$$

where $\vec{v}_{\mathrm{m}}^{\mathrm{dq}}(t) = (v_{\mathrm{m}}^{\mathrm{d}}(t),\, v_{\mathrm{m}}^{\mathrm{q}}(t))^{\top}$ [V]^2 is the generator side converter output voltage vector (to be specified in later), R_{s} is the stator resistance, $\vec{i}_{\mathrm{m}}^{\mathrm{dq}}(t) = (i_{\mathrm{m}}^{\mathrm{d}}(t),\, i_{\mathrm{m}}^{\mathrm{q}}(t))^{\top}$ [A]^2 is the generator current vector, $\vec{\psi}_{\mathrm{s}}^{\mathrm{dq}}(t) = (\psi_{\mathrm{s}}^{\mathrm{d}}(t),\, \psi_{\mathrm{s}}^{\mathrm{q}}(t))^{\top}$ [Wb]^2 is the flux linkage (in the stator of the generator). The flux linkage is assumed linearly related to current $\vec{i}_{\mathrm{m}}^{\mathrm{dq}}(t)$, stator inductance L_{s} [Vs/A] and (constant) permanent-magnet flux linkage ψ_{pm} as follows

$$\vec{\psi}_{\mathrm{s}}^{\mathrm{dq}}(t) = L_{\mathrm{s}}\vec{i}_{\mathrm{m}}^{\mathrm{dq}}(t) + \left(\psi_{\mathrm{pm}}, 0\right)^{\top} \tag{2.40}$$

$$T_{\mathrm{e}}(t) = N_{\mathrm{p}}\psi_{\mathrm{pm}} i_{\mathrm{m}}^{\mathrm{q}}. \tag{2.41}$$

Taking all equations of (2.39), (2.40), (2.37) and (2.41) into consideration, and applying the Euler-forward method, yields the discrete format of the generator as

$$\left.\begin{aligned}
\vec{i}^{\,\mathrm{dq}}_{\mathrm{m[k+1]}} &= \underbrace{\begin{bmatrix} 1-\frac{R_\mathrm{s}}{L_\mathrm{s}} & T_\mathrm{s}\omega_{\mathrm{e[k]}} \\ -T_\mathrm{s}\omega_{\mathrm{e[k]}} & 1-\frac{T_\mathrm{s}R_\mathrm{s}}{L_\mathrm{s}} \end{bmatrix}}_{=:\mathbf{A}_{\mathrm{m[k]}}} \vec{i}^{\,\mathrm{dq}}_{\mathrm{m[k]}} + \underbrace{\begin{bmatrix} \frac{T_\mathrm{s}}{L_\mathrm{s}} & 0 \\ 0 & \frac{T_\mathrm{s}}{L_\mathrm{s}} \end{bmatrix}}_{=:\mathbf{B}_\mathrm{m}} \vec{v}^{\,\mathrm{dq}}_{\mathrm{m[k]}} + \underbrace{\begin{pmatrix} 0 \\ -\frac{T_\mathrm{s}\psi_\mathrm{pm}}{L_\mathrm{s}}\omega_{\mathrm{e[k]}} \end{pmatrix}}_{=:\mathbf{H}_{\mathrm{m[k]}}} \\
\vec{\psi}^{\,\mathrm{dq}}_{\mathrm{s[k+1]}} &= L_\mathrm{s}\vec{i}^{\,\mathrm{dq}}_{\mathrm{m[k+1]}} + \begin{pmatrix} \psi_\mathrm{pm}, 0 \end{pmatrix}^\top \\
\omega_{\mathrm{e[k+1]}} &= \omega_{\mathrm{e[k]}} + \tfrac{T_\mathrm{s}}{\Theta_\mathrm{m} N_\mathrm{p}} \Big(T_{\mathrm{t[k]}} - \underbrace{N_\mathrm{p}\psi_\mathrm{pm} i^\mathrm{q}_{\mathrm{m[k]}}}_{=:T_{\mathrm{e[k]}}} - B\cdot\omega_{\mathrm{m[k]}} \Big)
\end{aligned}\right\}. \tag{2.42}$$

2.4.3 Grid side dynamics: grid and filter

Typically, for a MW level wind turbine system, a LCL or LC filter is usually used to connect the power converter to the grid. The proper design of a LCL[12] or LC filter results in much smaller inductance values to achieve a comparable filtering performances as L-filter (See [46, 54] and the reference therein). However, given a properly designed hardware system, both the properly designed LC and LCL filter can be simplified as the same type of a L filter in the fundamental frequency domain for the controller design process. Therefore, in this work, only a (R) L filter is considered and constructed in the laboratory due to its simplicity.

The (controllable) grid side power converter is also named as an active front end (AFE) power converter or (boost) PWM rectifier in many publications and in this dissertation, it is named as GSC or AFE for consistency. A typical two or three-level AFE with RL filter is shown at the right side of Fig. 2.5. It can be described in both $\alpha\beta$ and dq frames.

2.4.3.1 AFE with RL filter modeling in $\alpha\beta$ frame

An AFE with RL-filter connected to an ideal (balanced) grid in $\alpha\beta$ frame is given by (see e.g., [8, 10]):

$$\vec{e}^{\,\alpha\beta}_\mathrm{g}(t) = \vec{v}^{\,\alpha\beta}_\mathrm{g}(t) + R_\mathrm{g}\cdot\vec{i}^{\,\alpha\beta}_\mathrm{g}(t) + L_\mathrm{g}\cdot\frac{\mathrm{d}\vec{i}^{\,\alpha\beta}_\mathrm{g}(t)}{\mathrm{d}t},\ \vec{i}^{\,\alpha\beta}_\mathrm{g}(0) = \vec{i}^{\,0}_\mathrm{g} \in \mathbb{R}^2. \tag{2.43}$$

Transferring into the discrete format, one obtains

$$\vec{i}^{\,\alpha\beta}_{\mathrm{g[k+1]}} = \underbrace{\big(1-\tfrac{T_\mathrm{s}R_\mathrm{g}}{L_\mathrm{g}}\big)}_{:=\hat{\mathbf{A}}_\mathrm{g}} \vec{i}^{\,\alpha\beta}_{\mathrm{g[k]}} + \underbrace{\tfrac{T_\mathrm{s}}{L_\mathrm{g}}}_{:=\hat{\mathbf{B}}_\mathrm{g}} \big(\vec{v}^{\,\alpha\beta}_{\mathrm{g[k]}} - \vec{e}^{\,\alpha\beta}_{\mathrm{g[k]}}\big), \tag{2.44}$$

where $R_\mathrm{g}\,[\Omega]$ and $L_\mathrm{g}\,[\mathrm{Vs/A}]$ are filter resistance and inductance, respectively, $\vec{i}^{\,\alpha\beta}_\mathrm{g} = (i^\alpha_\mathrm{g},\, i^\beta_\mathrm{g})^\top\,[\mathrm{A}]^2$ is the current vector to the grid, $\vec{v}^{\,\alpha\beta}_\mathrm{g} = (v^\alpha_\mathrm{g},\, v^\beta_\mathrm{g})^\top\,[\mathrm{V}]^2$ is the output voltage vector of the GSC, and $\vec{e}^{\,\alpha\beta}_\mathrm{g} = (e^\alpha_\mathrm{g},\, e^\beta_\mathrm{g})^\top\,[\mathrm{V}]^2$ is the grid voltage vector: all in $\alpha\beta$ frame.

[12] For which a damping of the resonant frequency is very important.

2.4.3.2 AFE with RL filter modeling in dq frame

The input current dynamics in rotating dq frame can be modeled as follows [8]

$$\frac{\mathrm{d}\vec{i}_{\mathrm{g}}^{\mathrm{dq}}(t)}{\mathrm{d}t} = \frac{1}{L_{\mathrm{g}}}\big(\vec{e}_{\mathrm{g}}^{\mathrm{dq}}(t) - \vec{v}_{\mathrm{g}}^{\mathrm{dq}}(t)\big) - R_{\mathrm{g}}\vec{i}_{\mathrm{g}}^{\mathrm{dq}} + \omega_{\mathrm{g}}L_{\mathrm{g}}\mathbf{J}\vec{i}_{\mathrm{g}}^{\mathrm{dq}}, \vec{i}_g(0) = \vec{i}_g^0 \in \mathbb{R}^2 \tag{2.45}$$

Applying Euler-forward discretization method to equation (2.45), yields the following result

$$\vec{i}_{\mathrm{g[k+1]}}^{\mathrm{dq}} = \big(1 - \tfrac{T_{\mathrm{s}}R_{\mathrm{g}}}{L_{\mathrm{g}}}\big)\vec{i}_{\mathrm{g[k]}}^{\mathrm{dq}} + \omega_{\mathrm{g}}L_{\mathrm{g}}T_{\mathrm{s}}\mathbf{J}\vec{i}_{\mathrm{g[k]}}^{\mathrm{dq}} + \tfrac{T_{\mathrm{s}}}{L_{\mathrm{g}}}\Big(\vec{v}_{\mathrm{g[k]}}^{\mathrm{dq}} - \vec{e}_{\mathrm{g[k]}}^{\mathrm{dq}}\Big), \tag{2.46}$$

where $\vec{i}_{\mathrm{g}}^{\mathrm{dq}} = (i_{\mathrm{g}}^{\mathrm{q}},\, i_{\mathrm{g}}^{\mathrm{q}})^\top\,[\mathrm{A}]^2$ is the current vector to the grid, $\vec{v}_{\mathrm{g}}^{\mathrm{dq}} = (v_{\mathrm{g}}^{\mathrm{d}},\, v_{\mathrm{g}}^{\mathrm{q}})^\top\,[\mathrm{V}]^2$ is the output voltage vector of the GSC, and $\vec{e}_{\mathrm{g}}^{\mathrm{dq}} = (e_{\mathrm{g}}^{\mathrm{d}},\, e_{\mathrm{g}}^{\mathrm{q}})^\top\,[\mathrm{V}]^2$ is the grid voltage vector: all in dq frame.

2.4.3.3 Grid side power dynamics

In the following chapters, the power dynamics are used. Therefore, to ease the reading, I will present the relevant equations of the grid side power dynamics also in this chapter.

Invoking the instantaneous power theory [33, 34], grid side power can be calculated as

$$\vec{S} = (P,\, Q)^\top = \big((\vec{e}_{\mathrm{g}}^{\alpha\beta})^\top\vec{i}_{\mathrm{g}}^{\alpha\beta},\, (\vec{e}_{\mathrm{g}}^{\alpha\beta})^\top\mathbf{J}\vec{i}_{\mathrm{g}}^{\alpha\beta}\big)^\top = \big((\vec{e}_{\mathrm{g}}^{\mathrm{dq}})^\top\vec{i}_{\mathrm{g}}^{\mathrm{dq}},\, (\vec{e}_{\mathrm{g}}^{\mathrm{dq}})^\top\mathbf{J}\vec{i}_{\mathrm{g}}^{\mathrm{dq}}\big)^\top, \tag{2.47}$$

where P and Q are active and reactive power at the point of common coupling, respectively. For $\frac{\mathrm{d}}{\mathrm{d}t}P = (\vec{e}_{\mathrm{g}}^{\mathrm{dq}})^\top\frac{\mathrm{d}}{\mathrm{d}t}\vec{i}_{\mathrm{g}}^{\mathrm{dq}}$ and $\frac{\mathrm{d}}{\mathrm{d}t}Q = (\vec{e}_{\mathrm{g}}^{\mathrm{dq}})^\top\mathbf{J}\frac{\mathrm{d}}{\mathrm{d}t}\vec{i}_{\mathrm{g}}^{\mathrm{dq}}$ (assuming $\vec{e}_{\mathrm{g}}^{\mathrm{dq}} = (\hat{e}_{\mathrm{g}},\, 0) = (\hat{e}_{\mathrm{g}}^{\mathrm{d}},\, 0)$ is constant, i.e. $e_{\mathrm{g}}^{\mathrm{d}} = \hat{e}_{\mathrm{g}} > 0$), the dynamics of active and reactive power in the dq-reference frame can be computed as follows

$$\left.\begin{aligned}\tfrac{\mathrm{d}}{\mathrm{d}t}P &\overset{(2.45)}{=} \tfrac{1}{L_{\mathrm{g}}}\Big(-R_{\mathrm{g}}P + v_{\mathrm{g}}^{\mathrm{d}}\hat{e}_{\mathrm{g}} - \omega_g L_{\mathrm{g}}Q + \hat{e}_{\mathrm{g}}^2\Big)\\ \tfrac{\mathrm{d}}{\mathrm{d}t}Q &\overset{(2.45)}{=} \tfrac{1}{L_{\mathrm{g}}}\Big(-R_{\mathrm{g}}Q - v_{\mathrm{g}}^{\mathrm{q}}\hat{e}_{\mathrm{g}} + \omega_g L_{\mathrm{g}}P\Big).\end{aligned}\right\} \tag{2.48}$$

For a balanced grid, the grid side source voltage is in the format of $\vec{e}_{\mathrm{g}}^{\alpha\beta} = Ae^{\mathrm{j}\omega_{\mathrm{g}}\mathrm{t}}$, where A and ω_{g} are the magnitude and frequency, respectively. Therefore, $\frac{\mathrm{d}\vec{e}_{\mathrm{g}}^{\alpha\beta}}{\mathrm{d}t} = j\omega_{\mathrm{g}}\vec{e}_{\mathrm{g}}^{\alpha\beta}$. So the dynamics of the grid side power can be obtained in the $\alpha\beta$ frame in discrete format invoking Euler-forward method, as[13]

$$\vec{G}_{\mathrm{S[k]}} = \frac{\mathrm{d}\vec{S}_{\mathrm{[k]}}}{\mathrm{d}t} = \big[g_{\mathrm{P[k]}}, g_{\mathrm{Q[k]}}\big]^\top = \frac{1}{L_{\mathrm{g}}}\begin{bmatrix} e_{\mathrm{g[k]}}^{\alpha} & e_{\mathrm{g[k]}}^{\beta} \\ e_{\mathrm{g[k]}}^{\beta} & -e_{\mathrm{g[k]}}^{\alpha}\end{bmatrix}\begin{pmatrix} e_{\mathrm{g[k]}}^{\alpha} - v_{\mathrm{g[k]}}^{\alpha} \\ e_{\mathrm{g[k]}}^{\beta} - v_{\mathrm{g[k]}}^{\beta}\end{pmatrix} - \begin{pmatrix}\frac{R_{\mathrm{g}}}{L_{\mathrm{g}}}P_{\mathrm{[k]}} + \omega_{\mathrm{g}}Q_{\mathrm{[k]}} \\ \frac{R_{\mathrm{g}}}{L_{\mathrm{g}}}Q_{\mathrm{[k]}} - \omega_{\mathrm{g}}P_{\mathrm{[k]}}\end{pmatrix}. \tag{2.49}$$

Therefore, the grid side power at $k+1$ can be predicted as

$$\vec{S}_{\mathrm{[k+1]}} = \big(P_{\mathrm{[k+1]}}, Q_{\mathrm{[k+1]}}\big)^\top = \big(P_{\mathrm{[k]}}, Q_{\mathrm{[k]}}\big)^\top + T_{\mathrm{s}}\cdot\vec{G}_{\mathrm{S[k]}} \tag{2.50}$$

[13] $\vec{G}_{\mathrm{S}}(t)$ can be regarded as a slope/gradient of the power, with the same definition, which can also be applied in the dq frame, as $\vec{G}_{\mathrm{S}}(t) := \frac{\mathrm{d}\vec{S}(t)}{\mathrm{d}t} = \hat{e}_{\mathrm{g}}^{\mathrm{d}}\big(\frac{\mathrm{d}i_{\mathrm{g}}^{\mathrm{d}}}{\mathrm{d}t}, \frac{\mathrm{d}i_{\mathrm{g}}^{\mathrm{q}}}{\mathrm{d}t}\big)^\top$.

2.5 Lab-constructed test-benches and real-time controller

This section describes the self-designed hardware test-benches, which include a two-level back-to-back power converter system with both RL load and a PMSG, three-level NPC back-to-back power converter system with PMSG and an FPGA based HiL simulation system with NI-cRIO real-time controller. The controller development process with this FPGA real-time controllers is also briefly introduced.

2.5.1 Two-level back-to-back power converter system

A two-level back-to-back power converter with both a RL load and PMSM(G) were constructed using Infineon MIPAQ modules and the relevant drives in our institute. An overview of this set-up is shown in Fig. 2.9. The power rating of the power converter set-up is 60kVA. The available RL load is limited to 300VA and the machines for both generator and turbine emulator are limited to around 2.7kVA.

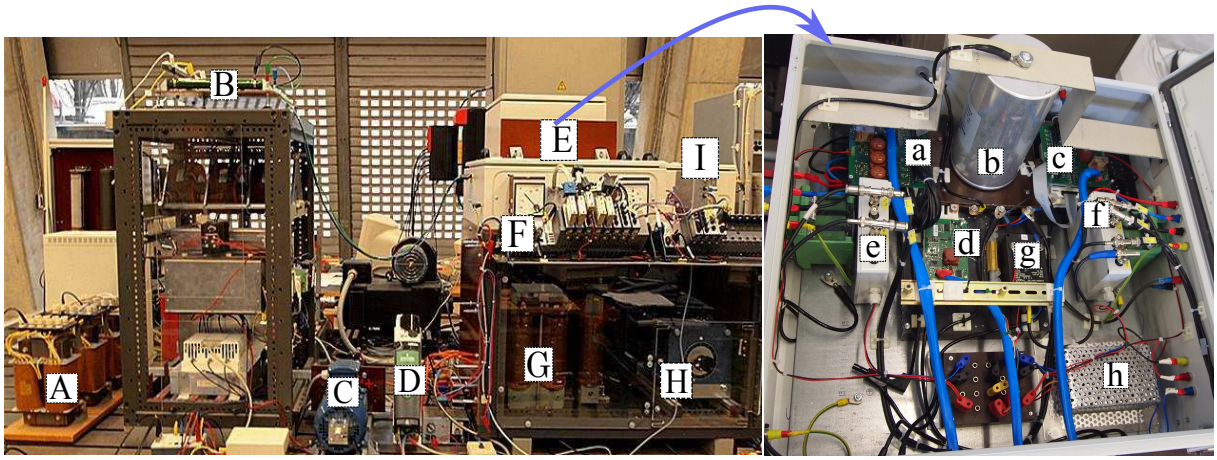

Fig. 2.9: Self-designed two-level back-to-back power converter system with RL load and PMSG. **A** and **B** are the inductance and the resistance of the RL load; **C** is the PMSG coupled with a load side AC motor and its commercial converter of **D**; (inside of) **E** is a self-constructed two-level back-to-back power converter using Infineon MIPAQ modules; **F** is the fully configurable FPGA based real-time controller (NI-cRIO-9082); **G** is the grid side L(R) filter, **H** is the grid side variac and **I** is the protection devices (against short circuit and input inrush current). The detailed depictions of inside of E are shown in the right side: **a** is the machine/load side converter and its driver circuits, **b** is the DC-link, **c** is grid side converter and driver circuits, **d** is DC-link switch and its driver circuits, **e** and **f** are the current and voltage measurements boards, **g** is the DC-link transducer and **h** is the power sources for the drivers and measurement boards.

The inside figure of the self-constructed two-level back-to-back power converter is shown in the right side of Fig. 2.9. Parameters of the back-to-back 2L power converter configured with RL-load and PMSG are collected in Table 2.2 and Table 2.3, respectively.

Parameter	Experiment
Grid-side Phase Voltages $e_g^{a,b,c}$ [V] (peak)	80 to 120
Grid-side Voltage Frequency ω_n [rad/s]	100π
Grid-side Reactor Resistor R_g [Ohm]	$1.56 \cdot e^{-3}$
Grid-side Reactor Inductance L_g [H]	$16 \cdot e^{-3}$
Load-side Inductance L_l [H]	$10e^{-3}$
Load-side Resistor R_l [Ohm]	10
Load Reference Current Frequency f_l [Hz]	50

Table 2.2: System configuration of the 2L back-to-back power converter with RL load for evaluations in Chp. 3 to Chp. 8.

Parameters	Values
Grid-Side Phase Voltage $\vec{e}_\mathrm{g}^{\mathrm{abc}}$ [V] (peak)	80 to 120
Grid-Side Voltage Frequency ω_g [rad/s]	100π
Grid-side Reactor Resistor R_g [Ohm]	$1.56e-3$
Grid-side Reactor Inductance L_g [H]	$16e-3$
DC-link Capacitor C [μF]	1100
Generator Stator Inductance L_s = [H]	8e-3
Generator Stator Resistor R_s [Ohm]	1.3
Generator Pole Pairs N_p [1]	3
Rotor Permanent-Magnet Flux ψ_pm [Wb]	0.41

Table 2.3: System configuration of the 2L back-to-back power converter with PMSG for evaluations in Chp. 3, to Chp. 8.

2.5.2 Three-level back-to-back power converter system

The three-level NPC back-to-back power converter using also Infineon power switches is depicted in Fig. 2.10. The switches are with a power rating of 30kVA. However, the heat-sink and the measurement board are designed to work within 5 kVA to reduce cost and ease its design and realization for laboratory use. More parameters are listed in Table 2.4. The inside configuration of the self-designed three-level NPC back-to-back

Parameters	Values	Parameters	Values
Grid Phase Vol. $\vec{e}_\mathrm{g}^{\mathrm{abc}}$ [V] (peak)	80 to 120	PMSG Stator Induc. L_s = [H]	8e-3
PMSG Stator Resis.r $\mathrm{R_s}$ [Ohm]	1.3	PMSG nominal $\mathrm{T_e^n/I_m^n}$ [Nm/A]	7.5/5.5
Grid Vol. Freq. ω_g [rad/s]	100π	PMSG Pole Pairs N_p [1]	3
Grid Reactor Resis. R_g [Ohm]	$1.56e-3$	Permanent-Magnet ψ_pm [Wb]	0.41
Grid Reactor Induc.e L_g [H]	$16e-3$	Sampling Interval T_s [μs]	50/100
DC-Link cap. $C_1 = C_2 = C$ [F]	1000×10^{-6}		

Table 2.4: System parameters for the three-level system.

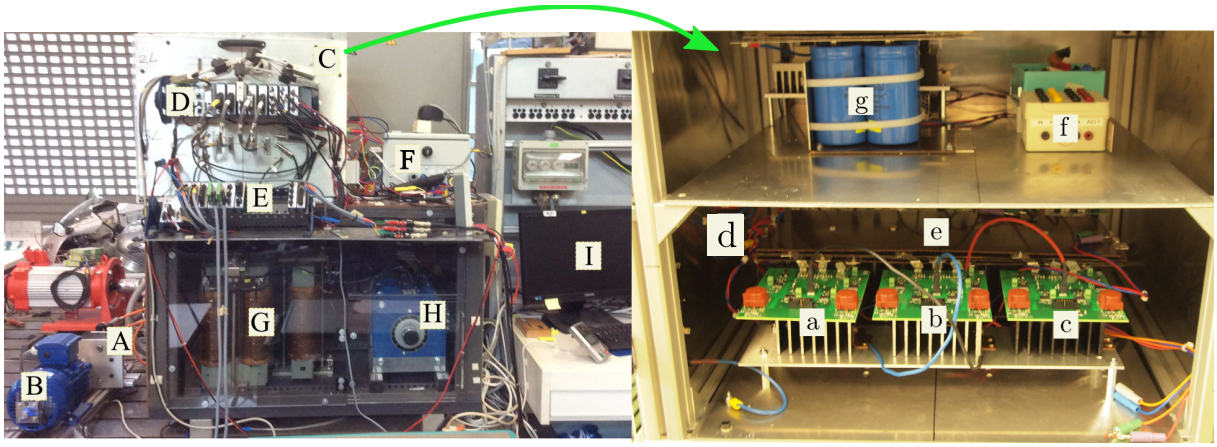

Fig. 2.10: Three-level NPC back-to-back power converter system with PMSG. **A** and **B** are the PMSG and an asynchronous motor (controlled by a commercial drive) emulating the turbine; (inside of) **C** is a self-designed three-level NPC back-to-back power converter using Infineon switching modules; **D** is a fully configurable FPGA based real-time controller (NI-cRIO-9082) for deploying the control algorithms; **G** is the grid side L(R) filter, **H** is the grid side variac and **F** is the protection devices against short circuit and input inrush current. The detailed depictions of in side **C** are shown in the right side: **a, b, c** are the machine/load side three-phase three-level NPC power converter and its heat-sink, beyond **e** (not visible due to its position is a four/three-leg three-level NPC power converter serving as the grid side AFE); **d** is the DC-link voltage measurement interface; **e** is the layered DC-bus (its bellow are the capacitors), **g** (and its behind) is a DC-bus with a two-level voltage source power inverter serving as a SVG for extension and **f** is the power source for the gate driver, the current and voltage measurements boards.

Parameter	Variable	Value
Rated Voltage	V_B	690V
Rated Current	I_B	1896A
Rated Frequency (Generator)	f_B	14.4 Hz
Rated Speed	Ω_n	18 RPM
Stator Resistor	R_s	$3.52e^{-3}$ Ohm
Stator Inductance	L_s	2.54mH
DC-link Voltage	V_{dc}	1200V
Rated Frequency (Grid)	f_{gB}	50 Hz
Filter Inductance	L_g	3.52mH

Table 2.5: Parameters of a 2MW PMSG used for investigation the HiL refreshing rate effects.

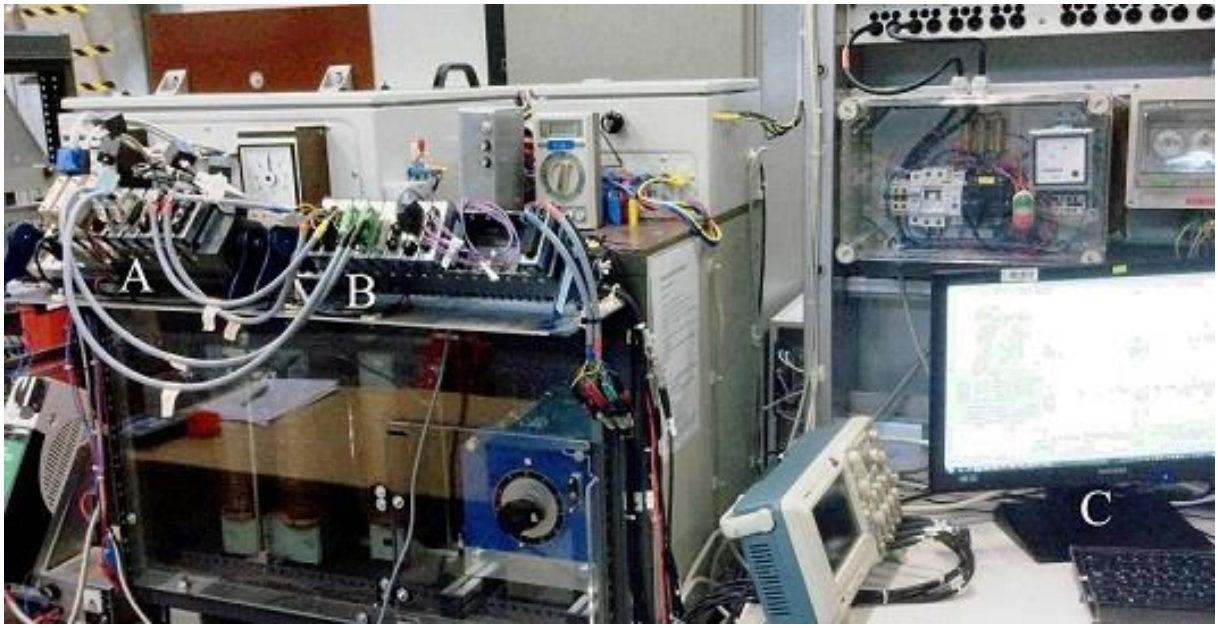

Fig. 2.11: FPGA HiL platform of a back-to-back power converter PMSG wind turbine system. *A: FPGA platform (NI-cRIO-9082)*, for implementing the ECU; *B: FPGA platform (NI-9159)*, for implementing the back-to-back converter PMSG wind turbine emulator; *C: User interface*, programmed using Labview running in a PC.

power converter is shown in the right side of Fig. 2.10. Noticeably, from the hardware design and realization level, the as-constructed three-level NPC power converter can be also configured as a four-leg NPC on the grid side. Due to the experimental verifications of such configuration have not yet been done. Therefore its detailed parameters are not given in this dissertation.

2.5.3 FPGA based HiL simulation system configuration

The FPGA based signal level Hardware-in-the-Loop (HiL) system is depicted in Fig. 2.11. Detailed instruction of each controller chassis is given in the caption of Fig. 2.11. This test-bench is mainly used for the research topics introduced in Chp. 9. The 2MW PMSG wind turbine system parameters for using such HiL system to evaluate its refreshing rate effects are listed in Table 2.5.

2.5.4 Real-time system structure and utilization

The reconfigurable real-time system used for the controller deployment is depicted in Fig. 2.12. The controller deploying system used in this dissertation can be divided into three main levels with regarding to their implementation environments, namely, the personal computer (PC), the real-time processor (RT) and the field-programmable gate array (FPGA).

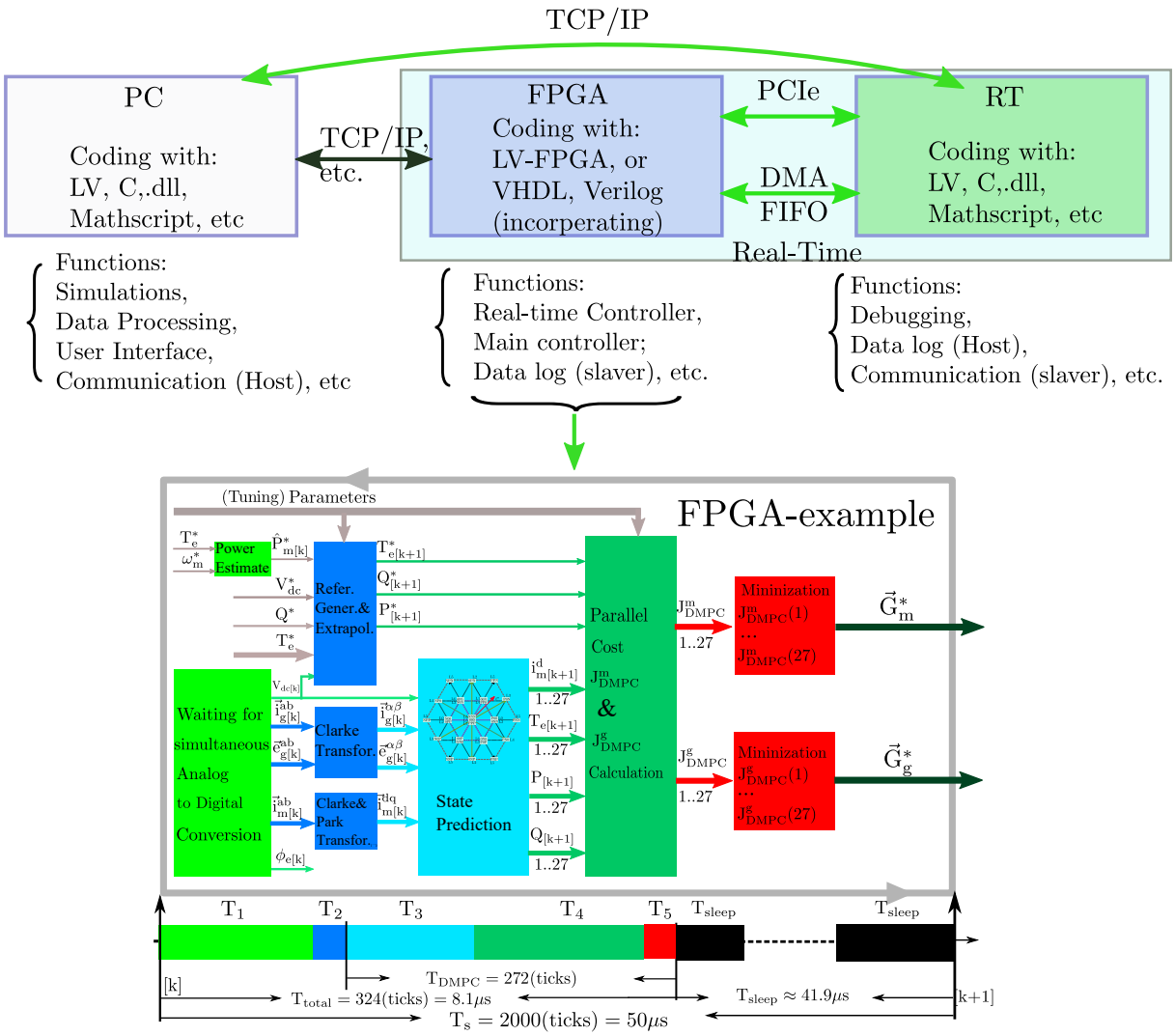

Fig. 2.12: Real-time deploying system structure.

In the PC, the simulations are preliminarily done through Matlab/Labview-PC environments. These can be coded with Matlab (m-files), Labview graphical coding (VIs), C, generated .dll and math-scripts. Meanwhile the data/result processing procedure, user interface and communication host to the real-time controller are also done here.

The real-time controller is in charge of the real-time debugging, (real-time) data logging (as the host) and communication with the host PC. It can be coded with VIs, C, math-scripts and incorporating ".dll" files generated from certain third-part software (e.g., Visual Studio, Matlab/Simulink, etc.).

The FPGA is used as the main controller and coded with LV-FPGA (it can also incorporate hardware description languages such as VHDL, Verilog, etc.). The mains functions of the FPGA are real-time host of the controllers, real-time data-logging slaver, etc. TCP/IP are used in between the PC and RT in non-real-time; while PCI-e and DMA-FIFO are used as the real-time communication solution in between the RT and the FPGA.

For FPGA realizations of the control algorithms, a so-called single-cycle-time-loop (SCTL) NI-FPGA technique is widely used in this dissertation. With a slightly higher implementation efforts the technique introduces two considerable benefits, namely, reduced resource usage and improved code execution speed. More details of such technique can be found online taking SCTL as the key word, and is therefore not described here. Noticeably, the execution time of each sub-routines can be easily measured with an accuracy of 25[ns]. As an example, the realization overview of a classical direct model predictive control scheme for the 3L back-to-back power converter PMSG system is shown in the lower side of Fig. 2.12, where different colors represent different time durations. In the the following chapters, except a dedicated comparison, the FPGA realizations of the relevant control algorithms has followed such instructions, but will not be detailed again.

2.6 Summary

This chapter has introduced the mathematical basics for the system modeling. All the models for both two- and three-level NPC back-to-back power converters, RL load and PMSG wind turbine system have been explicitly developed in both *continuous* and *discrete time* formats. The self-designed and lab-constructed two- and three-level NPC back-to-back power converter test-benches have also been depicted. The real-time controller utilization and the control algorithm deploying environments in this dissertation have also been briefly described.

Chapter 3

Classical control techniques

This chapter describes and summarizes the actual control schemes for back-to-back power converters and PMSG wind turbine systems. These include:

- *Field-oriented-control* (FOC) for machine side converter (MSC), and *voltage oriented control* (VOC) for grid side converter (GSC), both with space vector modulator (SVM) (see Sec. 3.2),
- *Direct torque control* (DTC) for MSC and *direct power control* (DPC) for GSC both with switching table (see Sec. 3.5),
- DTC and DPC with modulators for MSC and GSC (see Sec. 3.3), respectively,
- And deadbeat-like predictive control with modulator for both the MSC and GSC (see Sec. 3.4).

Their basic principles are revisited and discussed, their digital realizations are presented in detail and the performances are evaluated with experimental data (see Sec. 3.6) at the test-benches described in Chp. 2.

3.1 Introduction

A controller which produces a continuous reference actuating signal will require a modulator to decode the gate signals to assign to the switches of the power converters. There are different ways to modulate a continuous reference to the gate signals [25]. Due to its merits such as wider DC-link utilization range, smaller total harmonic distortions (THDs) and ease for embedded system realizations, space vector modulation (SVM) becomes one of the most standard ones. SVM (both for two- and three-level three-phase power converters) is already a well-known technique. Its design and realization processes are, therefore, not redundantly repeated in this dissertation.

Control schemes of (i) FOC for MSC, VOC for GSC; (ii) DTC-DPC with modulator and (iii) *deadbeat control* share some common properties such as using extra modulations

and *vector orientation* concept[1]. Therefore they are referred to as linear controller based *vector control* [21, 25, 55]. A general control block diagram for these three techniques is given in Fig. 3.1a.

Control schemes of (i) DTC for MSC, DPC for GSC, both with switching table; and (ii) *direct model predictive control* for MSC, GSC, respectively, are all nonlinear control schemes, sharing the similar properties, such as, no modulator or inner linear control loops. Therefore, both can be regarded as "nonlinear direct control" [25, 56, 57]. A general control block diagram for these schemes is given in Fig. 3.1b.

DTC-DPC with (offline designed) switching table is introduced in Sec. 3.5, and direct model predictive control class is discussed in the follow chapter for the sake of completeness. Note that, without special declaration all the variables/symbols used in this chapter have same definition/meaning as introduced in Chp 2.

3.2 Field and voltage oriented control

The key principle of both VOC and FOC is the so-called "vector orientation" [25, 58]. By transferring the system into the "synchronous" frame, the control variables will be "DC components" and the inner part of the system (both the grid and machine sides) can be simplified as a one-order system. For such system, proportional integration (PI) controller can achieve nice steady state performances. In the following sections, system dynamics of both the machine and grid sides in *dq* frame are revisited to ease the controller descriptions. Their respective controller design processes are introduced in brief.

3.2.1 Field oriented control for MSC

3.2.1.1 Inner control loop

For a surface-mounted PMSG, similar assumption as in Chp. 2, i.e., $L_{\mathrm{s}}^{\mathrm{d}} \approx L_{\mathrm{s}}^{\mathrm{q}} := L_{\mathrm{s}}$ is made. Rearranging Equation (2.39) yields the state current dynamics in *dq* frame as [17]

$$L_{\mathrm{s}} \frac{\mathrm{d}i_{\mathrm{m}}^{\mathrm{d}}}{\mathrm{d}t} = v_{\mathrm{m}}^{\mathrm{d}} - R_{\mathrm{s}} i_{\mathrm{m}}^{\mathrm{d}} + L_{\mathrm{s}} \omega_{\mathrm{e}} i_{\mathrm{m}}^{\mathrm{q}}, \tag{3.1a}$$

$$L_{\mathrm{s}} \frac{\mathrm{d}i_{\mathrm{m}}^{\mathrm{q}}}{\mathrm{d}t} = v_{\mathrm{m}}^{\mathrm{q}} - R_{\mathrm{s}} i_{\mathrm{m}}^{\mathrm{q}} - L_{\mathrm{s}} \omega_{\mathrm{e}} (i_{\mathrm{m}}^{\mathrm{d}} + \psi_{\mathrm{pm}}), \tag{3.1b}$$

[1] Deadbeat controller for grid side power control when designed in the $\alpha\beta$ frame requires no synchronous frame transformation (see Sec. 3.4 for details) or vector orientation concept. Therefore, it can be also regarded as a *direct control*. However, modulation is still required.

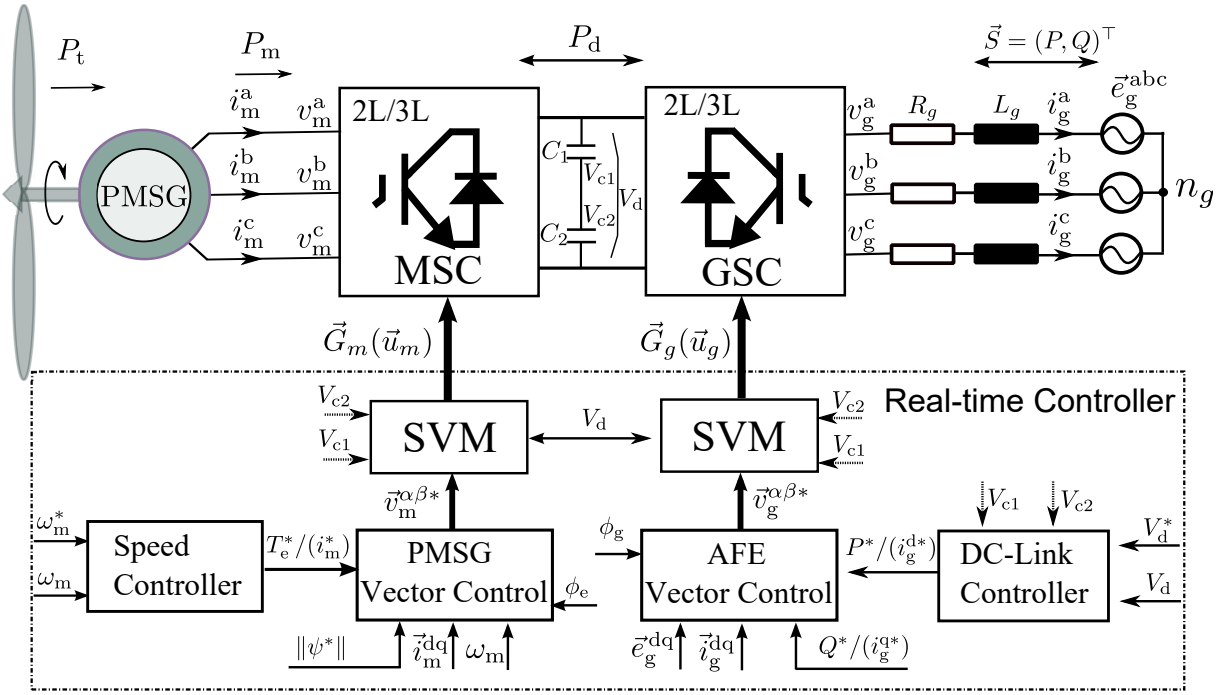

(a) Linear vector control scheme.

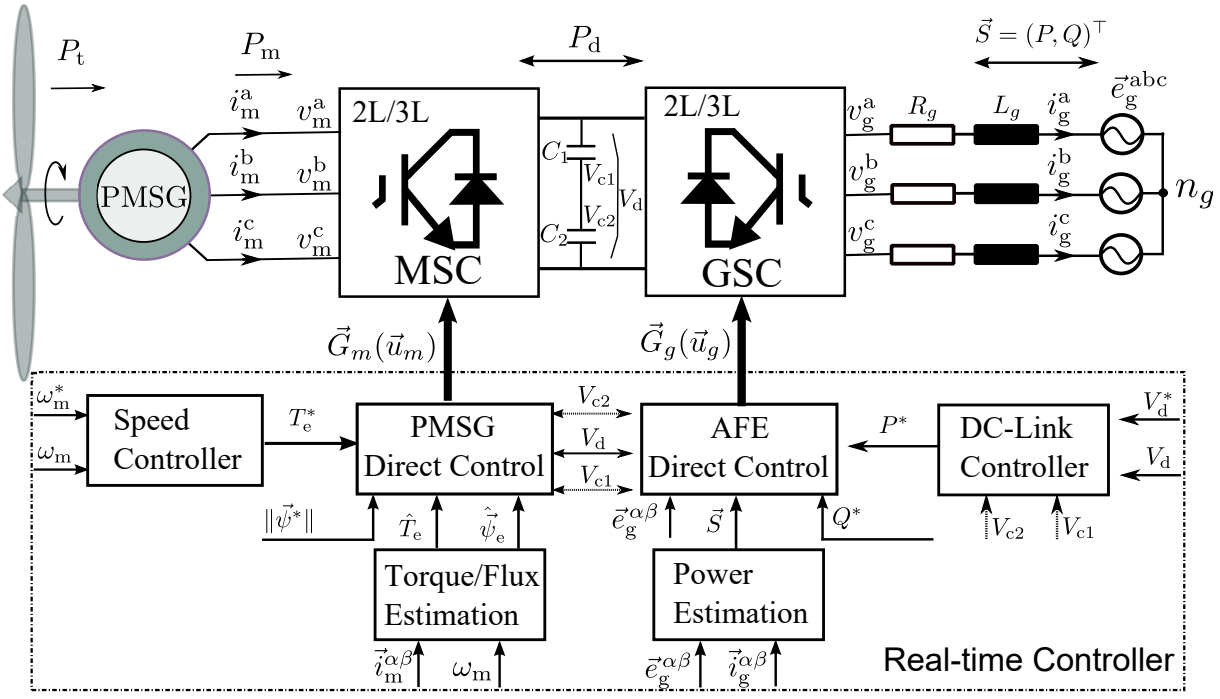

(b) Nonlinear direct control scheme.

Fig. 3.1: Block diagrams of a two- and three-level back-to-back power converter PMSG wind turbine system with RL-filter on the grid-side and its controller with linear vector control methods (a) and nonlinear direct control methods (b). The dashed lines of the controller represent the specific parts of the structure for 3L NPC power converter system control.

Rearranging equations (3.1a) and (3.1), yields the voltage equations in dq frame, as

$$\overbrace{v_{\mathrm{m}}^{\mathrm{d}} + L_{\mathrm{s}}\omega_{\mathrm{e}} i_{\mathrm{m}}^{\mathrm{q}}}^{v_{\mathrm{m}}^{\mathrm{d,eq}}} = L_{\mathrm{s}}\frac{\mathrm{d}i_{\mathrm{m}}^{\mathrm{d}}}{\mathrm{d}t} + R_{\mathrm{s}} i_{\mathrm{m}}^{\mathrm{d}}, \tag{3.2a}$$

$$\underbrace{v_{\mathrm{m}}^{\mathrm{q}} - \omega_{\mathrm{e}}(L_{\mathrm{s}} i_{\mathrm{m}}^{\mathrm{d}} + \psi_{\mathrm{pm}})}_{v_{\mathrm{m}}^{\mathrm{q,eq}}} = L_{\mathrm{s}}\frac{\mathrm{d}i_{\mathrm{m}}^{\mathrm{q}}}{\mathrm{d}t} + R_{\mathrm{s}} i_{\mathrm{m}}^{\mathrm{q}}. \tag{3.2b}$$

The inner transfer function $\mathrm{TF}_{\mathrm{m}}^{\mathrm{i}}(\mathrm{S})$ between the output current $\mathrm{I}_{\mathrm{m}}^{\mathrm{d}}(\mathrm{S})$, $\mathrm{I}_{\mathrm{m}}^{\mathrm{q}}(\mathrm{S})$ and their equivalent control voltage $\mathrm{V}_{\mathrm{m}}^{\mathrm{d,eq}}(\mathrm{S})$ and $\mathrm{V}_{\mathrm{m}}^{\mathrm{q,eq}}(\mathrm{S})$ in dq frame is

$$\mathrm{TF}_{\mathrm{m}}^{\mathrm{i}}(\mathrm{S}) = \frac{\mathrm{I}_{\mathrm{m}}^{\mathrm{d}}(\mathrm{S})}{\mathrm{V}_{\mathrm{m}}^{\mathrm{d,eq}}(\mathrm{S})} = \frac{\mathrm{I}_{\mathrm{m}}^{\mathrm{q}}(\mathrm{S})}{\mathrm{V}_{\mathrm{m}}^{\mathrm{q,eq}}(\mathrm{S})} = \frac{1}{L_{\mathrm{s}}S + R_{\mathrm{s}}}. \tag{3.3}$$

Since the system is now in dq frame. Hence the inner loop control variables $\mathrm{I}_{\mathrm{m}}^{\mathrm{d}}(\mathrm{S})$ and $\mathrm{I}_{\mathrm{m}}^{\mathrm{q}}(\mathrm{S})$ (during steady state) are DC variables. Considering the plant inner loop transfer function of Equation (3.3), a simple PI controller with the following transfer function

$$\mathrm{G}_{\mathrm{m}}^{\mathrm{i}}(\mathrm{S}) = \frac{\mathrm{V}_{\mathrm{m}}^{\mathrm{d,q,eq*}}(\mathrm{S})}{\mathrm{I}_{\mathrm{m}}^{\mathrm{d,q*}}(\mathrm{S}) - \mathrm{I}_{\mathrm{m}}^{\mathrm{d,q}}(\mathrm{S})} = \frac{K_{\mathrm{m}}^{\mathrm{ip}} T_{\mathrm{m}}^{i} S + K_{\mathrm{m}}^{\mathrm{ii}}}{T_{\mathrm{m}}^{i} S} \tag{3.4}$$

can manipulate the plant to follow a DC reference with zero steady state tracking error. $T_{\mathrm{m}}^{i}, K_{\mathrm{m}}^{\mathrm{ii}}, K_{\mathrm{m}}^{\mathrm{ip}}$ are the PI time constant and coefficients, respectively. The *equivalent control voltages* $v_{\mathrm{m}}^{\mathrm{d,q,eq*}}$, generated by the PI controller, contain also a coupling pair of $v_{\mathrm{m}}^{\mathrm{d,coupling}} = L_{\mathrm{s}}\omega_{\mathrm{e}} i_{\mathrm{m}}^{\mathrm{q}}$, and $v_{\mathrm{m}}^{\mathrm{q,coupling}} = -L_{\mathrm{s}}\omega_{\mathrm{e}}(i_{\mathrm{m}}^{\mathrm{d}} + \psi_{\mathrm{pm}})$, respectively (see equations (3.2a) and (3.2b)). Both $v_{\mathrm{m}}^{\mathrm{d,q,coupling}}$ cannot be directly reflected by the inner PI controller. Therefore, a better solution is to decouple the controller by adding a compensation to the $v_{\mathrm{m}}^{\mathrm{d,q,eq*}}$ produced by the PI controller as follows

$$v_{\mathrm{m}}^{\mathrm{d*}} = v_{\mathrm{m}}^{\mathrm{d,eq*}} - L_{\mathrm{s}}\omega_{\mathrm{e}} i_{\mathrm{m}}^{\mathrm{q}}, \tag{3.5a}$$

$$v_{\mathrm{m}}^{\mathrm{q*}} = v_{\mathrm{m}}^{\mathrm{q,eq*}} + \omega_{\mathrm{e}}(L_{\mathrm{s}} i_{\mathrm{m}}^{\mathrm{d}} + \psi_{\mathrm{pm}}), \tag{3.5b}$$

where $v_{\mathrm{m}}^{\mathrm{d,q*}}$ are the control voltages to assign to the modulator after transferring to $\alpha\beta$ frame. The as-described VOC scheme is shown in the left part of Fig. 3.2.

3.2.1.2 Outer (speed) control loop

The mechanical dynamics are

$$J\frac{\mathrm{d}\omega_{\mathrm{m}}}{\mathrm{d}t} = T_{\mathrm{t}} - T_{\mathrm{e}} + B(\omega_{\mathrm{m}}), \tag{3.6a}$$

$$T_{\mathrm{e}} = N_{\mathrm{p}}\psi_{\mathrm{pm}} \cdot i_{\mathrm{m}}^{\mathrm{q}}, \tag{3.6b}$$

Similarly, the speed loop transfer function $\mathrm{TF}_{\mathrm{m}}^{\omega_{\mathrm{m}}}(\mathrm{S})$, i.e., the speed output $\Omega_{\mathrm{m}}(\mathrm{S})$ to the torque input $\mathrm{T}_{\mathrm{t}}(\mathrm{S}) - \mathrm{T}_{\mathrm{e}}(\mathrm{S})$ is

$$\mathrm{TF}_{\mathrm{m}}^{\omega_{\mathrm{m}}}(\mathrm{S}) = \frac{\Omega_{\mathrm{m}}(\mathrm{S})}{\mathrm{T}_{\mathrm{t}}(\mathrm{S}) - \mathrm{T}_{\mathrm{e}}(\mathrm{S})} = \frac{1}{JS + B}. \tag{3.7}$$

where $\mathrm{T_e(S)}, \mathrm{T_t(S)}$ are the electro-magnetic and the load (drive) torques, respectively. Easy to see, it is again a one-order system. Therefore, the speed loop can also be controlled using a PI controller with the following transfer function

$$\mathrm{G_m^{\omega_m}(S)} = \frac{\mathrm{T_e^*(S)}}{\omega_\mathrm{m}^*(\mathrm{S}) - \Omega_\mathrm{m}(\mathrm{S})} = \frac{K_\mathrm{m}^{\omega_\mathrm{m} p} T_\mathrm{m}^{\omega_\mathrm{m}} S + K^{\omega_\mathrm{m} i}}{T_\mathrm{m}^{\omega_\mathrm{m}} S}, \tag{3.8}$$

where $T_\mathrm{m}^{\omega_\mathrm{m}}, K_\mathrm{m}^{\omega_\mathrm{m} i,p}$ are the PI time constant and coefficients, respectively.

Without specific declaration, in the following parts of this chapter, all the machine side outer loop (speed loop) controllers are the same as in Equation (3.8), i.e., a PI controller. Note that, the output of the controller can also be regarded as $\mathrm{I_m^{q*}(S)}$ (in time-domain $i_\mathrm{m}^{\mathrm{q}*}(t)$) since the difference between the torque and the current is simply a (constant) proportional coefficient here (See (3.6b)). Physical explanation is that, once "field orientation" reaches, the quadrature current, i.e., i_m^q, *directly* will correlate to electromagnetic torque production.

The whole system controller for the machine side is now a cascaded structure (See Fig. 3.2) using two PI controllers for the speed and inner current regulations, respectively.

3.2.2 Voltage oriented control for GSC

Rearranging the equations in (2.45), yields the voltage dynamics of the grid tied AFE (right side of Fig. 2.5) as

$$\left.\begin{aligned} \overbrace{e_\mathrm{g}^\mathrm{d} + L_\mathrm{g}\omega_\mathrm{g} i_\mathrm{g}^\mathrm{d} - v_\mathrm{g}^\mathrm{d}}^{v_\mathrm{g}^{\mathrm{d,eq}}} &= L_\mathrm{g}\frac{\mathrm{d}i_\mathrm{g}^\mathrm{d}}{\mathrm{d}t} + R_\mathrm{g} i_\mathrm{g}^\mathrm{d}, \\ \underbrace{e_\mathrm{g}^\mathrm{q} - L_\mathrm{g}\omega_\mathrm{g} i_\mathrm{g}^\mathrm{d} - v_\mathrm{g}^\mathrm{q}}_{v_\mathrm{g}^{\mathrm{q,eq}}} &= L_\mathrm{g}\frac{\mathrm{d}i_\mathrm{g}^\mathrm{q}}{\mathrm{d}t} + R_\mathrm{g} i_\mathrm{g}^\mathrm{q}. \end{aligned}\right\} \tag{3.9}$$

Similarly to the generator side, the transfer function $\mathrm{TF_g^i(S)}$ between the output current $\mathrm{I_g^{d,q}(S)}$ and their equivalent control voltage $\mathrm{V_g^{d,q,eq}(S)}$ in dq frame is

$$\mathrm{TF_g^i(S)} = \frac{\mathrm{I_g^d(S)}}{\mathrm{V_g^{d,eq}(S)}} = \frac{\mathrm{I_g^q(S)}}{\mathrm{V_g^{q,eq}(S)}} = \frac{1}{L_\mathrm{g} S + R_\mathrm{g}}. \tag{3.10}$$

In the analogy, a PI controller with the following transfer function,

$$\mathrm{G_g^i(S)} = \frac{\mathrm{V_g^{d,q,eq*}(S)}}{\mathrm{I_g^{d,q*}(S)} - \mathrm{I_g^{d,q}(S)}} = \frac{K_\mathrm{g}^{\mathrm{ip}} T_\mathrm{g}^i S + K_\mathrm{g}^{\mathrm{ii}}}{T_\mathrm{g}^\mathrm{i} S}, \tag{3.11}$$

can be used to regulate the inner "DC" current in dq frame, where $T_\mathrm{g}^\mathrm{i}, K_\mathrm{g}^{\mathrm{ii,ip}}$ are the PI time constant and coefficients, respectively. Note that, the equivalent voltages also contains the coupling terms of $v_\mathrm{g}^{\mathrm{d,coupling}} = L_\mathrm{g}\omega_\mathrm{g} i_\mathrm{g}^\mathrm{q} + e_\mathrm{g}^\mathrm{d}$, and $v_\mathrm{g}^{\mathrm{q,coupling}} = e_\mathrm{g}^\mathrm{q} - L_\mathrm{g}\omega_\mathrm{g} i_\mathrm{g}^\mathrm{d}$, respectively. Both $v_\mathrm{g}^{\mathrm{d,q,coupling}}$ cannot be *directly* reflected by the inner PI controller. The command voltages to assign to the converter shall be $v_\mathrm{g}^{\mathrm{d,q*}}$. Therefore, based on Equation (3.9) they can be computed by

$$v_\mathrm{g}^{\mathrm{d,q*}} = v_\mathrm{g}^{\mathrm{d,q,coupling}} - v_\mathrm{g}^{\mathrm{d,q,eq*}}, \tag{3.12}$$

where $v_{\mathrm{g}}^{\mathrm{d,q}*}$ are the voltages to be assigned to the modulator (after transferring into $\alpha\beta$ frame[2]).

3.2.2.1 DC-link controller

The DC-link control is one of the key parts for a back-to-back power converter (which will be more detail presented in Chp. 6. For the sake of completeness, only a *physical explanation* of why a PI controller can be used to regulate the DC-link voltage is given in the following paragraphs.

Considering the current flow, the DC-link voltage dynamics can be modeled as

$$C\frac{\mathrm{d}V_{\mathrm{d}}}{\mathrm{d}t} = \overbrace{\underbrace{(u_{\mathrm{m}}^{\mathrm{d}} \cdot i_{\mathrm{m}}^{\mathrm{d}} + u_{\mathrm{m}}^{\mathrm{q}} \cdot i_{\mathrm{m}}^{\mathrm{q}})}_{I_{\mathrm{m}}} - \underbrace{(u_{\mathrm{g}}^{\mathrm{d}} \cdot i_{\mathrm{g}}^{\mathrm{d}} + u_{\mathrm{g}}^{\mathrm{q}} \cdot i_{\mathrm{g}}^{\mathrm{q}})}_{I_{\mathrm{g}}}}^{I_{\mathrm{d}}}. \tag{3.13}$$

Therefore, it is the (charging/discharging) current I_{d} that causes the DC-link voltage to change. A controller which takes the difference between the reference and real value of the DC-link voltage should produce a reference of *a current* quantity to the inner controller loop. To this end, a simple PI controller with the following transfer function

$$H_{PI}(S) = \frac{I_{\mathrm{g}}^{*}(S)}{V_{\mathrm{d}}^{*}(S) - V_{\mathrm{d}}(S)} = \frac{K_p \cdot S + K_i}{S} \tag{3.14}$$

can be used as the DC-link controller here[3]. Its output

$$I_{\mathrm{PI[k]}}^{*} = \mathcal{L}^{-1}\big\{H_{PI}(S) \cdot (V_{\mathrm{d}}^{*}(S) - V_{\mathrm{d}}(S))\big\} \tag{3.15}$$

shall contribute to the "active current" since any current consumption from the load side will turn out to be an active power with the exiting DC-link voltage. Given the grid voltage vector aligns with the d-axis of the dq frame, the command current signal $I_{\mathrm{PI[k]}}^{*}$ from the DC-controller should be regarded as $i_{\mathrm{g}}^{\mathrm{d}*}$, which can be directly assigned to the inner loop controller of the VOC schemes.

As for the power regulating based inner loop control schemes (e.g., DPC or deadbeat like DPC which will be introduced in the following sections), the reference active power can be computed by

$$P_{\mathrm{PI[k]}}^{*} = V_{\mathrm{dc[k]}} \cdot \underbrace{\mathcal{L}^{-1}\big\{H_{PI}(S) \cdot (V_{\mathrm{d}}^{*}(S) - V_{\mathrm{d}}(S))\big\}}_{=:I_{\mathrm{g[k]}}^{*}}. \tag{3.16}$$

In most operations, it is the machine side DC-link current I_{m} or the machine side power flow P_{m} that cause the DC-link voltage (2.18) to change. Therefore, taking the estimation

[2]Note that, the phase lock loop (PLL), which is used to obtain position of the grid side voltage vector, is not going to be detailed in this thesis. Since it is already a matured technique in particular for balanced grid. Many publications with regarding to PLL design and tuning can be found in the literature (see e.g., [59]).

[3]Issues such as *instability* and *non-minimum phase* situations requires a careful tuning of the DC-link PI controller parameters (see e.g., [44]).

of the machine side current $\hat{I}_{\mathrm{m}}$ or machine side power $\hat{P}_{\mathrm{m}}$ as feed-forward term to the active current/power references as follows

$$I^*_{\mathrm{n[k]}} = I^*_{\mathrm{PI[k]}} + \hat{I}_{\mathrm{m[k]}}, \tag{3.17}$$

$$P^*_{[k]} = P^*_{\mathrm{PI[k]}} + \hat{P}_{\mathrm{m[k]}}, \tag{3.18}$$

will (greatly) reduce the voltage fluctuations in reality [10, 57, 60].

Based on the descriptions presented in this section, the overall control structure of a FOC-VOC scheme is given in Fig. 3.2.

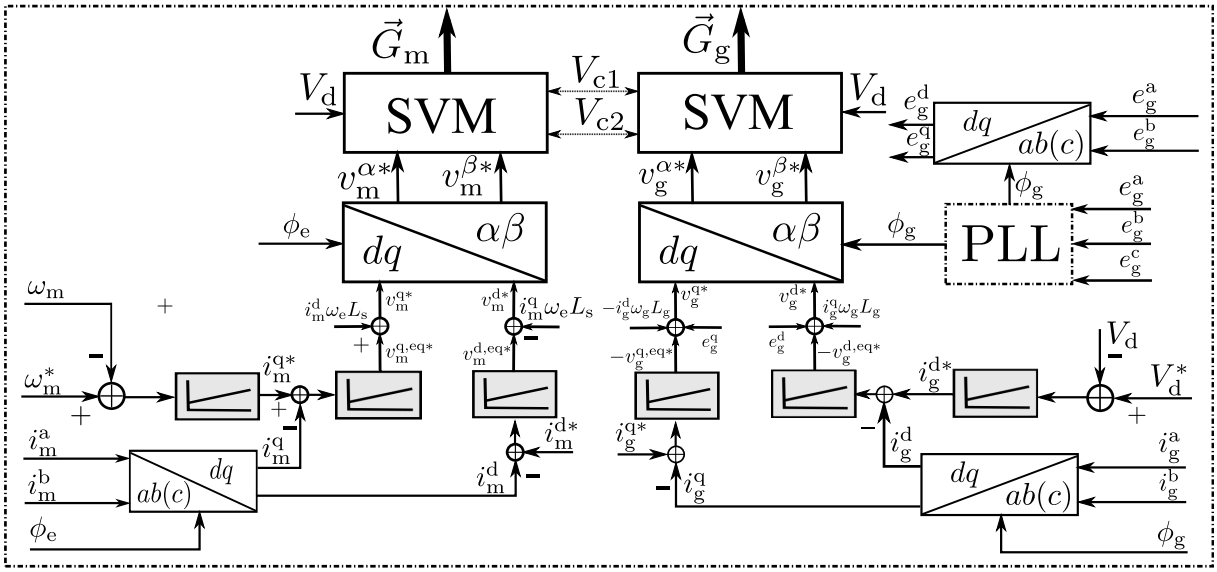

Fig. 3.2: Control scheme of FOC for generator side and VOC for grid side, both with space vector modulator.

3.3 Direct torque and power control with SVM

Different from FOC, DTC-SVM is a more "model based" scheme. In general, there are two variants, namely *torque close loop* and *flux close loop* DTC-SVM [25, 61, 62]. In this section, the mathematical basics of DTC-SVM and its application procedures are firstly re-formulated and analyzed. Since both the techniques of DTC-SVM and DTC with switching table were developed based on the relationship between stator flux and the electromagnetic torque, in the following paragraphs, the fundamentals between the torque and flux position are introduced briefly. For the sake of generality, PMSM(G)s, both with and without structural saliency, are here considered. Then the implementation procedures for non-saliency based PMSM(G), i.e, the main focused type in this work, are introduced in details.

3.3.1 Direct torque control (with SVM) for MSC

3.3.1.1 Mathematical fundamentals for DTC and DTC-SVM [63]

Goal of this section is to derive analytical expressions for the changes of torque and stator flux. First the estimates of actual torque and flux must be found. Estimated stator flux $\hat{\vec{\psi}}_{\mathrm{s}}^{\mathrm{dq}} = (\hat{\psi}_{\mathrm{s}}^{\mathrm{d}}, \hat{\psi}_{\mathrm{s}}^{\mathrm{q}})^{\top}$ and torque $\hat{T}_{\mathrm{e}}$ in the dq-reference frame can be obtained from current measurements as follows

$$\hat{\vec{\psi}}_{\mathrm{s}}^{\mathrm{dq}} = \boldsymbol{L}_{\mathrm{s}}^{\mathrm{dq}} \vec{i}_{\mathrm{m}}^{\mathrm{dq}} + \vec{\psi}_{\mathrm{pm}}^{\mathrm{dq}} \quad \text{and} \quad \hat{T}_{\mathrm{e}} = N_{\mathrm{p}} \big(\hat{\psi}_{\mathrm{s}}^{\mathrm{d}} i_{\mathrm{m}}^{\mathrm{d}} - \hat{\psi}_{\mathrm{s}}^{\mathrm{q}} i_{\mathrm{m}}^{\mathrm{q}} \big). \tag{3.19}$$

Fig. 3.3 illustrates the system variables in different reference frames. Invoking Park's

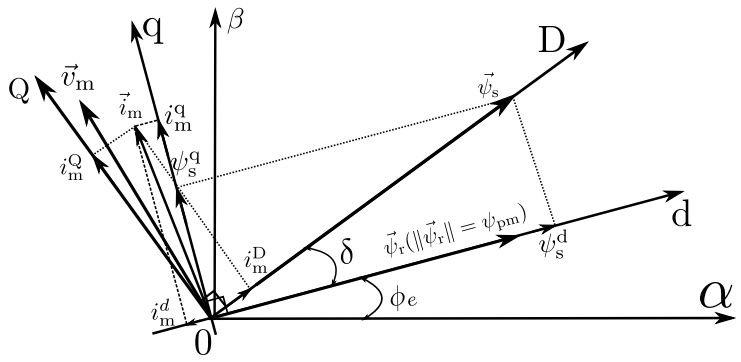

Fig. 3.3: Variables in different reference frames for PMSM(G), where DQ, dq and $\alpha\beta$ are the stator and rotor flux and stationary reference frames, respectively; δ and ϕ_e are the load angle and rotor flux position, respectively, $\vec{\psi}_s, \vec{\psi}_r$ and ψ_{pm} are the stator, rotor and permanent-magnet flux linkages, respectively [63–65]

transformation $\mathbf{T}_{\mathrm{P}}(\delta) := \left[\begin{smallmatrix} \cos(\delta) & \sin(\delta) \\ -\sin(\delta) & \cos(\delta) \end{smallmatrix}\right]$ [10], the variables in stator flux and permanent magnet flux orientation are connected as follows

$$\vec{x}^{DQ} = \mathbf{T}_{\mathrm{P}}^{-1}(\delta) \cdot \vec{x}^{dq} \quad \Longleftrightarrow \quad \vec{x}^{dq} = \mathbf{T}_{\mathrm{P}}(\delta) \cdot \vec{x}^{DQ}. \tag{3.20}$$

Inserting Eq. (3.20) with $\sin(\delta) = \frac{\hat{\psi}_{\mathrm{s}}^{\mathrm{q}}}{\|\hat{\vec{\psi}}_{\mathrm{s}}^{\mathrm{dq}}\|}$ and $\cos(\delta) = \frac{\hat{\psi}_{\mathrm{s}}^{\mathrm{d}}}{\|\hat{\vec{\psi}}_{\mathrm{s}}^{\mathrm{dq}}\|}$ (see Fig. 3.3) into both equations in (3.19) yields

$$\hat{T}_{\mathrm{e}} = N_{\mathrm{p}} \|\hat{\vec{\psi}}_{\mathrm{s}}^{\mathrm{dq}}\| i_{\mathrm{m}}^{\mathrm{Q}} = N_{\mathrm{p}} \sqrt{(\hat{\psi}_{\mathrm{s}}^{\mathrm{d}})^2 + (\hat{\psi}_{\mathrm{s}}^{\mathrm{q}})^2} \cdot i_{\mathrm{m}}^{\mathrm{Q}} \tag{3.21}$$

and

$$\begin{pmatrix} \hat{\psi}_{\mathrm{s}}^{\mathrm{d}} \\ \hat{\psi}_{\mathrm{s}}^{\mathrm{q}} \end{pmatrix} = \mathbf{T}_{\mathrm{P}}^{-1}(\delta) \boldsymbol{L}_{\mathrm{s}}^{\mathrm{dq}} \mathbf{T}_{\mathrm{P}}(\delta) \begin{pmatrix} i_{\mathrm{m}}^{\mathrm{D}} \\ i_{\mathrm{m}}^{\mathrm{Q}} \end{pmatrix} + \mathbf{T}_{\mathrm{P}}^{-1}(\delta) \begin{pmatrix} \psi_{\mathrm{pm}} \\ 0 \end{pmatrix}. \tag{3.22}$$

3.3.1.1.1 For PMSGs without saliency

(i.e., $L_{\mathrm{s}}^{\mathrm{d}} \approx L_{\mathrm{s}}^{\mathrm{q}} =: L_{\mathrm{s}}$ and $\boldsymbol{L}_{\mathrm{s}}^{\mathrm{dq}} = L_{\mathrm{s}} \left[\begin{smallmatrix} 1 & 0 \\ 0 & 1 \end{smallmatrix}\right]$) and, by observing that

$$\begin{bmatrix} L_{\mathrm{s}}^{\mathrm{d}}(\cos(\delta))^2 + L_{\mathrm{s}}^{\mathrm{q}}(\sin(\delta))^2 & -L_{\mathrm{s}}^{\mathrm{d}} \sin(\delta)\cos(\delta) + L_{\mathrm{s}}^{\mathrm{q}} \sin(\delta)\cos(\delta) \\ -L_{\mathrm{s}}^{\mathrm{d}} \sin(\delta)\cos(\delta) + L_{\mathrm{s}}^{\mathrm{q}} \sin(\delta)\cos(\delta) & L_{\mathrm{s}}^{\mathrm{d}}(\cos(\delta))^2 + L_{\mathrm{s}}^{\mathrm{q}}(\sin(\delta))^2 \end{bmatrix} = \mathbf{T}_{\mathrm{P}}^{-1}(\delta) \boldsymbol{L}_{\mathrm{s}}^{\mathrm{dq}} \mathbf{T}_{\mathrm{P}}(\delta) = \begin{bmatrix} L_{\mathrm{s}} & 0 \\ 0 & L_{\mathrm{s}} \end{bmatrix}, \tag{3.23}$$

Equation (3.22) simplifies to [63]

$$\hat{\vec{\psi}}_{\mathrm{s}}^{\mathrm{DQ}} = \begin{pmatrix} \hat{\psi}_{\mathrm{s}}^{\mathrm{D}} \\ \hat{\psi}_{\mathrm{s}}^{\mathrm{Q}} \end{pmatrix} = L_{\mathrm{s}} \begin{pmatrix} i_{\mathrm{m}}^{\mathrm{D}} \\ i_{\mathrm{m}}^{\mathrm{Q}} \end{pmatrix} + \psi_{\mathrm{pm}} \begin{pmatrix} \cos(\delta) \\ \sin(\delta) \end{pmatrix}. \tag{3.24}$$

In case of a perfect stator flux orientation (see Fig. 3.3), the following holds $\hat{\psi}_{\mathrm{s}}^{\mathrm{Q}} \approx \psi_{\mathrm{s}}^{\mathrm{Q}} = 0$. Hence, $i_{\mathrm{m}}^{\mathrm{Q}} \overset{(3.24)}{=} \frac{\psi_{\mathrm{pm}}}{L_{\mathrm{s}}} \sin(\delta)$ and the torque in (3.21) becomes $\hat{T}_{\mathrm{e}} = \frac{N_{\mathrm{p}}}{L_{\mathrm{s}}} \|\hat{\vec{\psi}}_{\mathrm{s}}\| \psi_{\mathrm{pm}} \sin(\delta)$. Assuming that the stator flux magnitude remains constant, the time derivative of the torque is $\frac{\mathrm{d}}{\mathrm{d}t}\hat{T}_{\mathrm{e}} = \frac{N_{\mathrm{p}}}{L_{\mathrm{s}}} \|\hat{\vec{\psi}}_{\mathrm{s}}\| \psi_{\mathrm{pm}} \cos(\delta) \frac{\mathrm{d}}{\mathrm{d}t}\delta$, which, for sampling time $T_{\mathrm{s}} \ll 1s$, in the discrete time (using Euler forward, i.e. $\frac{\mathrm{d}}{\mathrm{d}t}x \approx \frac{x_{[\mathrm{k}+1]} - x_{[\mathrm{k}]}}{T_{\mathrm{s}}} =: \frac{\Delta x_{[\mathrm{k}+1]}}{T_{\mathrm{s}}}$) becomes

$$\Delta\hat{T}_{\mathrm{e}[\mathrm{k}+1]} = \frac{N_{\mathrm{p}}}{L_{\mathrm{s}}} \|\hat{\vec{\psi}}_{\mathrm{s}}^{\mathrm{dq}}\| \psi_{\mathrm{pm}} \cos(\delta_{[\mathrm{k}]}) \cdot \Delta\delta_{[\mathrm{k}]}. \tag{3.25}$$

For small $\delta_{[\mathrm{k}]} \ll 1$ it holds that $\cos(\delta_{[\mathrm{k}]}) \approx 1$. Hence, Equation (3.25) shows that the *torque change* $\Delta\hat{T}_{\mathrm{e}[\mathrm{k}+1]}$ is directly proportional to the *change of the stator flux angle* $\Delta\delta_{[\mathrm{k}]}$.

Next, the expression for the stator flux change will be derived. In the $\alpha\beta$-reference frame, it is given by

$$\frac{\mathrm{d}}{\mathrm{d}t}\vec{\psi}_{\mathrm{s}}^{\alpha\beta} = \vec{v}_{\mathrm{m}}^{\alpha\beta} - R_{\mathrm{s}}\vec{i}_{\mathrm{m}}^{\alpha\beta} \tag{3.26}$$

which becomes

$$\Delta\vec{\psi}_{\mathrm{s}[\mathrm{k}+1]}^{\alpha\beta} := \vec{\psi}_{\mathrm{s}[\mathrm{k}+1]}^{\alpha\beta} - \vec{\psi}_{\mathrm{s}[\mathrm{k}]}^{\alpha\beta} = (\vec{v}_{\mathrm{m}[\mathrm{k}]}^{\alpha\beta} - R_{\mathrm{s}}\vec{i}_{\mathrm{m}[\mathrm{k}]}^{\alpha\beta}) \cdot T_{\mathrm{s}}. \tag{3.27}$$

in discrete time (again using the Euler forward method). In most cases, the stator resistor R_{s} is quite small (i.e. $R_{\mathrm{s}} \approx 0$), hence, the flux change is approximately given by $\Delta\vec{\psi}_{\mathrm{s}[\mathrm{k}+1]}^{\alpha\beta} \approx \vec{v}_{\mathrm{m}[\mathrm{k}]}^{\alpha\beta} \cdot T_{\mathrm{s}}$. Concluding, for direct torque control (either with or without modulator), the key expressions are found by equations (3.25) and (3.27). Eq. (3.25) illustrates how the torque and (3.27) how the flux can be changed by adequately applied voltages $\vec{v}_{\mathrm{m}[\mathrm{k}]}^{\alpha\beta}$ which in combination allow for direct torque control. Note that the (electrical) time constant of the *stator flux* is *smaller* than the time constant of the *rotor flux* or the angle δ (associated to the mechanical time constant). In other words, "direct torque control" is nothing else than "direct flux control" which allows to directly control magnitude and angle of the stator flux [63].

3.3.1.1.2 PMSM with pole saliency, i.e., $L_{\mathrm{s}}^{\mathrm{d}} \neq L_{\mathrm{s}}^{\mathrm{q}}$. Solving (3.22) with $\hat{\psi}_{\mathrm{s}}^{\mathrm{Q}} = 0$ one obtains

$$i_{\mathrm{m}}^{\mathrm{D}} = \frac{2\psi_{\mathrm{pm}} \sin(\delta) - [(L_{\mathrm{s}}^{\mathrm{d}} + L_{\mathrm{s}}^{\mathrm{q}}) + (L_{\mathrm{s}}^{\mathrm{d}} - L_{\mathrm{s}}^{\mathrm{q}}) \cos(2\delta)]}{(L_{\mathrm{s}}^{\mathrm{d}} - L_{\mathrm{s}}^{\mathrm{q}}) \sin(2\delta)}. \tag{3.28}$$

Substituting (3.28) into (3.22), yields

$$i_{\mathrm{m}}^{\mathrm{Q}} = \frac{1}{2L_{\mathrm{s}}^{\mathrm{d}}L_{\mathrm{s}}^{\mathrm{q}}} \Big[2\psi_{\mathrm{pm}} L_{\mathrm{s}}^{\mathrm{q}} \sin(\delta) - \|\hat{\vec{\psi}}_{\mathrm{s}}\| (L_{\mathrm{s}}^{\mathrm{d}} - L_{\mathrm{s}}^{\mathrm{q}}) \sin(2\delta) \Big]. \tag{3.29}$$

Therefore,

$$\hat{T}_\mathrm{e} = \frac{3N_\mathrm{p}\|\hat{\vec{\psi}}_\mathrm{s}\|}{4L_\mathrm{s}^\mathrm{d}L_\mathrm{s}^\mathrm{q}}\Big[2\psi_\mathrm{pm}L_\mathrm{s}^\mathrm{q}\sin(\delta) - \|\hat{\vec{\psi}}_\mathrm{s}\|(L_\mathrm{s}^\mathrm{d} - L_\mathrm{s}^\mathrm{q})\sin(2\delta)\Big]. \tag{3.30}$$

Note that, only for all $\frac{\mathrm{d}T_\mathrm{e}}{\mathrm{d}t}$ a positive $\frac{\mathrm{d}\delta}{\mathrm{d}t}$ is kept, the torque can be consistently controlled by changing the flux angle. This condition requires [64, 65]

$$\|\vec{\psi}_s\| < \frac{L_\mathrm{s}^\mathrm{q}}{L_\mathrm{s}^\mathrm{d} - L_\mathrm{s}^\mathrm{q}}\psi_\mathrm{pm}. \tag{3.31}$$

Otherwise, a negative derivative of the torque near zero-crossing of δ appears, which means the torque cannot be consistently controlled by changing the flux angle without changing the flux magnitude. As a conclusion, for PMSM with saliency, $\|\vec{\psi}_s\| < \frac{L_\mathrm{s}^\mathrm{q}}{L_\mathrm{s}^\mathrm{d}-L_\mathrm{s}^\mathrm{q}}\psi_\mathrm{pm}$ shall be guaranteed to apply DTC.

In our case, a surface mounted PMSG is used, i.e., $L_\mathrm{s}^\mathrm{d} \approx L_\mathrm{s}^\mathrm{q} = L_\mathrm{s}$, both DTC and DTC-SVM can be applied and the torque control can be achieved by directly controlling the position of the stator flux through proper voltage vector. In the following sections, the implementation procedures of DTC-SVM is firstly introduced (and the DTC with switching table is introduced in the next section) for the machine side control.

3.3.1.2 Control implementation of DTC-SVM

Based on the key equations (3.25) and (3.27), the reference voltages $\vec{v}_\mathrm{m[k]}^{\alpha\beta *}$ must be computed. To do so, the estimated stator flux and its angle are required. The stator flux estimate $\hat{\vec{\psi}}_\mathrm{s[k]}^{\alpha\beta} = (\hat{\psi}_\mathrm{s[k]}^{\beta}, \hat{\psi}_\mathrm{s[k]}^{\alpha})^\top$ can directly be estimated via Eq. (3.27) in the $\alpha\beta$-reference frame. Hence, its angle is obtained for each sampling instant k by

$$\angle\hat{\psi}_\mathrm{s[k]} = \mathrm{atan2}(\hat{\psi}_\mathrm{s[k]}^{\beta}, \hat{\psi}_\mathrm{s[k]}^{\alpha}). \tag{3.32}$$

For any torque difference between reference T_e^* (generated by the outer speed control loop) and actual (estimated) value $\hat{T}_\mathrm{e}$ (see Fig. 3.4), the torque controller will output an *angle command* $\delta_\mathrm{[k]}^*(\angle\hat{\psi}_\mathrm{s})$ (reference angle, see Fig. 3.4) which, with (3.32), allows to set the new (reference) stator flux angle to

$$\angle\psi_\mathrm{s[k]}^* = \angle\hat{\psi}_\mathrm{s[k]} + \delta_\mathrm{[k]}^*(\angle\hat{\psi}_\mathrm{s}). \tag{3.33}$$

Therefore, the reference stator flux can be computed by

$$\vec{\psi}_\mathrm{s[k+1]}^* = \Big(\|\psi_\mathrm{s}^*\|\cos(\angle\psi_\mathrm{s[k]}^*),\ \|\psi_\mathrm{s}^*\|\sin(\angle\psi_\mathrm{s[k]}^*)\Big)^\top \tag{3.34}$$

where $\|\psi_\mathrm{s}^*\|$ is the reference stator flux magnitude which is set slightly higher than the permanent-magnet flux[4] ψ_pm. Finally, based on Eq. (3.26), one can calculate the reference voltage

$$\vec{v}_\mathrm{m[k]}^{\alpha\beta *} = (\vec{\psi}_\mathrm{s[k]}^* - \hat{\vec{\psi}}_\mathrm{s[k]}^{\alpha\beta})/T_\mathrm{s} + R_\mathrm{s}\vec{i}_\mathrm{m[k]}^{\alpha\beta}, \tag{3.35}$$

which is then assigned to a SVM to generate the corresponding switching sequences.

[4] The choice of this parameter will affect the current magnitude in steady-state: A too high or too low choice will lead to (i) very high ripples of the currents and the torque at zero and high load (which, both, is not desirable [64, 65]). In this paper, it is chosen as $\|\psi_\mathrm{s}^*\| = 1.02\psi_\mathrm{pm}$ (102%).

3.3.2 Direct power control with SVM for GSC

Invoking the instantaneous power theory [33,34], the grid side apparent power is given by

$$\vec{S} = (P,\ Q)^\top = \Big((\vec{e}_{\rm g}^{\rm dq})^\top \vec{i}_{\rm g}^{\rm dq},\ (\vec{e}_{\rm g}^{\rm dq})^\top \boldsymbol{J} \vec{i}_{\rm g}^{\rm dq} \Big)^\top,$$

where P and Q are active and reactive power at the point of common coupling, respectively. For $\frac{\rm d}{{\rm d}t}P = (\vec{e}_{\rm g}^{\rm dq})^\top \frac{\rm d}{{\rm d}t}\vec{i}_{\rm g}^{\rm dq}$ and $\frac{\rm d}{{\rm d}t}Q = (\vec{e}_{\rm g}^{\rm dq})^\top \boldsymbol{J} \frac{\rm d}{{\rm d}t}\vec{i}_{\rm g}^{\rm dq}$ (assuming $\vec{e}_{\rm g}^{\rm dq} = (\hat{e}_{\rm g},\, 0)$ is constant, i.e. $e_{\rm g}^{\rm d} = \hat{e}_{\rm g} > 0$), the dynamics of active and reactive power in the dq-reference frame, recalling the equations (2.48) given in Ch. 2, are

$$\left.\begin{aligned} \tfrac{\rm d}{{\rm d}t}P &= \tfrac{1}{L_{\rm g}}\Big(-R_{\rm g}P + v_{\rm g}^{\rm d}\hat{e}_{\rm g} - \omega_g L_{\rm g} Q + \hat{e}_{\rm g}^2 \Big) \\ \tfrac{\rm d}{{\rm d}t}Q &= \tfrac{1}{L_{\rm g}}\Big(-R_{\rm g}Q - v_{\rm g}^{\rm q}\hat{e}_{\rm g} + \omega_g L_{\rm g} P \Big). \end{aligned}\right\} \tag{3.36}$$

Introducing the reference voltages (see Fig. 3.4) as follows

$$\left.\begin{aligned} v_{\rm g}^{\rm d*} &= \tfrac{1}{\hat{e}_{\rm g}}\big(\omega_{\rm g} L_{\rm g} Q - \hat{e}_{\rm g}^2 + v_{\rm g}^{\rm d,eq*}\big), \\ v_{\rm g}^{\rm q*} &= \tfrac{1}{\hat{e}_{\rm g}}\big(-\omega_{\rm g} L_{\rm g} Q - v_{\rm g}^{\rm d,eq*}\big) \end{aligned}\right\} \tag{3.37}$$

allows to compensate for the cross-coupling/disturbance terms in the power dynamics (3.36). For active $P^\star$ and reactive $Q^\star$ power references, the used PI controllers with proportional gain K_p and time constant T_n have the transfer function(s)

$$G_{PI}(s) = \tfrac{v_{\rm g}^{\rm d,eq*}(s)}{P^\star(s) - P(s)} = \tfrac{v_{\rm g}^{\rm q,eq*}(s)}{Q^\star(s) - Q(s)} = K_p\big(\tfrac{1+sT_n}{T_g s}\big) \tag{3.38}$$

and are designed for the (identical and decoupled) active and reactive power dynamics transfer functions[5]

$$G_{P/Q}(s) = \frac{P(s)}{v_{\rm g}^{\rm d,eq*}(s)} = \frac{Q(s)}{v_{\rm g}^{\rm q,eq*}(s)} = \frac{\frac{\hat{e}_{\rm g}}{L_{\rm g}}}{1 + s\frac{L_{\rm g}}{R_{\rm g}}}. \tag{3.39}$$

The PI controllers (3.38) can be tuned according to the "Magnitude Optimum" [63] with $K_p = \frac{1}{2} L_{\rm g} f_{\rm sw}$ (with switching frequency $f_{\rm sw}$) and $T_g = L_{\rm g}/R_{\rm g}$.

Finally, the reference voltages $v_{\rm g}^{\rm q*}$ & $v_{\rm g}^{\rm d*}$ are transformed to the $\alpha\beta$-reference frame and send to the modulator (see Fig. 3.4).

Remark 1 (Comments to VOC-SVM and DPC-SVM) *VOC-SVM and DPC-SVM are both linear controllers with modulator to deal with the grid side converter control. There are certain similarities and also some differences between these two techniques.*

*a. The **similarities** are: both are developed in the dq frame, and use linear (PI) controllers with modulator.*

[5] It is assumed that the cross-coupling/disturbance terms are perfectly compensated for [46,58].

*b. The main **difference** is: VOC is developed based on the grid side current dynamics (i.e., Eq. (2.45)) while DPC is originated from the power dynamics (i.e., Eq. (2.48)).*

c. Their relationship: it is easy to find once the grid voltage vector is (perfectly) oriented and grid side is balanced and symmetrical, i.e., after orientation, $e_g^d = A, e_g^q = 0$, then $P = i_g^d \cdot e_g^d, Q = -i_g^q \cdot e_g^d$. Then fundamental equation (3.36) (the basis for DPC-SVM) will turn out to be (3.9) (i.e., the basis for VOC-SVM) .

As is already introduced in Sec. 3.2.2, the active power reference is generated by the DC-link controller. So far the modulator based DTC and DPC control schemes are introduced and an overview of this control is given in Fig. 3.4.

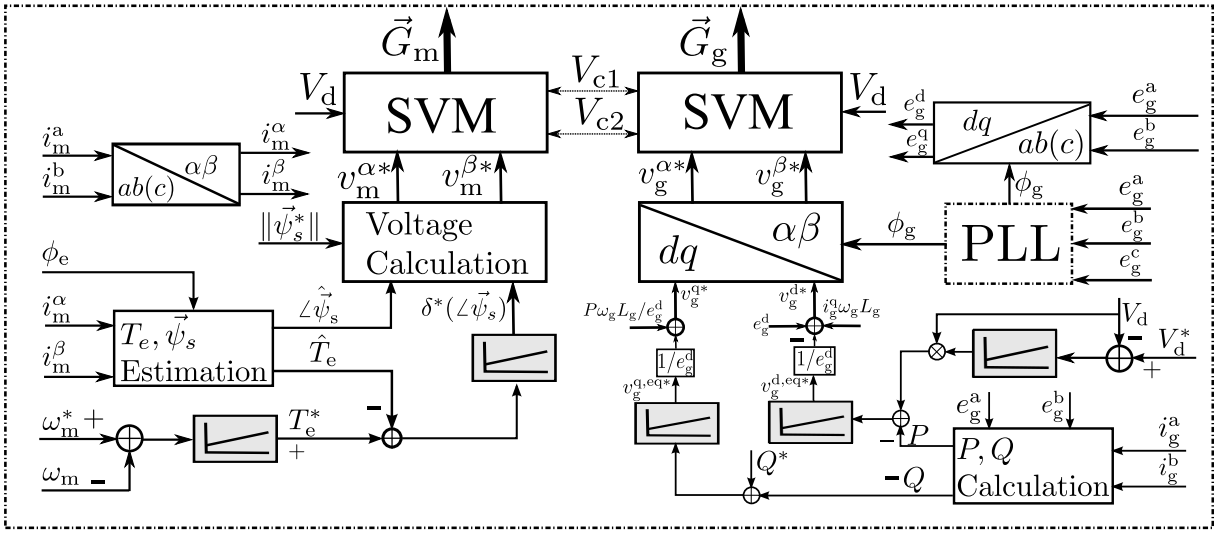

Fig. 3.4: Control scheme of DTC-SVM for generator side and DPC-SVM for grid side.

3.4 Deadbeat control with SVM

Deadbeat control aims to manipulate the system to fully reach certain references in a finite number of control intervals by assigning to the plant (e.g., electrical power converter) some control input (e.g., voltage references) calculated using the discrete system model. *However, whether the references are reachable or not, highly depends on the reach-ability of the system (i.e, the rank of the system reachability matrix); for the systems, where* $r = n = m$, with $r, n, m \in \mathbb{N}$ being the system reach-ability matrix rank, the numbers of state and control inputs, respectively, the references of the state can be reached in *one step* and the solution of the control input is *unique*[6] [60, 66]. It is a fully model based linear control scheme and due to a one-step state prediction is required, in some publications it is also referred to as *predictive control* in the power electronics community (see e.g., [8, 60]

[6] A close look at the system models (See equations (3.40) (3.41)) will yield that for both the machine and grid side system $r = n = m$ holds true, i.e., the references of the state can be reached in *one step* [66, Chp:5] and the solution of the control input is *unique*.

and the reference therein). Moreover, since the actuating signals are continuous, it can also be put into the *continuous-set model predictive control* class[7]. In the following sections, both deadbeat (torque) control for machine side and deadbeat (power) control for the grid side are introduced.

3.4.1 Deadbeat (torque) control for machine side

The propose of the deadbeat torque controller is to manipulate the torque to reach its reference until the end of (one or several) sampling interval(s). The key process is to take the references into the *system model* and solve the corresponding reference voltages to assign to the converter. For the sake of completeness and to ease the understanding of this section, the generator model in discrete format is re-visited as follows

$$\vec{i}^{\,\mathrm{dq}}_{\mathrm{m[k+1]}} = \underbrace{\begin{bmatrix} 1-\frac{T_\mathrm{s}R_\mathrm{s}}{L_\mathrm{s}} & T_\mathrm{s}\omega_{\mathrm{e[k]}} \\ -T_\mathrm{s}\omega_{\mathrm{e[k]}} & 1-\frac{T_\mathrm{s}R_\mathrm{s}}{L_\mathrm{s}} \end{bmatrix}}_{=:\mathbf{A}_{\mathrm{m[k]}}} \vec{i}^{\,dq}_{\mathrm{m[k]}} + \underbrace{\begin{bmatrix} \frac{T_\mathrm{s}}{L_\mathrm{s}} & 0 \\ 0 & \frac{T_\mathrm{s}}{L_\mathrm{s}} \end{bmatrix}}_{=:\mathbf{B}_\mathrm{m}} \vec{v}^{\,dq}_{\mathrm{m[k]}} + \underbrace{\begin{pmatrix} 0 \\ -\frac{T_\mathrm{s}\psi_\mathrm{pm}}{L_\mathrm{s}}\omega_{\mathrm{e[k]}} \end{pmatrix}}_{=:\mathbf{H}_{\mathrm{m[k]}}}, \tag{3.40}$$

$$T_{\mathrm{e[k]}} = N_\mathrm{p}\psi_\mathrm{pm} i^{q}_{\mathrm{m[k]}}, \tag{3.41}$$

In the analogy to DTC or DTC-SVM, the reference torque $T^*_{\mathrm{e[k+1]}}$ comes from the speed controller and the reference current $i^{\mathrm{d}*}_{\mathrm{m[k+1]}} = 0$ is set for maximum torque per ampere (MTPA)[8]. Therefore, taking the torque equation of (3.41) into consideration, one obtains the reference current as follows

$$\vec{i}^{\,\mathrm{dq}*}_{\mathrm{m[k+1]}} = \vec{i}^{\,\mathrm{dq}}_{\mathrm{m[k+1]}} = \left(i^{\mathrm{d}*}_{\mathrm{m[k+1]}},\ \frac{T^*_{\mathrm{e[k+1]}}}{N_\mathrm{p}\psi_\mathrm{pm}} \right)^\top. \tag{3.42}$$

Following the concept of deadbeat control, i.e., the reference voltage shall be computed such that dead-beat torque control is (approximately) achieved using the system model. Therefore, we may insert (3.42) into (3.40) to compute the *machine-side reference voltage vector* as

$$\vec{v}^{\,\mathrm{dq}*}_{\mathrm{m[k]}} = \mathbf{B}_\mathrm{m}^{-1}\left[\vec{i}^{\,dq*}_{\mathrm{m[k+1]}} - \mathbf{A}_{\mathrm{m[k]}}\vec{i}^{\,dq}_{\mathrm{m[k]}} - \mathbf{H}_{\mathrm{m[k]}}\right]. \tag{3.43}$$

The voltage vector to assign to a SVM can be calculated as $\vec{v}^{\,\alpha\beta*}_{\mathrm{m[k]}} = \mathbf{T}_\mathrm{P}^{-1}(\phi_\mathrm{e})\vec{v}^{\,\mathrm{dq}*}_{\mathrm{m[k]}}$. Applying $\vec{v}^{\,\alpha\beta*}_{\mathrm{m[k]}}$ would (ideally) control the current $\vec{i}^{\,\mathrm{dq}}_{\mathrm{m[k+1]}}$ to reach its reference $\vec{i}^{\,\mathrm{dq}*}_{\mathrm{m[k+1]}}$ in the next sampling interval, thereby a dead-beat torque control is achieved, i.e., $T_{\mathrm{e[k+1]}} = T^*_{\mathrm{e[k]}}$. An overview of this method is shown in the left side of Fig. 3.5.

[7] Deadbeat control can be regarded as a one-step predictive control of which a unconstrained cost-function is used. Its relationship with one-step direct (FCS) model predictive control is formulated in [66, Chp:5].

[8] Here $L^\mathrm{d}_\mathrm{s} = L^\mathrm{q}_\mathrm{s} = L_\mathrm{s}$ is considered. Otherwise, $i^{\mathrm{d}*}_{\mathrm{m[k+1]}} = \frac{1}{2}\left(\frac{\psi_\mathrm{pm}}{L^\mathrm{d}_\mathrm{s}-L^\mathrm{q}_\mathrm{s}} + \sqrt{\frac{\psi^2_\mathrm{pm}}{4(L^\mathrm{d}_\mathrm{s}-L^\mathrm{q}_\mathrm{s})^2} + 2(i^*_\mathrm{r})^2}\right)$, $i^{\mathrm{q}*}_{\mathrm{m[k+1]}} = \mathrm{sign}(i^*_\mathrm{r})\sqrt{(i^*_\mathrm{r})^2 - (i^{\mathrm{d}*}_{\mathrm{m[k+1]}})^2}$, following the MTPA condition of $i^\mathrm{d}_\mathrm{m} + \frac{L^\mathrm{d}_\mathrm{s}-L^\mathrm{q}_\mathrm{s}}{\psi_\mathrm{pm}}\left((i^\mathrm{d}_\mathrm{m})^2 - (i^\mathrm{q}_\mathrm{m})^2\right) = 0$, where $i^*_\mathrm{r}(\leq I_n)$ is the reference generated by a out loop controller, I_n is the rated value of the plant [67].

3.4.2 Deadbeat (power) control for grid side

To achieve deadbeat control for the grid side, in principle the system model both in dq and $\alpha\beta$ frames can be used, i.e., there are two types of the controller design formats: i) deadbeat power control in $\alpha\beta$ frame, and ii) deadbeat power control in dq frame. Both are introduced in the following sections. For the sake of completeness and to ease the reading, the discrete time models which have already been introduced in Chp. 2, are re-visited.

3.4.2.1 Deadbeat (power) control in $\alpha\beta$ frame

To achieve a deadbeat power control performance for the grid side, $\left(P_{[\mathrm{k+1}]}, Q_{[\mathrm{k+1}]}\right)^\top := \left(P^*_{[\mathrm{k+1}]}, Q^*_{[\mathrm{k+1}]}\right)^\top$ is set in Eq. (2.50). Thus the grid side reference voltage vector as

$$\begin{pmatrix} v^{\alpha*}_{\mathrm{g[k]}} \\ v^{\beta*}_{\mathrm{g[k]}} \end{pmatrix} = \begin{pmatrix} e^{\alpha}_{\mathrm{g[k]}} \\ e^{\beta}_{\mathrm{g[k]}} \end{pmatrix} - \frac{L_\mathrm{g}}{T_\mathrm{s}\|\vec{e}^{\,\alpha\beta}_{\mathrm{g[k]}}\|^2} \begin{bmatrix} e^{\alpha}_{\mathrm{g[k]}} & e^{\beta}_{\mathrm{g[k]}} \\ e^{\beta}_{\mathrm{g[k]}} & -e^{\alpha}_{\mathrm{g[k]}} \end{bmatrix} \begin{pmatrix} P^*_{[\mathrm{k+1}]} - P_{[\mathrm{k}]} + \frac{T_\mathrm{s}R_\mathrm{g}}{L_\mathrm{g}} P_{[\mathrm{k}]} + \omega_\mathrm{g} T_\mathrm{s} Q_{[\mathrm{k}]} \\ Q^*_{[\mathrm{k+1}]} - Q_{[\mathrm{k}]} + \frac{T_\mathrm{s}R_\mathrm{g}}{L_\mathrm{g}} Q_{[\mathrm{k}]} - \omega_\mathrm{g} T_\mathrm{s} P_{[\mathrm{k}]} \end{pmatrix}. \quad (3.44)$$

Applying $\vec{v}^{\,\alpha\beta*}_{\mathrm{g[k]}}$ would (ideally) control the power to reach its reference at the end of the current sampling interval, thereby achieving a dead-beat power control in $\alpha\beta$ frame.

3.4.2.2 Deadbeat (power) control in dq frame

According to the instant power theory, the active (P) and reactive power (Q) of the grid-side can be expressed in the dq frame as

$$\begin{pmatrix} P_{[\mathrm{k}]} \\ Q_{[\mathrm{k}]} \end{pmatrix} = \begin{bmatrix} e^{\mathrm{d}}_{\mathrm{g[k]}} & e^{\mathrm{q}}_{\mathrm{g[k]}} \\ e^{\mathrm{q}}_{\mathrm{g[k]}} & -e^{\mathrm{d}}_{\mathrm{g[k]}} \end{bmatrix} \begin{pmatrix} i^{\mathrm{d}}_{\mathrm{g[k]}} \\ i^{\mathrm{q}}_{\mathrm{g[k]}} \end{pmatrix}. \quad (3.45)$$

In practice the filter self-resistance is quite small and therefore can be neglected. Taking this into consideration and re-arranging (3.45), yields the following

$$\begin{pmatrix} i^{\mathrm{d}}_{\mathrm{g[k+1]}} - i^{\mathrm{d}}_{\mathrm{g[k]}} \\ i^{\mathrm{q}}_{\mathrm{g[k+1]}} - i^{\mathrm{q}}_{\mathrm{g[k]}} \end{pmatrix} = \frac{T_\mathrm{s}}{L_\mathrm{g}} \begin{pmatrix} e^{\mathrm{d}}_{\mathrm{g[k]}} \\ e^{\mathrm{q}}_{\mathrm{g[k]}} \end{pmatrix} - \frac{T_\mathrm{s}}{L_\mathrm{g}} \underbrace{\begin{pmatrix} v^{\mathrm{d}}_{\mathrm{g[k]}} - \omega_\mathrm{g} L_\mathrm{g} i^{\mathrm{q}}_{\mathrm{g[k]}} \\ v^{\mathrm{q}}_{\mathrm{g[k]}} + \omega_\mathrm{g} L_\mathrm{g} i^{\mathrm{d}}_{\mathrm{g[k]}} \end{pmatrix}}_{:=\vec{v}^{\mathrm{dq,eq}}_{\mathrm{g[k]}} = [v^{\mathrm{d,eq}}_{\mathrm{g[k]}}, v^{\mathrm{q,eq}}_{\mathrm{g[k]}}]^T}, \quad (3.46)$$

where T_s is the sampling interval in the domain of tens of μs, and compared to the system constant or the fundamental period of the grid-side voltage, it is considerably small[9], hence $e^{\mathrm{d}}_{\mathrm{g[k+1]}} \approx e^{\mathrm{d}}_{\mathrm{g[k]}}$ and $e^{\mathrm{q}}_{\mathrm{g[k+1]}} \approx e^{\mathrm{q}}_{\mathrm{g[k]}}$. Therefore, Equation (3.45) can be reformulated as

$$\begin{pmatrix} P_{[\mathrm{k+1}]} - P_{[\mathrm{k}]} \\ Q_{[\mathrm{k+1}]} - Q_{[\mathrm{k}]} \end{pmatrix} = \begin{bmatrix} e^{\mathrm{d}}_{\mathrm{g[k]}} & e^{\mathrm{q}}_{\mathrm{g[k]}} \\ e^{\mathrm{q}}_{\mathrm{g[k]}} & -e^{\mathrm{d}}_{\mathrm{g[k]}} \end{bmatrix} \begin{pmatrix} i^{\mathrm{d}}_{\mathrm{g[k+1]}} - i^{\mathrm{d}}_{\mathrm{g[k]}} \\ i^{\mathrm{q}}_{\mathrm{g[k+1]}} - i^{\mathrm{q}}_{\mathrm{g[k]}} \end{pmatrix} \quad (3.47)$$

[9] Otherwise a simple rotation compensation can be added.

To achieve the deadbeat power control performance, i.e., the active and reactive power at the beginning of sampling interval $[\mathrm{k}+1]$ reach the reference values of $P^*_{[\mathrm{k}]}$ and $Q^*_{[\mathrm{k}]}$. Therefore substituting (3.46) into (3.47), and replacing $P_{[\mathrm{k+1}]}, Q_{[\mathrm{k+1}]}$ with $P^*_{[\mathrm{k}]}, Q^*_{[\mathrm{k}]}$, we get the *equivalent reference voltages* as

$$\vec{v}^{\,\mathrm{dq,eq*}}_{\mathrm{g[k]}} = \begin{pmatrix} v^{\mathrm{d,eq*}}_{\mathrm{g[k]}} \\ v^{\mathrm{q,eq*}}_{\mathrm{g[k]}} \end{pmatrix} = \begin{pmatrix} e^{\mathrm{d}}_{\mathrm{g[k]}} \\ e^{\mathrm{q}}_{\mathrm{g[k]}} \end{pmatrix} - \frac{L_\mathrm{g}}{T_\mathrm{s}\big((e^{\mathrm{d}}_{\mathrm{g[k]}})^2 + (e^{\mathrm{q}}_{\mathrm{g[k]}})^2\big)} \begin{bmatrix} e^{\mathrm{d}}_{\mathrm{g[k]}} & e^{\mathrm{q}}_{\mathrm{g[k]}} \\ e^{\mathrm{q}}_{\mathrm{g[k]}} & -e^{\mathrm{d}}_{\mathrm{g[k]}} \end{bmatrix} \begin{pmatrix} P^*_{[\mathrm{k}]} - P_{[\mathrm{k}]} \\ Q^*_{[\mathrm{k}]} - Q_{[\mathrm{k}]} \end{pmatrix}. \quad (3.48)$$

Note that, assuming the adopted PLL works properly, i.e., the grid-side voltage vector alines correctly to d-axis (i.e., $e^{\mathrm{q}}_{\mathrm{g}} = \|\vec{e}^{\,\mathrm{abc}}_{\mathrm{g}}\|, e^{\mathrm{q}}_{\mathrm{g}} = 0$)[10]. Therefore, Equation (3.48) can be simplified as

$$\vec{v}^{\,\mathrm{dq,eq*}}_{\mathrm{g[k]}} = \begin{pmatrix} v^{\mathrm{d,eq*}}_{\mathrm{g[k]}} \\ v^{\mathrm{q,eq*}}_{\mathrm{g[k]}} \end{pmatrix} = \begin{pmatrix} e^{\mathrm{d}}_{\mathrm{g[k]}} \\ 0 \end{pmatrix} - \frac{L_\mathrm{g}}{T_\mathrm{s}(e^{\mathrm{d}}_{\mathrm{g[k]}})^2} \begin{pmatrix} e^{\mathrm{d}}_{\mathrm{g[k]}}\big(P^*_{[\mathrm{k}]} - P_{[\mathrm{k}]}\big) \\ -e^{\mathrm{d}}_{\mathrm{g[k]}}\big(Q^*_{[\mathrm{k}]} - Q_{[\mathrm{k}]}\big) \end{pmatrix}. \quad (3.49)$$

So the reference voltage vector in dq frame, by considering the term $\vec{v}^{\,\mathrm{dq,eq*}}_{\mathrm{g[k]}}$ in (3.46), can be obtained as

$$\begin{pmatrix} v^{\mathrm{d*}}_{\mathrm{g[k]}} \\ v^{\mathrm{q*}}_{\mathrm{g[k]}} \end{pmatrix} = \begin{pmatrix} v^{\mathrm{d,eq*}}_{\mathrm{g[k]}} + \omega_\mathrm{g} L_\mathrm{g} i^{\mathrm{q}}_{\mathrm{g[k]}} \\ v^{\mathrm{q,eq*}}_{\mathrm{g[k]}} - \omega_\mathrm{g} L_\mathrm{g} i^{\mathrm{d}}_{\mathrm{g[k]}} \end{pmatrix}. \quad (3.50)$$

The voltage vector to assign to a SVM is computed by using $\vec{v}^{\,\alpha\beta\,*}_{\mathrm{g[k]}} = \mathbf{T}^{-1}_{\mathrm{P}}(\phi_g)\vec{v}^{\,dq\,*}_{\mathrm{g[k]}}$. Similarly, applying $\vec{v}^{\,\alpha\beta\mathrm{*}}_{\mathrm{g[k]}}$ would (ideally) control the power to reach its reference at the end of the current sampling interval, thereby achieving a dead-beat power control in dq frame.

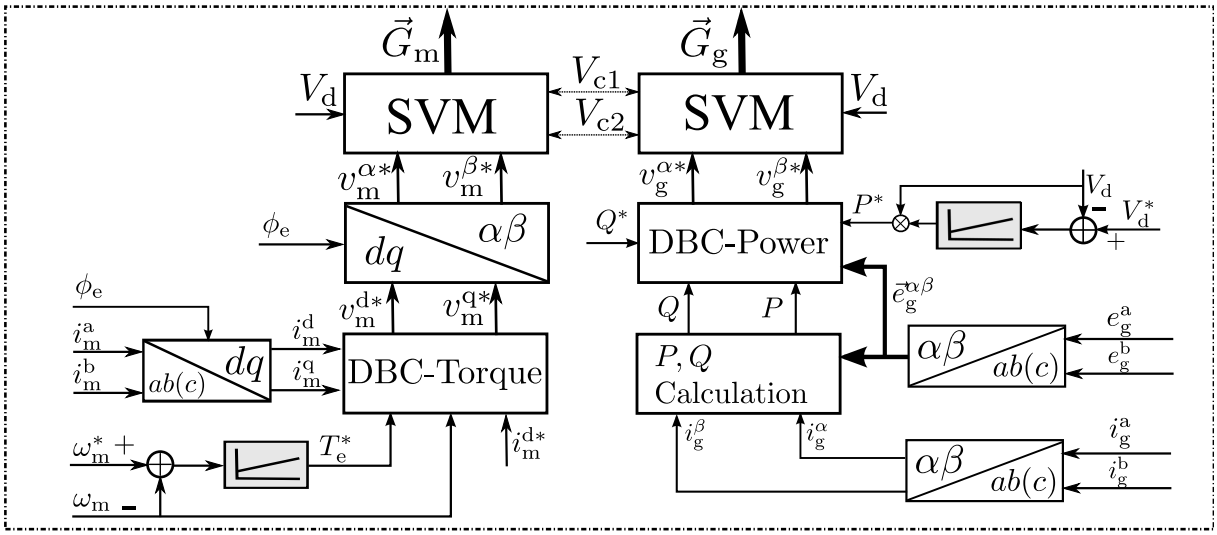

Fig. 3.5: Control scheme of deadbeat torque control for generator side and deadbeat power control for grid side.

The top level control structure of deadbeat control for generator and grid side is given in Fig. 3.5. Note that, the grid side controller is designed in $\alpha\beta$ frame for the experimental evaluation due to its simplicity in the FPGA realization.

[10]The grid side voltage can be also aligned to q-axis, in this case, $e^{\mathrm{d}}_{\mathrm{g}} = 0$, and $i^{\mathrm{d}}_{\mathrm{g}}$ is used to control the reactive power.

3.5 Direct torque and power control with switching table

3.5.1 Direct torque control for MSC

Direct torque control (DTC) does not apply in every case to a PMSM(G) without a proper setting of the reference flux magnitude (see Sec. 3.3). However, for PMSM(G) with surface mounted structure, DTC can be applied. The basic principle for DTC is Equation (3.25) and (3.27). After rearranging these two equations, one obtains the following

$$\Delta\hat{T}_{\mathrm{e[k+1]}} = \hat{T}_{\mathrm{e[k+1]}} - \hat{T}_{\mathrm{e[k+1]}} \approx \tfrac{N_\mathrm{P}}{L_\mathrm{s}} \|\vec{\psi}_\mathrm{s}\| \cdot \psi_\mathrm{pm} \cdot \Delta\delta, \tag{3.51a}$$

$$\Delta\vec{\psi}^{\alpha\beta}_{\mathrm{s[k]}} = \vec{\psi}^{\alpha\beta}_{\mathrm{s[k+1]}} - \vec{\psi}^{\alpha\beta}_{\mathrm{s[k]}} = \vec{v}^{\alpha\beta}_{\mathrm{m[k]}} T_\mathrm{s} - \underbrace{T_\mathrm{s} R_\mathrm{s} \vec{i}^{\alpha\beta}_{\mathrm{m[k]}}}_{:\approx 0} \approx \vec{v}^{\alpha\beta}_{\mathrm{m[k]}} \cdot T_\mathrm{s}. \tag{3.51b}$$

The electrical time constant for the *stator flux* to change is much smaller than the mechanical time constant for the *rotor flux* to change. Therefore, the so-called "direct torque control" is realized by "direct flux control" concept, i.e., to directly control the magnitude and position of the stator flux through a proper voltage vector for a control interval of T_s. Due to the structure and control target difference of two- and three-level power converter driven systems, DTC techniques shall be designed differently. To apply the classical DTC scheme for a two level power converter driven PMSG systems, the flux and torque control are the main focus and only 8 switching vectors[11] are available. While for a three-level NPC power converter driven PMSG system, besides the torque and flux control, the DC-link voltage balancing control shall also be taken into consideration and 27 vectors (with different magnitudes) are available. In the following sections both the classical DTC for two- and three-level machine side converters are re-visited.

3.5.1.1 DTC for two-level converter driven PMSG

For two-level power converters, classical DTC directly selects the optimal switching sequence from a predefined witching table by indexing (i) the flux location information and (ii) hysteresis controller output signals (for both torque and flux). The hysteresis controllers are usually defined as [63]

$$H^{\mathrm{2L}}_{\psi} = \begin{cases} 1, & \Delta\vec{\psi}_\mathrm{s} \in [W_\psi, +\infty) \\ -1, & \Delta\vec{\psi}_\mathrm{s} \in (-\infty, -W_\psi) \end{cases}, \quad H^{\mathrm{2L}}_{\mathrm{T_e}} = \begin{cases} 1, & \Delta T_\mathrm{e} \in (W_{T_\mathrm{e}}, +\infty) \\ 0, & \Delta T_\mathrm{e} \in (-W_{T_\mathrm{e}}, W_{T_\mathrm{e}}) \\ -1, & \Delta T_\mathrm{e} \in (-\infty, -W_{T_\mathrm{e}}) \end{cases}. \tag{3.52}$$

where $\Delta\vec{\psi}_\mathrm{s} := \|\vec{\psi}^{\alpha\beta}_{\mathrm{s[k+1]}}\| - \|\vec{\psi}^{\alpha\beta}_{\mathrm{s[k]}}\|$, $\Delta T_\mathrm{e} := \hat{T}_{\mathrm{e[k+1]}} - \hat{T}_{\mathrm{e[k+1]}}$, and $\mathrm{W}_{\mathrm{T_e}}, \mathrm{W}_\psi$ are the hysteresis bandwidths[12] of the torque and flux controllers, respectively. In practice, the flux and

[11] In the classical cases, only the active vectors are applied. However, in this section including the DTC for 3L NPC case, both the active and zero vectors are considered for a fair comparison with the DMPC schemes.

[12] The bandwidth of the flux linkage hysteresis controller will affect the final switching frequency, control variable ripples, which is normally set at 1% to 5% of the rated value depending on the control interval and DC-bus value [63, 64]. The

torque can be estimated by Equation (3.19). The location of the estimated flux can be calculated by

$$\theta_{\vec{\psi}_s} = \text{arc2tan}\left(\frac{\psi_s^\beta}{\psi_s^\alpha}\right). \tag{3.53}$$

It is divided into six regions (sectors) in the $\alpha\beta$ plane through the following equation

$$(2n-3)\cdot\frac{\pi}{6} \leq \theta_{\vec{\psi}_s} \leq (2n-1)\cdot\frac{\pi}{6},\ n \in \{1,2,\cdots,5,6\}. \tag{3.54}$$

Fig. 3.6-A illustrates how the switching table is designed for the two-level power converter in the first sector: If the flux hysteresis controller output is $H_\psi = 1$ (i.e., a flux increase is desired) and the torque hysteresis controller output is $H_T = 1$ (i.e., a torque increase is desired), then, PPN(110) is the "optimal" vector to be applied. If $H_\psi = 1$ but $H_T = -1$ (i.e., a torque *de*crease is desired), then PNP(101) should be applied; etc. Following this idea for all the sectors, the complete switching table[13] as given in Tab. 3.1 can be derived.

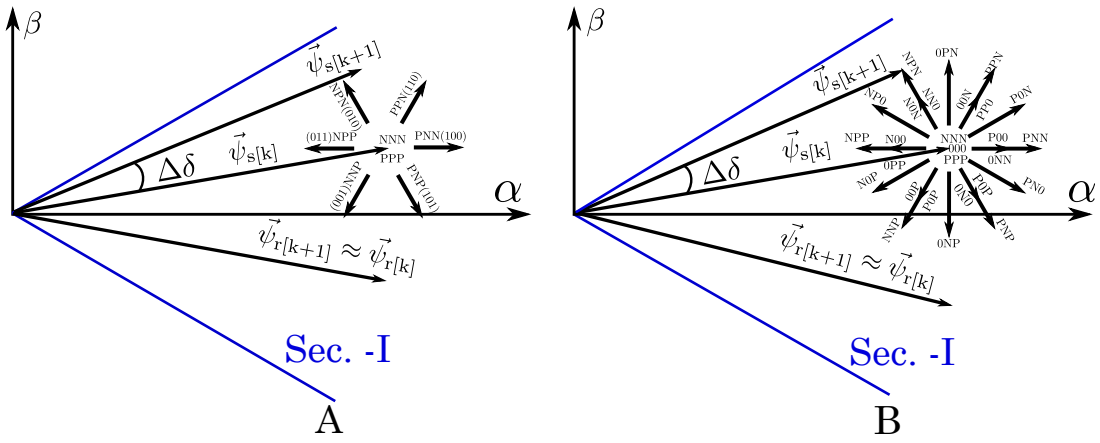

Fig. 3.6: Voltage vector selection of the DTC scheme with table. A: for two-level power converters; B: for three-level NPC power converters.

3.5.1.2 DTC for three-level converter driven PMSG

Principally, the same switching table as in Table 3.1 can be adopted for three-level NPC power converter driven systems as well. However, in this case, only the large and zero voltage vectors are used and the DC-link voltage balancing requirements are not met.

Benefiting from its increased numbers of the voltage vectors with multiple magnitudes and phases (intermediate voltage vectors), hysteresis controllers for three-level NPC power converter driven system can be designed as a "multiple-level" comparator/selector. Fig. 3.7 depicts the differences between two- and three-level power converter cases: when the

change of the flux linkage is equal to the product of the DC-link voltage and sampling time, therefore, the sampling time for low-voltage, high speed motors (which have small value of stator flux linkages) should be extremely small, otherwise, DTC cannot apply. A nice reference for such topics is [65].

[13] This table can be also used for induction motor control since the same stator flux estimation principle is used [63].

H_{ψ}^{2L}	$H_{T_e}^{2L}$	**n=1**	**n=2**	**n=3**	**n=4**	**n=5**	**n=6**
	1	PPN	NPN	NPP	NNP	PNP	PNN
1	0	PPP	NNN	PPP	NNN	PPP	NNN
	-1	PNP	PNN	PPN	NPN	NPP	NNP
	1	NPN	NPP	NNP	PNP	PNN	PPN
-1	0	NNN	PPP	NNN	PPP	NNN	PPP
	-1	NNP	PNP	PNN	PPN	NPN	NPP

Table 3.1: Switching table for two-level power converter driven machine using DTC scheme.

difference between control variable x ($x \in \{T_e, \vec{\psi}_s\}$) and its reference reach the upper band, a bigger driving force or a bigger changing slope is required, so a voltage vector with a bigger magnitude should be selected, otherwise a voltage vector with a smaller magnitude shall be used, hence to better utilize the multi-level of the voltage vectors to reduce the ripples. The hysteresis controllers for the flux and torque are designed as (3.55) with multi-levels.

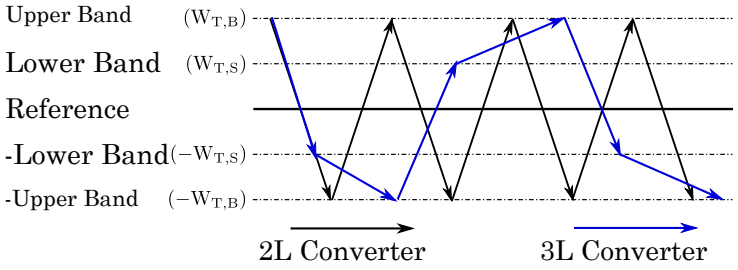

Fig. 3.7: Cases for two- and three-level power converters using DTC.

$$H_{\psi}^{3L} = \begin{cases} 1, & \Delta\vec{\psi}_s \in (W_{\psi}, +\infty) \\ 0, & \Delta\vec{\psi}_s \in [-W_{\psi}, -W_{\psi}] \\ -1, & \Delta\vec{\psi}_s \in (-\infty, -W_{\psi}) \end{cases}; \qquad H_{T_e}^{3L} = \begin{cases} 2, & \Delta T_e \in (W_{T,B}, +\infty) \\ 1, & \Delta T_e \in [W_{T,S}, W_{T,B}) \\ 0, & \Delta T_e \in (-W_{T,S}, W_{T,s}] \\ -1, & \Delta T_e \in (-W_{T,B}, -W_{T,S}] \\ -2, & \Delta T_e \in (-\infty, -W_{T,B}) \end{cases} \tag{3.55}$$

where $\Delta\vec{\psi}_s := \|\psi_s^*\| - \|\vec{\psi}_{s[k]}^{\alpha\beta}\|, \Delta T_e := T_e^* - \hat{T}_{e[k+1]}$, and $W_{T,B}, W_{T,S}, W\psi$ are the hysteresis bandwidth, respectively. The level of bandwidth for torque is more than that for flux, which is due to small torque ripples are desired to reduce mechanical vibrating stress to the coupling shaft.

For three-level NPC power converter, the DC-link balancing control shall also be taken into consideration, and therefore another hysteresis controller should be included. As can be found in the system modeling part of Chp. 2, the DC-link neutral point voltage is affected by both the small and medium voltage vectors. However, the medium voltage vector can only change the voltage balancing in a single direction for a given current flow. While the small vectors, always existing in pairs, can change the voltage in bi-directions

with the same slope. In this work, the small voltage vectors are therefore considered for the voltage balancing and one-level hysteresis control is used since all small vectors are with the same length. The hysteresis controller for the DC-link balancing is designed as

$$H_{\mathrm{V_o}}^{\mathrm{3L}} = \begin{cases} +1, & \Delta V_{\mathrm{o}} \in (BD_{V_{\mathrm{o}}}, +\infty) \\ -1, & \Delta V_{\mathrm{o}} \in (-\infty, -BD_{V_{\mathrm{o}}}) \end{cases} \tag{3.56}$$

where $\Delta V_{\mathrm{o}} := V_{\mathrm{c1[k]}} - V_{\mathrm{c2[k]}}$, and $BD_{V_{\mathrm{o}}}$ is its hysteresis bandwidth.

To better utilize the intermediate voltage vectors, the flux location is arranged into, in stead of 6 sectors, 12 sections by

$$(n-1)\cdot\frac{\pi}{6} \leq \theta_{\vec{\psi}_{\mathrm{s}}} \leq n\cdot\frac{\pi}{6},\ n \in \{1,2,\cdots,11,12\}, \tag{3.57}$$

where $\theta_{\vec{\psi}_{\mathrm{s}}}$ is obtained through equation (3.53).

In Fig. 3.6-B, the selection of the optimal voltage vectors are illustrated: if $\{H_{T_{\mathrm{e}}} = 2, H_{\vec{\psi}_{\mathrm{s}}} = 2\}$, i.e., the torque and flux differences reach or beyond the big band (which means a heavy decrease is required), then PPN should be selected, no matter which situation of the DC-link neutral point voltage is. While if $\{H_{T_{\mathrm{e}}} = 1, H_{\vec{\psi}_{\mathrm{s}}} = 1\}$, i.e., the torque and flux differences reach or beyond the small bandwidth only (i.e., a light decrease is needed), both $P00$ and $0NN$ can be used, since they are of the same contribution to torque and flux change; however, they lead to different neutral point voltage change directions: $P00$ will cause increase and $0NN$ leads to a decrease of the neutral point voltage. Therefore, $P00$ shall be selected, if the DC-link neutral point voltage needs to increase, i.e, when $H_{V_{\mathrm{o}}} = -1$; while $0NN$ shall be selected when the DC-link neutral point voltage needs to decrease, i.e, when $H_{V_{\mathrm{o}}} = 1$. Following this rule, the mostly used switching table as in [68, 69] are applied, which are given in the appendix of Table D.2.

3.5.2 Direct power control for GSC

Similarly to DTC, the instantaneous active and reactive powers are regulated using a hysteresis controller with pre-defined bandwidth and switching table using DPC method. In more details, the estimated active and reactive powers are compared with their references, which are obtained from outer control loops. The differences are taken as inputs to certain hysteresis controllers, which output the determination signals of how the active and reactive powers should be regulated. Those signals, together with grid voltage vector location information (and voltage balancing information for 3L NPC power converter), are used to index a pre-defined switching table, so to output the optimal switching sequence.

The grid voltage vector is allocated through

$$\theta_{\mathrm{g}} = \mathrm{arc2tan}(\tfrac{e_{\mathrm{g}}^{\beta}}{e_{\mathrm{g}}^{\alpha}}). \tag{3.58}$$

The whole $\alpha\beta$ plane is divided into 12 sectors by

$$(n-1)\cdot\frac{\pi}{6} \leq \theta_{\mathrm{g}} \leq n\cdot\frac{\pi}{6},\ n \in \{1,2,\cdots,11,12\}. \tag{3.59}$$

Similarly to the machine side control, the hysteresis controllers for DPC method of two- and three-level power converters are designed as follows

$$H_{\mathrm{P}}^{2\mathrm{L}} = \begin{cases} 1, & \Delta P \in [BD_P, +\infty) \\ -1, & \Delta P \in (-\infty, -BD_P) \end{cases}, \qquad H_{\mathrm{Q}}^{2\mathrm{L}} = \begin{cases} 1, & \Delta Q \in [w_Q, +\infty) \\ -1, & \Delta Q(-\infty, -w_Q) \end{cases}, \tag{3.60}$$

$$H_{\mathrm{P}}^{3\mathrm{L}} = \begin{cases} 1, & \Delta P \in (BD_P, +\infty) \\ 0, & \Delta P \in (0, BD_P) \\ -1, & \Delta P \in (-\infty, 0) \end{cases}, H_{\mathrm{Q}}^{3\mathrm{L}} = \begin{cases} 1, & \Delta Q \in (BD_Q, +\infty) \\ 0, & \Delta Q \in (0, BD_Q) \\ -1, & \Delta Q \in (-\infty, 0) \end{cases}, H_{\mathrm{V_o}}^{3\mathrm{L}} = \begin{cases} 1, & \Delta V_{\mathrm{o}} \in (BD_{V_{\mathrm{o}}}), +\infty) \\ -1, & \Delta V_{\mathrm{o}} \in (-\infty, -BD_{V_{\mathrm{o}}}) \end{cases}. \tag{3.61}$$

Different from the DTC scheme, the switching table of DPC is based on an analytical process of this equation (detail development see 3.4.2.2)

$$\vec{v}_{\mathrm{g[k]}}^{\mathrm{dq,eq*}} = \begin{pmatrix} v_{\mathrm{g[k]}}^{\mathrm{d,eq*}} \\ v_{\mathrm{g[k]}}^{\mathrm{q,eq*}} \end{pmatrix} = \begin{pmatrix} e_{\mathrm{g[k]}}^{\mathrm{d}} \\ e_{\mathrm{g[k]}}^{\mathrm{q}} \end{pmatrix} - \frac{L_{\mathrm{g}}}{T_{\mathrm{s}}((e_{\mathrm{g[k]}}^{\mathrm{d}})^2 + (e_{\mathrm{g[k]}}^{\mathrm{q}})^2)} \begin{bmatrix} e_{\mathrm{g[k]}}^{\mathrm{d}} & e_{\mathrm{g[k]}}^{\mathrm{q}} \\ e_{\mathrm{g[k]}}^{\mathrm{q}} & -e_{\mathrm{g[k]}}^{\mathrm{d}} \end{bmatrix} \begin{pmatrix} P_{\mathrm{[k]}}^{*} - P_{\mathrm{[k]}} \\ Q_{\mathrm{[k]}}^{*} - Q_{\mathrm{[k]}} \end{pmatrix}, \tag{3.62}$$

i.e.,

$$\Delta P_{\mathrm{[k]}} := P_{\mathrm{[k+1]}}^{*} - P_{\mathrm{[k]}} \propto T_{\mathrm{s}} \frac{e_{\mathrm{g[k]}}^{\mathrm{d}}}{L_{\mathrm{g}}} (e_{\mathrm{g[k]}}^{\mathrm{d}} - v_{\mathrm{g[k]}}^{\mathrm{d,eq*}}), \tag{3.63a}$$

$$\Delta Q_{\mathrm{[k]}} := Q_{\mathrm{[k+1]}}^{*} - Q_{\mathrm{[k]}} \propto T_{\mathrm{s}} \frac{e_{\mathrm{g[k]}}^{\mathrm{d}}}{L_{\mathrm{g}}} v_{\mathrm{g[k]}}^{\mathrm{q,eq*}}. \tag{3.63b}$$

The influences of all the voltage vectors in every sector can be analyzed and an influence relationship can be set up based on equations (3.63a) and (3.63b). Taking the three-level power converter in the first sector as an example: re-examining equations (3.63a), (3.63b) with all the available non-redundant vectors (vector list is presented in Appendix D.2) yields the following relationship in Table 3.2. Based on such analytical relationships,

Vector	Influence on P	Influence on Q	Vector	Influence on P	Influence on Q
V_1	+	−	V_{15}	++	−−
V_4	+	+	V_{18}	non	−−
V_7	++	++	V_2	− − −	−
V_{10}	++	+	V_5	non	++
V_{13}	++	−	V_8	+	+ + +
V_{16}	+	−−	V_{11}	+ + +	+
V_3	−−	+	V_{14}	++	−−
V_6	+	++	V_{17}	+	− − −
V_9	++	++	V_0	++	0
V_{12}	++	−			

Table 3.2: Influence of voltage vectors on the active and reactive power in sector 1, where "+, −, non" represent the influence of "increase", "decrease", and "non-influence", respectively. The mount of these symbols represents influence level.

off-line switching tables can be designed. The as-used switching tables for two level power

$H_{\mathrm{P}}^{2\mathrm{L}}$	$H_{\mathrm{Q}}^{2\mathrm{L}}$	Sector											
		1	2	3	4	5	6	7	8	9	10	11	12
1	-1	pnp	ppp	pnn	nnn	ppn	ppp	npn	nnn	ppp	ppp	nnp	nnn
	1	ppp	ppp	nnn	nnn	ppp	ppp	nnn	nnn	ppp	ppp	nnn	nnn
-1	-1	pnp	pnn	pnn	ppn	ppn	npn	npn	npp	npp	nnp	nnp	pnp
	1	pnn	ppn	ppn	npn	npn	npp	npp	nnp	nnp	pnp	pnp	pnn

Table 3.3: Switching table for two-level direct instantaneous power control.

converter system is given as Table 3.3. The table for three-level NPC power converter is presented in the appendix Table D.2

So far direct control schemes with switching table for both two- and three-level power converter systems are described. Fig. 3.8 illustrates the overall control scheme.

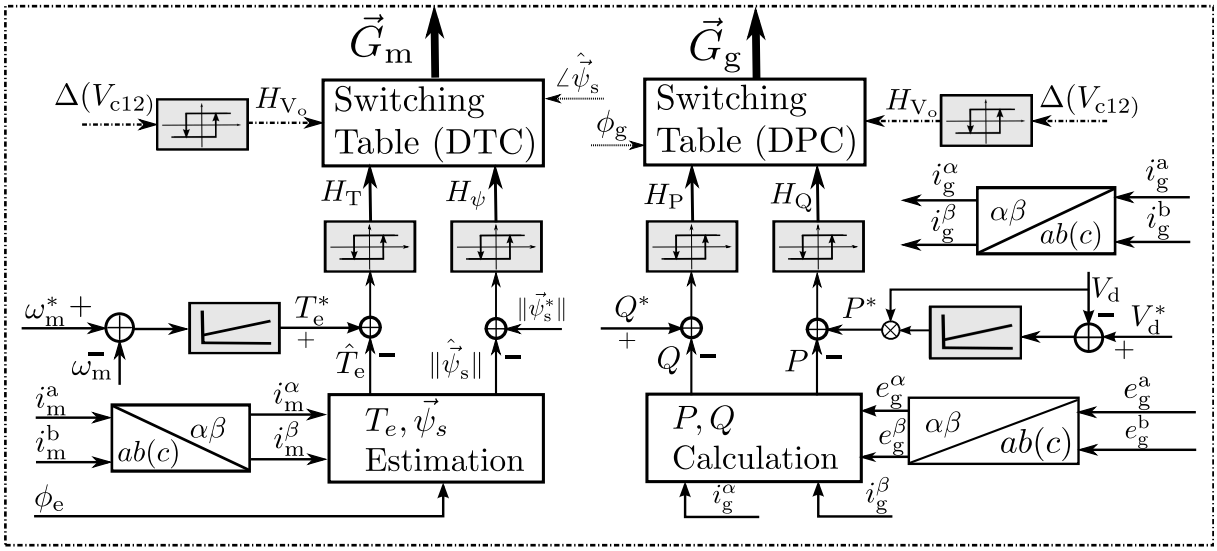

Fig. 3.8: Classical switching-table based direct torque and power control for two- and three-level power converter PMSG wind turbine systems.

3.6 Performance evaluation with experimental data

In this section, the control performances of the aforementioned control techniques (e.g., FOC-VOC, DBC for torque and power, and DTC-DPC both with switching table and modulator) are experimentally evaluated.

All the experimental results presented in the following parts are obtained using the test-benches described in Chp. 2. The control system design procedure follows the descriptions given in Sec. 2.5.4 using a fully FPGA based solution. Note that, due to their similarity (to the realizations presented in the following chapters), all FPGA realizations

processes for these classical control methods are not presented in this chapter. For readers who are interested to the FPGA realization may directly refer to our publications (e.g., [42, 46, 47, 57, 60, 63, 70]) or Chp. 6, 7 and 8.

3.6.0.0.1 Identical Test Setting In the following, *if not specifically mentioned*, the overall testing scenarios are as follows: we assume the optimal speed reference ω_{m}^{*} (i.e., the so-called "maximum power point tracking speed reference") in Eq. (2.33), which shall come from a MPPT controller, is already known and changes (abruptly with a slope of 3 [rpm/ms]) following certain (unpredictable) wind speeds. The turbine drive torque T_{t} is mounted to its rated value **to emulate the most harsh operation situations**, although in reality few hours (per day) will see a turbine working in full/rated load. All the realizations of the classical control techniques presented in this chapter have been realized on the FPGA, representing the future trend (see Remark 2).

Remark 2 (On controller realizations using FPGA) *Increasing many real-time electrical drive controllers are realized using FPGA. The reasons are mainly as follows [60, 71, 72]:*

(i) the volume of a single FPGA chip increases drastically, while its price is falling. Moore's law is becoming much more loose and conservative to predict the integrated chip development.

(ii) the capability of FPGAs to process in parallel[14] *is becoming more and more important to deal with the modern advanced control methods (optimal control, predictive control, etc.) which require high computational power;*

(iii) modern rapid-prototyping tools for FPGA design enable the user to program/develop their algorithms with higher level languages (e.g., Labview FPGA) or allows for directly using third-party code generation tools (e.g. Matlab/Simulink), which has drastically increased the development/tuning efficiency. Besides, FPGAs also provides benefits of combining hardware-software seamlessly, offering a more stable and cheaper system-on-the-chip (SOP) solution.

It is therefore quite reasonable to predict that FPGA based targets will be more widely used for realizing control algorithms in the fields of power electronics and electrical drives. The biggest short-coming in the eyes of the author for using FPGA is its long compilation time in general.

3.6.1 Control performances of FOC-VOC and DBC with SVM

Besides the identical testing scenarios mentioned in Sec. 3.6.0.0.1, the DC-link voltage reference remains at 350 [V], the reactive power reference is set at 0 [Var]. For both

[14] FPGAs are clocked with much lower rates (smaller than hundreds MHz) than normal Central Processing Units (CPUs) (faster than 1 GHz). However, FPGAs compensate for that by a highly customized and paralleled processing capability, e.g. FPGAs can perform sequential, multiple and parallel processes in a single clock cycle. This feature makes it more suitable for the fast computational demanding in fields with quite small time constant (e.g., power electronics).

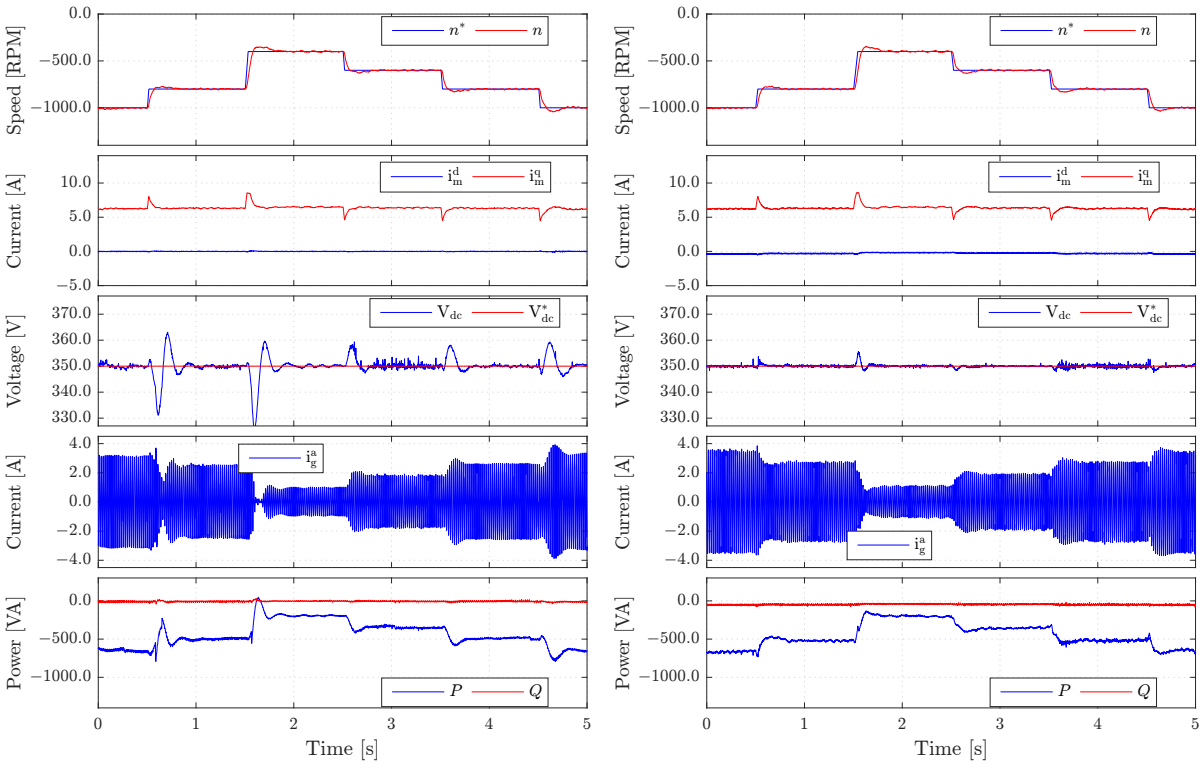

(a) Overall results for FOC-VOC (with $T_s = 100e^{-6}$ s).

(b) Overall results of SVM-DBC ($T_s = 100e^{-6}$ s).

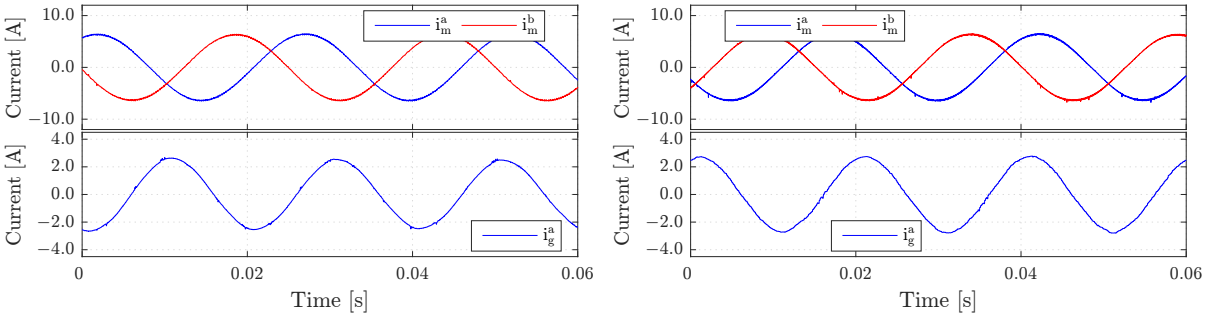

(c) Steady-state control performance of SVM-FOC-VOC.

(d) Steady-state control performance of SVM-DBC.

Fig. 3.9: [Experimental results:] Overall results and steady-state current control performance of SVM-FOC-VOC and SVM-DBC (torque and power) methods for the back-to-back power converter PMSG wind turbine system emulator. From top to bottom: generator speed, stator currents, DC-link voltage, grid side current, active and reactive power, and zoomed in view of stator and grid side filter currents, respectively.

methods, both the grid and machine side control interval of 100 [μs] is set (a switching frequency of 10 kHz is used) and identical outer control loops (the speed and DC-link control loops) are used. The control performances of the filed- & voltage oriented control and deadbeat torque & power control methods for the two-level back-to-back power converter PMSG wind turbine system are illustrated by Fig. 3.9.

As can be seen similar steady state control performances are achieved. However, due to

its cascaded structure, for FOC-VOC scheme (See Fig. 3.2) too many parameters need to be well-tuned to achieve an comparable dynamic performances as the DBC approach (See Fig. 3.5). Also, limited by this, its inner loop bandwidth is not only determined by the control interval, but also the PI controller parameters, which results in a lower overall dynamics hence will also affect the general performances (e.g., the bigger DC-link fluctuations are affected by the grid side controller bandwidth, and an obvious second order phenomenon is observed at both the current and grid side active power control results). Note that, theoretical calculations of the PI parameters are not acceptable if the relevant (speed and DC-link voltage) filters and un-considered time delay are not taken into account, which makes the whole procedure much more tedious than its counterpart technique (DBC), for which, given a known parameter set, no complex calculations or trial-and-error tuning process are required.

3.6.2 Control performances of DTC-DPC with SVM and switching table

At a self-constructed back-to-back power converter PMSG wind turbine system emulator, both SVM-DTC-DPC and ST-DTC-DPC are implemented and experimentally verified. The experimental results are shown in Fig. 3.10. The sampling periods T_{s} for the SVM-DTC-DPC is set as $100e^{-6}[s]$ and for ST-DTC-DPC methods $50e^{-6}[s]$, respectively (to achieve a similar maximum switching frequencies).

Besides the identical testing scenarios mentioned in Sec. 3.6.0.0.1, both schemes use the same outer (speed and DC-link voltage) control loops, the DC-link voltage reference remains at 300 [V], the reactive power reference is set at 0 [Var] for an operation with unity power factor.

The obtained overall and steady-state current control performances for DTC and DPC with and without modulator are shown in Fig. 3.10.

As can be seen, the SVM-DTC-DPC method achieves much smoother current, torque and power waveforms than the ST-DTC-DPC technique. In particular, comparing Fig. 3.10 (a) and Fig. 3.10 (b) yields the following conclusion: SVM-DTC-DPC gives a better steady-state control performance with much slower ripples in current, while even using only the half of the sampling frequency (control period $T_{\mathrm{s}} = 100\mu s$). The smooth waveforms of the currents and powers are desirable, in particular, on the grid side to meet the grid code requirements. In contrast, the sampling frequency for ST-DTC-DPC is twice that of SVM-DTC-DPC, however, its steady state performances are far worse than SVM-DTC-DPC solution, which suggest that, to obtain a better current quality, an even higher sampling frequency for ST-DTC-DPC is required which might lead to unfeasible hardware specifications (e.g. measurement boards with very high sampling frequency) for industrial application.

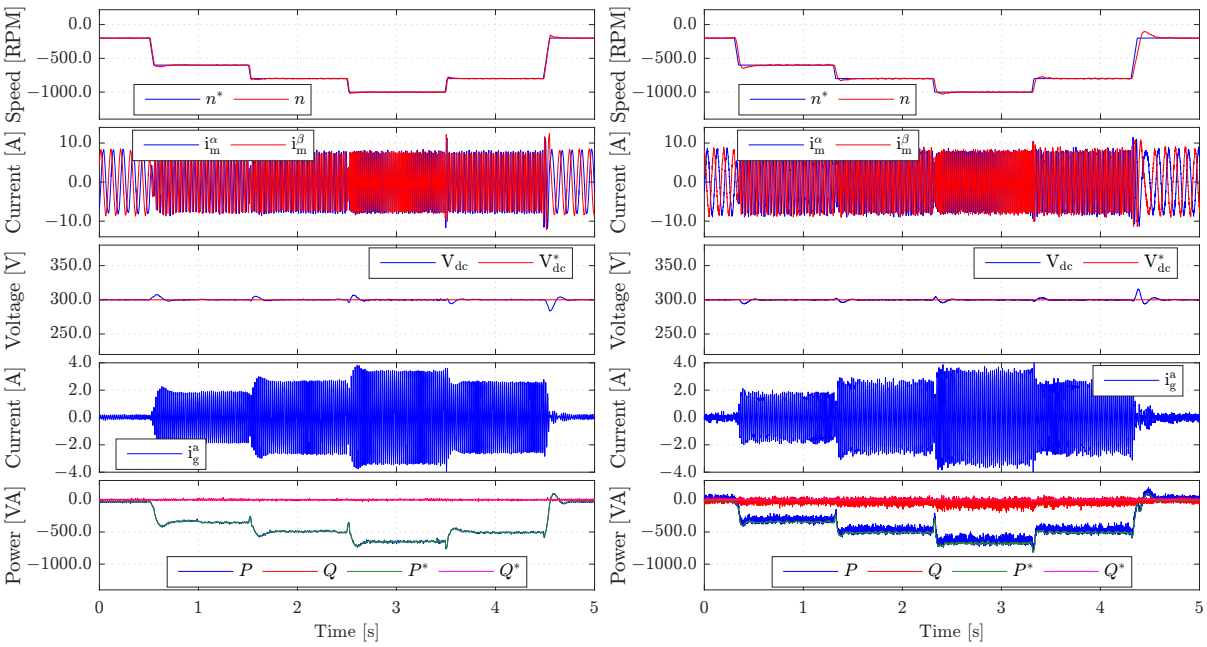

(a) Overall results for SVM-DTC-DPC (with $T_s = 100e^{-6}$ s).

(b) Overall results of ST-DTC-DPC ($T_s = 50e^{-6}$ s).

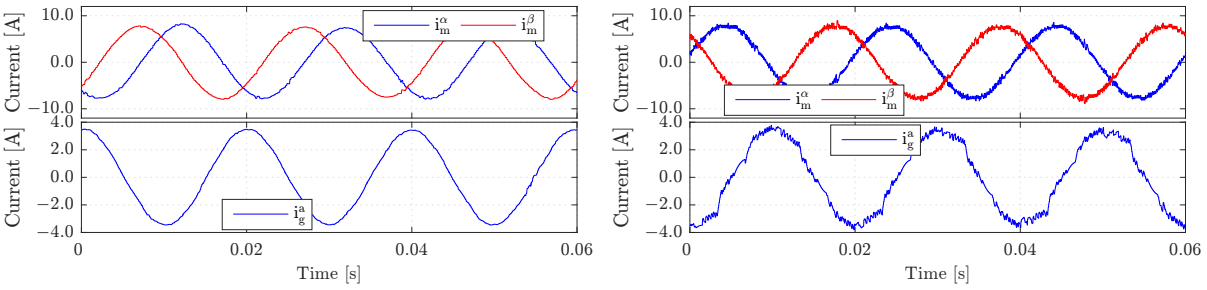

(c) Steady-state control performance of SVM-DTC-DPC.

(d) Steady-state control performance of ST-DTC-DPC.

Fig. 3.10: [Experimental results:] Overall results and steady-state current control performance of SVM-DTC-DPC and ST-DTC-DPC methods for the back-to-back power converter PMSG wind turbine system emulator. From top to bottom: generator speed, stator currents, DC-link voltage, grid side current, active and reactive power, and zoomed in view of stator and grid side filter currents, respectively.

3.6.3 Control performances of ST-DTC-DPC for the three-level system

The control performances of the direct torque and power control method with switching table for the 3L NPC back-to-back power converter PMSG wind turbine system are evaluated at a self-designed three-level NPC back-to-back power converter PMSG wind turbine system emulator (presented in Chp. 2).

Besides the identical testing scenarios mentioned in Sec. 3.6.0.0.1, the DC-link voltage reference remains at 350 [V], the reactive power reference is set at 0 [Var] for an operation with unity power factor. The sampling frequency is set to be $50e^{-6}$ [s], the upper and lower

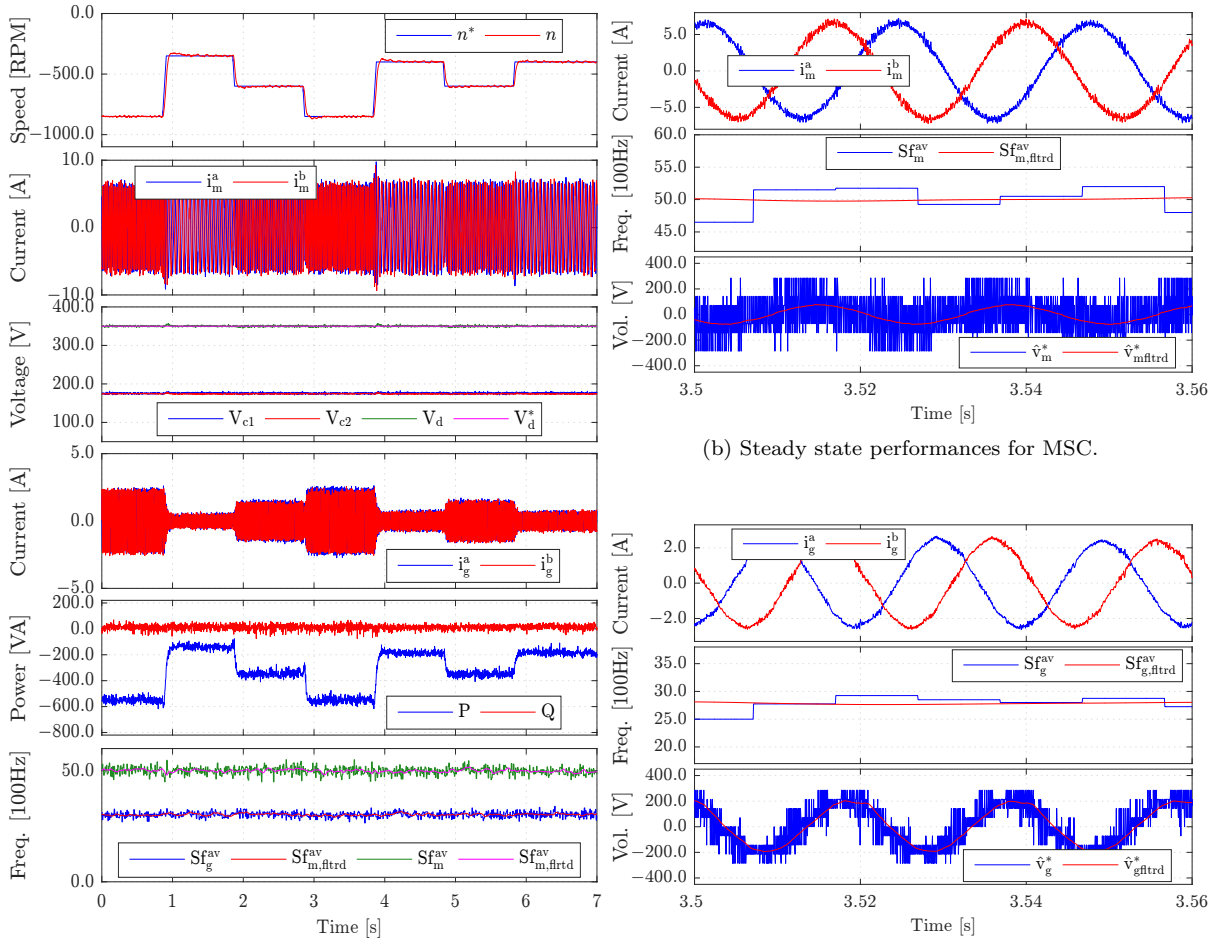

(a) Overall control performances.

(b) Steady state performances for MSC.

(c) Steady state performances for GSC.

Fig. 3.11: [Experimental results] of the overall and steady state control performances using ST-DTC-DPC for the **three-level** NPC system. For sub-figure (a), from up to down are: speed, machine stator (ab-phase) currents, DC-link voltages, grid side phase current, grid side active and reactive power and the average switching frequencies, respectively. Symbols of $\mathrm{Sf}_{\mathrm{y}}^{\mathrm{av}}, \mathrm{Sf}_{\mathrm{y,fltrd}}^{\mathrm{av}}, \mathrm{y} \in \{\mathrm{g}, \mathrm{m}\}$ represent the average switching frequency of each switches in the power converter, and its filtered value with a cut-off switching frequency of 5Hz, respectively. Sub-figure (b) and (c) illustrate of the zoomed performance of the machine (b) and grid (c) side phase currents, switching frequency and estimated voltages, where, $\hat{v}_y^*, y \in \{g, m\}$ is the estimated α -axis voltage from its switching position, and $\hat{v}_{y,fltrd}^*, y \in \{g, m\}$ is its filtered value with a cut-off frequency of 300Hz.

bandwidths are set to 2% and 1% of the their respective rated values for an acceptable switching frequency (bellow 5kHz). The experimental results are illustrated by Fig. 3.11, where sub-figure (a) shows the overall control performances, while (b) and (c) illustrates the steady state control performances. As can be seen from sub-figure (a), a (very) good speed, DC-link voltage (and the voltages of serial connected capacitors), and grid side power control performance have been achieve, except the unfixed switching frequency for both sides.

However, through Fig. 3.11 (b) and (c), we see the detailed control performances during the steady state of the system operation with considerable ripples in comparison with the

modulator based method (even for the two-level systems). The reason can be found from its switching patterns: a (quite) "noisy" and less sinusoidal switching patterns is seen using ST-DTC-DPC method (see the last sub-figures in Fig. 3.11 (b) and (c)). However, as expected, the currents for both sides are more smoother than that of the two-level systems with switching table based direct control (in particular for the grid side). More details with regarding to this part of work can be found in our publications of [73, 74]. Its comparison with direct model predictive control solution is presented in our next chapter after introducing direct model predictive control methods.

3.7 Summary

This chapter has presented the actual classical control techniques for back-to-back power converters and PMSG wind turbine systems, all with their very original but intelligent formats. These include cascaded linear controller with modulator (SVM-FOC-VOC), direct control methods with modulator (SVM-DTC-DPC), deadbeat like predictive control with modulators (SVM-DBC) and direct control with switching table (ST-DTC-DPC). Their design processes and detailed theoretical principles are clearly (at least with such intention) presented. Their control performances (both an overall and detailed steady state control performances) are evaluated using a fully FPGA based platform (to avoid certain repeating process, the FPGA design processes are not collected here).

From the steady state control variable quality point of view, with a similar (even lower) sampling frequency, all modulator based methods will outperform the direct control methods with switching table. From perspectives of both the required realization/tuning efforts and the control performances, deadbeat like predictive control is recommended among all the afore-presented control techniques within this chapter, due to its good control dynamics and steady state control performances, while less realization and tuning efforts are required. However, a proper parameter estimation solution would be desirable to reduce its inner loop tracking bias (as is mentioned in our publication of [60]). A more detailed comparison of the classical control methods can be seen (some are still under preparation) from our publications [56, 58, 75], etc.

Chapter 4

Direct model predictive control

In this chapter, the classic concept of model predictive control is revisited and summarized (see Sec. 4.1). Then direct model predictive control schemes with prediction horizon-one *for both two- and three-level NPC* back-to-back power converters in PMSG wind turbine systems are discussed. In more details, the direct torque/current control for machine side converter and direct power/current control for grid side converters for both the two- and three-level NPC power converters systems are presented in Sec. 4.2 and Sec. 4.3, respectively. Their performances are evaluated *all* with experimental results (see Sec. 4.4).

4.1 Model predictive control: a brief introduction

Model predictive control (MPC) (also referred to as "receding horizon control") was originally developed in the early 1970s [76–79], and has already been comprehensively applied in the petrochemical industry area for many years, where the long system time constant allows for long control interval and has therefore no strict requirement for a high computation power of its online optimization process. Different from the conventional control concepts introduced in the last chapter, in MPC, the optimum values of the actuating variables are not computed by the "post-error" between the reference and the feedback signals, but through minimizing a flexibly designed "cost function" with penalized errors between the reference values and the predicted behaviors of the system using a system model and the control action sequences over a receding prediction horizon. Multiple "weighted targets" can be included into a customer-designed cost function, resulting in a flexible "customized-optimal" control.

There are in general three main basic elements (components) to apply MPC [76–78]:

i) The *mathematical model* of the plant. For most cases, in particular for the field of power electronics and electrical drives, the plant models are usually available;

ii) *Customized optimal control targets*, i.e., the objective/cost function, which maps the customized control objectives into a scalar over a prediction horizon N. In other words, the cost function connects the N-step control actions with a customized control

goal. However, only the first element after the current sampling interval k is predicted in a "closed loop" manner (i.e., with measurement feedback or estimate), and all the system behaviors in the control interval $h > k + 1$ are acquired in an "open-loop" prediction;

iii) The "*receding horizon policy*" is used for "close-looping" the control process, i.e., only the first element of the optimal control action sequence is chosen to apply, the others are discarded. The horizon is shifted one sampling step forward. Such procedure is then repeated in the next time step with new measurements or estimates.

Invoking the plant model, this control strategy is equipped with a "foreseen" or "prediction" capability, which allows predictive control to have more freedoms to further improve the system control performances since the future behaviors of the system can be "known". Its "weighted optimal" property increases its control flexibility and hence will reduce the engineering efforts. Such positive features allow predictive control to deal with more complex even nonlinear dynamics with multiple input and multiple output (MIMO). From a concept point of view, it remains in a quite straightforward level. The tricky part lies at: solving the optimization problem is usually a trade-off between the control performances and the prediction horizon (which "equals" to computational complexity), i.e., with a longer prediction horizon, system stability and control performances will be generally improved [80, 81], however, the computational complexity will increase as well.

Since the last decade, this control concept has attracted significant attention in the area of power electronics and electrical drives [40, 41, 77, 82–85] due to its multiple merits (e.g., intuitive concept, ease for inclusion of multiple control targets, easier to implement in particular for multi-level and multiphase converter topologies in comparison with the conventional methods, etc). It has emerged as a viable alternative in the field of power electronics and electrical drives [21, 25, 55, 86–90].

4.1.1 MPC for power electronics and electrical drives

The MPC concept for controlling power electronics and electrical drives is applied in various formats (see e.g., [10, 88, 91–95]). Considering whether the control input is continuous or not, it can be divided into *continuous/general (model) predictive control* (GPC) [40, 88, 91] and *direct/finite-control-set model predictive control* (DMPC) schemes [25, 39, 86, 96]. For the former, an extra modulator is utilized to generate the switching sequences based on the controller outputs (which usually are continuous values of duty-cycles or reference voltages, see Fig. 4.1a) and was investigated and reported in [40, 77, 87, 88]. While the latter combines both the cost optimization and modulation into one single process and directly output the switching sequence. No extra modulation is required (See Fig. 4.1b). Only after the beginning of this century (2004) [97], DMPC has become well-known in the form of "finite-control-set model predictive control" (FCS-MPC) [97–99].

Considering whether a longer prediction horizon is used or not, it can be divided into *horizon-one MPC* and *long horizon MPC*. Although increasing the prediction horizon will lead to better control performances, the required computational efforts may make the

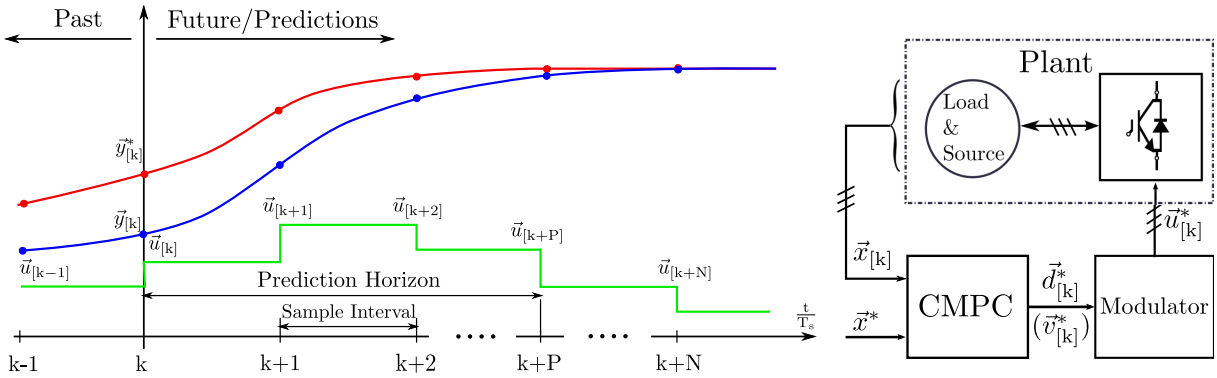

(a) General/continuous predictive control concept (R. Kennel, et al., 1983).

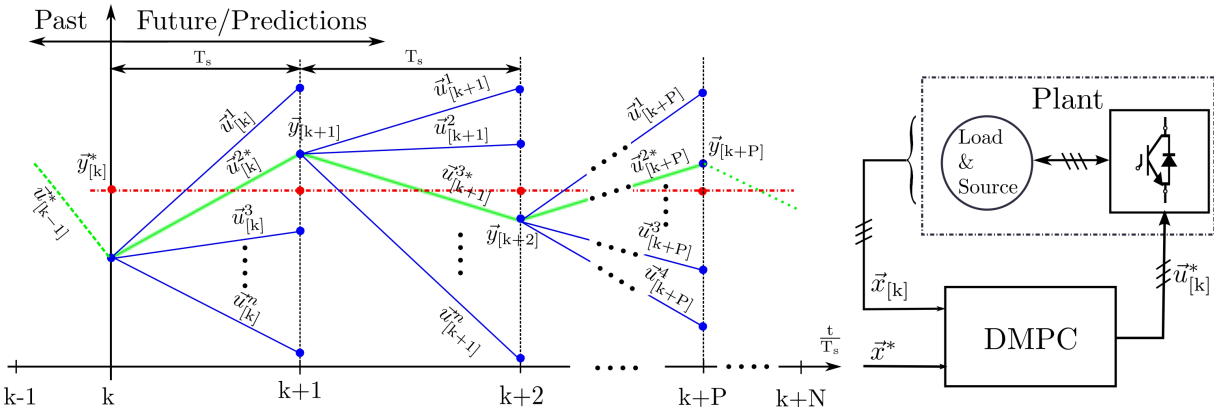

(b) Direct (finite-control-set) model predictive control concept (J. Rodriguez, et al., 2004).

Fig. 4.1: Basic concepts of general and direct (finite-control-set) model predictive control techniques for power electronics and electrical drives.

real-time realization not feasible in general. Horizon-one methods, in particular horizon-one DMPC methods, are straightforward to realize and can produce (mostly) satisfactory results in power electronics and electrical control areas. Therefore, such category is commonly applied in power electronics and electrical drives and have been applied in many different applications such as synchronous motor and asynchronous motor drives, two and multilevel power converter control, matrix converter control, HVDC and renewable energy generation systems (See e.g., [21, 93, 100–102] and the reference therein).

Robustness against system parameter variations and model uncertainties is one of the concerns [95, 103–105], since predictive control class is an entirely model based technique. Steady-state tracking bias for short (one) prediction horizon is also an open issue. Apart from its higher computational power demanding (in particular for multilevel power converter cases), in comparison with the classical control methods presented in Chp. 3, relatively poor steady state control performances in particular for two-level cases in comparison with modulator based techniques, due to its *one-vector-per-control-interval* nature [47], remains to be further improved. Despite of this, this scheme achieves very satisfactory control performances with straight-forward concept and reduced implementation efforts for most applications [21, 106].

In this chapter, the mostly investigated predictive control branch, i.e., direct model predictive control method is discussed. Its applications for both the machine/generator and grid sides of the back-to-back two- and three-level NPC power converters are introduced and experimentally evaluated.

To ease the reading and description, the classical direct model predictive control guidelines are firstly revisited in Sec. 4.1.2. Following the guidelines, the direct model predictive control methods for two- and three-level back-to-back power converter PMSG wind turbine systems are presented in Sec. 4.2, and Sec. 4.3, where both the direct model prediction torque (for machine side) and power control (for grid side), and direct model predictive current control (for both sides) methods are experimentally evaluated at the self-constructed test-benches introduced in Chp. 2 using a fully FPGA based solution.

4.1.2 Concept of classical direct model predictive control

Classical DMPC/FCS-MPC schemes evaluate a cost function of

$$J = \underbrace{\sum_{h=k}^{k+N-1}\sum_{i=1}^{m}\gamma_{\mathrm{TS_i}}\|TS^{*}_{\mathrm{i[h+1]}} - TS^{p}_{\mathrm{i[h+1]}}(\vec{u}_i)\|}_{=:J_{\mathrm{TS}}} + \underbrace{\sum_{h=k}^{k+N-1}\sum_{j=1}^{n}\gamma_{\mathrm{CS_j}}\|CS^{*}_{\mathrm{j[h+1]}} - CS^{p}_{\mathrm{j[h+1]}}(\vec{u}_j)\|}_{=:J_{\mathrm{CS}}}, \quad (4.1)$$

where N is the prediction horizon, m and n are the element number for targeting and constraint sets, respectively. In general, J represents the control objectives, and comprises two parts: J_{TS} and J_{CS} (with corresponding weighting factors of their elements as $\gamma_{\mathrm{TS_i}}$ and $\gamma_{\mathrm{CS_j}}$, respectively), which maps the control targets to N steps of the control actions. J_{TS} and J_{CS} represent sub-costs for the *Target Set* $\mathrm{TS_i}$ (such as: reference tracking of current, voltage, torque, or power with reference $\mathrm{TS^*_i}$) *and* the *Constraint Set* $\mathrm{CS_j}$ (such as: current/torque, or power limitations, switching frequency, with reference $\mathrm{CS^*_j}$), respectively. For a two level converter, the switching vector (control action) $\vec{u}_i$ is chosen from the set

$$\vec{u}_i \in \mathcal{U}_8 := \{000, 001, \ldots, 100, \ldots 101, 111\} \quad (4.2)$$

of *8 admissible switching vectors*. For a three level NPC power converter it is chosen from

$$\vec{u}_i \in \mathcal{U}_{27} := \{\mathrm{NNN}, \mathrm{NN0}, \ldots, 000, \ldots \mathrm{PP0}, \mathrm{PPP}\} \quad (4.3)$$

of *27 admissible switching vectors*. Definitions of the switching states can be found in equations (2.7) and (2.14) in Chp. 2.

The simplified steps for DMPC/FCS-MPC scheme are summarized by Algorithm 4.1.

Algorithm 4.1 : Classical DMPC algorithm with $\vec{u}_i \in \mathcal{U}$

Step I: Reference $TS^*_{\mathrm{i[k+1]}}, CS^*_{\mathrm{i[k+1]}}$ generation and target prediction for all $\vec{u}_i \in \mathcal{U}$:

$$TS_{\mathrm{i[k+1]}}(\vec{u}_i) = M_{TS_i}(\vec{u}_i), \tag{4.4a}$$
$$CS_{\mathrm{j[k+1]}}(\vec{u}_i) = M_{CS_j}(\vec{u}_i). \tag{4.4b}$$

Step II: Cost evaluation and optimal switching vector selection: $\{\vec{u}^*_x := \arg\min_{\vec{u}_{i,j}\in\mathcal{U}} J(\vec{u}_{i,j})\}$, where J is defined as in (4.1).

Step III: Apply gate signal vector: $\vec{G}^*_x = \mathcal{G}^{-1}(\vec{u}^*_x)$. $\mathcal{G}$ was presented in chapter 2.

where $\mathrm{M_{TS_i}}$ *and* $\mathrm{M_{CS_j}}$ are abbreviations of the *prediction model for the Target Set* $\mathrm{TS_i}$ and the *prediction model for the Constraint Set* $\mathrm{CS_j}$, respectively.

In the following sections, based on such concept, direct model predictive torque control (DMPTC) for the machine side and direct model predictive power control (DMPPC) for the grid side, and direct model predictive current control (DMPCC) methods for both sides, for both the two and three-level NPC back-to-back power converter PMSG wind turbine systems will be presented. Note that, for machine (PMSG) side control, apart from DMPTC and DMPCC, there exists also direct model predictive flux control (DMPFC). The relationship and performance evaluations among DMPTC, DMPCC and DMPFC[1] methods for PMSM(G) drives are theoretically analyzed and evaluated in [75]. Theoretical investigation and evaluations of DMPPC and DMPCC methods for grid side control (AFE control) have been reported in [74].

4.2 DMPC for two-level back-to-back PMSG systems

In this section the state-of-the-art direct model predictive control methods for two-level back-to-back power converter systems are going to be presented. More specifically, in Sec. 4.2.1, the direct model predictive torque control (DMPTC) for the machine side and direct model predictive power control (DMPPC) for the grid side of a two level back-to-back power converter PMSG wind turbine system will be presented. While in Sec. 4.2.2, the direct model predictive current control (DMPCC) methods for both the machine and grid side are introduced.

[1] In the analogy, for the grid side, when taking the "virtual-flux" and "virtual machine"[2] concepts, there also exists predictive virtual flux control (DMPVFC) method, and potentially DMPVFC shall be more "robust" to certain grid voltage distortion in comparison with DMPPC, due to the integration relationship between voltage and the "virtual flux". However, so far such solution remains to be reported and currently the author of this thesis is investing such concept.

4.2.1 Direct model predictive torque and power control

4.2.1.1 Direct model predictive torque control of 2L-MSC

For the MSC of a two-level power converter, besides the current limitations, the torque tracking subjecting to a so called "maximum torque per Ampere" (MTPA) law (i.e., $i_{\mathrm{m}}^{\mathrm{d}} + \frac{L_{\mathrm{s}}^{\mathrm{d}} - L_{\mathrm{s}}^{\mathrm{q}}}{\psi_{\mathrm{pm}}}\left((i_{\mathrm{m}}^{\mathrm{d}})^2 - (i_{\mathrm{m}}^{\mathrm{q}})^2\right) = 0$) is desired. In our set-up, $L_{\mathrm{s}}^{\mathrm{d}} \approx L_{\mathrm{s}}^{\mathrm{q}} = L_{\mathrm{s}}$. Therefore, $i_{\mathrm{m}}^{\mathrm{d}*} := 0$ can be set in the controller. Thus, the generator/machine-side cost function is defined as

$$J_{\mathrm{DMPC}}^{\mathrm{m}}(\vec{u}_{\mathrm{m}}) = \underbrace{\gamma_{T_{\mathrm{e}}}\Big(T_{\mathrm{e}}^{*} - T_{\mathrm{e[k+1]}}(\vec{u}_{\mathrm{m}})\Big)^2}_{=:\mathrm{J(T_e)}} + \underbrace{\gamma_{i_{\mathrm{m}}^{\mathrm{d}}}\Big(0 - i_{\mathrm{m[k+1]}}^{\mathrm{d}}(\vec{u}_{\mathrm{m}})\Big)^2}_{=:\mathrm{J(i_m^d)}} + \underbrace{\gamma_{\mathrm{cs}}\Big\{(i_{\mathrm{m}}^{\mathrm{d\,max}} \leq \|i_{\mathrm{m[k+1]}}^{\mathrm{d}}\|) \text{ or } (T_{\mathrm{e}}^{\mathrm{max}} \leq \|T_{\mathrm{e[k+1]}}(\vec{u}_{\mathrm{m}})\|)\Big\}}_{=:\mathrm{J}_{\mathrm{CS_m}}^{\mathrm{m}}}, \quad (4.5)$$

where $\mathrm{J(T_e)}$ is the sub-cost for torque tracking, while $\mathrm{J}(\mathrm{i}_{\mathrm{m}}^{\mathrm{d}})$ is to regulate the d-axis current to be zero hence to achieve the MTPA control, the constraint set $\mathrm{J}_{\mathrm{CS_m}}^{\mathrm{m}}$ is to assure the current and torque limitations are respected. The predicted torque $T_{\mathrm{e[k+1]}}(\vec{u}_{\mathrm{m}})$ and current $i_{\mathrm{m[k+1]}}^{\mathrm{d}}(\vec{u}_{\mathrm{m}})$ are given by equations (2.42), with $\vec{u}_{\mathrm{m}} \in \mathcal{U}_8$. The torque reference is generated by an upper speed control loop with PI controller (see Fig. 4.2a), where the reference is supposed to be generated from a proper MPPT controller[3]. After evaluating and minimizing the costs obtained from equation (6.15) for $\vec{u}_{\mathrm{m}} \in \mathcal{U}_8$, an optimal gate vector of $\vec{G}_{\mathrm{m}}$ will be obtained and assigned to the machine side converter.

4.2.1.2 Direct model predictive power control of 2L-GSC

The cost function for the grid side control to achieve both active and reactive power tracking objectives is designed as

$$J_{\mathrm{DMPC}}^{\mathrm{g}}(\vec{u}_{\mathrm{g}}) = \underbrace{\Big(P^{*} - P_{\mathrm{[k+1]}}(\vec{u}_{\mathrm{g}})\Big)^2 + \Big(Q^{*} - Q_{\mathrm{[k+1]}}(\vec{u}_{\mathrm{g}})\Big)^2}_{=:\mathrm{J_{TS_g}}} + \underbrace{\gamma_{\mathrm{CS_g}}\Big\{(i_{\mathrm{g}}^{\alpha\,\mathrm{max}} \leq \|i_{\mathrm{g[k+1]}}^{\alpha}(\vec{u}_{\mathrm{g}})\|) \text{ or } (i_{\mathrm{g}}^{\beta\,\mathrm{max}} \leq \|i_{\mathrm{g[k+1]}}^{\beta}(\vec{u}_{\mathrm{g}})\|)\Big\}}_{=:\mathrm{J_{CS_g}}}. \quad (4.6)$$

The predicted power $P_{\mathrm{[k+1]}}(\vec{u}_{\mathrm{g}}), Q_{\mathrm{[k+1]}}(\vec{u}_{\mathrm{g}})$, currents $i_{\mathrm{g[k+1]}}^{\alpha}(\vec{u}_{\mathrm{g}}), i_{\mathrm{g[k+1]}}^{\beta}(\vec{u}_{\mathrm{g}})$ are given by Equations (2.50) and (2.44), respectively. After evaluating and minimizing the costs obtained from Equation (4.6) for $\vec{u}_{\mathrm{g}} \in \mathcal{U}_8$ of the two level GSC, an optimal gate vector of $\vec{G}_{\mathrm{g}}$ will be obtained and assigned to the grid side converter.

[3]MPPT is a control technique to guarantee a maximum power is generated from the available wind energy in the operation range-II, for which see Chp. 2. The weighting factor selection rules are not introduced and for the readers who are interested please refer to [10] and the reference therein.

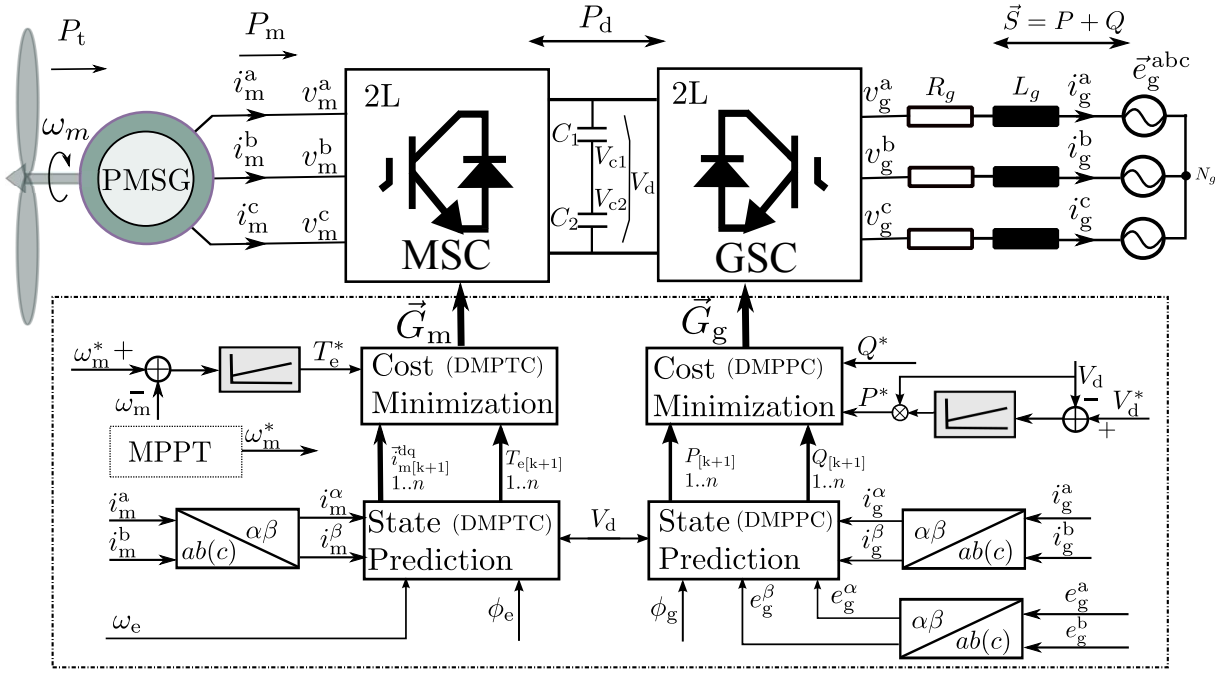

(a) DMPTC and DMPPC scheme for two-level back-to-back power converter PMSG system.

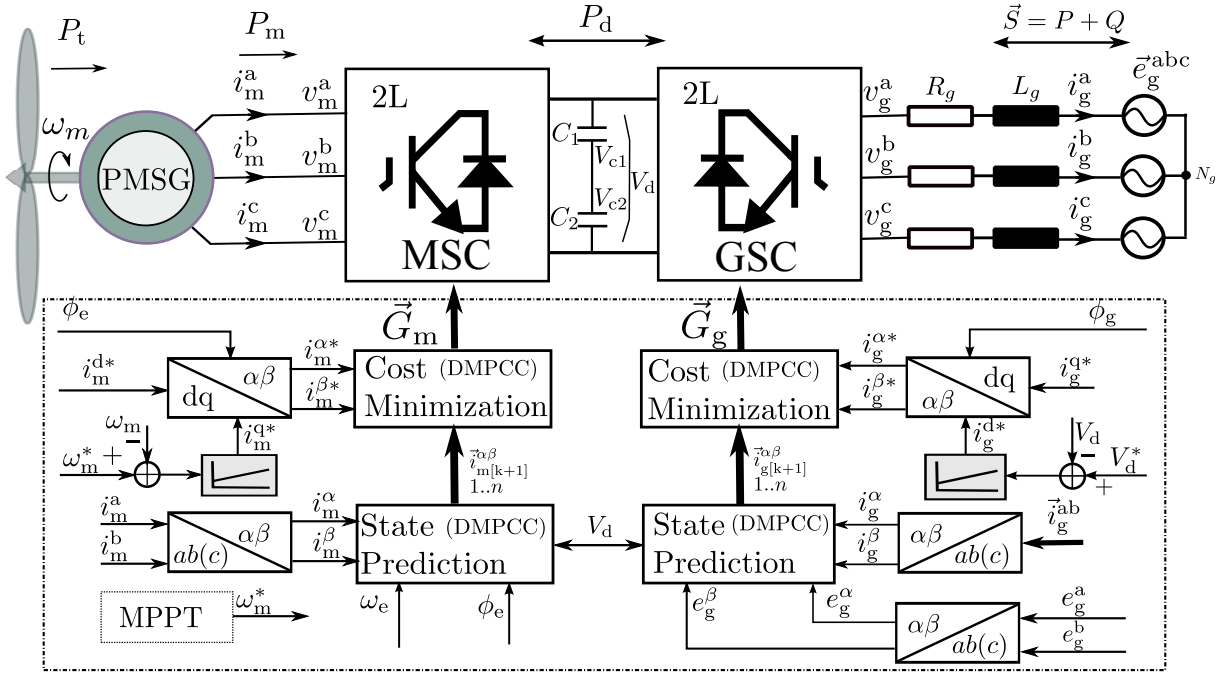

(b) DMPCC scheme for the two-level back-to-back PMSG system.

Fig. 4.2: Direct model predictive control schemes for the two-level back-to-back power converter PMSG wind turbine system: direct model predictive torque control for machine side and direct model predictive power control for grid side (a), and direct model predictive current control for both the machine and grid side (b).

Remark 3 (System limit constraint simplification) *Re-examining the control structure shown in Fig. 4.2, it is easy to find that, both the MSC and GSC sides require an outer control loop to generate the references, which in most cases is PI controllers, or controllers which can easily incorporate an upper and lower output limits. Those limits have already considered the rated values of the system, i.e., the limit constraints [55]. Therefore, assuming the references can be tracked properly, there are no necessities to re-consider them again in the cost function, which are computationally heavy. In the following, for predictive current, power, and torque control, for both two and three-level systems, the constraints are included into the outer control loops, and the cost functions are therefore simplified for the sake for reducing computational efforts. The cost function for predictive torque and power control can be simplified as*

$$J^{\mathrm{m}}_{\mathrm{DMPC}}(\vec{u}_{\mathrm{m}}) = \gamma_{T_{\mathrm{e}}}\Big(T^{*}_{\mathrm{e}} - T_{\mathrm{e[k+1]}}(\vec{u}_{\mathrm{m}})\Big)^{2} + \gamma_{i^{\mathrm{d}}_{\mathrm{m}}}\Big(i^{\mathrm{d}}_{\mathrm{m[k+1]}}(\vec{u}_{\mathrm{m}})\Big)^{2} \tag{4.7a}$$

$$J^{\mathrm{g}}_{\mathrm{DMPC}}(\vec{u}_{\mathrm{g}}) = \Big(P^{*} - P_{\mathrm{[k+1]}}(\vec{u}_{\mathrm{g}})\Big)^{2} + \Big(Q^{*} - Q_{\mathrm{[k+1]}}(\vec{u}_{\mathrm{m}})\Big)^{2} \tag{4.7b}$$

respectively. (The experimental results have also shown that, the current/torque, and power have not violated the limitations.) However, for the cases, where the system is not limited/constrained by certain outer loop controllers with output limitations, simply simplifying the cost function in such a manner is not an effective solution [55].

4.2.2 Direct model predictive current control

4.2.2.1 Direct model predictive current control of 2L-MSC

Instead of using the torque (and d-axis current) as tracking targets, for direct model predictive current control, the current performances are of higher priority. The inner loop itself can be designed in the $\alpha\beta$ frame to eliminate the otherwise required synchronous frame transformations. Therefore, the generator/machine-side cost function for predictive current control is defined as

$$J^{\mathrm{m}}_{\mathrm{DMPC}}(\vec{u}_{\mathrm{m}}) = \Big(i^{\alpha *}_{\mathrm{m}} - i^{\alpha}_{\mathrm{m[k+1]}}(\vec{u}_{\mathrm{m}})\Big)^{2} + \Big(i^{\beta *}_{\mathrm{m}} - i^{\beta}_{\mathrm{m[k+1]}}(\vec{u}_{\mathrm{m}})\Big)^{2}. \tag{4.8}$$

The predicted current vector of $\vec{i}^{\,\alpha\beta}_{\mathrm{m[k+1]}}(\vec{u}_{\mathrm{m}})$ is calculated by Equation (2.38), with $\vec{u}_{\mathrm{m}} \in \mathcal{U}_8$. The current reference is generated by a proper outer control loop (here a PI controller regulating the speed control is used for generating the q-axis current and the d-axis current reference is set to be zero for a MTPA control. These references are then transferred into $\alpha\beta$ frame to assign to the machine side inner predictive current control loop). Note here, due to the currents in both α and β axis are equally important to the system, so no extra weightings are required for these target sets. After evaluating and minimizing the costs obtained from Equation (4.8) for $\vec{u}_{\mathrm{m}} \in \mathcal{U}_8$ for the two level MSC, an optimal gate vector of $\vec{G}^{*}_{m} = \mathcal{G}^{-1}(\vec{u}^{*}_{\mathrm{m}})$ will be obtained and assigned to the machine side converter.

4.2.2.2 Direct model predictive current control of 2L-GSC

In the analogy to DMPCC for MSC, instead of using the grid side instantaneous power as tracking targets, the grid side current performances are of higher level priority for direct model predictive current control. The inner loop itself can be designed in the $\alpha\beta$ frame, and the grid side cost function is defined as

$$J^{\mathrm{g}}_{\mathrm{DMPC}}(\vec{u}_{\mathrm{g}}) = \left(i^{\alpha*}_{\mathrm{g}} - i^{\alpha}_{\mathrm{g[k+1]}}(\vec{u}_{\mathrm{g}})\right)^2 + \left(i^{\beta*}_{\mathrm{g}} - i^{\beta}_{\mathrm{g[k+1]}}(\vec{u}_{\mathrm{g}})\right)^2. \tag{4.9}$$

The predicted current vector $\vec{i}^{\,\alpha\beta}_{\mathrm{g[k+1]}}(\vec{u}_{\mathrm{g}})(\vec{u}_{\mathrm{m}} \in \mathcal{U}_8)$ can be obtained by Equation (2.44). The current references are generated/set by a proper outer control loop (here a PI controller for the DC-link control is used to generate the d-axis current reference and the q-axis current is set to be zero for unit power factor control. These two references are then transferred into $\alpha\beta$ frame). In the analogy, due to the currents both in α and β axis are equally important to the system, again no extra weightings are required for these targets.

After evaluating and minimizing the costs obtained from Equation (4.9) for $\vec{u}_{\mathrm{m}} \in \mathcal{U}_8$ for the two level MSC, an optimal gate vector of $\vec{G}_{\mathrm{g}}$ will be obtained and assigned to the machine side converter.

The overview of the predictive current control method for both the grid and machine side control is shown in Fig. 4.2b.

4.3 DMPC for three-level back-to-back PMSG systems

In Sec. 4.3.1, the direct model predictive torque control (DMPTC) for the machine side and direct model predictive power control (DMPPC) for the grid side of a three-level NPC back-to-back power converter PMSG wind turbine system will be presented. While in Sec. 4.3.2, the direct model predictive current control (DMPCC) methods for both the machine and grid side of a three-level NPC back-to-back power converter PMSG wind turbine system are to be discussed.

4.3.1 Direct model predictive torque and power control

Characterized by its physical structure, for a three-level NPC power converter, the DC-link voltage balancing has to be assured. Therefore, an extra DC-Link voltage balancing term should be included into the cost function design. For a 3L NPC power converter driven PMSG, the cost function using predictive torque control shall therefore be designed as

$$J^{\mathrm{m}}_{\mathrm{DMPC}}(\vec{u}_{\mathrm{m}}) = \underbrace{\gamma_{\mathrm{T_e}}\left(T^*_{\mathrm{e}} - T_{\mathrm{e[k+1]}}(\vec{u}_{\mathrm{m}})\right)^2}_{=:J_{T_{\mathrm{e}}}} + \underbrace{\gamma_{i^{\mathrm{d}}_{\mathrm{m}}}\left(i^{\mathrm{d}}_{\mathrm{m[k+1]}}(\vec{u}_{\mathrm{m}})\right)^2}_{=:J_{i^{\mathrm{d}}_{\mathrm{m}}}} + \underbrace{\gamma_{V_{\mathrm{o}}}\left(V_{\mathrm{o[k+1]}}(\vec{u}_{\mathrm{m}})\right)^2}_{J_{V_{\mathrm{o}}}=:J_{\mathrm{CS_m}}} \tag{4.10}$$

with weighting factors $\gamma_{T_\mathrm{e}}[1/\mathrm{Nm}]$, $\gamma_{i_\mathrm{m}^\mathrm{d}}[1/\mathrm{A}]$ and $\gamma_{V_\mathrm{o}}[1]$. The predicted torque $T_{\mathrm{e}[\mathrm{k}+1]}(\vec{u}_\mathrm{m})$, currents $\vec{i}^{\,\mathrm{dq}}_{\mathrm{m}[\mathrm{k}+1]}(\vec{u}_\mathrm{m})$ and neutral point voltage difference $V_{\mathrm{o}[\mathrm{k}+1]}(\vec{u}_\mathrm{m})$ are given by Equations (2.42) and (2.21), respectively, both with $\vec{u}_\mathrm{m} \in \mathcal{U}_{27}$.

In the analogy, including the DC-link balancing control targets, for the GSC with a three-level NPC power converter, its cost function for using predictive power control is designed as

$$J^{\mathrm{g}}_{\mathrm{DMPC}}(\vec{u}_\mathrm{g}) = \underbrace{\left(P^* - P_{[\mathrm{k}+1]}(\vec{u}_\mathrm{g})\right)^2}_{=:J_P} + \underbrace{\left(Q^* - Q_{[\mathrm{k}+1]}(\vec{u}_\mathrm{g})\right)^2}_{=:J_Q} + \underbrace{\gamma_{V_\mathrm{o}}\left(V_\mathrm{o}(\vec{u}_\mathrm{g})\right)^2}_{J_{V_\mathrm{o}}=:J_{\mathrm{CS_g}}} \tag{4.11}$$

with weighting factors $\gamma_{V_\mathrm{o}}[1]$. The predicted active and reactive power and currents are given by Equation (2.50) and (2.21), respectively, both with $\vec{u}_\mathrm{m} \in \mathcal{U}_{27}$.

After evaluating and minimizing cost-functions (4.11) and (4.10) for $\vec{u}_\mathrm{g}, \vec{u}_\mathrm{m} \in \mathcal{U}_{27}$, optimal gate vectors of $\vec{G}_{\mathrm{g,m}}$ will be obtained and assigned to the grid and machine side converters, respectively. The overview of such control method is depicted by Fig. 4.3a.

4.3.2 Direct model predictive current control

Similar to the two-level converter predictive current control scheme, instead of using the torque (and d-axis current) or power as tracking targets, for direct model predictive current control of the grid and machine sides of the three-level NPC back-to-back power converter PMSG wind turbine system, the current tracking belongs to the targeting set. The inner loop itself can be designed in the $\alpha\beta$ frame to eliminate the otherwise required synchronous frame transformations. However, the voltage balancing requirement shall be taken into consideration. Therefore, the machine and grid-side cost functions for the three-level back-to-back power converter case are defined as

$$J^{\mathrm{m}}_{\mathrm{DMPC}}(\vec{u}_\mathrm{m}) = \underbrace{\left(i^{\alpha*}_\mathrm{m} - i^{\alpha}_{\mathrm{m}[\mathrm{k}+1]}(\vec{u}_\mathrm{m})\right)^2 + \left(i^{\beta*}_\mathrm{m} - i^{\beta}_{\mathrm{m}[\mathrm{k}+1]}(\vec{u}_\mathrm{m})\right)^2}_{=:J_{\mathrm{TS_m}}} + \underbrace{\gamma_{V_\mathrm{o}}\left(V^*_\mathrm{o} - V_{\mathrm{o}[\mathrm{k}+1]}(\vec{u}_\mathrm{m})\right)^2}_{J_{V_\mathrm{o}}=:J_{\mathrm{CS_m}}}, \tag{4.12}$$

and

$$J^{\mathrm{g}}_{\mathrm{DMPC}}(\vec{u}_\mathrm{g}) = \underbrace{\left(i^{\alpha*}_\mathrm{g} - i^{\alpha}_{\mathrm{g}[\mathrm{k}+1]}(\vec{u}_\mathrm{g})\right)^2 + \left(i^{\beta*}_\mathrm{g} - i^{\beta}_{\mathrm{g}[\mathrm{k}+1]}(\vec{u}_\mathrm{g})\right)^2}_{=:J_{\mathrm{TS_g}}} + \underbrace{\gamma_{V_\mathrm{o}}\left(V^*_\mathrm{o} - V_\mathrm{o}(\vec{u}_\mathrm{g})\right)^2}_{J_{V_\mathrm{o}}=:J_{\mathrm{CS_g}}}, \tag{4.13}$$

respectively, where $\gamma_{\vec{i}^{\,\alpha\beta}_\mathrm{m}}[1]$ is the weighting factor for DC-link voltage balancing control items. The predicted currents of $\vec{i}^{\,\alpha\beta}_{\mathrm{m}[\mathrm{k}+1]}(\vec{u}_\mathrm{m})$, $\vec{i}^{\,\alpha\beta}_{\mathrm{g}[\mathrm{k}+1]}(\vec{u}_\mathrm{g})$, and neutral point voltage are given by equations (2.38), (2.44), and (2.21), respectively, with $\vec{u}_\mathrm{m}, \vec{u}_\mathrm{g} \in \mathcal{U}_{27}$.

After evaluating and minimizing cost-function (4.12) and (4.13) for $\vec{u}_\mathrm{g}, \vec{u}_\mathrm{m} \in \mathcal{U}_{27}$, optimal gate vectors of $\vec{G}_{\mathrm{g,m}}$ will be obtained and assigned to the grid and machine side converters. The structural overview of such control method is depicted by Fig. 4.3b.

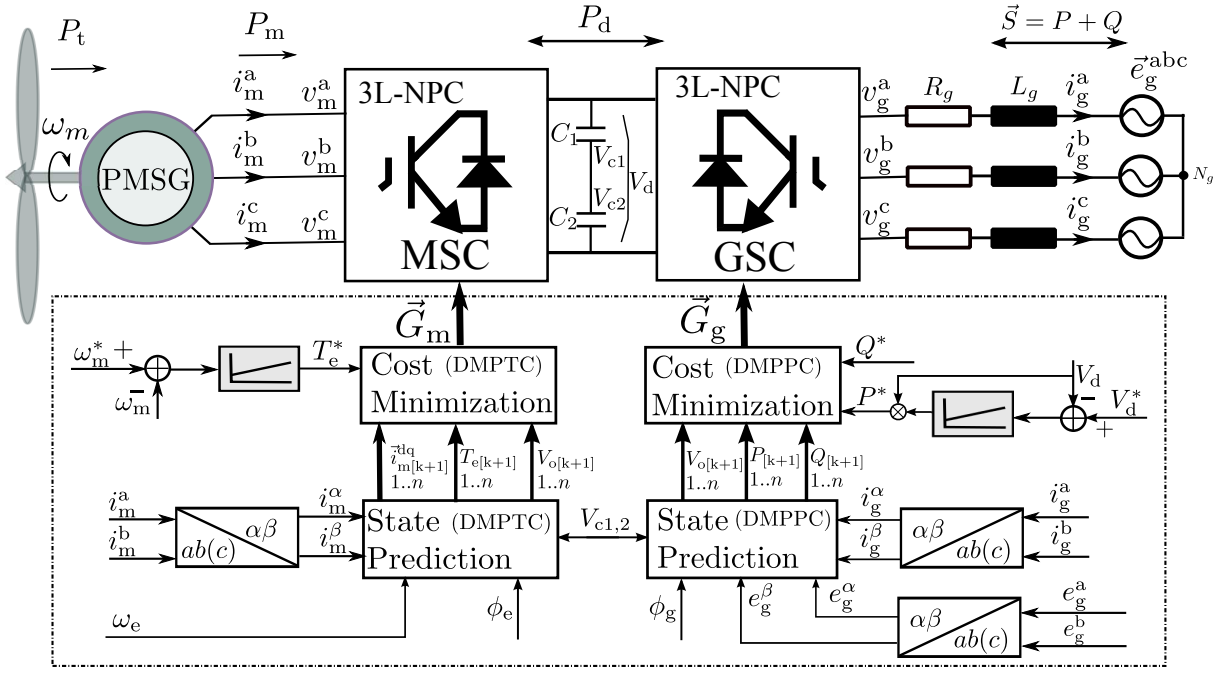

(a) FCS-DTC-DPC method for three-level NPC back-to-back power converter PMSG wind turbine systems.

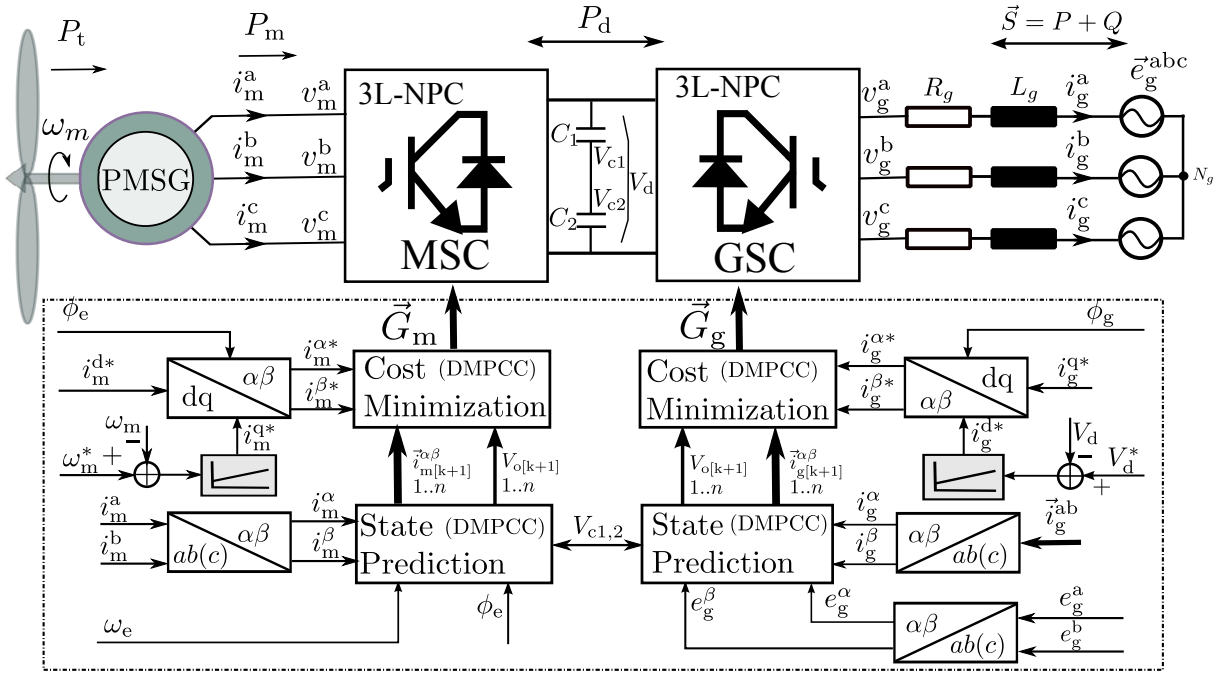

(b) DMPCC scheme for three-level NPC back-to-back power converter PMSG wind turbine systems.

Fig. 4.3: Control structure of direct model predictive torque-power control (a) and direct model predictive current control (b) for three-level NPC back-to-back power converter PMSG wind turbine system.

Remark 4 (Analysis of DTC, DPC, DMPTC, DMPPC and DMPCC) *So far, several direct control methods for both the machine and grid side control have been introduced. These are DTC, DMPTC and DMPCC for MSC, DPC, DMPPC and DMPCC for GSC. A deep view at these methods will reveal the following similarities and differences among these schemes.*

(i) ***Similarities:*** *All do not require any modulator or inner linear control loops, and belong to the nonlinear control class.*

(ii) ***Differences:***

(a) For both MSC and GSC control, from the structure level DMPTC, DMPPC and DMPCC all use a cost function and the explicit system model to determine the optimal switching sequence, while DTC uses an offline defined switching table to achieve so. The cost-function based concept brings more flexibility to achieve the relevant control targets.

(b) For the machine side control, from the "torque per current ratio" point of view, classical DTC scheme will produce the worst ratio since a constant stator flux magnitude (slightly bigger than that of the permanent-magnet flux) is usually set from the outer loop for surface-mounted PMSM(G) [64], hence a very big flux-weakling current component will be produced during the heavy load situations, because the torque angle is very big in this situation (See Equation (2.40)). This makes its torque per current ratio (much) smaller than that of the predictive control schemes, where almost all the current can be manipulated to produce torque with a flexible cost function.

(c) Directly examining the cost-function formulation between DMPTC and DMPCC will yield that, DMPCC might simplify the weighting factor tuning process (for the targeting set), since, currents both in $\alpha\beta$ frame are equivalently important and require not different weighting. However, for non-saliency (i.e., $L_{\mathrm{s}}^{\mathrm{d}} = L_{\mathrm{s}}^{\mathrm{q}}$) based PMSG it can be proven that, theoretically both DMPTC & DMPCC and DMPPC & DMPCC shall achieve same steady control performances, for this a detailed presentation can be found in our publication [74, 75], with different computational requirements.

For switching state power converters, the switching frequency and the control variable ripples are always a conflicting pair. In general, smaller control variable ripples will be observed with a higher switching frequency, at a same modulation technique (even without modulator), and vice versa. Since during our experimental verification part, certain comparison will be performed between the cost-function based methods and the switching table based solutions. For a fair comparison (during the steady state), the switching frequency has to be regulated into a similar range. To this end, the cost-function based techniques, i.e., FCS-MPC or DMPC, show great flexibility: the cost functions can be modified to include switching frequency regulation objective for both the MSC and GSC, easily. Taking the 3L NPC back-to-back system as an example, the realization is presented

as follows: Cost functions for the machine and grid side control using FCS-DTC-DPC, with switching frequency regulation are defined as

$$J^{\mathrm{m}}_{\mathrm{DMPC}}(\vec{u}_{\mathrm{m}}) = \underbrace{\overbrace{\gamma_{\mathrm{T_e}}\left(T^*_{\mathrm{e}} - T_{\mathrm{e[k+1]}}(\vec{u}_{\mathrm{m}})\right)^2}^{=:J_{T_{\mathrm{e}}}} + \overbrace{\gamma_{i^{\mathrm{d}}_{\mathrm{m}}}\left(i^{\mathrm{d}}_{\mathrm{m[k+1]}}(\vec{u}_{\mathrm{m}})\right)^2}^{=:J_{i^{\mathrm{d}}_{\mathrm{m}}}}}_{=:J_{\mathrm{TS_m}}} + \underbrace{\overbrace{\gamma_{V_{\mathrm{o}}}\left(V^*_{\mathrm{o}} - V_{\mathrm{o[k+1]}}(\vec{u}_{\mathrm{m}})\right)^2}^{J_{V_{\mathrm{o}}}} + \overbrace{\gamma_{\mathrm{sf}}\Delta_{\vec{u}_{\mathrm{m}}}}^{J_{\mathrm{sfm}}}}_{=:J_{\mathrm{CS_m}}}, \tag{4.14}$$

and

$$J^{\mathrm{g}}_{\mathrm{DMPC}}(\vec{u}_{\mathrm{g}}) = \underbrace{\overbrace{\left(P^* - P_{\mathrm{[k+1]}}(\vec{u}_{\mathrm{g}})\right)^2}^{=:J_P} + \overbrace{\left(Q^* - Q_{\mathrm{[k+1]}}(\vec{u}_{\mathrm{g}})\right)^2}^{=:J_Q}}_{=:J_{\mathrm{TS_g}}} + \underbrace{\overbrace{\gamma_{V_{\mathrm{o}}}\left(V^*_{\mathrm{o}} - V_{\mathrm{o[k+1]}}(\vec{u}_{\mathrm{g}})\right)^2}^{J_{V_{\mathrm{o}}}} + \overbrace{\gamma_{\mathrm{sf}}\Delta_{\vec{u}_{\mathrm{g}}}}^{J_{\mathrm{sfg}}}}_{=:J_{\mathrm{CS_g}}}, \tag{4.15}$$

respectively, where $\Delta_{\vec{u}_{\mathrm{y}}}, y \in \{m, g\}$ is responsible for the switching frequency regulation, and is defined as

$$\Delta_{\vec{u}_{\mathrm{y}}} = |u^{\mathrm{a}}_{\mathrm{y[k+1]}} - u^{\mathrm{a}}_{\mathrm{y[k]}}| + |u^{\mathrm{b}}_{\mathrm{y[k+1]}} - u^{\mathrm{b}}_{\mathrm{y[k]}}| + |u^{\mathrm{c}}_{\mathrm{y[k+1]}} - u^{\mathrm{c}}_{\mathrm{y[k]}}|. \tag{4.16}$$

4.4 Performance evaluations with experimental data

In this section, the control performances of the aforementioned direct model predictive control techniques, i.e, direct model predictive torque and power control (we name it here as FCS-DTC-DPC for the sake of a clear comparison with ST-DTC-DPC presented in the last chapter), direct model predictive current control (similarly we name it as FCS-DCC), are presented. Experimental evaluations of these control methods applied to (i) the two level systems are presented in Sec. 4.4.1, (ii) three-level are presented in Sec. 4.4.2. Their comparison with the switching table based methods are presented in Sec. 4.4.3.1 and 4.4.3.2.

All the experimental results presented in the following parts are obtained using the test-benches described in Chp. 2. The control system design procedure follows the descriptions given in Sec. 2.5.4. All the realizations of these control techniques presented in this chapter have been realized on the FPGA. Due to their similarity (to the realizations presented in the following chapters), all FPGA realizations processes for these classical DMPC methods are not presented in this chapter. Readers who are interested in the FPGA realization may directly refer to our publications (e.g., [42, 46, 47, 57, 60, 63, 70]) or Chp. 6, 7 and 8.

4.4.0.0.1 Identical Test Setting In the following, *if not specifically mentioned*, the overall testing scenarios are as follows: we assume the optimal speed reference ω^*_{m} (i.e., the so-called "maximum power point tracking speed reference") in Eq. (2.33), which shall come from a proper MPPT controller, is already known and changes (abruptly with a slope of 3 [rpm/ms]) following certain (unpredictable) wind speeds. A rated torque is mounted under such (fast) speed changing rate to test the most harsh operation situations.

4.4.1 FCS-DTC-DPC and FCS-DCC for two level PMSG systems

In this section, both the direct FCS-DTC-DPC (See Sec. 4.4.1.2) and FCS-DCC control (See Sec. 4.4.1.2) methods for **2L back-to-back power converter PMSG wind turbine system** are evaluated. Both the overall control performances and the steady state of the machine and grid side control performances are given.

4.4.1.1 Evaluations of FCS-DTC-DPC method for 2L back-to-back PMSG system

The experimental data of direct model predictive torque (for MSC) and direct model predictive power control (for GSC) methods for the 2L back-to-back power converter PMSG wind turbine system are depicted in Fig. 4.4. The control interval is set to be $50e^{-6}$[s], and the calculation time is around 4.6 [μs] (therefore no compensation is required to insert into the predictions). The DC-link voltage reference is set at 350 [V], while the reactive power reference is set to be 0 [var] for a unit power factor control. The overall control performances are shown in Fig. 4.4-(a). The zoomed steady state control performances of both the generator and grid side currents are illustrated in Fig. 4.4-(b) and (c). As can be seen, besides its good control dynamics, and large changing range of the switching frequency is seen. The synthesized switching patterns (represented by the estimated command voltage here) are in general satisfying (sinusoidal and symmetrical, see the last sub-figures in both (b) and (c)).

4.4.1.2 Evaluations of FCS-DCC method for 2L back-to-back PMSG system

The experimental data of direct model predictive current control method (for both MSC and GSC) of the 2L back-to-back power converter PMSG wind turbine system are depicted in Fig. 4.5. Similar to the FCS-DTC-DPC test setting: the control interval is set to be $50e^{-6}$[s], and no compensation was inserted into the predictions. The DC-link voltage reference is set at 350 [V], while the reactive power reference is set to be 0 [var]. The overall control performances are shown in Fig. 4.5-(a). The zoomed steady state control performances of both the generator and grid side currents are illustrated in Fig. 4.5-(b) and (c). As can be seen, besides its good control dynamics, a big change of the switching frequency is seen. The current tracking performances are also (quite) good. The synthesized switching patterns (represented by the estimated command voltage here) are in general satisfying (sinusoidal and symmetrical, see the last sub-figures in both (b) and (c)).

4.4.2 FCS-DTC-DPC and FCS-DCC for three-level NPC PMSG systems

In this section, both the direct FCS-DTC-DPC (See Sec. 4.4.2.1) and FCS-DCC control (See Sec. 4.4.2.2) methods for the **3L NPC back-to-back power converter PMSG**

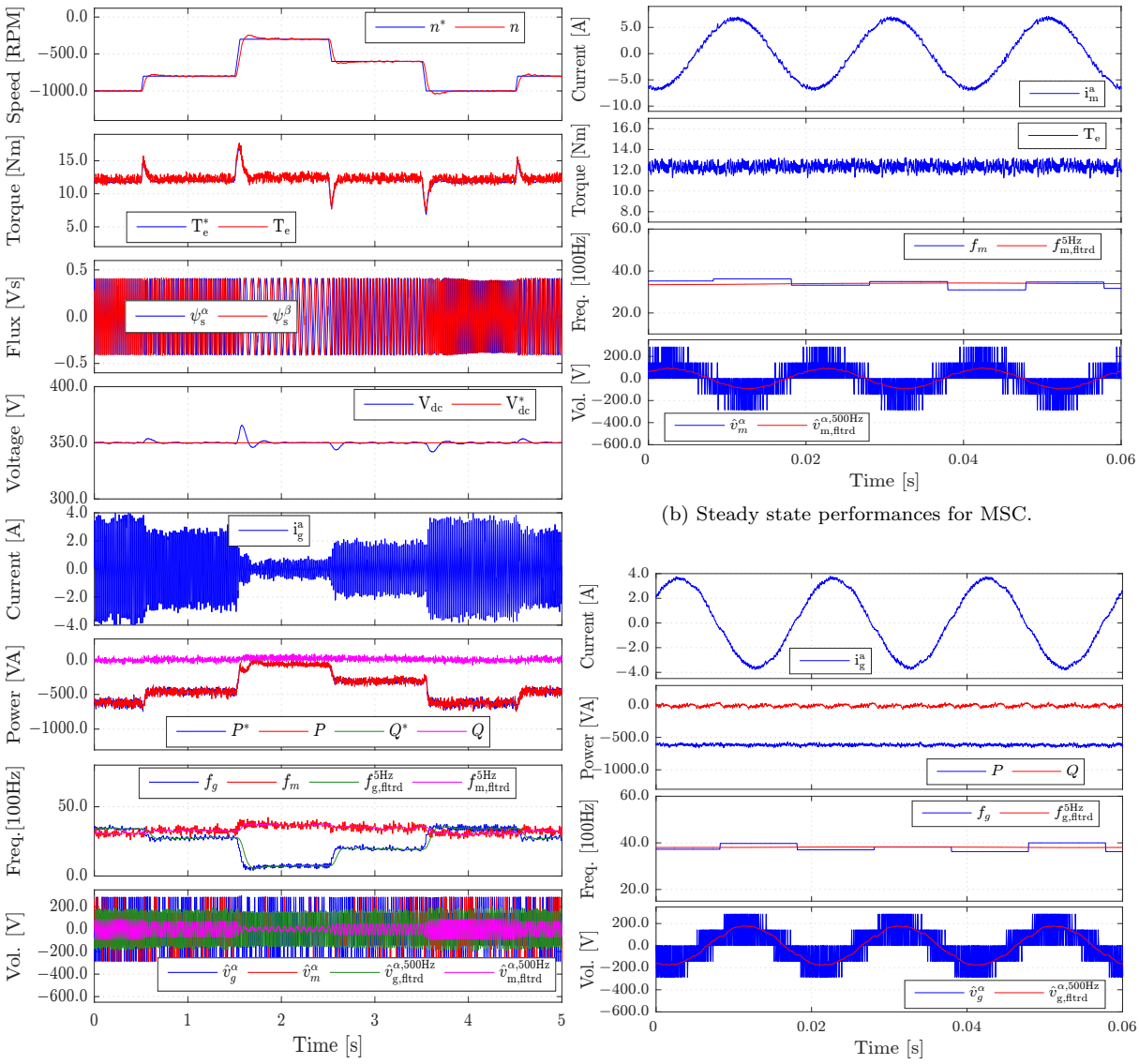

(a) Overall control performances.

(b) Steady state performances for MSC.

(c) Steady state performances for GSC.

Fig. 4.4: [Experimental results:] Overall control performance of **FCS-DTC-DPC** for the two-level back-to-back power converter PMSG wind turbine system. From top to bottom for sub-figure (a) are: generator speed, (estimated) electromagnetic torque, (estimated) stator flux, DC-link voltage, grid side current, active and reactive power, switching frequency and estimated grid and machine side converter voltages (in α phase), respectively. $f_x, f_{x,fltrd}^{5Hz}$ and $\hat{v}_x, \hat{v}_{x,fltrd}^{500Hz}$ are the switching frequency *versus* its filtered values (with cut-off frequency of 5Hz), and the estimated converter voltage *versus* its filtered (with cut-off frequency of 500Hz) values, for machine (m) and grid (g), respectively. Sub-figure (b) and (c) illustrate of the zoomed performance of the machine (b) and grid (c) side phase currents, electromagnetic torque, active and reactive power, switching frequency and estimated voltages.

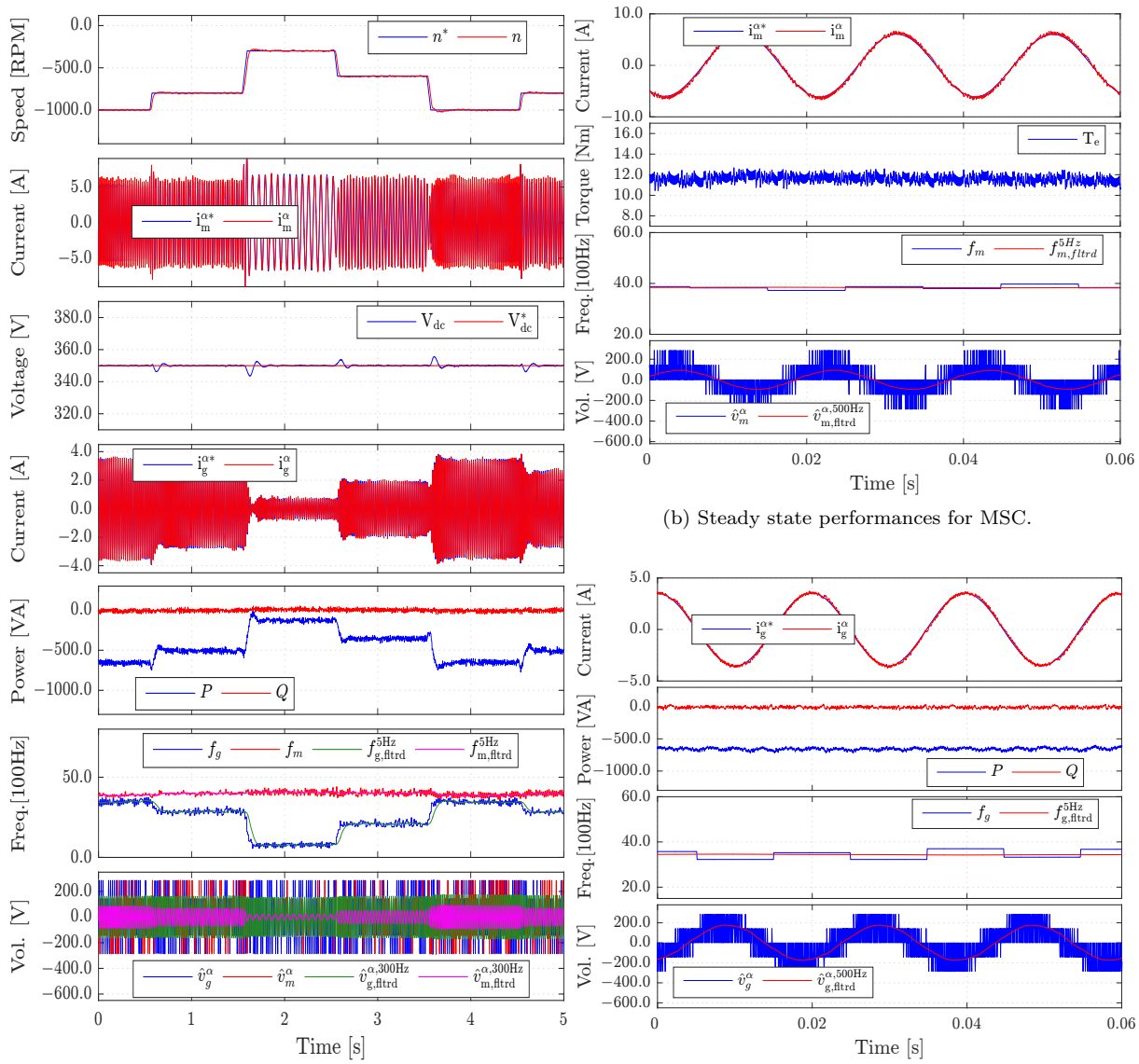

(a) Overall control performances.

(b) Steady state performances for MSC.

(c) Steady state performances for GSC.

Fig. 4.5: [Experimental results:] Overall control performance of **FCS-DCC** for the two-level back-to-back power converter PMSG wind turbine system. From top to bottom for sub-figure (a) are: generator speed, generator stator current in α phase, DC-link voltage, grid side current, active and reactive power, switching frequency and estimated grid and machine side converter voltages (in α phase), respectively. $f_x, f_{\text{x,fltrd}}^{\text{5Hz}}$ and $\hat{v}_x, \hat{v}_{\text{x,fltrd}}^{\text{500Hz}}$ are the switching frequency *versus* its filtered values (with cut-off frequency of 5Hz), and the estimated converter voltage *versus* its filtered (with cut-off frequency of 500Hz) values, for machine (m) and grid (g) sides, respectively. Sub-figure (b) and (c) illustrate of the zoomed performance of the machine (b) and grid (c) side phase currents, electromagnetic torque, active and reactive power, switching frequency and estimated voltages.

wind turbine system are evaluated. In the analogy to the two-level system testing, both the overall control performances and the steady state performances of both the machine and grid side control are presented.

4.4.2.1 Evaluations of FCS-DTC-DPC for 3L NPC back-to-back power converter PMSG system

The experimental evaluation results of predictive torque and power control of the three-level back-to-back power converter PMSG wind turbine systems are given in Fig. 4.6. The control interval is set to be $50e^{-6}$[s]. The DC-link voltage reference is set at 350 [V], while the reactive power reference is set to be 0 [var] for a unit power factor control. The overall control performances are shown in Fig. 4.6-(a). As can be seen, (quite) nice control dynamics, and reduced control variable ripples (in comparison with the two-level case) are seen. The DC-link control performances (for both the overall voltage tracking and DC-link capacitor voltage balancing control) are (very) good, which comes from the nice combination of a power feed-ward in the DC-link control loop and good dynamics of the inner power control loop. Note that, a fluctuation-free DC-link control requires also a good (fluctuation-free) speed control on the machine side, when power (estimated using speed and torque) feed-forward is used. However, large chattering of the switching frequency is observed. The zoomed steady state control performances of both the generator and grid side currents, the switching frequency (updated with a period of 10 [ms]) and the (estimated) command voltage in α-phase (which is the same as in a-phase) are illustrated in Fig. 4.6-(b) and (c).

4.4.2.2 Evaluations of FCS-DCC for 3L NPC back-to-back power converter PMSG system

The experimental evaluation results of predictive current control of the three-level back-to-back power converter PMSG wind turbine systems are given in Fig. 4.7. The control interval is set to be $50e^{-6}$[s]. The DC-link voltage reference is set at 350 [V], while the reactive power reference is set to be 0 [var] for a unit power factor control. The overall control performances are shown in Fig. 4.7-(a). As can be seen, (quite) nice control dynamics, and reduced control variable ripples (in comparison with the two-level case) are seen. The DC-link control performances (for both the overall voltage tracking and DC-link capacitor voltage balancing control) are (very) good, which comes from the nice combination of a power feed-forward in the DC-link control loop and good dynamics of the inner power control loop. Note that, a fluctuation-free DC-link control requires also a good (fluctuation-free) speed control on the machine side, when power (estimated using speed and torque) feed-forward is used. However, chattering of the switching frequency is observed. The zoomed steady state control performances of both the generator and grid side currents, the switching frequency (updated with a period of 10 [ms]) and the (estimated) command voltage in α-phase (which is the same as in a-phase) are illustrated in Fig. 4.7-(b) and (c).

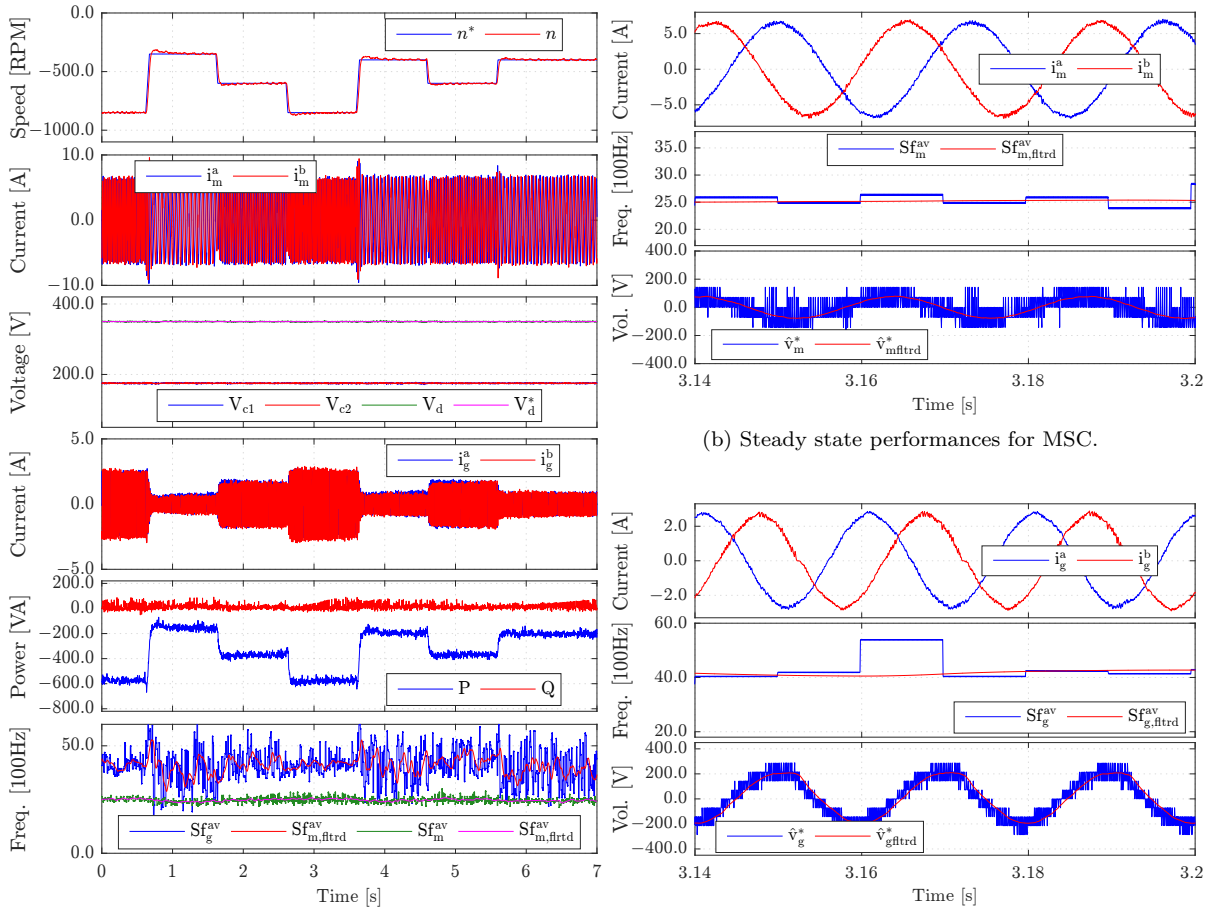

(a) Overall control performances.

(b) Steady state performances for MSC.

(c) Steady state performances for GSC.

Fig. 4.6: [Experimental results:] Overall control performance of **FCS-DTC-DPC** for the three-level back-to-back power converter PMSG wind turbine system. From top to bottom for sub-figure (a) are: generator speed, generator side phase currents, DC-link and capacitor voltages, grid side current, active and reactive power, and the average switching frequencies, respectively. $f_x, f_{x,fltrd}^{5Hz}$ are the switching frequency *versus* its filtered values (with cut-off frequency of 5Hz), and the estimated converter voltage *versus* its filtered (with cut-off frequency of 500Hz) values, for machine (m) and grid (g) sides, respectively. Sub-figure (b) and (c) illustrate of the zoomed performance of the machine (b) and grid (c) side phase currents, switching frequency and estimated voltages.

4.4.3 FCS-DTC-DPC and ST-DTC-DPC for back-to-back PMSG systems

Theoretical analysis and detailed realization steps of the switching table based DTC-DPC method (ST-DTC-DPC) have been presented in our last chapter. In comparison with the cost function based DTC-DPC method (FCS-DTC-DPC) some similarities can be easily found in between, such as, both are direct nonlinear control methods, no modulation is required, switching frequency not fixed and both have fast control dynamics [21, 25].

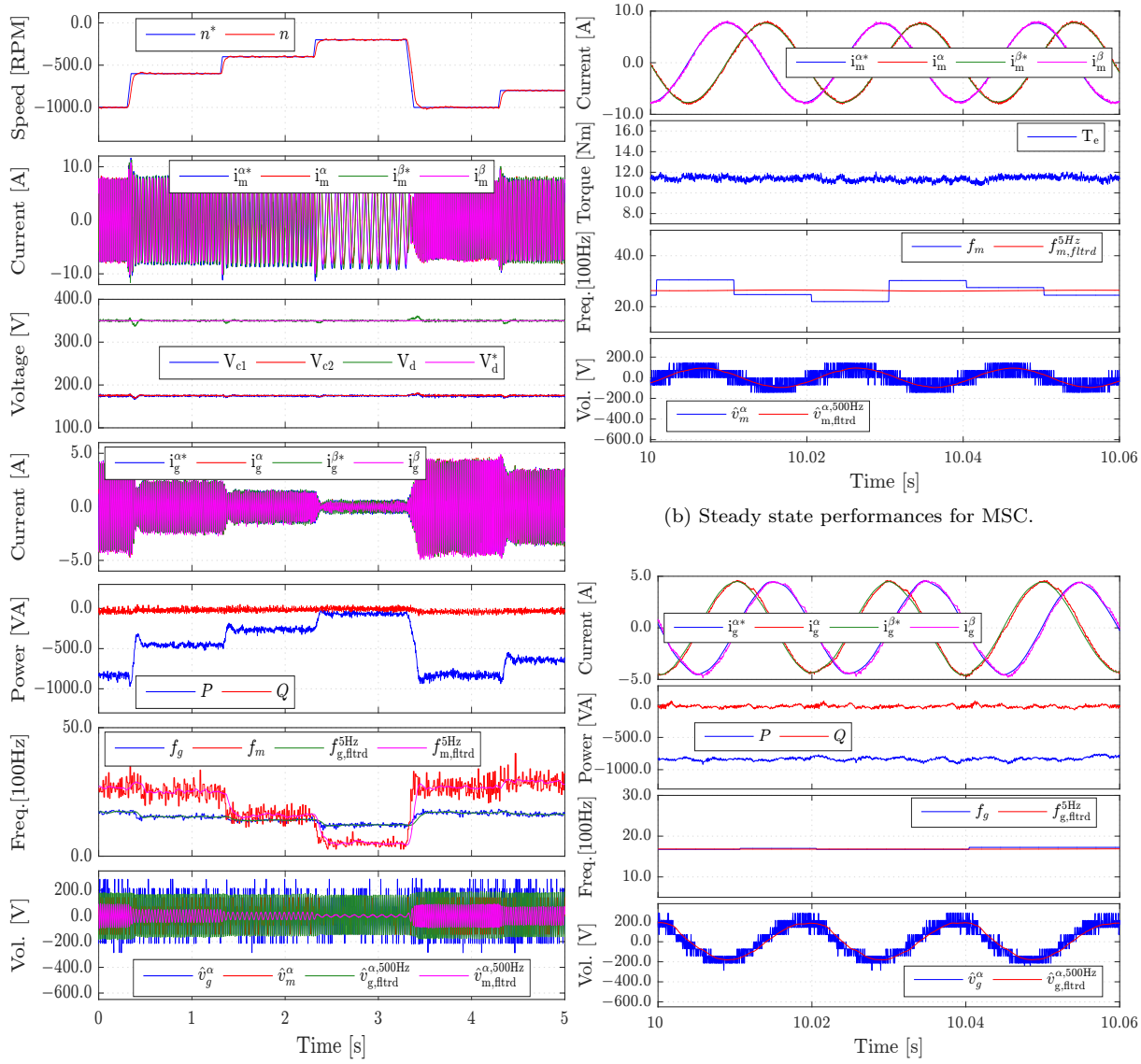

(a) Overall control performances.

(b) Steady state performances for MSC.

(c) Steady state performances for GSC.

Fig. 4.7: [Experimental results:] Overall control performance of **FCS-DCC** for the three-level back-to-back power converter PMSG wind turbine system. From top to bottom for sub-figure (a) are: generator speed, generator side phase currents, DC-link and capacitor voltages, grid side current, active and reactive power, and the average switching frequencies, respectively. $f_x, f^{5\text{Hz}}_{\text{x,fltrd}}$ and $\hat{v}^{*}_{\text{x,fltrd}}, x \in \{g, m\}$ are the switching frequency *versus* its filtered values (with cut-off frequency of 5Hz), and the estimated converter voltage *versus* its filtered (with cut-off frequency of 500Hz) values, for machine (m) and grid (g) sides, respectively. Sub-figure (b) and (c) illustrate of the zoomed performance of the machine (b) and grid (c) side phase currents, switching frequency and estimated voltages.

Therefore, it is worthwhile to take the efforts to give a deeper investigation of both methods experimentally, to illustrate their differences in control performances, in particular at steady state phase under a similar switching frequency. In the following sections, the experimental evaluations of the FCS- and ST-DTC-DPC techniques for both the two- and three-level NPC back-to-back power converter systems are presented.

4.4.3.1 FCS-DTC-DPC and ST-DTC-DPC for 2L back-to-back PMSG systems: A comparative evaluation

The experimental evaluations of the FCS-DTC-DPC and ST-DTC-DPC techniques for the two-level system at the same outer control loop parameters are performed. For the ST-DTC-DPC the bandwidths around 2% of their rated values are set, which results in the switching frequencies around 5kHz for the machine side and 4kHz for the grid side. The weighting factors to regulate the switching frequencies are set as 0.43 for the machine side while 0.56 for the grid side to achieve the similar operating switching frequency values for FCS-DTC-DPC method. The overall and the steady state control performances are shown in Fig. 4.8 and Fig. 4.9, respectively.

As can be seen from Fig. 4.8, the general overall control performances for both FCS-DTC-DPC and ST-DTC-DPC are quite similar, except these:

(1) the torque ripples with FCS-DTC-DPC are smaller than that of ST-DTC-DPC method (See the second sub-figure for both Fig. 4.9a and Fig. 4.9a), while,

(2) the switching frequency (in particular for the grid side converter) with the ST-DTC-DPC method changed in a narrower range in comparison with the FCS-DTC-DPC method (See the last second sub-figure for both Fig. 4.9a and Fig. 4.9a), under the same tested scenarios.

A deep view into Fig. 4.9 will yield the following discovery: during steady state under the given testing scenario, much smaller ripples for both the stator and grid side filter currents, the torque and grid side power are achieved with the FCS-DTC-DPC solution, at a similar switching frequency (of around 4 kHz). The reason can be found from their switching patterns synthesized by the respective control methods (i.e., the last sub-figure in both (a) v.s. (b) and (c) v.s. (d) of Fig. 4.9): with the similar average magnitudes of the expected (control) voltages (i.e., the filtered values for both sides), much smoother (and "sinusoidal") switching patterns are generated with the proposed FCS-DTC-DPC technique.

To test the transient control performances for both methods, the following scenarios are set: a torque reference changes from -7 to $+7$ [Nm] abruptly without using the speed PI control loop, while the grid side reactive power reference changes from $+500$ to -500 [var][4]. As is expected, their transient control performances for both the machine and grid

[4]For a back-to-back power converter system the active power reference is generated by controlling the DC-link voltage. Therefore, it is not possible to independently test the inner loop power control dynamics by directly setting the active power reference. Because the outer DC-link control loop has always to exist to guarantee an assured DC-link voltage value for safety concerns.

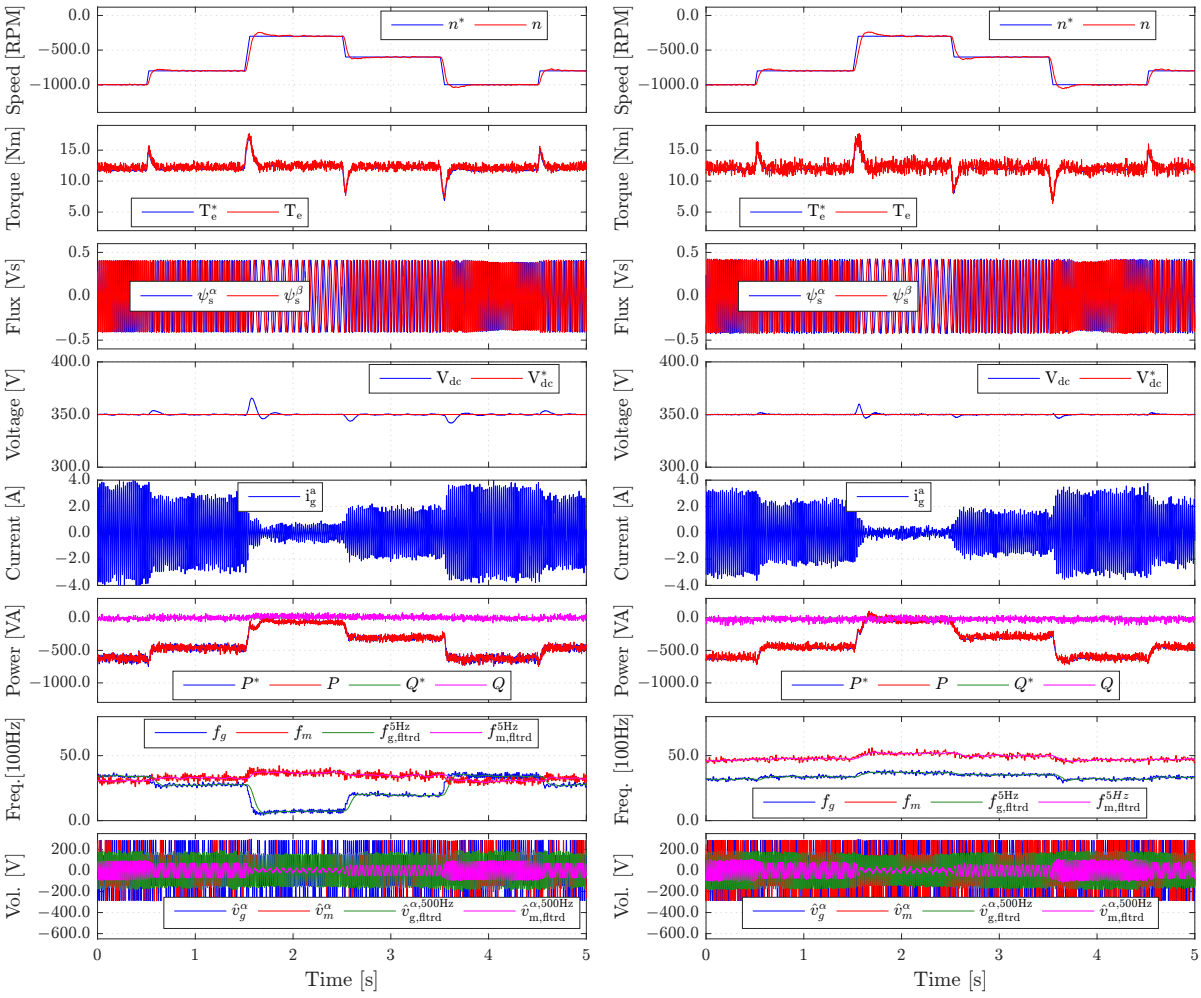

(a) Overall results for FCS-DTC-DPC (with $T_s = 50e^{-6}$ s).

(b) Overall results of ST-DTC-DPC ($T_s = 50e^{-6}$ s).

Fig. 4.8: [Experimental results:] Overall control performance of FCS-DTC-DPC and ST-DTC-DPC methods for the two-level back-to-back power converter PMSG wind turbine system emulator. From top to bottom for both *(a)* and *(b)* are: generator speed, (estimated) electromagnetic torque, (estimated) stator flux, DC-link voltage, grid side current, active and reactive power, switching frequency and estimated grid and machine side converter voltages (in α phase), respectively. $f_x, f^{5\text{Hz}}_{\text{x,fltrd}}$ and $\hat{v}_x, \hat{v}^{500\text{Hz}}_{\text{x,fltrd}}$ are the switching frequency *versus* its filtered values (with cut-off frequency of 5Hz), and the estimated converter voltage *versus* its filtered (with cut-off frequency of 500Hz) values, for machine (when $x = m$) and grid (when $x = g$), respectively.

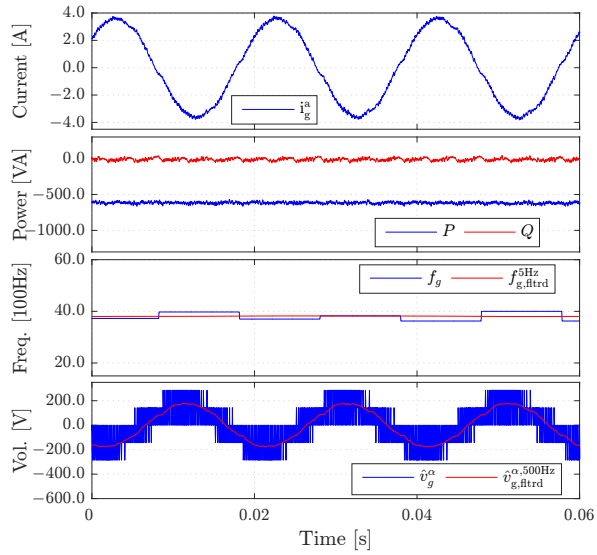

(a) Grid side steady state control performances for FCS-DMPTC-PC.

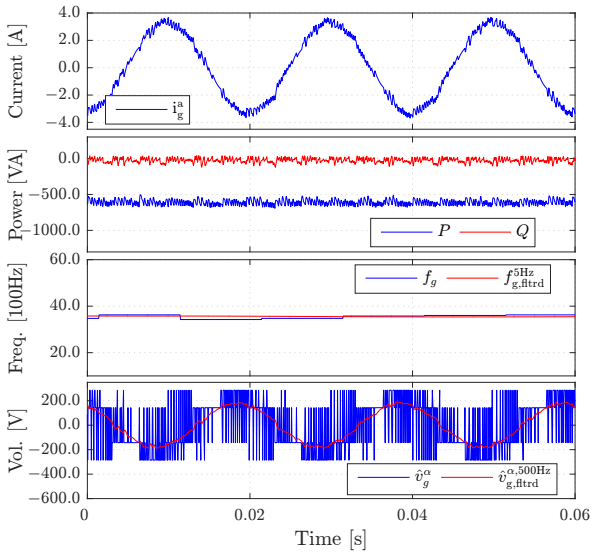

(b) Grid side steady state control performances for ST-DTC-DPC.

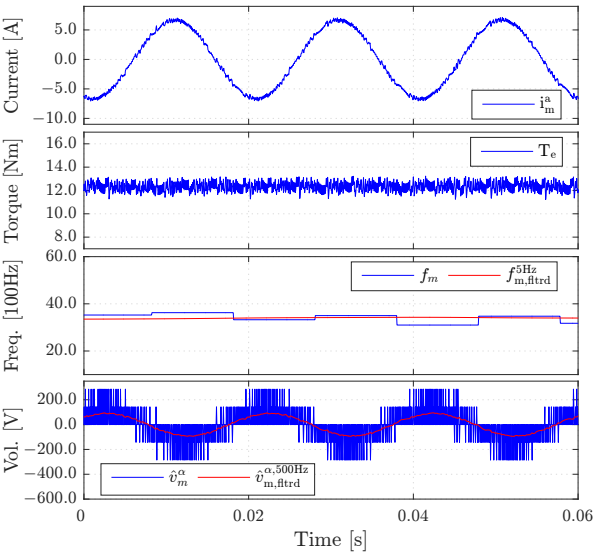

(c) Machine side steady state control performances for FCS-DMPTC-PC.

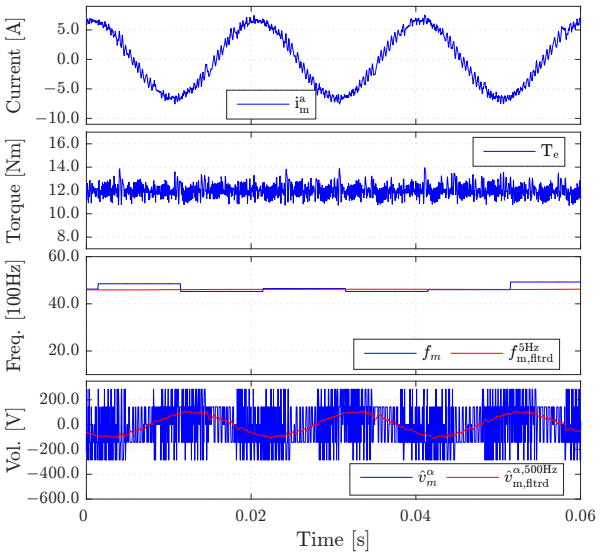

(d) Machine side steady state control performances for ST-DTC-DPC.

Fig. 4.9: [Experimental results:] Steady-state control performance of FCS-DPC-DTC and ST-DTC-DPC methods for the two-level back-to-back power converter PMSG wind turbine system emulator. From top to bottom: i) for (a) and (b) are grid side phase current, active and reactive power, switching frequency, estimated grid side converter output voltage; ii) for (c) and (d) are generator stator current, electromagnetic torque, switching frequency and estimated grid side converter output voltage, respectively.

sides with FCS-DTC-DPC and ST-DTC-DPC are quite similar: for the machine side, tracking a torque change from -7 to $+7$ [Nm], i.e., tracking a step change of 14 [Nm], costs (a similar period) less than 0.8 [ms] for both the FCS-DTC and ST-DTC methods (See Fig. 4.14d and Fig. 4.14e); while tracking a reactive power change from +500 to -500 [var], i.e., a 1000 [var] step, lasts for less (a similar period) than 1 [ms] for both the FCS-DPC and ST-DPC methods (See Fig. 4.14f and Fig. 4.13d), under the same DC-link voltage of 350 [V] (i.e., under the same magnitude of the "driving" voltage vectors).

4.4.3.2 FCS-DTC-DPC and ST-DTC-DPC for three-level PMSG systems: A comparative evaluation

The experimental results of the ST-DTC-DPC and FCS-DTC-DPC methods have been illustrated in this part. Identical test scenarios for both control methods are configured for a fair comparison: e.g., both schemes use the same outer (speed and DC-link voltage) control loops and under the same condition for each testing scenario. In the following, both overall control, steady/transient performances and performances under parameter variations of both method under consideration are compared.

4.4.3.2.1 Overall control performances The test scenario is as follows: we assume the "maximum power point tracking speed reference" changes abruptly (with a slope of 3[rpm/ms], see top rows in Fig.6) while the load side torque remains at its rated (maximum) value to test the most harsh conditions. The DC-link voltage reference V_{d}^{*} is set to 350 [V] and reactive power reference is set to be 0 [var] to achieve a unit power factor control. The overall control performances are illustrated in Fig. 5.26. The switching frequency for both methods are recorded during the testing and depicted in Fig. 4.11. From these two figures, we can see that: quite similar overall performances (for both the generator and the grid side control, including the DC-link control part) are achieved (See Fig. 5.26). However, the switching frequency changes within a larger range using the proposed FCS-DTC-DPC method (See Fig. 4.11).

4.4.3.2.2 Steady state control performance comparison The upper and lower hysteresis bandwidths of the ST-DTC-DPC methods are set as 2% and 1% of their rated values, respectively, while for FCS-DTC-DPC, the switching frequency weighting factors are tuned in such way that the system operates at a similar switching frequency as the ST-DTC-DPC method. The generator operates at 800[RPM] with rated turbine torque. Under such configurations, the steady state control performances for both the generator and grid side are obtained, which is shown in Fig. 4.12: for both the generator and grid side control, the proposed FCS-DTC-DPC method will outperform the classical ST-DTC-DPC solution at a similar switching frequency. The reason is their differing switching patterns: as can be seen from the last sub-figures of Fig. 4.12, at the same operating point, FCS based method "selects" much smoother switching patterns and almost no full voltage pattern (i.e., the "P" position of the phase switches) is selected; while ST-DTC synthesizes much more "noisy" switching patterns with lead to higher instantaneous voltage magnitudes

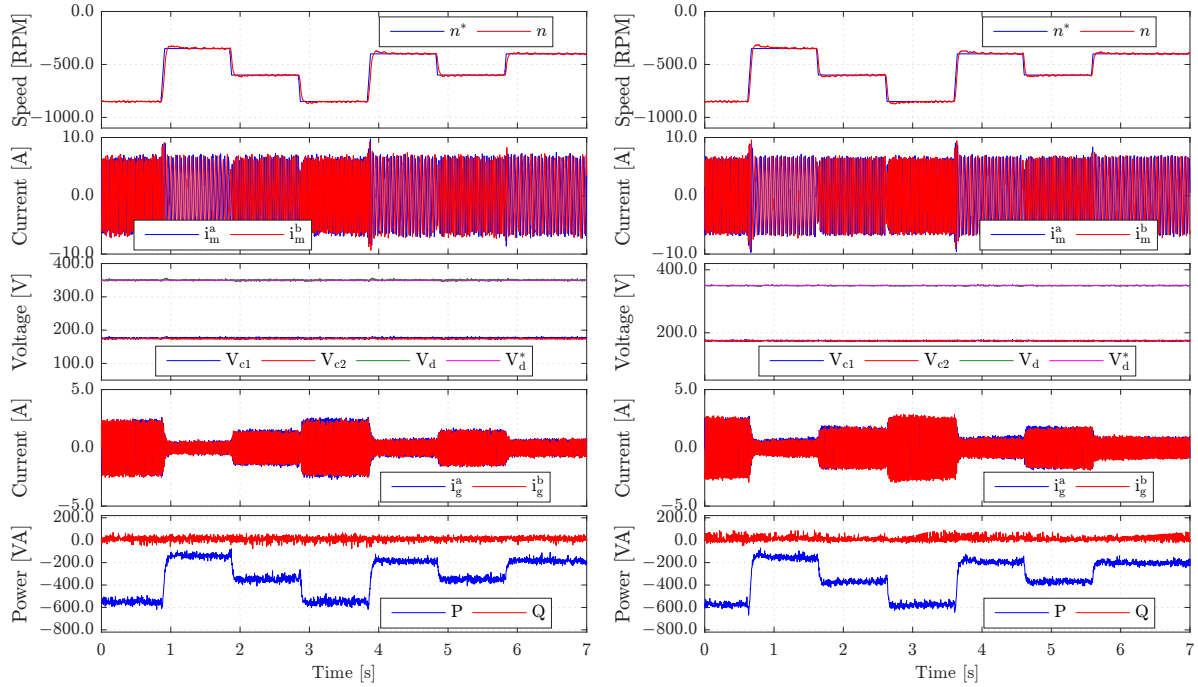

(a) Overall control performances of the proposed FCS-DTC-DPC.

(b) Overall control performances of ST-DTC-DPC.

Fig. 4.10: [Experimental results:] of the overall performances of the proposed FCS-DTC-DPC (left) and classical ST-DTC-DPC (right) control methods. For both sides, from up to down are: speed, machine stator (ab-phase) currents, DC-link overall and capacitor voltages, grid side phase current, grid side active and reactive power, respectively.

(see the last sub-figure in Fig. 4.12), although the magnitude of the fundamental is the same as for the DMPCC method (i.e., both the filtered command voltages from FCS-DTC and ST-DTC have a similar magnitude). More details with regarding to this part of work can be found in our publications of [73, 74, 107].

4.4.3.2.3 Transient phase control performance comparison The transient control performances for both the generator and grid side are shown in Fig. 4.13. Testing scenarios for both methods are that: for the generator side, the torque reference is directly manipulated to generate a "step-like" change from -7[Nm] to 7[Nm] and back, without using the outer speed loop (to get rid of its bandwidth influences); while for the grid side, the reactive power reference is "step" changed from 500[var] to -500[var][5]. As can be seen from Fig. 4.13, both methods achieves similar fast control dynamics: tracking a 14[Nm] torque and 1000[var] reactive power change cost around 1[ms].

4.4.3.2.4 Parameter sensitivity investigation The inductance values for the generator and grid side filter used inside both controllers are varied (to 50% and 200% of its

[5]Active power control is linked to the DC-link control for a back-to-back power converter and cannot be directly assigned to such changes.

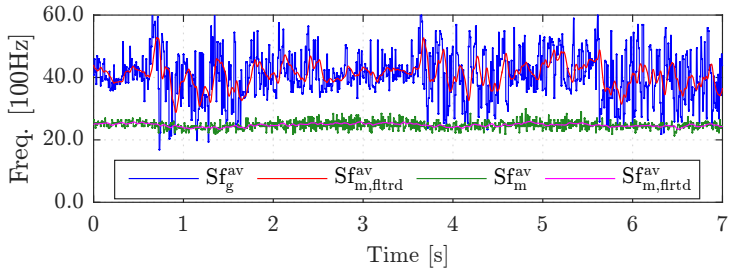

(a) Average switching frequency for FCS-DTC-DPC.

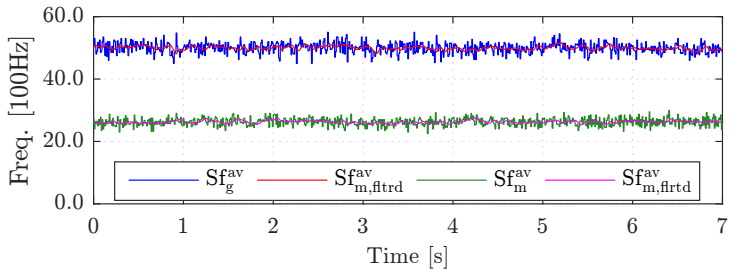

(b) Average switching frequency for ST-DTC-DPC.

Fig. 4.11: [Experimental results:] average switching frequency (update rate 10 [ms]) for FCS-DTC-DPC and ST-DTC-DPC during the overall test, where $\{Sf_{x,fltrd}^{av} \mid x \in \{m, g\}\}$ represents the filtered values (cut-off frequency 5Hz) of the generator (m) and grid side (g) average switching frequencies.

measured values) under same conditions (with same outer loops and during rated turbine torque) to investigate their parameter sensitivities. Results are collected in Fig. 4.14. As can be seen, the ST-DTC-DPC is quite robust against parameter variations while the FCS-DTC-DPC solution shows tracking bias (and increased ripples) when parameters are changed.

Short conclusions from the above experimental data with both FCS-DTC-DPC and ST-DTC-DPC methods for the 3L-NPC back-to-back power converter PMSG wind turbine system are that:

(i) Both methods achieve equivalently fast control dynamics with the same sampling interval.

(ii) However, in comparison with ST-DTC-DPC, much smaller current/torque, and power ripples are achieved at a similar switching frequency by using the FCS-DTC-DPC method.

(iii) The cost-function based concept brings much design and tuning flexibility to FCS-DTC-DPC (e.g., easier to include DC-link balancing and switching frequency regulation capabilities).

(iv) In terms of computational demanding, the ST-DTC-DPC approach cost much fewer resources and can be calculated around 1 μs, while FCS-DTC-DPC costs around 7 μs on the same FPGA.

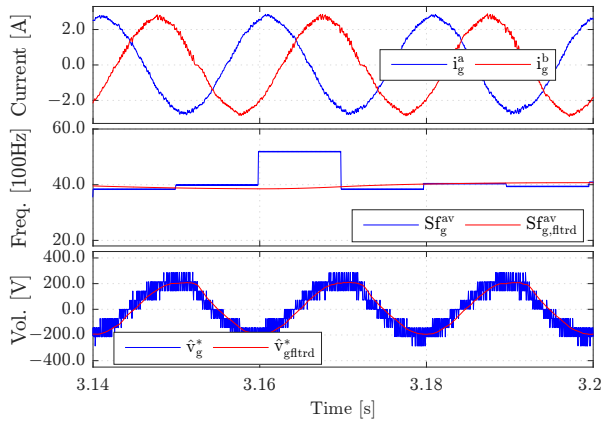

(a) Steady state performances of FCS for GSC (THD 2.57%).

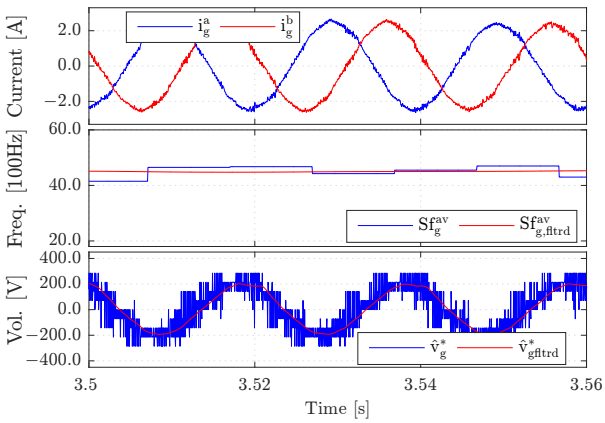

(b) Steady state performances of ST for GSC (THD 2.93%).

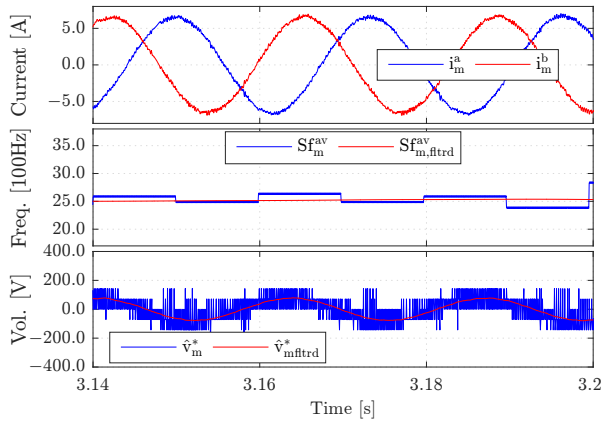

(c) Steady state performances of FCS for MSC (THD 2.88%).

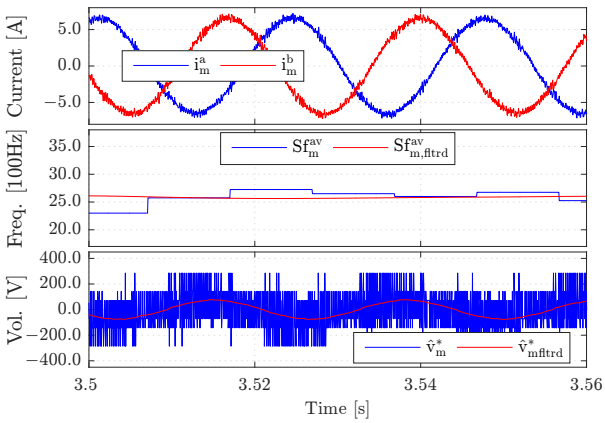

(d) Steady state performances of ST for MSC (THD 4.46%).

Fig. 4.12: [Experimental results:] of the steady state control performances for both methods: for (a) and (b) are machine side phase currents, switching frequency and estimated commanded phase-a voltage , while for (c) and (d) are grid side phase currents, switching frequency and estimated commanded phase-a voltage, respectively, where $\{\hat{v}^*_{x,\text{fltrd}} \mid x \in \{m, g\}\}$ represents the filtered values (cut-off frequency 300Hz) of the generator (m) and grid side (g) estimated commanded voltages.

(v) Although both methods operate at an un-fixed switching frequency, the ST-DTC-DPC solution achieves much smaller switching frequency operation range. Meanwhile, ST-DTC-DPC method is more robust to parameter variations because of its less model-dependent properties.

4.5 Summary

In this chapter, the classical direct model predictive control concept and its application guidelines have been revisited and summarized. Based on this, its application has been illustrated on both the two- and three-level NPC back-to-back power converter PMSG wind

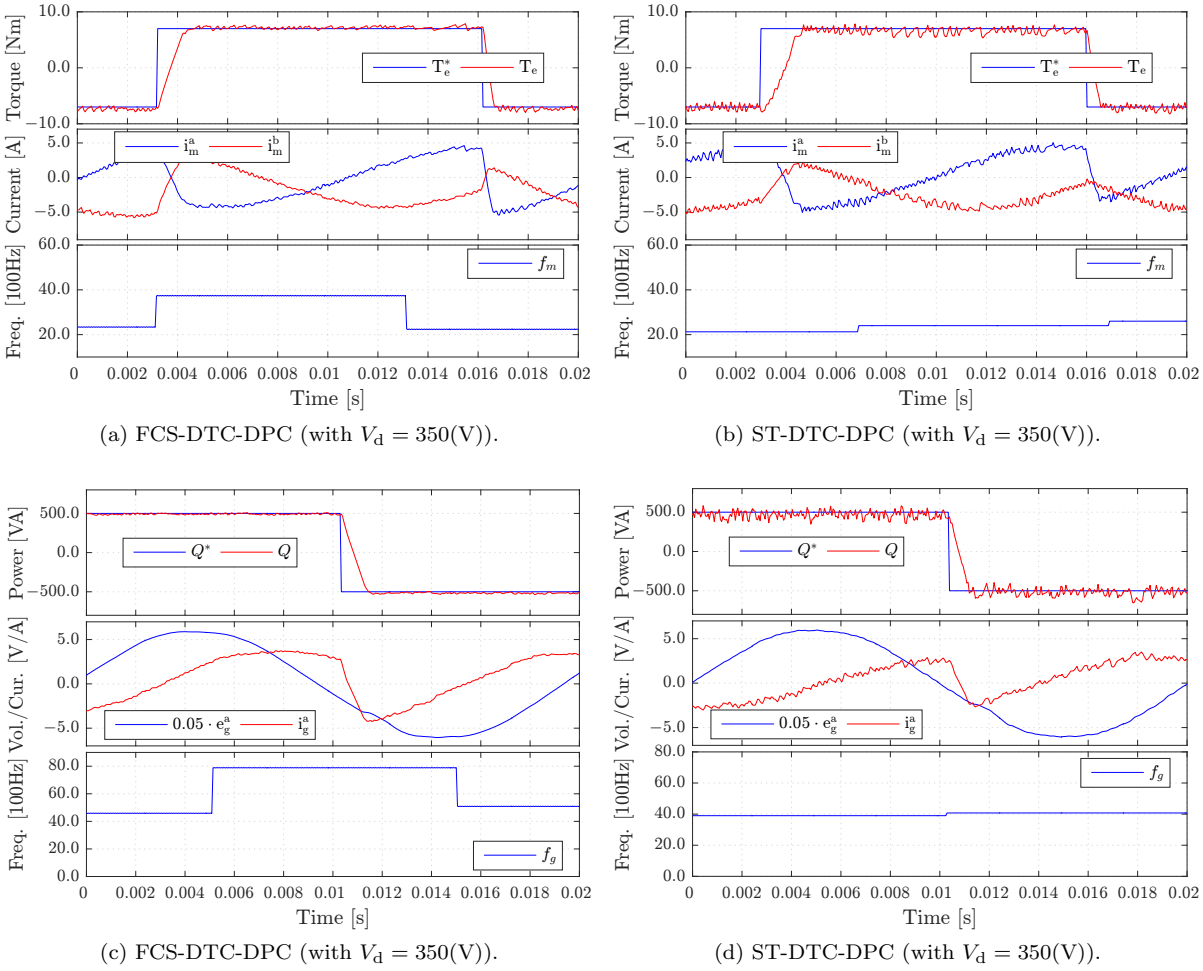

(a) FCS-DTC-DPC (with $V_d = 350$(V)).

(b) ST-DTC-DPC (with $V_d = 350$(V)).

(c) FCS-DTC-DPC (with $V_d = 350$(V)).

(d) ST-DTC-DPC (with $V_d = 350$(V)).

Fig. 4.13: [Experimental results:] of transient phase control performances of FCS-DTC-DPC and ST-DTC-DPC methods. For (a) and (b): from top to bottom are generator electromagnetic torque, stator currents, and converter average switching frequency, respectively, while For (c) and (c) are grid side reactive power, phase-a voltage and current, and converter switching frequency, respectively.

turbine systems taking "current, power, torque" as the targeting set[6]. As for the constraint set, neutral point voltages and the switching frequency are considered. Experimental evaluations of the relevant applications have also been given using a fully FPGA based realization solution. Experimental results confirmed that better performances are achieved when applying DMPC to three-level power converters in comparison with the two-level cases at a same control interval, which also confirms that DMPC technique has more potentials dealing with multi-level power converter based application in comparison with conventional switching table based methods. In comparison with switching table based direct torque and power control methods, the direct model predictive control methods, by using the cost-function based solution, makes both the controller design and tuning process much more straight-forward, in particular when the frequency regulations and

[6]This concept can also be applied to deal with "flux" and "voltage" control. A generalized relationship among parts of its diversities for PMSM(G) control can be found from our on-coming publication [75].

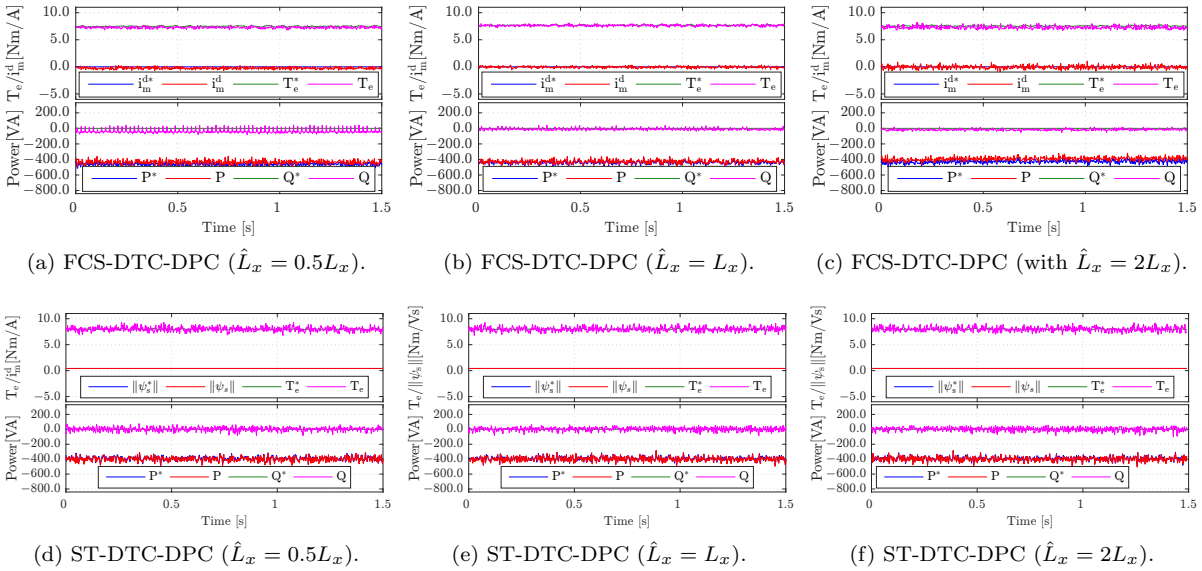

(a) FCS-DTC-DPC ($\hat{L}_x = 0.5L_x$). (b) FCS-DTC-DPC ($\hat{L}_x = L_x$). (c) FCS-DTC-DPC (with $\hat{L}_x = 2L_x$).

(d) ST-DTC-DPC ($\hat{L}_x = 0.5L_x$). (e) ST-DTC-DPC ($\hat{L}_x = L_x$). (f) ST-DTC-DPC ($\hat{L}_x = 2L_x$).

Fig. 4.14: [Experimental results:] of the parameter sensitivity investigation. Sub-figures (a), (b) and (c) stand for the FCS-DTC-DPC methods, from up to down are: electromagnetic torque, d-axis current and active/reactive power and their references; (d) (e) and (f) are for ST-DTC-DPC methods, from top to bottom are electromagnetic torque and flux, grid side active/reactive power and their references, respectively. $\hat{\mathrm{L}}_{\mathrm{x}}$ is the inductance value used in the controller, while L_{x} is the measured value, with $x \in \{s, g\}$, representing the generator stator and grid side filter inductance, respectively.

DC-link capacitor voltage balancing control are considered. With regarding to the steady state control variable ripples, the experimental results confirm that, DMPC technique might achieve smaller ripples, at the similar switching frequency, in particular for the three-level power converter control.

Chapter 5

Advanced direct model predictive control

In this chapter, certain problems and drawbacks of the classical DMPC schemes are analyzed and formulated in Sec. 5.1. Following, in Sec. 5.2 two computational-efficient DMPC (CE-DMPC) schemes for three-level NPC power converters are introduced to reduce the computational efforts of the classical DMPC techniques. The proposed CE-DMPC concepts are applied to three-level NPC back-to-back power converter PMSG wind turbine systems: generator side with predictive torque control, and grid side with predictive power control. In Sec. 5.3, Sec. 5.4 two performance-enhanced DMPC (PE-DMPC) concepts are proposed to reduce the ripples of steady state control variables to conquer the big-ripple drawbacks of the classical DMPC for two-level power converters without increasing the sampling frequency. Experimental results are also given which confirm the effectiveness of the proposed methods. In Sec. 5.5, by using the recently reported reactive power definition, a proposed direct model model predictive control method dealing with unbalanced grid control is verified for the grid-tied three-level NPC back-to-back power converter PMSG wind turbine system.

5.1 Problems of classical DMPC

DMPC, also named Finite-Control-Set Model Predictive Control (FCS-MPC) (See e.g., [10, 21, 82, 91, 108]), has received more and more attention. This technique exploits the finite number of the switching states of a power converter and combines current (torque) or power control and modulation into one computational step. Straightforward concept, fast control dynamics and flexibility in terms of the control target realization are the advantages. In the past decade, research on DMPC has spread out across various fields, e.g., renewable energy systems, matrix and multi-level converters, and electrical drives [21, 25, 73, 74, 82, 109]. In particular, for multi-level and multi-phase converters with more than eight switching states, DMPC increases the system performances and eases controller design process.

The concept of the classical DMPC has already been introduced in Chp. 4. To ease the problem description, this concept is depicted in Fig. 5.1 and named as C-DMPC (for the sake of a clear comparison with other schemes to be presented).

C-DMPC evaluates a given cost function (representing the control targets/objectives) for each switching state $\vec{u}_y$ (where $y \in \{m, g\}$, representing machine (m) and grid side (g), respectively) of an admissible (finite) set $\mathcal{U}$. The switching sequence which minimizes the cost function will be chosen and applied for a whole control interval. Typically, this technique *enumerates* all the admissible switching states to perform the state prediction and cost minimization, i.e., using "exhausting search" manner to solve the optimization problem. This leads to extremely *heavy computational efforts*, in particular for multilevel power converters or long-horizon prediction where a great amount of switching states are available [41, 110].

5.1.0.1 Drawback 1: heavy computational efforts caused by the enumeration concept

One severe drawback of C-DMPC for multi-level converters (even for one prediction step) is that: the amount of switching states (e.g. 27 switching states for a 3L-NPC converter) increases the computation time drastically thus real-time implementation is *not* feasible in general [82, 111, 112]. In particular, when certain functionality, e.g., parameter online estimations, encoderless/voltage sensorless control and multiple switching sequence selection methods, etc., are considered.

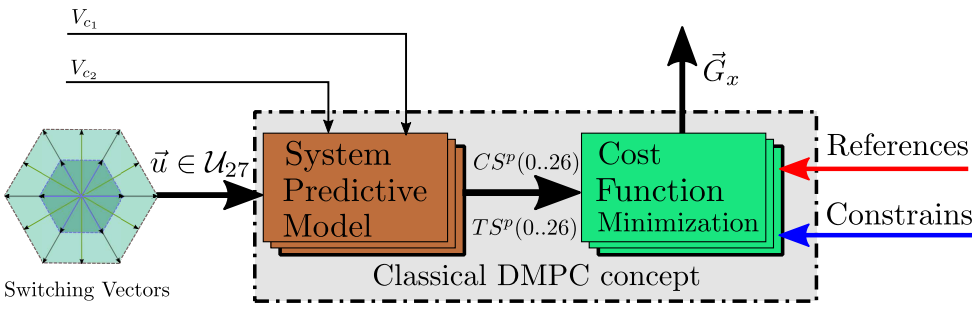

Fig. 5.1: Classical DMPC calculation efforts illustration, where CS and TS are the abbreviations for "constraint set" and "targeting set", respectively, ^{p} stands for "prediction".

Recent papers, e.g., [90, 113], have already shown that longer prediction horizon results in a drastically improved system performance: e.g., lower torque ripples and lower current THDs will be obtained. However, the computation time will increase exponentially as the number of prediction steps increases, impeding the real-time realization in many cases. This again emphasizes the necessity to investigate on computational efficient solutions. Therefore many of the recent research efforts are made to reduce the computation load of (direct) model predictive control schemes so to ease its real-time implementation. In [85, 113] a sphere decoding method (originated from the signal processing fields) was adopted for a 3L-NPC inverter-fed induction machine control. It was proven to be effective in particular for multilevel and multiple prediction cases. However, the computation time is reduced *statistically* and whether the decoding is feasible or not *heavily depends on* the chosen cost function format (for instance, the voltage balancing control target of a NPC power converter cannot be encoded/decoded with such approach). Its application is therefore quite limited. In [106] three computationally efficient schemes, namely, move

blocking, extrapolation, and event-based horizon MPC, are discussed. However, each has its disadvantages. In [114], a simplified predictive current control combining a deadbeat concept is used to reduce the computational efforts for grid-tied AFEs. The computational load reduction is effective. The most widely used direct model predictive control schemes, such as predictive power and torque control, remains to be discussed. Additionally, there are still rooms to reduce the computational load even further.

Within this chapter, two computational efficient solutions for three level NPC back-to-back power converter systems using DMPTC and DMPPC schemes are proposed, combining the deadbeat and DMPC concept with an intelligent off-line searching solution. The proposed concepts and their real-time realization details for NPC three-level back-to-back power converter PMSG wind turbine systems[1] are introduced in Sec. 5.2.

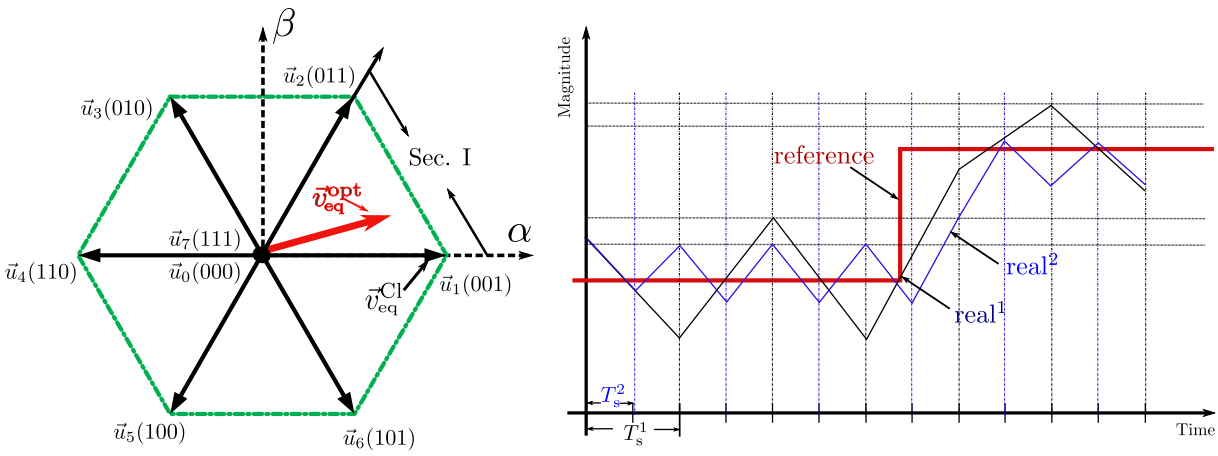

Fig. 5.2: Vector plane and control variable ripple effect using classical DMPC. Left side shows the vector plane of a two level voltage source power converter, where the black ones are the seven available switching vectors, the red one is assumed to be the desired voltage vector $\vec{v}_{eq}^{opt}$; $\vec{v}_1^{Cl}$ is assumed to be the selected optimal vector with a classical DMPC controller. The right side shows the control variable ripples using the classical DMPC scheme, where the red line is the reference, the blue and black lines are the tracking lines using sampling time of $T_s^1, T_s^1(= 2T_s^2)$, respectively.

Based on the C-DMPC concept, minimizing the cost-function yields the optimal *one* voltage vector, which is kept for a whole control interval, i.e., *one-vector-per-control-interval*. With a similar sampling frequency, the ripples of the control variables are much bigger (particularly for a two-level power converter due to its limited switching states and admissible voltage vectors) in comparison with the classical modulator based techniques, where typically three switching state/switching vectors (for instance, SVM based solutions) are applied for a whole control interval. This has already been illustrated by the experimental data in Chp. 3 and Chp. 4.

One possible solution (similar to DTC or DPC techniques) is to increase the sampling frequency (with which, the ripple reduction effect is illustrated in Fig. 5.2). It is not difficult to understand, increasing the sampling frequency will not generate different slopes

[1] This concept can also be applied to two-level power converters topologies [8].

of the control variables. The ripple reduction effects are caused only by the reduced actuating time of the chosen vector, i.e., the fast refreshing rate of the controller. To realize this, however, requires fast measuring/sampling of the controller hardware set-up [115].

5.1.0.2 Drawback 2: big steady state ripples caused by the *one-vector* concept

Therefore, *how to reduce the control variable ripples (without increasing the sampling frequency) thus to enhance the steady state performances is another question remains to be further investigated.*

To cope with this, a duty optimal direct model predictive power control method (DutyOpt-DMPPC) was reported in [17] for an AFE control, where instead of *one-vector-per-control-interval*, two vectors, namely, one active and one zero vectors, were chosen to minimize the cost-function. An equivalent voltage vector in phase with the selected active vector with an optimized length can be synthesized. Therefore, better steady state performance than the classical schemes can be achieved. However, with only one active and a zero vector, an equivalent vector with phases (directions) other than that of the fundamental active vectors cannot be synthesized; the performance improvement is therefore quite limited. Inspired by these, two performance-enhanced DMPC (PE-DMPC) concepts with two and three switching vector based solutions are introduced in this work. Different from both the classical and the DutyOpt-DMPPC schemes is that with the proposed methods, an equivalent vector with both optimized "phase" or/and "length" is synthesized to minimize the cost-function. The steady state performances are comparable with the classical modulator based schemes meanwhile the fast transient dynamics remains similar to C-DMPC. The main ideas and their realization procedures are introduced in Sec. 5.3 and 5.4 of this chapter.

Some other issues, such as unfixed switching frequency and wide spread harmonic spectrum, optimal design of the cost functions, MPC incorporated with parameter online estimation, MPC with selective harmonic elimination (SHE) or optimal pulse pattern design for very low switching frequency, systematical level design of (quasi) centralized MPC for back-to-back power converters, etc., remain also open. However, they are not the focus of this dissertation.

5.2 Computationally efficient DMPC for three-level NPC power converters

5.2.1 Introduction

Fig. 5.3 illustrates a direct-drive wind turbine system with PMSG and 3L-NPC back-to-back power converter. The back-to-back converter consists of machine-side converter (MSC) and grid-side converter (GSC) which share a common DC-link. Control objectives

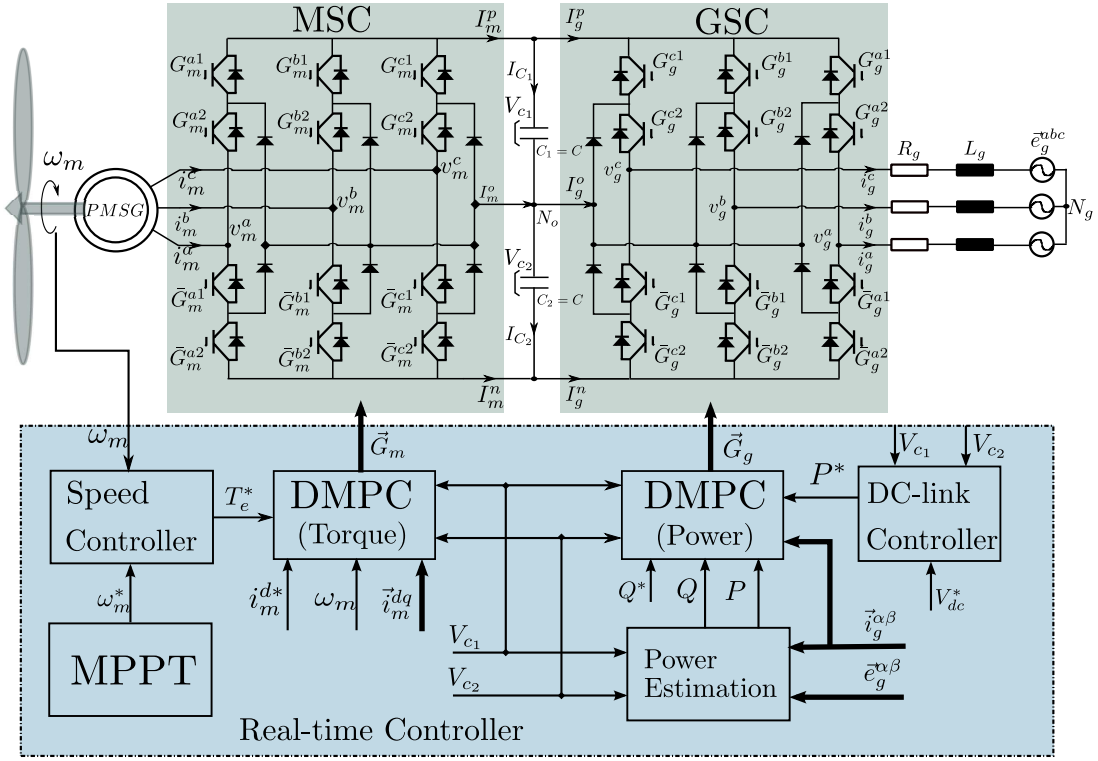

Fig. 5.3: Simplified electrical circuit of a 3L-NPC back-to-back PMSG wind turbine system with RL-filter on the grid-side and its controller with DMPC scheme.

for MSC and GSC include (see e.g. [10, 17] and the references therein): (co_1) Fast and accurate *torque control* to assure (a) maximum power point tracking (MPPT) of the wind turbine system or (b) nominal torque generation for wind speeds above the nominal wind speed. In addition, to achieve a high efficiency and to reduce the stress on the mechanical components, a low torque ripple and a low THD should be guaranteed; (co_2) *Power control*, i.e., the GSC shall assure grid-side active and reactive power control with fast dynamics to have small the DC-link voltage fluctuations (active power is controlled indirectly by the DC-link voltage controller). Moreover, the underlying GSC current controller(s) must guarantee a certain power quality to fulfill grid codes; and (co_3) *DC-link capacitor voltage balancing control*. For 3L-NPC back-to-back converters, (at least) one side needs to assure balancing of the voltages V_{c1} [V] and V_{c2} [V] of the upper and lower DC-link capacitors. (see Fig. 5.3), i.e.,

$$V_{\mathrm{c1}} \stackrel{!}{=} V_{\mathrm{c2}} > 0 \quad \Longrightarrow \quad V_{\mathrm{d}} := V_{\mathrm{c1}} + V_{\mathrm{c2}} > 0. \tag{5.1}$$

These objectives can be achieved through a classical direct model predictive control method to apply two switching states $\vec{u}_{\mathrm{m}}$ and $\vec{u}_{\mathrm{g}}$ which result in *two* gate signal vectors $\vec{G}_m = \mathcal{G}^{-1}(\vec{u}_{\mathrm{m}})$ and $\vec{G}_g = \mathcal{G}^{-1}(\vec{u}_{\mathrm{g}})$ on *machine* and *grid* side converters, respectively (see Fig. 5.3). However, the required computational effort is one of the concerns. The C-DMPC concept has already been given in Algorithm 4.1. Following these steps, the relevant controller for machine and grid side converters are designed as follows.

5.2.1.1 Machine-side torque control and voltage balancing

For classical DMPC, the machine-side cost function is defined by

$$J^{\mathrm{m}}_{\mathrm{DMPC}}(\vec{u}_{\mathrm{m}}) = \underbrace{\underbrace{\gamma_{\mathrm{T_e}}\frac{|T^*_{\mathrm{e}} - T_{\mathrm{e}}(\vec{u}_{\mathrm{m}})|}{J^{\max}_{T_{\mathrm{e}}}}}_{=:J_{T_{\mathrm{e}}}} + \underbrace{\gamma_{i^{\mathrm{d}}_{\mathrm{m}}}\frac{|i^{\mathrm{d}*}_{\mathrm{m}} - i^{\mathrm{d}}_{\mathrm{m}}(\vec{u}_{\mathrm{m}})|}{J^{\max}_{i^{\mathrm{d}}_{\mathrm{m}}}}}_{=:J_{i^{\mathrm{d}}_{\mathrm{m}}}}}_{=:J_{TS_m}} + \underbrace{\gamma_{V_{\mathrm{o}}}\frac{|V^*_{\mathrm{o}} - V_{\mathrm{o[k+1]}}|}{J^{\max}_{V_{\mathrm{o}}}}}_{J_{V_{\mathrm{o}}}=:J_{\mathrm{CS_m}}} \tag{5.2}$$

with weighting factors $\gamma_{T_{\mathrm{e}}}\,[1]$, $\gamma_{i^{\mathrm{d}}_{\mathrm{m}}}\,[1]$ and $\gamma_{V_{\mathrm{o}}}\,[1]$ and normalization factors $J^{\max}_{T_{\mathrm{e}}} > 0\,[\mathrm{Nm}]$, $J^{\max}_{i^{\mathrm{d}}_{\mathrm{m}}} > 0\,[\mathrm{A}]$ and $J^{\max}_{V_{\mathrm{o}}} > 0\,[\mathrm{V}]$ (e.g. representing the expected maximal value of each sub-cost or the rated value of each quantity).

The target set cost function $J_{TS_m} = J_{T_{\mathrm{e}}} + J_{i^{\mathrm{d}}_{\mathrm{m}}}$ is represented by the sum of the sub-costs $J_{T_{\mathrm{e}}}$ and $J_{i^{\mathrm{d}}_{\mathrm{m}}}$ for torque control with torque reference $T^*_e\,[\mathrm{Nm}]$ and d-axis current control to guarantee a constant flux (i.e. $i^{\mathrm{d}*}_{\mathrm{m}} = 0[A]$ for maximum torque per ampere). The constraint set $J_{V_{\mathrm{o}}} = J_{\mathrm{CS_m}}$ shall assure voltage balancing with *difference voltage reference* $V^*_{\mathrm{o}} = 0\,\mathrm{V}$.

5.2.1.2 Grid-side power control and voltage balancing

For classical DMPC, the grid-side cost function is defined by

$$J^{\mathrm{g}}_{\mathrm{DMPC}}(\vec{u}_{\mathrm{g}}) = \underbrace{\underbrace{\gamma_P\frac{|P^* - P_{\mathrm{[k+1]}}(\vec{u}_{\mathrm{g}})|}{J^{\max}_{P}}}_{=:J_P} + \underbrace{\gamma_Q\frac{|Q^* - Q_{\mathrm{[k+1]}}(\vec{u}_{\mathrm{g}})|}{J^{\max}_{Q}}}_{=:J_Q}}_{=:J_{TS_g}} + \underbrace{\gamma_{V_{\mathrm{o}}}\frac{|V^*_{\mathrm{o}} - V_{\mathrm{o[k+1]}}(\vec{u}_{\mathrm{g}})|}{J^{\max}_{V_{\mathrm{o}}}}}_{J_{V_{\mathrm{o}}}=:J_{CS_g}} \tag{5.3}$$

with weighting factors $\gamma_P\,[1/\mathrm{W}]$, $\gamma_Q\,[1/\mathrm{var}]$ and $\gamma_{V_{\mathrm{o}}}\,[1/\mathrm{V}]$ and normalization factors $J^{\max}_{P} > 0\,[\mathrm{W}]$, $J^{\max}_{Q} > 0\,[\mathrm{var}]$ and $J^{\max}_{V_{\mathrm{o}}} > 0\,[\mathrm{V}]$. The target set cost function $J_{TS_g} = J_P + J_Q$ is represented by the sum of the sub-costs J_P and J_Q for *active* and *reactive* power control, respectively. The constraint set $J_{V_{\mathrm{o}}} = J_{CS_g}$ shall also assure voltage balancing. Note that, since $J_{\mathrm{CS_m}} = J_{CS_g}$, both converters may contribute to voltage balancing.

Remark 5 (On the tuning of weighting factors) *Basically, there exist cost functions with equally important terms (sub-costs) and cost functions with secondary (important) terms. In [116], for some particular control problems, reasonable tuning intervals for the weighing factors of these cost function types are presented. In this section, the considered cost functions comprise equally important* and *secondary (important) terms. Hence, the given guidelines in [117] are not directly applicable. The essential step, to make it intuitive again, is the use of* normalized *sub-costs and to choose the weighting factors of the* normalized *sub-costs within an interval of* [0, 1] *[10]. Moreover, since, for different operation points different sub-costs might be more important, the use of varying or adaptive weighting factors might be useful. In this chapter, normalized sub-costs in* (5.3) *and* (5.2) *are used for C-DMPC. The* equivalent *weighting factors for the computationally efficient DMPC schemes are derived by the formulas given in* (5.6) *and* (5.11)*, respectively.*

Remark 6 (Discussion of the computational load) *In view of Algorithm 4.1, the following computational load is to be expected: In Step I, each of the prediction models (2.42), (2.21) and (2.50) needs to be computed* for all $\vec{u}_{\mathrm{m}}, \vec{u}_{\mathrm{g}} \in \mathcal{U}_{27}$ *(i.e. 27 times each). Then, in Step II, the cost functions* $J^{\mathrm{m}}_{\mathrm{DMPC}}(\vec{u}_{\mathrm{m}})$ *as in (5.2) and* $J^{\mathrm{g}}_{\mathrm{DMPC}}(\vec{u}_{\mathrm{g}})$ *as in (5.3) must be evaluated* for all $\vec{u}_{\mathrm{m}}, \vec{u}_{\mathrm{g}} \in \mathcal{U}_{27}$ *(i.e. 27 times each) to find the optimal switching vectors* $\vec{u}^*_{\mathrm{m}}$ *and* $\vec{u}^*_{\mathrm{g}}$ *on machine and grid side, respectively. Finally, in Step III, the optimal gate vectors* $\vec{G}^*_m = \mathcal{G}^{-1}(\vec{u}^*_{\mathrm{m}})$ *and* $\vec{G}^*_g = \mathcal{G}^{-1}(\vec{u}^*_{\mathrm{g}})$ *are generated and applied.*

As can be seen the computational load for applying the C-DMPC scheme to such a three-level NPC back-to-back power converter PMSG wind turbine system is considerably heavy. The following sections introduces the proposed computationally efficient DMPC (CE-DMPC) concept, based on which two applicable solutions are then presented.

5.2.2 Concept of the proposed computationally efficient DMPC

The idea of the proposed computationally efficient DMPC (CE-DMPC) schemes is the intelligent (offline) selection of admissible and reasonable but smaller sub-sets of $\mathcal{U}_{27}$ such that fewer switching vectors must be tested during prediction and cost function evaluation. Hence, the goal is to find a smaller switching vector set within an admissible region (later called candidate region) such that it is still feasible to minimize the sub-costs J_{TS_x} and J_{CS_x} in (4.1) adequately. Within this context[2], two methods for selection of the candidate regions will be proposed: CE-DMPC with hexagon candidate region (HCR, see Sec. 5.2.3) and CE-DMPC with triangle candidate region (TCR, see Sec. 5.2.4). The general idea of the proposed CE-DMPC schemes is illustrated in Fig. 5.4 and consists of five steps (also listed as pseudo code in Algorithm 5.1):

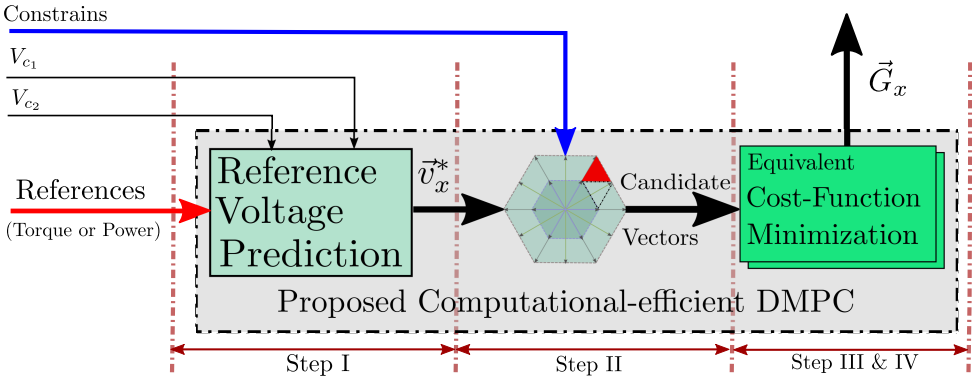

Fig. 5.4: Block diagrams of the proposed computationally efficient (CE) direct model predictive control (DMPC) schemes for torque and power control.

[2]Note that a similar idea has been proposed recently in [114] for predictive current control of voltage source AFEs. This work adopts and extends the idea from [114]. The differences are: (i) Instead of using predictive current control, the proposed CE-DMPC schemes are utilized in the frames of predictive *torque* and *power* control on the machine and the grid side control of a grid-tied 3L-NPC back-to-back power converter for wind turbine systems with permanent-magnet synchronous generator (PMSG), and (ii) *two* candidate regions, i.e. hexagon candidate region (HCR) and triangle candidate region (TCR), are proposed for wind turbine systems with PMSG and 3L-NPC back-to-back power converters.

Algorithm 5.1 Proposed CE-DMPC algorithm with $\vec{u}_{\mathrm{y}} \in \mathcal{U}_{CR}$ $(\subset \mathcal{U}, y \in \{m, g\})$

Step I: Dead-beat reference voltage prediction for given target reference TS^*:

$$\{\ \vec{v}_y^* = M_{TS}^{-1}(TS^*)\ \}$$

Step II: Selection of candidate region CR according to constraint set CS

$$\{\ \mathcal{U}_{CR} \subset \mathcal{U} \text{ with respect to } \vec{v}_y^* \text{ and } CS^p = M_{CS}(\vec{u}_{\mathrm{y}})\ \}$$

Step III: Prediction for all $\vec{u}_{\mathrm{y}} \in \mathcal{U}_{CR} \subset \mathcal{U}$:

$$\{\ TS^p(\vec{u}_{\mathrm{y}}) = M_{TS}(\vec{u}_{\mathrm{y}}) \text{ and } CS^p(\vec{u}_{\mathrm{y}}) = M_{CS}(\vec{u}_{\mathrm{y}})\ \}$$

Step IV: Cost evaluation and selection of optimal switching vector out of $\mathcal{U}_{CR}$:

$\{\ \vec{u}_{\mathrm{y}}^* := \arg\min_{\vec{u}_{\mathrm{y}} \in \mathcal{U}_{CR}} J_{\mathrm{CE-DMPC}}(\vec{u}_{\mathrm{y}})$ with equivalent cost $J_{\mathrm{CE-DMPC}}(\vec{u}_{\mathrm{y}})$ as in (5.4) $\}$

Step V: Application of optimal gate signal vector:

$$\{\ \vec{G}^* = \mathcal{G}^{-1}(\vec{u}_{\mathrm{y}}^*)\ \}$$

- *Step I - Reference voltage prediction:* Instead of evaluating the cost function (4.1) for all 27 possible switching states, the proposed algorithm directly computes the reference voltage $\vec{v}_y^*$ *only* for the target set by using a dead-beat/like approach. The constraints are neglected.

- *Step II - Selection of the candidate region (CR):* In view of the predicted reference voltage $\vec{v}_{\mathrm{y}}^*$ and the constraint set, a *candidate region* $\mathcal{U}_{CR} \subset \mathcal{U}$ (subset of $\mathcal{U}$) is selected which will comprise (much) less than 27 switching vectors.

- *Step III - Prediction over the reduced candidate region:* For the evaluation of the cost function in Step IV, the prediction models of target and constraint set must then be computed only for the switching vectors $\vec{u}_{\mathrm{y}}$ element of the *reduced* candidate region $\mathcal{U}_{CR} \subset \mathcal{U}$.

- *Step IV - Cost evaluation and selection of optimal switching vector:* For all switching vectors $\vec{u}_{\mathrm{y}} \in \mathcal{U}_{CR}$ the *equivalent* cost

$$J_{\mathrm{DMPC}}^{\mathrm{m}}(\vec{u}_{\mathrm{y}}) = \underbrace{\gamma_{TS_{y,1}}^{\mathrm{eq}} |v_{\mathrm{y}}^{\alpha *} - v_{\mathrm{y}}^{\alpha}(\vec{u}_{\mathrm{y}})| + \gamma_{TS_{y,2}}^{\mathrm{eq}} |v_{\mathrm{y}}^{\beta *} - v_{\mathrm{y}}^{\beta}(\vec{u}_{\mathrm{y}})|}_{=: J_{TS_y}^{\mathrm{eq}}} + \underbrace{\sum_{j=1}^{n} \gamma_{CS_{y,j}} |CS_{y,j}^* - CS_{y,j}^p(\vec{u}_{\mathrm{y}})|}_{J_{CS_y}} \quad (5.4)$$

is evaluated and the optimal switching vector

$$\vec{u}_{\mathrm{y}}^* := \arg \min_{\vec{u}_{\mathrm{y}} \in \mathcal{U}_{CR}} J_{\mathrm{CE-DMPC}}(\vec{u}_{\mathrm{y}})$$

is selected. The *equivalent* sub-cost J_{TS}^{eq} weights deviations between predicted reference voltage $\vec{v}_{\mathrm{y}}^* = (v_{\mathrm{y}}^{\alpha *}, v_{\mathrm{y}}^{\beta *})^\top$ and to be applied voltage vector $\vec{v}_{\mathrm{y}}(\vec{u}_{\mathrm{y}}) = (v_{\mathrm{y}}^1(\vec{u}_{\mathrm{y}}), v_{\mathrm{y}}^2(\vec{u}_{\mathrm{y}}))^\top$. Note that, by adjusting the *equivalent* weighting factors $\gamma_{TS_{y,1}}^{\mathrm{eq}}$ and $\gamma_{TS_{y,2}}^{\mathrm{eq}}$ in (5.4) to a certain value, an *equivalent* sub-cost for the targeting set can be maintained, i.e. $J_{TS_y}^{\mathrm{eq}} = J_{TS_y}$ as in (4.1).

- *Step V - Application of optimal gate signal vector:* Based on the optimal switching vector $\vec{u}_{\mathrm{y}}^{*}$ the optimal gate signal vector $\vec{G}_{y}^{*} = \mathcal{G}^{-1}(\vec{u}_{\mathrm{y}}^{*})$ is generated and applied.

In the following sections, to illustrate and compare the computational effort reduction of the proposed concept, two computationally efficient DMPC schemes based on such concept are introduced and applied to torque and power control of wind turbine systems with PMSG and 3L-NPC back-to-back power converter. Control objectives are (co_1) torque control, (co_2) power control and (co_3) voltage balancing as introduced in Sec. 8.1. The control objective (co_3) will be considered as a constraint.

5.2.3 CE-DMPC with hexagon candidate region

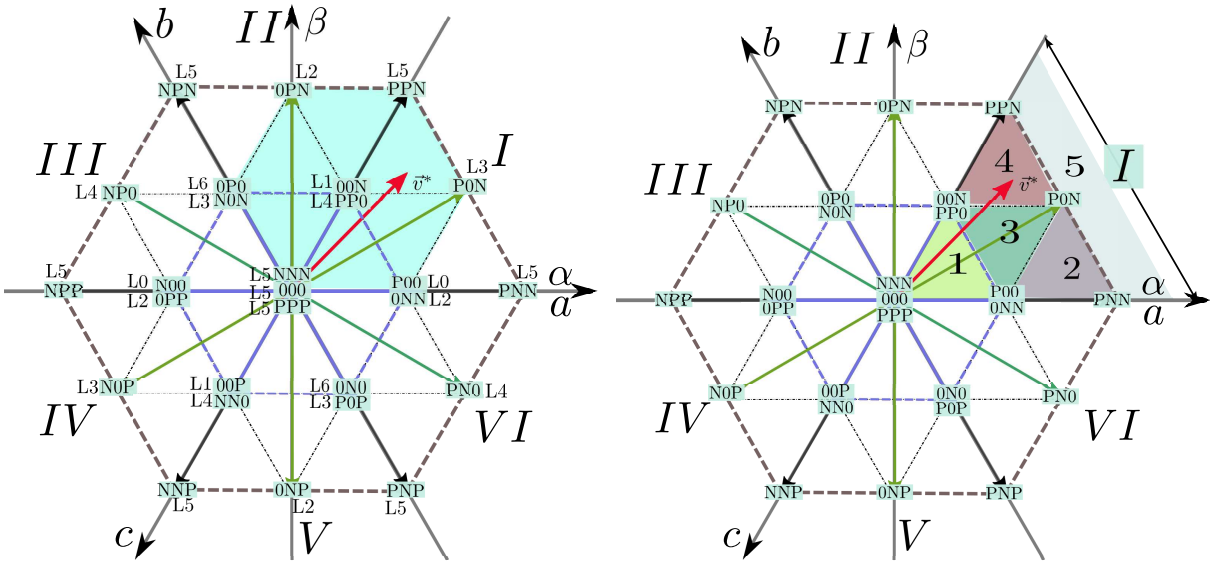

(a) Hexagon candidate region.

(b) Triangle candidate region.

Fig. 5.5: Candidate regions with reduced number of switching vectors to be evaluated for CE-DMPC schemes: (a) CE-DMPC with hexagon candidate region (HCR) and (b) CE-DMPC with triangle candidate region (TCR).

This subsection introduces CE-DMPC with hexagon candidate region (HCR) for torque and power control of wind turbine systems with PMSG and 3L-NPC back-to-back power converter.

The basic idea is illustrated in Fig. 5.4 and Fig. 5.5a. Computation and optimization follow Algorithm 5.1. More details are explicitly given for machine-side and grid-side as follows.

5.2.3.1 Machine-side torque control and voltage balancing

To achieve the control objectives (co_1) and (co_2), the following *equivalent* cost function (similar to (5.4)) is proposed

$$J^{m}_{\mathrm{CE-DMPC}}(\vec{u}_{\mathrm{m}}) = \underbrace{\gamma^{\mathrm{eq}}_{v^{\mathrm{d}}_{\mathrm{m}}} |v^{\mathrm{d}*}_{\mathrm{m[k]}} - v^{\mathrm{d}}_{\mathrm{m}}(\vec{u}_{\mathrm{m}})| + \gamma^{\mathrm{eq}}_{v^{\mathrm{q}}_{\mathrm{m}}} |v^{\mathrm{q}*}_{\mathrm{m[k]}} - v^{\mathrm{q}}_{\mathrm{m}}(\vec{u}_{\mathrm{m}})|}_{=J^{\mathrm{eq}}_{TS_m}} + \underbrace{\gamma_{V_{\mathrm{o}}} \frac{|V^{*}_{\mathrm{o}} - V_{\mathrm{o[k+1]}}|}{J^{\mathrm{max}}_{V_{\mathrm{o}}}}}_{=J_{\mathrm{CS_m}}} \tag{5.5}$$

with the *equivalent* weighting factors (with [unit])

$$\gamma^{\mathrm{eq}}_{v^{\mathrm{d}}_{\mathrm{m}}} = \frac{T_{\mathrm{s}}}{L_s J^{\mathrm{max}}_{i^{\mathrm{d}}_{\mathrm{m}}}} \gamma_{i^{\mathrm{d}}_{\mathrm{m}}} \quad [1/\mathrm{V}] \qquad \text{and} \qquad \gamma^{\mathrm{eq}}_{v^{\mathrm{q}}_{\mathrm{m}}} = N_{\mathrm{p}} \psi_{\mathrm{pm}} \frac{T_{\mathrm{s}}}{L_s J^{\mathrm{max}}_{T_{\mathrm{e}}}} \gamma_{T_{\mathrm{e}}} \quad [1/\mathrm{V}] \tag{5.6}$$

where $\gamma_{i^{\mathrm{d}}_{\mathrm{m}}}$, $\gamma_{T_{\mathrm{e}}}$, $J^{\mathrm{max}}_{i^{\mathrm{d}}_{\mathrm{m}}}$ and $J^{\mathrm{max}}_{T_{\mathrm{e}}}$ are as in (5.2) and v^{d*}_{m}, $v^{\mathrm{d}}_{\mathrm{m}}$ [V] and v^{q*}_{m}, $v^{\mathrm{q}}_{\mathrm{m}}$ [V] are reference and actual voltages of the direct and quadrature component, respectively.

• Step I of Algorithm 5.1: The reference voltage is computed such that dead-beat torque control is (approximately) achieved. The constraints are neglected in this step. As references for the *next* sampling instant the *machine-side current references*

$$\vec{i}^{\mathrm{dq}*}_{\mathrm{m[k+1]}} = \vec{i}^{\mathrm{dq}}_{\mathrm{m[k+1]}} = \left(i^{\mathrm{d}*}_{\mathrm{m[k+1]}}, \frac{T^{*}_{\mathrm{e[k+1]}}}{N_{\mathrm{p}} \psi_{\mathrm{pm}}} \right)^{\top} \tag{5.7}$$

are chosen where the reference torque $T^{*}_{\mathrm{e[k+1]}}$ comes from the speed controller (see Fig. 5.3) and the reference current $i^{\mathrm{d}*}_{\mathrm{m[k+1]}} = 0$ is set for maximum torque per ampere. Following the deadbeat concept introduced in Chp. 3, yields the (predicted) *machine-side reference voltage vector*

$$\vec{v}^{\mathrm{dq}*}_{\mathrm{m[k]}} = \mathbf{B}^{-1}_{\mathrm{m}} \left[\vec{i}^{\mathrm{dq}*}_{\mathrm{m[k+1]}} - \mathbf{A}_{\mathrm{m[k]}} \vec{i}^{\mathrm{dq}}_{\mathrm{m[k]}} - \mathbf{H}_{\mathrm{m[k]}} \right]. \tag{5.8}$$

This computation is simple and requires solely one computation step. Applying $\vec{v}^{\mathrm{dq}*}_{\mathrm{m[k]}}$ would (ideally) control the current $\vec{i}^{\mathrm{dq}}_{\mathrm{m[k+1]}}$ to reach its reference $\vec{i}^{\mathrm{dq}*}_{\mathrm{m[k+1]}}$ in the next sampling interval. Hence, dead-beat torque control could be achieved with $T_{\mathrm{e[k+1]}} = T^{*}_{\mathrm{e[k+1]}}$. The predicted reference voltage $\vec{v}^{\mathrm{dq}*}_{\mathrm{m[k]}}$ might not be applied instantaneously (in view of the switching nature of converter), however its knowledge allows to *restrict* the candidate region.

• Step II of Algorithm 5.1: The selection of the candidate region is the crucial step in Algorithm 5.1 which allows to reduce the computation time of the prediction of the constraint set $V_{\mathrm{o[k+1]}} = V_{\mathrm{o}}(\vec{u}_{\mathrm{m}}, \vec{u}_{\mathrm{g}})$ and the evaluation of the cost function (5.2). To illustrate the offline procedure of the selection of the candidate regions, assume that the predicted reference voltage vector $\vec{v}^{*}_{\mathrm{m}} := \vec{v}^{\alpha\beta*}_{\mathrm{m}} = \mathbf{T}_{\mathrm{P}}(\phi_{\mathrm{e}}) v^{\mathrm{d,q}*}_{\mathrm{m}}$ (obtained in Step I by (5.8)) is located at the position shown in Fig. 5.5a. Without the constraint of voltage balancing (i.e. without the sub-cost $J_{\mathrm{CS_m}}$ in (5.2)) solely the *four* switching vectors "P0N, PP0, 00N, PPN" will yield the lowest cost. However, control objective (co_3) also needs to be taking into account. Therefore, an intelligent selection of the candidate region must be found. For simplicity, assume that the grid-side current vector $\vec{i}^{\mathrm{abc}}_{\mathrm{g[k]}}$ will *not* change

over the small sampling interval $[kT_\mathrm{s}, (k+1)T_\mathrm{s}]$, then $|\vec{u}_\mathrm{g}|^\top \cdot \vec{i}^{\,\mathrm{abc}}_{\mathrm{g[k]}}$ in (2.21) is constant and the sub-cost $J_{\mathrm{CS_m}} = \gamma_{V_\mathrm{o}}|V_\mathrm{o}^* - V_{\mathrm{o[k+1]}}|$ in (5.2) can only be minimized by switching vectors $\vec{u}_\mathrm{m}$ which compensates for $-\frac{C}{T_\mathrm{s}}V_\mathrm{o}(k) + |\vec{u}_\mathrm{g}|\,\vec{i}^{\,\mathrm{abc}}_{\mathrm{g[k]}}$ in (2.21). An offline analysis of the effect of each switching vector $\vec{u}_\mathrm{m} \in \mathcal{U}_{27}$ on the difference voltage V_o in (2.21) yields that there are seven "impact levels" $L0$, $L1$, …, $L5$, $L6$ (see Fig. 5.5a) with similar impact on the minimization [54]. For instance, level $L0$ comprises the switching states $N00$ and $P00$ which both give $|\vec{u}_\mathrm{m}| = (|1|, |0|, |0|)^\top = (|-1|, |0|, |0|)^\top = (1, 0, 0)^\top$. Level $L5$ comprises "NPN, PNP, PNN, NPP, PPN, PPP, NNN" which all yield $|\vec{u}_\mathrm{y}| = (1, 1, 1)^\top$. Clearly, evaluation of (2.21) gives different values for $L0$ and $L5$. Hence, for the considered reference vector $\vec{v}_m^*$ in Fig. 5.5a, all *seven* levels must be considered and the *smallest* admissible hexagon candidate region is the *light green hexagon* in Fig. 5.5a. It has 12 elements and is given by

$$\mathcal{U}^{\mathrm{HCR}}_{\mathrm{CR_m}} := \{\mathrm{NNN}, \mathrm{000}, \mathrm{PPP}, \mathrm{0P0}, \mathrm{N0N}, \mathrm{00N}, \mathrm{PP0}, \mathrm{P00}, \mathrm{0NN}, \mathrm{0PN}, \mathrm{PPN}, \mathrm{0P0}\} \subset \mathcal{U}_{27}. \quad (5.9)$$

Therefore, instead of 27 evaluations of the cost function (5.2), 12 evaluations of the *equivalent* cost function (5.2) are required. One of these 12 switching state vectors will be the optimal vector to minimize (5.2), since (at least) one element of the seven levels $L0$, …, $L6$ belongs to selected hexagon candidate region $\mathcal{U}^{\mathrm{HCR}}_{\mathrm{CR_m}}$ (see Fig. 5.5a). Note that *all* hexagon candidate regions (like the light green hexagon) in Fig. 5.5a will result in sets $\mathcal{U}^{\mathrm{HCR}}_{\mathrm{CR_m}}$ with *not* more than 12 elements.

• Step III, IV and V of Algorithm 5.1: The remainder of Algorithm 5.1 is now to evaluate the constraint set prediction model (2.21) and the equivalent cost function (5.2) for all $\vec{u}_\mathrm{m} \in \mathcal{U}_{CR_m}$ (i.e. 12 times each) to find the optimal switching vector $\vec{u}^*_\mathrm{m}$ which will be used to generate and apply the optimal gate vector $\vec{G}^*_m = \mathcal{G}^{-1}(\vec{u}^*_\mathrm{m})$.

5.2.3.2 Grid-side power control and voltage balancing

To achieve the control objectives (co_2) and (co_3), the following *equivalent* cost function (equivalent to (5.3)) is proposed

$$J^{\mathrm{g}}_{\mathrm{CE-DMPC}}(\vec{u}_\mathrm{g}) = \underbrace{\gamma^{\mathrm{eq}}_{v^\alpha_\mathrm{g}}|v^{\alpha*}_{\mathrm{g[k]}} - v^\alpha_\mathrm{g}(\vec{u}_\mathrm{g})| + \gamma^{\mathrm{eq}}_{v^\beta_\mathrm{g}}|v^{\beta*}_{\mathrm{g[k]}} - v^\beta_\mathrm{g}(\vec{u}_\mathrm{g})|}_{=J^{\mathrm{eq}}_{TS_\mathrm{g}}} + \underbrace{\gamma_{V_\mathrm{o}}\frac{|V_\mathrm{o}^* - V_{\mathrm{o[k+1]}}|}{J^{\max}_{V_\mathrm{o}}}}_{=J_{CS_\mathrm{g}}} \quad (5.10)$$

with *equivalent* weighting factors (with [unit])

$$\gamma^{\mathrm{eq}}_{v^\alpha_\mathrm{g}} = \frac{T_\mathrm{s}\|\vec{e}^{\,\alpha\beta}_\mathrm{g}\|}{L_s J^{\max}_P}\gamma_P \quad [1/\mathrm{V}] \qquad \text{and} \qquad \gamma^{\mathrm{eq}}_{v^\beta_\mathrm{g}} = \frac{T_\mathrm{s}\|\vec{e}^{\,\alpha\beta}_\mathrm{g}\|}{L_s J^{\max}_Q}\gamma_Q \quad [1/\mathrm{V}], \quad (5.11)$$

respectively, where γ_P, γ_Q, $J^{\max}_P$ and $J^{\max}_Q$ are as in (5.3).

Note that, the equivalent cost function $J^m_{\mathrm{CE-DMPC}}(\vec{u}_\mathrm{m})$ in (5.2) and $J^g_{\mathrm{CE-DMPC}}(\vec{u}_\mathrm{g})$ in (5.10) share the same sub-cost $J_{\mathrm{CS_m}} = J_{CS_g} = J_{V_\mathrm{o}}$ for the constraint set. Therefore, grid-side CE-DMPC with HCR is almost identical to that on the machine side. So, only essential steps are highlighted in the following.

• Step I of Algorithm 5.1: The reference voltage on the grid-side is computed to achieve a dead-beat like behavior for active and reactive power. The constraints are neglected. In the next sampling instant, *active* P [W] and reactive Q [var] power should equal their respective reference values, hence

$$\left(P_{[\mathrm{k+1}]},\, Q_{[\mathrm{k+1}]}\right)^{\top} = \left(Q^{*}_{[\mathrm{k+1}]},\, Q^{*}_{[\mathrm{k+1}]}\right)^{\top} \tag{5.12}$$

are chosen in (2.50) where the *active power reference* $Q^{*}_{[\mathrm{k+1}]}$ comes from the DC-link controller (see Fig. 5.3) and the *reactive power reference* $Q^{*}_{[\mathrm{k+1}]}$ from the operation management of the wind turbine (according to specifications by the grid operator). Inserting (5.12) into (2.50) and re-arranging yields the (predicted) *grid-side reference voltage vector*

$$\begin{pmatrix} v^{\alpha *}_{\mathrm{g[k]}} \\ v^{\beta *}_{\mathrm{g[k]}} \end{pmatrix} = \begin{pmatrix} e^{\alpha}_{\mathrm{g[k]}} \\ e^{\beta}_{\mathrm{g[k]}} \end{pmatrix} - \frac{L_{\mathrm{g}}}{T_{\mathrm{s}}||\vec{e}^{\,\alpha\beta}_{\mathrm{g[k]}}||^2} \begin{bmatrix} e^{\alpha}_{\mathrm{g[k]}} & e^{\beta}_{\mathrm{g[k]}} \\ e^{\beta}_{\mathrm{g[k]}} & -e^{\alpha}_{\mathrm{g[k]}} \end{bmatrix} \cdot \begin{pmatrix} Q^{*}_{[\mathrm{k+1}]} - P_{[\mathrm{k}]} + \frac{T_{\mathrm{s}}R_{\mathrm{g}}}{L_{\mathrm{g}}} P_{[\mathrm{k}]} + \omega_{\mathrm{g}} T_{\mathrm{s}} Q_{[\mathrm{k}]} \\ Q^{*}_{[\mathrm{k+1}]} - Q_{[\mathrm{k}]} + \frac{T_{\mathrm{s}}R_{\mathrm{g}}}{L_{\mathrm{g}}} Q_{[\mathrm{k}]} - \omega_{\mathrm{g}} T_{\mathrm{s}} P_{[\mathrm{k}]} \end{pmatrix} \tag{5.13}$$

• Step II of Algorithm 5.1: In view of the dead-beat like prediction of the reference voltage vector (5.13), only the constraint set limits the reduction of the candidate region on the grid side. Since the constraint set on machine and grid-side are identical (i.e. $J_{\mathrm{CS_m}} = J_{CS_g}$), the offline selection of the hexagon candidate region(s) on the grid side is identical to the one on the machine side. Hence, the candidate region(s) $\mathcal{U}^{\mathrm{HCR}}_{\mathrm{CR_g}} = \mathcal{U}^{\mathrm{HCR}}_{\mathrm{CR_m}}$ on the grid side are the same as those on the machine side (see e.g. (5.9)) and do *not* have more than 12 elements.

• Step III, IV and V of Algorithm 5.1 on the grid side are identical to those on the machine side.

Remark 7 (Discussion of the computational load) *The CE-DMPC schemes with HCR on machine* and *grid side allow to make the evaluation of the prediction models for the target sets obsolete. Due to the dead-beat like prediction of the voltage vectors in* (5.8) *and* (5.13)*, instead of 27 computations, only one computation is required, respectively. Hence, the computation times for the evaluation of the prediction models for the target sets* $J_{TS_m} = J_{T_{\mathrm{e}}} + J_{i^d_s}$ *and* $T_{TS_g} = J_P + J_Q$ *are reduced by* $1 - \frac{1}{27} \approx 96\,\%$ *to nearly* $4\,\%$ *of the computation time required by classical DMPC. Moreover, the CE-DMPC schemes with HCR allow to shrink down the reasonable candidate regions on machine* and *grid side: Instead of 27* only *12 switching vectors must be considered. Hence, the computation time of the CE-DMPC with HCR can be reduced by*

$$1 - \frac{12}{27} \approx 55.6\% \text{ (i.e., the potential computation time reduction by CE-DMPC with HCR)} \tag{5.14}$$

to nearly $44.4\,\%$ *of the computation time of classical DMPC. Note that, additional computations are required for the determination of the location of the predicted reference voltages* $v^{\mathrm{d,q}*}_{\mathrm{m}}$ *and* $\vec{v}^{\,\alpha\beta *}_{\mathrm{g}}$ *within the hexagon. However, such calculations are easy to implement and not computationally demanding: Classical algorithms from space vector modulation can be applied.*

5.2.4 CE-DMPC with triangle candidate region

This subsection introduces CE-DMPC with triangle candidate region (TCR) for torque and power control of wind turbine systems with PMSG and 3L-NPC back-to-back power converter. The basic idea is illustrated in Fig. 5.4 and Fig. 5.5b. Again, the procedure and computation follow Algorithm 5.1 where the same equivalent cost functions (5.2) and (5.10) on machine and grid-side are used, respectively. Moreover, Step I (dead-beat like reference prediction) is identical to Step I of CE-DMPC with HCR. But now, the selection of the triangle candidate regions allows to reduce the computation time compared to CE-DMPC with HCR *even more* if fulfillment of the dynamic specifications for the constraint set (i.e. $J_{\mathrm{CS_m}} = J_{\mathrm{CS_g}} = J_{V_\mathrm{o}}$ in (5.2) or (5.10)) are less significant than the target set objectives (i.e. $J_{\mathrm{TS_m}} = J_{T_\mathrm{e}} + J_{i_\mathrm{m}^\mathrm{d}}$ in (5.2) and $J_{\mathrm{TS_g}} = J_P + J_Q$ in (5.10)). To omit the redundant part as is introduced in the above sections, only the key idea and the essential changes to CE-DMPC with HCR are discussed for *machine-side torque control and voltage balancing*. The derivation for grid-side power control and voltage balancing follows analogously.

5.2.4.1 Machine-side torque control and voltage balancing

Steps I, III, IV and V of Algorithm 5.1 are identical to CE-DMPC with HCR (see Sec. 5.2.3) only Step II, as the crucial step, yields a different outcome.

• Step II of Algorithm 5.1: Again, to illustrate the offline selection of the candidate region, assume that the reference voltage vector $\vec{v}^* := \vec{v}_\mathrm{m}^{\alpha\beta *} = \mathbf{T}_\mathrm{P}(\phi_\mathrm{e}) v_\mathrm{m}^{\mathrm{d,q}*}$ (obtained by (5.8)) is located at the position shown in Fig. 5.5b. Clearly, sector I can be divided further into five sub-regions or *triangles* (those labeled with 1, ..., 5 in Fig. 5.5b). By analyzing the geometric relations between those triangles within sector I, it is not difficult to see that one can differentiate the triangles from each other by checking the following rules in order of appearance (i.e. start with (rule-i) and stop with (rule-iv))

(rule-i) $v_m^{\alpha *} + \frac{\sqrt{3}}{3} v_m^{\beta *} \leq \frac{U}{2}$,

(rule-ii) $v_m^{\alpha *} + \frac{\sqrt{3}}{3} v_m^{\beta *} \geq U$,

(rule-iii) $v_m^{\alpha *} - \frac{\sqrt{3}}{3} v_m^{\beta *} \leq \frac{U}{2}$,

(rule-iv) $v_m^{\beta *} > \frac{\sqrt{3}}{4} U$ where $U = \sqrt{2/3}(V_{\mathrm{c1}} + V_{\mathrm{c2}}) = \sqrt{2/3} V_\mathrm{d}$.

Evaluation of the rules gives the triangle (see Tab. 5.1) which has to be considered and evaluated for a given reference voltage vector. A specific judgment about the relevant triangle and the number of the relevant switching vectors is made such that the cost function (5.2) can be minimized within the corresponding triangle. Tab. 5.1 lists these judgments and the number of switching vectors to be evaluated for each of the triangles. For instance, if (*rule*-iv) is satisfied, then the switching vector set of this triangle candidate region (i.e. "triangle 4") becomes

$$\mathcal{U}_{\mathrm{CR_m}}^{\mathrm{TCR}\,4} = \{\mathrm{00N},\ \mathrm{PP0},\ \mathrm{PPN},\ \mathrm{P0N}\} \subset \mathcal{U}_{27}, \tag{5.15}$$

Triangle	(rule-i)	(rule-ii)	(rule-iii)	(rule-iv)	No. of $\vec{u}_{\mathrm{y}}$ to be evaluated
1	true	-	-	-	7
5	false	true	-	-	3
2	false	false	true	-	4
4	false	false	false	true	4
3	false	false	false	false	5

Table 5.1: Determination of triangle candidate region (TCR): Decision rules and resulting number of switches $\vec{u}_{\mathrm{y}}$, $y \in \{m, g\}$, to be evaluated.

whereas, if (*rule*-ii) holds, i.e. "triangle 5" (the outer most line of sector I), the triangle candidate region (reduced switching vector set) is given by

$$\mathcal{U}_{\mathrm{CR_m}}^{\mathrm{TCR\,5}} = \{\mathrm{PPN},\ \mathrm{P0N},\ \mathrm{PNN}\} \subset \mathcal{U}_{27}. \tag{5.16}$$

The remaining switching vector sets $\mathcal{U}_{\mathrm{CR_m}}^{\mathrm{TCR\,i}}$, $i = 1, 2, 3$ follow by inspection from Fig. 5.5b and Tab. 5.1.

Remark 8 (Sector determination and mirroring to sector I) *For situations where the reference voltage vector $\vec{v}_{\mathrm{y}}^{*\mathrm{N}}$ ($y \in \{m, g\}$) is located in sector $N \in \{II, \ldots, VI\}$ and is* not *located in sector I (see Fig. 5.5b), simple* mirroring *of the reference voltage vector $\vec{v}_{\mathrm{y}}^{*\mathrm{N}}$ into sector I allows to re-use the sub-region determination procedure introduced above for all sectors I, II, ..., VI. To mirror the reference voltage vector the following rotation has to be performed*

$$\vec{v}_{\mathrm{y}}^{*\mathrm{I}} = \mathbf{T}_{\mathrm{P}}(\widetilde{\phi})\, \vec{v}_{\mathrm{y}}^{*\mathrm{N}}, \tag{5.17}$$

where $\widetilde{\phi} = \frac{\pi}{3}(N-1)$ and N is the number of the sector in which $\vec{v}_{\mathrm{y}}^{*\mathrm{N}}$ is located.

5.2.4.2 Grid-side power control and voltage balancing

Again, Steps I, III, IV and V of Algorithm 5.1 are identical to the steps of CE-DMPC with HCR on the machine side (see Sec. 5.2.3). Moreover, Step II of Algorithm 5.1 – the selection of the triangle candidate regions – follows the same rules as introduced in Sec. 5.2.4 for the machine side (see Tab. 5.1). Details are omitted.

Remark 9 (Discussion of the computational load) *The CE-DMPC with TCR achieves an even further reduction of the reasonable candidate regions: Instead of 27 only* 3, 4, 5 *or* 7 *switching vectors must be considered and evaluated on machine* and *grid-side (see Tab. 5.1). Considering the mean value of the numbers of switching vectors to be evaluated for all five triangles, i.e.*

$$\frac{7+3+4+4+5}{5} = \frac{23}{5} = 4.6,$$

(assuming a uniform distribution of the reference voltage) yields that the computation time for CE-DMPC with TCR is reduced on average *by*

$$1 - \frac{4.6}{27} \approx 83\,\% \text{ (i.e., the potential computation time reduction by CE-DMPC with TCR)} \quad (5.18)$$

to nearly 17 % *of the computation time of classical DMPC on machine* and *grid side. However, the constraint sets, i.e.* $J_{\mathrm{CS_m}} = J_{CS_g} = J_{V_o}$ *(see* (5.2) *and* (5.10)*), are* not *explicitly considered during the selection of the triangle candidate regions, which may lead to a less optimal control performance with respect to voltage balancing and current ripples.*

5.2.5 Evaluation and analysis

In this section the control performances of CE-DMPC with HCR and CE-DMPC with TCR are illustrated by simulation results and compared with the control performance of C-DMPC. As simulation scenario, a grid-tied 3L-NPC back-to-back PMSG wind turbine system (described in Chp. 2) is implemented in Matlab/Simulink. Simulation and system data are collected in Tab. 5.5.

5.2.5.1 Simulative evaluations

The test scenario is as follows: Within the interval $[0, 0.5]$ s, the wind speed is kept constant at $12\mathrm{m\,s^{-1}}$, which leads to a maximum grid-side output power of 1kW and a machine torque of approximately $-9\mathrm{N\,m}$. At 0.5s the wind speed increases to $17\mathrm{m\,s^{-1}}$ and is kept constant until 1s; then it starts to change to $21\mathrm{m\,s^{-1}}$ at 1s. From 1.5s on, the wind speed reduces again to $17\mathrm{m\,s^{-1}}$ and is kept at this speed until 2.5s. The initial DC-link capacitor voltages are chosen differently with $V_{c1}(0) = 350\,\mathrm{V}$ and $V_{c2}(0) = 400\,\mathrm{V}$ to investigate the DC-link voltage balancing performance of the three control schemes. The machine starts with an initial speed of $40\pi\mathrm{rad\,s^{-1}}$. For all simulation results in the Fig. 5.6, 5.7 and **??**, the grid voltages are balanced and non-faulty.

Figures 5.6(a), 5.6(c) and 5.6(e) illustrate the overall control performances of the direct model predictive torque controllers on the machine side and the direct model predictive power controllers on the grid side using classical DMPC, the proposed CE-DMPC with HCR and the proposed CE-DMPC with TCR, respectively. The evolutions of torque T_e, grid-side active power P and reactive power Q are almost identical for classical DMPC and the proposed CE-DMPC schemes.

In Figures 5.6(b), 5.6(d) and 5.6(f), the corresponding machine-side currents $\vec{i}_m^{abc}$, the grid-side current i_g^a and voltage e_g^a of phase a, the DC-link voltage V_d and the capacitor voltages V_{c1} and V_{c2} are plotted for the three different control schemes. The current evolutions are almost identical for all the DMPC schemes (see the 1st and 2nd subplots in Fig. 5.6(b), 5.6(d) and 5.6(f), respectively.). The CE-DMPC with TCR shows higher ripples in the currents and the DC-link voltage than classical DMPC and CE-DMPC with HCR (see Fig. 5.6(f)). The DC-link balancing control performances of all three DMPC schemes are shown in the 3rd and 4th subplot of Fig. 5.6(b), 5.6(d) and 5.6(f), respectively.

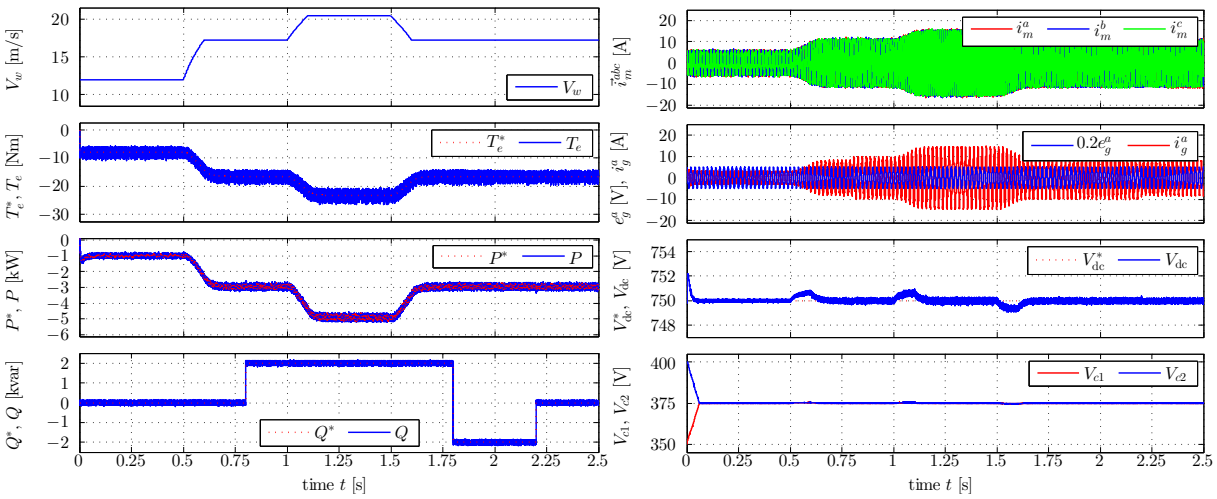

(a) Classical DMPC.

(b) Classical DMPC.

(c) CE-DMPC with HCR.

(d) CE-DMPC with HCR.

(e) CE-DMPC with TCR.

(f) CE-DMPC with TCR.

Fig. 5.6: Comparison of overall control performance: Wind V_w, torque T_e, active power P and reactive power Q *(*left*)* and machine-side currents $\vec{i}_m^{abc}$, grid-side current i_g^a and voltage e_g^a, DC-link voltage V_{d} and capacitor voltages V_{c1}, V_{c2} *(*right*)*, respectively.

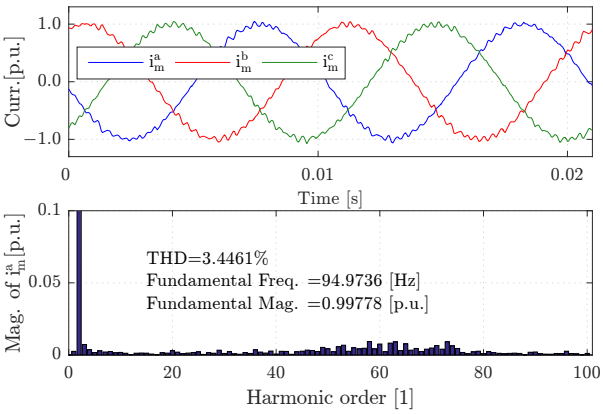

(a) Classical DMPC: Machine-side spectra and THD.

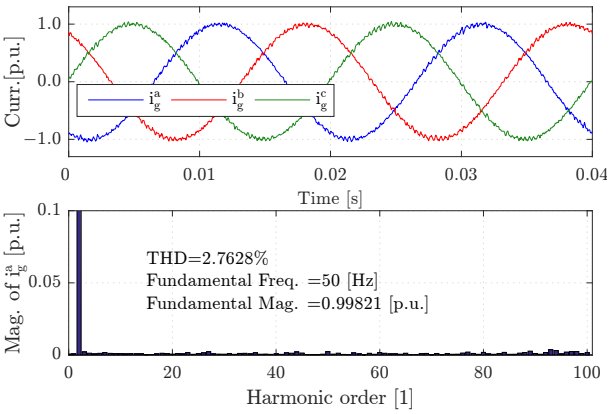

(b) Classical DMPC: Grid-side spectra and THD.

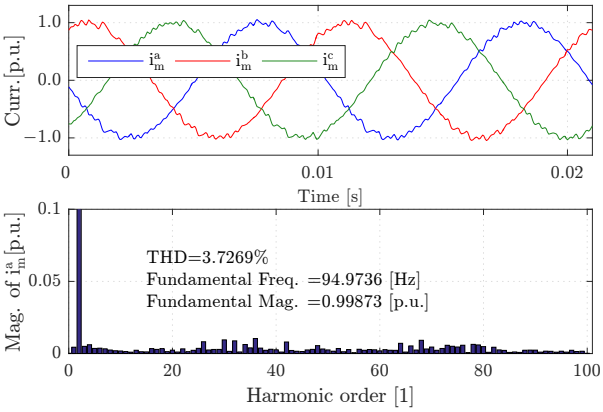

(c) CE-DMPC with HCR: Machine-side spectra and THD.

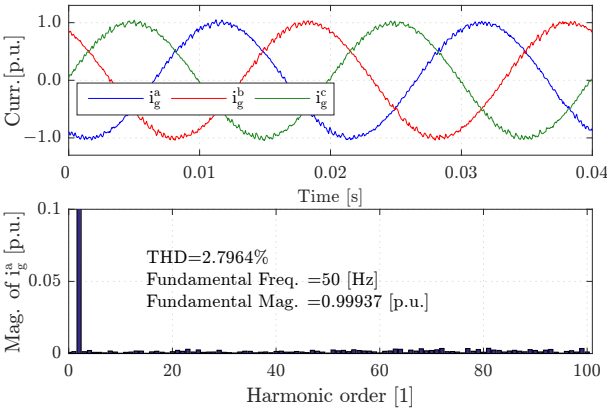

(d) CE-DMPC with HCR: Grid-side spectra and THD.

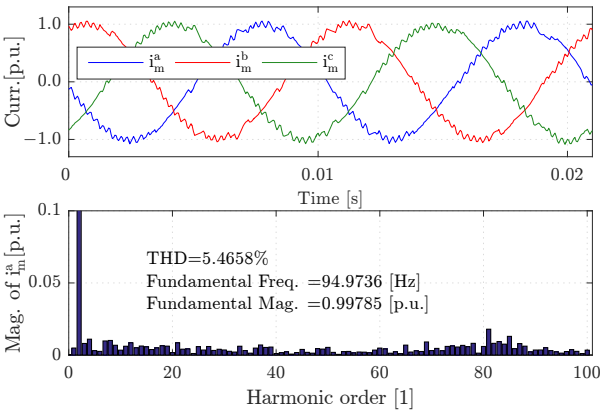

(e) CE-DMPC with TCR: Machine-side spectra and THD.

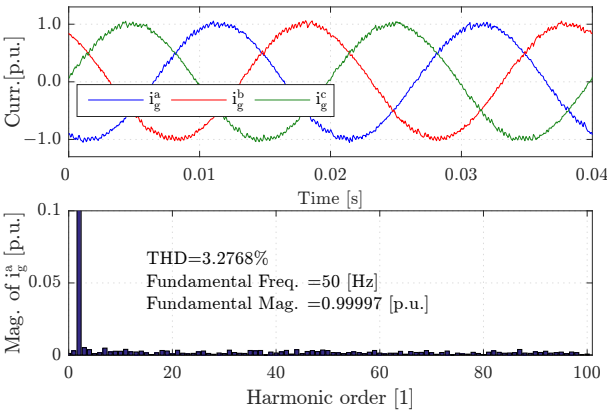

(f) CE-DMPC with TCR: Grid-side spectra and THD.

Fig. 5.7: Comparison of machine-side (left) and grid-side (right) current spectra and THDs for (a)-(b) classical DMPC, (c)-(d) CE-DMPC with HCR and (e)-(f) CE-DMPC with TCR, respectively (base values for machine and grid side currents are 12.88 A and 11.85 A, respectively.), respectively.

Parameters	**Simulation**	**Experiment**
Turbine quantities		
Air density ρ	$1.225\,\mathrm{kg\,m^{-3}}$	
Turbine radius R_t	$0.8\,\mathrm{m}$	
Maximum power coefficient C_p	0.48	
Tip speed ratio λ	8.4	
Pitch angle β	$0°$	
Grid-side quantities		
Grid-side phase voltage $\|\vec{e}_g\|$	$250\,\mathrm{V}$	$120\,\mathrm{V}$
Grid-side voltage frequency ω_g	$100\pi\,\mathrm{rad\,s^{-1}}$	$100\pi\,\mathrm{rad\,s^{-1}}$
Grid-side resistance R_g	$1.56 \times 10^{-3}\,\Omega$	$1.56 \times 10^{-3}\,\Omega$
Grid-side inductance L_g	$16 \times 10^{-3}\,\mathrm{H}$	$16 \times 10^{-3}\,\mathrm{H}$
3L-NPC back-to-back converter quantities		
DC-Link cap. $C_1 = C_2 = C$	$1000 \times 10^{-12}\,\mathrm{F}$	$1000 \times 10^{-12}\,\mathrm{F}$
Sampling frequency f_s	$20\,\mathrm{kHz}$	$20\,\mathrm{kHz}$
Machine-side quantities		
PMSG stator inductance $L_d = L_q$	$9 \times 10^{-3}\,\mathrm{H}$	$9 \times 10^{-3}\,\mathrm{H}$
PMSG stator resistance R_s	$1.1\,\Omega$	$1.1\,\Omega$
PMSG flux linkage ψ_{pm}	$4.1 \times 10^{-3}\,\mathrm{V\,s}$	$4.1 \times 10^{-3}\,\mathrm{V\,s}$
Weighting factors for C-DMPC (for CE-DMPC, given by (5.6) and (5.11))		
Weighting factor γ_{T_e}	1 ($J_{T_e}^{\max} = 16\,\mathrm{N\,m}$)	1 ($J_{T_e}^{\max} = 16\,\mathrm{N\,m}$)
Weighting factor $\gamma_{i_m^d}$	1 ($J_{i_m^d}^{\max} = 20\,\mathrm{A}$)	1 ($J_{i_m^d}^{\max} = 20\,\mathrm{A}$)
Weighting factor γ_{V_o}	0.01 ($J_{V_o}^{\max} = 10\,\mathrm{V}$)	0.01 ($J_{V_o}^{\max} = 10\,\mathrm{V}$)
Weighting factor $\gamma_P = \gamma_Q$	1	1

Table 5.2: System data of implementation, simulation, measurement, and controller design.

For classical DMPC and CE-DMPC with HCR, the DC-link voltages are balanced with nearly identical performance, whereas voltage balancing for CE-DMPC with TCR takes slightly longer; which is due to the limited number of switching vectors allowed for this scheme (*not* all elements of the seven levels are considered in contrast to CE-DMPC with HCR and classical DMPC). After 0.1s all three DMPC schemes achieve an almost ideal DC-link balancing control performance, i.e. $V_{c1}(t) = V_{c2}(t)$ holds true for almost all $t \in (0.1,\, 2.5]$.

To compare the current quality for all three control schemes in more detail, the current

spectra and the total harmonic distortions (THDs[3]) are shown in Fig. 5.7(a), 5.7(c) and 5.7(e) for the machine-side currents and in Fig. 5.7(b), 5.7(d) and 5.7(f) for the grid-side currents, respectively. Since all switching vectors are used during optimization/prediction, the classical DMPC scheme shows (slightly) better results than the proposed CE-DMPC with HCR scheme. CE-DMPC with TCR shows the highest THD values on machine and grid side, since only very few switching vectors are used during optimization. However, the grid-side THD value is still below the grid code requirements [119].

5.2.5.2 FPGA based real-time controller realization comparison

To illustrate and compare the real-time realization feasibility and calculating time details, all three DMPC schemes (i.e. classical DMPC, CE-DMPC with HCR and CE-DMPC with TCR) are implemented on an FPGA-based real-time system (NI-CRIO 9082 FPGA from National Instruments). Implementation of each DMPC scheme is visualized in Fig. 5.8. The different parts of the computation are highlighted by different colors (e.g. Clarke and Park transformation in dark blue or minimization/evaluation of the cost functions in red) and contribute individually to the overall computation time $T_{\text{total}} = T_1 + T_2 + T_3 + T_4 + T_5 = T_1 + T_2 + T_{\text{MPC}}$. Since T_1 and T_2 are the same for all three DMPC schemes, the overall computation time T_{total} will only differ due to different computation times $T_{\text{MPC}} = T_3 + T_4 + T_5$ of different the model predictive control schemes. Sleeping time $T_{\text{sleep}} = T_{\text{s}} - T_{\text{total}}$ is shown in black.

All DMPC schemes are implemented using an identical FPGA optimization method: The so-called Single-Cycle-Timed-Loop technique. Note that, since the usage of FPGA resources and the resulting execution times would not be comparable anymore, possible parallelizations of certain sub-routines were *not* considered. The execution times and the usage of the FPGA resources of all three DMPC implementations are collected in Tab. 5.4. The proposed computationally efficient DMPC schemes run faster with a decreased execution time compared to the classical DMPC scheme. Evaluation of the model predictive control execution times yields a reduction of the computational load by

$$100\% \cdot \frac{T_{\text{DMPC}} - T_{\text{CE-HCR}}}{T_{\text{DMPC}}} = 100\% \cdot \frac{6.8\mu s - 3.05\mu s}{6.8\mu s} = 55.1\%$$

for the CE-DMPC with HCR and by

$$100\% \cdot \frac{T_{\text{DMPC}} - T_{\text{CE-TCR}}}{T_{\text{DMPC}}} = 100\% \cdot \frac{6.8\mu s - 1.625\mu s}{6.8\mu s} = 79.6\%$$

for CE-DMPC with TCR, respectively. These results confirm the predicted reductions in computational load as discussed in Sec. 5.2.3 3) and Sec. 5.2.4 3), respectively. Moreover,

[3]The THD value of a current $i(t)$ with fundamental frequency $f_1 = \frac{1}{T_1} = \frac{\omega_1}{2\pi}$ is computed according to the IEEE Std 1459-2010 [118, Sec. 3.1.2.1] by using the formula $\text{THD}_{[\%]} := 100 \cdot \sqrt{\frac{I_{\text{rms}}^2}{I_{1,\text{rms}}^2} - 1}$ where $I_{1,\text{rms}}$ is the root-mean square value of the fundamental component of $i(t)$ and $I_{\text{rms}}^2 := \frac{1}{kT_1} \int_{\tau}^{\tau+kT_1} i(t)^2 \text{d}t$ with $k \in \mathbb{N}$ and $T_1 = \frac{2\pi}{\omega_1}$ is the (averaged) root-mean square value of the distorted current $i(t)$ over the time interval kT_1. k should be a natural number larger or equal to one, i.e. $k \geq 1$. In the paper, $k = 10$ is used. Note that, $i(t)$ is still T_1-periodic.

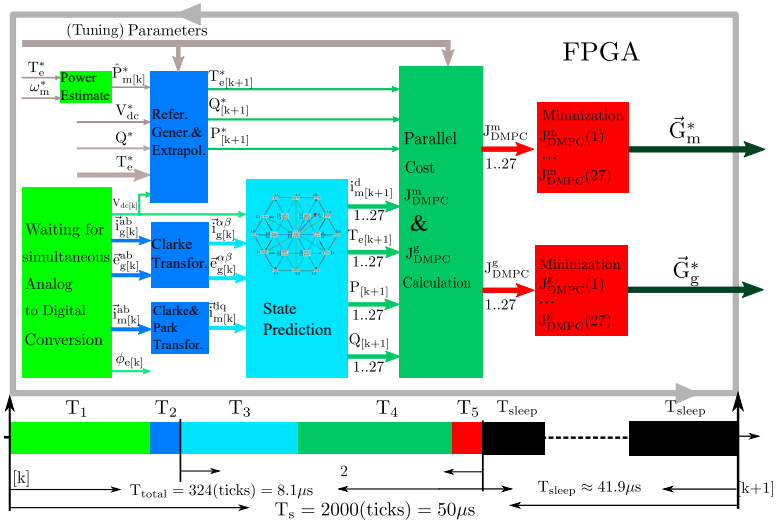

(a) Classical DMPC: FPGA implementation.

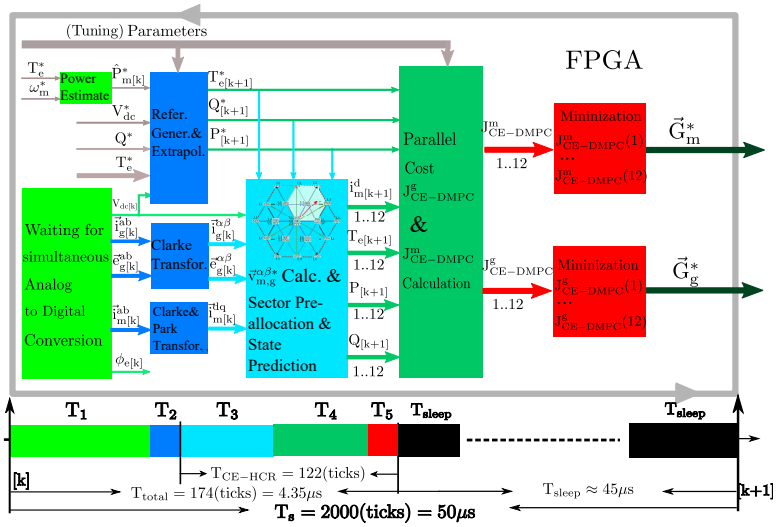

(b) CE-DMPC with HCR: FPGA implementation.

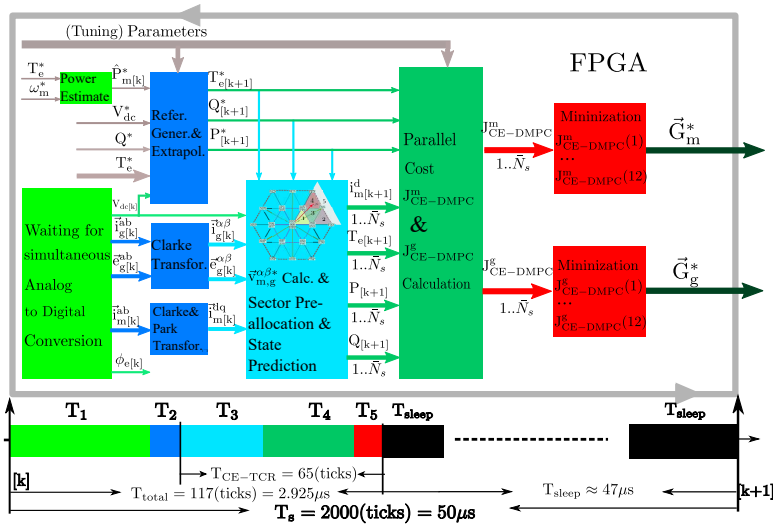

(c) CE-DMPC with TCR: FPGA implementation.

Fig. 5.8: Block diagrams and execution times of the FPGA implementations.

	C-DMPC	DMPC-HCR	DMPC-TCR
Execution times (top clock of FPGA is 40 MHz, i.e., $T_{\text{tick}} = \frac{1s}{40M} = 0.025\mu s$)			
T_1	1.000 μs (40 ticks)	1.000 μs (40 ticks)	1.000 μs (40 ticks)
T_2	0.300 μs (12 ticks)	0.300 μs (12 ticks)	0.300 μs (12 ticks)
T_3	3.375 μs (135 ticks)	1.450 μs (58 ticks)	0.750 μs (30 ticks)
T_4	2.725 μs (109 ticks)	1.275 μs (51 ticks)	0.725 μs (29 ticks)
T_5	0.700 μs (28 ticks)	0.325 μs (13 ticks)	0.150 μs (6 ticks)
T_{MPC}	6.800 μs (272 ticks)	3.050 μs (122 ticks)	1.625 μs (65 ticks)
Resources (total/number of used units)			
Slices	3227	2992	2974
Slice registers	8872	8372	8072
Slice LUTs	9606	6021	4807
DSP48s	45	54	54
Block RAMs	0	0	0

Table 5.3: FPGA implementation details.

in comparison to the classical DMPC implementation, the required FPGA resources are also reduced by CE-DMPC with HCR and CE-DMPC with TCR (see Tab. 5.4). Solely, the usage of the DSP48 slices is (slightly) increased due to the necessary reference voltage computation as in (5.8) and (5.13), respectively. The classical DMPC scheme does not require this step.

5.2.5.3 Experimental validation

To finally show the effectiveness of the proposed solutions and their real-time applicability on a hardware setup, a grid-tied 3L-NPC back-to-back power converter PMSG wind turbine system emulator was constructed in the laboratory. An overview of the this test-bench is shown in Fig. 2.10. A step-down variac is installed between the grid and the L(R) filter to lower the grid voltages for safety reasons. In the following, the overall control performances during steady-state *and* transient phase of the proposed solutions are experimentally verified. The measurement results are shown in Figures 5.9, 5.10 & 5.11.

Overall control performance: The testing scenario is maximum power point tracking where the wind speed (and hence the reference speed) changes rapidly (with a large slope) while the load-side torque remains at its rated value to test the most severe condition. The DC-link voltage reference V_{dc}^* is set to 350 V and the reactive power reference Q^* is set to 0 var to achieve a unit power factor. The overall control performance of the three DMPC schemes are illustrated in Fig. 5.9. As can be seen: Quite similar overall performances for generator *and* grid-side control (including the DC-link control) are obtained (see Fig. 5.9). Solely, CE-DMPC with TCR shows slightly bigger ripples in torque and power.

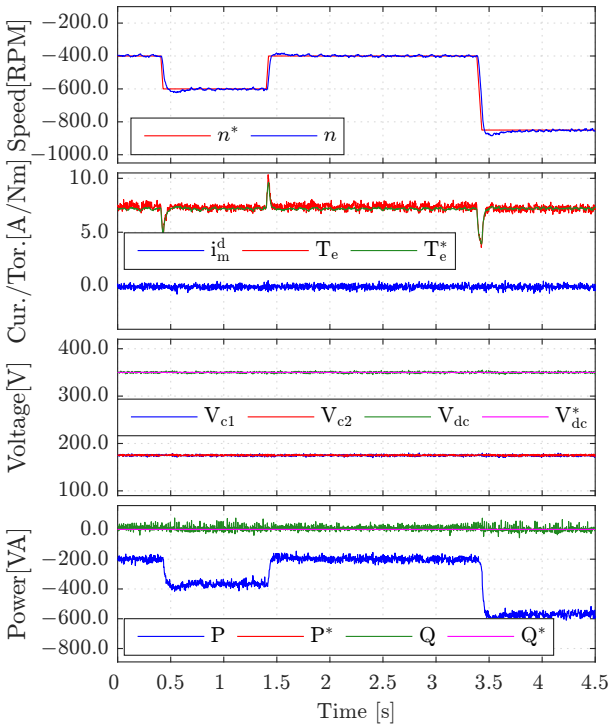

(a) Overall control performance of the classical DMPC.

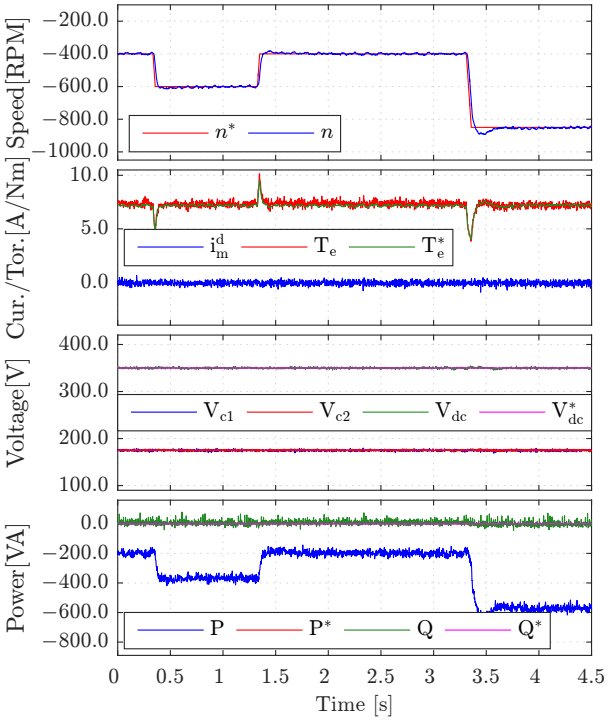

(b) Overall control performance of the CE-DMPC with HCR.

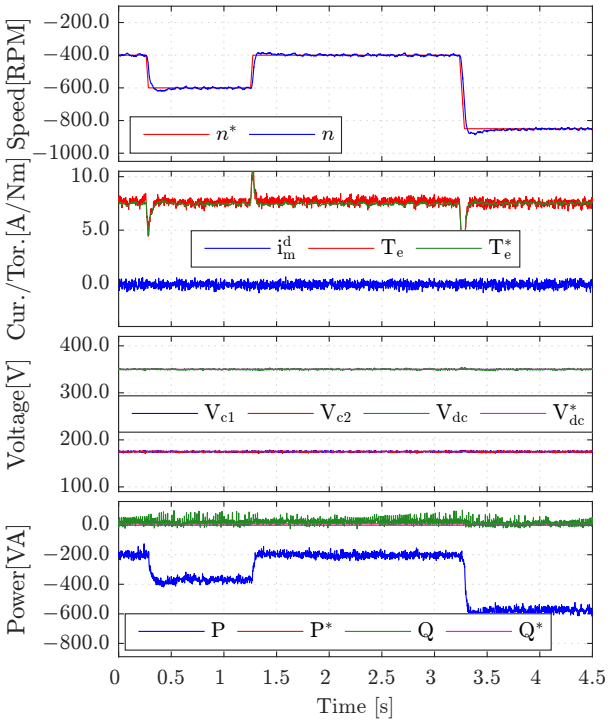

(c) Overall control performance of the CE-DMPC with TCR.

Fig. 5.9: [Experimental results] Overall control performances of classical DMPC (a), CE-DMPC with HCR (b) and CE-DMPC with HCR (c). Each subplot (from top to bottom) shows speed, machine stator (d-axis) current and electromagnet torque, DC-link and capacitor voltages, grid-side active and reactive power (and their references), respectively.

Transient control performance: The closed-loop dynamics are one of the key measures to judge the performance of a controller. Fast closed-loop control dynamics is one of the key benefits for using the DMPC solution, in comparison with the conventional cascaded control structures. Therefore, the transient control performances of both, the machine and grid side, are tested for all three DMPC schemes. To obtain the fastest possible closed-loop dynamics of the inner torque and reactive power controllers (covered by the discussed DMPC schemes), the slow dynamics of outer control loops (e.g. due to the slow speed controller (2.32) of the wind turbine system) are not considered. The testing scenario for the classical and the proposed DMPC schemes is as follows: The DC-link voltage set-point is set to 350 V. On generator side, the torque reference is manipulated directly (and is *not* coming from the slow speed controller (2.32)) to obtain *fast* and *step-like* changes in the reference torque varying from $-7\,\mathrm{N\,m}$ to $7\,\mathrm{N\,m}$ and back to $-7\,\mathrm{N\,m}$. On grid side, during steady-state operation of the generator (i.e., the generator operates with constant torque and speed), the reactive power reference[4] is changed step-like from 500 var to −500 var. The machine-side and grid-side transient control performances of all three DMPC schemes are depicted in Fig. 5.10 and Fig. 5.11, respectively. All three DMPC schemes achieve similarly fast closed-loop dynamics: Set-point tracking of a 14 N reference torque step on machine side (see Fig. 5.10) and of a 1000 var reference reactive power step on grid side (see Fig. 5.11) take around 1 ms, respectively.

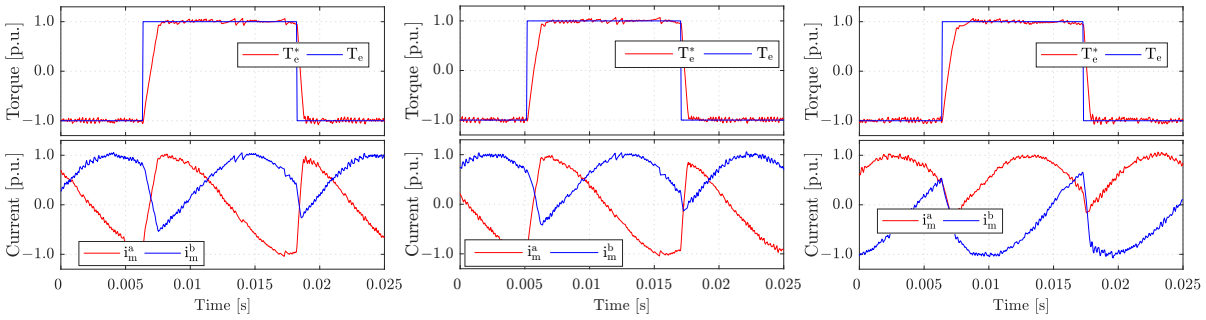

(a) Classical DMPC. (b) CE-DMPC with HCR. (c) CE-DMPC with TCR.

Fig. 5.10: [Measurement results:] Generator-side transient control performance of (a) classical DMPC, (b) CE-DMPC with HCR and (c) CE-DMPC with HCR (base values for electro-magnetic torque and machine-side current are $7\,\mathrm{N\,m}$ and 5.8 A, respectively).

5.2.5.4 Remark and analysis

This section has presented two computationally efficient DMPC schemes (CE-DMPC) for three-level neutral-point clamped (3L-NPC) back-to-back power converters in wind turbine systems with direct-drive permanent-magnet synchronous generator (PMSG). The following have been the main contributions:

(i) A detailed, discrete-time mathematical model of wind turbine systems with PMSG and 3L-NPC back-to-back power converter for DMPC schemes has been derived;

[4] Active power control is linked to DC-link control for a back-to-back power converter and, hence, step-like reference changes in active power are not feasible.

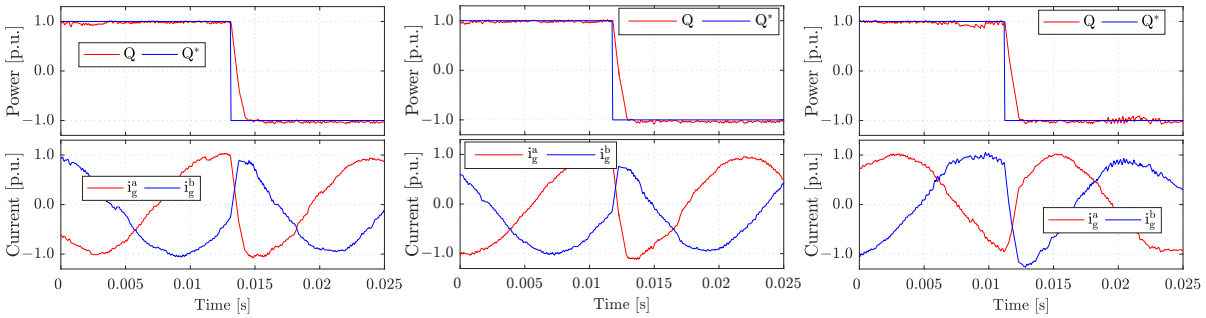

(a) Classical DMPC. (b) CE-DMPC with HCR. (c) CE-DMPC with TCR.

Fig. 5.11: [Measurement results] Grid-side transient control performance of (a) classical DMPC, (b) CE-DMPC with HCR and (c) CE-DMPC with HCR (base values for reactive power and grid-side current are 500 var and 4 A, respectively).

(ii) The classical direct model predictive control (DMPC) schemes for torque and power control have been revisited and applied to the wind turbine system;

(iii) To reduce the computational load of classical DMPC schemes, *two* CE-DMPC schemes with either *hexagon candidate region* (HCR) or *triangle candidate region* (TCR) have been introduced and applied to torque and power control of wind turbine systems with PMSG and 3L-NPC back-to-back power converter (see Sec. 5.2.3 and Sec. 5.2.4, respectively). The possible reductions of the computational load for CE-DMPC with HCR and for CE-DMPC with TCR have been theoretically analyzed: By CE-DMPC with HCR up to 55.6 % and by CE-DMPC with TCR up to 83.0 % of the computational power can be saved (see Sec. 5.2.3-3 and Sec. 5.2.4-3);

(iv) All three DMPC schemes have been implemented in Matlab/Simulink and applied to wind turbine systems with PMSG and 3L-NPC back-to-back power converter. The comprehensive simulation results have illustrated that the overall control performances of CE-DMPC with HCR and TCR are still acceptable, although not all available switching state are evaluated during prediction and optimization (see Sec. 5.5.4);

(v) The implementation of all three DMPC schemes on a FPGA-based real-time system. It was shown that real-time implementation is feasible. Moreover, the theoretically derived bounds on the potential reduction of the computational load for the CE-DMPC schemes were validated on the FPGA-based real-time system: The computation times can be reduced by 55.1% with CE-DMPC with HCR and by 79.6% with CE-DMPC with TCR (see Sec. 5.2.5.2 and cf. (5.14) and (5.18)).

(vi) Finally, all three DMPC schemes were experimentally tested at a lab-constructed 3L-NPC back-to-back power converter PMSG wind turbine system prototype. The presented measurement results clearly illustrated that the control performances of CE-DMPC with HCR and TCR are still very satisfactory and comparable to the control performance of the classical DMPC scheme while significantly lower computation times were achieved (see Sec. 5.2.5.3).

In conclusion, the saved computation time of the proposed CE-DMPC schemes eases real-time implementation on common industrial real-time platforms without the need of newer/more powerful processors or FPGAs. Moreover, it might give room to combine the CE-DMPC schemes with online parameter estimation algorithms (to improve robustness) and with long, i.e. multi-step, prediction horizons (to improve control performance). Future research will focus on the experimental verification of the proposed CE-DMPC schemes on a wind turbine emulator, the reduction of current ripples and the extension to unbalanced grids.

5.3 Performance-enhanced DMPC with two switching vectors

The big ripple drawback of the classical DMPC scheme has already been summarized in Sec. 5.1 which is (mainly) caused by its inherent *one-switching-vector-per-interval* character. Oversampling (See e.g., [120]) or online state estimation based multiple prediction (See e.g., [115]) techniques can be used to increase the switching actuating events of each control interval hence to reduce the ripples. However, either even higher requirements will be imposed on the hardware set-up (e.g., high sampling frequency measurement board and high power real-time controller [120]) or precise system model and parameters are required to achieve so. Due to the hardware limitations, controller refreshing rate cannot be too high. Therefore, with a similar sampling frequency, the steady state performance of DMPC scheme is less satisfying than the modulator based approaches.

5.3.1 Concept of the proposed two-vector DMPC

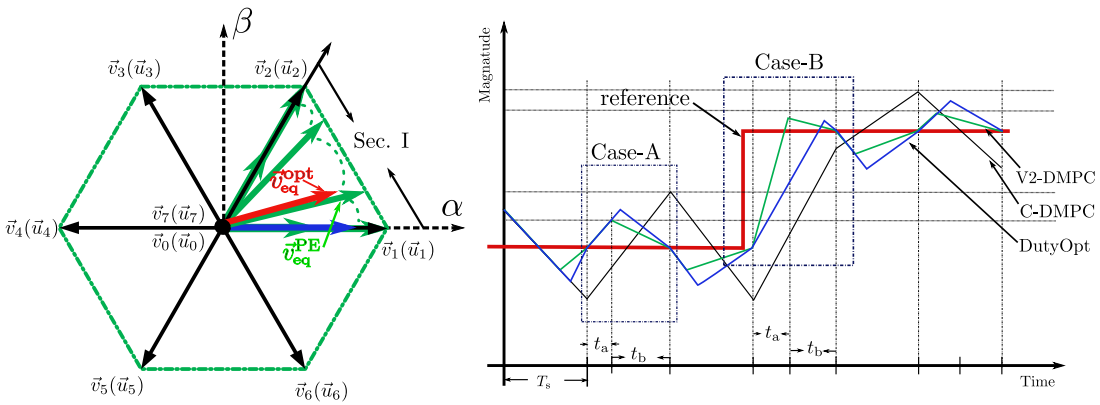

Fig. 5.12: Vector plane and ripple-reduction effect of the proposed V2-DMPC.

In this section, a new solution with (also) two switching vectors in each sampling interval (in the following it is named as V2-DMPC) are proposed and verified. Different from the DutyOpt method (See e.g., [17, 121]), the proposed V2-DMPC [122, 123] utilizes not

only the *active plus zero* vector combination but also *a pair of two active vectors*[5]. With such configurations, the controller uses an equivalent synthesized voltage vector with *an arbitrary phase*, or voltage vector *with arbitrary length on the phases of the six fundamental active ones*. Therefore, more freedoms and precise tracking possibilities are included into the predictive controller design. To better illustrate the propose V2-DMPC, its concept and principles are shown in Fig. 5.12. The left side of Fig. 5.12 depicts the concept, while the right side of this figure shows the expected performances. Detailed explanation of this concept is as follows.

In the left part of Fig. 5.12, the black lines/point represent all the admissible vectors for the classical DMPC (C-DMPC) scheme with a control interval of T_s; the blue lines/point and the green lines/point are the diminishable vectors for the DutyOpt-DMPC and the proposed V2-DMPC scheme with the same control period. It is not difficult to understand, the DutyOpt-DMPC scheme extended the candidate vectors from the original 8 vectors (2 zeros and 6 active ones)[6] to an infinite number of vectors. However, vector phases *other* than the original active ones are not admissible for this scheme. While for the proposed V2-DMPC scheme, admissible (equivalent) vectors to apply can be divided into two classes: i) *vectors with the same direction of the active vectors but with (infinite number of) different lengths*, and ii) *vectors with the maximum length but different phases/directions.*

Differences in the equivalent voltage vectors will lead to different control performances. As is depicted in the right side of Fig. 5.12, during steady state, i.e, **Case-A** in Fig. 5.12, the driving force produced by any vector for an entire control interval becomes too large. Therefore, with a second vector working for t_b time, a more flexible (optimal) vector phase can be equivalently synthesized, resulting in a better slope of the control variable. Thus a smaller ripple of the control variable is expected[7]. While during the transient phases, i.e, **Case-B** in Fig. 5.12, a bigger drive force is required to reach a sudden change of the reference. In this case, both C-DMPC and DutyOpt-DMPC schemes, may utilized one of the six (fundamental) active vectors while the V2-DMPC scheme may take the combination of two active vectors (working for t_a and t_b, respectively) resulting in a better slope than that of the CDMPC and DutyOpt-DMPC method.

5.3.2 Realization of V2-DMPC

The realization of the proposed V2-DMPC method includes two separate procedures using a *time-optimal concept*, namely, *arbitrary length determination* (at fundamental vector phases) and *arbitrary phase determination*. They are detailed in the following.

[5]To reduce the switching transient, the active vector pairs are adjacent to each other, i.e., only $\vec{u}_{1,2}, \vec{u}_{2,3}, ..., \vec{u}_{5,6}, \vec{u}_{6,1}$ can be pairs. For the applications, where MOSFET or silicon-carbide semiconductors are used, higher switching frequency is not an issue. Then the vectors not necessarily adjacent can be applied, which may have even better steady state performances. A similar idea for a PMSM drive was found in [123].

[6]It may also be seen as 7 original vectors, since 2 zeros are the same in drive force, but may lead to different switching transient (switching frequency).

[7]The V2-DMPC (the green line in Fig. 5.12) is allowed to choose both the zero and an active vector as the second vector, which makes it may outperform the DutyOpt-DMPC (the blue line in Fig. 5.12) during steady state.

5.3.2.1 Time-optimal concept

Assuming the predictive controller tries to optimize the following targeting set[8]

$$J = \sum_{1}^{n} \left(Z_{\mathrm{i}}^{*} - Z_{\mathrm{i[k+1]}} \right)^{2}, \tag{5.19}$$

of a cost function, where Z_{i}^{*} is the reference of the $i-th$ control target, and $Z_{\mathrm{i[k+1]}} = Z_{\mathrm{i[k]}} + t_{\mathrm{j}} \cdot Sl^{\mathrm{uj}}_{\mathrm{Z_{i[k]}}} + t_{\mathrm{k}} \cdot Sl^{\mathrm{uk}}_{\mathrm{Z_{i[k]}}}$ is the predicted state using control variable with slopes of $Sl^{\mathrm{vj,k}}_{\mathrm{Z_{i[k]}}}$ produced by the switching states of $\vec{u}_{j,k}$, respectively. In practice, the current state $Z_{\mathrm{i[k]}}$ and all the relevant slopes $Sl^{\mathrm{vj}}_{\mathrm{Z_{i[k]}}}(\vec{u}_{\mathrm{j}})$ produced by $\vec{u}_{\mathrm{j}} \in \mathcal{U}_8$ can be obtained by measurement or estimation. The whole control interval is occupied by $\vec{u}_{j,k}$ only, i.e., $t_{\mathrm{j}} + t_{\mathrm{k}} = T_{\mathrm{s}}$. Therefore the optimal control times of $t_{\mathrm{j}}, t_{\mathrm{k}}$ for switching vector $\vec{u}_{j,k}$ can be calculated through assuring the following equation[9]

$$\begin{aligned} &\frac{\partial J(t_{\mathrm{j}}, t_{\mathrm{k}})}{\partial t_{\mathrm{j}}, \partial t_{\mathrm{k}}} := 0, \\ \text{Subj. to } &: (i)\ t_{\mathrm{j}} + t_{\mathrm{k}} = T_{\mathrm{s}}; \\ &\ (ii)\ t_{\mathrm{j}}, t_{\mathrm{k}} \in [0, T_{\mathrm{s}}]. \end{aligned} \tag{5.20}$$

Actuating times in reality cannot be negative. Therefore, solely Equation (5.20) cannot always yield admissible results (the calculated times may turn out to be negative or bigger than the control interval of T_{s}). So in practice Equation (5.20) will be firstly solved to obtain of t_{j}. Then the following restraint

$$\text{if } \ t_{\mathrm{j}} \leq 0, \text{then} \quad t_{\mathrm{j}} = 0; \ \text{if} \quad t_{\mathrm{j}} \geq T_{\mathrm{s}}, \quad \text{then}\, t_{\mathrm{j}} = T_{\mathrm{s}}; \quad \text{else}\, t_{\mathrm{j}} = t_{\mathrm{j}}; \tag{5.21}$$

is taken into account to assure $t_{\mathrm{j}} \in [0, T_{\mathrm{s}}]$, and t_{k} is calculated through $t_{\mathrm{k}} = T_{\mathrm{s}} - t_{\mathrm{j}}$.

5.3.2.2 Optimal length determination (at fundamental vector phases)

One of the vector pairs are chosen from one of $\vec{u}_1, ..., \vec{u}_6$; the second is always $\vec{u}_{\mathrm{null}}$[10]. Starting from Sec-I (See Fig. 5.12), taking the first vector pair of $\vec{u}_{1,\mathrm{null}}$ as an example, their optimal times will be calculated using (5.20). The obtained times will be re-ranged using (5.21), and marked as $t^{I}_{1,0}$. The cost of $J^{I}_{1,0}$ will be obtained and recorded.

5.3.2.3 Optimal phase determination

The vector pairs in this case are chosen from one of $\vec{u}_{(1,2),(2,3),...(5,6),(6,1)}$. Starting also from Sec-I (See Fig. 5.12), actuating times of $t_{(1,2)}$ for $\vec{u}_{(1,2)}$ can be calculated invoking

[8] Such as the current, torque, power and/or flux tracking targets, which are globally differentiable.

[9] The nonlinear constraints (current, power and torque limitations) are limited by the outer controller loops with regarding to the power ratings, such as the speed and DC-link PI controllers, which makes the whole cost function differentiable to the time variable.

[10] Here to lower the switching frequency, $\vec{u}_{\mathrm{null}}$ can be $\vec{u}_0$ if the active one is $\vec{u}_1$,$\vec{u}_3$, or $\vec{u}_5$; or $\vec{u}_7$ if the active one is $\vec{u}_2$,$\vec{u}_4$, or $\vec{u}_6$

Equations (5.20) and (5.21). These times are recorded as $t^I_{1,2}$. The cost for this pair can be calculated as $J^I_{1,2}$. Between $J^I_{1,0}$ and $J^I_{1,2}$, the smaller is recorded as J^I_{opt}; the correlated vectors and actuating times are recorded as $\vec{u}^{\text{I,a,b}}_{opt}$, and $t^{\text{I,a,b}}_{opt}$, respectively.

Carrying out the above procedures for all the six sectors yields six cost values $J^{\text{I,..,VI}}_{\text{opt}}$, and their correlated vectors $\vec{u}^{\text{I,..,VI;a,b}}_{opt}$ and duration times $t^{\text{I,..,VI;a,b}}_{opt}$. The optimal vector pair and their times with the smallest cost value will be selected and recorded as $\vec{u}^{\text{a,b}}_{opt}$, $t^{\text{a,b}}_{opt}$. Applying $\vec{u}^{\text{a}}_{opt}$, $\vec{u}^{\text{b}}_{opt}$ for t^{a}_{opt} and t^{b}_{opt}, respectively for a whole control interval will yield the optimal control performances with such switching vector combinations.

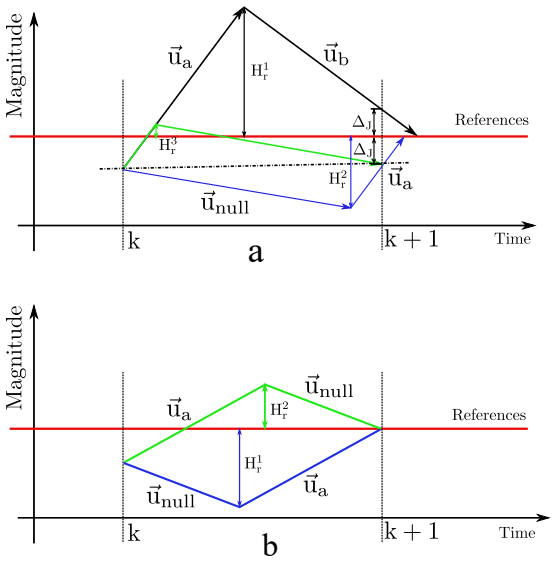

Fig. 5.13: Discussion of the potential sub-optimal solutions. In **a**, the black line is triggered using two active vectors, the blue and green lines are triggered by one zero and one active vectors. While in **b**, both the blue and green lines are triggered by one active and one zero vectors, but the actuating order is different.

Remark 10 (Sub-optimal solution analysis) *A careful analysis will yield the following conclusion as shown in Fig. 5.13: certain situations will produce the same cost of J, but with different intermediate ripples, which may produce undesired or sub-optimal results. For instance, both situations in Fig. 5.13-**a** and -**b** have the same cost values, i.e., the control will choose any of these vector and time pairs which triggers however different trajectories of the control variable (i.e., the blue and green lines). Obviously the blue lines produces much bigger ripples since $|\text{H}^1_\text{r}| > |\text{H}^2_\text{r}|$.*

5.3.2.3.1 Optimization 1 To conquer the problem induced by the situation in the Remark 10, a solution using two extra steps as follows is proposed

i) Change the cost function for comparison from (5.19) as

$$J^{\text{com}} = \sum_1^n \left(Z^*_\text{i} - Z_{\text{i}(1+\frac{\text{t}_1}{\text{T}_\text{s}})[\text{k}]}\right)^2 + \sum_1^n \left(Z^*_\text{i} - Z_{\text{i[k+1]}}\right)^2 \tag{5.22}$$

which will help the controller to discard the vector pair of the blue line in the situation showed in **a** of Fig. 5.13.

ii) For each of an obtained vector pair ($\vec{u}_{\mathrm{a,b}}$) and their time pair ($t_{\mathrm{a,b}}$), calculate both the costs of $J^{\mathrm{com}}_{(\mathrm{a,b})}$ and $J^{\mathrm{com}}_{(\mathrm{b,a})}$, compare and record only the smaller one. This will help the controller to discard the vector pair of the blue line in the situation showed in **b** of Fig. 5.13.

Remark 11 (Discussions on the calculation load) *The aforementioned two extra optimization steps in Sec. 5.3.2.3.1 settle the un-optimal solution problem. However, it will further increase the computational load drastically from 12 cost calculations/comparisons to 24 iterations; the cost function for the comparison step becomes also more complicated (See (5.22)). The increased computational load may lead to the proposed scheme not feasible for hardware realizations.*

5.3.2.3.2 Optimization 2 To conquer the problem stated in Remark 11, the same computational efficient concept introduced in Sec. 5.2.2 is used, i.e., in-cooperating the deadbeat concept to pre-allocate a smaller region (sector) of the candidate voltage vectors to evaluate. For instance, once we know the optimal voltage vector is located in Sec-I in Fig. 5.12, then only the vector pairs of $\vec{u}_{1,2}, \vec{u}_{2,1}, \vec{u}_{1,0}, \vec{u}_{0,1}, \vec{u}_{2,0}, \vec{u}_{0,2}$ will be compared[11], thus the real computational load reduces from 24 cases to 6 only.

So far the concept, realization procedures, and optimization steps of the proposed V2-DMPC scheme have all been introduced. Note that, this concept can theoretically be applied to both two and multilevel converters. However, multilevel power converters (e.g., three- or more voltage level power converters) have multiple voltage levels and the steady state control variable ripples are much smaller than that of the two level situations. The improvements using the proposed methods will not be as remarkable as the two-level cases [54]. Therefore, in the following sections the proposed V2-DMPC method is only applied to the two-level back-to-back power converter system, for both the grid side and machine side converter control.

5.3.3 Application of the V2-DMPC to grid side control

5.3.3.1 Introduction

Characterized by bidirectional power flow, flexible DC-link voltage regulation ability with smaller DC-link capacitors and sinusoidal input currents with low harmonic pollution [8,10], active front-end power converters (AFEs) i.e., the grid side converter (GSC) has been widely used in a variety of industrial applications, such as advanced machine drives with regenerative capability, renewable energy systems [17,124,125]. The most popular strategy in the industrial to control AFEs is VOC [125,126], where the grid currents is decomposed into active and reactive power components in synchronous (dq) frame in the format of

[11] By locating the optimal voltage vector in to a 30° sector, another two evaluations will be saved. For instance, if the optimal voltage vector can be located with the lower half of Sec-I, then only $\vec{u}_{1,2}, \vec{u}_{2,1}, \vec{u}_{1,0}, \vec{u}_{0,1}$ are to evaluated.

"DC" quantities. Therefore, simple PI controllers can be adopted to regulate the d-axis and q-axis components and generate the relevant reference voltage vectors. This method achieves nice steady response, but the final performance largely depends on the PI tuning for the inner current loops [3, 104, 127] and an extra modulator is required.

Contrary to voltage oriented control, *direct power control technique*, using an offline designed switching table, is a simple and effective control strategy for grid-tied AFE control. It was derived from the well-known DTC technique and requires no line voltage vector position, no Park's transformation or extra modulator [35, 93]. Due to its merits of fast dynamic response and simple structure, DPC has attracted much attention. However, the discrete nature and the available model of the power converter had not been fully considered by the classical table based DPC schemes.

In 2008, the author of [93] presented a direct model predictive power control (DMPPC) algorithm for AFEs based on the FCS-MPC concept, which requires no linear current controller, coordinate transformations, or modulators. A cost function representing the control objectives, is defined with flexibility, and then minimized to determine the optimal switching sequence to be applied in the next control interval. It becomes a nice alternative for AFE control. However, characterized by its *single-voltage-vector-per-control-interval*, big control variable ripples/high THDs of the grid side currents are seen.

For a grid-tied AFE using DMPPC the control targets are active power control (tracking) and reactive power control (tracking) [10]. Therefore the cost function to fulfill these two control targets is defined as

$$J(\vec{S}^{\vec{u}_\mathrm{x}}_{[\mathrm{k+1}]}) = \underbrace{\left(P^* - P_{[\mathrm{k+1}]}(\vec{u}_\mathrm{x})\right)^2}_{=:J_\mathrm{P}} + \underbrace{\left(Q^* - Q_{[\mathrm{k+1}]}(\vec{u}_\mathrm{x})\right)^2}_{=:J_\mathrm{Q}} \tag{5.23}$$

where J_P and J_Q represent the targets for active and reactive power control, respectively.

In this section, with the same cost function of (5.23) the C-DMPPC, recently reported DutyOpt-DMPPC schemes are firstly revisited and then a proposed V2-DMPPC method using the V2-DMPC concept introduced in last section is introduced in detail. To cope with its heavy computational load, a fully FPGA based solution is utilized for the controller implementation. To clearly illustrate the effectiveness of performance enhancement, all approaches are compared with both simulation and experimental data in Sec. 5.4.5.

5.3.3.2 Classical DMPPC scheme (C-DMPPC)

C-DMPPC scheme evaluates the cost function of (5.23) for each switching state $\vec{u}_i$ of the admissible (finite) set $\mathcal{U}_8$ to find the optimal switching vector by using the following prediction model

$$(P^{\vec{u}_\mathrm{i}}_{[\mathrm{k+1}]}, Q^{\vec{u}_\mathrm{i}}_{[\mathrm{k+1}]})^\top = (P^{\vec{u}_\mathrm{i}}_{[\mathrm{k}]}, Q^{\vec{u}_\mathrm{i}}_{[\mathrm{k}]})^\top + T_\mathrm{s}(Sl^{\vec{u}_\mathrm{i}}_{\mathrm{P[k]}}, Sl^{\vec{u}_\mathrm{i}}_{\mathrm{Q[k]}})^\top, \tag{5.24}$$

where all the variables are the same as in Chp. 2, and

$$\left(Sl^{\vec{u}_\mathrm{i}}_{\mathrm{P[k]}}, Sl^{\vec{u}_\mathrm{i}}_{\mathrm{Q[k]}}\right)^\top = \frac{1}{L_\mathrm{g}} \begin{bmatrix} e^{\alpha}_{\mathrm{g[k]}} & e^{\beta}_{\mathrm{g[k]}} \\ e^{\beta}_{\mathrm{g[k]}} & -e^{\alpha}_{\mathrm{g[k]}} \end{bmatrix} \begin{pmatrix} e^{\alpha}_{\mathrm{g[k]}} - v^{\alpha}_{\mathrm{g[k]}}(\vec{u}_\mathrm{i}) \\ e^{\beta}_{\mathrm{g[k]}} - v^{\beta}_{\mathrm{g[k]}}(\vec{u}_\mathrm{i}) \end{pmatrix} - \begin{pmatrix} \frac{R_\mathrm{g}}{L_\mathrm{g}} P_{\mathrm{[k]}} + \omega_\mathrm{g} Q_{\mathrm{[k]}} \\ \frac{R_\mathrm{g}}{L_\mathrm{g}} Q_{\mathrm{[k]}} - \omega_\mathrm{g} P_{\mathrm{[k]}} \end{pmatrix}. \tag{5.25}$$

The chosen optimal (*one*) switching vector is applied for a whole control interval. Details have been introduced in Chp. 4.

5.3.3.3 Duty Optimal DMPPC (DutyOpt-DMPPC)

DutyOpt-DMPPC (See [47, 122] and the reference therein) applies instead of "*one-vector-per-control-interval*", two vectors, i.e., *one active* and *one zero* vectors to minimize the cost-function. An equivalent voltage vector in phase with the selected active vector with an optimized length can be synthesized. Therefore, better steady state performance than the classical scheme can be achieved.

However, with only one active and a zero vector, the synthesized equivalent vector with phases (directions) other than that of the *fundamental* active vector cannot be generated.

5.3.3.4 DMPPC with V2-DMPC concept (V2-DMPPC)

V2-DMPPC is also a two-vector based solution. However, different from the DutyOpt-DMPPC method, candidate vectors with both different lengths and phases can be synthesized. In the following its realization will be introduced in detail following the descriptions[12] given in Sec. 5.3.2.

5.3.3.5 Arbitrary length determination (at fundamental vector phases)

Starting from Sec. I, the optimal vector is (assumed to be) synthesized with $\vec{u}_1$ and $\vec{u}_0$; their operating times are assumed as t_1 and t_0, respectively. Therefore, the power vector can be predicted as

$$\vec{S}^{\vec{u}_{0,1}}_{[\mathrm{k+1}]} = \vec{S}_{[k]} + \vec{Sl}^{\vec{u}_1}_{\mathrm{S[k]}} \cdot t_1 + \vec{Sl}^{\vec{u}_0}_{\mathrm{S[k+1]}} \cdot t_0 \tag{5.26}$$

where $\vec{Sl}^{\vec{u}_1}_{\mathrm{S[k]}} = (Sl^{\vec{u}_1}_{\mathrm{P[k]}}, Sl^{\vec{u}_1}_{\mathrm{Q[k]}})^\top$, $\vec{Sl}^{\vec{u}_0}_{\mathrm{S[k+1]}} = (Sl^{\vec{u}_0}_{\mathrm{P[k+1]}}, Sl^{\vec{u}_0}_{\mathrm{Q[k+1]}})^\top$. Inserting (5.26) to (5.23), and using the time optimal concept (Equations (5.20) and (5.21)) yields the duration times as

$$\begin{aligned} t_1 =& \frac{(P^* - P_{\mathrm{[k]}})\big(Sl^{\vec{u}_1}_{\mathrm{P[k]}} - Sl^{\vec{u}_0}_{\mathrm{P[k+1]}}\big) + (Q^* - Q_{\mathrm{[k]}})\big(Sl^{\vec{u}_1}_{\mathrm{Q[k]}} - Sl^{\vec{u}_0}_{\mathrm{Q[k+1]}}\big)}{(Sl^{\vec{u}_1}_{\mathrm{P[k]}} - Sl^{\vec{u}_0}_{\mathrm{P[k+1]}})^2 + (Sl^{\vec{u}_1}_{\mathrm{Q[k]}} - Sl^{\vec{u}_0}_{\mathrm{Q[k+1]}})^2} \\ &+ \frac{T_\mathrm{s}\big(||Sl^{\vec{u}_0}_{\mathrm{S[k+1]}}||^2 - Sl^{\vec{u}_1}_{\mathrm{P[k]}} Sl^{\vec{u}_0}_{\mathrm{P[k+1]}} - Sl^{\vec{u}_1}_{\mathrm{Q[k]}} Sl^{\vec{u}_0}_{\mathrm{Q[k+1]}}\big)}{(Sl^{\vec{u}_1}_{\mathrm{P[k]}} - Sl^{\vec{u}_0}_{\mathrm{P[k+1]}})^2 + (Sl^{\vec{u}_1}_{\mathrm{Q[k]}} - Sl^{\vec{u}_0}_{\mathrm{Q[k+1]}})^2} \end{aligned} \tag{5.27a}$$

$$t_0 = T_\mathrm{s} - t_1. \tag{5.27b}$$

With the calculated times $t_{0,1}$, a modified cost function (based on Optimization1 in Sec. 5.3.2.3.1) of $J(\vec{S}^{\vec{\mathrm{I}}0,1}_{[\mathrm{k+2}]})$ is defined by (5.28) to guarantee both the tracking performance

[12] The calculation optimization solution proposed in Sec. 5.3.2.3.2 was not used for this realization due to that a FPGA is used for the real-time implementation.

at time instant [k + 1] and ripple-reducing performance at $(1+\frac{T_i}{T_s})$[k] can be obtained.

$$J(\vec{S}^{\mathrm{I}0,1}_{[k+2]}) = \underbrace{\left(P^* - P_{(1+\frac{T_i}{T_s})[k]}(\vec{u}_0)\right)^2}_{=:J_{P1}} + \underbrace{\left(Q^* - Q_{(1+\frac{T_i}{T_s})[k]}(\vec{u}_0)\right)^2}_{=:J_{Q1}} + \underbrace{\left(P^* - P_{[k+1]}(\vec{u}_1)\right)^2}_{=:J_{P2}} + \underbrace{\left(Q^* - Q_{([k+1]}(\vec{u}_1)\right)^2}_{=:J_{Q2}}. \quad (5.28)$$

5.3.3.6 Arbitrary phase determination

In this step, instead of using $\vec{u}_{0,1}$, the optimal vector is assumed to be synthesized with the two active ones of $\vec{u}_{1,2}$. Then the power vector can be predicted as

$$\vec{S}^{\vec{u}_{1,2}}_{[k+1]} = \vec{S}_{[k]} + \vec{Sl}^{\vec{u}_1}_{\mathrm{S}[k]} \cdot t_1 + \vec{Sl}^{\vec{u}_2}_{\mathrm{S}[(1+\frac{t_1}{T_s})k]} \cdot t_2. \quad (5.29)$$

Following the similar procedures as in Sec. 5.3.3.5 and applying equations (5.26) to (5.28) (replace the relevant variables related to $\vec{u}_o$ with those related to $\vec{u}_2$), the cost in this case is calculated and marked as $J(\vec{S}^{\vec{u}_{1,2}}_{[k+1]})$. Compare $J(\vec{S}^{\mathrm{I}0,1}_{[k+1]})$ with $J(\vec{S}^{\mathrm{I}1,2}_{[k+1]})$ and record the smaller one together with its correlating vectors and duration times as $J^{\mathrm{I}}_{\mathrm{opt}}$, $\vec{u}^{\mathrm{I,a,b}}_{\mathrm{opt}}$, $t^{\mathrm{I,a,b}}_{\mathrm{opt}}$.

Carrying out the procedures in both Sec. 5.3.3.5 and Sec. 5.3.3.6 for all the six sectors yields *six* cost of $J^{\mathrm{I...VI}}_{\mathrm{opt}}$, and the relevant vectors $\vec{u}^{\mathrm{I..VI,a,b}}_{\mathrm{opt}}$ and their corresponding duration times $t^{\mathrm{I...VI,a,b}}_{\mathrm{opt}}$. The remaindering steps are to record the vectors their times with the smallest cost as $\vec{u}^{\mathrm{a,b}}_{\mathrm{opt}}$, $t^{\mathrm{a,b}}_{\mathrm{opt}}$ *and* apply $\vec{u}^{\mathrm{a}}_{\mathrm{opt}}$, and $\vec{u}^{\mathrm{b}}_{\mathrm{opt}}$ for $t^{\mathrm{a}}_{\mathrm{opt}}$ and $t^{\mathrm{b}}_{\mathrm{opt}}$ within a control interval, respectively.

Remark 12 *Due to its complex calculation procedures, even implemented on a FPGA based platform, the calculation time, cannot be neglected. Therefore, a time compensation step using the same concept, as presented in [128], is used*[13]*. Simplified steps are:*

i) Collecting the measurement data of $\vec{i}^{\alpha\beta}_{\mathrm{g}[k]}, \vec{e}^{\alpha\beta}_{\mathrm{g}[k]}$ *and* $V_{\mathrm{d}[k]}$ and *sending out the gating signals* $\vec{G}^*_{\mathrm{x}[k]} := \mathcal{G}^{-1}(\vec{u}^*_{[k]})$*, at the starting point of sampling interval k;*

ii) One-step-shifted estimation is then made for power vector $\hat{\vec{S}}_{[k+1]}$ *based on the output average voltage* $\vec{v}^{\mathrm{av}}_{[k]}$*, which is*:

$$\vec{v}^{\mathrm{av}}_{[k]} = \boldsymbol{T}_c \boldsymbol{T}_{\mathrm{SW}} \frac{t^{\mathrm{a}}_{\mathrm{opt}} \cdot \vec{u}^{\mathrm{a}}_{\mathrm{opt}} + t^{\mathrm{a}}_{\mathrm{opt}} \cdot \vec{u}^{\mathrm{b}}_{\mathrm{opt}}}{T_s} \quad (5.30)$$

[13] For a simple one-prediction-step C-MDPPC scheme, implemented using FPGA, its calculation time is quite small, and the time compensation is in general not required [10]; However, in order to make a fair performance comparison, the same time compensation concept is also included into the C-DMPPC and DutyOpt-DMPPC approaches.

iii) Predict the future power vectors $\vec{S}_{[k+2]}$ *and the cost based on* $\hat{\vec{S}}_{[k+1]}$*. The cost function in this case is also* one-step-shifted*, and it is:*

$$J(\vec{S}^{\vec{u}_{x,y}}_{[k+2]}) = \underbrace{\left(P^* - P_{(1+\frac{T_i}{T_s})[k]}(\vec{u}_x)\right)^2}_{=:J_{P1}} + \underbrace{\left(Q^* - Q_{(1+\frac{T_i}{T_s})[k]}(\vec{u}_x)\right)^2}_{=:J_{Q1}} + \underbrace{\left(P^* - P_{[k+2]}(\vec{u}_y)\right)^2}_{=:J_{P2}} + \underbrace{\left(Q^* - Q_{([k+2]}(\vec{u}_y)\right)^2}_{=:J_{Q2}}. \quad (5.31)$$

Fig. 5.14 depicts the structure overview of V2-DMPPC.

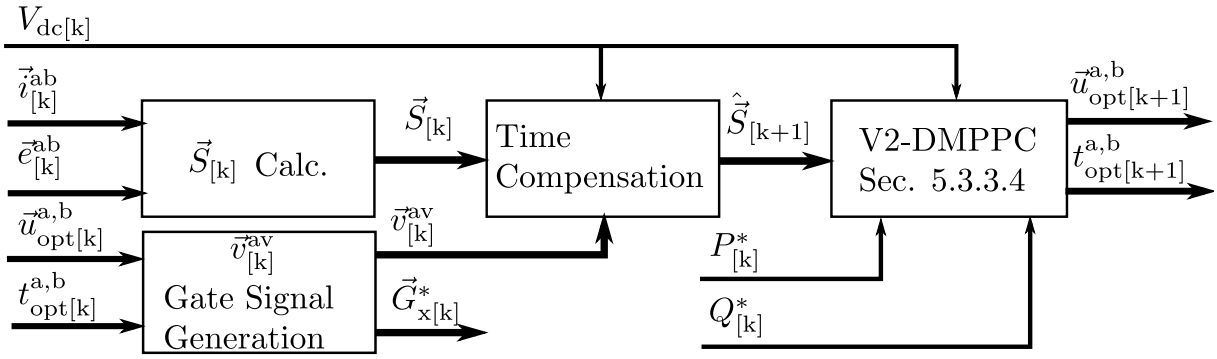

Fig. 5.14: Overall control structure of the proposed V2-DMPC.

5.3.4 Application of the V2-DMPC to machine side control

The machine side control in essence is to realize the torque or current control, meanwhile to achieve maximum torque per ampere control for a higher efficiency. The outer control loop considers already the limitations of the references (here T^*_e). Thus the cost function is defined as

$$J_m(\vec{u}_m) = \underbrace{\gamma_{T_e}\left(T^*_e - T_{e[k+1]}(\vec{u}_m)\right)^2}_{=:J_{T_e}} + \underbrace{\gamma_{i^d_m}\left(i^d_{m[k+1]}(\vec{u}_m)\right)^2}_{=:J_{i^d_m}} \quad (5.32)$$

From Equation (2.42) with the same definition of a variable slope as in last section, we calculate the slopes for both the currents and the torque as

$$Sl^{\vec{u}_i}_{i^d_m[k]} = \tfrac{R_s}{L_s} i^d_{m[k]} + N_p \omega_{m[k]} i^q_{m[k]} + \tfrac{v^{d,\vec{u}_i}_{m[k]}}{L_s}, \quad (5.33a)$$

$$Sl^{\vec{u}_i}_{i^q_m[k]} = \tfrac{-R_s}{L_s} i^q_{m[k]} - N_p \omega_{m[k]} i^d_{m[k]} - N_p \omega_{m[k]} \tfrac{\psi_{pm}}{L_s} + \tfrac{v^{q,\vec{u}_i}_{m[k]}}{L_s}, \quad (5.33b)$$

$$Sl^{\vec{u}_i}_{T_e[k]} = N_p \psi_{pm} Sl_{i^q_m}. \quad (5.33c)$$

Following the realization steps of V2-DMPC concept introduced in Sec. 5.3.2, the following two steps are required to apply V2-DMPTC into the machine side control.

5.3.4.1 Arbitrary length determination (at fundamental vector phases)

The selection/vector synthesizing starts also from Sec. I. Assuming the optimal vector is synthesized with $\vec{u}_1$ and $\vec{u}_0$; their operating times are assumed as t_1 and t_0, respectively. Therefore, the current and torque can be predicted as

$$i_{\mathrm{m[k+1]}}^{\mathrm{d},\vec{u}_{0,1}} = i_{\mathrm{m[k]}}^{\mathrm{d}} + Sl_{i_{\mathrm{m}}^{\mathrm{d}}}^{\vec{u}_1} \cdot t_1 + Sl_{i_{\mathrm{m}}^{\mathrm{d}}}^{\vec{u}_0} \cdot t_0, \tag{5.34a}$$

$$T_{\mathrm{e[k+1]}}^{\vec{u}_{0,1}} = T_{\mathrm{e[k]}} + Sl_{T_{\mathrm{e}}}^{\vec{u}_1} \cdot t_1 + Sl_{T_{\mathrm{e}}}^{\vec{u}_0} \cdot t_0. \tag{5.34b}$$

Inserting (5.34) to (5.32), and using the time optimal concept yields the duration times as

$$\begin{aligned} t_1 =& \frac{\gamma_{i_{\mathrm{m}}^{\mathrm{d}}}(i_{\mathrm{m}}^{\mathrm{d}*} - i_{\mathrm{m[k+1]}}^{\mathrm{d}})(Sl_{i_{\mathrm{m}}^{\mathrm{d}}}^{\vec{u}_1} - Sl_{i_{\mathrm{m}}^{\mathrm{d}}}^{\vec{u}_{\mathrm{null}}}) + \gamma_{T_{\mathrm{e}}}(T_{\mathrm{e}}^{*} - T_{\mathrm{e[k+1]}})(Sl_{T_{\mathrm{e}}}^{\vec{u}_1} - Sl_{T_{\mathrm{e}}}^{\vec{u}_{\mathrm{null}}})}{\gamma_{i_{\mathrm{m}}^{\mathrm{d}}}\left(Sl_{i_{\mathrm{m}}^{\mathrm{d}}}^{\vec{u}_1} - Sl_{i_{\mathrm{m}}^{\mathrm{d}}}^{\vec{u}_{\mathrm{null}}}\right)^2 - \gamma_{T_{\mathrm{e}}}\left(Sl_{T_{\mathrm{e}}}^{\vec{u}_1} - Sl_{T_{\mathrm{e}}}^{\vec{u}_{\mathrm{null}}}\right)^2} \\ &+ \frac{T_{\mathrm{s}}\left((Sl_{i_{\mathrm{m}}^{\mathrm{d}}}^{\vec{u}_{\mathrm{null}}})^2 + (Sl_{T_{\mathrm{e}}}^{\vec{u}_{\mathrm{null}}})^2 - Sl_{T_{\mathrm{e}}}^{\vec{u}_1} Sl_{i_{\mathrm{m}}^{\mathrm{d}}}^{\vec{u}_{\mathrm{null}}} - Sl_{T_{\mathrm{e}}}^{\vec{u}_{\mathrm{null}}} Sl_{i_{\mathrm{m}}^{\mathrm{d}}}^{\vec{u}_1}\right)}{\gamma_{i_{\mathrm{m}}^{\mathrm{d}}}\left(Sl_{i_{\mathrm{m}}^{\mathrm{d}}}^{\vec{u}_1} - Sl_{i_{\mathrm{m}}^{\mathrm{d}}}^{\vec{u}_{\mathrm{null}}}\right)^2 - \gamma_{T_{\mathrm{e}}}\left(Sl_{T_{\mathrm{e}}}^{\vec{u}_1} - Sl_{T_{\mathrm{e}}}^{\vec{u}_{\mathrm{null}}}\right)^2} \end{aligned} \tag{5.35a}$$

$$t_0 = T_{\mathrm{s}} - t_1. \tag{5.35b}$$

With the calculated times $t_{0,1}$, and following the optimization step proposed in Sec. 5.3.2.3.1 the cost function to guarantee both the tracking performance at time instant $[\mathrm{k}+1]$ and ripple-reducing performance at $(1+\frac{\mathrm{T_i}}{\mathrm{T_s}})[\mathrm{k}]$ can be obtained as

$$\begin{aligned} J_{\mathrm{m}}^{\mathrm{com}}(\vec{u}_{\mathrm{m}}) = \gamma_{\mathrm{T_e}} \Bigg(\underbrace{\left(T_{\mathrm{e}}^{*} - T_{\mathrm{e}(1+\frac{\mathrm{t_1}}{\mathrm{T_s}})[\mathrm{k}]}(\vec{u}_{\mathrm{m}})\right)^2 + \left(T_{\mathrm{e}}^{*} - T_{\mathrm{e[k+1]}}(\vec{u}_{\mathrm{m}})\right)^2}_{=:J_{\mathrm{T_e}}} \Bigg) \\ + \gamma_{\mathrm{i_m^d}} \Bigg(\underbrace{\left(i_{\mathrm{m}(1+\frac{\mathrm{t_1}}{\mathrm{T_s}})[\mathrm{k}]}^{\mathrm{d}}(\vec{u}_{\mathrm{m}})\right)^2 + \left(i_{\mathrm{m[k+1]}}^{\mathrm{d}}(\vec{u}_{\mathrm{m}})\right)^2}_{=:J_{i_{\mathrm{m}}^{\mathrm{d}}}} \Bigg). \end{aligned} \tag{5.36}$$

The cost is recorded as $J_{\mathrm{m}}^{\mathrm{comp,I1,0}}$.

5.3.4.2 Arbitrary phase determination

Starting also from Sec. I, however, instead of using $\vec{u}_{0,1}$, the control variables are calculated with two active vectors, i.e., $\vec{u}_{1,2}$ as

$$i_{\mathrm{m[k+1]}}^{\mathrm{d},\vec{u}_{1,2}} = i_{\mathrm{m[k]}}^{\mathrm{d}} + Sl_{i_{\mathrm{m}}^{\mathrm{d}}}^{\vec{u}_1} \cdot t_1 + Sl_{i_{\mathrm{m}}^{\mathrm{d}}}^{\vec{u}_2} \cdot t_2 \tag{5.37a}$$

$$T_{\mathrm{e[k+1]}}^{\vec{u}_{1,2}} = T_{\mathrm{e[k]}} + Sl_{T_{\mathrm{e}}}^{\vec{u}_1} \cdot t_1 + Sl_{T_{\mathrm{e}}}^{\vec{u}_2} \cdot t_2 \tag{5.37b}$$

Following the similar procedures as Sec. 5.3.4.1, the cost in this case is calculated and marked as $J_{\mathrm{m}}^{\mathrm{com,I1,2}}$. Compare $J_{\mathrm{m}}^{\mathrm{com,I1,0}}$ with $J_{\mathrm{m}}^{\mathrm{com,I1,2}}$, and record the smaller one together with the corresponding vectors and their duration times as $J_{\mathrm{opt}}^{\mathrm{I}}$, $\vec{u}_{\mathrm{opt}}^{\mathrm{I,a,b}}$, $t_{\mathrm{opt}}^{\mathrm{I,a,b}}$.

Carrying out the procedures of both Sec. 5.3.4.1 and Sec. 5.3.4.2 for all the six sectors yields *six* cost of $J_{\text{opt}}^{\text{I...VI}}$, and the relevant vectors $\vec{u}_{\text{opt}}^{\text{I..VI,a,b}}$ and their corresponding duration times $t_{\text{opt}}^{\text{I...VI,a,b}}$. Rest steps are to record the vectors their times with the smallest cost as $\vec{u}_{\text{opt}}^{\text{a,b}}$, $t_{\text{opt}}^{\text{a,b}}$, and apply $\vec{u}_{\text{opt}}^{\text{a}}$, and $\vec{u}_{\text{opt}}^{\text{b}}$ for $t_{\text{opt}}^{\text{a}}$ and $t_{\text{opt}}^{\text{b}}$ within a control interval, respectively.

5.4 Performance-enhanced DMPC with three switching vectors

5.4.1 Concept of three-vector DMPC (V3-DMPC)

In deep view of V2-DMPC introduced in the Sec. 5.3.1 yields the following conclusion: since only two vectors $\vec{u}_{\text{a,b}}$ are used for a whole control interval, i.e., $t_{\text{a}} + t_{\text{b}} = T_{\text{s}}$, the synthesized equivalent voltage vector in phases *different from* the original ones will always have a *full length*, i.e., reaching the edge of the hexagon as is shown in Fig 5.15. This limits the performance improvements. Obviously, if the length of the vectors with phases other than the original ones can also be optimized, the performances of the controller will be further improved. Inspired by this another *three*-vector based solution (in the following it is named as V3-DMPC) is proposed. The main concept is to optimally tune the length of the synthesized vectors in all phases, i.e., to make the vectors with a fully range of the hexagon area. Fig. 5.15 depicts its concept and the expected control performances.

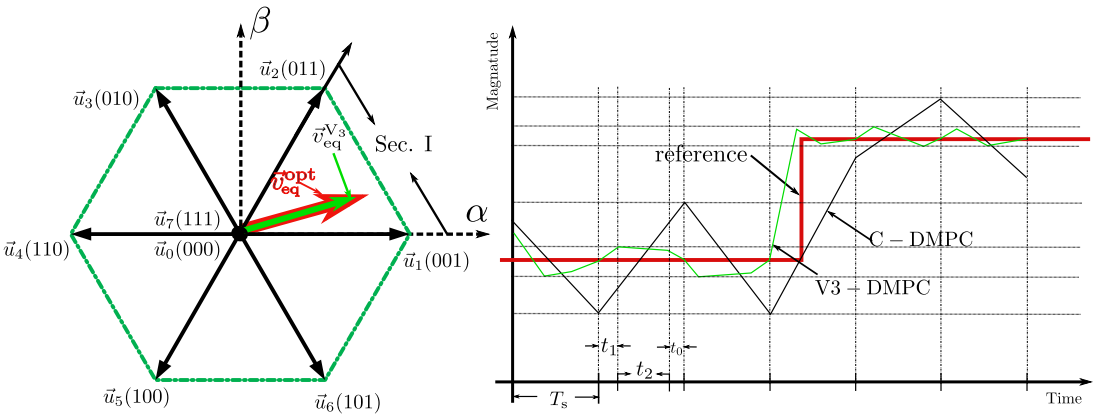

Fig. 5.15: Vector plane and ripple-reduction effect of the proposed V3-DMPC.

As is illustrated in Fig. 5.15, the optimal control voltage vectors can now be approximated by using the synthesized vector of $\vec{v}_{\text{eq}}^{\text{V3}}$, which is optimal both in length and phase, and can be synthesized with maximally three vectors (two active vectors and a zero one). *This brings another freedom to minimize the cost function: optimal length at the phases different from the six original active ones.* Therefore, as shown in the right side of Fig. 5.15, it produces more chances to minimize the cost within one control interval. Also during the transient phases, a synthesized vector with an angle (slope) bigger than the original ones will be available, same as the V2-DMPC scheme, which might drive the system with better

dynamics.

5.4.2 Realization of the proposed V3-DMPC

Similar to the V2-DMPC scheme, the proposed V3-DMPC can be realized also through two steps: i) phase (direction) detection of the optimal (equivalent) vector; ii) length determination of the optimal (equivalent) vector. For both steps, the cost function is minimized via the same time-optimal control concept as is given in Equation (5.20). Details are given as follows.

5.4.2.1 Optimal equivalent vector *Phase* (direction) detection

In this step the length of the optimal equivalent vector is assumed to be the maximum value, i.e., the boundary of the hexagonal plane. Assuming the candidate switching states $\vec{u}_i$ and $\vec{u}_{i+1}$ actuate with the duration times, t_{i} and $t_{\mathrm{i+1}}$, receptively, then $t_{\mathrm{i}} + t_{\mathrm{i+1}} = T_{\mathrm{s}}$ holds. The system states are therefore predicted using $\vec{u}_i$ and $\vec{u}_{i+1}$ as

$$Z^{\vec{u}_{\mathrm{i,i+1}}}_{i[k+1]} = Z_{i[k]} + \vec{Sl}^{\vec{u}_{\mathrm{i}}}_{\mathrm{Zi[k]}} \cdot t_{\mathrm{i}} + \vec{Sl}^{\vec{u}_{\mathrm{i+i}}}_{\mathrm{Zi[k]}} \cdot t_{\mathrm{i+1}}. \tag{5.38}$$

Inserting Eq. (5.38) to (5.19), and using the time optimal concept, i.e., to assure

$$\begin{aligned} &\frac{\partial J(\vec{Z}^{\vec{u}_{\mathrm{i,i+1}}}_{\mathrm{i[k+1]}})}{\partial t_{\mathrm{i}}, \partial t_{\mathrm{i+1}}} := 0, \\ \text{Subj. to } &: (i)\ t_{\mathrm{i}} + t_{\mathrm{i+1}} = T_{\mathrm{s}}; \\ &(ii)\ t_{\mathrm{i}}, t_{\mathrm{i+1}} \in [0, T_{\mathrm{s}}]. \end{aligned} \tag{5.39}$$

Solving Eq. (5.39), yields the duration times of $t_{\mathrm{i}}, t_{\mathrm{i+1}}$.

Then the cost function is minimized by enumerating all the calculated $t_{\mathrm{i,i+1}}$ and $Z^{\vec{u}_{\mathrm{i,i+1}}}_{i[k+1]}$ for all *adjacent* active fundamental vectors[14] by

$$\vec{u}^{*}_{\mathrm{i,i+1}}, t^{*}_{\mathrm{i,i+1}} := \arg \min_{i \in \{1,\ldots,6\}} J^{\mathrm{com}}(\vec{u}_{\mathrm{i,i+1}}, t_{\mathrm{i,i+1}}) \tag{5.40}$$

The minimization procedure includes also the proposed optimization step introduced in Sec. 5.3.2.3.1. It is not difficult to find, after solving (5.40), depending on t^{*}_{i}, there are the following two cases with regarding to the obtained optimal vector(s):

case-I: (for $t^{*}_{\mathrm{i}} = T_{\mathrm{s}}$) one optimal vector $\vec{u}^{*}_{\mathrm{i}}$ is selected, whose phase (direction) is the same as one of the six active (*fundamental*) vectors, *or*

case-II: (for $0 < t^{*}_{\mathrm{i}} < T_{\mathrm{s}}$) two adjacent vectors of $\vec{u}^{*}_{\mathrm{i}}$ and $\vec{u}^{*}_{\mathrm{i+1}}$ with the actuating times of t^{*}_{i} and $t^{*}_{\mathrm{i+1}}$ are selected, which will synthesize a *new* vector. This new vector is

[14] To obey the *adjacent* rule, when $i = 6$, i.e., the last vector of the six active ones, $\vec{v}_{\mathrm{i+1}} = \vec{v}_1$ (See Fig. 5.15).

phase-optimally-oriented and can be expressed as[15]

$$\vec{u}_{\text{new}} = \frac{t_{\text{i}}^*}{T_{\text{s}}} \cdot \vec{u}_{\text{i}}^* + \frac{t_{\text{i+1}}^*}{T_{\text{s}}} \cdot \vec{u}_{\text{i+1}}^*. \tag{5.41}$$

With (5.41), the relevant control variable slope vector $Sl_{\text{Zi[k]}}^{\vec{u}_{\text{new}}}$, in correspondence to $\vec{u}_{\text{new}}$, can be calculated, which will be used to minimize the cost with another extra freedom, i.e., with optimized length. Details are introduced as follows.

5.4.2.2 Optimal equivalent vector *length* determination

The cost function is already "minimized" by extended vectors with arbitrary phases as is analyzed in Sec. 5.4.2.1. However, they are all with *full length*, i.e., vectors reaching the boundary of the hexagon in Fig. 5.15. This has already greatly extends the candidate vectors in comparison with the classical and DutyOpt-DMPC and schemes. The possibilities for further performance-enhancement, the *length* of $\vec{u}_{\text{new}}$ can be further optimized.

The basic idea is that, assuming the final optimal equivalent vector $\vec{v}_{\text{eq}}^{\text{opt}}$ is "shorter" than the *full length*. To achieve so, it shall be synthesized with the *phase-optimally-oriented vector* of $\vec{u}_{\text{new}}$ (actuating time t_{new}) *and* an extra zero vector $\vec{u}_{\text{null}}$[16] (actuating time t_{null}). By optimizing their actuating times, with the time optimal control concept, as given in (5.39), the length of the synthesized vector is therefore also optimized. Details are given as follows.

After the control variable slope $Sl_{\text{Zi[k]}}^{\vec{u}_{\text{new}}}$ of the *phase-optimally-oriented* vector $\vec{u}_{\text{new}}$ is obtained, the future system state can be predicted using $Sl_{\text{Zi[k]}}^{\vec{u}_{\text{new}}}$, $Sl_{\text{Zi[k]}}^{\vec{u}_{\text{null}}}$ and their relevant duration times t_{new} and t_{null} as

$$Z_{\text{i[k+1]}}^{\vec{u}_{\text{new,null}}} = \vec{Z}_{\text{i[k]}} + Sl_{\text{Zi[k]}}^{\vec{u}_{\text{new}}} \cdot t_{\text{new}} + Sl_{\text{Zi[k]}}^{\vec{u}_{\text{null}}} \cdot t_{\text{null}}. \tag{5.42}$$

Substituting the predicted vectors with (5.42) into (5.19), and solving

$$\begin{aligned} &\frac{\partial J(Z_{\text{i[k+1]}}^{\vec{u}_{\text{new,null}}})}{\partial t_{\text{new}}, \partial t_{\text{null}}} := 0, \\ \text{Subj. to } &: (i)\ t_{\text{new}} + t_{\text{null}} = T_{\text{s}}; \\ &\quad (ii)\ t_{\text{new}}, t_{\text{null}} \in [0, T_{\text{s}}], \end{aligned} \tag{5.43}$$

the duration times of the t_{new} and t_{null} will be obtained, which, as analyzed above, will lead to an optimized vector *length*. At the end, the optimal actuating times for the already selected fundamental vectors of $\vec{u}_{\text{i}}^*$, $\vec{u}_{\text{i+1}}^*$ and $\vec{u}_{\text{null}}^*$ can be calculated as

$$t_{\text{i}}^{\text{opt}} = m \cdot t_{\text{i}}^*; \tag{5.44a}$$

$$t_{\text{i+1}}^{\text{opt}} = m \cdot t_{\text{i+1}}^*; \tag{5.44b}$$

$$t_{\text{null}}^{\text{opt}} = T_{\text{s}} - t_{\text{i}}^{\text{opt}} - t_{\text{i+1}}^{\text{opt}}. \tag{5.44c}$$

[15] Note that, to simply and unify the following required calculations, *case-I* can be included into *case-II* as a special condition (condition of $t_{\text{i+1}}^* = 0$).

[16] Vector $\vec{u}_{\text{null}}$ can be selected from $\vec{u}_0$ or $\vec{u}_7$, which obeys the rule of fewest switching actions, for instance, if the vector applied before $\vec{u}_{\text{null}}$ is $\in \{000, 001, 010, 100\}$, then $\vec{u}_{\text{null}}$ ="000"; otherwise, $\vec{u}_{\text{null}}$ = "111".

respectively, where $m = \frac{t_{\text{new}}}{T_s} \in (0, 1]$. The proposed optimization steps in Sec. 5.3.2.3.1 is further used to avoid the sub-optimal solution, i.e.,

$$\left(\vec{u}^*_{\text{i,i+1,null}}, t^*_{\text{i,i+1,null}}\right) := \arg\min \left\{ J^{\text{com}}(\vec{u}_{\text{new,null}}, t_{\text{new,null}}), J^{\text{com}}(\vec{u}_{\text{null,new}}, t_{\text{null,new}}) \right\} \quad (5.45)$$

The rest step is to apply the obtained switching vectors and their times following the proper order.

So far the concept and the implementation procedures of the proposed V3-DMPC scheme is introduced. In the following sections, its application to the grid and machine side control of the 2L back-to-back power converter system, both for the machine and grid side, is introduced and verified.

5.4.3 Application of V3-DMPC to grid side control

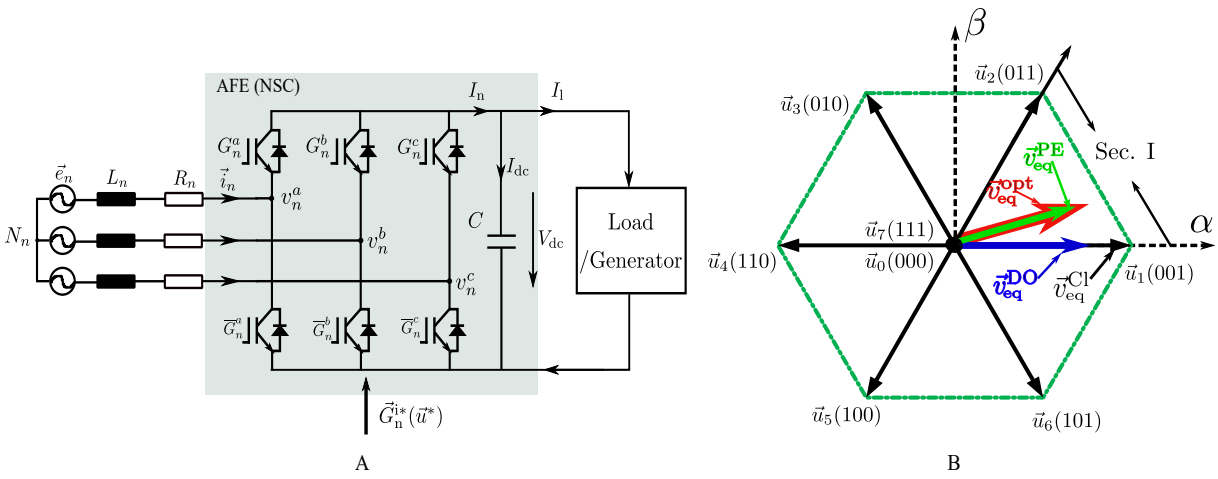

Fig. 5.16: A: Grid-tied Active Front End power converter with $(R)L$ filter; B: Switching vector plane, fundamental and equivalent candidate vectors: $\vec{u}_0, ..., \vec{u}_7$ are the 8 *fundamental* vectors; $\vec{v}^{\text{opt}}_{\text{eq}}$ is an *example* optimal (synthesized) vector "zeroing" the cost function; while $\vec{v}^{\text{Cl}}_{\text{eq}}$, $\vec{v}^{\text{DO}}_{\text{eq}}$ and $\vec{v}^{\text{PE}}_{\text{eq}}$ are the example equivalent vectors for using the Classical, Duty-Opt and the proposed V3-DMPPC schemes, respectively.

Following the descriptions in Sec. 5.4.2, applying the V3-DMPC concept to achieve power control of a grid-tied AFE shown in Fig. 5.16 requires two steps: i) phase (direction) detection of the optimal equivalent vector; ii) length determination of the optimal equivalent vector. For both steps, the cost function minimization via a time-optimal control concept is performed. Details are given as follows.

5.4.3.1 Optimal equivalent vector *phase* (direction) detection

In this step the length of the optimal equivalent vector is maintained to be the maximum value, i.e., the boundary of the hexagonal plane (See the green line in Fig. 5.16-B). Assuming the candidate switching states $\vec{u}_i$ and $\vec{u}_{i+1}$ are actuating with the duration times

of t_i and $t_{\mathrm{i}+1}$, receptively, then $t_\mathrm{i} + t_{\mathrm{i}+1} = T_\mathrm{s}$ will hold true. The relevant predicted power vector using $\vec{u}_i$ and $\vec{u}_{i+1}$ in this case is

$$\vec{S}^{\vec{u}_{\mathrm{i,i+1}}}_{[k+1]} = \vec{S}_{[k]} + \vec{Sl}^{\vec{u}_\mathrm{i}}_{\mathrm{S[k]}} \cdot t_\mathrm{i} + \vec{Sl}^{\vec{u}_{\mathrm{i+i}}}_{\mathrm{S[k]}} \cdot t_{\mathrm{i}+1} \tag{5.46}$$

Inserting (5.46) to (5.23), and solving the time optimal equations

$$\begin{aligned} &\frac{\partial J(\vec{S}^{\vec{u}_{\mathrm{i,i+1}}}_{[k+1]})}{\partial t_\mathrm{i}, \partial t_{\mathrm{i}+1}} := 0, \\ \text{Subj. to } &:(i)\ t_\mathrm{i} + t_{\mathrm{i}+1} = T_\mathrm{s}; \\ &(ii)\ t_\mathrm{i}, t_{\mathrm{i}+1} \in [0, T_\mathrm{s}], \end{aligned} \tag{5.47}$$

yields

$$\begin{aligned} t_\mathrm{i} =& \frac{(P^* - P_{\mathrm{n[k]}})\big(Sl^{\vec{u}_\mathrm{i}}_{\mathrm{P[k]}} - Sl^{\vec{u}_0}_{\mathrm{P[k+1]}}\big) + (Q^* - Q_{\mathrm{n[k]}})\big(Sl^{\vec{u}_\mathrm{i}}_{\mathrm{Q[k]}} - Sl^{\vec{u}_{\mathrm{i+1}}}_{\mathrm{Q[k+1]}}\big)}{(Sl^{\vec{u}_1}_{\mathrm{P[k]}} - Sl^{\vec{u}_\mathrm{i}}_{\mathrm{P[k+1]}})^2 + (Sl^{\vec{u}_1}_{\mathrm{Q[k]}} - Sl^{\vec{u}_{\mathrm{i+1}}}_{\mathrm{Q[k+1]}})^2} \\ &+ \frac{T_\mathrm{s}\big(||Sl^{\vec{u}_{\mathrm{i+1}}}_{\mathrm{S[k+1]}}||^2 - Sl^{\vec{u}_\mathrm{i}}_{\mathrm{P[k]}} Sl^{\vec{u}_\mathrm{i}}_{\mathrm{P[k+1]}} - Sl^{\vec{u}_\mathrm{i}}_{\mathrm{Q[k]}} Sl^{\vec{u}_{\mathrm{i+1}}}_{\mathrm{Q[k+1]}}\big)}{(Sl^{\vec{u}_\mathrm{i}}_{\mathrm{P[k]}} - Sl^{\vec{u}_{\mathrm{i+1}}}_{\mathrm{P[k+1]}})^2 + (Sl^{\vec{u}_\mathrm{i}}_{\mathrm{Q[k]}} - Sl^{\vec{u}_{\mathrm{i+1}}}_{\mathrm{Q[k+1]}})^2} \end{aligned} \tag{5.48a}$$

$$t_{\mathrm{i}+1} = T_\mathrm{s} - t_\mathrm{i}. \tag{5.48b}$$

The cost function is then minimized by enumerating all the calculated $t_{\mathrm{i,i+1}}$ and $\vec{S}^{\mathrm{i,i+1}}_{[k+1]}$ for all *adjacent* active fundamental vectors through

$$\vec{u}^*_{\mathrm{i,i+1}}, t^*_{\mathrm{i,i+1}} := \arg \min_{i \in \{1,\ldots,6\}} J(\vec{u}_{\mathrm{i,i+1}}, t_{\mathrm{i,i+1}}). \tag{5.49}$$

A phase-optimally-oriented new vector is then obtained as

$$\vec{u}_\mathrm{new} = \frac{t^*_\mathrm{i}}{T_\mathrm{s}} \cdot \vec{u}^*_\mathrm{i} + \frac{t^*_{\mathrm{i+1}}}{T_\mathrm{s}} \cdot \vec{u}^*_{\mathrm{i+1}}. \tag{5.50}$$

Substituting (5.50) into (2.8), (2.10) and then into (5.25), the relevant power slope vector $\vec{Sl}^{\vec{u}_\mathrm{new}}_{\mathrm{S[k]}}$, in correspondence to $\vec{u}_\mathrm{new}$, can be calculated, which will be used to minimize the cost with another extra freedom, i.e., optimized length. Details are given as follows.

5.4.3.2 Optimal equivalent vector *length* determination

After the power slope $\vec{Sl}^{\vec{u}_\mathrm{new}}_{\mathrm{S[k]}}$ of the phase-optimally-oriented vector $\vec{u}_\mathrm{new}$ is obtained, the future power vector can be predicted using $\vec{Sl}^{\vec{u}_\mathrm{new}}_{\mathrm{S[k]}}$, $\vec{Sl}^{\vec{u}_\mathrm{null}}_{\mathrm{S[k]}}$ and their relevant duration times t_new and t_null as

$$\vec{S}^{\vec{u}_{\mathrm{new,null}}}_{[k+1]} = \vec{S}_{[k]} + \vec{Sl}^{\vec{u}_\mathrm{new}}_{\mathrm{S[k]}} \cdot t_\mathrm{new} + \vec{Sl}^{\vec{u}_\mathrm{null}}_{\mathrm{S[k]}} \cdot t_\mathrm{null} \tag{5.51}$$

Substituting the predicted active and reactive powers $P^{\text{new}}_{[k+1]}$ and $Q^{\text{new}}_{[k+1]}$ into (5.59), and solving

$$\begin{aligned} &\frac{\partial J(\vec{S}^{\vec{u}_{\text{new,null}}}_{[k+1]})}{\partial t_{\text{new}}, \partial t_{\text{null}}} := 0, \\ \text{Subj. to } &:(i)\ t_{\text{new}} + t_{\text{null}} = T_{\text{s}}; \\ &(ii)\ t_{\text{new}}, t_{\text{null}} \in [0, T_{\text{s}}], \end{aligned} \tag{5.52}$$

the duration times of the t_{new} and t_{null} will be obtained, which, as analyzed above, will lead to an optimized vector *length*. At the end, the optimal actuating times for the already selected fundamental vectors of $\vec{u}^*_{\text{i}}$, $\vec{u}^*_{\text{i+1}}$ and $\vec{u}^*_{\text{null}}$ can be calculated as

$$t^{\text{opt}}_{\text{i}} = m \cdot t^*_{\text{i}}; \tag{5.53a}$$

$$t^{\text{opt}}_{\text{i+1}} = m \cdot t^*_{\text{i+1}}; \tag{5.53b}$$

$$t^{\text{opt}}_{\text{null}} = T_{\text{s}} - t^{\text{opt}}_{\text{i}} - t^{\text{opt}}_{\text{i+1}}. \tag{5.53c}$$

respectively, where $m = \frac{t_{\text{new}}}{T_{\text{s}}} \in (0, 1)$. Similar time compensation step as introduced in Remark 8 is used.

So far the proposed V3-DMPPC with both optimized vector *phase* and *length* is introduced. Its structure overview is given in Fig. 5.17.

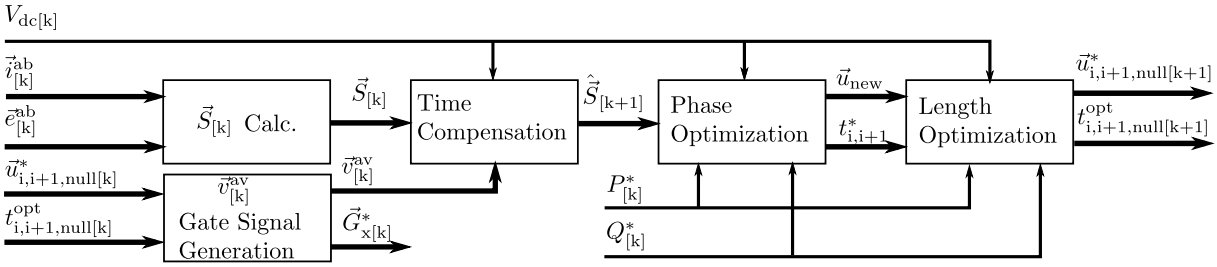

Fig. 5.17: Overall control structure of the proposed V3-DMPPC.

Remark 13 *Note that, after these two steps of phase and length optimizations, voltage vectors with the entire* whole hexagon plane *(similar to the well-know space-vector modulation (SVM) method) of a power converter can be used to minimize the targeting set of the cost function. Hence the system steady state control performances will be optimized. The controller still can directly select one of the fundamental vectors (e.g., when* ***Case I*** *and* and $m = 0$ *or* 1 *occur) during the transient phases. Fast control dynamics as the C-DMPPC method will therefore remain. However, system constraints* $J_{\boldsymbol{CS}}$ *(e.g., torque, current, or power limits) is so far not considered. In the following a solution to include the operation (limit) constraint is introduced.*

5.4.3.3 Constraint inclusion

Constraint violence happens when the system limit has already been reached but the reference tracking is still not met. A deep analysis for this situation will yield that,

since the length of the vector obtained after the *phase-optimization* process (**step-I**) can be tuned down to zero in the step of *length optimization* procedure, only an un-proper direct/phase (i.e., direction optimization process in **step-I** is un-proper) will lead to such violence. Inspired by this, a solution to include the system constraint $J_{\mathbf{CS}}$ was further proposed, by adding a modification process after the afore-mentioned two steps. To put it clearly, the proposed method is introduced through Algorithm 5.2.

Algorithm 5.2 : Constraint inclusion for MV-DMPC

Step I: Predict $J_{\mathbf{CS}}$ with $t^{\text{opt}}_{\text{i,i+1,null}}$ and $\vec{u}^{*}_{\text{i,i+1,null}}$.
Step II: if $J_{\mathbf{CS}} > 0$, replace $J^{\mathbf{com}}$ with J in Eq. (5.45) and repeat the relevant procedures in Sec. 5.4.3.1 and Sec. 5.4.2.2.
Step III: Application of the optimal gate signal vector(s) $\vec{u}^{*}_{\text{i,i+1,null}}$ and their duration time(s) $t^{\text{opt}}_{\text{i,i+1,null}}$.

5.4.4 Application of V3-DMPC to machine side control

The application of the V3-DMPC concept to the machine side control is quite similar to the V3-DMPPC introduced in last section. Therefore, also two steps are required, which are introduced as follows.

5.4.4.1 Arbitrary phase determination

In this step assuming the candidate switching states $\vec{u}_i$ and $\vec{u}_{i+1}$ actuate with the duration times of t_{i} and $t_{\text{i+1}}$, receptively. Therefore, the current and torque can be predicted as

$$i^{\text{d},\vec{u}_{\text{i,i+1}}}_{\text{m[k+1]}} = i^{\text{d}}_{\text{m[k]}} + Sl^{\vec{u}_1}_{i^{\text{d}}_{\text{m}}} \cdot t_{\text{i}} + Sl^{\vec{u}_{\text{i+1}}}_{i^{\text{d}}_{\text{m}}} \cdot t_{\text{i+1}}, \tag{5.54a}$$

$$T^{\vec{u}_{\text{i,i+1}}}_{\text{e[k+1]}} = T_{\text{e[k]}} + Sl^{\vec{u}_{\text{i}}}_{T_{\text{e}}} \cdot t_{\text{i}} + Sl^{\vec{u}_{\text{i+1}}}_{T_{\text{e}}} \cdot t_{\text{i+1}}. \tag{5.54b}$$

Inserting (5.54) to (5.32), and using the time optimal concept yields the duration times as

$$\begin{aligned} t_{\text{i}} =& \frac{\gamma_{i^{\text{d}}_{\text{m}}}(i^{\text{d}*}_{\text{m}} - i^{\text{d}}_{\text{m[k+1]}})(Sl^{\vec{u}_1}_{i^{\text{d}}_{\text{m}}} - Sl^{\vec{u}_{\text{null}}}_{i^{\text{d}}_{\text{m}}}) + \gamma_{T_{\text{e}}}(T^{*}_{\text{e}} - T_{\text{e[k+1]}})(Sl^{\vec{u}_1}_{T_{\text{e}}} - Sl^{\vec{u}_{\text{null}}}_{T_{\text{e}}})}{\gamma_{i^{\text{d}}_{\text{m}}}\left(Sl^{\vec{u}_1}_{i^{\text{d}}_{\text{m}}} - Sl^{\vec{u}_{\text{null}}}_{i^{\text{d}}_{\text{m}}}\right)^2 - \gamma_{T_{\text{e}}}\left(Sl^{\vec{u}_1}_{T_{\text{e}}} - Sl^{\vec{u}_{\text{null}}}_{T_{\text{e}}}\right)^2} \\ &+ \frac{T_{\text{s}}\left((Sl^{\vec{u}_{\text{null}}}_{i^{\text{d}}_{\text{m}}})^2 + (Sl^{\vec{u}_{\text{null}}}_{T_{\text{e}}})^2 - Sl^{\vec{u}_1}_{T_{\text{e}}} Sl^{\vec{u}_{\text{null}}}_{i^{\text{d}}_{\text{m}}} - Sl^{\vec{u}_{\text{null}}}_{T_{\text{e}}} Sl^{\vec{u}_1}_{i^{\text{d}}_{\text{m}}}\right)}{\gamma_{i^{\text{d}}_{\text{m}}}\left(Sl^{\vec{u}_1}_{i^{\text{d}}_{\text{m}}} - Sl^{\vec{u}_{\text{null}}}_{i^{\text{d}}_{\text{m}}}\right)^2 - \gamma_{T_{\text{e}}}\left(Sl^{\vec{u}_1}_{T_{\text{e}}} - Sl^{\vec{u}_{\text{null}}}_{T_{\text{e}}}\right)^2} \end{aligned} \tag{5.55a}$$

$$t_{\text{i+1}} = T_{\text{s}} - t_{\text{i}}. \tag{5.55b}$$

The cost function is then minimized by enumerating all the calculated $t_{\text{i,i+1}}$ and $\vec{S}^{\text{i,i+1}}_{[k+1]}$ for all *adjacent* active fundamental vectors through

$$\vec{u}^{*}_{\text{i,i+1}}, t^{*}_{\text{i,i+1}} := \arg \min_{i \in \{1,\dots,6\}} J(\vec{u}_{\text{i,i+1}}, t_{\text{i,i+1}}). \tag{5.56}$$

A phase-optimally-oriented new vector is then obtained as

$$\vec{u}_{\text{new}} = \frac{t_{\text{i}}^*}{T_{\text{s}}} \cdot \vec{u}_{\text{i}}^* + \frac{t_{\text{i+1}}^*}{T_{\text{s}}} \cdot \vec{u}_{\text{i+1}}^*; \tag{5.57}$$

Substituting (5.57) into (2.8), (2.10) and (5.33), the relevant current and torque slopes $Sl_{\text{id}_{\text{m[k]}}}^{\vec{u}_{\text{new}}}$, $Sl_{\text{T}_{\text{e[k]}}}^{\vec{u}_{\text{new}}}$, in correspondence to $\vec{u}_{\text{new}}$, can be calculated. The following step, i.e., optimal length determination, is quite similar as the V3-DMPPC method. To avoid redundancy this part is omitted.

5.4.5 Evaluation and analysis

In this section, the performance evaluations of the proposed multiple-vector DMPC schemes, namely, the V2-DMPC and V3-DMPC methods, are carried out with *both* simulation *and* experimental results for both the grid and machine side control.

5.4.5.1 Simulation evaluations

Experimental results can be influenced by a lot of non-ideal factors such as noises in the measurement channels, intermediate data precisions of the real-time processors. In particular, the fixed-data type based processors such as FPGAs may introduce certain un-wanted rough approximations of the intermediate variables because of its limited word-length, which makes the off-line simulation[17] necessary to pre-check the functionality of a proposed method. Therefore, the performance comparisons among the classical-, the DutyOpt-DMPC, the proposed V2-DMPC, V3-DMPC control methods are firstly compared in simulation with all same scenarios (simulation step $T_{\text{sim}} = 1e^{-6}$[s], control/sampling interval $T_{\text{s}} = 100e^{-6}$[s], all the outer control loops have the same parameter values). Overall performance comparison is shown in Fig. 5.18, while steady state control performances for each method are shown Fig. 5.18. As can be seen: both the proposed V2-DMPC and (in particular) the V3-DMPC outperform the classical and DutyOpt-DMPC methods and best performances are seen with the proposed V3-DMPC method. More detailed comparison including the current THDs and zoomed transient performances can be found in the publication (5) of Appendix E.

5.4.5.2 Experimental evaluations

In this work, all the algorithms (including C-DMPC, DutyOpt-DMPC and the proposed V2- and V3-DMPC) are divided into sub-routines and are implemented using the Single-Cycle-Timed-Loop (SCTL) technique on the entirely FPGA based platform introduced in Chp. 2. To save some space, only the FPGA design overall structures of the proposed V2- and V3-DMPPC methods are illustrated in Fig. 5.20. The system configuration and parameters are collected in TABLE I as given in Chp. 2.

[17] which is always ideal in terms of processor data precision and can be set as noise-free.

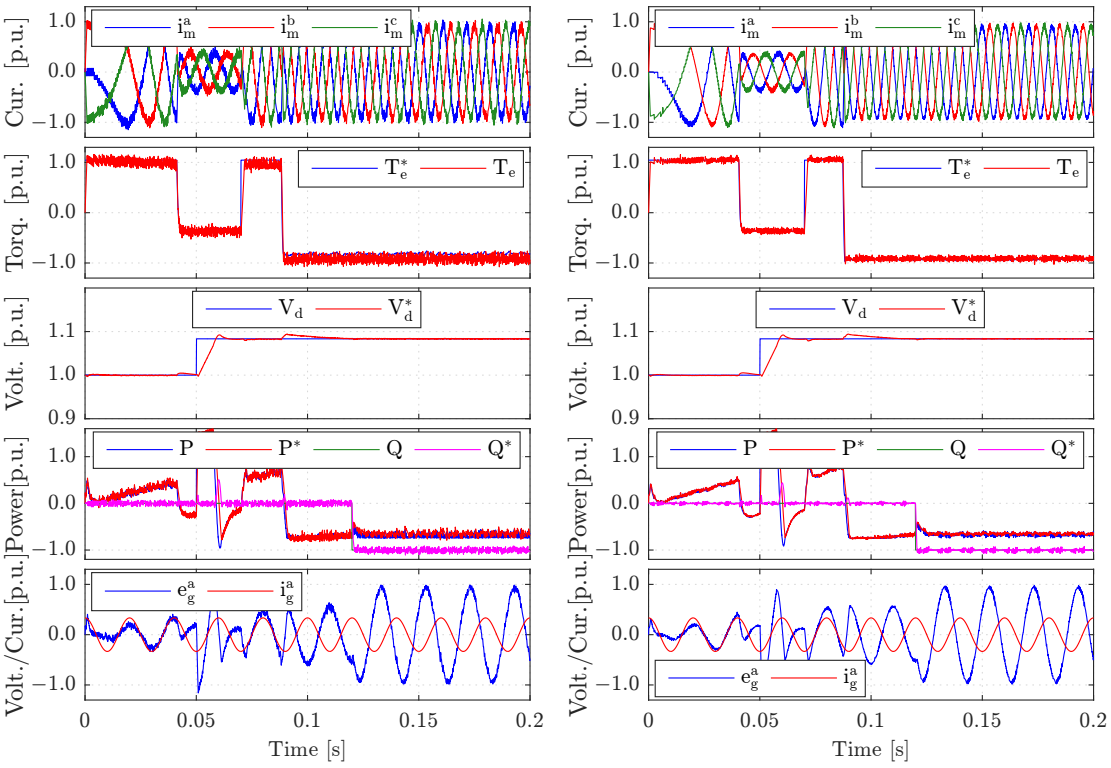

(a) CDMPC.

(b) DutyOpt-DMPC.

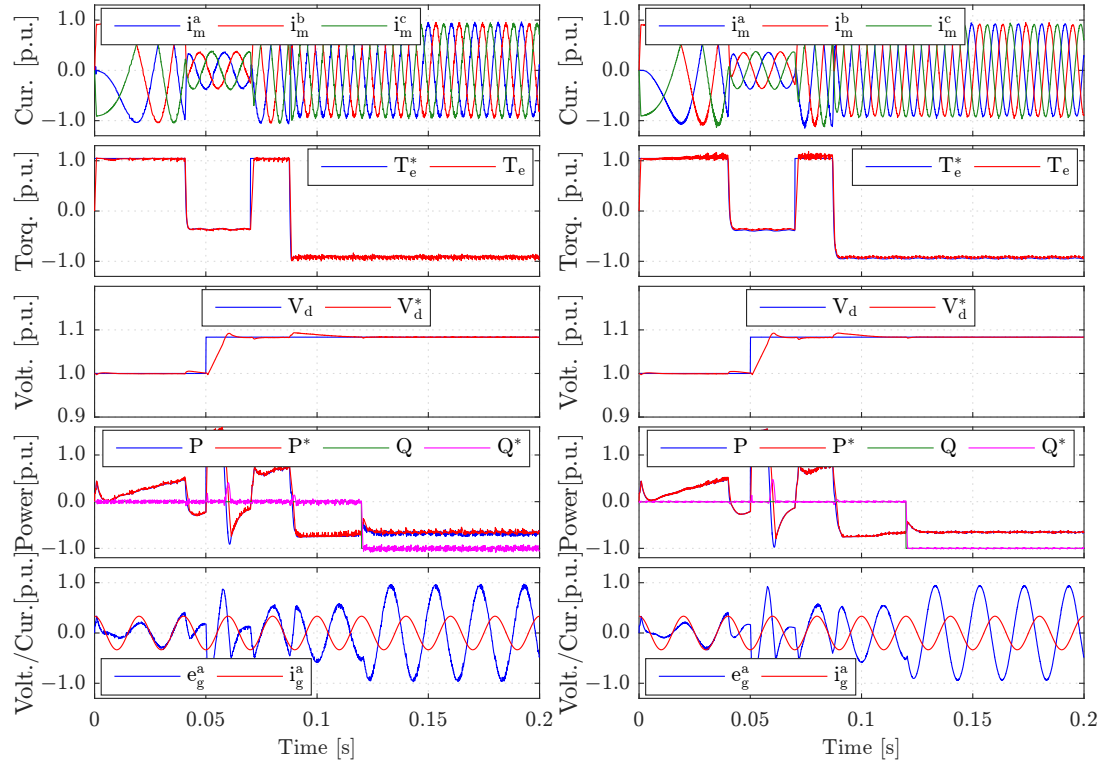

(c) V2-DMPC.

(d) V3-DMPC.

Fig. 5.18: [Simulation data:] Overall control performance comparison. For each figure, from up to down are: the stator currents, electro-magnetic torque, DC-link voltage, grid side power, grid side phase voltage and current, respectively, all in p.u. values.

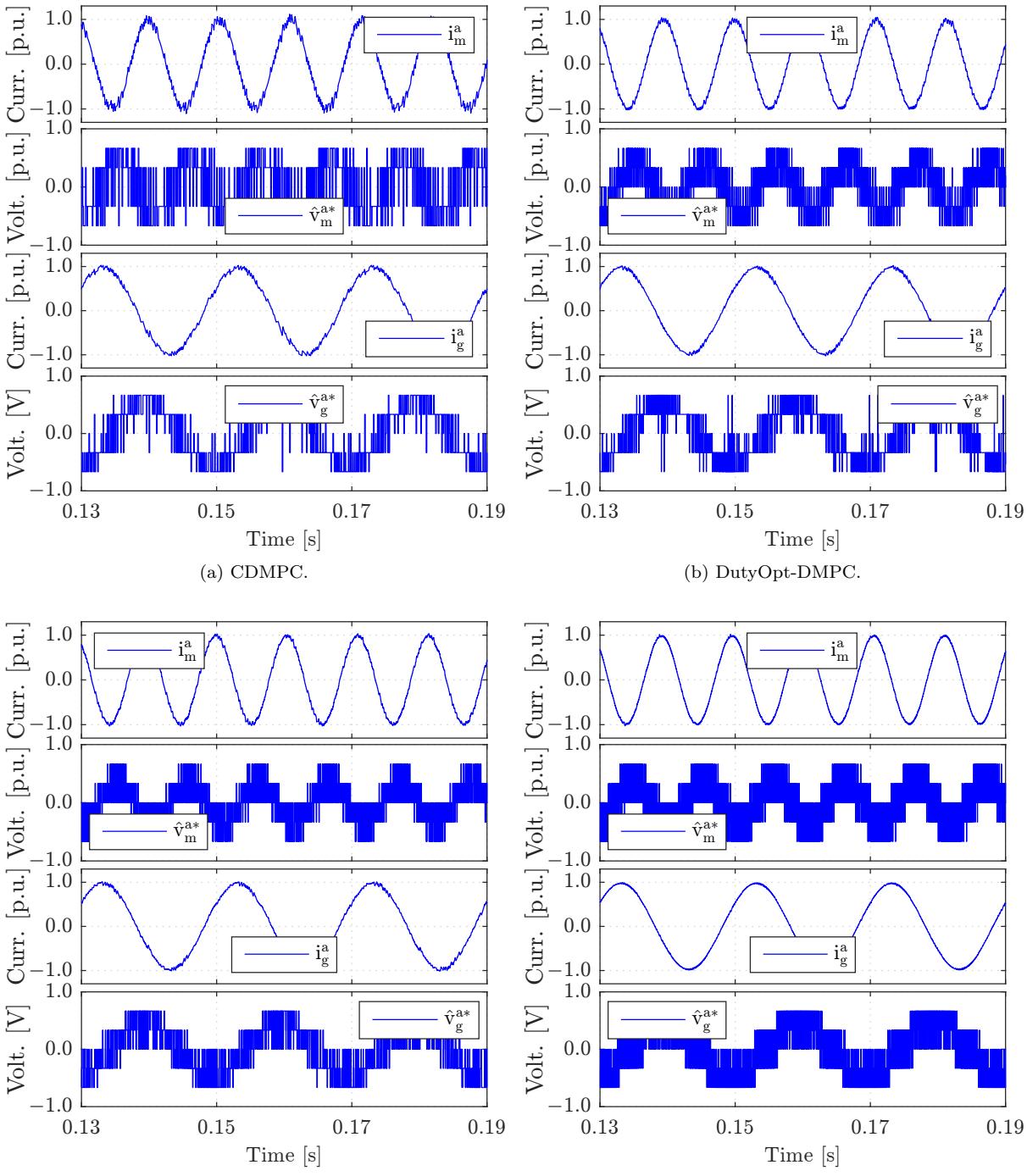

(a) CDMPC.

(b) DutyOpt-DMPC.

(c) The proposed V2-DMPC.

(d) The proposed V3-DMPC.

Fig. 5.19: [Simulation data:] Steady state control performances. For each figure, from up to down are: the generator stator currents and generator side converter (estimated) commanded voltages; grid side current and grid side converter (estimated) voltage, respectively.

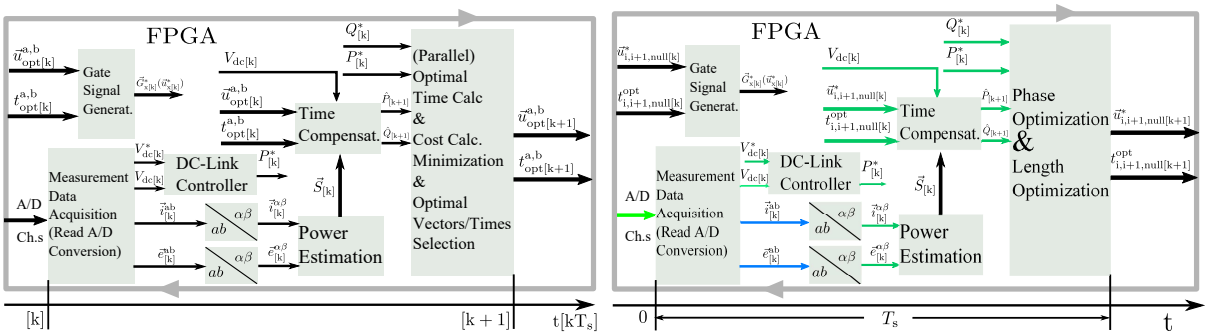

(a) Overall structure of the V2-DMPPC scheme.

(b) Overall structure of the V3-DMPPC scheme.

Fig. 5.20: FPGA design of the proposed control scheme.

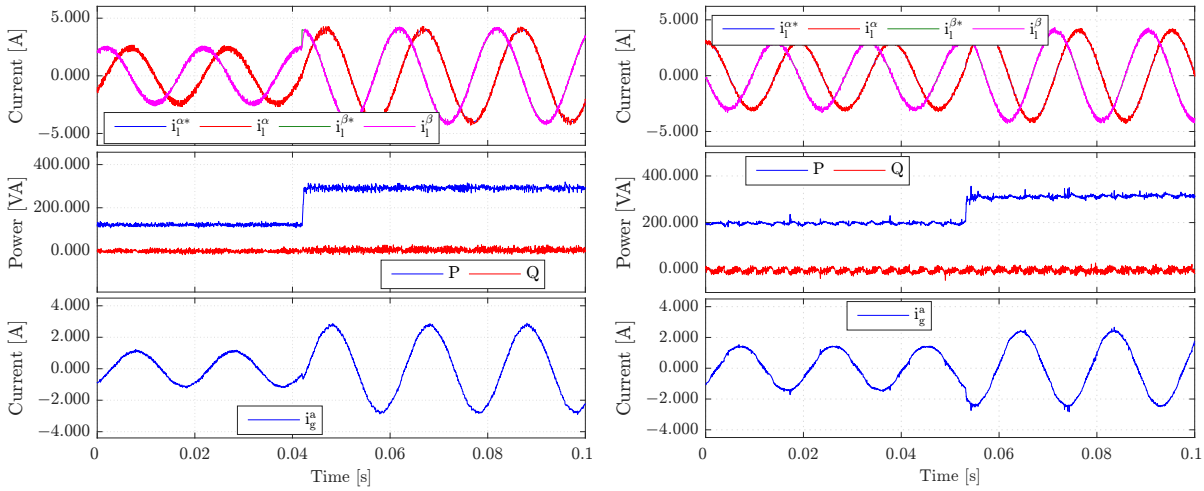

(a) C-DMPPC (load change from 2 to 4A).

(b) DutyOpt-DMPPC (load change from 3 to 4A).

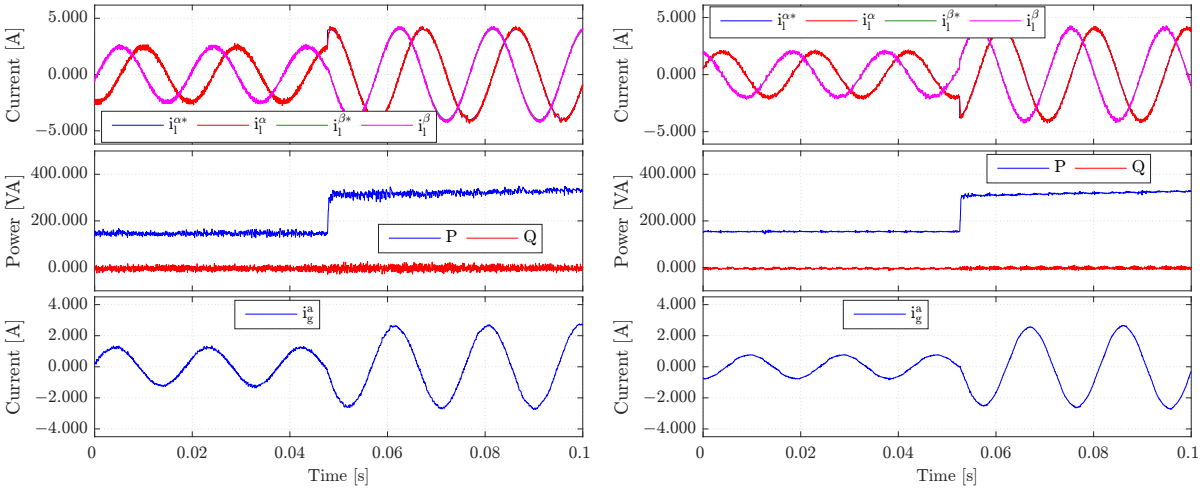

(c) V2-DMPPC (load change from 2 to 4A).

(d) V3-DMPPC (load change from 2 to 4A).

Fig. 5.21: [Experimental results:] Performances of the classical, DutyOpt, proposed V2- and V3-DMPPC methods. From up to down are the load side current, grid side active and reactive power, Grid side phase current, respectively.

5.4.5.2.1 Grid side control The grid side control performances using the proposed V2- and V3-DMPPC methods are evaluated on the back-to-back power converter with RL load. The results are shown in Fig. 5.21. As can be seen, without loosing any dynamic performances, the proposed V2- and V3-DMPPC methods obviously outperform the C-DMPPC and DutyOpt-DMPPC approaches. Best results are seen using the proposed V3-DMPPC solution, which confirms both the theoretical and simulation analysis.

5.4.5.2.2 Machine side control The control performances using the proposed V3-DMPTC method are evaluated on the back-to-back power converter with PMSM(G). To emphasize its performance enhancement, the same situation performance comparison with the classical DMPTC method are performed. The results are shown in Fig. 5.22. As expected, both steady and transient phase performance improvements are seen.

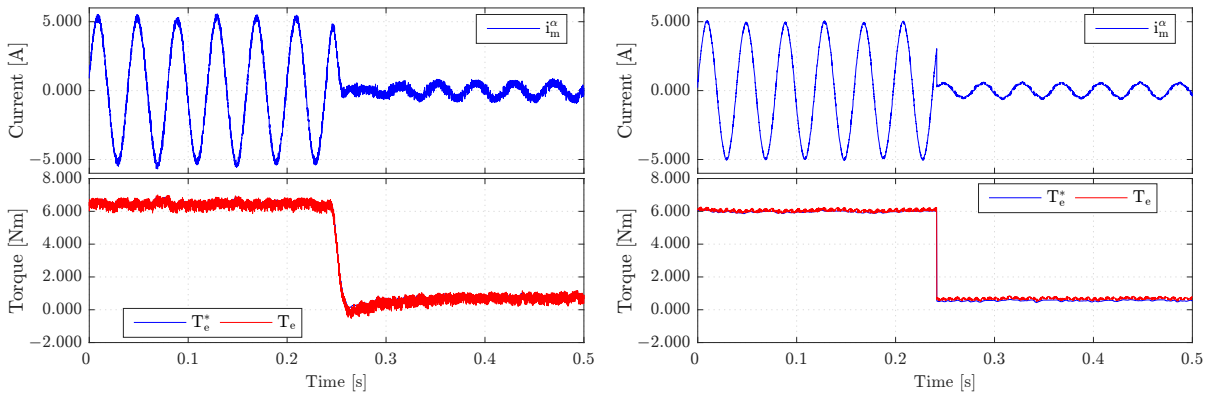

(a) C-DMPTC performances.

(b) V3-DMPTC performances.

Fig. 5.22: [Experimental results:] Performances of the classical, and proposed V3-DMPTC methods. From up to down are the load side current, grid side active and reactive power, Grid side phase current, respectively.

5.4.5.3 Remark and discussion

Direct model predictive control (DMPC) becomes already a viable alternative for both grid-tied active front end and machine side power converter control. However, the inherent one-vector-per-control-interval character of the classical DMPC leads to relatively big control variable ripples, in particular for the two-level cases. This makes the investigation on steady state performance enhanced approaches quite necessary. Following such requirement, the DutyOpt-DMPC method applies one active and one zero vector during a control interval, which greatly reduces the ripples. Limitation for such approach is that the equivalent vector have no phases (directions) other than the six fundamental active ones. In my work two performance-enhanced multiple-vector DMPC concepts with the purpose of reducing the steady state control variable ripples have been proposed, namely, the V2-DMPC and V3-DMPC solutions. The former utilizes (maximum) two vectors (which can be two active ones or one active and one zero vector), extending the candidate synthesized vector range to another freedom: phases (directions) other than the fundamental active ones. The

latter (V3-DMPC) by using (maximum) three vectors makes the whole hexagon plane reachable. These two concepts have been applied to both the grid side AFE with power control, and machine side control with torque control solutions. Note that, they can also be applied into the classical predictive current/voltage/flux/speed control methods.

In deep view of any control method for a switching power converter based system (including both the modulator and non-modulator based techniques) will yield such a conclusion: for all the available methods, forces to fulfill the control objectives are no more than *three* types: *the admissible vector slopes during one control interval*, *duration time of each slope* and *their actuating arrangement* (i.e., the pulse pattern). Considering only the first two, we can category the four direct model predictive control methods discussed in this chapter with Table 5.4. Easy to understand, with unlimited, optimized slopes of

Methods	**Vector slopes**	**Vector actuating time**
Classical DMPC	Fixed and limited-choices	Fixed ($= T_\mathrm{s}$)
Duty-Opt DMPC	Fixed and limited-choices	Unlimited, partially optimized
V2-DMPC	Unlimited and optimized	Unlimited, partially optimized
V3-DMPC	Unlimited and optimized	Unlimited, optimized

Table 5.4: Properties of the four direct model predictive control schemes.

the candidate vectors and their actuating times, best performances are achieved by the proposed V3-DMPC scheme. It can also be expected that with a proper pulse pattern design, the proposed V3-DMPC will yield even improved steady state control performances (with a similar sampling frequency, the current quality will be comparable with the SVM based solution). Its control dynamics during transient phases remain similar as the classical DMPC method since the V3-DMPC incorporates still the nature of the classical DMPC concept (when $t_i = T_\mathrm{s}$ in Equation (5.45), it turns out to be the C-DMPC approach).

Since a comparing process of a cost function are still available for the proposed multiple-vector DMPC solutions, (See e.g., Eq. (5.45) and (5.40)), *certain constraints* (which have direct relationship with the predicted system states, such as, current, power, torque/flux limitations) *can still be added into the minimization process*, though they cannot be added into the time optimization procedure (due to that, mostly a limitation is not "continuous" or "differentiable" with regard to time).

In regard to the computational efforts, both the proposed V2-DMPC and V3-DMPC solutions require increased computational power due to their time optimal process. However, since multiple voltage vectors can be selected, a much longer sampling/control period is allowed.

The proposed multiple-vector DMPC (V3-DMPC) concept can, theoretically, achieve similar steady state control performances as the space vector modulation based control solutions. However, there are also differences:

- The proposed solution still belongs to the *direct control* class, i.e., without requiring

a separately designed *modulator*, while the space vector modulation based technique belongs to the *indirect control* class, i.e., a separate modulation stage is required;

- With the proposed solution, the equivalent vector can reach any corner of the whole hexagon from its inherent design phase. To achieve so, extra *over-modulation techniques* are required for the space vector modulation based methods;

- The (optimal) pulse pattern design procedures can still be included into the proposed solution.

5.5 Predictive control of back-to-back power converter under unbalanced grid

More than 75% of today's grid faults are asymmetric faults where the grid voltage is (temporarily) *un*balanced, i.e. for some period of time, the sum of the grid voltage do *not* cancel: $e_g^a + e_g^b + e_g^c \neq 0$ [24]. An unbalanced grid has a severe impact on the performance and safety of the wind turbine system and should be considered and investigated carefully. Control of grid-tied wind turbine systems under unbalanced grid is therefore one the challenges.

This section studies and illustrates several unbalanced grid control methods combined with DMPC schemes for three-level NPC back-to-back power converter PMSG wind turbine systems. Within this section, three different compensation schemes, i.e., *symmetrical current compensation*, *constant active power compensation*, and *constant reactive power compensation*, using the conventional instantaneous power theory are over-viewed and compared. Then based on a newly proposed instantaneous power theory, a direct model predictive control scheme for unbalanced grid three-level NPC back-to-back power converter PMSG wind turbine systems is presented. The performance comparison is illustrated through simulation results (*due to the fact that: our current set-up lacks a grid emulator with unbalanced voltage output capability*).

5.5.1 Introduction

A big amount of references and publications are dealing with low-voltage ride through control of a grid-tied wind turbines systems (See e.g., [19, 129–131]). Within the DMPC concept, a profound overview and comparative study of the three compensation schemes, namely *symmetrical current compensation*, *constant active power compensation*, and *constant reactive power compensation* within the classical instantaneously power definition frame are lacking. Few studies was reported using DMPC concept under the novel instantaneously power definition for a grid-tied wind turbine system control. To cope with these, three different compensation schemes under the DMPC frame for 3L-NPC back-to-back power converter PSMG wind turbine systems are revisited and their performances are compared. Moreover, combined with the novel instantaneous power calculation [132],

a direct model predictive control scheme for 3L-NPC back-to-back power converter PMSG wind turbine systems under unbalanced grid situations was considered is presented. Its effectiveness is verified and compared with the classical compensation based schemes. With such scheme[18], no complex current/voltage sequence decoupling procedure is required, but similar or even better current/reactive power control performance is achieved.

5.5.1.1 Overall control structure

This section illustrates the overall control structure of a grid-tied 3L-NPC back-to-back power converter PMSG wind turbine system under unbalanced grid taking the DMPC as the control framework. For simplicity, the switching frequency regulations for both sides are neglected.

5.5.1.1.1 Machine-side torque control and voltage balancing The generator side cost function is defined by

$$J^{\mathrm{m}}_{\mathrm{DMPC}}(\vec{u}_m) = \underbrace{\gamma_{T_\mathrm{e}}|T_e^* - T_{\mathrm{e[k+1]}}(\vec{u}_m)|}_{=:J_{T_\mathrm{e}}} + \underbrace{\gamma_{i^{\mathrm{d}}_{\mathrm{m}}}|i_m^{d*} - i^d_{\mathrm{m[k+1]}}(\vec{u}_m)|}_{=:J_{i^{\mathrm{d}}_{\mathrm{m}}}} + \underbrace{\gamma_{V_\mathrm{o}}|V_\mathrm{o}^* - V_{\mathrm{o[k+1]}}(\vec{u}_m)|}_{J_{V_\mathrm{o}}=:J_{\mathrm{CS_m}}} \tag{5.58}$$

with weighting factors $\gamma_{T_\mathrm{e}}[1/\mathrm{Nm}]$, $\gamma_{i^{\mathrm{d}}_{\mathrm{m}}}[1/\mathrm{A}]$ and $\gamma_{V_\mathrm{o}}[1/\mathrm{V}]$. The target set is represented by the sum of the sub-costs J_{T_e} and $J_{i^{\mathrm{d}}_{\mathrm{m}}}$ for torque control with reference T_e^* and d-axis current control to guarantee a constant flux (i.e. $i_m^{d*} = 0\,\mathrm{A}$ for maximum torque per ampere). The constraint set $J_{V_\mathrm{o}} = J_{\mathrm{CS_m}}$ shall assure voltage balancing with $V_\mathrm{o}^* = 0\,\mathrm{V}$. The predicted torque of $T_{\mathrm{e[k+1]}}(\vec{u}_m)$, current of $i^d_{\mathrm{m[k+1]}}(\vec{u}_m)$ and voltage difference $V_{\mathrm{o[k+1]}}(\vec{u}_m)$ have been given in Chp. 2.

5.5.1.1.2 Grid-side power control and voltage balancing Here, the grid/net-side cost function is defined by

$$J^{n}_{\mathrm{DMPC}}(\vec{u}_g) = \underbrace{\gamma_P|P^* - P_{\mathrm{[k+1]}}(\vec{u}_g)|}_{=:J_P} + \underbrace{\gamma_Q|Q^* - Q_{\mathrm{[k+1]}}(\vec{u}_g)|}_{=:J_Q} + \underbrace{\gamma_{V_\mathrm{o}}|V_\mathrm{o}^* - V_{\mathrm{o[k+1]}}(\vec{u}_g)|}_{J_{V_\mathrm{o}}=:J_{CS_g}} \tag{5.59}$$

with weighting factors $\gamma_P[1/\mathrm{W}]$, $\gamma_Q[1/\mathrm{var}]$ and $\gamma_{V_\mathrm{o}}[1/\mathrm{V}]$. The target set is represented by the sum of the sub-costs J_P and J_Q for active and reactive power control, resp. The constraint set $J_{V_\mathrm{o}} = J_{CS_g}$ shall also assure voltage balancing. Note that, since $J_{\mathrm{CS_m}} = J_{CS_g}$, both converters may contribute to voltage balancing. The predicted active and reactive powers, depending on two instantaneous power definitions, are given by Equation (5.63) and (5.73), respectively.

A block diagram of the control structure is given by the lower part of Fig. 5.23, where the "Power Estimation" and "Compensator" parts are introduced in the following section.

[18] A similar contribution with regard to the two-level grid-tied power converter control was presented in [133]. The differences, in this work, are: control of a 3L-NPC back-to-back power converter PMSG wind turbine system under unbalanced grid situations was considered, two detailed sequence decoupling solutions were presented, and a direct model predictive control framework with DC-link balancing was used.

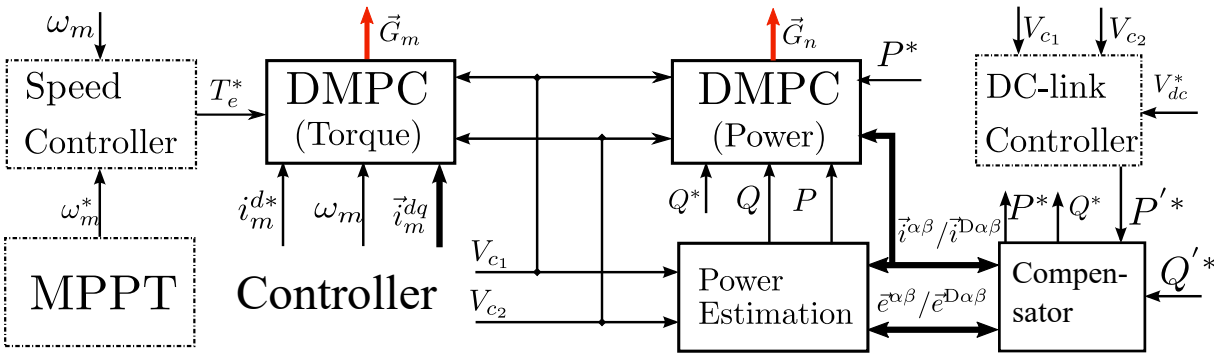

Fig. 5.23: Simplified DMPC controller for a 3L NPC back-to-back converter PMSG wind turbine system.

5.5.2 Conventional unbalanced grid control

In this section three different compensation for control of grid tied three level NPC back-to-back power converter PMSG wind turbine systems under unbalanced grid using the conventional instantaneous power theory are firstly discussed. *Note that, within this work only the unbalanced situations without zero sequence voltage is under consideration.* Then base on a newly proposed instantaneous power theory, a novel direct model predictive control scheme achieving current symmetrical/constant reactive power control without sequence decomposition and complicated compensation is presented.

5.5.2.1 Unbalanced grids and sequence decoupling

Under unbalanced operating conditions without zero sequence voltage, both grid voltage $\vec{e}_g^{\alpha\beta}$ and grid side current in $\alpha\beta$ frame can be expressed as the sum of a positive and a negative sequence components

$$\vec{e}_g(t) = \vec{e}_g^{+}(t) + \vec{e}_g^{-}(t) = A_e^+ e^{j(\omega_g t+\phi_e^+)} + A_e^- e^{-j(\omega_g t+\phi_e^-)}, \tag{5.60a}$$

$$\vec{i}_g(t) = \vec{i}_g^{+}(t) + \vec{i}_g^{-}(t) = A_i^+ i^{j(\omega_g t+\phi_i^+)} + A_i^- i^{-j(\omega_g t+\phi_i^-)}. \tag{5.60b}$$

The relationship of the positive and negative sequence voltage/current vectors is illustrated in Fig. 5.24.

To obtain the positive and negative sequences of the voltage/current vectors, taking voltage vector as an example, two methods are available [24], namely, synchronous frame phase lock loop (SFLL) based method and delayed signal cancellation (DSC) based method. Details are shown in Fig. 5.25. Detailed descriptions for each are given as follows.

SFLL method goes in this way: projecting the voltage vector to a reference frame fixed to the positive sequence, i.e., the reference frame rotating at ω_g (dq frame), then the voltage vector can be interpreted as the sum of a constant value (*dq* components of the positive sequence) and an oscillation of twice the grid frequency (dq components of the negative sequence). In practice the mean value of each component can be calculated by integrating the oscillating components over integer times of its period. These mean values,

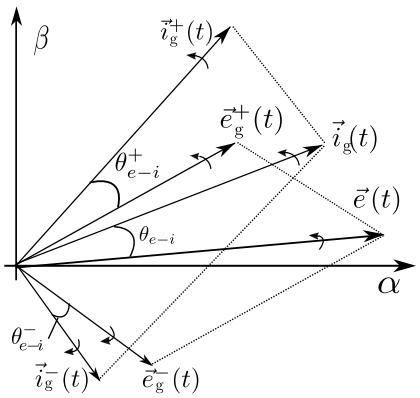

Fig. 5.24: Voltage and current vectors in $\alpha\beta$ frame under unbalanced situations.

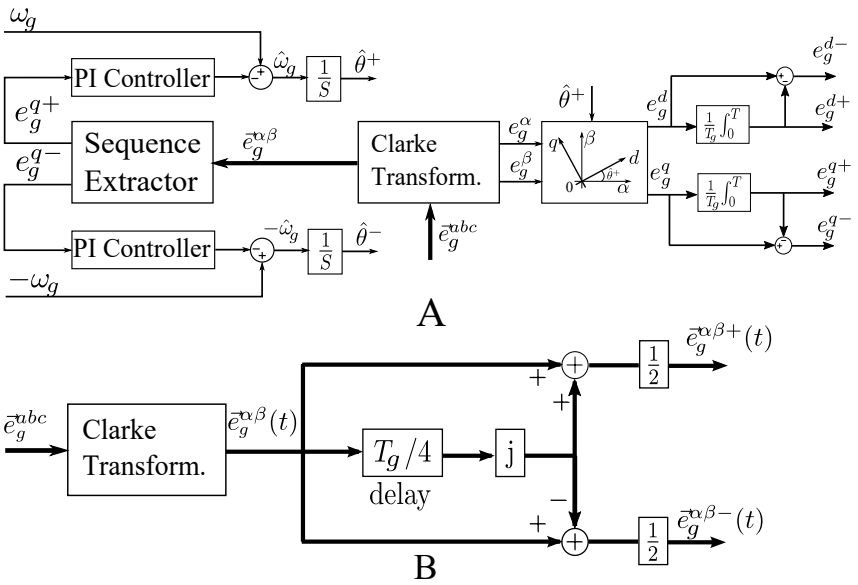

Fig. 5.25: Two sequence decoupling methods A: SFLL method, B: DSC based method.

being therefore constant, are the dq components e_g^{d+} and e_g^{q+} of the positive sequence voltage vector in its own reference frame. Negative sequence voltage vector components are obtained by subtracting the positive sequence vector components from $e_{\mathrm{g}}^{\mathrm{d}}$ and $e_{\mathrm{g}}^{\mathrm{q}}$, respectively. After the relevant inverse Park transformation using $\hat{\theta}^+$ and $\hat{\theta}^-$, all the positive and negative sequences of the voltage/current vectors in $\alpha\beta$ frame are obtained.

The DSC method applied in $\alpha\beta$ frame is based on the equations below

$$\vec{e}_g^{\alpha\beta+}(t) = \frac{1}{2}\left[\vec{e}_g^{\alpha\beta}(t) + j\vec{e}_g^{\alpha\beta}(t - \frac{T_g}{4})\right], \tag{5.61a}$$

$$\vec{e}_g^{\alpha\beta-}(t) = \frac{1}{2}\left[\vec{e}_g^{\alpha\beta}(t) - j\vec{e}_g^{\alpha\beta}(t - \frac{T_g}{4})\right], \tag{5.61b}$$

where T_g is the fundamental period of the grid side voltage. Obviously, it is much more simple and computational less demanding than the SFLL based method. Therefore it is adopted in this work to obtain the positive and negative sequences of the voltage/current

vectors for using the conventional sequence compensation based methods.

5.5.2.2 Conventional instantaneous power theory

According to [34, 134], the complex power $\vec{S}^{\mathrm{C}}$ with its elements of active power P^{C} and reactive power Q^{C}, can be expressed as

$$\vec{S}^{\mathrm{C}} = \vec{i}_g^{*}\vec{e}_g = P^{\mathrm{C}} + jQ^{\mathrm{C}} \tag{5.62}$$

In this case, the predicted active and reactive power are given as [10]

$$P_{[\mathrm{k+1}]} = P^{\mathrm{C}}_{[\mathrm{k+1}]} = P^{\mathrm{C}}_{[\mathrm{k}]} + \frac{T_{\mathrm{s}}}{L_{\mathrm{g}}}\Big(||\vec{e}^{\,\alpha\beta}_{\mathrm{g[k]}}||^2 - e^{\alpha}_{\mathrm{g[k]}}v^{\alpha}_{\mathrm{g[k]}} - e^{\beta}_{\mathrm{g[k]}}v^{\beta}_{\mathrm{g[k]}} - R_{\mathrm{g}}P^{\mathrm{C}}_{[\mathrm{k}]} - \omega_{\mathrm{g}}Q^{\mathrm{C}}_{[\mathrm{k}]}\Big); \tag{5.63a}$$

$$Q_{[\mathrm{k+1}]} = Q^{\mathrm{C}}_{[\mathrm{k+1}]} = Q^{\mathrm{C}}_{[\mathrm{k}]} + \frac{T_{\mathrm{s}}}{L_{\mathrm{g}}}\big(e^{\alpha}_{\mathrm{g[k]}}v^{\beta}_{\mathrm{g[k]}} - e^{\beta}_{\mathrm{g[k]}}v^{\alpha}_{\mathrm{g[k]}} - R_{\mathrm{g}}Q^{\mathrm{C}}_{[\mathrm{k}]} + \omega_{\mathrm{g}}P^{\mathrm{C}}_{[\mathrm{k}]}\big). \tag{5.63b}$$

In $\alpha\beta$ frame, under unbalanced grid as is described in last section, the active and reactive power can be calculated as

$$\begin{aligned} P^{C} &= P_0 + P_1 + P_2 \\ Q^{C} &= Q_0 + Q_1 + Q_2 \end{aligned} \tag{5.64}$$

where

$$\begin{cases} P_0 &= e_g^{\alpha+}i_g^{\alpha+} + e_g^{\beta+}i_g^{\beta+} + e_g^{\alpha-}i_g^{\alpha-} + e_g^{\beta-}i_g^{\beta-} = A_e^{+}A_i^{+}\cos(\theta_{e-i}^{+}) + A_e^{-}A_i^{-}\cos(\theta_{e-i}^{-}), \\ P_1 &= e_g^{\alpha+}i_g^{\alpha-} + e_g^{\beta+}i_g^{\beta-} = A_e^{+}A_i^{-}\cos(2\omega_{\mathrm{g}}t - \theta_{e-i}^{-}), \\ P_2 &= e_g^{\alpha-}i_g^{\alpha+} + e_g^{\beta-}i_g^{\beta+} = A_e^{-}A_i^{+}\cos(2\omega_{\mathrm{g}}t + \theta_{e-i}^{+}); \\ Q_0 &= e_g^{\beta+}i_g^{\alpha+} - e_g^{s\alpha+}i_g^{s\beta+} + e_g^{\beta-}i_g^{\alpha-} - e_g^{\alpha-}i_g^{\beta-} = A_e^{+}A_i^{+}\sin(\theta_{e-i}^{+}) + A_e^{-}A_i^{-}\sin(\theta_{e-i}^{-}), \\ Q_1 &= e_g^{\beta+}i_g^{\alpha-} - e_g^{\alpha+}i_g^{\beta-} = A_e^{+}A_i^{-}\sin(2\omega_{\mathrm{g}}t - \theta_{e-i}^{-}), \\ Q_2 &= e_g^{\beta-}i_g^{\alpha+} - e_g^{\alpha-}i_g^{\beta+} = A_e^{-}A_i^{+}\sin(2\omega_{\mathrm{g}}t + \theta_{e-i}^{+}). \end{cases} \tag{5.65}$$

Easy to know from (5.64) and (5.65), terms $P, Q_{1,2}$ are with an oscillation of twice the grid voltage frequency and only P, Q_0 can be constant values. However, under unbalanced grid situation, similar as normal situations, the controller also tries to smooth/track both the active and reactive powers/reference powers, i.e., to assure $(\mathrm{co}_1) : \{P_0 = P^*, Q_0 = Q^*\}$ and $(\mathrm{co}_2) : \{Q_1 + Q_2 = 0, P_1 + P_2 = 0\}$. (co_1) is achievable, but to achieve (co_2) means the following should hold true (See (5.65))

$$\begin{aligned} A_e^{+}A_i^{-}\cos(2\omega_{\mathrm{g}}t - \theta_{e-i}^{-}) &= -A_e^{-}A_i^{+}\cos(2\omega_{\mathrm{g}}t + \theta_{e-i}^{+}), \\ A_e^{+}A_i^{-}\sin(2\omega_{\mathrm{g}}t - \theta_{e-i}^{-}) &= A_e^{-}A_i^{+}\sin(2\omega_{\mathrm{g}}t + \theta_{e-i}^{+}), \end{aligned} \tag{5.66}$$

which requires

$$\begin{cases} A_e^{+}A_i^{-} &= -A_e^{-}A_i^{+} \\ \cos(2\omega_{\mathrm{g}}t - \theta_{e-i}^{-}) &= \cos(2\omega_{\mathrm{g}}t + \theta_{e-i}^{+}) \\ A_e^{+}A_i^{-} &= A_e^{-}A_i^{+} \\ \sin(2\omega_{\mathrm{g}}t - \theta_{e-i}^{-}) &= \sin(2\omega_{\mathrm{g}}t + \theta_{e-i}^{+}) \end{cases} \tag{5.67}$$

Obviously, conditions of (5.67) cannot hold true for all the time throughout a fundamental period of the grid side voltage. Therefore, for unbalanced situations, (co_1) and (co_2) are not able to be achieved simultaneously. In the literature, three compensation schemes are available for doing direct power control of a grid side power converter under unbalanced grid, to achieve: (i) sinusoidal and symmetrical current, and/or (ii) to reduce or eliminate reactive power oscillation or (iii) to reduce or eliminate active power/DC-link voltage oscillation. In this work those three compensation schemes are incorporated into the DMPC concept. The basic principle is to calculate the relevant compensating components and add them to the power references which are assigned to the inner predictive controller, as follows

$$P^* = P'^* + P_{comp};\ Q^* = Q'^* + Q_{comp}; \tag{5.68}$$

In the following the compensating components to achieve (i) to (iii) are introduced.

5.5.2.3 Sinusoidal and symmetrical current compensation

The target is to eliminate negative sequence current component thereby obtaining sinusoidal and symmetrical grid current. Therefore, the power ripples generated by the negative sequence current components should be depressed. The other oscillating power components generated by the negative sequence voltage and positive sequence current will still exist in the instantaneous active and reactive powers. The compensating components for such case are

$$P_{comp} = e_g^{\alpha-} i_g^{\alpha+} + e_g^{\beta-} i_g^{\beta+}, \qquad Q_{comp} = e_g^{\beta-} i_g^{\alpha+} - e_g^{\alpha-} i_g^{\beta+}. \tag{5.69}$$

5.5.2.4 Oscillation-reduced reactive power compensation

This control target is to allow the existence of negative sequence current components but to eliminate the reactive power oscillations. In order to obtain constant reactive power, the reactive power reference must be kept constant. Based on Equation (5.64), the active power components in this case are not zero and the compensation terms are

$$Q_{comp} = 0, \qquad P_{comp} = e_g^{\alpha-} i_g^{\alpha+} + e_g^{\beta-} i_g^{\beta+} + e_g^{\alpha+} i_g^{\alpha-} + e_g^{\beta+} i_g^{\beta-}. \tag{5.70}$$

5.5.2.5 Oscillation-reduced active power/DC-link voltage compensation

This control target is to allow the existence of negative sequence current components but to eliminate the active power ripple thereby also eliminating the DC-link voltage ripples. Based on Equation (5.64), the reactive power components are not zero and the compensation terms are

$$P_{comp} = 0, \qquad Q_{comp} = e_g^{\beta+} i_g^{\alpha-} - e_g^{\alpha+} i_g^{\beta-} + e_g^{\beta-} i_g^{\alpha+} - e_g^{\alpha-} i_g^{\beta+}. \tag{5.71}$$

5.5.3 Extended instantaneous power theory and its combination to DMPC

An extended instantaneous power theory was proposed in [132]. Under this concept, a new complex power $\vec{S}^{\mathrm{N}}$ is introduced as

$$\vec{S}^{\mathrm{N}} = \vec{i}_g^{*}\vec{e}_g^{D}. \tag{5.72}$$

where $\vec{e}_g^{D}$ is a voltage vector lagging $\vec{e}_g$ by 90 electrical degrees. In this new definition, the instantaneous active and reactive power can be expressed as

$$P^{\mathrm{N}} = \Re\{\vec{S}^{\mathrm{N}}\} = \Re\{\vec{i}_g^{*}\vec{e}_g\} = P^{\mathrm{C}}, \qquad Q^{\mathrm{N}} = \Re\{\vec{i}_g^{*}\vec{e}_g^{D}\}. \tag{5.73}$$

Remark 14 (On the new reactive power definition) *Good part for using this new definition is that under unbalanced situations without providing any compensation components to the reference powers, i.e., $P_{comp} = Q_{comp} = 0$, the reactive power (Q^{N}) can be oscillation-free meanwhile the grid side currents are sinusoidal and symmetrical (See Fig 5.28). This saves the complex sequence decoupling part and greatly eases the controller design. Note that the new definition in Eq. (5.73) is the same as conventional definition in Eq. (5.64) under balanced voltages. Then it can be applied for both balanced and unbalanced conditions.*

The predicted active and reactive powers in this case are

$$P_{[\mathrm{k+1}]} = P^{\mathrm{N}}_{[\mathrm{k+1}]} = P^{\mathrm{N}}_{[\mathrm{k}]} + \frac{T_{\mathrm{s}}}{L_{\mathrm{g}}}\Big(||\vec{e}^{\alpha\beta}_{\mathrm{g[k]}}||^2 - e^{\alpha}_{\mathrm{g[k]}}v^{\alpha}_{\mathrm{g[k]}} - e^{\beta}_{\mathrm{g[k]}}v^{\beta}_{\mathrm{g[k]}} - R_{\mathrm{g}}P^{\mathrm{N}}_{[\mathrm{k}]} - \omega_{\mathrm{g}}Q^{\mathrm{N}}_{[\mathrm{k}]}\Big); \tag{5.74a}$$

$$Q_{[\mathrm{k+1}]} = Q^{\mathrm{N}}_{[\mathrm{k+1}]} = Q^{\mathrm{N}}_{[\mathrm{k}]} + \frac{T_{\mathrm{s}}}{L_{\mathrm{g}}}\Big(e^{D\alpha}_{\mathrm{g[k]}}v^{\beta}_{\mathrm{g[k]}} - e^{D\beta}_{\mathrm{g[k]}}v^{\alpha}_{\mathrm{g[k]}} - R_{\mathrm{g}}Q^{\mathrm{N}}_{[\mathrm{k}]} + \omega_{\mathrm{g}}P^{\mathrm{N}}_{[\mathrm{k}]}\Big). \tag{5.74b}$$

So far, the conventional instantaneous power theory, three compensation schemes, and the newly proposed instantaneous power theory are introduced. Thus, the predictive control scheme is entirely introduced and the general overview is given by Fig. 5.23.

5.5.4 Evaluation and analysis

In this section overall control performances of the proposed DMPC scheme under both balanced and unbalanced grid situations for a three level NPC back-to-back power converter PMSG wind turbine system are firstly illustrated through simulation data. Then the effectiveness of the three compensation schemes under conventional instantaneous power theory are verified and compared with the novel instantaneous power theory based DMPC scheme. Simulation and system data are collected in Table 5.5.

An overall control performance under unbalanced grid situations (to test only the DMPC scheme, but without any unbalance control solution) is illustrated in Fig. 5.26.

Parameter [unit]	Value	Parameter [unit]	Value
Air density ρ [kg/m^3]	1.225	DC-Link cap. $C_1 = C_2$ [F]	1000×10^{-12}
Turbine radius R_t [m]	0.8	Stator induc. $L_{\mathrm{s}}^{\mathrm{d}} = L_{\mathrm{s}}^{\mathrm{q}}$[H]	19×10^{-3}
Max. power coeff. C_p [1]	0.48	Stator resistance R_s [Ω]	1.3
Tip speed ratio λ [1]	8.4	PMSG flux linkage ψ_{pm} [Vs]	4.26×10^{-2}
Pitch angle β [°]	0	Sampling frequency f_s [kHz]	20
Grid phase volt. $\|\vec{e}_g\|$ [V]	250	$\gamma_{T_{\mathrm{e}}}$ [1]	$\frac{1}{N_{\mathrm{p}}\psi_{\mathrm{pm}}}$
Grid volt. freq. ω_n [rad/s]	100π	$\gamma_{i_{\mathrm{m}}^{\mathrm{d}}}$ [1]	1
Filter resistance R_{g} [Ω]	1.56×10^{-3}	$\gamma_{V_{\mathrm{o}}}$ [1]	0.001
Filter inductance L_{g} [Wb]	16×10^{-3}	γ_P[1] $= \gamma_Q$ [1]	1

Table 5.5: Implementation and system data.

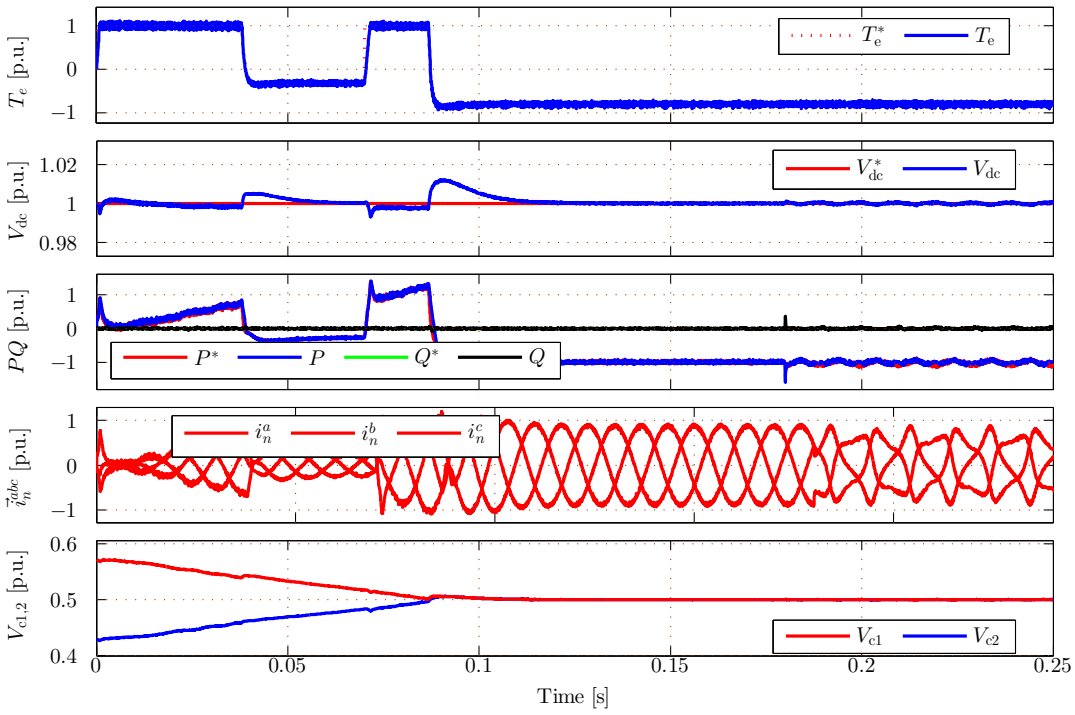

Fig. 5.26: Overall control performances of the proposed DMPC scheme under both balanced and unbalance grid.

Test scenarios are: for $t \in [0, 0.04]$ [s] to test its "motor mode" operation, a MPPT torque reference is set as 1 [p.u.] (based value 25 [Nm]); it changes to -1 [p.u.] at $t = 0.04$ [s] and back to 1 [p.u.] at $t = 0.75$ [s], then changes back to -1 [p.u.] and keeps this values for the rest time. The DC-link reference is set as 1 [p.u.] (base value 700 [V]) for all the testing period. DC-link capacitors C_1, C_2 are initialized with difference voltages of 300 [V] and 400 [V] respectively, to invest the DC-link balancing control performances. Reactive power reference is set to zero to achieve unit power factor control. The grid side voltage is set balanced for $t \in [0, 0.175]$ [s], and for the rest time, $A_e^- = 25\%A_e$ is set to the source. As can be seen from Fig. 5.26, generator side, nice torque tracking performances are achieved.

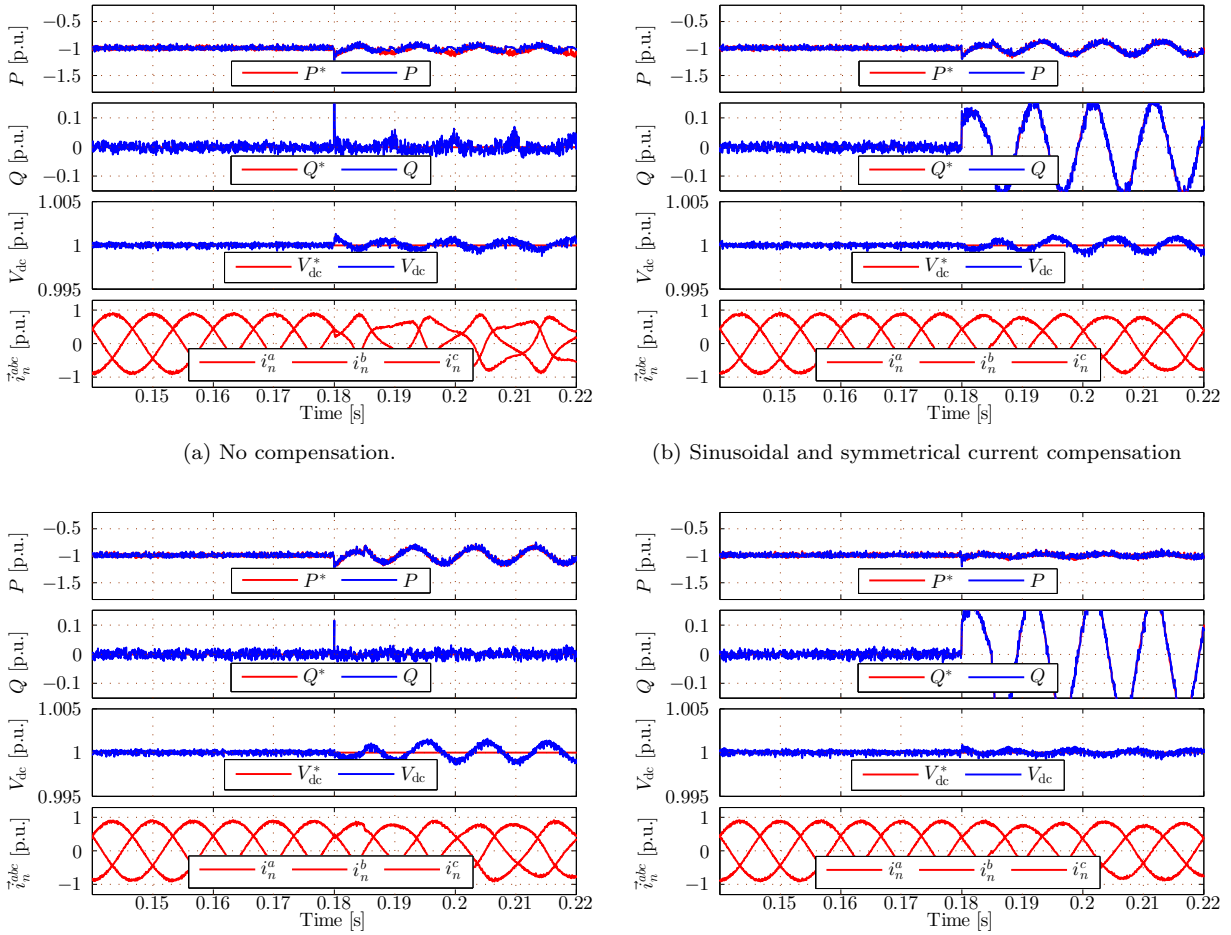

(a) No compensation.

(b) Sinusoidal and symmetrical current compensation

(c) Oscillation-relied reactive power compensation

(d) Oscillation-relied active power/DC-link voltage compensation

Fig. 5.27: DMPC with different compensation schemes using conventional instantaneous power calculation. From up to down are: grid side voltages, active power, reactive power, DC-link voltage, grid side currents.

The DC-link voltage and DC-link balancing control are also with nice accuracy and fast dynamics. Grid side active and reactive powers are nicely controlled before unbanning grid happens. However, due to the controller is in this case without any compensation scheme, and the power is calculated using the conventional instantaneous power concept,

so evident grid current distortions and active power (DC-link voltage) fluctuations are observed for $t \in [0.18, 0.25]$ [s].

5.5.4.1 DMPC with different compensation schemes

The comparison results of DMPC with different compensation schemes using conventional instantaneous power calculation are illustrated in Fig. 5.27. As can be clearly seen, with *symmetrical current compensation*, the current waveform is much better than the others (See Fig. 5.27-(b)). In the same situation, with *Oscillation-relied reactive and active power compensation*, the reactive and active ripples are much smaller than the others. However, as analyzed in last section, no scheme can achieve simultaneously current, active and reactive power optimal control, due to their un-compatible mathematical relationship.

5.5.4.2 DMPC using novel instantaneous power calculation

Fig. 5.28-(a) shows the control performances using the novel instantaneous power calculation concept without compensation. As can be seen, nice current waveforms are maintained, meanwhile, the reactive power Q^N under novel instantaneous power calculation concept is quite smooth. The active power and DC-link voltage control performances are also better compared with the *sinusoidal and symmetrical current compensation* using conventional instantaneous power calculation concept (Fig. 5.28-(b)). Therefore, together with the

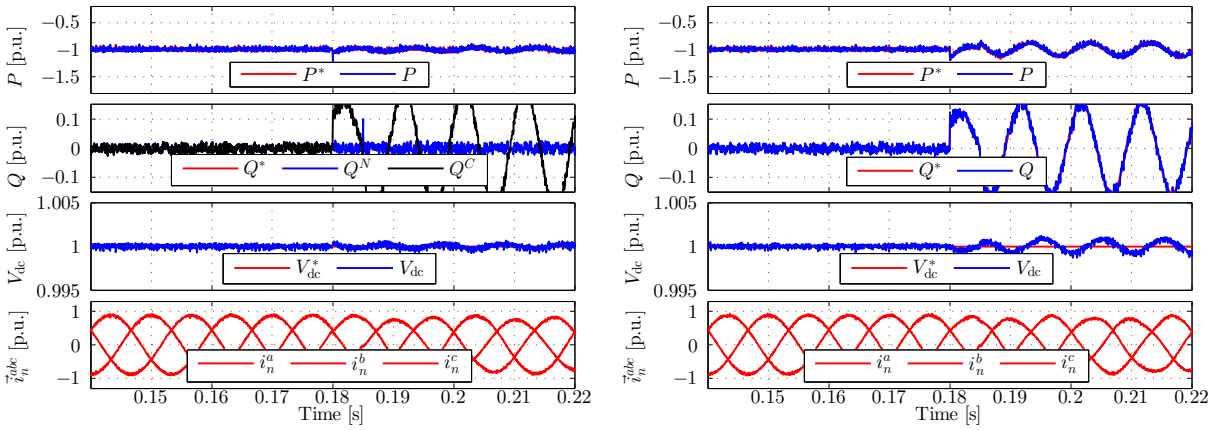

(a) DMPC without compensation using novel instantaneous power calculation.

(b) DMPC without sinusoidal and symmetrical current compensation using conventional instantaneous power calculation.

Fig. 5.28: Comparison between *DMPC without compensation using novel instantaneous power calculation* and *DMPC without sinusoidal and symmetrical current compensation using conventional instantaneous power calculation*. From up to down are: grid side voltages, active power, reactive power, DC-link voltage, grid side currents.

calculation procedures introduced in last section, the novel instantaneous power calculation concept based DMPC scheme is of better performances (sinusoidal and symmetrical current, lower active and DC-link voltage ripples) and easier realization character (no sequence decoupling is required).

5.6 Summary

Within this chapter, two main drawbacks (high computational demanding and poor steady state control variable qualities) of the classical DMPC concept have been formulated. To conquer its high computational demanding drawback for multi-level power converters, two computational efficient DMPC techniques have been proposed for both the grid and machine side control of the three-level NPC back-to-back power converter PMSG wind turbine systems, combining the deadbeat control concept and an intelligent offline search solution. To deal with its big control variable ripple problems for two-level power converters, two multi-vector based solutions have been proposed and verified for both the grid and machine side control of the two-level back-to-back power converter systems. Moreover, different methods dealing with *unbalanced grid* control of grid-tied PMSG wind turbine systems within the direct model predictive control framework have been studied. A newly proposed instantaneously power theories have been incorporated into the DMPC scheme for controlling the grid-tied three-level NPC back-to-back power converter PMSG wind turbine system.

Chapter 6

Quasi-centralized direct model predictive control

This chapter presents the quasi-centralized direct model predictive control (QC-DMPC) methods for back-to-back power converter using the so-called dynamic reference generation concept. Its performance improvements and also the potential drawbacks in comparison with the classical proportional-integration (PI) DC-link controller based method have been evaluated in Sec. 6.2, taking a two-level back-to-back power converter system with RL load as an example. Following, to conquer its DC-link tracking bias problem, Sec. 6.3 presents a revised QC-DMPC method and its application to the back-to-back power converter driven PMSG system with reduced computational efforts. The effectiveness has all been evaluated with experimental data using a fully FPGA based solution.

6.1 Background

Back-to-back power converter driven systems permit instant power reverse and allows for true four-quadrant operations, which is an important property for high performance drives, grid-tied distributed energy generation systems, etc. For such topology, model predictive control becomes a nice alternative [10]. The flexibly defined cost function eases the realizations of the control objectives without using any modulator.

The DC-link voltage control represents a key part of a back-to-back power converter based system. Therefore, a great amount of investigations have been made in this direction. In [135], a feedback linearization scheme was proposed for controlling the DC-link voltage of a back-to-back system with an extremely small DC-link capacitor. In [136] a similar feedback linearization idea is used for controlling a grid-tied AFE. In [137], a nonlinear controller that uses a new complex state-space modeling method was proposed and verified against a grid-tied AFE. In [138], the DC-Link control was fulfilled by using a proportional-integration (PI) controller, which generates the reference for grid-side inner predictive power controller. For steady state, the DC-link voltage and grid side active power are controlled nicely. However, a typical second-order fluctuation of sizable magnitude is

observed during system transient phases. In [104], by using a dynamic reference generation concept the DC-link voltage control was directly included into the grid-side predictive controller for a grid-tied AFE with a DC-link R-Load.

The comprehensive relation and performance comparison investigation of the available control techniques provide a platform not only to transform from one to another, but also to develop different DC-link controllers with enhanced performances. Therefore, many efforts have been made to compare and study the different methods mentioned above. In [139], a state feedback control was analyzed and compared with a conventional cascaded control scheme for a single phase AC/DC converter with respect to DC-link control, while in [140], the linear and nonlinear control strategies of a back-to-back converter with respect to DC-link voltage control were compared. However, few publications compare conventional PI controller and the recently reported dynamic reference generation concept with regards to DC-link voltage control.

In the following sections of this chapter two fully FPGA based quasi-centralized direct model predictive control (QC-DMPC) schemes for both back-to-back power converter with RL load (See Sec. 6.2) and back-to-back power converter PMSG wind turbine systems (See Sec. 6.3) are introduced extending the dynamic reference generation concept proposed in [104]. The performances of both the proposed schemes have been compared with the classical PI controller based DC-link control methods.

6.2 QC-DMPC for back-to-back power converter with RL load

This section presents a QC-DMPC method for a voltage source back-to-back power converter with RL load (See Fig. 6.1). A thorough comparison between the conventional PI-DMPC and the proposed QC-DMPC is presented using both simulation and experimental data. Furthermore, DC-link voltage control performance and robustness under parameter variations are experimentally compared between the QC-DMPC and PI-DMPC schemes. Both schemes are implemented using a platform that is entirely based on FPGA. The implementation, timing, and FPGA resource usage are all introduced in detail.

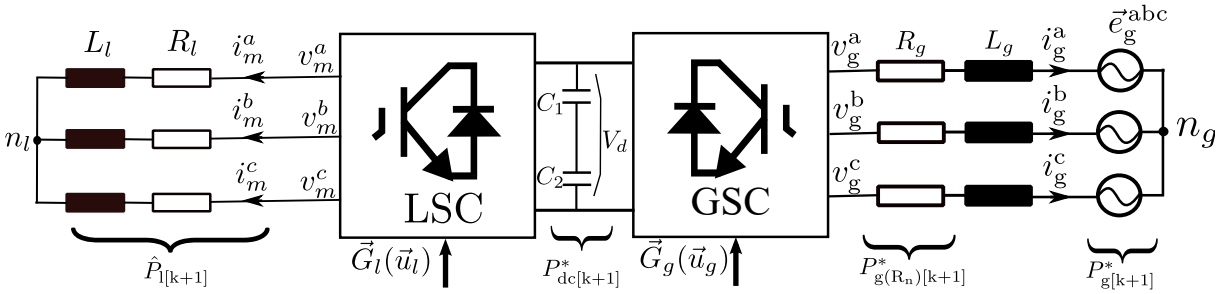

Fig. 6.1: Simplified power circuit of a voltage source back-to-back converter with (R)L filter and RL load.

The modeling of the system shown in Fig. 6.1 has already been developed in Chp. 2. The main control objectives for such a system are: (Co_1) load side current tracking, (Co_2) DC-link voltage control, and (Co_3) grid side power control. The system is supposed to be operated under certain current and power limits. In the following parts of this section, a conventional PI DC-link controller-based DMPC (PI-DMPC) scheme (see Fig. 6.14 A) and a proposed quasi-centralized DMPC (QC-DMPC) scheme (see Fig. 6.14 B) are presented. They are introduced following the order of **Step-II** to **Step-I** in Algorithm 4.1 to ease the reading, i.e., firstly the cost functions and then the required state predictions and reference generation are given.

6.2.1 PI DC-link controller based DMPC scheme

In general, three separate controllers are required for the PI DC-link controller based DMPC (PI-DMPC) scheme to achieve the above mentioned control objectives of $\mathrm{Co}_{1,2,3}$, namely: a load side predictive current control for Co_1, PI based DC-link controller for Co_2 and an inner predictive power controller for Co_3. The cost functions which represent the control objectives of the load and grid side mentioned above can be designed as

$$J_{\mathrm{LSC}} = \underbrace{\|i^{\alpha*}_{\mathrm{l}[\mathrm{k}+1]} - i^{\alpha}_{\mathrm{l}[\mathrm{k}+1]}\| + \|i^{\beta*}_{\mathrm{l}[\mathrm{k}+1]} - i^{\beta}_{\mathrm{l}[\mathrm{k}+1]}\|}_{=:J_{\mathrm{TS}_{\mathrm{LSC}}}} + \underbrace{\begin{cases} 0 & , \sqrt{(i^{\alpha}_{\mathrm{l}[\mathrm{k}+1]})^2 + (i^{\beta}_{\mathrm{l}[\mathrm{k}+1]})^2} \leq i_{\mathrm{l}}^{\max} \\ \gamma_{\mathrm{l}} & , \sqrt{(i^{\alpha}_{\mathrm{l}[\mathrm{k}+1]})^2 + (i^{\beta}_{\mathrm{l}[\mathrm{k}+1]})^2} > i_{\mathrm{l}}^{\max} \end{cases}}_{=:J_{\mathrm{CS}_{\mathrm{LSC}}}}, \tag{6.1a}$$

$$J^{\mathrm{PI}}_{\mathrm{GSC}} = \underbrace{\|P^{*}_{[\mathrm{k}+1]} - P_{[\mathrm{k}+1]}\| + \|Q^{*}_{[\mathrm{k}+1]} - Q_{[\mathrm{k}+1]}\|}_{=:J^{\mathrm{PI}}_{\mathrm{TS}_{\mathrm{GSC}}}} + \underbrace{\begin{cases} 0 & , \sqrt{(P_{[\mathrm{k}+1]})^2 + (Q_{[\mathrm{k}+1]})^2} \leq \|\vec{S}\|^{\max} \\ \gamma_{\mathrm{g}} & , \sqrt{(P_{[\mathrm{k}+1]})^2 + (Q_{[\mathrm{k}+1]})^2} > \|\vec{S}\|^{\max} \end{cases}}_{=:J^{\mathrm{PI}}_{\mathrm{CS}_{\mathrm{GSC}}}}, \tag{6.1b}$$

respectively, where $J_{\mathrm{TS}_{\mathrm{LSC}}}$ and $J^{\mathrm{PI}}_{\mathrm{TS}_{\mathrm{GSC}}}$ represent the *Targeting Set* of load and grid side; $J^{\mathrm{PI}}_{\mathrm{CS}_{\mathrm{GSC}}}$, $J_{\mathrm{CS}_{\mathrm{LSC}}}$ represent the *Constraint Set* for load and grid side, respectively, γ_{l} and γ_{g} (all > 0), are the weighting factors; $\|\vec{S}\|^{\max}$ and $i_{\mathrm{l}}^{\max}$ (all > 0) are the power and current limits.

6.2.1.1 System state prediction

For a PI-DMPC scheme, the required system states, for the cost evaluation, are load side current of $\vec{i}^{\,\alpha\beta}_{\mathrm{l}[\mathrm{k}+1]}$ and grid side active and reactive powers $P_{[\mathrm{k}+1]}$ and $Q_{[\mathrm{k}+1]}$, respectively. They are calculated using equations (2.24) and (2.50), respectively.

6.2.1.2 Reference extrapolation (generation)

The purpose of reference generation is to obtain the future system reference required by the cost functions, i.e., equations (6.1a) and (6.1b). Those reference values are load side currents $\vec{i}^{\alpha\beta*}_{\mathrm{l}[\mathrm{k}+1]}$, grid side active and reactive powers $P^*_{[\mathrm{k}+1]}$ and $Q^*_{[\mathrm{k}+1]}$. In practice, the load side current and grid side reactive power at the current sampling instant of [k], and past instants of [k − 1] and [k − 2] can be recorded, which allows the future reference values to be obtained with a second order extrapolation scheme [128, 141] of

$$x^*_{[\mathrm{k}+1]} = 3(x^*_{[\mathrm{k}]} - x^*_{[\mathrm{k}-1]}) + x^*_{[\mathrm{k}-2]}, \text{ where } x \text{ can be } \vec{i}^{\alpha\beta*}_{\mathrm{l}} \text{ or } Q^*. \tag{6.2}$$

The active power reference $P^*_{[\mathrm{k}+1]}$ is produced by an outer DC-link PI controller by (See Fig. 6.14 A)

$$P^*(t) = V_{\mathrm{d}}(t) \cdot \mathcal{L}^{-1}\{T_{\mathrm{PI}}(s) * (V^*_{\mathrm{d}}(s) - V_{\mathrm{d}}(s))\} + \hat{P}_l(t), \text{ with } T_{\mathrm{PI}}(s) = \frac{K_p \cdot s + K_i}{s} \tag{6.3}$$

where $\mathcal{L}^{-1}$ represents the inverse Laplace transformation, and $\hat{P}_l(t)$ is the estimated active power of the load side (See Equation (6.8)). Note that, with the presence of $\hat{P}_l(t)$ in Equation (6.3), the power control forms a feed-forward structure, resulting in a much smaller DC-link voltage fluctuation during load change. The structure overview of PI-DMPC is given in Fig. 6.2 A.

6.2.2 The proposed quasi-centralized DMPC scheme

6.2.2.1 Cost function design

The load side cost-function for QC-DMPC scheme is designed the same way as described by Equation (6.1a), since the control objectives are same. However, the DC-link voltage for the proposed QC-DMPC is directly included into the grid side predictive controller using a dynamic reference generation concept and no outer PI control loop is required [10, 104]. The cost function for the grid side is designed as

$$\begin{aligned} J^{QC}_{\mathrm{GSC}} = & \underbrace{\|P^*_{[\mathrm{k}+1]} - P_{[\mathrm{k}+1]}\| + \|Q^*_{[\mathrm{k}+1]} - Q_{[\mathrm{k}+1]}\| + \gamma^{QC}_{V_{\mathrm{d}}} \|V^*_{\mathrm{d}[\mathrm{k}+1]} - V_{\mathrm{d}[\mathrm{k}+1]}\|}_{=:J^{QC}_{\mathrm{TS}_{\mathrm{GSC}}}} \\ & + \underbrace{\begin{cases} 0 & , \sqrt{(P_{[\mathrm{k}+1]})^2 + (Q_{[\mathrm{k}+1]})^2} \leq \|\vec{S}\|^{\max} \\ \gamma_{\mathrm{g}} & , \sqrt{(P_{[\mathrm{k}+1]})^2 + (Q_{[\mathrm{k}+1]})^2} > \|\vec{S}\|^{\max} \end{cases}}_{=:J^{QC}_{CS_{\mathrm{GSC}}}}. \end{aligned} \tag{6.4}$$

6.2.2.2 System state prediction *and* reference generation (extrapolation)

6.2.2.2.1 System state (TS^p, CS^p) prediction For the QC-DMPC scheme, the system states to predict are load side currents $\vec{i}^{\alpha\beta}_{\mathrm{l}[\mathrm{k}+1]}$, grid side active and reactive powers $P_{[\mathrm{k}+1]}$ and $Q_{[\mathrm{k}+1]}$, and the DC-link voltage $V_{\mathrm{d}[\mathrm{k}+1]}$, which are predicted by equations (2.24), (2.50) and (2.18), respectively.

6.2.2.2.2 Reference generation (extrapolation) The same method for the load side current and grid side reactive power reference generation used in PI-DMPC scheme is again adopted for QC-DMPC (See Equation (6.2)). The DC-link voltage reference $V^*_{\mathrm{d[k+1]}}$ and grid side active power reference $P^*_{\mathrm{[k+1]}}$ are obtained here using a dynamic reference generation concept and load side power estimation. The details are explained as follows.

i) DC-link voltage reference generation: To obtain the *one step reference value* $V^*_{\mathrm{d[k+1]}}$ of the DC-link voltage, a gradually-approaching manner with a limited-step size is introduced by using $N_s(>1)$ to limit the charging and discharging current of the DC-link capacitor

$$V^*_{\mathrm{d}} := V_{\mathrm{d[k]}} + \frac{1}{N_s}(V^*_{\mathrm{d},\infty} - V_{\mathrm{d[k]}}), \tag{6.5}$$

where N_s defines how many control intervals it needs to reach the *general reference value* of $V^*_{\mathrm{d},\infty}$.

ii) Grid side active power reference generation: Assuming that $V^*_{\mathrm{d[k+1]}}$ is reached in the next sampling interval, the required capacitor charging (or discharging) current reference $I^*_{\mathrm{d[k+1]}}$ can be calculated by

$$I^*_{\mathrm{d[k+1]}} = \frac{C}{N_s T_{\mathrm{s}}}(V^*_{\mathrm{d[k+1]}} - V_{\mathrm{d[k]}}). \tag{6.6}$$

By defining the estimated load side current reflected at the DC-link part as $\hat{I}_{\mathrm{l[k+1]}}$, the reference DC-link current on the grid side $I^*_{\mathrm{g[k+1]}}$ can be calculated as

$$I^*_{\mathrm{g[k+1]}} = I^*_{\mathrm{d[k+1]}} + \hat{I}_{\mathrm{l[k+1]}}, \tag{6.7}$$

where, in order to reduce the influences of the DC-link voltage measurement noises, $\hat{I}_{\mathrm{l[k+1]}}$ is calculated by $\hat{I}_{\mathrm{l[k+1]}} = \frac{\hat{P}^*_{\mathrm{l[k+1]}} + \hat{P}^*_{\mathrm{l[k]}}}{V^*_{\mathrm{d[k+1]}} + V_{\mathrm{d[k]}}}$. The load side power estimation $\hat{P}^*_{\mathrm{l[k+1]}}$ is obtained by

$$\hat{P}^*_{\mathrm{l[k+1]}} = \{(i^{\alpha *}_{\mathrm{l[k+1]}})^2 + (i^{\beta *}_{\mathrm{l[k+1]}})^2\} \cdot R_{\mathrm{l}}. \tag{6.8}$$

The power reference $P^*_{\mathrm{g(dc)[k+1]}}$ of the DC-link at grid side can be calculated by equations (6.7) and (6.5) as

$$P^*_{\mathrm{g(dc)[k+1]}} = I^*_{\mathrm{g[k+1]}} \cdot V^*_{\mathrm{d[k+1]}}. \tag{6.9}$$

By defining the power reference for the resistor at the grid side filter as $P^*_{\mathrm{g(R_g)[k+1]}}$ (See Fig. 6.1), the power reference $P^*_{\mathrm{[k+1]}}$ (See Fig. 6.1) for the grid side predictive controller is

$$P^*_{\mathrm{[k+1]}} = P^*_{\mathrm{g(R_g)[k+1]}} + P^*_{\mathrm{g(dc)[k+1]}}, \tag{6.10}$$

where $P^*_{\mathrm{g(R_g)[k+1]}} = \frac{2R_{\mathrm{g}}}{3A^2}\{(P^*_{\mathrm{[k+1]}})^2 + (Q^*_{\mathrm{[k+1]}})^2\}$. Solving (6.10) we obtain the following

$$P^{\mathrm{calc}*}_{\mathrm{g[k+1]}} = \frac{3A^2}{4R_{\mathrm{g}}} - \sqrt{\frac{9A^4}{16R^2_{\mathrm{g}}} - \frac{3A^2}{2R_{\mathrm{g}}} \cdot (P^*_{\mathrm{g(dc)[k+1]}} + \frac{2R_{\mathrm{g}}}{3A^2} \cdot (Q^*_{\mathrm{[k+1]}})^2}. \tag{6.11}$$

Note here, for safety concerns, the grid side power reference has to be limited. To be more specific, the power reference $P^*_{[k+1]}$ assigned to the predictive power controller is defined by the following function

$$P^*_{[k+1]} = \begin{cases} P^{calc*}_{g[k+1]} & , \mid P^{calc*}_{g[k+1]} \mid \leq P^{max}_g \\ P^{max}_g & , P^{calc*}_{g[k+1]} > P^{max}_g \\ -P^{max}_g & , P^{calc*}_{g[k+1]} < -P^{max}_g. \end{cases} \tag{6.12}$$

By defining the maximum grid side power as $\|\vec{S}\|^{max}$ (obtained from the system hardware limits), the maximum admissible grid side active power is calculated by

$$P^{max}_g = \sqrt{\left(\|\vec{S}\|^{max}\right)^2 - \left(Q^*_{[k+1]}\right)^2}. \tag{6.13}$$

The structure overview of the proposed QC-DMPC is depicted in Fig. 6.2b.

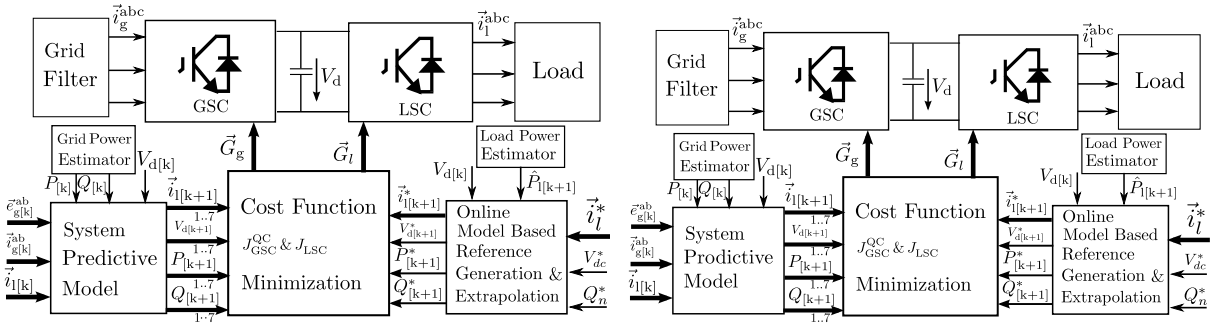

(a) The PI-DMPC scheme.

(b) The proposed QC-DMPC scheme.

Fig. 6.2: Control structure of the PI-DMPC and the proposed QC-DMPC schemes.

Remark 15 (Comparison of QC-DMPC and PI-DMPC schemes) *A primary comparison of the QC-DMPC and PI-DMPC methods is described as follows.*

(a) *For the QC-DMPC scheme, theoretically no big over- or undershoot of the DC-link voltage will happen, which is due to:* (i) *the reference DC-link voltage is generated by using a gradually-approaching manner (see Equation (6.5)). This leads to the* one-step-reference-value ($V^*_{d[k+1]}$ *in Equation (6.5))), which cannot be larger (when positive) or smaller (when negative) than the* general-reference-value (V^*_d *in Equation (6.5)).* (ii) *The power and current constraints are included inside the cost function. So when the constraints are fully respected (by choosing a big enough weighting factor), no over-limit charging and discharging current will happen. Since big voltage over- or undershoot can be damaging to the DC-link capacitors, which are usually one of the most vulnerable parts of a real power converter. From this aspect, the QC-DMPC scheme is more suitable when considering the life-span of the DC-link capacitors.*

(b) *The QC-DMPC scheme uses only one parameter N_s in the DC-link part; moreover, it can be chosen according to the specific charging or discharging current limit of the DC-link capacitor and the intended steps for reaching the DC-link voltage reference. This makes the tuning procedure considerably easier than PI-DMPC schemes.*

Time	PI-DMPC	QC-DMPC	**Resources**	PI-DMPC	QC-DMPC
T_1	40 ticks, 1 μs	40 ticks, 1 μs	Total Slices	2755	2792
T_2	1 tick, 25 ns	1 tick, 25 ns	Slice Registers	1690	1710
T_3	7 ticks, 175 ns	9 ticks, 225 ns	Slice LUTs	1838	1864
T_4	19 ticks, 475 ns	19 ticks, 475 ns	DSP48s	48	54
T_5	8 ticks, 200 ns	8 ticks, 200 ns	Block RAMs	0	0
T_s	50 μs	50 μs			
T_{mpc}	$\leq$ 2 μs	$\leq$ 2 μs			
T_{sleep}	$\geq$ 48 μs	$\geq$ 48 μs			

Table 6.1: FPGA design details of both schemes.

(c) *The calculation of the DC-link and grid-side active power reference values involves all of the system parameters. The correct value of the load side resistor is particularly important for the generated active power reference. Intuitively, the QC-DMPC scheme is more vulnerable to system parameter deviations. In terms of the computational efforts required, the QC-DMPC scheme is more demanding than the PI-DMPC scheme.*

(d) *The selections of weighting parameters is still an open question, but there are some rule-of-thumb. An "equal weighing" tuning method as is used in this paper is highly recommended due to its simplicity and effectiveness. "Equal weighting" means the targeted quantities are regarded as equally important, and the weighting factors for targeted quantities can be chosen with normalized value by*

$$\frac{\gamma_i}{i_n} = \frac{\gamma_p}{p_n}, \tag{6.14}$$

where γ_i, γ_p are the weightings for current and power, respectively.

But the weighting factors for the constraints can be chosen with values big enough (exact requirements depends on the data type of the digital controller employed), to assure all the constraints are respected.

6.2.3 FPGA implementation comparison

In this section, a FPGA-based platform (NI-CRIO reconfigurable system) is used to implement both control schemes. The implementation procedures, resource usage and the timing information are introduced in this section. Note that, for the subscribes, both x_n and x_g represent the grid/net side quantity of x.

The overview of the FPGA implementations for both schemes are depicted in Fig. 6.3, where different colors represent different calculation times. FPGA design procedure is introduced hereafter following the respective duration time of $T_1, T_2..T_5, T_{sleep}$ in Fig. 6.3.

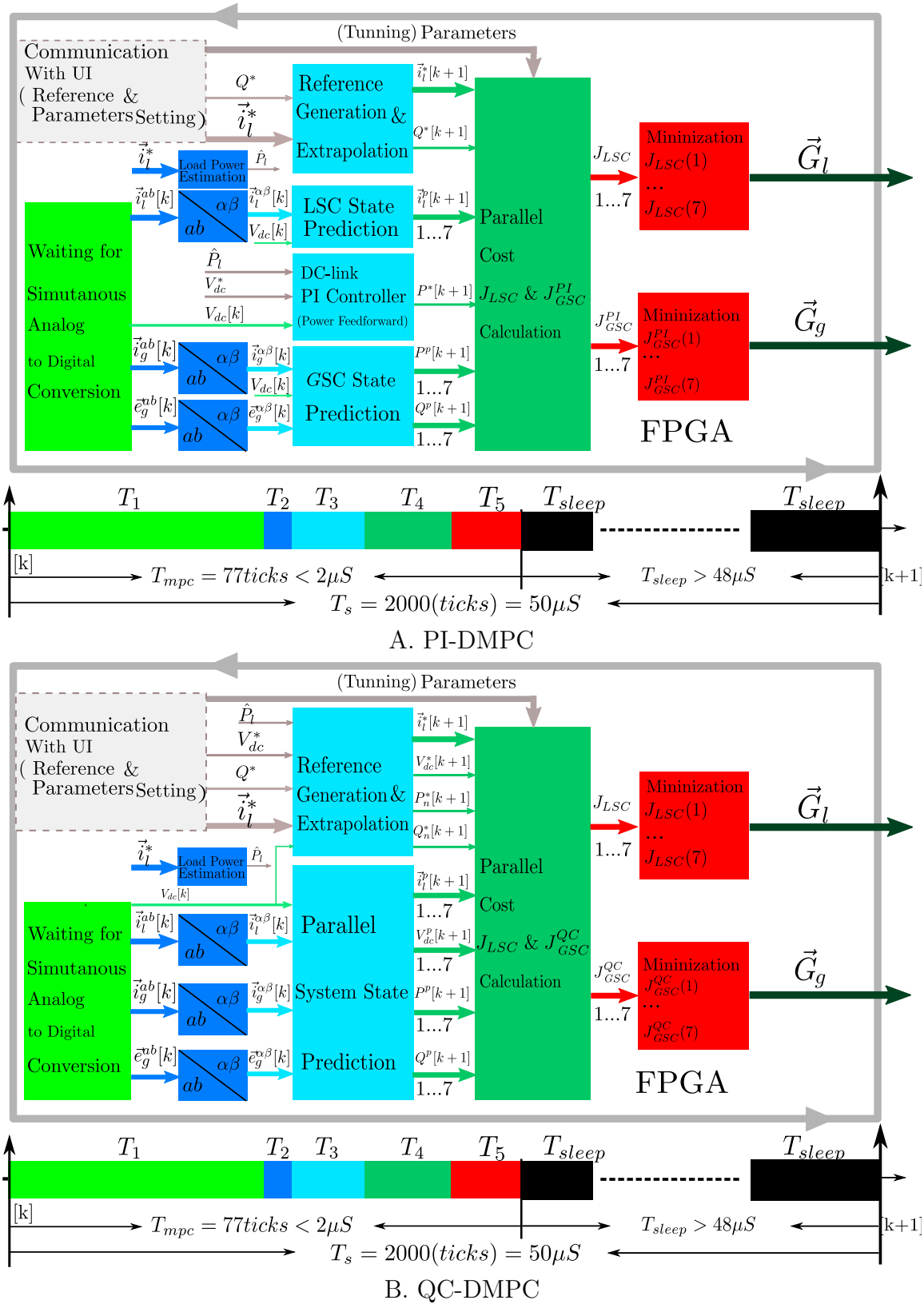

Fig. 6.3: FPGA implementation overview of PI-DMPC and QC-DMPC schemes.

During T_1 (40 ticks, i.e., 1μs)[1] : For both PI-DMPC and QC-DMPC, the analog-to-digital conversion (ADC) interface subroutine is executed and the feedback signals are obtained.

During T_2 (1 tick): Measured signals are transformed into $\alpha\beta$ frame, using a so-called Single-Circle-Timed-Loop (SCTL) technique in parallel running subroutines; meanwhile the subroutine of load side power estimation is executed in parallel, for both PI-DMPC and QC-DMPC (See Fig. 6.3).

During T_3 (7 ticks for PI-DMPC; **9 ticks** for QC-DMPC)**:** *(i)* For PI-DMPC, the reference generation (extrapolation), load side state prediction, DC-link PI controller and grid side state are implemented in parallel. Note that, the heaviest parts in terms of computation are the load and grid state predictions which run in **7 ticks**. The PI controller itself only runs for **1 tick** but a waiting routine (**6 ticks**) is added for synchronizing purpose; *(ii)* For QC-DMPC, the system state prediction and reference generation (extrapolation) subroutines are implemented in parallel and the time duration is **9 ticks**.

During T_4 and T_5 (19 ticks): For both schemes the cost calculation (T_4) and minimization (T_5) parts are implemented in parallel in the same way. For both, the durations of these two steps (cost calculation and minimization) are $T_4 = 19$ ticks and $T_5 = 8$ ticks.

During T_{sleep} (1925 ticks for PI-DMPC; **1923 ticks** for QC-DMPC)**:** For both schemes, this part represents the period from sending out the gate signals to the beginning of a new control interval.

The calculation time is quite small (77 ticks for QC-DMPC, and 75 ticks for PI-DMPC) compared to the whole sampling interval $T_s = 2000$ ticks. Therefore the computation compensation is not necessary. Table 6.1 summarizes the FPGA design details.

6.2.4 Evaluations and analysis

6.2.4.1 Simulation evaluations

To verify the effectiveness of the proposed QC-DMPC scheme and also the DC-link voltage control comparison between the presented QC-DMPC and PI-DMPC (a conditional integration anti-windup PI strategy, for which see [10] and the references therein, is used for a fair comparison) schemes, a simulative comparison in Matlab/Simulink environment is performed. The weighting parameters in equations (6.1a), (6.1b) and (6.4) are set using the equal-weighting method (See Eq. (6.14)) as: $\gamma l = 5000, \gamma_g = 5000; \gamma_{V_d}^{QC} = \frac{V_d}{\|\vec{S}\|^{max}}, \gamma_g = 5000$. Note that, for a fair comparison, the parameters of the PI controller are tuned in a trial-and-error manner to reach a similar rising-time[2] of T_r ($T_r \approx 0.22$s, See Fig. 6.4 (c) and (d)) as the QC-DMPC, and all the other conditions are set the same. The other parameters of the simulation are collected in Table 6.2.

The simulation scenario is as follows: within the interval [0, 0.08]s, the load side current reference has a frequency of 50Hz and a magnitude of 10 [A] (peak). At $t = 0.03$s, DC-link

[1] The FPGA top-level clock is 40MHz, and one 1 tick $= \frac{1}{40\text{MHz}} = 25$ns

[2] Here instead of using the definition for "rising time" on the text book, the time for the state to reach 100% of its status value is regarded as the"rising time" here for easing the measuring accuracy.

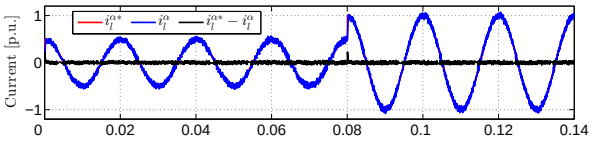

(a) Load side current with PI-DMPC (base value 20A)

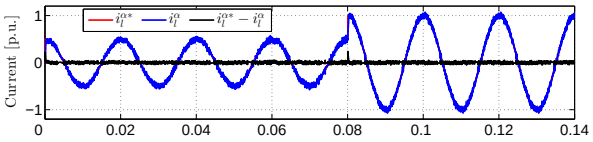

(b) Load side current with QC-DMPC (base value 20A)

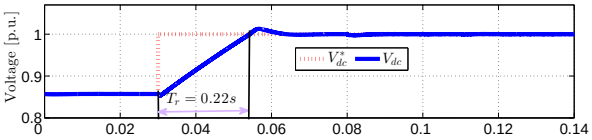

(c) DC-Link voltage with PI-DMPC (base value 700V)

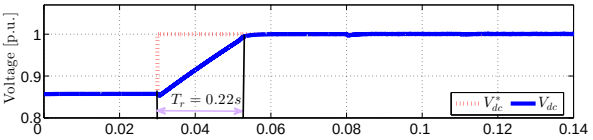

(d) DC-Link voltage with QC-DMPC (base value 700V)

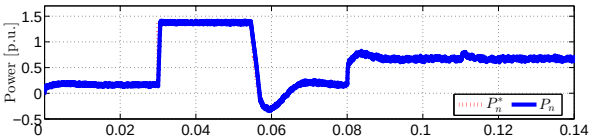

(e) Grid side power with PI-DMPC (base value 5000VA)

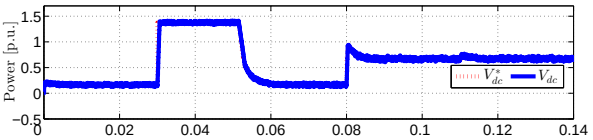

(f) Grid side power with QC-DMPC (base value 5000VA)

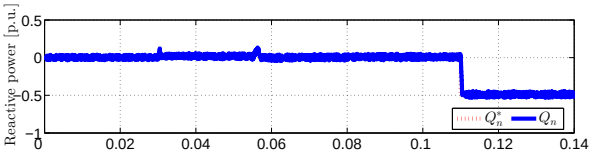

(g) Reactive power with PI-DMPC (base value 5000VA)

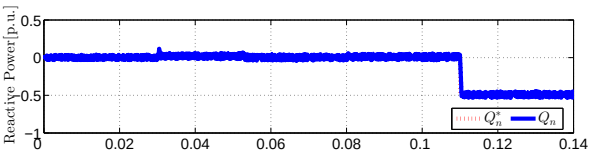

(h) Reactive power with QC-DMPC (base value 5000VA)

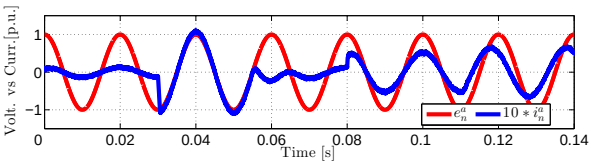

(i) Grid volt./curr. with PI-DMPC (base value 311V/20A)

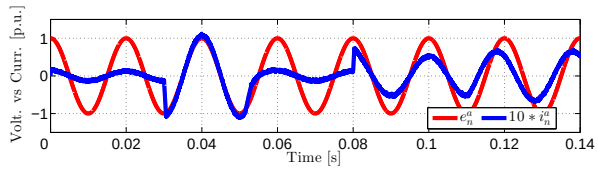

(j) Grid volt./curr. with QC-DMPC (base value 311V/20A)

Fig. 6.4: Simulation data: performance comparison with both PI-DMPC and QC-DMPC.

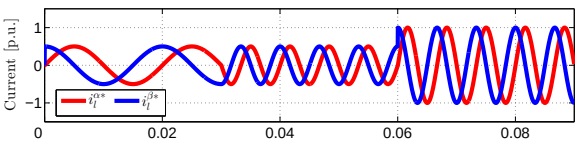

(a) Load side current (base value, 20A)

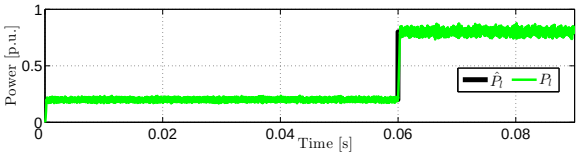

(b) Load side power estimation (base value, 8000VA)

Fig. 6.5: Simulation data: Load side power estimation during load current changes.

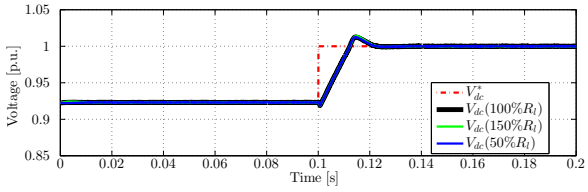

(a) V_{d} with PI-DMPC (base value, 650V).

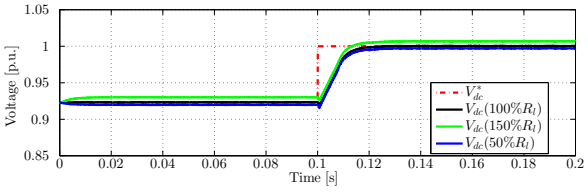

(b) V_{d} with QC-DMPC (base value, 650V).

Fig. 6.6: Simulation data: Robustness to system parameter (load resistor R_l) variation.

voltage reference steps up from 600 [V] to 700 [V](base value), whereas at $t = 0.08$ [s], the current reference magnitude changes to 20 [A]. The reactive power changes from 0var to -3000 [var] at $t = 0.11$ [s]. The effectiveness of the proposed QC-DMPC scheme is illustrated in (b), (d), (f), (h) and (j) of Fig. 6.4. The two schemes demonstrate similar performance for the load side current tracking (See Fig. 6.4 (a) and(b)). The power tracking performances during the steady state for both schemes are also similarly good (See Fig. 6.4 (e) to (f)). However, the QC-DMPC scheme outperforms the PI-DMPC scheme in controlling the the DC-link voltage, active power and grid side current during the transient state (See Fig. 6.4 (c) to (j)). For the PI controller, a typical second-order phenomenon is seen with noticeable over- and undershoot magnitudes (See the transient phases (around $t = 0.6$ and $t = 0.8$ [s]) of Fig. 6.4 (d) and (f)). However, as expected, no over- or undershoot is observed for the QC-DMPC scheme.

Parameters	simulation	experiment
Grid-Side Phase Voltage $\vec{e}_{\mathrm{g}}^{\mathrm{abc}}$ [V] (peak)	250	70
Grid-Side Voltage Frequency ω_{g} [rad/s]	100π	100π
Grid-side Reactor Resistor R_{g} [Ohm]	$1.56e-3$	$1.56e-3$
Grid-side Reactor Inductance L_{g} [H]	$16e-3$	$16e-3$
DC-link Capacitor C [uF]	1100	1100
Load-side Inductance L_l [H]	10e-3	10e-3
Load-side Resistor R_l [Ohm]	10	10
Sampling Frequency f_s [kHz]	20	20

Table 6.2: System configuration.

6.2.4.2 Experimental evaluations

The load side power estimation is an essential step for the proposed QC-DMPC scheme, because the load side power reflected at the DC-link part is required for calculating $I^*\mathrm{g}[\mathrm{k}+1]$ (See Eq. (6.7)). Simulation results in Fig. 6.5 confirm the effectiveness of the proposed load side power estimation. The testing scenario is as follows: within the interval [0, 0.03] [s], the load side current reference has a frequency of 50Hz and a magnitude of 10 [A] (peak). At $t = 0.3$ [s], it changes from 50 to 150 [Hz], then at $t = 0.06$ [s] the magnitude changes to 20 [A] (peak) (See Fig. 6.5(a)). Clearly, the load power estimation is working accurately during both magnitude and frequency change (See Fig. 6.5(b)).

The robustness under parameter (load side resistor) variations of the two schemes is also compared in the simulation. The results in Fig. 6.6 emphasize that PI-DMPC is less sensitive to parameter variation than QC-DMPC: for QC-DMPC, when changing the load side resistor (to 150% and 50% of its measured value), noticeable DC-link voltage steady state errors are seen (See Fig. 6.6 (b)); while for PI DMPC, neither transient nor steady state performances are (evidently) affected by changing R_l (See Fig. 6.6 (a)).

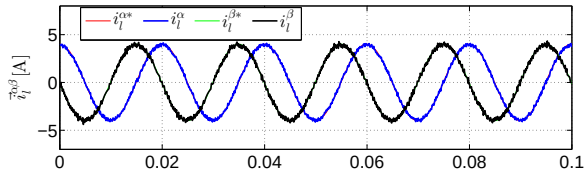

(a) Load side current: steady state performance

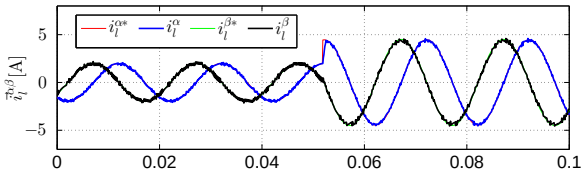

(b) Load side current: transient state performance

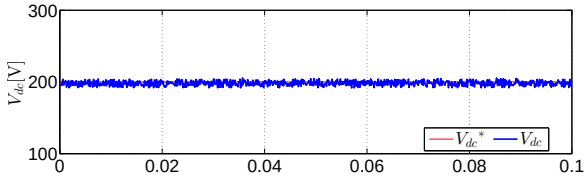

(c) DC-Link voltage control: steady state performance

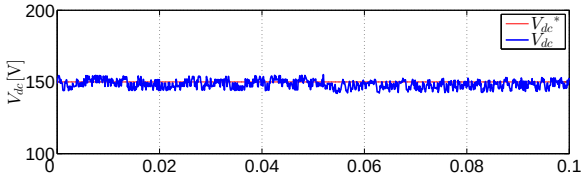

(d) DC-Link voltage control: transient state performance

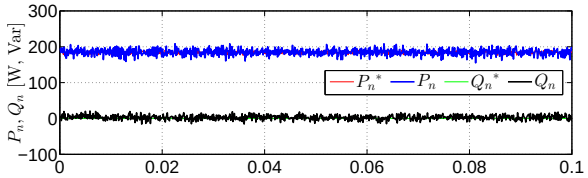

(e) Grid side power: steady state performance

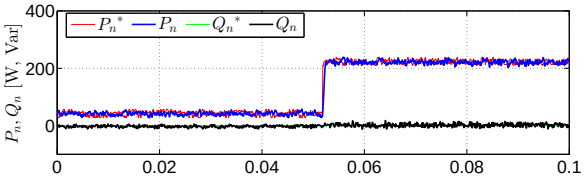

(f) Grid side power: transient state performance

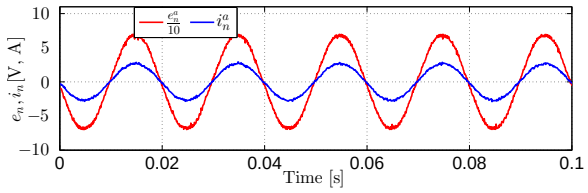

(g) Grid side voltage and current: steady state performance

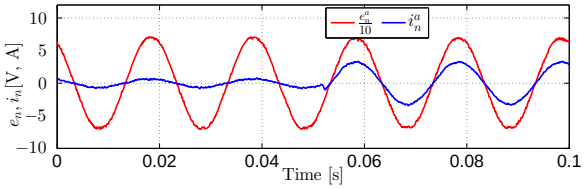

(h) Grid side voltage and current: transient state performance

Fig. 6.7: Experimental results: performance of QC-DMPC for a Back-to-Back converter.

Experimental verification of the proposed QC-DMPC scheme and its performance comparison with PI-DMPC are carried out on a lab-constructed test bench (See Fig.2.9 presented in Chp. 2). For the test bench, the only difference from the topology depicted in Fig. 6.1 is that, a three-phase variac (H in Fig. 2.9) is added between the power line and the grid side filter for safety concerns. The parameters in experiments are collected in Table 6.2. Note that, for all test scenarios the reactive power reference Q^* is set to be 0 [var] for a unit power factor operation.

6.2.4.3 Experimental verification of the proposed QC-DMPC

Fig. 6.7 illustrates the steady state and dynamic performances of the proposed QC-DMPC control scheme. The load side current tracking performance during both steady state and transient phases are with fast dynamics and small tracking errors (See Fig. 6.7 (a) and (b)). The DC-link control performances are shown in Fig. 6.7 (c) and (d). In (d) the DC-link voltage is almost not affected during the load change. Grid side active and reactive

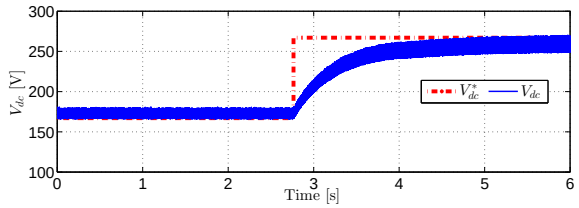

(a) Step changing of DC-link voltage: $N_s = 200$

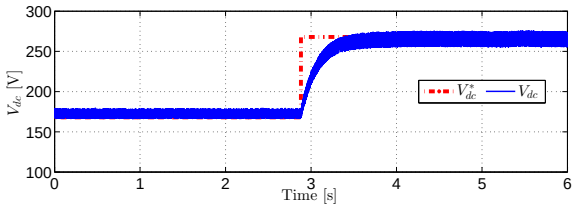

(b) Step changing of DC-link voltage: $N_s = 160$

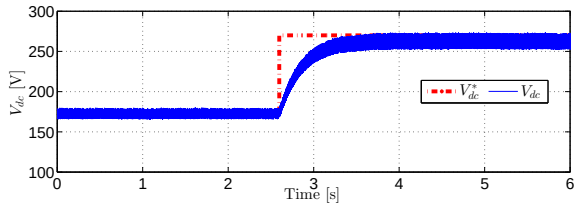

(c) Step changing of DC-link voltage: $N_s = 120$

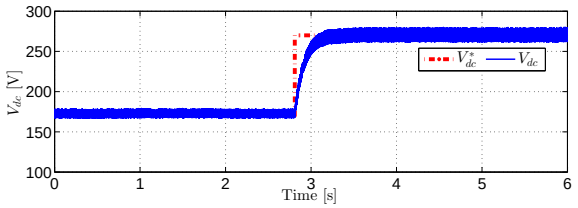

(d) Step changing of DC-link voltage: $N_s = 100$

Fig. 6.8: Experimental results: effects of N_s for QC-DMPC.

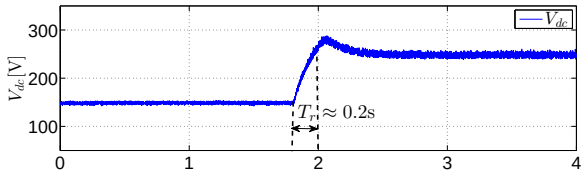

(a) DC-link voltage with PI-DMPC

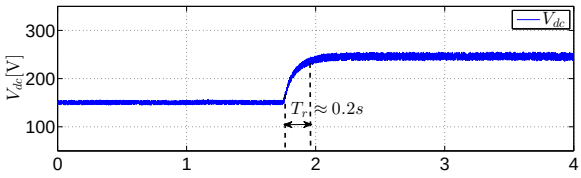

(b) DC-link voltage with QC-DMPC

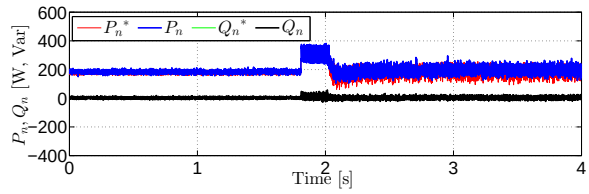

(c) Grid side Power with PI-DMPC

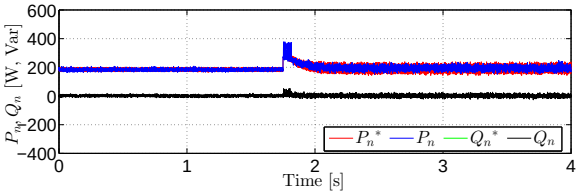

(d) Grid side Power with QC-DMPC

Fig. 6.9: Experimental results: dynamic performance comparison of PI-DMPC and QC-DMPC.

power control performances are shown in Fig. 6.7 (e) and (f). Especially, nice decoupling performance of using QC-DMPC is illustrated in Fig. 6.7 (f): At around $t = 0.052$ [s], a step change happens to the active power due to the load side current change, and the reactive power is almost not affected. The last pair of Fig. 6.7 illustrate the grid side current and voltage in phase-a: A unit power factor and also a nice dynamic performance are achieved (See Fig. 6.7 (f) at around $t = 0.052$ [s], grid side current immediately changes in accordance with the load change).

Fig. 6.8 illustrates the effects of N_s to the DC-link voltage control in QC-DMPC scheme: As N_s decreases, the dynamics, i.e. the rising time, for the DC-link change is getting shorter. This further confirms that the dynamics of the DC-link voltage is controllable by changing N_s.

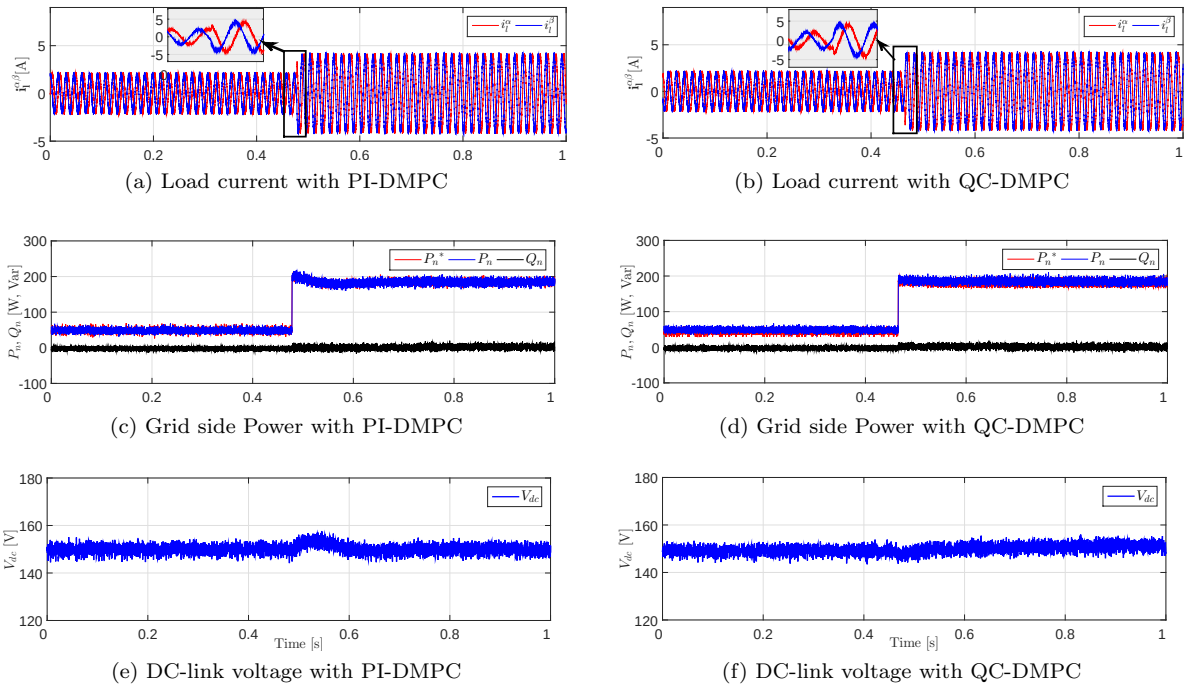

(a) Load current with PI-DMPC

(b) Load current with QC-DMPC

(c) Grid side Power with PI-DMPC

(d) Grid side Power with QC-DMPC

(e) DC-link voltage with PI-DMPC

(f) DC-link voltage with QC-DMPC

Fig. 6.10: Experimental results: dynamic performance comparison of PI-DMPC and QC-DMPC.

6.2.4.4 Experimental comparison of QC-DMPC and PI-DMPC

Note that, a constant value of N_s is chosen ($N_s = 100$) for QC-DMPC scheme, and the PI controller parameters for PI-DMPC scheme are tuned in a trial-and-error manner to reach the same rising time ($T_r \approx 0.2$ [s], See Fig. 6.9 (a) and (b)) as the QC-DMPC scheme. Within the PI-DMPC scheme a *conditional integration anti-windup* strategy as an industrial standard (See e.g., [10] and the reference therein) is used. A first-order low pass filter with a cutoff frequency of 1000 [Hz] is added to the DC-link voltage measurement for both controllers for a fair *grid current* performance comparison (Fig.11 and Fig.12). All the other operation conditions are kept the same.

The performance comparison of the DC-link voltage control is shown in Fig. 6.9. The test scenario is as follows: at $t \approx 1.8$ [s] the DC-link voltage reference is changed from 150 to 250 [V]; the load current is kept at 4 [A]. No overshoot occurs, but a fast dynamic (with $T_r \approx 0.2$ [s]) is achieved when using QC-DMPC (See Fig. 6.9 (b)) while a considerable overshoot showing a typical second order phenomenon is seen when using PI-DMPC (See Fig. 6.9 (a)). Notably, for the PI-DMPC scheme, the power ripples also increase in comparison to the QC-DMPC scheme (See Fig. 6.9 (c) and (d) for time interval of [2, 4] [s]).

Fig. 6.10 illustrates the DC-link control performance comparison in the presence of load disturbances. The test scenario is as follows: for the time range of [0, 0.48] [s], the load side current reference is set at a magnitude of 2 [A], and at around $t = 0.48$ [s] it changes to 4 [A] (See Fig. 6.10 (a) and (b)); while for all $t \in$[0, 1] [s] the DC-link voltage

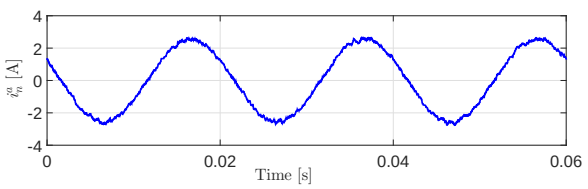

(a) Grid side current with PI-DMPC

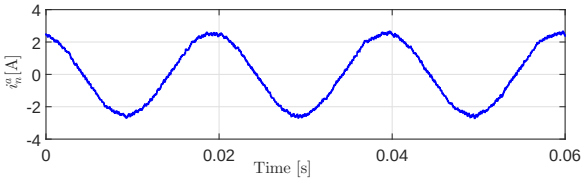

(b) Grid side current with QC-DMPC

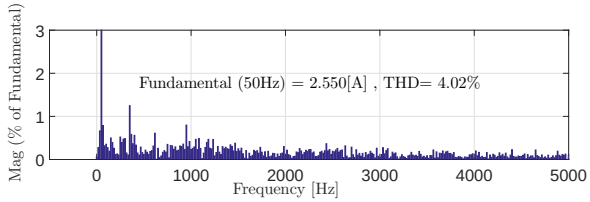

(c) Grid side current spectrum and THDs with PI-DMPC

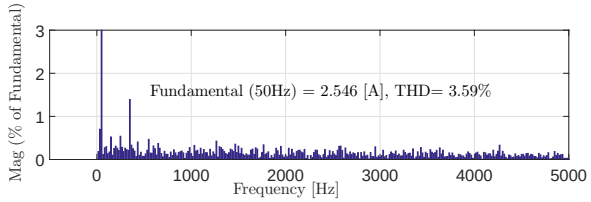

(d) Grid side current spectrum and THDs with QC-DMPC

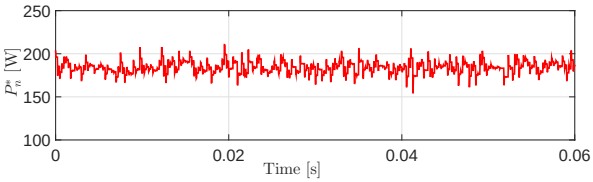

(e) Grid side active power reference with PI-DMPC

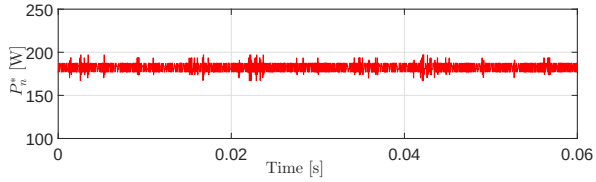

(f) Grid side active power reference with QC-DMPC

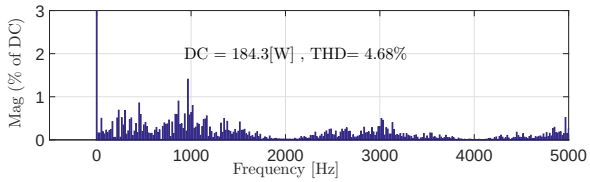

(g) Spectrum and THDs of P^* with PI-DMPC

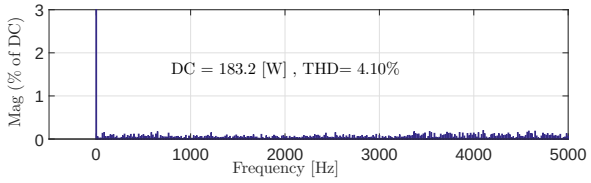

(h) Spectrum and THDs of P^* with QC-DMPC

Fig. 6.11: Experimental results: THD comparison of PI-DMPC and QC-DMPC for grid side current and active power reference.

reference is set to be 150 [V]. The DC-link voltage is almost not affected for QC-DMPC when the load is changed (See Fig. 6.10 (f)); this is due to the dynamic power reference which is immediately generated accordingly and tracked by the inner predictive control loop (See Fig. 6.10 (d)). However, a slight fluctuation occurs in the DC-link voltage and grid side active power in the PI-DMPC scheme (See Fig. 6.10 (e) and (c)) due to the slight mismatching of the load and grid side power with using PI DC-link controller.

In Fig. 6.11 (a) to (d) the grid side current control comparison of PI-DMPC and QC-DMPC are given. The Total Harmonic Distortions (THDs) of the grid side current with QC-DMPC (3.59%, See Fig. 6.11 (b) and (d)) outperforms PI-DMPC (4.02%, See Fig. 6.11 (a) and (c)). This is primarily due to the differences of the active power reference generation schemes involved. Therefore, in Fig. 6.11 (e) to (h) the spectrum and THDs of the active power references for PI-DMPC and QC-DMPC are illustrated. The active

power reference ripples in the QC-DMPC scheme are evidently smaller. The active power reference THDs for QC-DMPC is 4.10% and 4.68% for PI-DMPC (See Fig 6.11 (h), (g)).

6.2.4.5 Verification of the robustness under parameters variations.

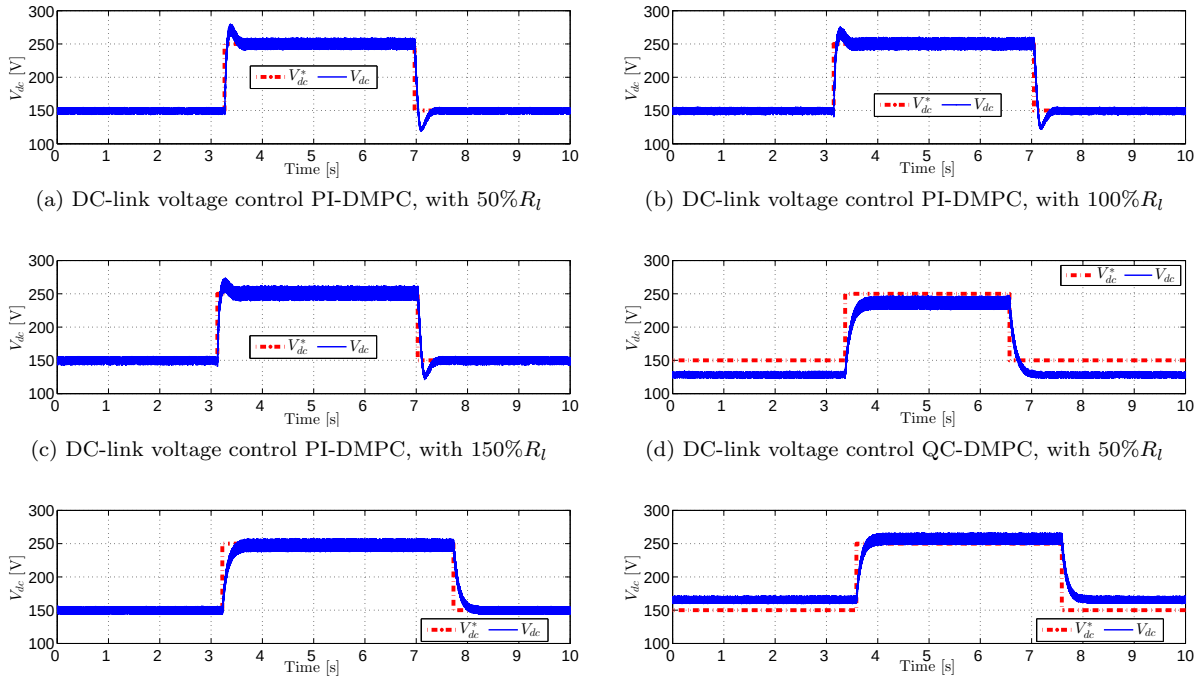

(a) DC-link voltage control PI-DMPC, with 50%R_l

(b) DC-link voltage control PI-DMPC, with 100%R_l

(c) DC-link voltage control PI-DMPC, with 150%R_l

(d) DC-link voltage control QC-DMPC, with 50%R_l

(e) DC-link voltage control QC-DMPC,with 100%R_l

(f) DC-link voltage control QC-DMPC, with 150%R_l

Fig. 6.12: Experimental results: Robustness to system parameter (load resistor R_l) variation.

Experimental results shown in Fig. 6.12 illustrate the robustness of the DC-link voltage control to load parameter (load resistor R_l) variation for the two schemes. As expected, the PI-DMPC scheme outperforms the QC-DMPC scheme when the value of load side resistor used in the controllers is changed to 150% or 50% of its measured value: QC-DMPC shows noticeable constant steady state errors (See Fig. 6.12 (d), (f)), while the steady state performance of PI-DMPC scheme is almost not affected (See Fig. 6.12 (a), (c)).

Remark 16 (On DC-link steady state tracking error of the QC-DMPC) *For QC-DMPC scheme, two sources may lead to DC-link voltage tracking errors in steady state:* (i) *modeling errors, especially the system parameter variations (like the load resistor parameter variation as is illustrated in this work);* (ii) *actual efficiency of the power converter. While developing the dynamic reference an ideal efficiency (i.e., 100% power converter efficiency) is assumed, so if in practice (especially for high power operation situations) the power converter efficiency is lower than 100%, evident DC-link voltage tracking errors can be observed.*

6.3 A revised QC-DMPC for back-to-back power converter with PMSG

6.3.1 Introduction

The Quasi-Centralized DMPC (QC-DMPC) scheme presented in Sec. 6.2 may serve as an alternative for controlling back-to-back power converter PMSG wind turbine systems. Compared with centralized DMPC scheme, instead of 64, 8 enumerations are required to minimize the cost function; the control complexity and computational load for QC-DMPC method are drastically reduced. Compared with the classical DC-link PI controller based control scheme, the QC-DMPC technique shows nice characters such as: easy to tune, fast and controllable DC-link dynamics, no extra PI DC-link controller, etc. However, as analyzed in Remark 16 and Fig. 6.12, model errors and imperfect power efficiency lead to evident steady status tracking offset of the DC-link voltage. Also, the cost-enumeration concept of the classical DMPC, which is used in [10], leads to heavy computational efforts and FPGA resource cost.

To deal with this, a revised quasi-centralized direct model predictive control (RQC-DMPC) scheme for back-to-back converter PMSG wind turbine systems is further proposed in this section. With the proposed (RQC-DMPC) scheme, the DC-link voltage is directly controlled by a grid side predictive controller with a flexibly designed cost function using a revised dynamic reference generation concept. Its steady status tracking errors are eliminated. To reduce the computational efforts of the classical scheme, the computational efficient concept introduced in Chp. 5 is utilized. The proposed scheme is again implemented on an entirely FPGA based platform. The effectiveness of the proposed method is verified through experimental data. DC-link control performance comparison with classical Proportional-Integration (PI) controller based methods and the QC-DMPC scheme under different scenarios are also experimentally investigated. The results emphasize the improvement of the proposed RQC-DMPC scheme.

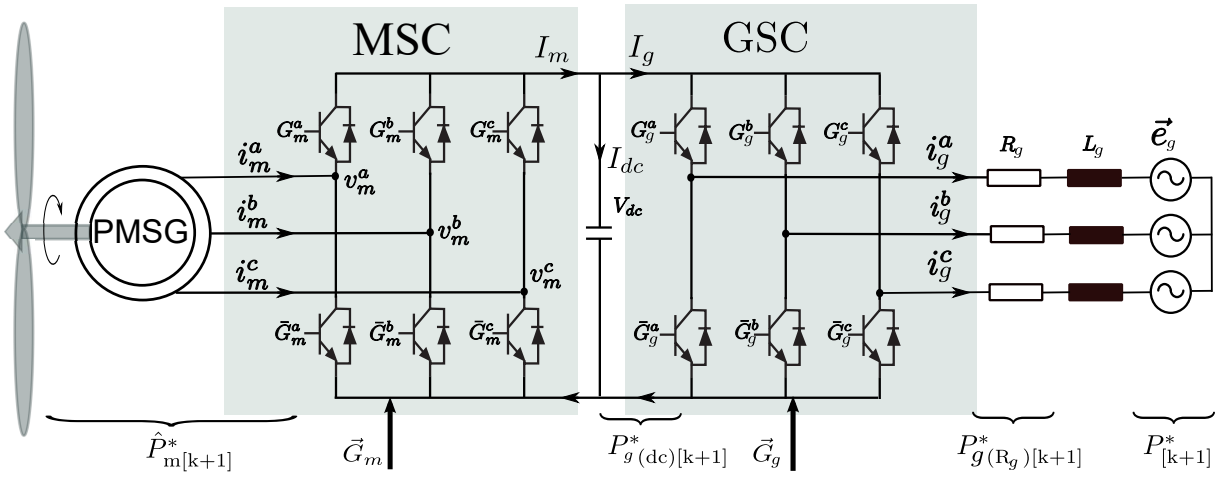

Fig. 6.13: Simplified power circuit of a voltage source Back-to-Back power converter PMSG wind turbine system with RL filter.

6.3.2 Classical PI-DMPC and QC-DMPC controllers

The main control objectives for a back-to-back converter PMSG wind turbine system shown in Fig. 6.13 are: Co_1: Torque reference T_e^* (generated by a maximum-power-point-tracking (MPPT) controller) tracking, Co_2: DC-link voltage reference V_d^* tracking, and Co_3: grid side power reference $\vec{S}^*$ tracking. For both PI-DMPC and newly reported QC-DMPC [10] scheme as in Sec. 6.2, the machine side control objective is the same, i.e., T_e^* tracking. Therefore, for both methods, the same machine side cost function to achieve Co_1 is used, which is

$$J^\mathrm{m}_\mathrm{DMPC}(\vec{u}_\mathrm{m}) = \underbrace{\gamma_{T_\mathrm{e}}\|T^*_{\mathrm{e[k+1]}} - T_{\mathrm{e[k+1]}}(\vec{u}_\mathrm{m})\|}_{=:J(T_\mathrm{e})} + \underbrace{\gamma_{i^\mathrm{d}_\mathrm{m}}\|i^\mathrm{d}_{\mathrm{m[k+1]}}(\vec{u}_\mathrm{m})\|}_{=:J(i^\mathrm{d}_\mathrm{m})} + \underbrace{\begin{cases} 0 & ,\|\vec{i}^{\,\mathrm{dq}}_{\mathrm{m[k+1]}}\| \le I^\mathrm{max}_\mathrm{m} \\ \gamma^{\mathrm{i_m}}_\mathrm{CS} & ,\|\vec{i}^{\,\mathrm{dq}}_{\mathrm{m[k+1]}}\| > I^\mathrm{max}_\mathrm{m} \end{cases}}_{=:\mathrm{J}^\mathrm{m}_{\mathrm{CS}_1}} + \underbrace{\begin{cases} 0 & ,\|(T_{\mathrm{e[k+1]}}\| \le T^\mathrm{max}_\mathrm{e}, \\ \gamma^{\mathrm{T_e}}_\mathrm{CS} & ,\|(T_{\mathrm{e[k+1]}}\| > T^\mathrm{max}_\mathrm{e}. \end{cases}}_{=:\mathrm{J}^\mathrm{m}_{\mathrm{CS}_2}} \tag{6.15}$$

where, $\vec{i}^{\,\mathrm{dq}}_{\mathrm{m[k+1]}}$ and $T_{\mathrm{e[k+1]}}$ are predicted by Equation (2.42). Note that $J(i^\mathrm{d}_\mathrm{m})$ is used to maintain a constant flux and to achieve the maximum torque/current control. $\mathrm{J}^\mathrm{m}_{\mathrm{CS}_{1,2}}$ are the constraints to restraint the current and torque within their limits of $I^\mathrm{max}_\mathrm{m}$ and $\mathrm{T}^\mathrm{max}_\mathrm{e}$, respectively; $\|\vec{i}^{\,\mathrm{dq}}_{\mathrm{m[k+1]}}\| = \sqrt{(i^\mathrm{d}_{\mathrm{m[k+1]}})^2 + (i^\mathrm{q}_{\mathrm{m[k+1]}})^2}$.

However, based on a dynamic reference generation concept, the DC-link and grid side control is designed within one centralized predictive voltage and power controller for the QC-DMPC method. It is therefore different from the PI-DMPC method, where an extra outer loop PI based DC-link controller is used to generate the active power reference for the inner predictive power controller, thereby controlling the DC-link voltage and grid side power, i.e., to achieve $\mathrm{Co}_{2,3}$.

The DC-link and grid side power control part for the PI-DMPC scheme and the QC-DMPC scheme are re-visited briefly in the following.

6.3.2.1 Grid side and DC-link voltage control of PI-DMPC Scheme

Two separate controllers namely: a PI based DC-link controller and an inner predictive power controller are used to achieve $\mathrm{Co}_{2,3}$ (See Fig. 6.14. For the inner predictive power controller, a cost function to achieve Co_3 is designed as

$$J^\mathrm{n,PI}_\mathrm{DMPC}(\vec{u}_\mathrm{g}) = \underbrace{\|P^*_{\mathrm{[k+1]}} - P_{\mathrm{[k+1]}}(\vec{u}_\mathrm{g})\|}_{=:\mathrm{J(P)}} + \underbrace{\|Q^*_{\mathrm{[k+1]}} - Q_{\mathrm{[k+1]}}(\vec{u}_\mathrm{g})\|}_{=:\mathrm{J(Q)}} + \underbrace{\begin{cases} 0 & ,\|S_{\mathrm{[k+1]}}\| \le S^\mathrm{max}, \\ \gamma^{S}_{CS} & ,\|S_{\mathrm{[k+1]}}\| > S^\mathrm{max}, \end{cases}}_{=:\mathrm{J}^\mathrm{n,PI}_\mathrm{CS}}. \tag{6.16}$$

where $||S_{[k+1]}|| = \sqrt{(P_{[k+1]})^2 + (Q_{[k+1]})^2}$. $J_{CS}^{n,PI}$ is used to restrain the grid side power within its limit of S^{max}.

The active power reference is produced by an outer DC-link PI controller. Depending on whether the machine side power is fed-forward or not, the DC-link PI controller can be designed as two cases of C − I and C − II:

$$P^*_{[k]} = \begin{cases} V_{d[k]}\mathcal{Z}^{-1}\{T_{PI}(Z) * (V^*_{d[k]} - V_{d[k]})\}, & C-I \\ V_{d[k]}\mathcal{Z}^{-1}\{T_{PI}(Z) * (V^*_{d[k]} - V_{d[k]})\} + \hat{P}_{m[k]}, & C-II \end{cases} \tag{6.17}$$

where $T_{PI}(Z) = \frac{K_p + K_i - K_p Z^{-1}}{1 - Z^{-1}}$ is the Z format of a PI controller, and

$$\hat{P}_{m[k]} = T^*_{e[k]} \cdot \omega_{m[k]} \tag{6.18}$$

is the estimated active power of the machine side. The controller structure of PI-DMPC is given in Fig. 6.14 A.

6.3.2.2 Grid side and DC-link control using QC-DMPC Scheme

The DC-link voltage and grid side power control, i.e., $Co_{2,3}$, are realized with one single predictive controller for the QC-DMPC scheme. An extra DC-link voltage control term is included inside the cost function (See (6.19)).

$$J^{g,QC}_{DMPC}(\vec{u}_g) = \underbrace{\|P^*_{[k+1]} - P_{[k+1]}(\vec{u}_g)\|}_{=:J(P)} + \underbrace{\|Q^*_{[k+1]} - Q_{[k+1]}(\vec{u}_g)\|}_{=:J(Q)} + \underbrace{\gamma_{V_{dc}}|V^*_{dc} - V_{dc[k+1]}|}_{=:J(V_d)} + \underbrace{\begin{cases} 0 & , ||S_{[k+1]}|| \le S^{max}, \\ \gamma^S_{CS} & , ||S_{[k+1]}|| > S^{max}. \end{cases}}_{=:J^n_{CS}} \tag{6.19}$$

Note that, V^*_{dc} in (6.19) is the generated "one-step" reference using the *general reference voltage* $V^*_{d,\infty}$ (the set value) with a gradually-approaching manner [10] as Eq. (6.5)

Defining the power reference for the resistor of the grid side filter as $P^*_{g(R_g)[k+1]}$ and the power reference for the DC-link on the grid side as $P^*_{g(dc)[k+1]}$ (See Fig. 6.13), the power reference $P^*_{[k+1]}$ for the grid side predictive controller is therefore can be calculated, following the similar steps as presented in Sec. 6.2.2.2.2, as Eq. (6.11). For this PMSG system, the controller structure of QC-DMPC is given by Fig. 6.14 B.

Remark 17 (Theoretical interpretation of the DC-link tracking bias) *It can be seen from Sec. 6.3.2.2, for QC-DMPC method the development of the power reference to achieve both the DC-link and grid side active power control requires an accurate system model and a power-loss conversion assumption. More specifically:*

(a) To calculate the reference power through $P^*_{[k+1]} = P^*_{g(R_g)[k+1]} + P^*_{g(dc)[k+1]}$, *where* $P^*_{g(R_g)[k+1]} = \frac{2R_g}{3A^2}\left\{(P^*_{[k+1]})^2 + (Q^*_{[k+1]})^2\right\}$, *implies that, a perfect power conversion efficiency of the grid side power converter is assumed;*

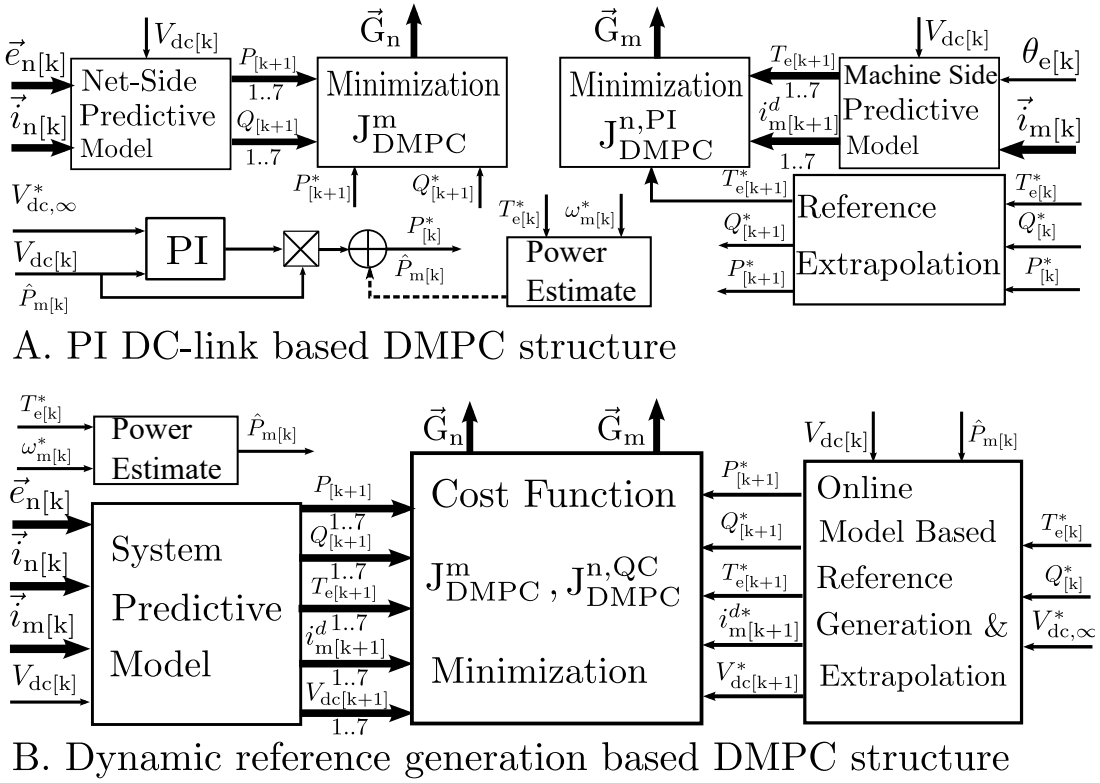

Fig. 6.14: Control structure of PI-DMPC and QC-DMPC schemes.

(b) Eq. (6.7), where $\hat{I}^*_{\mathrm{m(dc)[k+1]}} = \frac{\hat{P}_{\mathrm{m[k+1]}} + \hat{P}_{\mathrm{m[k]}}}{V^*_{\mathrm{dc[k+1]}} + V^*_{\mathrm{dc[k]}}}$*, contains the assumption that the load/machine side conversion is power loss-less and requires also that the load/machine side power estimation is accurate and has no time delay.*

Therefore, only both conditions (a) and (b) holding true will the calculated power reference in Eq. (6.11) lead to a bias-less DC-link tracking. However, in practice conditions (a) and (b) can hardly be guaranteed.

6.3.2.3 The proposed RQC-DMPC

Known from Sec. 6.3.2.2, to generate the active power reference, almost all the system parameters are involved by the QC-DMPC scheme. Especially, a perfect power converter efficiency (lossless power conversion) is assumed during the calculation for both the currents and power references. Therefore, as discussed in last section, the parameter variations and an imperfect power converter efficiency will lead to biased DC-link voltage tracking. To conquer this, a revised QC-DMPC method is proposed (named as RQC-DMPC in the following) in this work. Moreover, to address the heavy calculation efforts required by the classical DMPC concept, the computational efficient scheme as introduced in Chp. 5 is incorporated into the proposed RQC-DMPC method. Details are given in the following sections.

6.3.3 Revised QC-DMPC without DC-link voltage bias

One of the evident demerits for the PI based scheme is that, when a transient reference with a *big magnitude difference* from its previous value is newly given, due to the integration effect, an (evident) over-/undershoot will be observed. Even there is an anti-windup scheme. However, the integration term will on the other hand eliminate the infinite (small) tracking errors. Inspired by these, an extra bias elimination term is added to the power reference after the magnitude difference between the newly set reference and the real voltage is getting small, i.e.,

$$P^{\mathrm{RQC}*}_{[\mathrm{k+1}]} = P^{*}_{\mathrm{n(R_g)[k+1]}} + P^{*}_{\mathrm{n(d)[k+1]}} + P^{*}_{\mathrm{comp[k+1]}}, \text{ where,}$$

$$P^{*}_{\mathrm{comp[k+1]}} = \begin{cases} 0 & , k \leq N_s, \\ \lambda \sum\limits_{k=N_s}^{\infty} (V^{*}_{\mathrm{d},\infty} - V_{\mathrm{d[k]}}) & , k > N_s. \end{cases} \tag{6.20}$$

where $\lambda(>0)$ is the tuning parameter. Considering the drawbacks of a pure integration in practice, a Low Pass Filter (LPF) is used and therefore the term $P^{*}_{\mathrm{comp[k+1]}}$ is calculated as

$$P^{*}_{\mathrm{comp[k+1]}} = \begin{cases} 0 & , k \leq N_s, \\ \lambda \frac{1-Z^{-1}}{1-\alpha Z^{-1}} (V^{*}_{\mathrm{dc},\infty} - V_{\mathrm{d[k]}}) & , k > N_s. \end{cases} \tag{6.21}$$

Note that, the DC-link voltage regulation term of $J(\mathrm{V_d})$ in (6.19) is used to guarantee the DC-link voltage reference is gradually tracked; Now that a DC-link compensation term of $P^{*}_{\mathrm{comp[k+1]}}$ with the similar function is added into the power reference, to save part of the calculations and also to reduce the FPGA resource cost, the cost function in this case is simplified as

$$J^{\mathrm{n,RQC}}_{\mathrm{DMPC}}(\vec{u}_{\mathrm{g}}) = \underbrace{\gamma_P |P^{\mathrm{RQC}*}_{[\mathrm{k+1}]} - P_{[\mathrm{k+1}]}(\vec{u}_{\mathrm{g}})|}_{=:\mathrm{J(P)}} + \underbrace{\gamma_Q |Q^{*}_{[\mathrm{k+1}]} - Q_{[\mathrm{k+1}]}(\vec{u}_{\mathrm{g}})|}_{=:\mathrm{J(Q)}} + \underbrace{\begin{cases} 0 & , ||S_{[\mathrm{k+1}]}|| \leq S^{\max}, \\ \gamma^{S}_{CS} & , ||S_{[\mathrm{k+1}]}|| > S^{\max}. \end{cases}}_{=:\mathrm{J^{n}_{CS}}} \tag{6.22}$$

6.3.3.1 Low computational effort solutions

6.3.3.1.1 Cost function simplification The purpose of the constraint terms inside the cost functions (6.15) and (6.22) is to limit the current/torque, and power. However, to this end, based on the classical DMPC concept, 8 extra calculations of the predicted variables are required, which increases the computational load heavily. Given that the references are limited, the tracking terms themselves have already contained the limit constraints. Therefore, an alternative is to set limitations within the references instead of using those computationally demanding constraint terms. Therefore, the cost functions

can be simplified as[3]

$$J^{\mathrm{m,R}}_{\mathrm{DMPC}}(\vec{u}_{\mathrm{m}}) = \underbrace{\|T^{*}_{\mathrm{e[k+1]}} - T_{\mathrm{e[k+1]}}(\vec{u}_{\mathrm{m}})\|}_{=:\mathrm{J(T_e)}} + \underbrace{\gamma_{i^{\mathrm{d}}_{\mathrm{m}}} \|i^{\mathrm{d}}_{\mathrm{m[k+1]}}(\vec{u}_{\mathrm{m}})\|}_{=:\mathrm{J(i^d_m)}} \tag{6.23a}$$

$$J^{\mathrm{n,R}}_{\mathrm{DMPC}}(\vec{u}_{\mathrm{g}}) = \underbrace{\|P^{\mathrm{RQC}*}_{\mathrm{[k+1]}} - P_{\mathrm{[k+1]}}(\vec{u}_{\mathrm{g}})\|}_{=:\mathrm{J(P)}} + \underbrace{\|Q^{*}_{\mathrm{[k+1]}} - Q_{\mathrm{[k+1]}}(\vec{u}_{\mathrm{g}})\|}_{=:\mathrm{J(Q)}} \tag{6.23b}$$

where $T^{*}_{\mathrm{e[k+1]}} \in [-\mathrm{T^{max}_e}, \mathrm{T^{max}_e}]$, $P^{\mathrm{RQC}*}_{\mathrm{[k+1]}} \in [-\mathrm{P^{max}}, \mathrm{P^{max}}]$, and $Q^{*}_{\mathrm{[k+1]}} \in [-\mathrm{Q^{max}}, \mathrm{Q^{max}}]$. $\mathrm{T^{max}_e}$, $\mathrm{P^{max}}$ and $\mathrm{Q^{max}}$ are the torque, active power and reactive power limits, respectively.

6.3.3.1.2 A combined deadbeat process to reduce computational efforts The reference voltage to achieve perfect tracking of the control references can be computed using the system model with a deadbeat concept, i.e., $\vec{i}^{\,\mathrm{dq}}_{\mathrm{m[k+1]}} := \vec{i}^{\,\mathrm{dq}*}_{\mathrm{m[k+1]}} = [\frac{2T^{*}_{\mathrm{e[k+1]}}}{3N_{\mathrm{p}}\psi_{\mathrm{pm}}}, i^{\mathrm{d}*}_{\mathrm{m[k+1]}}]^{\top}$ is set in (2.42). Re-arranging of (2.42) yields the (predicted) reference voltage vector

$$\vec{v}^{\,\mathrm{dq}*}_{\mathrm{m[k]}} = \mathbf{B}^{-1}_{\mathrm{m}} \Big[\vec{i}^{\,dq*}_{\mathrm{m[k+1]}} - \mathbf{A}_{\mathrm{m[k]}} \vec{i}^{\,dq}_{\mathrm{m[k]}} - \mathbf{H}_{\mathrm{m[k]}}\Big], \tag{6.24}$$

where $\mathbf{A}_{\mathrm{m[k]}}, \mathbf{B}_{\mathrm{m}}, \mathbf{H}_{\mathrm{m[k]}}$ are the same as defined in chapter 2. Using the inverse Park transformation, $\vec{v}^{\,\alpha\beta*}_{\mathrm{m[k+1]}}$ is computed as $\vec{v}^{\,\alpha\beta*}_{\mathrm{m[k+1]}} = \mathbf{T}^{-1}_{\mathrm{P}}(\theta_{\mathrm{e}})\vec{v}^{\,\mathrm{dq}*}_{\mathrm{m[k+1]}}$.

Similarly, to achieve a deadbeat power control performance for the grid side, recalling the concept and the realization steps presented in Chp. 3, the reference voltage vector on grid side becomes:

$$\begin{pmatrix} v^{\alpha*}_{\mathrm{g[k+1]}} \\ v^{\beta*}_{\mathrm{g[k+1]}} \end{pmatrix} = \begin{pmatrix} e^{\alpha}_{\mathrm{g[k]}} \\ e^{\beta}_{\mathrm{g[k]}} \end{pmatrix} - \frac{L_{\mathrm{g}}}{T_{\mathrm{s}}\|\vec{e}^{\,\alpha\beta}_{\mathrm{g[k]}}\|^2} \begin{bmatrix} e^{\alpha}_{\mathrm{g[k]}} & e^{\beta}_{\mathrm{g[k]}} \\ e^{\beta}_{\mathrm{g[k]}} & -e^{\alpha}_{\mathrm{g[k]}} \end{bmatrix} \begin{pmatrix} P^{*}_{\mathrm{[k+1]}} - P_{\mathrm{[k]}} + \frac{T_{\mathrm{s}}R_{\mathrm{g}}}{L_{\mathrm{g}}} P_{\mathrm{[k]}} + \omega_{\mathrm{g}} T_{\mathrm{s}} Q_{\mathrm{[k]}} \\ Q^{*}_{\mathrm{[k+1]}} - Q_{\mathrm{[k]}} + \frac{T_{\mathrm{s}}R_{\mathrm{g}}}{L_{\mathrm{g}}} Q_{\mathrm{[k]}} - \omega_{\mathrm{g}} T_{\mathrm{s}} P_{\mathrm{[k]}} \end{pmatrix}. \tag{6.25}$$

The obtained information of $\vec{v}^{\,\alpha\beta*}_{\mathrm{x[k+1]}}$ ($x \in \{\mathrm{m}, \mathrm{g}\}$) is helpful to allocate the optimal switching state. For instance, if $\vec{v}^{\,\alpha\beta*}_{\mathrm{x[k+1]}}$ is located in the I sector of the plane (See Fig. 6.15), then instead of all 8 switching vectors, only the 3 green ones ($\vec{u}_1, \vec{u}_2$, and $\vec{u}_{0/7}$) are required to minimize the cost equivalently, thus allowing to reduce the computational efforts to 3/8 of the classical scheme[4].

The controller structure of the proposed RQC-DMPC with lower computational efforts is depicted in Fig. 6.15.

[3] However, for the cases, where, the system is not limited/constrained by certain out-loop controllers with output limitations, the limitation constraints cannot be eliminated from the cost function in such a manner.

[4] A deeper analysis will yield that a further computational load reduction can be achieved by an extra comparison: i.e., if $\|\vec{v}^{\,\alpha\beta*}_{\mathrm{x[k+1]}}\| > \frac{\sqrt{3}V_{\mathrm{d}}}{6}$, only $\vec{u}_1, \vec{u}_2$ are required to evaluate to minimize the cost.

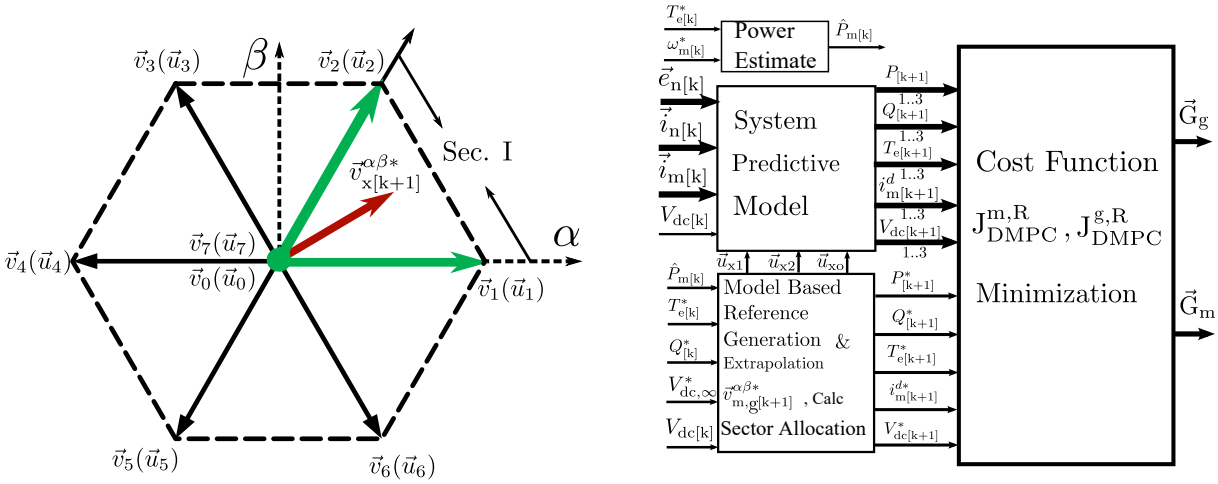

Fig. 6.15: Vector plane and control structure of the proposed RQC-DMPC scheme.

Parameters	Values
Grid-Side Phase Voltage $\vec{e}_n^{abc}$ [V] (peak)	120
Grid-Side Voltage Frequency ω_g [rad/s]	100π
Grid-side Reactor Resistor R_g [Ohm]	$1.56e-3$
Grid-side Reactor Inductance L_g [H]	$16e-3$
DC-link Capacitor C [uF]	1100
Generator Stator Inductance L_s = [H]	8e-3
Generator Stator Resistor R_s [Ohm]	1.3
Generator Pole Pairs N_p [1]	3
Rotor Permanent-Magnet Flux ψ_{pm} [Wb]	0.41
Sampling Interval T_s [μs]	50
Weighting Factors $\gamma_{i_m^d}$, λ	$\frac{I_m^n}{T_e^n}$, 0.05

Table 6.3: System configurations.

6.3.4 FPGA design and experimental evaluation

6.3.4.1 FPGA design

An FPGA-based platform is employed to implement all the presented control schemes for an experimental investigation. To omit redundancy, only the FPGA design process of the proposed RQC-DMPC scheme is introduced in this section.

The underlying RQC-DMPC controller is divided into small sub-routines and implemented using a Single-Cycle-Timed-Loop technique. An overview of the FPGA design is shown in Fig. 6.16. Notably, owning to the proposed computational efficient concept, the calculation time and the FPGA resource cost are both seen an remarkable reduction.

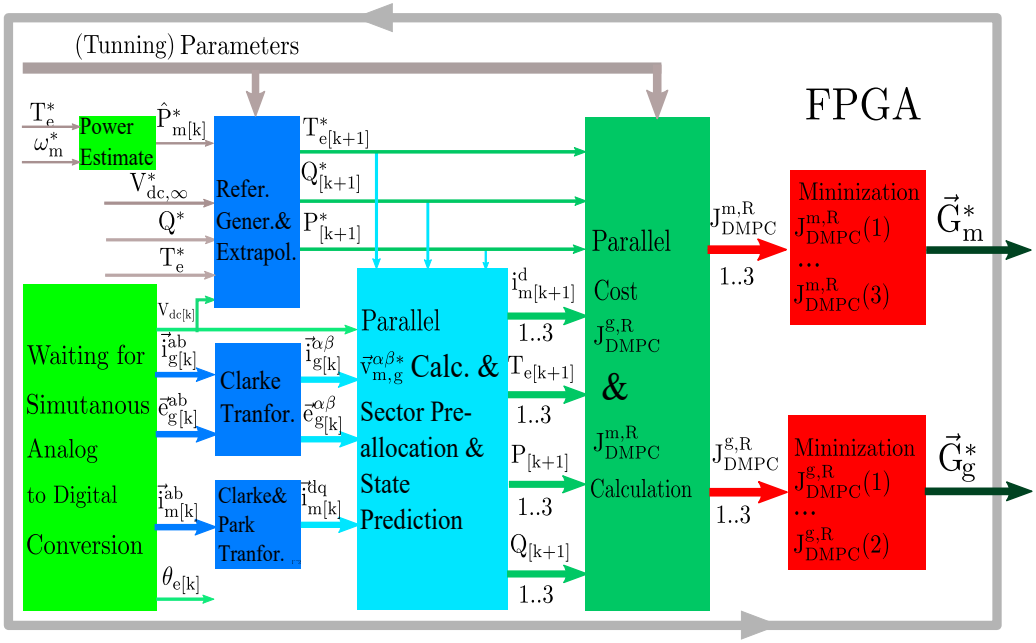

Fig. 6.16: FPGA design overview of the proposed RQC-DMPC scheme.

	PI-DMPC	QC-DMPC	RQC-DMPC
Calculation Time:	88ticks	91ticks	56ticks
Resources:	49%	51%	43%

Table 6.4: FPGA design comparison

Table 6.4 shows the comparison of the three control schemes discussed above[5].

6.3.4.2 Evaluation and analysis

Experimental verification of the proposed RQC-DMPC scheme and its DC-link control performance comparison with PI-DMPC, QC-DMPC are carried out on a lab-constructed test bench (See Fig. 2.9) introduced in Chp. 2. The differences between the test bench and the topology depicted in Fig. 6.13 are that, a three-phase variac (F in Fig. 2.9) is added between the power line and the grid side filter so as to reduce the grid-side phase voltage for safety concerns; the turbine is emulated using a commercial driven AC-Motor. The parameters in experiments are collected in Table 6.3. Note that: for all test scenarios the reactive power reference Q^* is set to be 0var to obtain a unit power factor operation; The DC-link voltage is limited below 350 [V] (operating set point maximum 300V) due to the isolation concerns in the self-constructed test-bench; Therefore, the generator speed is limited below 1500 [RPM] (operating set-point maximum ±1000 [RPM]).

The generator side control performances of using the proposed RQC-DMPC scheme is

[5]Only one of the two PI-DMPC schemes, i.e., the PI-DMPC with load power feed-forward, C – II, is compared for calculation time and FPGA resource usage testing.

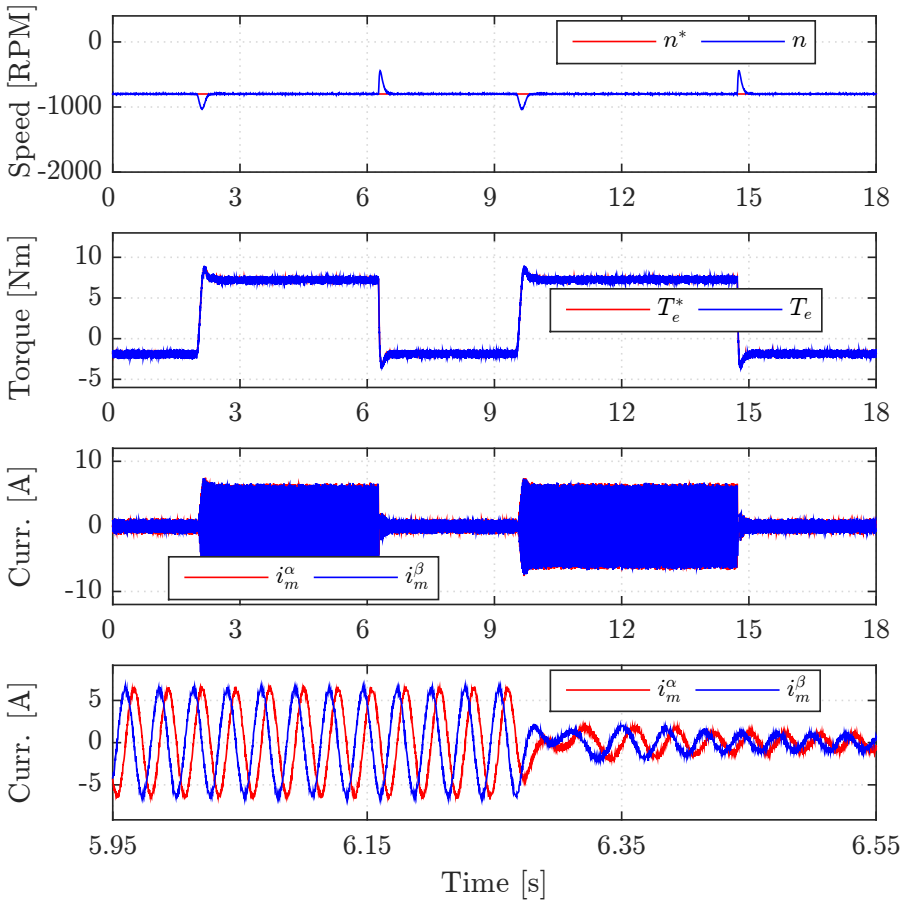

Fig. 6.17: Experimental results: Machine side control performances with the proposed scheme. From up to down are the speed, torque, stator current and zoomed stator current, respectively.

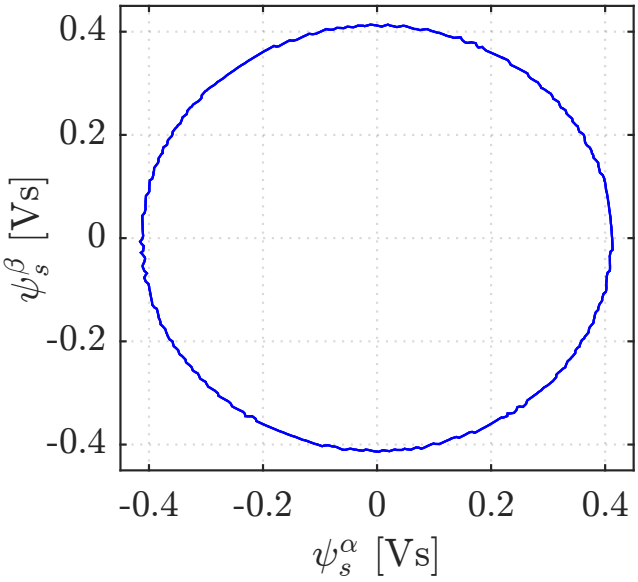

Fig. 6.18: Experimental results: generator stator flux.

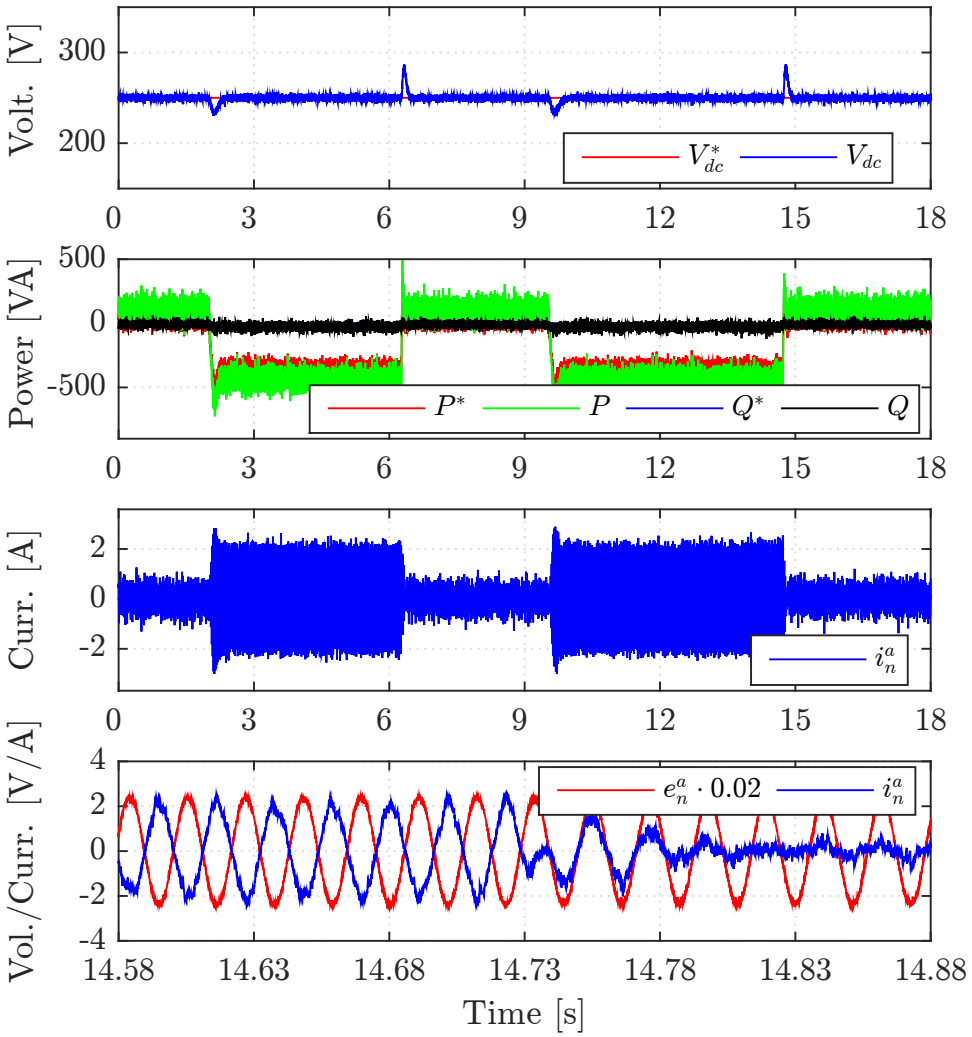

Fig. 6.19: Experimental results: Grid side control performances with the proposed scheme. From up to down are DC-link voltage, active and reactive power, grid side current, and zoomed grid side current.

shown in Fig. 6.17. To better illustrate both the transient and steady status predictive control performances, the speed reference (assuming it as the MPPT speed) of the generator is set as 1000 RPM for the whole period; the load torque changes abruptly between a negative 10% and the rated value (7.5 [Nm]) of the generator torque value at $t = 2, 6.5$ and 14.5 [s], respectively. Clearly, for these whole instants, the torque tracks its references with nice dynamics and steady status performances; the currents (in $\alpha\beta$ frame) and its zoomed figure (for $t \in [5.95, 6.55]$ [s]) are also shown. Smooth and a near-constant stator flux is also seen (shown in Fig. 6.18).

Fig. 6.19 illustrates the grid side control performances with the same scenarios as in Fig. 6.17. Noticeably good DC-link control performances are achieved. Also the grid side power is control with fast dynamics and tracking performances. The zoomed current and its phase voltage are shown in the last sub-figure of Fig. 6.19. Power factor of one is

maintained during the whole period.

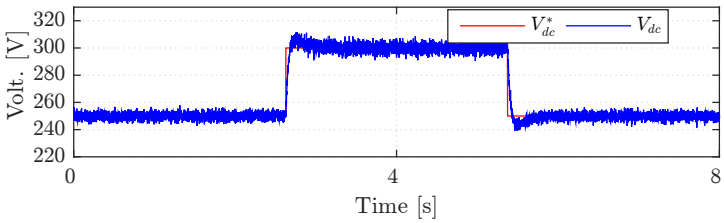

(a) DC-link voltage with PI-DMPC.

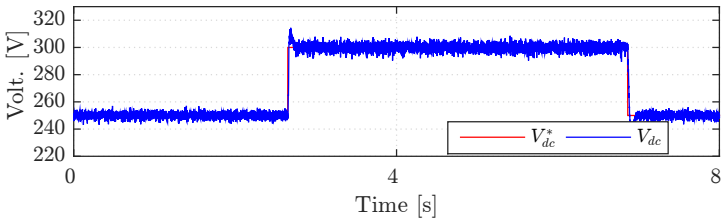

(b) DC-link voltage with PI-DMPC, with feedforward control.

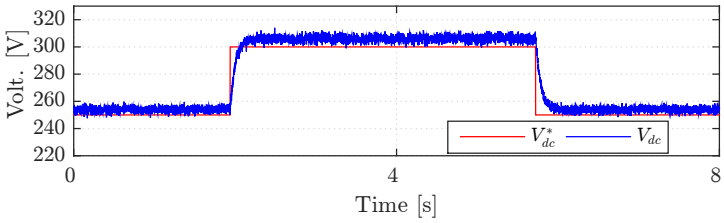

(c) DC-link voltage with QC-DMPC.

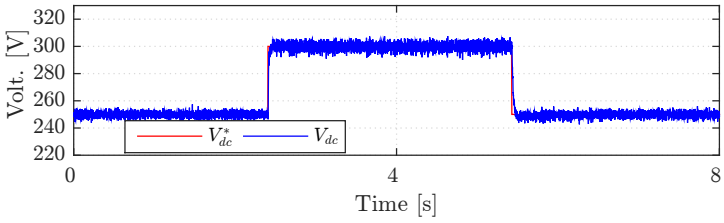

(d) DC-link voltage with the proposed RQC-DMPC.

Fig. 6.20: Experimental results: DC-link control performance with constant load torque.

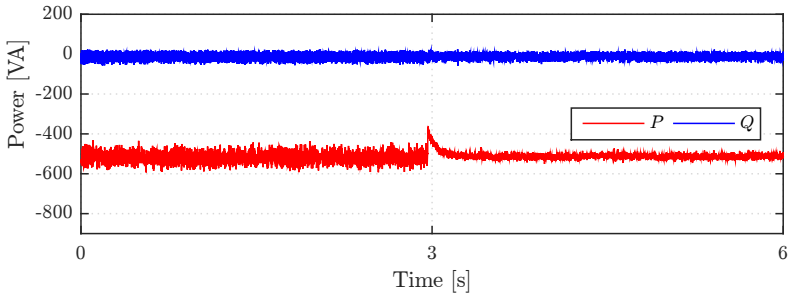

Fig. 6.21: Experimental results: Steady status power control performance comparison between PI-DMPC (with feed-forward) and the proposed RQC-DMPC scheme.

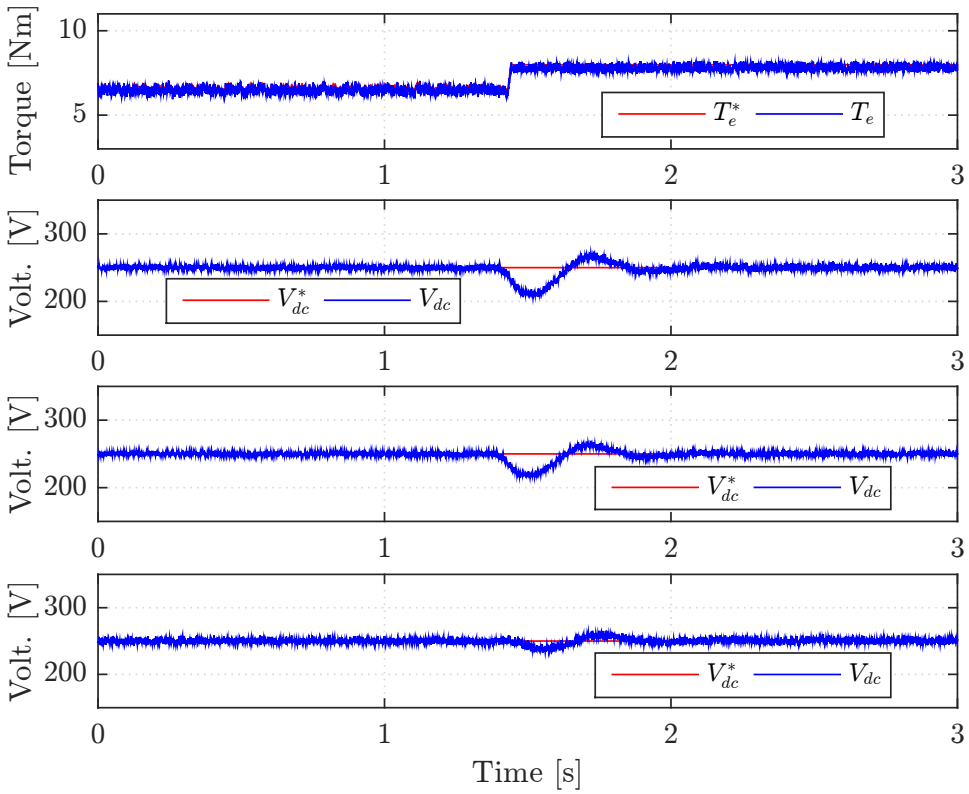

Fig. 6.22: Experimental results: DC-link control performance comparison: Load abrupt change situation. From up to down are: load torque change, DC-link voltage control performances with PI-DMPC, DC-link voltage with PI-DMPC using feed-forward control, and DC-link control performances with the proposed RQC-DMPC scheme, respectively.

6.3.4.3 Performance Comparison of PI-DMPC, QC-DMPC and the proposed RQC-DMPC.

DC-link control performance comparison under constant load torque situation (50% load torque) is illustrated in Fig. 6.20. A DC-link voltage reference change from 250V to 300V and back to 250V is set for all these four control schemes, namely: PI-DMPC, PI-DMPC with load side power feed-forward, QC-DMPC and the proposed RQC-DMPC control schemes. Sub-figures (a) and (b) are showing the two PI control schemes; as expected, with the feed-forward concept, a faster dynamic performance is seen with slightly bigger overshoots. In the contrary, no over- or undershoots are seen in (c) and (d), but an obvious tracking bias is seen in (c) (i.e., with QC-DMPC scheme), while, the DC-link voltage is tracking with nice dynamics and no tracking errors using the proposed RQC-DMPC control scheme.

Noticeably, the grid side power ripples are also reduced with the proposed RQC-DMPC scheme, in comparison with the PI-DMPC scheme. The test result is seen in Fig. 6.21. Testing scenario is that: the control scheme is changed from the PI-DMPC (with load power feed-forward) to the proposed RQC-DMPC at $t = 3.0$ [s], and a full load torque is set for the whole period.

Another DC-link control comparison under load abrupt change situation is also carried out. Since the big DC-link bias, which is not controllable when load is changing abruptly, will potentially lead to unsafe situation to the self-constructed test-bench, the QC-DMPC scheme is therefore not compared in this test scenario. The results are shown in Fig. 6.22. Best control performances are seen with the proposed QC-DMPC scheme. While, PI-DMPC with load power feed-forward shows smaller ripples than PI-DMPC.

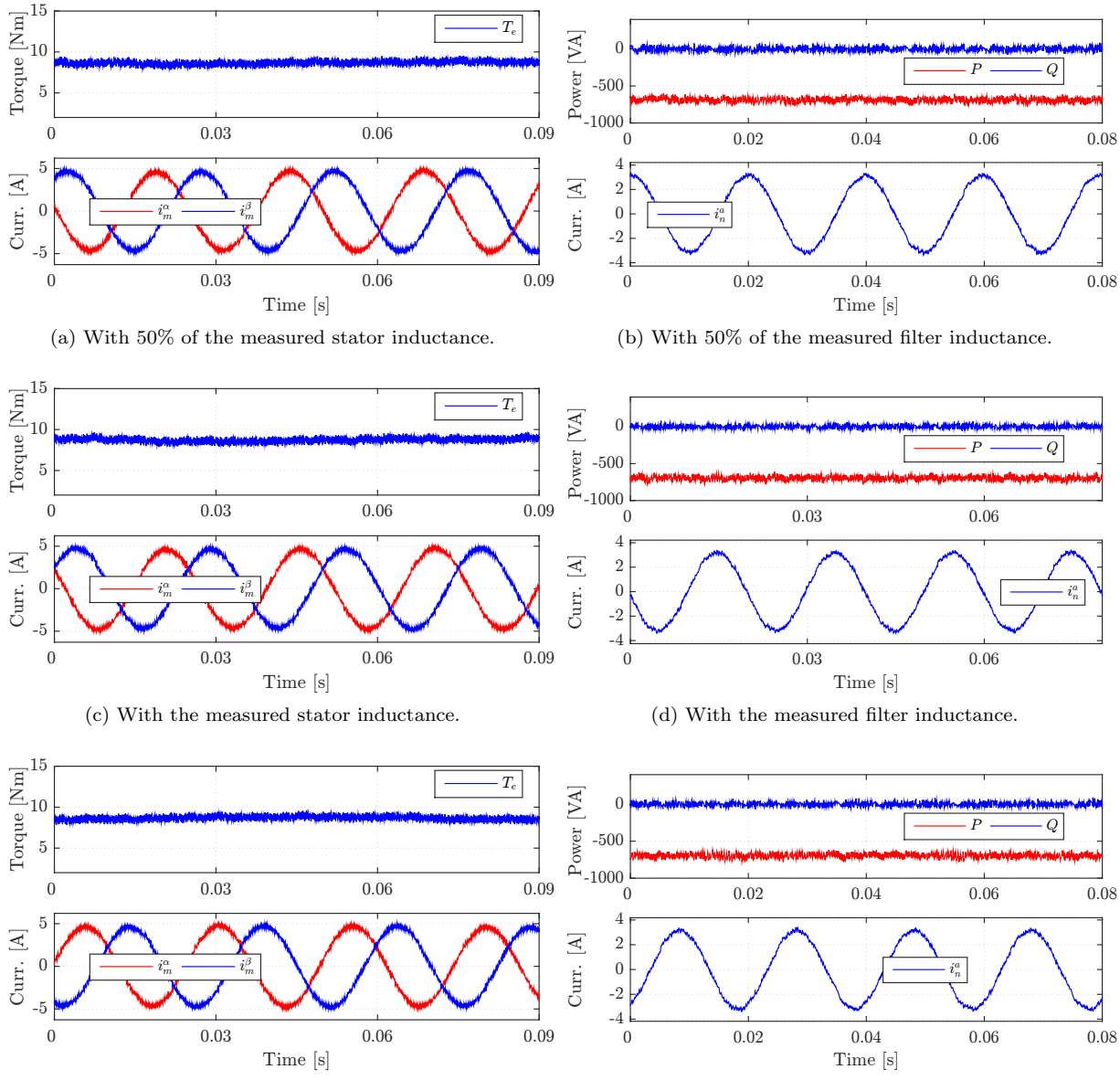

(a) With 50% of the measured stator inductance.

(b) With 50% of the measured filter inductance.

(c) With the measured stator inductance.

(d) With the measured filter inductance.

(e) With 150% of the measured stator inductance.

(f) With 150% of the measured filter inductance.

Fig. 6.23: Experimental results: where (a), (c) (e) are machine side control performance under parameter variations: for each sub-figure, from up to down are the torque and stator current in $\alpha\beta$ frame, respectively; while (b), (d) and (f) are grid side control performance under parameter variations: for each sub-figure, from up to down are the active and reactive power and grid side phase-a current, respectively.

6.3.4.4 Parameter sensitivity investigation of the proposed scheme

A deep view at Eq. (2.42) and Eq. (2.44) will yield that variations in R_y and L_y will lead to variations of $\boldsymbol{A}_y$ and $\boldsymbol{B}_y$, where $y \in \{s, m, g\}$, represents the generator stator or grid filter quantities, respectively. It means the variations of R_y (which is quite small, in particular for the grid side) cause a (quite) small portion ($\frac{\mathrm{T_s}\Delta\mathrm{R_y}}{L_y}$, where T_s is $50e^{-6}$ [s]) of the inaccuracy of current system state $\vec{i}^{\,\mathrm{dq}}_{\mathrm{m[k]}}$ or $\vec{i}^{\,\alpha\beta}_{\mathrm{g[k]}}$, while variations of L_y (greatly) impact the system input effects, which can also be clearly seen from Eq. (6.24) and Eq. (6.25): big variations of L_y may cause the system to produce an undesired voltage vector even a wrong selection of the switching state. Hence the inductance variation is of big impacts to the control performances.

Therefore, the performances of proposed method under generator (stator) and grid side filter inductance variations are illustrated. The testing scenarios are: both the generator stator and grid side filter inductance are changed to 50% and 150% of the measured (accurate) values under 60% of the nominal torque; the stator currents, generator eletromagnetic torque, grid side active and reactive powers, and grid side currents are measured and compared with the situation where measured parameter value is used. The results are illustrated in Fig. 6.23.

As can be seen from Fig. 6.23, (slight) performance degrading (relatively bigger power/torque and current ripples) is seen with parameter derivations of a ±50% range, but (even) such a variation range has not driven the system into instability. Even though, an effective parameter estimation solution is desirable for an optimal control performance using model based control methods, which is one of the research interests of the authors in the near future.

6.4 Summary

In this chapter the DC-link control issues of the back-to-back power converter systems have been discussed. Two quasi-centralized direct model predictive control methods have been proposed and experimentally compared with the conventional PI based DC-link control solutions for both back-to-back power converter with RL load and PMSG using fully FPGA based solution.

The investigation in Sec. 6.2 would suggest that quasi-centralized direct model predictive control (QC-DMPC) can be a nice alternative for back-to-back power converter based systems because of its easier tuning character, fast dynamics and under-/overshoot free performances. However, based on an entirely model based concept, evident DC-link tracking bias is seen under different operational scenarios due to imperfect power converter efficiency and model uncertainty. To further deal with this issue, Sec. 6.3 of this chapter has proposed a revised quasi-centralized direct model predictive control (QC-DMPC) scheme taking the voltage source back-to-back power converter driven PMSG wind turbine systems as an application target. With the proposed control scheme, the DC-link voltage is directly controlled by the grid side predictive controller using a revised QC-DMPC

concept without DC-link tracking errors. The computational load and FPGA resource cost are also reduced evidently with a simplified cost function and the combination of the deadbeat concept presented in Chp. 5.

Chapter 7

Grid side voltage sensorless control

This chapter introduces the grid side voltage sensorless control techniques for grid-tied back-to-back power converters. The virtual flux concept is revisited and formulated in Sec. 7.2.1; the classical filter based voltage sensorless control methods are summarized in Sec. 7.2.2. In Sec. 7.2.3 a novel *time domain initial bias compensation* based method is proposed and detailed, which estimates the grid side virtual flux/voltage with fast dynamics *with one sampling step* and nice accuracy *in both transient and steady state*. The proposed technique can be applied both to modulation based control schemes and also the nonlinear direct control frame without modulators. As a case study, the proposed method is incorporated into the deadbeat like predictive control technique for grid-tied two-level back-to-back power converter in Sec. 7.3.

7.1 Introduction

Back-to-back voltage source power converters with Active Front End (AFE) offer many advantages compared to those with Passive-Front-End (PFE) [15, 125]: (i) controllable sinusoidal currents on grid side with low harmonic pollution, (ii) controllable DC-link voltage which allows to reduce the DC-link capacitor size, (iii) a bi-directional power flow, and (iv) controllable reactive power on grid side.

These properties of a back-to-back converter make it possible to serve as a multi-functional converter: A back-to-back converter with DC-link can supply the full output power to its linear or non-linear load while controlling the active and reactive power drawn from the grid (net). The grid side converter functions as an active power filter by compensating harmonics and reactive power, whereas the load side converter (LSC) can act at the same time as supplier of an AC-load (like AC-motor or RL(C)-load). Moreover, such a fully controllable converter achieves a bi-directional power flow, i.e., allows for instant inverse power flow. Therefore it represents a promising solution to applications where regenerative operation or reactive power and harmonic compensation are needed [15, 17, 125, 142].

Control of the grid-connected AFE part (i.e. the net/grid side converter) is one of the

most important tasks for a back-to-back converter. Whether grid side voltage sensors are needed (or not) and whether active and reactive power are to be controlled, the AFE control schemes can be classified into four groups [17,47,63]: (i) voltage sensor based Direct Power Control (DPC), (ii) cascaded (current) control (in the following named "indirect power control"), (iii) Virtual Flux (VF) based DPC and (iv) VF based indirect power control. Due to the fast dynamics of DPC and model predictive control schemes [8,93,108], recently many reports were published dealing with direct power control and model predictive control concepts: In [47] an improved DMPPC scheme with duty cycle optimization was used. In [93] a Finite-Control-Set Model Predictive DPC (FCS-MP-DPC) was developed and in [143] a Sliding-Mode DPC (SM-DPC) is proposed. In [144] a constant-switching-frequency model predictive DPC was realized utilizing SVM. In [145] a predictive current controller for grid-tied wind turbine applications with extended state observer was proposed with fast dynamics and constant switching frequency. Besides, MPC becomes more and more popular in power electronics and electrical drives due to its promising results (see e.g. [10,41,74,146–149]).

All control schemes which rely on a voltage sensor depend on the measurement accuracy provided by the sensor hardware. Moreover, voltage sensor based schemes are costly and vulnerable to noise and may complicate the system setup [125]. In [150] a voltage sensorless method utilizing a switching table in DPC is firstly proposed. By using virtual flux estimation schemes, several publications extended Voltage Oriented Control (VOC), DPC (with look-up table) and FCS-MP-DPC methods such that a voltage sensor is not required anymore (see e.g. [125]). Most of these VF estimation schemes rely either on a band-pass or high-pass filter to extract the related component(s) of the estimated VF. However, due to the inevitable transient time (time delay) of the filters, a relatively long delay occurs at the beginning and during the transient phases of the estimation yielding inaccurate control during these phases. E.g. a huge overshoot in the estimation error will be observed and the control system might suffer from limitation problems.

In this chapter a novel VF estimation method with Initial Bias Compensation (IBC-VF) solution will be presented. The proposed method numerically analyzes the estimated VF components and eliminates the initial bias due to the converter voltage integration *and* due to the initial flux in the filter inductance. The proposed algorithm makes the VF estimation fast and accurate, achieving a dynamic response within *one* sampling step. The proposed IBC-VF estimation method can be applied in both modulator based control frames and nonlinear direct control frames. As a case study, it is combined with a deadbeat like predictive control scheme with SVM operating with constant switching frequency for a back-to-back power converter in Sec. 3.

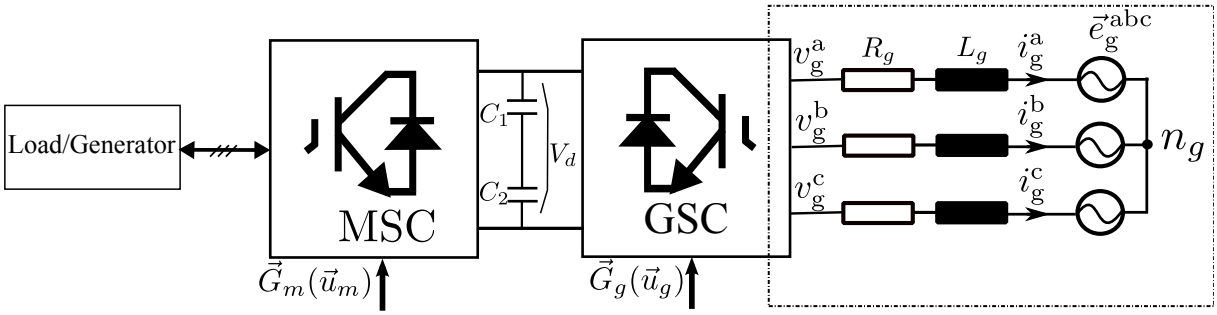

Fig. 7.1: Simplified electrical circuit of a voltage source back-to-back converter with (R)L-filter on the net/grid side.

7.2 Virtual flux concept and voltage sensorless control techniques

7.2.1 Virtual flux concept

The concept of virtual flux (VF) estimation was originally proposed to improve the VOC schemes (see [151]), and was developed further for AC voltage sensorless instantaneous active and reactive power estimation. This concept allows to replace AC voltage sensors by a VF estimator. It has advantages like hardware cost reduction and system simplification. By treating the net/grid side line choke (RL-filter) and the grid voltage as the stator circuit of an AC machine (see Fig. 7.1 and (2.43)), one may introduce the virtual flux as follows

$$\vec{\psi}_{\mathrm{e_g}}^{\alpha\beta}(t) := \left(\psi_{\mathrm{e_g}}^{\alpha}(t), \psi_{\mathrm{e_g}}^{\beta}(t)\right)^{\top} := \int_0^t \vec{e}_{\mathrm{g}}^{\alpha\beta}(\tau)\,\mathrm{d}\tau + \underbrace{\int_{-\infty}^{0^-} \vec{e}_{\mathrm{g}}^{\alpha\beta}(\tau)\,\mathrm{d}\tau}_{=0} = \underbrace{\int_0^t \vec{v}_{\mathrm{g}}^{\alpha\beta}(\tau)\,\mathrm{d}\tau}_{=:\vec{\psi}_{\mathrm{vg}}^{\alpha\beta}}$$
$$+ \underbrace{\int_0^t \vec{v}_{\mathrm{f}}^{\alpha\beta}(\tau)\,\mathrm{d}\tau}_{=:\vec{\psi}_{\mathrm{vf}}^{\alpha\beta}} \overset{(2.43)}{=} \int_0^t \left(\vec{v}_{\mathrm{g}}^{\alpha\beta}(\tau) + L_{\mathrm{g}} \cdot \frac{\mathrm{d}\vec{i}_{\mathrm{g}}^{\alpha\beta}(\tau)}{\mathrm{d}\tau} + \vec{i}_{\mathrm{g}}^{\alpha\beta}(\tau) \cdot R_{\mathrm{g}}\right)\mathrm{d}\tau\,. \quad (7.1)$$

Normally, $\vec{v}_{\mathrm{g}}^{\alpha\beta}$ is not measured. However, it can be estimated by invoking the switching sequence (2.8) or the on-duty time of each phase $\vec{T}_{\mathrm{g}}^{\mathrm{abc}}$ and the Clarke transformation $\mathbf{T}_{\mathrm{C}}$ as in (2.23), i.e.

$$\hat{\vec{v}}_{\mathrm{g}}^{\alpha\beta} \overset{(2.23)}{:=} \mathbf{T}_{\mathrm{C}}\vec{v}_{\mathrm{g}}^{\mathrm{abc}} \overset{(2.8)}{=} \mathbf{T}_{\mathrm{C}}\mathbf{T}_{\mathrm{SW}}\vec{T}_{\mathrm{g}}^{\mathrm{abc}}, \quad (7.2)$$

where $\vec{T}_{\mathrm{g}}^{\mathrm{abc}} := (T_{\mathrm{g}}^{\mathrm{a}}, T_{\mathrm{g}}^{\mathrm{b}}, T_{\mathrm{g}}^{\mathrm{c}})^{\top}$ with $T_{\mathrm{g}}^{\mathrm{a}}$, $T_{\mathrm{g}}^{\mathrm{b}}$, $T_{\mathrm{g}}^{\mathrm{c}} \in [0, T_{\mathrm{s}}]$. T_{s} is the switching period. $\vec{T}_{\mathrm{g}}^{\mathrm{abc}}$ can be obtained from the modulator for the indirect control schemes (e.g. VOC or DPC-SVM and MPC-SVM). Moreover, in most practical applications, the resistance of the choke (RL-Filter) on the net/grid side is very small, i.e. $R_{\mathrm{g}} \approx 0$. Hence, inserting (7.2) and

$R_\mathrm{g} = 0$ into (7.1), yields

$$\vec{\psi}_{\mathrm{e_g}}^{\alpha\beta}(t) = \int_0^t \vec{e}_\mathrm{g}^{\alpha\beta}(\tau)\,\mathrm{d}\tau \;= \int_0^t \hat{\vec{v}}_\mathrm{g}^{\alpha\beta}(\tau)\cdot\,\mathrm{d}\tau \;+ L_\mathrm{g}\cdot\vec{i}_\mathrm{g}^{\alpha\beta}(t) - L_\mathrm{g}\cdot\vec{i}_\mathrm{g}^{\alpha\beta}(0). \tag{7.3}$$

For the remainder of this paper, it is assumed that the grid is *balanced (ideal)* but *unknown*. Hence, the grid voltage has the following form

$$\vec{e}_\mathrm{g}^{\alpha\beta} = A\Big(\cos(\omega_\mathrm{g}\,t+\theta_0),\ \sin(\omega_\mathrm{g}\,t+\theta_0)\Big)^\top \tag{7.4}$$

with *constant* amplitude A, *constant* initial phase θ_0 and *constant* angular frequency ω_g. Now the virtual flux may be written as follows

$$\begin{aligned}\vec{\psi}_{\mathrm{e_g}}^{\alpha\beta}(t) = \int_0^t \vec{e}_\mathrm{g}^{\alpha\beta}(\tau)\cdot\,\mathrm{d}\tau \;&= \int_0^t A\cdot\begin{pmatrix}\cos(\omega_\mathrm{g}\,\tau+\theta_0)\\ \sin(\omega_\mathrm{g}\,\tau+\theta_0)\end{pmatrix}\cdot\,\mathrm{d}\tau\\ &= \underbrace{\frac{A}{\omega_\mathrm{g}}\cdot\begin{pmatrix}\sin(\omega_\mathrm{g}\,t+\theta_0)\\ -\cos(\omega_\mathrm{g}\,t+\theta_0)\end{pmatrix}}_{=:\vec{\psi}_{\mathrm{key}}^{\alpha\beta}(t)=\left(\psi_{\mathrm{key}}^{\alpha}(t),\,\psi_{\mathrm{key}}^{\beta}(t)\right)^\top} + \underbrace{\frac{A}{\omega_\mathrm{g}}\cdot\begin{pmatrix}-\sin(\theta_0)\\ \cos(\theta_0)\end{pmatrix}}_{=:\vec{\psi}_{\mathrm{bias}}^{\alpha\beta}=\left(\psi_{\mathrm{bias}}^{\alpha},\,\psi_{\mathrm{bias}}^{\beta}\right)^\top}.\end{aligned} \tag{7.5}$$

Equations (7.3) and (7.5) are the *key* equalities to obtain an estimate of the net/grid voltage.

7.2.2 Grid voltage estimation with filter based VF techniques

From (7.5), due to constant $\vec{\psi}_{\mathrm{bias}}^{\alpha\beta}$, it is easy to see that $\vec{e}_\mathrm{g}^{\alpha\beta}$ can directly be computed with the knowledge of $\vec{\psi}_{\mathrm{key}}^{\alpha\beta}(t)$, since

$$\vec{e}_\mathrm{g}^{\alpha\beta}(t) = \frac{\mathrm{d}}{\mathrm{d}t}\,\vec{\psi}_{\mathrm{e_g}}^{\alpha\beta}(t) \overset{(7.5)}{=} \omega_\mathrm{g}\begin{pmatrix}-\psi_{\mathrm{key}}^{\beta}(t)\\ \psi_{\mathrm{key}}^{\alpha}(t)\end{pmatrix}. \tag{7.6}$$

Now, the key question is how to extract $\vec{\psi}_{\mathrm{key}}^{\alpha\beta}$ from $\vec{\psi}_{\mathrm{e_g}}^{\alpha\beta}$ which can be computed by evaluating (7.3). Clearly, see (7.5), $\vec{\psi}_{\mathrm{bias}}^{\alpha\beta}$ is a constant which depends on the amplitude of the grid voltage and its initial phase. Moreover, without net/grid side voltage sensor(s), $\vec{\psi}_{\mathrm{bias}}^{\alpha\beta}$ is not available at system start. The simplest way, to extract $\vec{\psi}_{\mathrm{key}}^{\alpha\beta}$, is to use a high- or band-pass filter to filter out the constant influence of $\vec{\psi}_{\mathrm{bias}}^{\alpha\beta}$ in $\vec{\psi}_{\mathrm{e_g}}^{\alpha\beta}$.

Hereby, high-pass filters will be not further considered due to their undesirable amplification of noise (noise sensitivity). Moreover, first-order filters introduce an undesired phase shift (delay) to the closed-loop system dynamics, which is often not acceptable. So in recent publications (see e.g. [11, 152, 153]), a band-pass filter $F_\mathrm{bp}(s)$ has been proposed

with a cut-off frequency at ω_g to filter out the bias term $\vec{\psi}^{\alpha\beta}_{\text{bias}}$ in (7.5). The (filtered) estimate $\hat{\vec{\psi}}^{\alpha\beta}_{\text{key}}$ of the key component $\vec{\psi}^{\alpha\beta}_{\text{key}}$ in (7.5) is given by

$$\hat{\vec{\psi}}^{\alpha\beta}_{\text{key}}(t) := \mathcal{L}^{-1}\{F_{\text{bp}}(s)\} * \vec{\psi}^{\alpha\beta}_{\text{e}_g}(t). \tag{7.7}$$

The proposed band-pass filter has the following transfer function (for both α and β component)

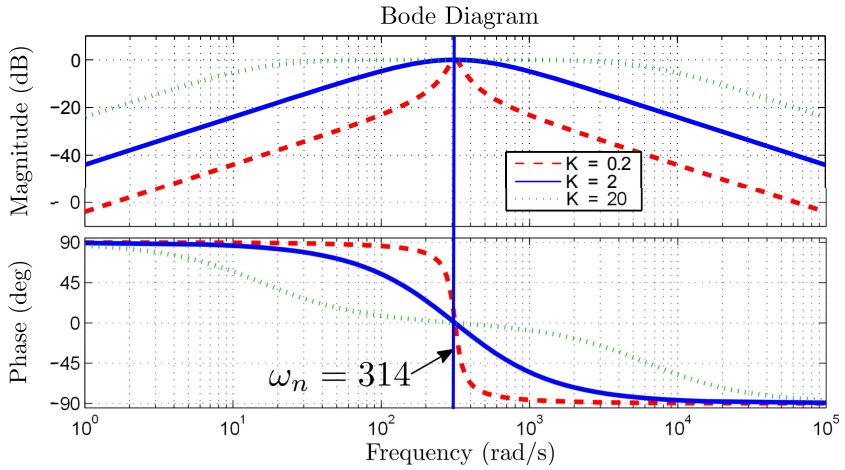

Fig. 7.2: Frequency response of band-pass filter (7.8).

$$F_{\text{bp}}(s) = \frac{\hat{\psi}^{\alpha}_{\text{key}}(s)}{\psi^{\alpha}_{\text{e}_g}(s)} = \frac{\hat{\psi}^{\beta}_{\text{key}}(s)}{\psi^{\beta}_{\text{e}_g}(s)} = \frac{K\omega_g s}{s^2 + K\omega_g s + \omega_g^2}. \tag{7.8}$$

The frequency response (bode plot) of filter (7.8) is depicted in Fig. 7.2. The time response of (7.8) for sinusoidal input signals, e.g. $\int_0^t e^{\alpha}_g(\tau)\,\mathrm{d}\tau = \int_0^t A\cos(\omega_g\tau + \theta_0)\,\mathrm{d}\tau$ as in (7.4), is given by: (i) for $K = 2$:

$$\hat{\psi}^{\alpha}_{\text{key}}(t) = -A\frac{(\cos(\theta_0) + \sin(\theta_0))\omega_g t + \sin(\theta_0)}{\omega_g}e^{-\omega_g t} + \underbrace{\frac{A}{\omega_g}\sin(\omega_g t + \theta_0)}_{\overset{(7.5)}{=}\psi^{\alpha}_{\text{key}}(t)} \tag{7.9}$$

and (ii) for $K \neq 2$:

$$\hat{\psi}^{\alpha}_{\text{key}}(t) = \frac{A}{2\omega_g M}[(e^{-\lambda_1 t} - e^{-\lambda_2 t})(2\cos(\theta_0) + K\sin(\theta_0)) - M(e^{-\lambda_1 t} + e^{-\lambda_2 t})\sin(\theta_0)] + \underbrace{\frac{A}{\omega_g}\sin(\omega_g t + \theta_0)}_{\overset{(7.5)}{=}\psi^{\alpha}_{\text{key}}(t)}, \tag{7.10}$$

where $M = \sqrt{K^2 - 4}$ and $\lambda_{1,2} = \frac{\omega_g}{2}(K \pm \sqrt{K^2 - 4})$. So, since $-\omega_g$, $-\lambda_1$ and $-\lambda_2$ have negative real parts, the terms $e^{-\omega_g t}$, $e^{-\lambda_1 t}$ and $e^{-\lambda_2 t}$ in (7.9) and (7.10) tend to zero for

$t \to \infty$. Hence, in steady state, the filter response gives the desired component $\psi^{\alpha}_{\text{key}}$. Analogously, for an input signal $\int_0^t e^{\beta}_{\text{g}}(\tau)\,\mathrm{d}\tau = \int_0^t A\sin(\omega_{\text{g}}\tau+\theta_0)\,\mathrm{d}\tau$, one obtains the component $\psi^{\beta}_{\text{key}}$. However, the initial accuracy of the filtered output depends on the filter dynamics which correlate with the real parts of the filter poles $\Re\{-\lambda_1\}$ and $\Re\{-\lambda_2\}$. More precisely, the transient response is related to the *slowest* pole, i.e. $\max\{\Re\{-\lambda_1\}, \Re\{-\lambda_2\}\}$. For $K=2$, the fastest transient response is obtained ($\approx \frac{5}{\omega_{\text{g}}} = 0.016$ s). In conclusion, in steady state, the band-pass filter (7.8) filters out the initial bias $\vec{\psi}^{\alpha\beta}_{\text{bias}}$ without any phase shift (at ω_{g}) which gives, for $t \gg 5/\omega_{\text{g}}$,

$$\hat{\psi}^{\alpha}_{\text{key}}(t) = \psi^{\alpha}_{\text{key}}(t) \quad \text{and} \quad \hat{\psi}^{\beta}_{\text{key}}(t) = \psi^{\beta}_{\text{key}}(t). \tag{7.11}$$

However, initial deviations of the estimation are inevitable (i.e. for $t \ll 5/\omega_{\text{g}}$). There are two ways to utilize the band-pass filter $F_{\text{bp}}(s)$: (i) The use of a Partial Band-Pass (PBP) filter and (ii) the use of a Full Band-Pass (FBP) filter. In the following subsections, both filter approaches are explained in more detail and the novel Initial Bias Compensation Virtual Flux (IBC-VF) estimation scheme is introduced and compared with the conventional approaches.

7.2.2.1 Partial band-pass filter virtual flux (PBP-VF) estimation method (see e.g. [154, 155])

The PBP filter method applies band-pass filter (7.8) only to filter the integration of the (approximated) converter side voltage $\hat{\vec{v}}^{\alpha\beta}_{\text{g}}$ as in (7.2), i.e.

$$\begin{aligned}\mathcal{L}^{-1}\{F_{\text{bp}}(s)\} * \int_0^t \vec{v}^{\alpha\beta}_{\text{g}}(\tau)\,\mathrm{d}\tau &\overset{R_{\text{g}}\approx 0}{=} \mathcal{L}^{-1}\{F_{\text{bp}}(s)\} * \Big\{ \int_0^t (\vec{e}^{\alpha\beta}_{\text{g}}(\tau) - L_{\text{g}}\frac{\mathrm{d}\vec{i}^{\alpha\beta}_{\text{g}}(\tau)}{\mathrm{d}\tau})\,\mathrm{d}\tau \Big\} \\ &\overset{(7.5)}{=} \mathcal{L}^{-1}\{F_{\text{bp}}(s)\} * \big\{\vec{\psi}^{\alpha\beta}_{\text{e}_{\text{g}}}(t) - L_{\text{g}}\vec{i}^{\alpha\beta}_{\text{g}}(t) + \underbrace{L_{\text{g}}\vec{i}^{\alpha\beta}_{\text{g}}(0)}_{=\hat{\vec{\psi}}^{\alpha\beta}_{\text{bias}}}\big\}. \end{aligned} \tag{7.12}$$

Clearly, $\hat{\vec{\psi}}^{\alpha\beta}_{\text{bias}}$ will be filtered out in steady state. So an estimate for $\vec{\psi}^{\alpha\beta}_{\text{key}}$ is obtained by adding $L_{\text{g}}\vec{i}^{\alpha\beta}_{\text{g}}(t)$ to (7.12), i.e.

$$\hat{\vec{\psi}}^{\alpha\beta}_{\text{key}}(t) = \mathcal{L}^{-1}\{F_{\text{bp}}(s)\} * \vec{\psi}^{\alpha\beta}_{\text{e}_{\text{g}}}(t) \underbrace{-\mathcal{L}^{-1}\{F_{\text{bp}}(s)\} * \{L_{\text{g}}\vec{i}^{\alpha\beta}_{\text{g}}(t)\} + L_{\text{g}}\vec{i}^{\alpha\beta}_{\text{g}}(t)}_{\approx 0}, \tag{7.13}$$

which gives an approximation of the desired filtered estimate as in (7.7).

7.2.2.2 Full band-pass filter virtual flux (FBP-VF) estimation method (see e.g. [11, 156])

The FBP filter method applies band-pass filter (7.8) to filter the integration of the (approximated) converter side voltage $\hat{\vec{v}}^{\alpha\beta}_{\text{g}}$ as in (7.2) *and* the current $\vec{i}^{\alpha\beta}_{\text{g}}(t)$ through L_{g}.

One obtains the following estimate $\hat{\vec{\psi}}^{\alpha\beta}_{\text{key}}(t)$ of the virtual flux

$$\begin{aligned}\hat{\vec{\psi}}^{\alpha\beta}_{\text{key}}(t) &= \mathcal{L}^{-1}\{F_{\text{bp}}(s)\} * \{\int_0^t \hat{\vec{v}}^{\alpha\beta}_{\text{g}}(\tau)\,\mathrm{d}\tau + L_{\text{g}}\vec{i}^{\,\alpha\beta}_{\text{g}}(t)\} \\ &\overset{R_{\text{g}}\approx 0}{=} \mathcal{L}^{-1}\{F_{\text{bp}}(s)\} * \{\int_0^t (\vec{e}^{\,\alpha\beta}_{\text{g}}(\tau) - L_{\text{g}}\frac{\mathrm{d}\vec{i}^{\,\alpha\beta}_{\text{g}}(\tau)}{\mathrm{d}\tau})\,\mathrm{d}\tau\} + \mathcal{L}^{-1}\{F_{\text{bp}}(s)\} * \{L_{\text{g}}\vec{i}^{\,\alpha\beta}_{\text{g}}(t)\} \\ &\overset{(7.5)}{=} \mathcal{L}^{-1}\{F_{\text{bp}}(s)\} * \{\vec{\psi}^{\alpha\beta}_{\text{eg}}(t) + \underbrace{L_{\text{g}}\vec{i}^{\,\alpha\beta}_{\text{g}}(0)}_{=\hat{\vec{\psi}}^{\alpha\beta}_{\text{bias}}}\} \approx \mathcal{L}^{-1}\{F_{\text{bp}}(s)\} * \{\vec{\psi}^{\alpha\beta}_{\text{eg}}(t)\}, \end{aligned} \tag{7.14}$$

which approximates the desired filtered estimate as in (7.7).

Inspection of (7.13) and (7.14) gives the following conclusions:

- **Steady state:** Since $\vec{i}^{\,\alpha\beta}_{\text{g}}(t)$ in (7.13) is a pure sinusoidal signal with frequency close to ω_{g} (neglecting measurement and switching noise), $F_{\text{bp}}(t) * \{L_{\text{g}}\vec{i}^{\,\alpha\beta}_{\text{g}}(t)\} - L_{\text{g}}\vec{i}^{\,\alpha\beta}_{\text{g}}(t) \approx 0$ holds true and, so, (7.13) equals (7.14).
- **Transient phase:** The PBP filter method with (7.13) is not accurate. Here the filter may loose information of $L_{\text{g}}\vec{i}^{\,\alpha\beta}_{\text{g}}(t)$ being not sinusoidal or having a different frequency than ω_{g}. In contrast to that, the FBP filter method in (7.14) is not affected.
- **Initial phase:** Due to the inevitable transient time of the filter dynamics, for both filter methods, the estimation is suffering from an initial delay time ($> 1/\omega_{\text{g}}$) yielding initial estimation errors. Any controller, using these delayed estimates, will be affected and will output non-ideal actuating signals and (large) overshoots are to be expected e.g. in power output (see Fig. 7.4(c) and 7.5(c)).

7.2.3 Proposed initial bias compensation based VF estimation

Based on (7.3) and (7.5), a novel time-domain Initial Bias Compensation Virtual Flux (IBC-VF) estimation method is proposed in this paper. The proposed method is analyzed and implemented in the discrete time-domain by introducing the sampling period T_{s} and the period

$$T_{\text{n}} := \frac{2\pi}{\omega_{\text{g}}} \tag{7.15}$$

of the grid fundamental voltage. For an arbitrary time instant $t \geq 0$ and some signal $x(t)$, the discrete signal is written as $x[k] := x(kT_{\text{s}}) \approx x(t)$. Moreover, it is assumed that T_{n} is a multiple of T_{s}. Hence, $T_{\text{n}} = N\,T_{\text{s}}$ for some fixed natural number $N \geq 1$ (sampling instant). Now, for any $l \geq 0$ and for a symmetrical grid, i.e. (7.4) holds (true in most applications), the following can be observed:

$$\sum_{i=0+l}^{N-1+l} \vec{\psi}^{\alpha\beta}_{\text{eg}}[i] \overset{(7.5)}{=} \underbrace{\sum_{i=0+l}^{N-1+l} \vec{\psi}^{\alpha\beta}_{\text{key}}[i]}_{=0} + \sum_{i=0+l}^{N-1+l} \vec{\psi}^{\alpha\beta}_{\text{bias}} = N \cdot \vec{\psi}^{\alpha\beta}_{\text{bias}}. \tag{7.16}$$

So, the constant[1] bias term $\vec{\psi}^{\alpha\beta}_{\text{bias}}$ can be estimated after one period T_{n} (i.e. after N samples) of the grid voltage by

$$\hat{\vec{\psi}}^{\alpha\beta}_{\text{bias}}[N-1] = \frac{1}{N} \cdot \sum_{i=0}^{N-1} \vec{\psi}^{\alpha\beta}_{\text{e}_\text{g}}[i]. \tag{7.17}$$

So, in the N^{th} sampling interval, the constant bias in (7.5) can be compensated and the key component is given by

$$\forall\, k \geq N\text{:} \qquad \hat{\vec{\psi}}^{\alpha\beta}_{\text{key}}[k] = \vec{\psi}^{\alpha\beta}_{\text{e}_\text{g}}[k] - \hat{\vec{\psi}}^{\alpha\beta}_{\text{bias}}[N-1]. \tag{7.18}$$

Clearly, in practice, measurement noise will deteriorate the estimation. Therefore, to improve the VF estimate, the bias term is updated for any new sampling instant $k > N$ by using a shifting-average method as follows

$$\forall\, k > N\text{:}\;\; \hat{\vec{\psi}}^{\alpha\beta}_{\text{bias}}[k] = \frac{1}{N} \cdot \sum_{i=k-N}^{k} \vec{\psi}^{\alpha\beta}_{\text{e}_\text{g}}[i] = \hat{\vec{\psi}}^{\alpha\beta}_{\text{bias}}[k-1] + \frac{\vec{\psi}^{\alpha\beta}_{\text{e}_\text{g}}[k] - \vec{\psi}^{\alpha\beta}_{\text{e}_\text{g}}[k-N]}{N}. \tag{7.19}$$

In conclusion, one may estimate the value of the key component of the virtual flux by

$$\forall\, k > N\text{:} \qquad \hat{\vec{\psi}}^{\alpha\beta}_{\text{key}}[k] = \vec{\psi}^{\alpha\beta}_{\text{e}_\text{g}}[k] - \hat{\vec{\psi}}^{\alpha\beta}_{\text{bias}}[k]. \tag{7.20}$$

So far, still a problem remains: The estimated key component $\hat{\vec{\psi}}^{\alpha\beta}_{\text{key}}[k]$ of the virtual flux lags behind during the initial estimation, i.e. for $0 \leq k \leq N$. In the following, a solution which overcomes this drawback for all $k \geq 1$ is proposed. Hence, an estimation with a delay of no more than T_{s} is achieved. From (7.5) it is known that α and β component of the virtual flux are given by $\psi^{\alpha}_{\text{e}_\text{g}}(t) = \frac{A}{\omega_{\text{g}}} \cdot [\sin(\omega_{\text{g}} t + \theta_0) - \sin\theta_0]$ and $\psi^{\beta}_{\text{e}_\text{g}}(t) = \frac{A}{\omega_{\text{g}}} \cdot [-\cos(\omega_{\text{g}} t + \theta_0) + \cos\theta_0]$, respectively. Considering the case $\omega_{\text{g}} t \to 0$, one may rewrite the equations above as follows

$$\begin{aligned}\lim_{\omega_{\text{g}} t \to 0} \begin{pmatrix} \psi^{\alpha}_{\text{e}_\text{g}}(t) \\ \psi^{\beta}_{\text{e}_\text{g}}(t) \end{pmatrix} &= \lim_{\omega_{\text{g}} t \to 0} \frac{A}{\omega_{\text{g}}} \begin{pmatrix} \sin(\omega_{\text{g}} t + \theta_0) - \sin\theta_0 \\ -\cos(\omega_{\text{g}} t + \theta_0) + \cos\theta_0 \end{pmatrix} = \lim_{\omega_{\text{g}} t \to 0} \frac{A\omega_{\text{g}} t}{\omega_{\text{g}}} \begin{pmatrix} \frac{\sin(\omega_{\text{g}} t + \theta_0) - \sin\theta_0}{\omega_{\text{g}} t} \\ \frac{-\cos(\omega_{\text{g}} t + \theta_0) + \cos\theta_0}{\omega_{\text{g}} t} \end{pmatrix} \\ &= \lim_{\omega_{\text{g}} t \to 0} \frac{A\omega_{\text{g}} t}{\omega_{\text{g}}} \begin{pmatrix} \cos(\theta_0) \\ \sin(\theta_0) \end{pmatrix}. \end{aligned} \tag{7.21}$$

Now, for a small sampling time $T_{\text{s}} \ll 1\text{s}$ ($T_{\text{s}} = 100\mu s$ for the employed setup) and $\omega_{\text{g}} t \to \omega_{\text{g}} T_s$ in (7.21), the virtual flux is already estimated after *one* sampling interval by

$$\begin{pmatrix} \hat{\psi}^{\alpha}_{\text{e}_\text{g}}[1] \\ \hat{\psi}^{\beta}_{\text{e}_\text{g}}[1] \end{pmatrix} = \lim_{\omega_{\text{g}} t \to \omega_{\text{g}} T_{\text{s}}} \begin{pmatrix} \hat{\psi}^{\alpha}_{\text{e}_\text{g}}(t) \\ \hat{\psi}^{\beta}_{\text{e}_\text{g}}(t) \end{pmatrix} \overset{(7.21)}{\approx} A T_{\text{s}} \begin{pmatrix} \cos(\theta_0) \\ \sin(\theta_0) \end{pmatrix}. \tag{7.22}$$

[1] Note that, $\vec{\psi}^{\alpha\beta}_{\text{bias}}[0] = \vec{\psi}^{\alpha\beta}_{\text{bias}}[l] = \vec{\psi}^{\alpha\beta}_{\text{bias}}$ for all $l \geq 0$.

Hence, for the initial estimation phase, the following estimate of the bias component can be used:

$$\forall\, 1 \leq k \leq N\colon\ \hat{\vec{\psi}}^{\alpha\beta}_{\text{bias}}[k] = \hat{\vec{\psi}}^{\alpha\beta}_{\text{bias}}[1] \overset{(7.5),(7.22)}{=} \left(-\frac{\hat{\psi}^{\beta}_{\text{e}_\text{g}}[1]}{T_\text{s}\cdot\omega_\text{g}}, \frac{\hat{\psi}^{\alpha}_{\text{e}_\text{g}}[1]}{T_\text{s}\cdot\omega_\text{g}} \right)^\top \tag{7.23}$$

To clarify and to ease implementation the proposed IBC-VF estimation method, the necessary steps for the computation/estimation are listed as quasi-code in Algorithm 7.1.

Algorithm 7.1 IBC-VF Estimation

function IBC-VF($\vec{i}^{\,\alpha\beta}_\text{g}[k], \hat{\vec{v}}^{\alpha\beta}_\text{g}[k]$, k)
  Record first sampled values as $\vec{i}^{\,\alpha\beta}_\text{g}[0]$ and $\hat{\vec{v}}^{\alpha\beta}_\text{g}[0]$;
  if $k < 1$ **then**
    Set $\vec{\psi}^{\alpha\beta}_{\text{e}_\text{g}}[0] = \vec{0}$; Set $\hat{\vec{\psi}}^{\alpha\beta}_{\text{bias}}[0] = \vec{0}$;
  end if
  if $k \geq 1$ **then**
    Compute $\vec{\psi}^{\alpha\beta}_{\text{e}_\text{g}}[k]$ with (7.3), i.e.,
    $\vec{\psi}^{\alpha\beta}_{\text{e}_\text{g}}[k] = \vec{\psi}^{\alpha\beta}_{\text{e}_\text{g}}[k-1] + T_\text{s}\hat{\vec{v}}^{\alpha\beta}_\text{g}[k] + L_\text{g}\cdot(\vec{i}^{\,\alpha\beta}_\text{g}[k] - \vec{i}^{\,\alpha\beta}_\text{g}[k-1])$;
    if $1 \leq k \leq N$ **then**
      Compute $\hat{\vec{\psi}}^{\alpha\beta}_{\text{bias}}[1]$ with (7.23), i.e.,
      $\hat{\vec{\psi}}^{\alpha\beta}_{\text{bias}}[1] = \frac{1}{T_\text{s}\cdot\omega_\text{g}} \left(-\hat{\psi}^{\beta}_{\text{e}_\text{g}}[1],\quad \hat{\psi}^{\alpha}_{\text{e}_\text{g}}[1] \right)^\top$;
      Set $\hat{\vec{\psi}}^{\alpha\beta}_{\text{bias}}[k] = \hat{\vec{\psi}}^{\alpha\beta}_{\text{bias}}[1]$;
    end if
    if $k > N$ **then**
      Compute $\hat{\vec{\psi}}^{\alpha\beta}_{\text{bias}}[k]$ with (7.19), i.e.,
      $\hat{\vec{\psi}}^{\alpha\beta}_{\text{bias}}[k] = \hat{\vec{\psi}}^{\alpha\beta}_{\text{bias}}[k-1] + \frac{\vec{\psi}^{\alpha\beta}_{\text{e}_\text{g}}[k] - \vec{\psi}^{\alpha\beta}_{\text{e}_\text{g}}[k-N]}{N}$;
    end if
  end if
  Compute $\hat{\vec{\psi}}^{\alpha\beta}_{\text{key}}[k]$ with (7.20), i.e.,
  $\hat{\vec{\psi}}^{\alpha\beta}_{\text{key}}[k] = \vec{\psi}^{\alpha\beta}_{\text{e}_\text{g}}[k] - \hat{\vec{\psi}}^{\alpha\beta}_{\text{bias}}[k]$.
end function

7.3 Deadbeat control of back-to-back power converter with IBC-VF

7.3.1 Overall control strategy

The overall control strategy is depicted in Fig. 7.3. On net/grid side, a predictive power controller (PPC) is implemented which is fed by the proposed IBF-VF estimator and the

output of the DC-link controller. On load side a predictive current controller (PCC) is implemented. Both predictive controllers are designed as dead-beat controllers and output reference voltages for net/grid and load side of the back-to-back converter, respectively. The corresponding switching patterns are generated by the respective SVM and so a constant switching frequency is assured. In the following the controller designs are explained in more detail.

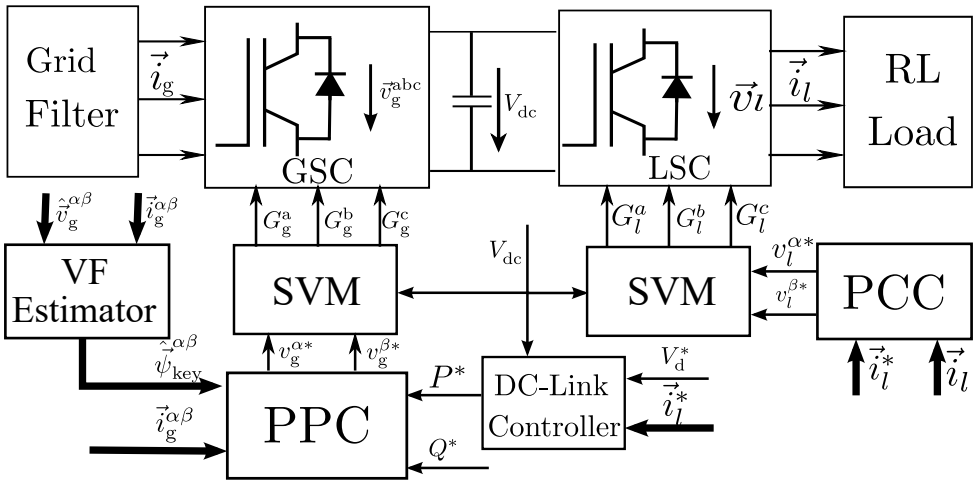

Fig. 7.3: Control structure of the deadbeat-like predictive current controller (PCC on load side) and the deadbeat-like predictive power controller (PPC on grid side) with IBC-VF estimation for a back-to-back converter with RL-load.

For the discrete implementation of the predictive algorithms, prediction models are to be derived in discrete time. For sufficiently small sampling periods $T_\mathrm{s} \ll 1$ (here: $T_\mathrm{s} = 100\mu s$), the application of the first-order (forward) Euler discretization method gives a sufficiently accurate approximation of time-continuous models (see e.g. [93, 138]). If the sampling interval is large (larger than hundreds of μs in the considered application), Euler discretization using Euler forward method may not meet the required approximation accuracy, then more sophisticated discretization methods (like Runge-Kutta or linear multistage) should be considered.

7.3.1.1 Predictive Current Control (PCC) of the Load Side Converter (LSC)

Applying Euler forward method to the load side dynamics (2.22) yields

$$\underbrace{\begin{pmatrix} v_{\mathrm{l[k]}}^{\alpha} \\ v_{\mathrm{l[k]}}^{\beta} \end{pmatrix}}_{=\vec{v}_{\mathrm{l[k]}}^{\alpha\beta}} = R_l \cdot \underbrace{\begin{pmatrix} i_{\mathrm{l[k]}}^{\alpha} \\ i_{\mathrm{l[k]}}^{\beta} \end{pmatrix}}_{=\vec{i}_{\mathrm{l[k]}}^{\alpha\beta}} + \frac{L_l}{T_\mathrm{s}} \cdot \begin{pmatrix} i_{\mathrm{l[k+1]}}^{\alpha} - i_{\mathrm{l[k]}}^{\alpha} \\ i_{\mathrm{l[k+1]}}^{\beta} - i_{\mathrm{l[k]}}^{\beta} \end{pmatrix}. \tag{7.24}$$

The load side predictive (dead-beat) current controller has the goal to drive the load side current to its reference $\vec{i}_l^{\,*} = (i_l^{\alpha *}, i_l^{\beta *})^\top$ in the *very next* interval, i.e.

$$\vec{i}_{\mathrm{l[k+1]}}^{\alpha\beta} = \vec{i}_{\mathrm{l[k+1]}}^{\alpha\beta *}. \tag{7.25}$$

Inserting (7.25) into (7.24) and solving for the load side voltage gives the reference voltage

$$\underbrace{\begin{pmatrix} v_{\mathrm{l[k]}}^{\alpha*} \\ v_{\mathrm{l[k]}}^{\beta*} \end{pmatrix}}_{=:\vec{v}_{\mathrm{l[k]}}^{\alpha\beta*}} = (R_l - \frac{L_l}{T_\mathrm{s}}) \cdot \begin{pmatrix} i_{\mathrm{l[k]}}^{\alpha} \\ i_{\mathrm{l[k]}}^{\beta} \end{pmatrix} + \frac{L_l}{T_\mathrm{s}} \cdot \begin{pmatrix} i_{\mathrm{l[k+1]}}^{\alpha*} \\ i_{\mathrm{l[k+1]}}^{\beta*} \end{pmatrix}, \tag{7.26}$$

which must then be modulated by the SVM. The future load side reference value is obtained by applying a second-order extrapolation algorithm (see [138] for more information):

$$\vec{i}_{\mathrm{l[k+1]}}^{\alpha\beta*} = 3(\vec{i}_{\mathrm{l[k]}}^{\alpha\beta*} - \vec{i}_{\mathrm{l[k-1]}}^{\alpha\beta*}) + \vec{i}_{\mathrm{l[k-2]}}^{\alpha\beta*}. \tag{7.27}$$

7.3.1.2 DC-link Controller

The objective of a DC-link voltage controller is to regulate the DC-link voltage. For simplicity, a PI controller with the following transfer function is used

$$H_{PI}(s) = \frac{I_n^*(s)}{V_{dc}^*(s) - V_{dc}(s)} = \frac{K_p \cdot s + K_i}{s}. \tag{7.28}$$

The output of the PI regulator can be regarded as the net/grid side DC-link current reference I_n^* with which the "PI part"

$$P_{PI}^*(t) = V_{dc}(t) \cdot \underbrace{\mathcal{L}^{-1}\{H_{PI}(s) \cdot (V_{dc}^*(s) - V_{dc}(s))\}}_{=:I_n^*(t)}. \tag{7.29}$$

of the active power reference P^* for the grid side controller is computed (see Fig. **??**). Clearly, the DC-link voltage (2.18) also depends on the load side DC-link current I_l or the load side power flow P_l. To improve the DC-link control performance, a rough estimate $\hat{P}_l$ of the load side resistive losses is introduced and added as feed-forward term to the active power reference as follows

$$P^*(t) = \underbrace{V_{dc}(t) \cdot I_g^*(t)}_{=P_{PI}^*(t)} + \underbrace{R_l \cdot ||\vec{i}_l^*(t)||^2}_{=\hat{P}_l(t)}. \tag{7.30}$$

7.3.1.3 Predictive Power Control (PPC) of the Grid Side Converter (GSC)

Invoking the instantaneous power theory [157], and recalling the deadbeat power control method presented in Chp. 2, yields: Thus the grid side reference voltage vector as

$$\begin{pmatrix} v_{\mathrm{g[k]}}^{\alpha*} \\ v_{\mathrm{g[k]}}^{\beta*} \end{pmatrix} = \begin{pmatrix} e_{\mathrm{g[k]}}^{\alpha} \\ e_{\mathrm{g[k]}}^{\beta} \end{pmatrix} - \frac{L_\mathrm{g}}{T_\mathrm{s}\|\vec{e}_{\mathrm{g[k]}}^{\alpha\beta}\|^2} \begin{bmatrix} e_{\mathrm{g[k]}}^{\alpha} & e_{\mathrm{g[k]}}^{\beta} \\ e_{\mathrm{g[k]}}^{\beta} & -e_{\mathrm{g[k]}}^{\alpha} \end{bmatrix} \begin{pmatrix} P_{\mathrm{[k+1]}}^* - P_{\mathrm{[k]}} + \frac{T_\mathrm{s}R_\mathrm{g}}{L_\mathrm{g}} P_{\mathrm{[k]}} + \omega_\mathrm{g} T_\mathrm{s} Q_{\mathrm{[k]}} \\ Q_{\mathrm{[k+1]}}^* - Q_{\mathrm{[k]}} + \frac{T_\mathrm{s}R_\mathrm{g}}{L_\mathrm{g}} Q_{\mathrm{[k]}} - \omega_\mathrm{g} T_\mathrm{s} P_{\mathrm{[k]}} \end{pmatrix}. \tag{7.31}$$

which is to be modulated by the grid side SVM.

Parameter	Simulation	Experiment
Grid-side Phase Voltages $e_g^{a,b,c}$ [V] (peak)	250	90
Grid-side Voltage Frequency ω_g [rad/s]	100π	100π
Grid-side Reactor Resistor R_g [Ohm]	$1.56 \cdot e^{-3}$	$1.56 \cdot e^{-3}$
Grid-side Reactor Inductance L_g [H]	$16 \cdot e^{-3}$	$16 \cdot e^{-3}$
Load-side Inductance L_l [H]	$10e^{-3}$	$10e^{-3}$
Load-side Resistor R_l [Ohm]	10	10
Load Reference Current Frequency f_l [Hz]	50	50
Sampling Frequency f_s [kHz]	10	10

Table 7.1: System Configuration.

If no grid side voltage information is available (as for the considered sensorless case), the virtual flux estimation in Algorithm 7.1 must be utilized to derive the estimate $\hat{\vec{e}}_g$ for the grid side voltage by invoking (7.6), i.e. in discrete time:

$$\hat{\vec{e}}_{g[k]} = \begin{pmatrix} \hat{e}^{\alpha}_{g[k]} \\ \hat{e}^{\beta}_{g[k]} \end{pmatrix} = \omega_\mathrm{g} \begin{pmatrix} -\hat{\psi}^{\beta}_{\mathrm{key[k]}} \\ \hat{\psi}^{\alpha}_{\mathrm{key[k]}} \end{pmatrix}. \tag{7.32}$$

Therefore, the active and reactive power can be estimated as

$$\begin{pmatrix} \hat{P}_{[\mathrm{k}]} \\ \hat{Q}_{[\mathrm{k}]} \end{pmatrix} = \omega_\mathrm{g} \begin{bmatrix} -\hat{\psi}^{\beta}_{\mathrm{key[k]}} & \hat{\psi}^{\alpha}_{\mathrm{key[k]}} \\ \hat{\psi}^{\alpha}_{\mathrm{key[k]}} & \hat{\psi}^{\beta}_{\mathrm{key[k]}} \end{bmatrix} \cdot \begin{pmatrix} i^{\alpha}_{\mathrm{g[k]}} \\ i^{\beta}_{\mathrm{g[k]}} \end{pmatrix} \tag{7.33}$$

and (since $||\hat{\vec{e}}_{\mathrm{g[k]}}||^2 \overset{(7.32)}{=} \omega_\mathrm{g}^2 ||\hat{\vec{\psi}}^{\alpha\beta}_{\mathrm{key[k]}}||^2$)

$$\begin{aligned} \begin{pmatrix} v^{\alpha *}_{\mathrm{g[k]}} \\ v^{\beta *}_{\mathrm{g[k]}} \end{pmatrix} = \omega_\mathrm{g} \begin{pmatrix} -\hat{\psi}^{\beta}_{\mathrm{key[k]}} \\ \hat{\psi}^{\alpha}_{\mathrm{key[k]}} \end{pmatrix} - \frac{L_\mathrm{g}}{T_\mathrm{s}\omega_\mathrm{g} ||\hat{\vec{\psi}}^{\alpha\beta}_{\mathrm{key[k]}}||^2} \cdot \begin{bmatrix} -\hat{\psi}^{\beta}_{\mathrm{key[k]}} & \hat{\psi}^{\alpha}_{\mathrm{key[k]}} \\ \hat{\psi}^{\alpha}_{\mathrm{key[k]}} & \hat{\psi}^{\beta}_{\mathrm{key[k]}} \end{bmatrix} \cdot \\ \cdot \begin{pmatrix} P^*_{[\mathrm{k+1}]} - \hat{P}_{[\mathrm{k}]} + \omega_\mathrm{g} T_\mathrm{s} \hat{Q}_{[\mathrm{k}]} + \frac{T_\mathrm{s} R_\mathrm{g}}{L_\mathrm{g}} \hat{P}_{[\mathrm{k}]} \\ Q^*_{[\mathrm{k+1}]} - \hat{Q}[k] - \omega_\mathrm{g} T_\mathrm{s} \hat{P}_{[\mathrm{k}]} + \frac{T_\mathrm{s} R_\mathrm{g}}{L_\mathrm{g}} \hat{Q}_{[\mathrm{k}]} \end{pmatrix}. \end{aligned} \tag{7.34}$$

7.3.2 Simulative verification

To illustrate and compare all three estimation schemes, i.e. **PBP-VF** (see Sec. 7.2.2.1), **FBP-VF** (see Sec. 7.2.2.2) and **IBF-VF** (see Sec. 7.2.3) are implemented in Matlab/Simulink. To perform the comparison, all three estimation methods feed a *deadbeat like predictive control* scheme with modulator as shown in Fig. 7.3. Note that the design of the *predictive control* scheme is *identical* for all three virtual flux estimation methods.

In the results, the subscript n has the same representation as g, representing the grid side quantities. The simulation parameters are listed in table 7.1.

The simulation scenario is as follows: Within the interval [0, 0.08]s, the load side current reference has a frequency of 50Hz and a magnitude of 15A (peak). At $t = 0.04$s, the DC-link voltage reference steps up from 600V to 650V, whereas at $t = 0.08$s, the net/grid side current reference magnitude changes to 20A. The simulation results for the **PBP-VF**, **FBP-VF** and **IBF-VF** estimation methods are shown in Fig. 7.4, Fig. 7.5 and Fig. 7.6, respectively. In Fig. 7.4 and Fig. 7.5, both the PBP-VF and FBP-VF estimation methods exhibit an initial delay in the estimation response (see interval [0, 0.017]s in Fig. 7.4(c) & 7.5(c)). This delayed estimation leads to large deviations in the estimated power feedback (see interval [0, 0.017]s in Fig. 7.4(a) & 7.5(a)): System output power and reactive power show great over- or undershoots, which may become a serious issue (e.g. damaging the hardware) for real application. In contrast to that, the proposed IBC-VF method estimates the virtual flux after one sampling instant (see Fig. 7.6(c)). Hence, active and reactive power control show a very acceptable performance. To compare the transient performance of active and reactive power control, Fig. 7.4(a), Fig. 7.5(a) and Fig. 7.6(a) at $t = 0.04$s and $t = 0.08$s are inspected: Obviously, the predictive power controller using the FBP-VF estimation method, shows a better performance than that using the PBP-VF estimation method. Best performance has the predictive power controller fed by the *proposed IBC-VF estimation method*.

7.3.3 Experimental verification

7.3.3.1 FPGA implementation

In this section the FPGA implementation of the proposed control scheme and the experimental results are described and explained in detail. The use of Field Programmable Gate Arrays (FPGAs) as part of the control platform in power electronics and electrical drive systems has increased notably both in academic and industrial applications (see e.g. [158]).

In this work, all the algorithms (e.g. (7.19), (7.23), (7.26), (7.27), (7.33) and (7.34)) are divided into small sub-routines and are implemented using the Single-Cycle-Timed-Loop (SCTL) structure. The FPGA top level clock is set to 40 MHz. Both the load side predictive current controller (PCC) and the grid side predictive power controller (PPC) — including the proposed IBC-VF estimation method — are executed within 2.6 μs (load side controller cost: 68 ticks $= \frac{68}{40\text{M}} 10^6$ μs $= 1.7$ μs and grid side cost: 101 ticks $= \frac{101}{40\text{M}} \cdot 10^6$ μs $= 2.53$ μs). With a sampling frequency of 10 kHz (i.e. $T_\text{s} = 100$ μs), a calculation time compensation is not necessary. The overall structure of the implementation is shown in Fig. 7.7.

7.3.3.2 Experimental verification of the proposed scheme

A grid-connected back-to-back converter system (power rating 5kVA) with RL-load (power rating 300VA) and grid side (R)L-filter has been constructed. The laboratory prototype is depicted in Chp. 2. Its parameters are collected in Tab. 7.1. A Variac is installed between

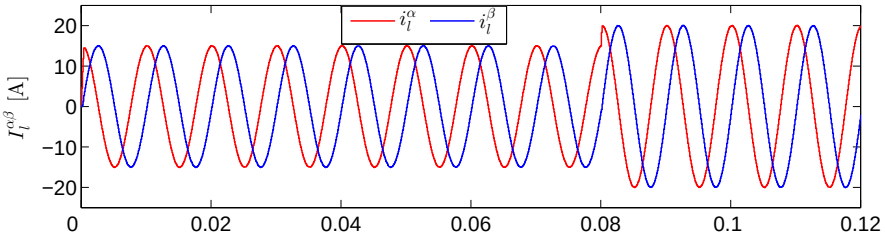

(a) Load side currents

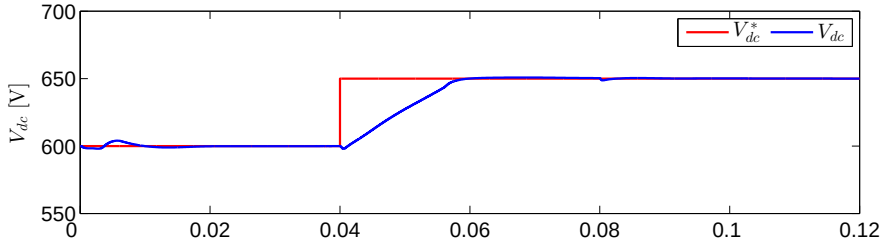

(b) DC-link voltage

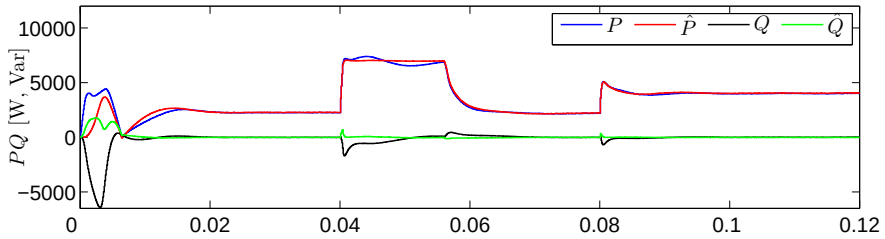

(c) Grid side power

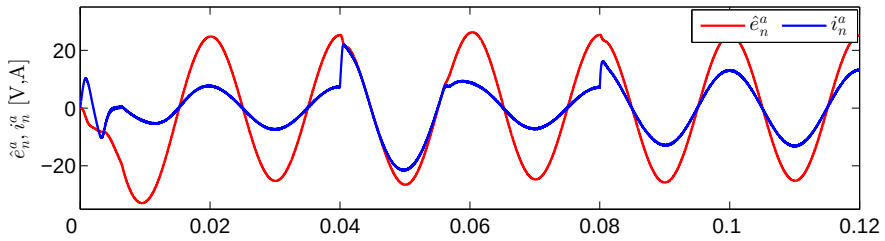

(d) Grid side estimated phase voltage and current

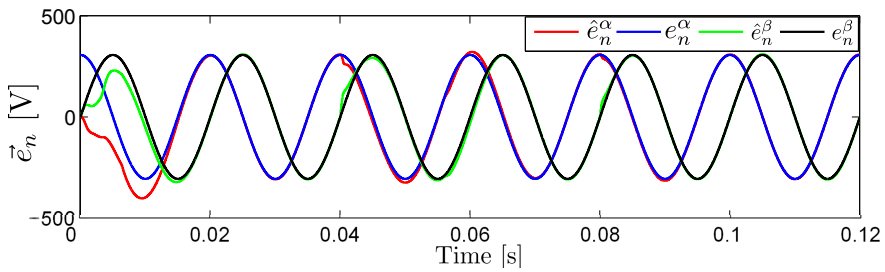

(e) Grid side estimated voltage in $\alpha\beta$ frame

Fig. 7.4: Simulation results for predictive control with **PBP-VF estimation method** for back-to-back power converter.

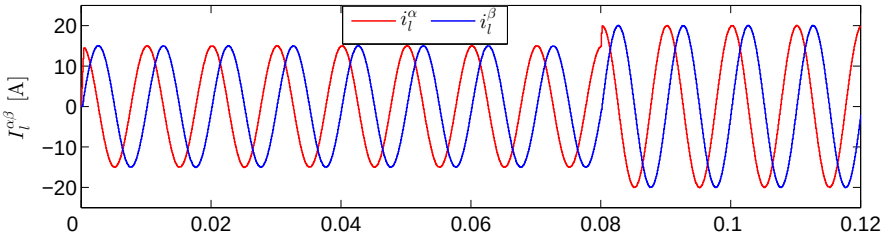

(a) Load side currents

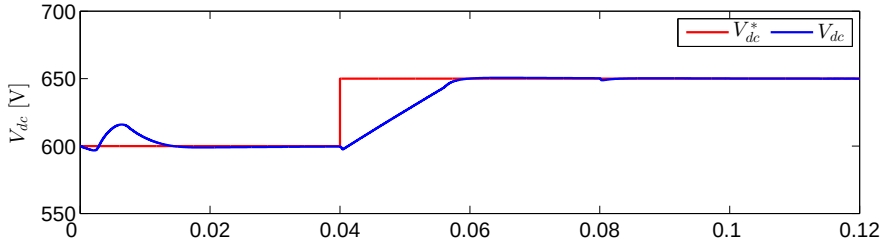

(b) DC-link voltage

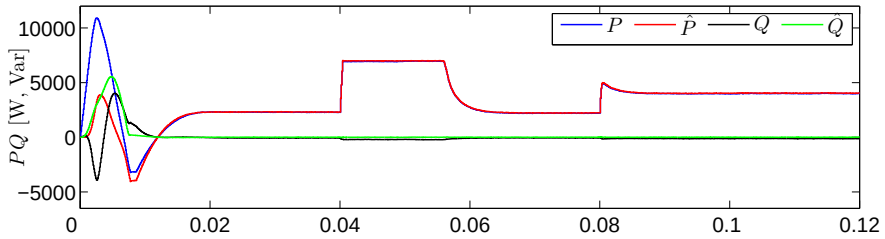

(c) Grid side power

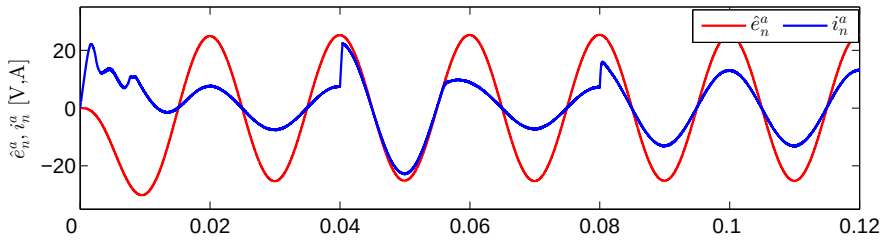

(d) Grid side estimated phase voltage and current

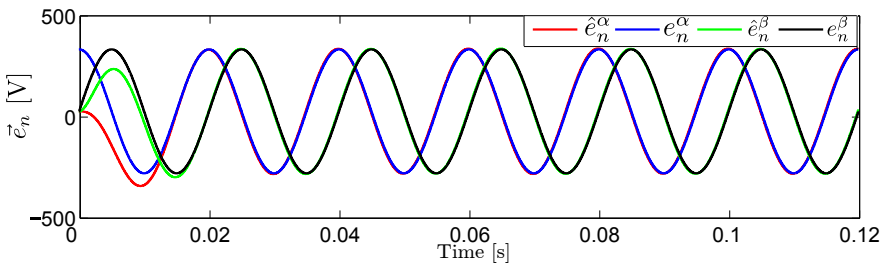

(e) Grid side estimated voltage in $\alpha\beta$ frame

Fig. 7.5: Simulation results for predictive control with **FBP-VF estimation method** for back-to-back power converter.

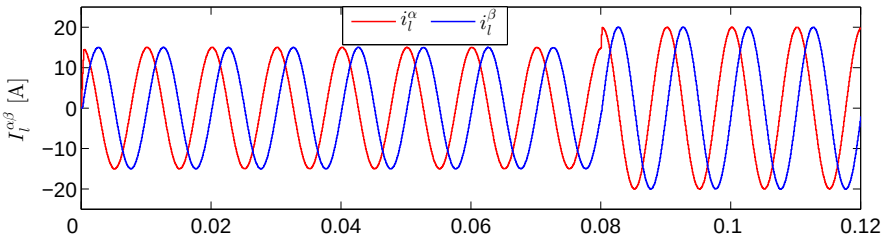

(a) Load side currents

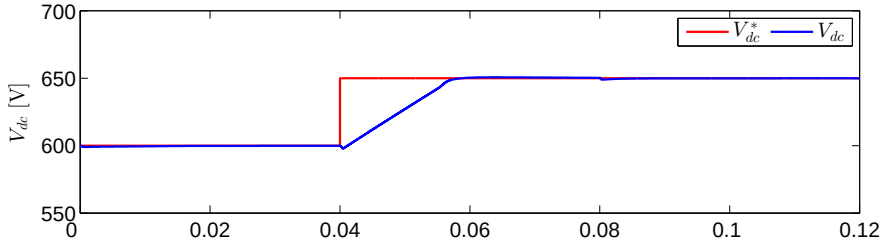

(b) DC-link voltage

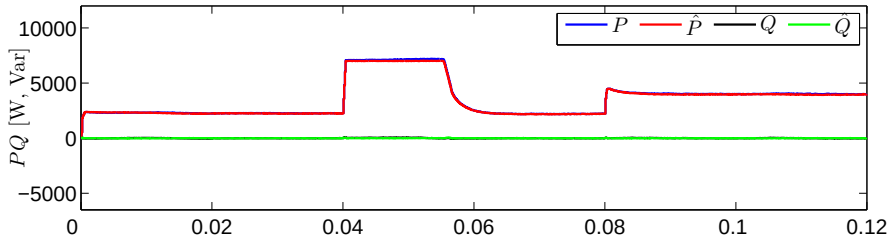

(c) Grid side power

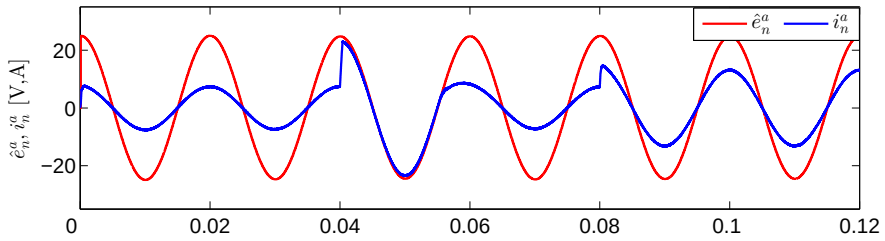

(d) Grid side estimated phase voltage and current

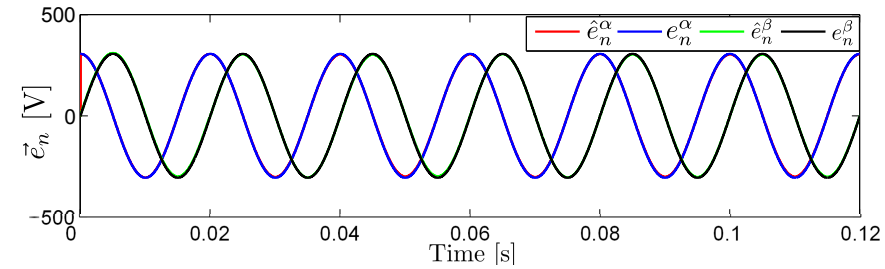

(e) Grid side estimated voltage in $\alpha\beta$ frame

Fig. 7.6: Simulation results for predictive control for back-to-back power converter with the proposed **IBC-VF estimation method**.

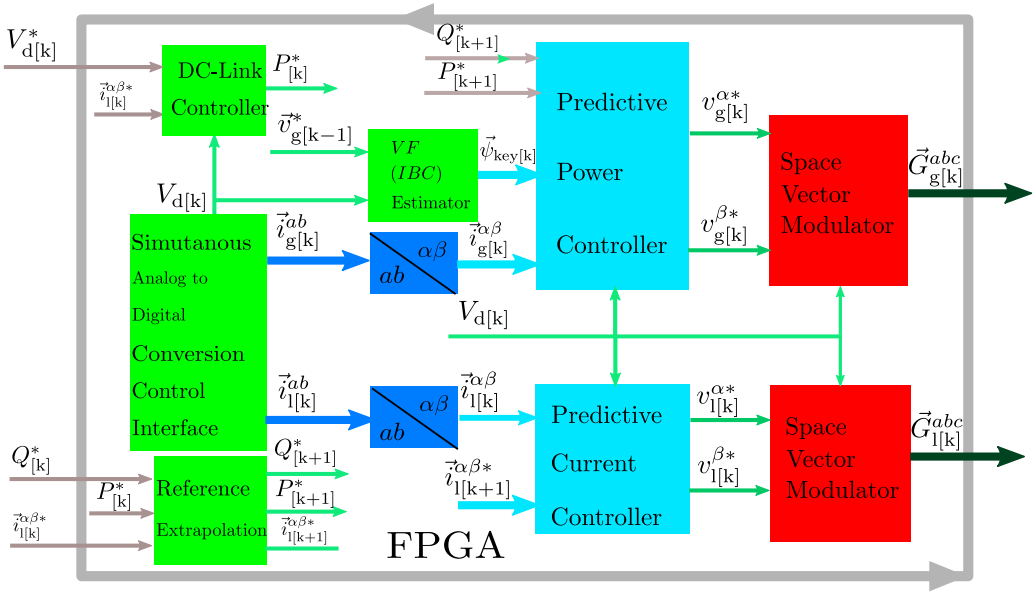

Fig. 7.7: FPGA implementation of the predictive current and power controller with the proposed **IBC-VF estimation method**.

grid and choke (RL-filter) to step down the grid side voltage from 311V (peak) to 90V (peak) for safety reasons. A NI-cRIO FPGA based reconfigurable real-time system is used to implement the predictive controllers (PCC & PPC) with the proposed initial bias compensation virtual flux (IBC-VF) estimation. The measurement results are shown in Fig. 7.8–7.13 (the subscript n has the same representation as g, representing the grid side quantities.). Fig. 7.8 shows the estimates obtained by the proposed IBC-VF estimation method. Estimated virtual flux, estimated grid side voltage and estimated active and reactive power are almost identical to the real signals, which illustrates the effectiveness of the proposed IBC-VF method.

Fig. 7.10 shows control and estimation performance of the predictive power controller (PPC) with IBC-VF estimation scheme during changes in active power (by changing the load currents). The load side current reference changes from 2A to 4A at around 2.39s and back to 2A at around 6s. The DC-link voltage reference is kept constant at 200V. The reactive power reference is set to 0var to perform an operation with unity power factor.

Fig. 7.9(a) shows the zoom of the load side predictive power control performance. Both the transient and the steady state response of the load side controller are fast. Fig. 7.9(b) shows the zoom of the a-phase voltage v.s. its current on the grid side. The good performance of the net/grid side controller – maintaining a unity power factor – is clearly visible.

Fig. 7.11 shows the control performance of the used DC-link controller and of the net side power controller. As can be seen in Fig. 7.11(a), the DC-link voltage follows the reference changes — from 180V to 230V at around 2s and from 230V back to 180V at 7s — with little overshoot and delay. The settling time is smaller than 0.3s. Fig. 7.11(b) shows the respective power control performance. The deviations in active power are caused by

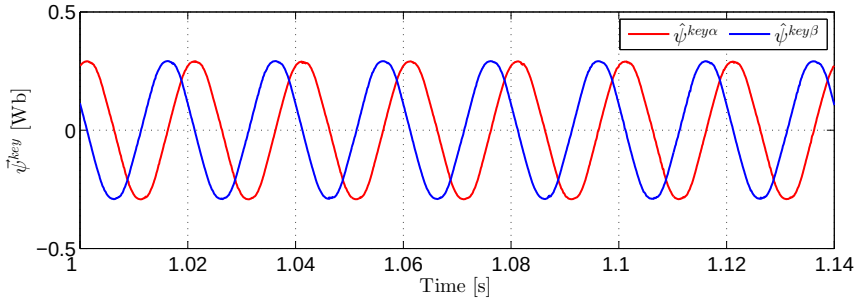

(a) Estimated virtual flux

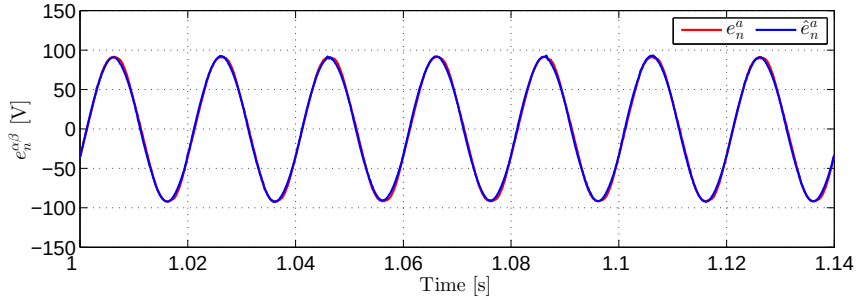

(b) Estimated grid side voltage vs. measured value

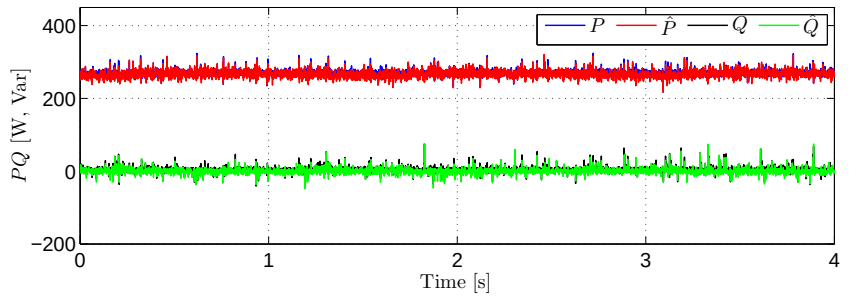

(c) Estimated grid side active and reactive power

Fig. 7.8: Experimental results for predictive power control with the proposed **IBC-VF estimation method**: Estimated virtual flux, voltage and active / reactive power.

the step-like changes in the DC-link voltage. In Fig. 7.12, reactive power control and estimation performance of the proposed IBC-VF scheme are shown. The load side current reference is kept at 4A (so the active power drawn from the grid is kept at around 280W), while the reactive power reference is changed from −50var to 100var at around 2s and then to −100var at 6s. Fig. 7.12(a) illustrates the decoupled dynamic performance of the proposed predictive power control scheme and the close match of estimated and real reactive power. Due to the changes in reactive power, the power factor also changes as illustrated in Fig. 7.12(b).

In Fig. 7.13 (a)–(d), the frequency spectra (with respective zooms) and the total harmonic distortions (THD) of (a) the load side current i_l^a, (b) the net side current i_n^a, (c) the estimated grid voltage $\hat{e}_n^a$ (each for phase a) and (d) the estimated net side active power $\hat{P}$ are shown. In addition, Fig. 7.13 (e) illustrates the spectrum of the net side active

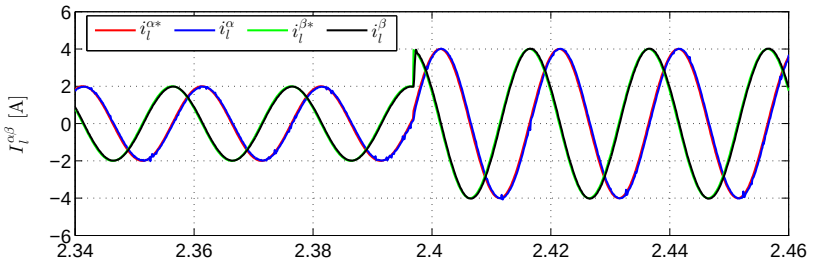

(a) Load side current controller performance

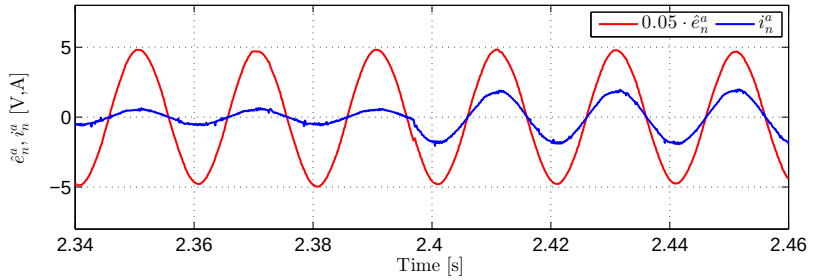

(b) Grid side phase current and estimated phase voltage

Fig. 7.9: Experimental results for predictive current and power control with the proposed **IBC-VF estimation method**: Zooms of load and grid side currents for the results shown in Fig. 7.10 within the interval [2.34, 2.46]s.

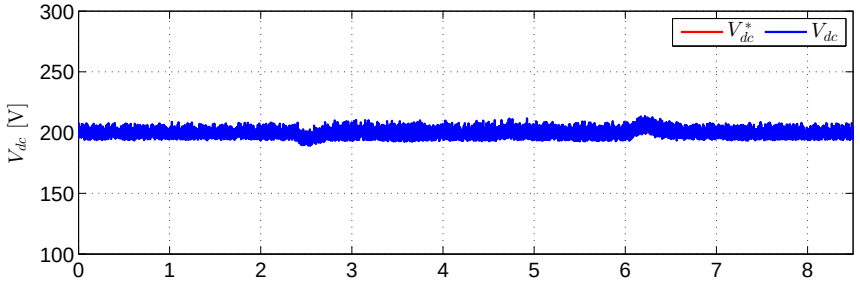

(a) DC-link voltage

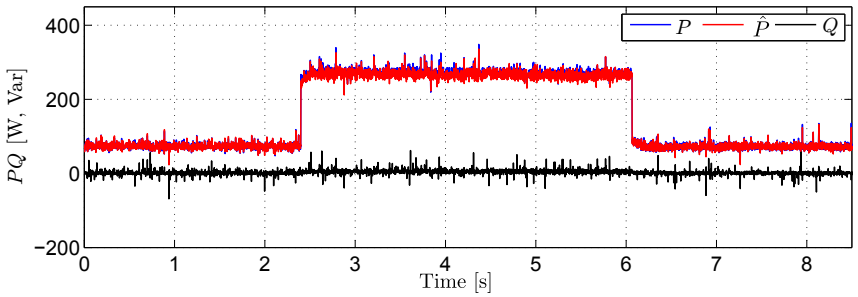

(b) Grid side active and reactive power

Fig. 7.10: Experimental results for predictive power control with the proposed **IBC-VF estimation method**: Overall view of the control/estimation performance. Load side current changes from 2A to 4A and back to 2A. The DC-link voltage reference is set to 200V and reactive power reference reference to 0var.

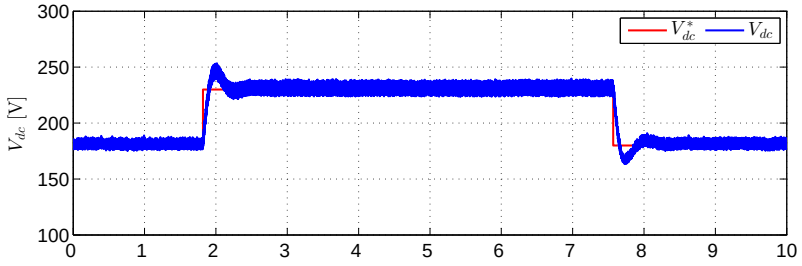

(a) DC-link voltage control

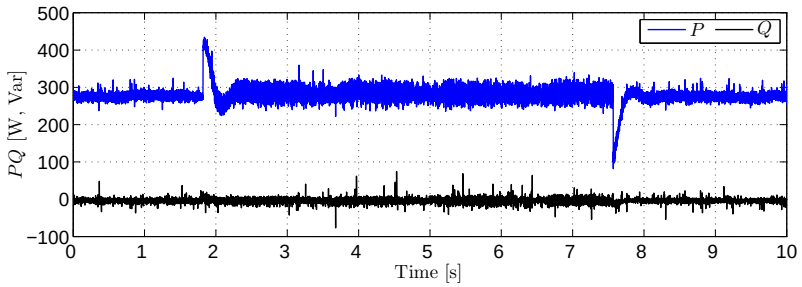

(b) Grid side active and reactive power

Fig. 7.11: Experimental results for predictive power control with the proposed **IBC-VF estimation method**: Performance of DC-link voltage control. DC-link voltage reference changes from 180V to 230V.

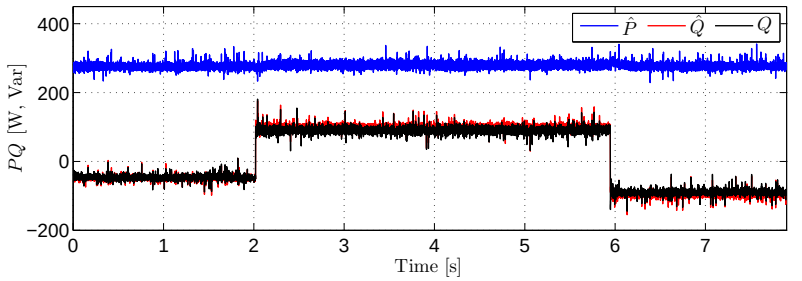

(a) Grid side active and reactive power

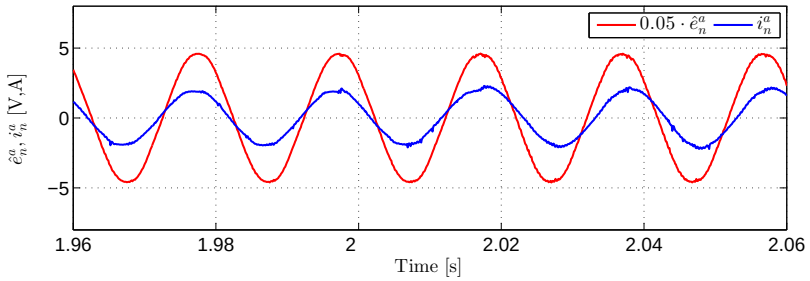

(b) Grid side estimated phase voltage and measured current (of the same phase)

Fig. 7.12: Experimental results for predictive power control with the proposed **IBC-VF estimation method**: Performance of reactive power control. Load side current is kept at 4A, DC-link voltage reference is 200V. The reactive power reference is changed from −50var to 100var and back to −100var at 2s and 6s, respectively.

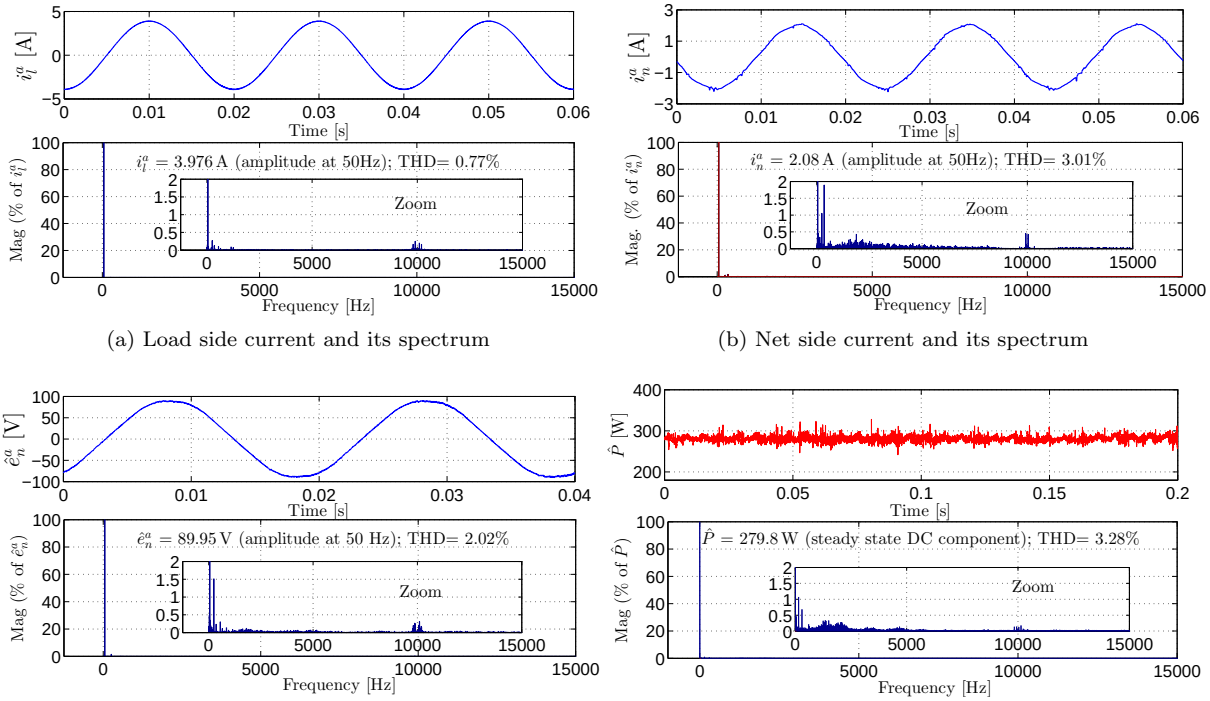

(a) Load side current and its spectrum

(b) Net side current and its spectrum

(c) Estimated grid side voltage and its spectrum

(d) Estimated net side active power and its spectrum

Fig. 7.13: Experimental results (FFT and THD) for predictive current and power control with the proposed **IBC-VF estimation method**. (a) load side current, (b) net side current, (c) estimated net side voltage, and (d) estimated net side active power.

power reference P^*. The THDs are computed with respect to a fundamental frequency of 50 Hz. All spectra in Fig. 7.13 (a)–(d) exhibit small peaks at 10kHz (see respective zooms of the spectra) which confirms a fixed (constant) switching frequency of 10 kHz of the predictive controllers with IBC-VF estimation scheme. The net side current in Fig. 7.13 (b) shows a noisy spectrum with frequencies ranging from 0 to 5kHz; this is due to the DC-link voltage measurement which induces measurement noise to the net side active power reference (the output of the DC-link controller, see Fig. 7.3 and Eq. (7.30)) and to the net side active power estimation (see Fig. 7.13 (d) & (e), resp.).

7.4 Summary

This chapter has closely studied the grid side voltage sensorless control methods of grid-tied power converters. A novel time domain initial bias compensation based virtual flux (IBC-VF) estimation technique for grid-tied back-to-back power converters to achieve grid side voltage sensorless control with nice control dynamics and estimate accuracy has been proposed and experimentally evaluated. The proposed methods can be also applied to direct model predictive control without modulators for multilevel power converters, which can be found in our publication [159]. Also, based on the same virtual flux concept, the proposed method can be a good base for realizing predictive flux control for grid connected power converter with and without voltage sensors.

Chapter 8

Encoderless control of PMSG wind turbine system

This chapter introduces the generator side encoderless control techniques. After a short review of the available encoderless control methods (See Sec. 8.1), two model based encoderless control techniques, namely, Extended Kalman Filter (EKF) based method (See Sec. 8.2) and Sliding Mode Observer (SMO) based method (See Sec. 8.3) are closely investigated. The former, due to its nice estimate performances, is implemented also on a FPGA based real-time controller and evaluated with experimental results (See Sec. 8.2.4.2).

8.1 Introduction

Installations of wind turbine systems with permanent-magnet synchronous generators (PMSG) have steadily increased over the last years [15, 17, 125, 142]. Usually, rotor speed and/or position of the generator are required, not only for a safe operation, but also for torque and power control of the wind energy conversion system. Although it is straight forward to utilize a speed/position sensor, according to [160], more than 14% of the system failures are directly related to sensor failures and more than 40% of the system failures are related to sensor failures in combination with failures of electrical and mechanical components. Clearly, system failures bring significant losses to the power production. This motivates the use of reliable and robust encoderless control strategies.

In general, two categories of techniques have been studied to achieve encodorless control [14, 161], namely, *machine model based* methods (i.e., to estimate the machine speed and position based on the system mathematical model) and *magnetic saliency decoding based* methods (i.e., to decode the position information from the magnetic flux saliency) [14, 162]. The latter takes the advantage of the asymmetrical distribution of the rotor flux, i.e., magnetic saliency, caused by either the *asymmetrical physical structure* or *stator inductance saturation* [162–164]. It is able to operate a motor/generator from stand-still. However, to achieve a decodable saliency ratio, external excitation signals[1]

[1]Mostly high frequency (HF) voltage signals injected in either the stationary (i.e., the so-called *rotating HF injection*

or modifying the modulator pulse patterns[2] are required, which may cause acoustic and power-loss problems or require a high performance hardware.

Starting from stand-still for generators in wind turbine systems is not commonly required because the wind turbine (driven by the flowing wind) may push the generator to a starting point. On the other side, many machine model based encoderless techniques have already been developed being able to achieve nice robustness against disturbances and good accuracy in terms of position and speed estimation above a cut-in speed. More importantly, they do not produce acoustic pollution and are injection power-lossless. Therefore, this group can be potentially applied for wind turbine generator encoderless control as a backup solution. Among this group, encoderless control with Extended Kalman Filter (EKF) [165–167] and Sliding Mode Observer (SMO) [168, 169] are two of the well-known solutions.

EKF is an extension of Kalman filter, which was firstly introduced by R.E. Kalman [170] as a recursive solution to the discrete-data linear filter problem. It is characterized by fast convergence and robustness in most cases. [171, 172]. However, for an AC motor drive system, due to its complex matrix calculation required by EKF, the heavy computational efforts make the whole controller calculation time considerably long; this introduces a delay deteriorating the control (estimation) performances. Therefore, Field Programmable Gate Array (FPGA) becomes more suitable to realize such schemes thanks to its nice flexibility and parallel calculation capability. However, only a few implementations of EKF using FPGA have been reported. Therefore, Sec. 8.2 of this chapter introduces the application of EKF based encoderless control and its FPGA realization in details.

In section 8.3 the SMO based encoderless control method is presented. By a properly chosen sliding mode manifold and stabilized by a proper feedback gain of the correction loop (mostly invoking the Lyapunov function), SMO achieves nice robustness to system disturbances and less sensitive to parameter deviations due to its inherent variable structure control nature. In section 8.3, instead of using the commonly used sign-um function for the feedback correction loop, a sigmoid function is adopted to reduce the chattering ripples of the estimated variables. The sliding mode observer utilizes a time-varying switching gain and a time-varying cut-off frequency to estimate rotor position and rotor speed with reduced chattering. The results which confirm the effectiveness are given.

8.2 Encoderless control with EKF

Nonlinear system state estimation using EKF is revisited and applied to encoderless control of PMSG for *both* without *and* with load estimation. This technique is then incorporated into the deadbeat control framework (introduced in Chp. 3). The effectiveness are evaluated and analyzed.

method), or rotational frames (i.e., the so-called *pulsating HF injection* method); or current signal injections (mostly a low frequency current signal is injected into the d-axis) of the systems are used to excite the motor hence to obtain a reacting signal containing the position information with a decodable ratio.

[2] Hence to use the so-called "*indirect flux detection by online inductance measurement*", i.e., INFORM, technique [162–164]

8.2.1 Nonlinear system state estimation with EKF

EKF targets to minimize the *covariance* of the state estimation errors for a *nonlinear system* and is an optimum filter when the system uncertainties and measurement noises exist. To ease the understanding and the algorithm description, the recursive algorithm including the implementation instruction using EKF to a generalized nonlinear system of

$$\left.\begin{array}{rcl} \vec{x}_{[\mathrm{k}+1]} & = & \overbrace{\vec{x}_{[\mathrm{k}]}+T_{\mathrm{s}}\vec{\mathbf{g}}\big(\vec{x}_{[\mathrm{k}]},\vec{u}_{[\mathrm{k}]}\big)}^{\vec{\mathbf{f}}(\vec{x}_{[\mathrm{k}]},\vec{u}_{[\mathrm{k}]})}+\vec{\omega}_{[\mathrm{k}]} \\ \vec{y}_{[\mathrm{k}]} & = & \vec{\mathbf{h}}\big(\vec{x}_{[\mathrm{k}]}\big)+\vec{v}_{[\mathrm{k}]},\ \vec{x}_{[0]}=\vec{x}_0 \end{array}\right\} \tag{8.1}$$

is listed in Algorithm 8.1, where $\vec{x}_{[\mathrm{k}]}=\big(x_{1[\mathrm{k}]},\cdots,x_{\mathrm{n}[\mathrm{k}]}\big)^{\top}\in\mathbb{R}^n$, $\vec{u}_{[\mathrm{k}]}=\big(u_{1[\mathrm{k}]},\cdots,u_{\mathrm{m}[\mathrm{k}]}\big)^{\top}\in\mathbb{R}^m$, $\vec{y}_{[\mathrm{k}]}=\big(y_{1[\mathrm{k}]},\cdots,y_{\mathrm{m}[\mathrm{k}]}\big)^{\top}\in\mathbb{R}^m$, are the system state, actuating and measurement vectors, respectively. $n,m\in\mathbb{N};\mathbb{N},\mathbb{R}$ are natural, real numbers. $\vec{\omega}_{[\mathrm{k}]}=\big(\omega_{1[\mathrm{k}]},\cdots,\omega_{\mathrm{n}[\mathrm{k}]}\big)^{\top}\in\mathbb{R}^n$ and $\vec{v}_{[\mathrm{k}]}=\big(v_{1[\mathrm{k}]},\cdots,v_{\mathrm{m}[\mathrm{k}]}\big)^{\top}\in\mathbb{R}^m$ are the system modeling uncertainties and measurement noises, respectively. Both are assumed to be independent (i.e., $\mathcal{E}\{\vec{\omega}_{[\mathrm{k}]}\vec{v}_{[\mathrm{k}]}\}=\mathbb{O}^{n\times m}$, while $\mathcal{E}\{\vec{\omega}_{[\mathrm{k}]}\}=\mathbb{O}^n$ and $\mathcal{E}\{\vec{v}_{[\mathrm{k}]}\}=\mathbb{O}^m$) and with *normal probability distributions* (i.e., $\mathcal{P}(\alpha_i)=\frac{1}{\delta\alpha_i\sqrt{2\pi}}\exp\big(\frac{-(\mathcal{E}\{\alpha_i\}-\alpha_i)^2}{2\delta_\alpha^2}\big)$ with $\delta_\alpha^2:=\mathcal{E}\big\{(\mathcal{E}\{\alpha_i\}-\alpha_i)^2\big\}$ and $\alpha_i\in\{\vec{\omega},\vec{v}\}$). $\mathcal{E}(\cdot)$ and $\mathcal{P}(\cdot)$ represent the expectation and distribution calculations, respectively. The covariance matrices of $\mathbf{Q}$ and $\mathbf{R}$ are assumed to be constant and semi- and positive definite (i.e., $\mathbf{Q}:=\mathcal{E}\big\{\vec{\omega}_{[\mathrm{k}]}\vec{\omega}_{[\mathrm{k}]}^{\top}\big\}\geq\mathbb{O}^{n\times n},\mathbf{R}:=\mathcal{E}\big\{\vec{v}_{[\mathrm{k}]}\vec{v}_{[\mathrm{k}]}^{\top}\big\}\geq\mathbb{O}^{m\times m}$).

Algorithm 8.1 EKF state estimation for nonlinear systems of (8.1)

function EKF($\vec{x}_{[\mathrm{k}]},\hat{\vec{u}}_{[\mathrm{k}]},k$)
  if $k=0$ **then**
    State Initialization: $\hat{\vec{x}}_{[\mathrm{k}]}=\vec{0},\mathbf{P}(0)=\mathbf{P}_0;\mathbf{K}_{[\mathrm{k}]}=\mathbf{P}_{[0]}\mathbf{J}_{h_{[0]}}^{\top}\big(\mathbf{J}_{h_{[0]}}\mathbf{P}_{[0]}\mathbf{J}_{h_{[0]}}^{\top}+\mathbf{R}\big)^{-1}$;
  end if
  if $k>1$ **then**
    Time Update, i.e., the *'priori prediction'* step.
    i) State prediction: $\hat{\vec{x}}_{[\mathrm{k}]}^{-}=\vec{\mathbf{f}}\big(\hat{\vec{x}}_{[\mathrm{k}-1]},\vec{u}_{[\mathrm{k}-1]}\big)$;
    ii) System *Jacobian* matrix calculation: $\mathbf{J}_{\vec{\mathbf{f}}_{[\mathrm{k}]}}=\frac{\partial\vec{\mathbf{f}}(\vec{x}(t)\vec{u}(t))}{\partial\vec{x}(t)}|_{\mathrm{t}=(\mathrm{k}-1)\cdot\mathrm{T_s}}$;
    iii) Error covariance matrix update: $\mathbf{P}_{[\mathrm{k}]}^{-}=\mathbf{J}_{\vec{\mathbf{f}}_{[\mathrm{k}]}}\mathbf{P}_{[\mathrm{k}-1]}\mathbf{J}_{\vec{\mathbf{f}}_{[\mathrm{k}]}}^{\top}+\mathbf{Q}$;
    iv) Measurement *Jacobian* matrix calculation: $\mathbf{J}_{\vec{\mathbf{h}}_{[\mathrm{k}]}}=\frac{\partial\vec{\mathbf{h}}(\vec{x}(t))}{\partial\vec{x}(t)}|_{\mathrm{t}=(\mathrm{k}-1)\cdot\mathrm{T_s}}$;
    v) Calculate Kalman Gain $\mathbf{K}_{[\mathrm{k}]}$: $\mathbf{K}_{[\mathrm{k}]}=\mathbf{P}_{[\mathrm{k}]}^{-}\mathbf{J}_{\vec{\mathbf{h}}_{[\mathrm{k}]}}^{\top}\Big(\mathbf{J}_{\vec{\mathbf{h}}_{[\mathrm{k}]}}\mathbf{P}_{[\mathrm{k}]}^{-}\mathbf{J}_{\vec{\mathbf{h}}_{[\mathrm{k}]}}^{\top}+\mathbf{R}\Big)^{-1}$;
    Measurement Update, i.e., the *'correction'* step.
    i) State estimation update with correction: $\hat{\vec{x}}_{[\mathrm{k}]}=\hat{\vec{x}}_{[\mathrm{k}]}^{-}+\mathbf{K}_{[\mathrm{k}]}\cdot\big(\vec{y}_{[\mathrm{k}]}-\vec{\mathbf{h}}(\vec{x}_{[\mathrm{k}]}^{-})\big)$;
    ii) Error covariance matrix update with correction: $\mathbf{P}_{[\mathrm{k}]}=\mathbf{P}_{[\mathrm{k}]}^{-}-\mathbf{K}_{[\mathrm{k}]}\mathbf{J}_{\vec{\mathbf{h}}_{[\mathrm{k}]}}\mathbf{P}_{[\mathrm{k}]}^{-}$.
  end if
  $k=k+1$; Output $\hat{\vec{x}}_{[\mathrm{k}]}$.
end function

Applying EKF to PMSG encoderless control requires the system model. The system models (introduced in Chp. 2) both in dq frame and $\alpha\beta$ frames can be used. However, an

extra *Park Transformation* is required for the model in dq, which increases the calculation and FPGA realization efforts. Therefore, in this work, the the EKF observer for encoderless control is realized using the PMSG model in $\alpha\beta$ frame[3].

In the following sections, both the system state estimations without (Case-I) and with turbine (Case-II) *drive torque* are introduced following the EKF frame listed in Algorithm 8.1.

8.2.2 Case-I: EKF estimation without turbine drive torque

The system state to estimate in this case (functions or quantities for this case are all marked with superscript of $(\cdot)^{\mathrm{I}}$) is $\hat{\vec{x}}^{\mathrm{I}}(t) = \big(\hat{i}^{\alpha}_{\mathrm{m}}(t), \hat{i}^{\beta}_{\mathrm{m}}(t), \hat{\omega}_{\mathrm{e}}(t), \hat{\theta}_{\mathrm{e}}(t)\big)^{\top}$. The measurement and actuating vectors are $\vec{y}(t) = \big(i^{\alpha}_{\mathrm{m}}(t), i^{\beta}_{\mathrm{m}}(t)\big)^{\top}$, and $\vec{u}(t) = \big(v^{\alpha}_{\mathrm{m}}(t), v^{\beta}_{\mathrm{m}}(t)\big)^{\top}$, respectively. With the *infinite inertia assumption*, i.e., $\frac{d\omega_{\mathrm{e}}}{dt} \approx 0$, transferring the PMSG model in $\alpha\beta$ frame following the state space description as in (8.1), one obtains the following

$$\vec{\mathbf{f}}^{\mathrm{I}}_{[\mathrm{k}]}\big(\,\cdot\,\big) = \vec{x}_{[\mathrm{k}]} + T_{\mathrm{s}} \cdot \vec{\mathbf{g}}^{\mathrm{I}}_{[\mathrm{k}]}\big(\,\cdot\,\big), \text{ with } \vec{\mathbf{g}}^{\mathrm{I}}_{[\mathrm{k}]}\big(\,\cdot\,\big) = \begin{bmatrix} \frac{v^{\alpha}_{\mathrm{m}[\mathrm{k}]}}{L_{\mathrm{s}}} - \frac{R_{\mathrm{s}}}{L_{\mathrm{s}}} i^{\alpha}_{\mathrm{m}[\mathrm{k}]} + \frac{\psi_{\mathrm{pm}}\omega_{\mathrm{e}[\mathrm{k}]}}{L_{\mathrm{s}}} \sin(\theta_{\mathrm{e}[\mathrm{k}]}) \\ \frac{v^{\beta}_{\mathrm{m}[\mathrm{k}]}}{L_{\mathrm{s}}} - \frac{R_{\mathrm{s}}}{L_{\mathrm{s}}} i^{\beta}_{\mathrm{m}[\mathrm{k}]} + \frac{\psi_{\mathrm{pm}}\omega_{\mathrm{e}[\mathrm{k}]}}{L_{\mathrm{s}}} \cos(\theta_{\mathrm{e}[\mathrm{k}]}) \\ 0 \\ \omega_{\mathrm{e}[\mathrm{k}]} \end{bmatrix}; \quad (8.2a)$$

$$\vec{\mathbf{h}}^{\mathrm{I}}_{[\mathrm{k}]}\big(\,\cdot\,\big) = \begin{bmatrix} i^{\alpha}_{\mathrm{m}[\mathrm{k}]} & 0 & 0 & 0 \\ 0 & i^{\beta}_{\mathrm{m}[\mathrm{k}]} & 0 & 0 \end{bmatrix}. \quad (8.2b)$$

Applying equations in step (ii) and (iv) of Algorithm 8.1 to (8.2a) and (8.2b), the system and measurement *Jacobian* matrices are obtained as

$$\mathbf{J}^{\mathrm{I}}_{\vec{\mathbf{f}}_{[\mathrm{k}]}} = \begin{bmatrix} \frac{L_{\mathrm{s}} - R_{\mathrm{s}}T_{\mathrm{s}}}{L_{\mathrm{s}}} & 0 & T_{\mathrm{s}}\frac{\psi_{\mathrm{pm}}}{L_{\mathrm{s}}}\sin(\theta_{\mathrm{e}[\mathrm{k}]}) & T_{\mathrm{s}}\frac{\psi_{\mathrm{pm}}\omega_{\mathrm{e}[\mathrm{k}]}}{L_{\mathrm{s}}}\cos(\theta_{\mathrm{e}[\mathrm{k}]}) \\ 0 & \frac{L_{\mathrm{s}} - R_{\mathrm{s}}T_{\mathrm{s}}}{L_{\mathrm{s}}} & -T_{\mathrm{s}}\frac{\psi_{\mathrm{pm}}}{L_{\mathrm{s}}}\cos(\theta_{\mathrm{e}[\mathrm{k}]}) & T_{\mathrm{s}}\frac{\psi_{\mathrm{pm}}\omega_{\mathrm{e}[\mathrm{k}]}}{L_{\mathrm{s}}}\sin(\theta_{\mathrm{e}[\mathrm{k}]}) \\ 0 & 0 & 1 & 0 \\ 0 & 0 & T_{\mathrm{s}} & 1 \end{bmatrix}; \quad (8.3a)$$

$$\mathbf{J}^{\mathrm{I}}_{\vec{\mathbf{h}}_{[\mathrm{k}]}} = \begin{bmatrix} 1 & 0 & 0 & 0 \\ 0 & 1 & 0 & 0 \end{bmatrix}. \quad (8.3b)$$

Then the targeted system state of $\hat{\vec{x}}^{\mathrm{I}}$ can be estimated following the algorithm outline.

[3]Note that, if the stator currents in $\alpha\beta$ frame are the estimation states for using EKF, then two groups of solutions can both satisfy the following equations, which may make the EKF converge to wrong state $(-\omega_{\mathrm{e}}, \theta_{\mathrm{e}} + \pi$, since $v^{\alpha}_{m} = R_{\mathrm{s}} i^{\alpha}_{\mathrm{m}} + L\frac{di^{\alpha}_{\mathrm{m}}}{dt} - \psi_{\mathrm{pm}}\omega_{\mathrm{e}}\sin(\theta_{\mathrm{e}})$; $v^{\beta}_{m} = R_{\mathrm{s}} i^{\beta}_{\mathrm{m}} + L\frac{di^{\beta}_{\mathrm{m}}}{dt} + \psi_{\mathrm{pm}}\omega_{\mathrm{e}}\cos(\theta_{\mathrm{e}})$;). A nice solution is to choose the stator flux as the estimation state, for more details please take "A novel sensorless Direct Torque Control for PMSM based Extended Kalman Filter"by Xiao Xi, Zhang Meng, etc., 2007 as a useful reference.

8.2.3 Case-II: EKF estimation with turbine drive torque

The system state to be estimated in this case (functions or quantities are marked with superscript of $(\cdot)^{\mathrm{II}}$) is $\hat{\vec{x}}^{\mathrm{II}}(t) = \big(\hat{i}^{\alpha}_{\mathrm{m}}(t), \hat{i}^{\beta}_{\mathrm{m}}(t), \hat{\omega}_{\mathrm{e}}(t), \hat{\theta}_{\mathrm{e}}(t), \hat{T}_t(t)\big)^{\top}$[4]. The measurement and actuating vectors remain the same as *case-I*. Assuming the load torque is unknown but changes slow enough, i.e., $\frac{dT_t(t)}{dt} \approx 0$ and comparing with equation (8.1), yields the following

$$\vec{\mathbf{f}}^{\mathrm{II}}_{[\mathrm{k}]}\big(\,\cdot\,\big) = \vec{x}_{[\mathrm{k}]} + T_{\mathrm{s}} \cdot \vec{\mathbf{g}}^{\mathrm{II}}_{[\mathrm{k}]}\big(\,\cdot\,\big), \text{ with } \vec{\mathbf{g}}^{\mathrm{II}}_{[\mathrm{k}]}\big(\,\cdot\,\big) = \begin{bmatrix} \frac{v^{\alpha}_{\mathrm{m}[\mathrm{k}]}}{L_{\mathrm{s}}} - \frac{R_{\mathrm{s}}}{L_{\mathrm{s}}} i^{\alpha}_{\mathrm{m}[\mathrm{k}]} + \frac{\psi_{\mathrm{pm}}\omega_{\mathrm{e}[\mathrm{k}]}}{L_{\mathrm{s}}} \sin(\theta_{\mathrm{e}[\mathrm{k}]}) \\ \frac{v^{\beta}_{\mathrm{m}[\mathrm{k}]}}{L_{\mathrm{s}}} - \frac{R_{\mathrm{s}}}{L_{\mathrm{s}}} i^{\beta}_{\mathrm{m}[\mathrm{k}]} + \frac{\psi_{\mathrm{pm}}\omega_{\mathrm{e}[\mathrm{k}]}}{L_{\mathrm{s}}} \cos(\theta_{\mathrm{e}[\mathrm{k}]}) \\ \frac{\hat{T}_{\mathrm{e}[\mathrm{k}]} - N_{\mathrm{p}} T_{\mathrm{t}[\mathrm{k}]}}{\Theta_{\mathrm{m}}} \\ \omega_{\mathrm{e}[\mathrm{k}]} \\ 0 \end{bmatrix}, \tag{8.4a}$$

$$\vec{\mathbf{h}}^{\mathrm{II}}_{[\mathrm{k}]}\big(\,\cdot\,\big) = \begin{bmatrix} i^{\alpha}_{\mathrm{m}[\mathrm{k}]} & 0 & 0 & 0 & 0 \\ 0 & i^{\beta}_{\mathrm{m}[\mathrm{k}]} & 0 & 0 & 0 \end{bmatrix}, \tag{8.4b}$$

where $\hat{T}_{\mathrm{e}[\mathrm{k}]} = N_{\mathrm{p}} \cdot \psi_{\mathrm{pm}}\big(i^{\beta}_{\mathrm{m}[\mathrm{k}]} \cos(\theta_{\mathrm{e}[\mathrm{k}]}) - i^{\alpha}_{\mathrm{m}[\mathrm{k}]} \sin(\theta_{\mathrm{e}[\mathrm{k}]})\big)$. Applying equations in step (ii) and (iv) of Algorithm 8.1 to (8.4a) and (8.4b), the system and measurement *Jacobian* matrices in this case are obtained as follows

$$\mathbf{J}^{\mathrm{II}}_{\vec{\mathbf{f}}_{[\mathrm{k}]}} = \begin{bmatrix} \frac{L_{\mathrm{s}} - R_{\mathrm{s}} T_{\mathrm{s}}}{L_{\mathrm{s}}} & 0 & T_{\mathrm{s}} \frac{\psi_{\mathrm{pm}}}{L_{\mathrm{s}}} \sin(\theta_{\mathrm{e}[\mathrm{k}]}) & T_{\mathrm{s}} \frac{\psi_{\mathrm{pm}}\omega_{\mathrm{m}[\mathrm{k}]}}{L_{\mathrm{s}}} \cos(\theta_{\mathrm{e}[\mathrm{k}]}) & 0 \\ 0 & \frac{L_{\mathrm{s}} - R_{\mathrm{s}} T_{\mathrm{s}}}{L_{\mathrm{s}}} & -T_{\mathrm{s}} \frac{\psi_{\mathrm{pm}}}{L_{\mathrm{s}}} \cos(\theta_{\mathrm{e}[\mathrm{k}]}) & T_{\mathrm{s}} \frac{\psi_{\mathrm{pm}}\omega_{\mathrm{m}[\mathrm{k}]}}{L_{\mathrm{s}}} \sin(\theta_{\mathrm{e}[\mathrm{k}]}) & 0 \\ \frac{-N_{\mathrm{p}}\psi_{\mathrm{pm}}}{\Theta_{\mathrm{m}}} \sin(\theta_{\mathrm{e}[\mathrm{k}]}) & \frac{-N_{\mathrm{p}}\psi_{\mathrm{pm}}}{\Theta_{\mathrm{m}}} \cos(\theta_{\mathrm{e}[\mathrm{k}]}) & 1 & F_{3,4} & \frac{-N_{\mathrm{p}}}{\Theta_{\mathrm{m}}} \\ 0 & 0 & T_{\mathrm{s}} & 0 & 0 \\ 0 & 0 & 0 & 0 & 0 \end{bmatrix}, \tag{8.5a}$$

$$\mathbf{J}^{\mathrm{II}}_{\vec{\mathbf{h}}_{[\mathrm{k}]}} = \begin{bmatrix} 1 & 0 & 0 & 0 & 0 \\ 0 & 1 & 0 & 0 & 0 \end{bmatrix}, \tag{8.5b}$$

where $F_{3,4} = -\frac{N_{\mathrm{p}}\psi_{\mathrm{pm}}}{\Theta_{\mathrm{m}}} \cdot \big(i^{\alpha}_{\mathrm{m}[\mathrm{k}]} \cdot \cos(\theta_{\mathrm{e}[\mathrm{k}]}) + i^{\beta}_{\mathrm{m}[\mathrm{k}]} \cdot \sin(\theta_{\mathrm{e}[\mathrm{k}]})\big)$.

Remark 18 (Parameter matrices determination [165, 173]) *The choice of the matrices* $\mathbf{P}_0$, $\mathbf{Q}$ *and* $\mathbf{R}$ *affects the EKF performance and even the convergence; therefore it is a crucial step.*

1. $\mathbf{P}_0$ *presents the covariance, i.e., mean-squared errors, starting from the initial conditions. It determines the initial amplitude of the transient behavior. The coupling effects between the system states are usually neglected and therefore* $\mathbf{P}_0$ *is often chosen as a diagonal matrix.*

[4]The motivation of an extra torque estimation is that feeding forward the load torque information provides multiple benefits for the speed control loop resulting in a performance-enhanced generator side controller.

2. $\mathbf{Q}$ *and* $\mathbf{R}$ *represent the model accuracy (or model confidence) and measurement noise characters, respectively. Larger values in* $\mathbf{Q}$ *represent the heavier uncertainties of the model parameters, and will lead to larger Kalman gain, i.e., a faster* ***filter dynamics****. On the other hand, small values in* $\mathbf{Q}$ *indicate a high confidence in the system model and may therefore lead to a slow measurement update, i.e.,* ***slow but smooth filter dynamics****. Similarly, enlarging the value in* $\mathbf{R}$ *only when the measurements are heavily affected by noises.*

3. *Explicit calculation of* $\mathbf{Q}$ *and* $\mathbf{R}$ *shows that both are composed a diagonal, time-invariant matrix plus a time-varying matrices, and the elements of the latter are (at least two) orders smaller than the smallest element of the former [167, 173]. Therefore, an acceptable solution for realization is to choose a constant diagonal, time-invariant matrix for both* $\mathbf{Q}$ *and* $\mathbf{R}$*.*

4. *Some general guidelines are given in [166, 167, 173] to choose proper parameters for EKF. In this work these parameters were chosen partially following these guideline and partially through the trial and error manner.*

5. *The estimated states (here currents) obtained from the EKF can be used as the feedback information for the controller. Better performances are therefore expected when the measurement channel is heavily noised because the estimated values will be corrected against* ***measurement noises*** *(See Algorithm 8.1).*

8.2.3.1 Incorporating EKF to deadbeat control scheme

Both cases of using EKF (Case-I in sec.8.2.2 and Case-II in sec.8.2.3) for state estimation have been incorporated into a deadbeat control scheme (i.e., deadbeat torque control for the generator side and deadbeat power control for the grid side as introduced in Chp. 3) for the finial encoderless control evaluations. The overall control scheme is shown in Fig. 8.1.

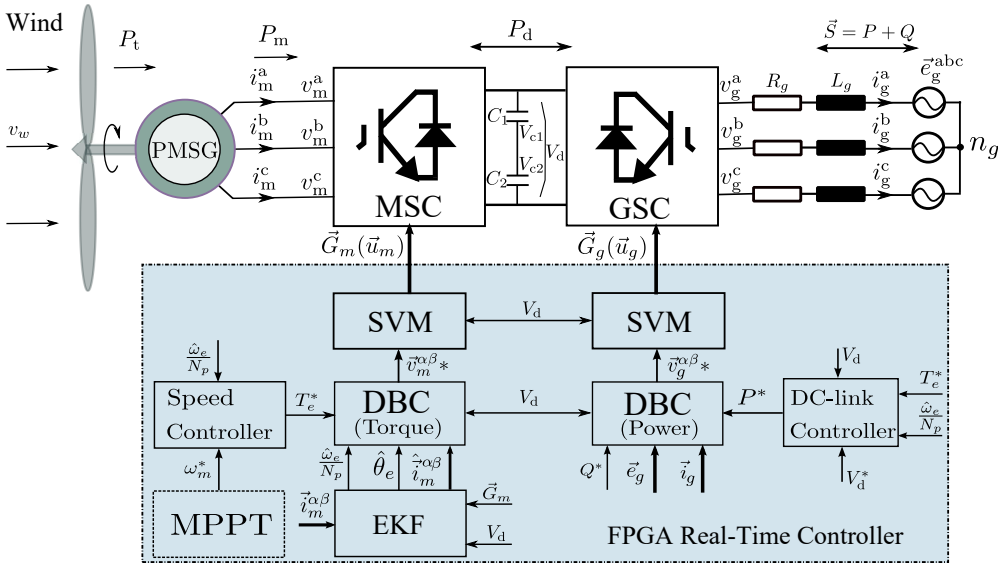

Fig. 8.1: Bock diagram of the proposed EKF-DBC control scheme.

8.2.4 FPGA design and experimental evaluations

In this section the FPGA implementation of the proposed control scheme is described and explained in detail. Note that, due to the limited FPGA resources available in the test-bench and also the costly but redundancy implementation efforts, only the EKF for currents, speed and position estimation, i.e., *Case-I* in sec.8.2.2, is implemented with the presented deadbeat like predictive controller.

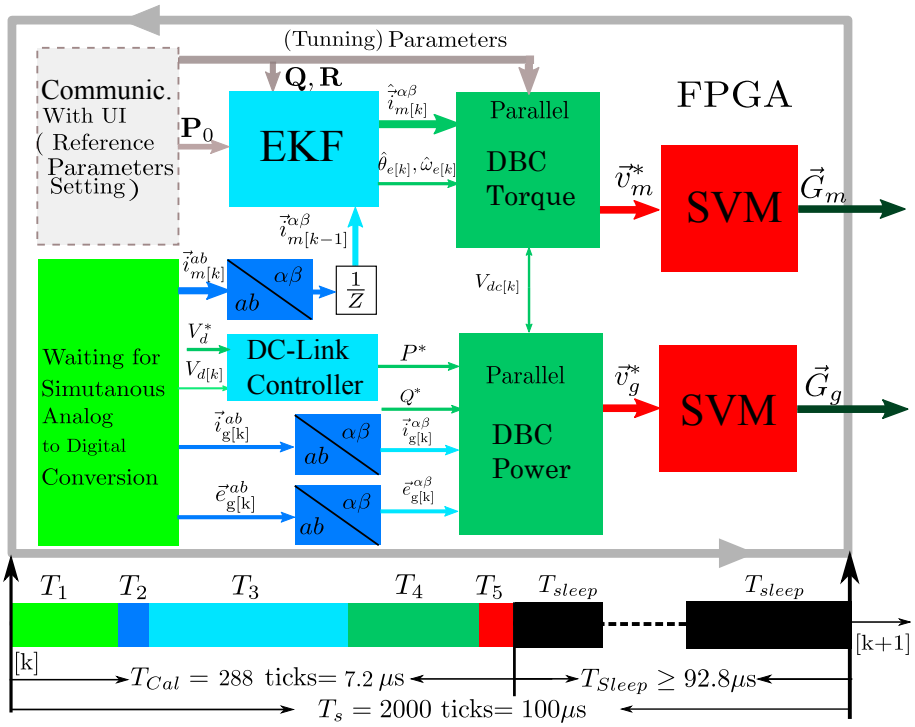

Fig. 8.2: Bock diagram of the FPGA design for the proposed EKF-DBC control scheme.

All the algorithms are divided into small sub-routines and are implemented using the Single-Cycle-Timed-Loop (SCTL) structure. The FPGA top level clock is set to 40 MHz. Both the generator side model predictive torque controller and the grid side predictive power controller — including the EKF observer — are executed within 7.2 μs (generator side controller cost: 288 ticks $= \frac{288}{40\text{M}}10^6$ μs $= 7.2$ μs and grid side cost: 101 ticks $= \frac{101}{40\text{M}} \cdot 10^6$ μs $= 2.53$ μs). The overall structure of the implementation is shown in Fig. 8.2. Notably, the color in Fig. 8.2 represents different duration time of $T_1, T_2..T_5, T_{sleep}$. With a sampling frequency of 10 kHz (i.e. $T_s = 100$ μs), the calculation time, including both the EKF and predictive controller parts (around 7 μs) in comparison to the whole control interval of 100 μs this value is very small, which makes the calculation time compensation not necessary.

Remark 19 (FPGA design tips [8, 10]) *An important issue for FPGA design of a given complicated algorithm is the trade-off between execution speed (parallelism) and resource usage (registers, Look-up Tables (LUTs), Memories and DSP slices, etc.). For the case that the FPGA chip under consideration is big enough, i.e., resources unlimited, which is very rare in practice, the best way to achieve the shortest calculation time is to*

program all (if possible) the sub-routines in parallel. Otherwise, the most recommenced tips when running into FPGA short-resource are:

i) Rearrange the equations (algorithms) to a more costing- and computing efficient format before coding, e.g. in stead of coding "$ab + ac$" (two multipliers and one adder are required) coding as "$a(b + c)$" (reduced to one multiplier and one multiplication step);

ii) Use shortest fixed point data type (without losing too much accuracy). A practical procedure is: firstly use floating point data type to verified the functionality of the algorithm, and then change it fixed point data type and tune the word and integer lengths until a satisfying approximation accuracy appears;

iii) Only parallel the subroutines when timing requirement is not met (i.e., the calculation time is too long); and during the implementation use shifting in stead of using dividing (or multiplying) if possible.

Parameter	Simulation	Experiment
Grid-side Phase Voltages $e_g^{a,b,c}$ [V] (peak)	250	120
Grid-side Voltage Frequency ω_g [rad/s]	100π	100π
Grid-side Reactor Resistor R_{g} [Ohm]	$1.56 \cdot e^{-3}$	$1.56 \cdot e^{-3}$
Grid-side Reactor Inductance L_{g} [H]	$16 \cdot e^{-3}$	$16 \cdot e^{-3}$
Generator Stator Inductance $\mathrm{L_s}$ = [H]	19e-3	8e-3
Generator Stator Resistor $\mathrm{R_s}$ [Ohm]	2.1	1.3
Generator Pole Pairs $\mathrm{N_p}$ [1]	3	3
Rotor Permanent-Magnet Flux ψ_{pm} [Wb]	0.42	0.41
Sampling Interval $\mathrm{T_s}$ [μs]	100	100

Table 8.1: System parameters.

8.2.4.1 Simulation verification

As described in the Sec. 8.2, the proposed encoderless deadbeat control with EKF for Case-II, i.e., with load estimation, is not realized on the real-time platform due to the limited resources available on the FPGA chip. Therefore, the verification for this part is done through simulation. And the results are shown in Fig.8.3. The parameters of the system are collected in Table 8.1.

As can be seen from Fig. 8.3, no matter during low speed range (See for $t \in [0, 0.15]$s), high speed range (See for $t \in [0.22, 0.3]$s), or transient phases (See for $t \in [0.3, 0.5]$s), the currents, speed, flux position, and load are estimated with nice accuracy, and system is stably under control.

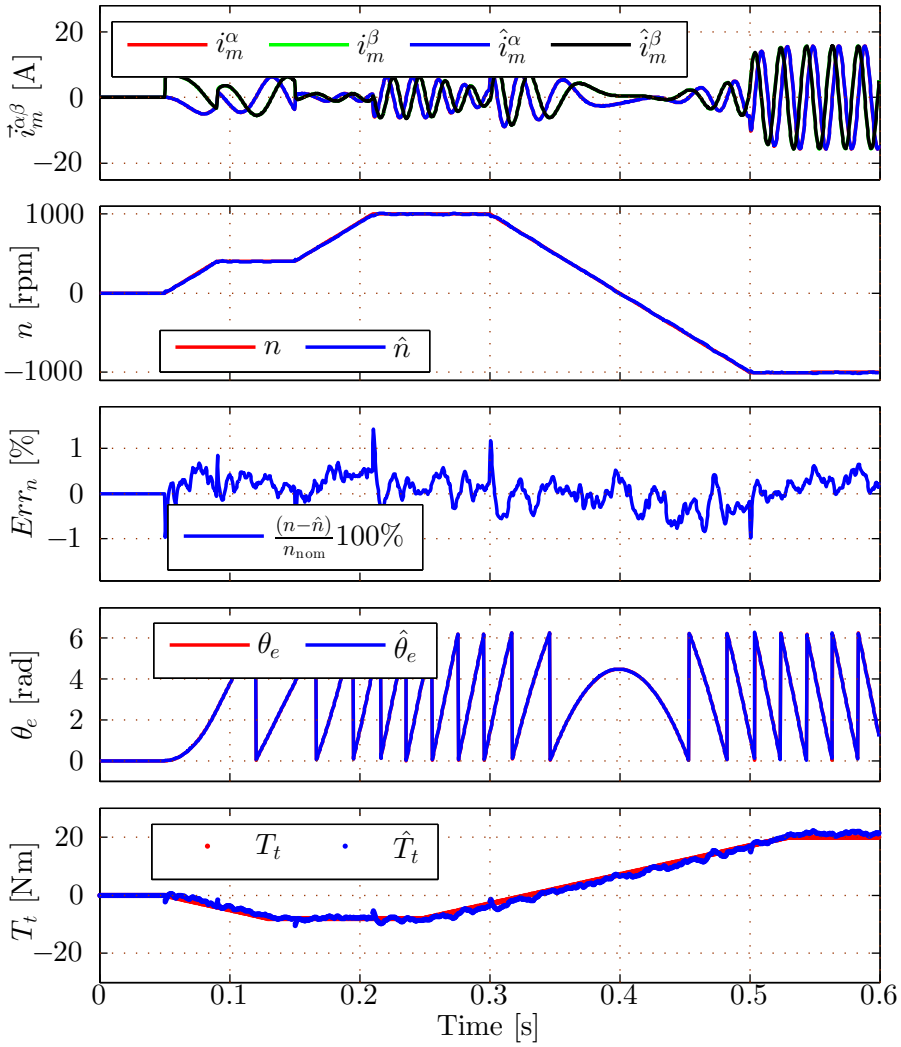

Fig. 8.3: [Simulation results:] of the proposed encoderless predictive control with EKF for *Case-II*, i.e, with load estimation. From up to down are: real and estimated generator currents of $\vec{i}_m^{\alpha\beta}$; real and estimated generator speed of n [RPM], ($n = \frac{30 \cdot \omega_e}{N_p \cdot \pi}$); speed estimated error of Err_n in percentage of the upper operating speed; real and estimated flux position of θ_e [rad]; real and estimated load of T_t [Nm].

8.2.4.2 Experimental verification

All the other parts, i.e., grid side converter control, generator side power converter and EKF with *Case-I*, are verified on the self-construed grid-tied back-to-back PMSG wind turbine system with a FPGA based real time controller (as introduced in Chp. 2).

The overall speed control performances with the proposed encoderless deadbeat control performance are shown in Fig. 8.4a (Note that the torque tracking bias is due to the same reason as introduced in Chp. 3). Its steady state performance during 200 [RPM] is given in Fig. 8.4b. Test scenarios are: a constant load torque is set during the whole time, while the speed (reference) changes with a slop, the DC-link voltage is set to 300 [V], reactive

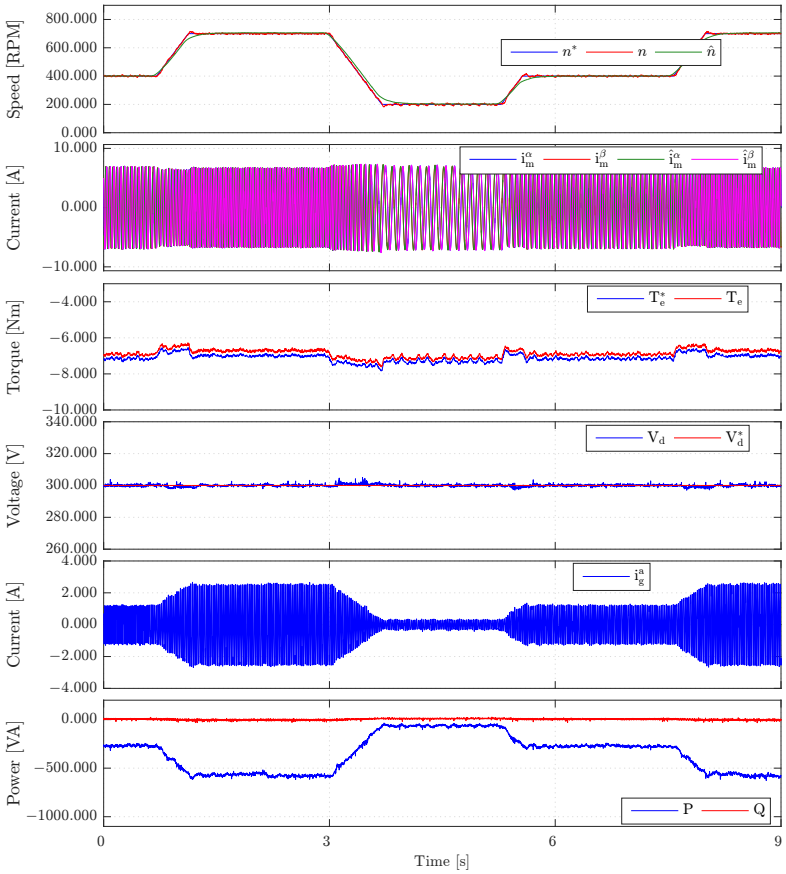

(a) Overall control performances.

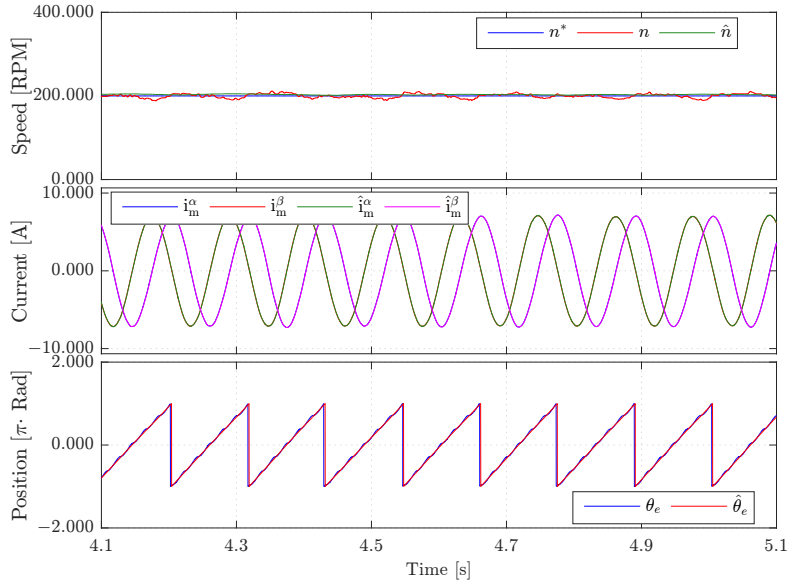

(b) Zoomed control performances during steady state.

Fig. 8.4: [Experimental results:] of the proposed deadbeat like predictive control with EKF. (a) Overall control performances with constant load while changing speed (reference), from up to down are generator reference, real and estimated speed, real and estimated stator current in $\alpha\beta$ frame; (estimated) and real torque, DC-link voltage, grid side phase current; grid side active and reactive power. (b) Zoomed control performances of generator reference, real and estimated speed, real and estimated stator current in $\alpha\beta$ frame, and real- and estimated- position.

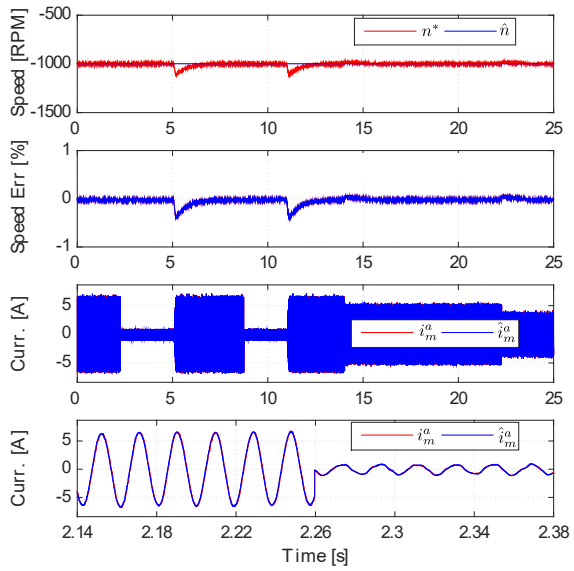

(a) Generator side control performances at high speed range with abrupt load (changing among rated, 0% (only friction load) and 80%, 60% and 50% rated load) changing.

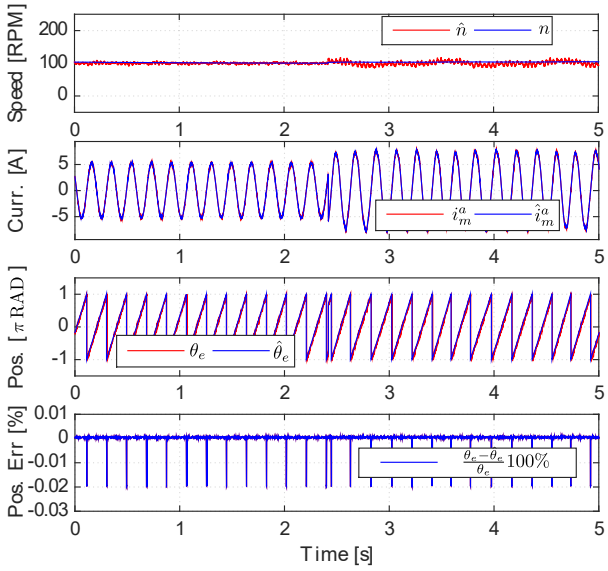

(b) EKF estimation performances at very low speed range (3% of the nominal speed) with abrupt load changing (changing from 80% to rated load at around 2.30s).

Fig. 8.5: [Experimental results] of the proposed encoderless deadbeat control with EKF with constant speed reference while changing load torque: generator side control performances at high and low speed.

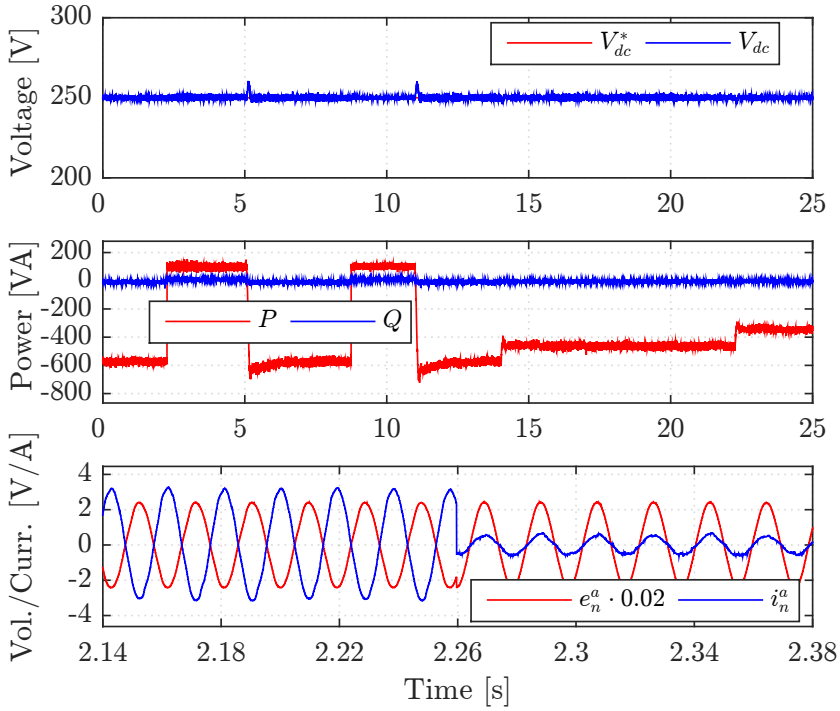

Fig. 8.6: [Experimental results]: DC-link and grid side control performances in accordance with Figure 8.5a: the system is working among generator-to-motor-generator mode at difference power levels, while the reactive power reference is kept at 0 [Var], the DC-link reference, 250 [V] for all the time.

power reference is set to be 0 [Var] for a unit power factor control.

The robustness to torque change at both high and low speed range are shown in Fig. 8.5. The testing scenarios are: constant speed reference is set (1000 [RPM] for Fig. 8.5a, and 100 [RPM] for Fig. 8.5b), while the load changes abruptly, the DC-link voltage is set to 250 [V], reactive power reference is set to be 0 [Var]. The grid side control performances in according to Fig. 8.5a are shown in Fig. 8.6.

8.3 Encoderless control with sliding mode observer

8.3.1 Sliding mode observer

Sliding mode observers (SMO) have the attractive features of robustness to disturbances, parameter deviations and system noise [168, 169, 174]. But for classical SMO techniques, to ensure general stability of the system, a high switching gain is required in the high speed range leading to a large amount of ripples in the back-EMF and, also, to large chattering in the estimated speed/position [14, 175]. Due to the use of a low pass filter with fixed cut-off frequency, phase compensation will vary according to the operating speed [14]. This needs to be considered and increases implementation effort [169, 174]. Therefore in this section a sliding mode observer with time-varying switching gain and time-varying cut-off frequency of the low-pass filter to achieve rotor speed/position estimation (almost) with constant phase compensation is presented.

8.3.2 Design of the time-varying sliding mode observer

Since estimating (electrical) speed $\omega_\mathrm{e} = N_\mathrm{p}\omega_\mathrm{m}$ and (electrical) position $\theta_\mathrm{e} = N_\mathrm{p}\theta_\mathrm{m}$ are interested, the PMSG model in $\alpha\beta$ reference frame can be used. The dynamics in the current can be expressed in the following nonlinear model (See Chp. 2 for more details)

$$\frac{d\vec{i}_\mathrm{m}^{\alpha\beta}(t)}{dt} = \underbrace{\frac{-R_\mathrm{s}}{L_\mathrm{s}}\boldsymbol{I}}_{\mathbf{A}_\mathrm{m}^{\alpha\beta}}\vec{i}_\mathrm{m}^{\alpha\beta}(t) + \underbrace{\frac{1}{L_\mathrm{s}}\boldsymbol{I}}_{\mathbf{B}_\mathrm{m}^{\alpha\beta}}\left(\vec{v}_\mathrm{m}^{\alpha\beta}(t) - \underbrace{\begin{pmatrix} -\psi_\mathrm{pm}\omega_\mathrm{e}(t)\sin\theta_\mathrm{e}(t) \\ \psi_\mathrm{pm}\omega_\mathrm{e}(t)\cos\theta_\mathrm{e}(t)\end{pmatrix}}_{=:\vec{e}_\mathrm{m}^{\alpha\beta}(t)}\right), \vec{i}_\mathrm{m}^{\alpha\beta}(0) = \vec{i}_\mathrm{m}^{\alpha\beta 0} \in \mathbb{R}^2, \tag{8.6}$$

where $\vec{e}_\mathrm{m}^{\alpha\beta} = (e_\mathrm{m}^{\alpha}, e_\mathrm{m}^{\beta})^\top$ V is the back-EMF voltage vector and $\vec{v}_\mathrm{m}^{\alpha\beta}$ is the output voltage vector of the machine side converter in $\alpha\beta$ frame. The other symbols are with the same meaning as introduced in Chp. 2. Based on such model, and following the idea in [176] [177], we introduce a sliding mode observer for indirect speed estimation from current observation. But similar to [175], we do not utilize a discontinuous "switching function" (such as sign$(\cdot)$) but rather a sigmoid "switching function" to reduce chattering in the estimate(s). For this work, we utilize the following smooth "switching function"

$$\mathbf{f}_{sig}\colon \mathbb{R}^2 \to [-1,1]\times[-1,1], \quad \varepsilon \mapsto \mathbf{f}_{sig}(\varepsilon) := \frac{2}{1+e^{-a\varepsilon}} - 1 \quad \text{with tuning parameter } a > 0. \tag{8.7}$$

Moreover, for the current estimation error

$$\vec{\varepsilon}_{\mathrm{m}}^{\alpha\beta}(t)=\Big(\varepsilon_{\mathrm{m}}^{\alpha}(t),\varepsilon_{\mathrm{m}}^{\beta}(t)\Big)^{\top}:=\hat{\vec{i}}_{\mathrm{m}}^{\alpha\beta}(t)-\vec{i}_{\mathrm{m}}^{\alpha\beta}(t)\quad\text{where }\hat{\vec{i}}_{\mathrm{m}}^{\alpha\beta}(t):=\Big(\hat{i}_{\mathrm{m}}^{\alpha}(t),\hat{i}_{\mathrm{m}}^{\beta}(t)\Big)^{\top},\tag{8.8}$$

we will reduce the noise sensitivity of our observer, by implementing a time-varying (adaptive) low pass filter of the following form

$$\frac{d\vec{x}_{\mathrm{f}}(t)}{dt}=-k_c\omega_{\mathrm{m}}^{*}(t)\Big(\vec{x}_{\mathrm{f}}(t)-\mathbf{f}_{sig}\big(\vec{\varepsilon}_{\mathrm{m}}^{\alpha\beta}(t)\big)\Big),\qquad\vec{x}_{\mathrm{f}}(0)=\Big(x_f^{\alpha}(0),x_f^{\beta}(0)\Big)^{\top}=\vec{x}_{\mathrm{f}}^{0}\in\mathbb{R}^2,\tag{8.9}$$

where $k_c>0$ is a tuning parameter. The filter in (8.9) has a time-varying cut-off frequency $k_c\omega_{\mathrm{m}}^{*}(t)$ and changes with speed reference $\omega_{\mathrm{m}}^{*}(t)$. Note that, in steady state (i.e. $\frac{d\vec{x}_{\mathrm{f}}(t)}{dt}=0$), we have $\vec{x}_{\mathrm{f}}(t)=\mathbf{f}_{sig}\big(\vec{\varepsilon}_{\mathrm{m}}^{\alpha\beta}(t)\big)$. Combining altogether, we introduce the following time-varying sliding mode observer (estimates indicated by $\hat{}$)

$$\frac{d\hat{\vec{i}}_{\mathrm{m}}^{\alpha\beta}(t)}{dt}=\mathbf{A}_{\mathrm{m}}^{\alpha\beta}\hat{\vec{i}}_{\mathrm{m}}^{\alpha\beta}(t)+\mathbf{B}_{\mathrm{m}}^{\alpha\beta}\Big(\vec{v}_{\mathrm{m}}^{\alpha\beta}(t)-k_f\vec{x}_{\mathrm{f}}(t)-k_s\omega_{\mathrm{m}}^{*}(t)\mathbf{f}_{sig}\Big(\vec{\varepsilon}_{\mathrm{m}}^{\alpha\beta}(t)\Big)\Big),\hat{\vec{i}}_{\mathrm{m}}^{\alpha\beta}(0)=\hat{\vec{i}}_{\mathrm{m}}^{\alpha\beta0}\in\mathbb{R}^2,\tag{8.10}$$

with tuning parameters $k_f,k_s>0$. Substraction of (8.10) and (8.6) yields the sliding mode dynamics

$$\frac{d\vec{\varepsilon}_{\mathrm{m}}^{\alpha\beta}(t)}{dt}=\mathbf{A}_{\mathrm{m}}^{\alpha\beta}\vec{\varepsilon}_{\mathrm{m}}^{\alpha\beta}(t)+\mathbf{B}_{\mathrm{m}}^{\alpha\beta}\Big(\vec{e}_{\mathrm{g}}^{\alpha\beta}(t)-k_f\vec{x}_{\mathrm{f}}(t)-k_s\omega_{\mathrm{m}}^{*}(t)\mathbf{f}_{sig}\big(\vec{\varepsilon}_{\mathrm{m}}^{\alpha\beta}(t)\big)\Big),$$
$$\vec{\varepsilon}_{\mathrm{m}}^{\alpha\beta}(0)=\hat{\vec{i}}_{\mathrm{m}}^{\alpha\beta0}-\vec{i}_{\mathrm{m}}^{\alpha\beta0}\in\mathbb{R}^2.\tag{8.11}$$

In [178] it is shown that, for $a\to\infty$ in (8.7) (i.e. $\mathbf{f}_{sig}\to\mathrm{sign}$), $k_f=0$ and $k_s\gg1$ (with $\omega_{\mathrm{m}}^{*}=1$), "sliding mode" (i.e. $\frac{d\vec{\varepsilon}_{\mathrm{m}}^{\alpha\beta}(t)}{dt}=0$) exists for (8.11) and the following holds $\hat{\vec{e}}_m^{\alpha\beta}(t):=k_s\,\mathrm{sign}(\vec{\varepsilon}_{\mathrm{m}}^{\alpha\beta}(t))$. Clearly, due to the sign-function the estimate is subject to chattering and highly noise sensitive. Our simulative analysis showed that for a sufficiently large value of $k_s\gg1$ and $-1<k_f<0$ in (8.11), "sliding mode" still exists and so we have the following equivalent signal which allows to estimate speed and position

$$\begin{aligned}\hat{\vec{e}}_m^{\alpha\beta}(t)&\overset{(8.11)}{:=}(1+k_f)\vec{x}_{\mathrm{f}}(t)\overset{(8.6)}{\Longrightarrow}\hat{\omega}_{\mathrm{e}}(t)\\&=-\tan^{-1}\left(\frac{\hat{e}_m^{\alpha}(t)}{\hat{e}_m^{\alpha}(t)}\right)=-\tan^{-1}\left(\frac{x_f^{\alpha}(t)}{x_f^{\beta}(r)}\right)\Longrightarrow\hat{\theta}_{\mathrm{e}}(t)=\int_0^t\hat{\omega}_{\mathrm{e}}(\tau)\,\mathrm{d}\tau\,.\end{aligned}\tag{8.12}$$

Remark 20 (Some remarks on the tuning parameters k_c and k_f) *k_c: Due to the low-pass filter, as described in [175], we need to introduce a position compensation $\theta_{com}=\tan^{-1}\left(\frac{\hat{\omega}_{\mathrm{e}}}{k_c\omega_m^{*}}\right)=\tan^{-1}\left(\frac{1}{k_cN_{\mathrm{p}}}\right)$ otherwise we would have a lag in the position estimate. In our case we achieve that by a constant compensation term, which highly simplifies the hardware implementation.*
k_f: From (8.11), it is evident that, $\vec{x}_{\mathrm{f}}=\frac{\hat{\vec{e}}_m^{\alpha\beta}}{1+k_f}$ can be increased for $0>k_f>-1$. Hence, even for small values of $\|\vec{e}_{\mathrm{g}}^{\alpha\beta}\|$, the filter output $\vec{x}_{\mathrm{f}}$ can be made large, increasing the estimation accuracy (even in the low speed range when $R_{\mathrm{s}}\vec{i}_{\mathrm{m}}^{\alpha\beta}$ is not *small and, so,* not *negligible).*

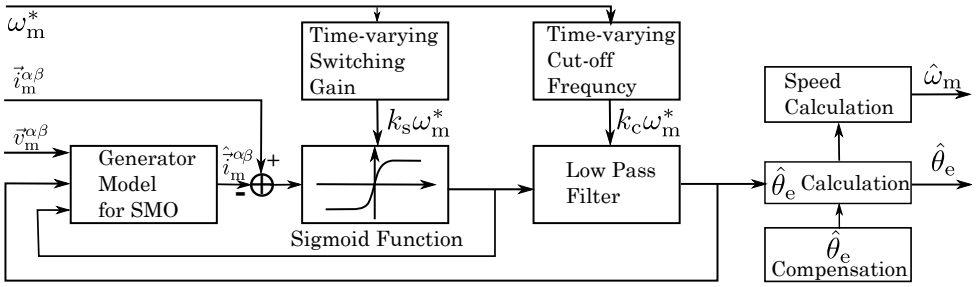

Fig. 8.7: Proposed time-varying sliding mode observer (SMO)

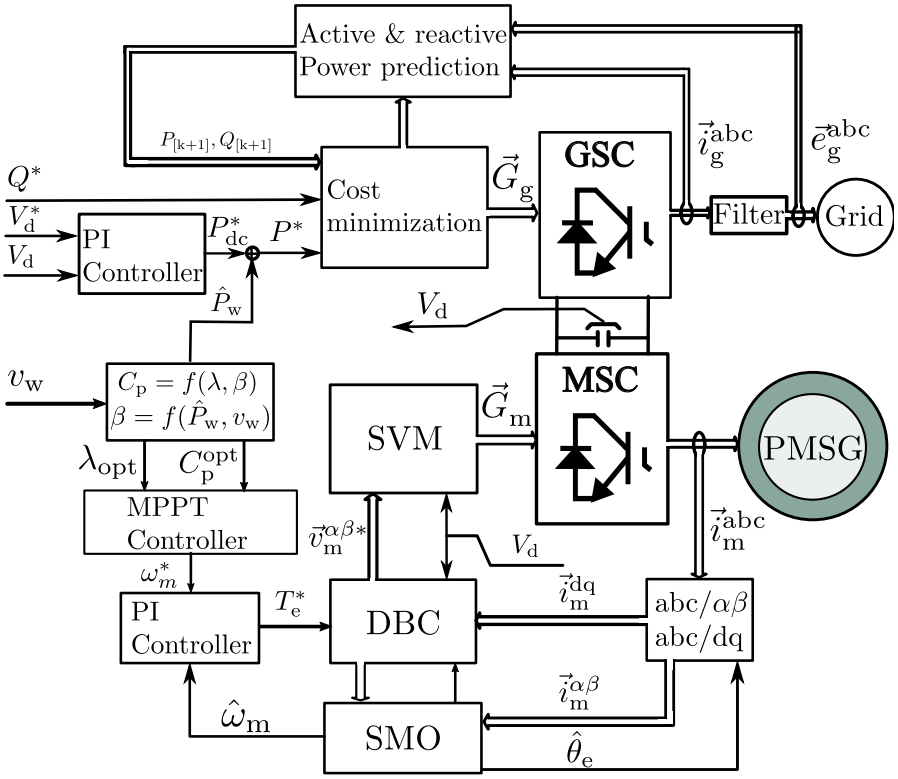

Fig. 8.8: Proposed model predictive control (MPC) scheme with time-varying sliding mode observer (SMO)

8.3.3 Evaluation

The proposed control strategy is also incorporated into the aforementioned deadbeat like predictive control framework (deadbeat torque control for the machine side and deadbeat power control for the grid side). To avoid the redundancy, it will not be repeated here. The overall control structure is illustrated in Fig. 8.8 and its effectiveness is verified by simulations using Matlab/Simulink as a first proof of concept. All simulation and controller parameters are collected in Tab. 8.2.

Testing scenarios are: Wind speed v_w is changing with a huge slop of 2000m/s^2 from 11.9m/s to 18.9m/s at 0.07s, which means that the wind power P_w changes from 1kW to 5kW at 0.07s. So, also the optimal reference speed $\frac{30}{\pi}\omega_m^*$ changes from around 1200rpm

Para.	Values	Unit	Para.	Values	Unit	Para.	Values	Unit
P_N	6.3	kW	ρ	1.225	kg/m^3	T_s	60	10^{-6}s
$\frac{30}{\pi}\omega_N$	2600	rpm	R_t	0.8	m	T_{SVM}	200	10^{-6}s
T_N	23	Nm	β	0	rad	$w_1 = w_2$	1	1
I_N	11.6	A	λ_{opt}	8.4	1	w_3	5000	1
L_s	20.4	mH	L_f	20	mH	k_s	80	1
R_s	0.138	Ohm	R_g	0.16	Ohm	k_f	-0.5	1
J	0.006	kg m^2	$\|\vec{v}_\mathrm{g}^{\alpha\beta}\|$	250	V	a	0.045	1
N_p	3	1	f_n	50	Hz	k_c	19.9	1

Table 8.2: Simulation and wind turbine parameters

to around 1900rpm at 0.07s. The reactive power reference Q_n^* changes from 0Var to -4KVar at 0.12s. The DC-link reference voltage is set to $V_\mathrm{d}^* = 600$V. The general control performances of using deadbeat control techniques have been illustrated both at the afore-discussed section and also Chp. 3. Therefore, here only the encoderless control performances are illustrated (for those who are interested in the overall control performances using SMO and deadbeat control method, please refer to [14] for more details). The encoderless control performances both under accurate and deviated parameter situations are given in Fig. 8.9. Fig. 8.9 (a) shows the performance of the proposed encoderless model predictive control scheme assuming perfect parameter match. In comparison to that, Fig. 8.9 (b) shows the performance with parameter deviations, i.e. $R_\mathrm{g} = 150\%\hat{R}_\mathrm{g}$ and $R_\mathrm{s} = 150\%\hat{R}_s$. The proposed sliding mode observer is still capable of estimating speed and position quite accurately, showing high robustness to resistance deviations. Moreover, Fig. 8.9 (b) highlights the effect of the use of the time-varying low pass filter. Without filter (i.e. $k_f = 0$) the estimate is more noisy than with filter (i.e. $k_f = -0.5$).

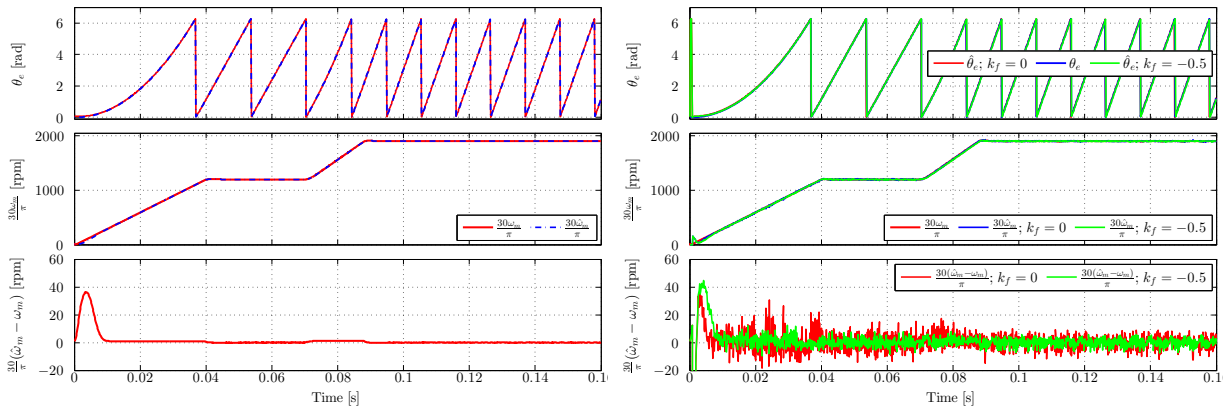

(a) $k_f = -0.5$, $a = 0.045$, $R_\mathrm{g} = \hat{R}_\mathrm{g}$, $R_\mathrm{s} = \hat{R}_s$

(b) $k_f = -0.5$, $k_f = 0$, $a = 0.045$, $R_\mathrm{g} = 150\%\hat{R}_\mathrm{g}$, $R_\mathrm{s} = 150\%\hat{R}_s$

Fig. 8.9: Performance of the proposed encoderless model predictive control scheme.

8.4 Summary

This chapter has introduced the encoderless control techniques for PMSG wind turbine systems. Two observer based solutions, namely, Extended Kalman Filter (EKF) and Sliding Mode Observer (SMO) incorporated into the deadbeat control framework for back-to-back power converter PMSG wind turbine systems have been closely investigated and verified. The EKF based solution is also verified with experimental data. In the near future, the experimental verification of the SMO based solution will be experimentally evaluated.

Chapter 9

FPGA HiL technique and low voltage ride through control

This chapter introduces the hardware-in-the-loop (HiL) technique, in particular the FPGA based signal level HiL method for electrical control unit (ECU) real-time evaluations (See Sec. 9.1). The refreshing rate effects of the emulator implemented on a digital hardware are evaluated and theoretically interpreted (See Sec. 9.2). After a survey of the state-of-the-art low-voltage-ride-through (LVRT) control techniques, a LVRT method combining the inertia energy storage and an active crowbar circuit incorporated within the direct model predictive current control framework has been verified using the proposed FPGA Signal-level HiL simulation solution (See Sec. 9.3).

9.1 Introduction

For most industrial products, before their commercialization and massive production a sound testing via certain qualified solutions are required. *Safety, efficiency (cost), and fidelity* (See [46] and the references therein) are the main concerns for such testing. *Safety* means no man power or instruments are allowed to be injured or destroyed, *efficiency* requires less time and money investigations, while *fidelity* means the testing results should be as effective and reliable as the on-site evaluations. Different from the off-line simulation based testing, the real-time HiL techniques provide chances to evaluate the unit under test (UUT) with nice efficiency and great flexibility, and more importantly, in a "real-time" manner.

For power electronics and electrical drive areas, the relevant testing includes the power circuit loop testing and the ECU testing. Accordingly, there are two branches of HiL techniques [46, 179–181] considering the communicating power level (See Fig. 9.1) in between the UUT and emulator, namely, (i) *Power-level* HiL (P-HiL) simulation systems, where high power flow (kW or higher) communicates between the emulator and the UUT, the emulator is usually constructed with power converter units, this group is mainly used for testing power sources or electrical drives [46, 179]; (ii) Real-time *signal-level* HiL

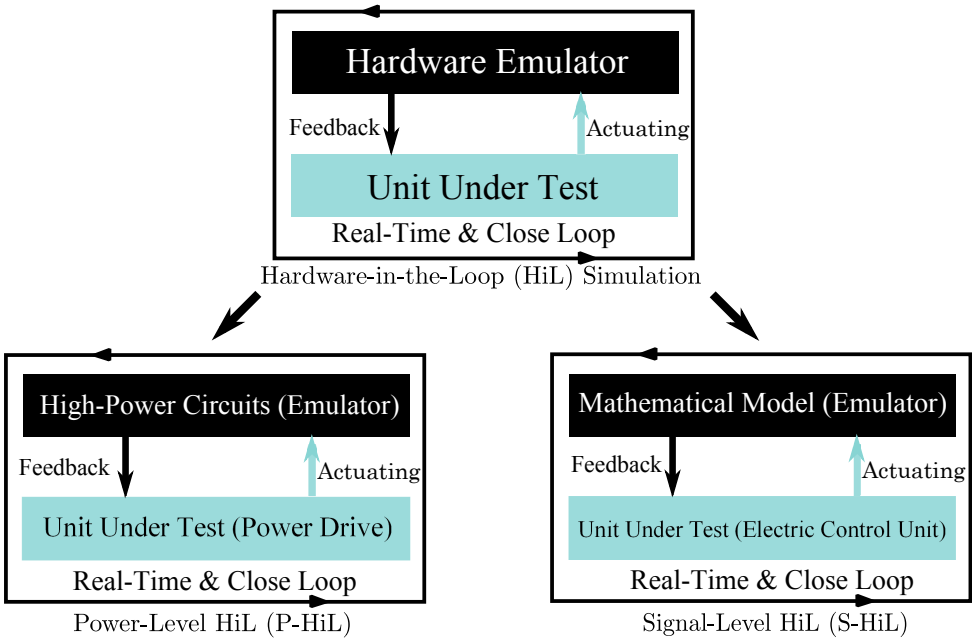

Fig. 9.1: Hardware-in-the-Loop techniques.

(S-HiL) simulation system, where, instead of high power-flow, only signal level closed loop communication is interacting between the emulator and UUT. The emulator is usually realized by implementing a high-fidelity system model within a digital processors. S-HiL systems are mainly used to test ECUs [179, 181].

P-HiL techniques have many interesting properties (e.g., it makes the true power level testing of the UUT achievable and offers even more freedom than the on-site evaluations). However, considerable investigations (cost) for the power level emulator construction are inevitable. In particular for a MW wind turbine system, due to safety and efficiency reasons, it is difficult for most institutions to construct a real MW level P-HiL set-up [182, 183]. In most cases, the ECU requires many testing processes before deployed to an expensive power level set-up. For instance, for a real MW hardware test-bench, the on-site operation of the controllers in certain scenarios (unbalanced grid, or low voltage ride through ability) is under great risks if the effectiveness of the ECUs cannot be 100% assured. A sound testing of the ECU in real-time against a S-HiL emulator in all the possible situations will help to prevent many damaging and costly potentials. Such requirements make the S-HiL techniques for testing the ECUs with real-time feedback signals highly desirable [179–181].

9.2 FPGA based S-HiL technique for wind turbine ECU evaluations

In S-HiL systems, in order to produce results of nice fidelity, the refreshing interval of the emulator shall be much smaller than the control (or sampling) interval of the ECU [46]. Otherwise, inaccurate instant of the gate-signal edges captured by the emulator may lead

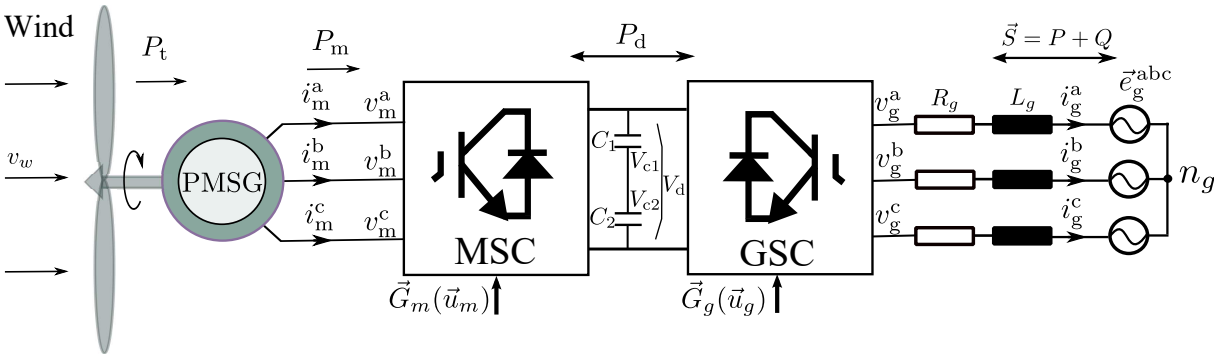

Fig. 9.2: Simplified structure of two-level back-to-back power converter PMSG wind turbine system.

to undesired results for the ECU closed loop verifications. Emulator short refreshing interval (or high refreshing rate) requirement makes the field-programmable-gate-array (FPGA) based solution an ideal choice, due to its parallel processing ability.

9.2.1 FPGA S-HiL realization for PMSG wind turbine systems

To realize a FPGA S-HiL based PMSG wind turbine system two separate parts are required: the FPGA realization of the system model as an emulator and the realization of the ECU. As a case study the well known FOC-VOC control scheme is used for the ECU development, which has already been introduced in Chp. 3 of this dissertation. The per-unit (P.U.)[1] system models of a two-level back-to-back power converter PMSG wind turbine system (depicted in Fig. 9.2) are used for the realization for the emulator. Detail information of the P.U. system models can be found in Appendix C. The above introduced emulator and the ECU are implemented on two separate commercial-off-the-shelf FPGA based platforms[2] programmed using Labview-FPGA. Fig. 9.3 and Fig. 9.4 illustrate the overview of the back-to-back PMSG wind turbine system emulator and the ECU with FOC-VOC control scheme. A detailed realization process for each is introduced as follows.

9.2.1.1 Hardware realization of the emulator

For the emulator design (See Fig. 9.3), the system engineering unit parameters are given by the user interface running on a Personal Computer (named as PC in Fig. 9.3), and via

[1]There are two ways to develop the system models: engineering unit (E.U.) models and Per-Unit (P.U.) system models. The general system model of a back-to-back power converter PMSG wind turbine system is developed in the E.U. format. However, in the E.U. mode, to describe mega-watt level wind turbine system quantities (vary in a wide range) using an FPGA hardware requires long word lengths which costs considerably much resources; While by choosing proper base values, the current, voltage, speed, etc. are scaled to 1 at their nominal operating condition for using P.U. models. This greatly eases the word length selection for the digital implementation process. Another benefit is that similar types of apparatus have the impedance lying within a narrow numerical range when expressed as a P.U. fraction of the equipment rating, even if the power rating varies widely. This may greatly ease the controller parameter tuning for testing systems with different power ratings.

[2]Codes in FPGA are allowed to work parallel and in different time domains, therefore, both the ECU and emulator can be realized with the same FPGA chip if the hardware resources (e.g., multipliers, memories, flip-flops, etc.) are enough without affecting the ECU's functionality.

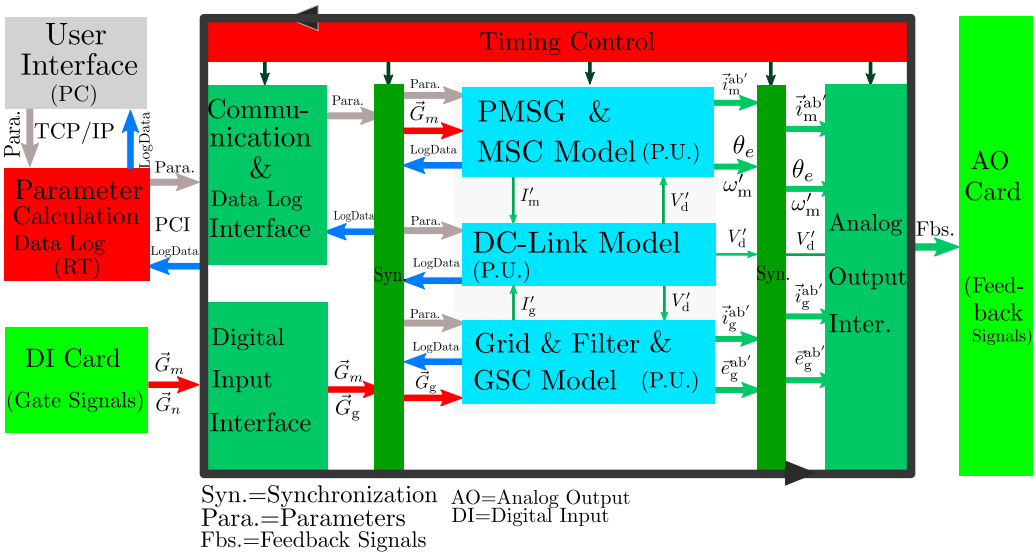

Fig. 9.3: FPGA realization of the back-to-back 2L-PMSG wind turbine system emulator.

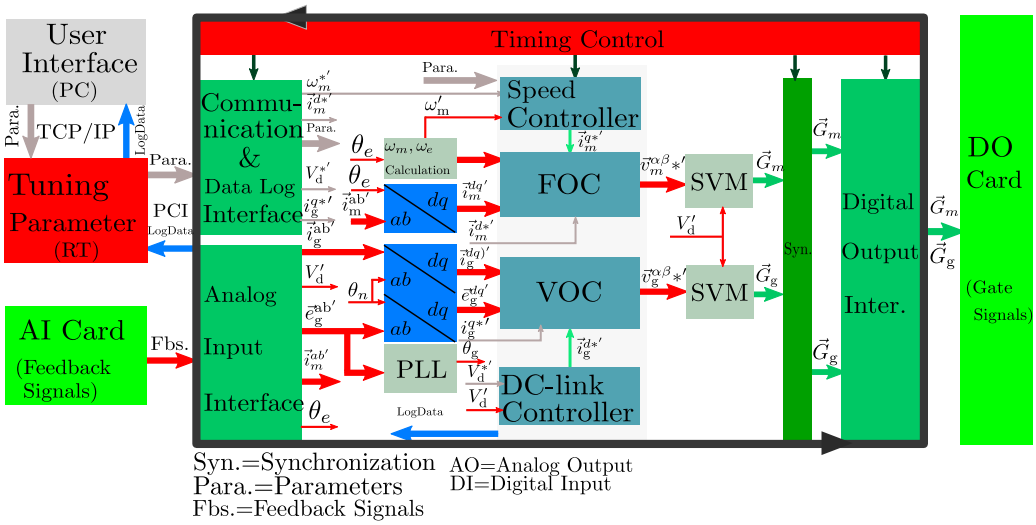

Fig. 9.4: FPGA design of the electrical control unit with FOC-VOC control scheme.

Ethernet bus the parameters are sent to a real time floating point processor (named as RT, see Fig. 9.3) of the real time hardware. Because many dividing operations are required and high speed real-time updating is unnecessary, the per-unit parameters ($R'_{\mathrm{s}}, L'_{\mathrm{s}}, \psi'_{\mathrm{M}}$ and so on) are calculated within the RT at the system start to make the best use of the floating point data processing ability of it. The RT and the FPGA communicate via a PCI bus and the per-unit parameters and logging data (system state variables and parameters) are transferred in between (See Fig. 9.3).

In the FPGA, related to the emulator, mainly three aspects are designed: (i) the interface parts, including the *digital input interface* for obtaining the gate triggering signals ($\vec{G}_{\mathrm{g}}, \vec{G}_{\mathrm{m}}$) from the ECU and *analog output interface* for outputting the feedback signals. (ii) The emulator discrete models. Per-unit back-to-back PMSG wind turbine system is

implemented by using a Single-Cycle-Timed-Loop technique with a controllable refreshing loop rate. (iii) Timing control and synchronous mechanism, which is implemented by using sequence frame and occurrence scheme of Labview-FPGA techniques to achieve synchronized in- and output data, also to make the refreshing rate controllable for the evaluations (introduced in 9.2.2).

9.2.1.2 Hardware configurations of the ECU

For the ECU design (See Fig. 9.4), a user interface running on the PC is designed to set the tuning parameters (mainly PI controller parameters) and observe the system running status. The RT is used in between the FPGA and PC for communication (transferring the tuning parameters to the ECU (which runs in the FPGA), and logging system state variables back to the PC. See Fig. 9.4). The FPGA design of the ECU requires also three parts: (i) Interface, including an *analog inputting interface* (for obtaining the feedback signals from an analog input card) and *a digital output interface* (for sending out the gate triggering signals to the Emulator via a digital output card) (See Fig. 9.4). (ii) Controller part, including the park transformation, PLL, DC-link, VOC-FOC controllers and space vector modulator. (iii) Timing control and synchronous mechanism, for which, a sequence frame and occurrence scheme are used similarly.

The system hardware configuration is given by Fig. 2.11 (in Chp. 2), where the left side (A) is the platform on which the ECU based on FOC-VOC scheme is implemented as introduced in Sec. 9.2.1.2; and the right side (B) is the emulator described in Sec. 9.2.1.1.

From the ECU's point of view, the operating and parameter tuning process are similar to the "on-site" or power level evaluation process, since the ECU obtains real-time feedback signals and produces the gate signals in the same way as controlling the real power level system. However, the updating frequency, i.e., the refreshing rate, of the emulator (which differs depending on the chosen hardware) affects the testing results. Therefore, in the following the refreshing rate effects of the emulator are illustrated and analyzed using real-time testing data.

9.2.2 Emulator refreshing rate effects and analysis

In Fig. 9.5 three different refreshing rates of the emulator with a same ECU controller setting are illustrated. These results confirm that, with an increased refreshing rate the currents (here the generator stator currents are given) shows clearly smaller ripples and accurate waveforms.

Remark 21 (Interpretation of the emulator refreshing rate effect) *Ideally when neglecting the dead-time of the switches, the* on-time T_{on} *of a switching period* T_{s} *captured by the emulator will be the* output time T^*_{on} *of the ECU (See Fig. 9.6). However, due to the existence of the* refreshing-period T_h *of the emulator, time errors will happen at both the rising and dropping edges of a switching action (named as* T^r_{Er} *and* T^d_{Er} *in Fig. 9.6,*

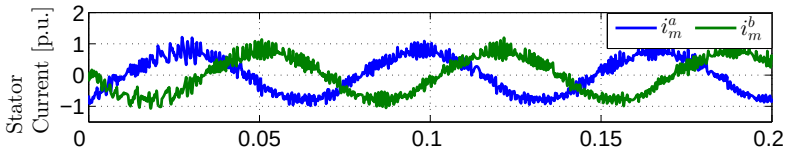

(a) Emulator refreshing rate of 100kHz.

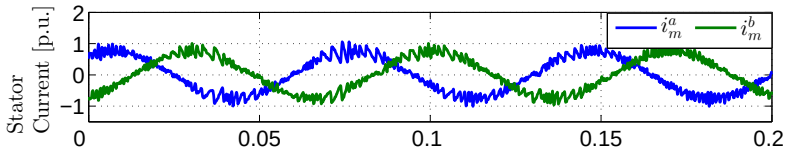

(b) Emulator refreshing rate of 200kHz.

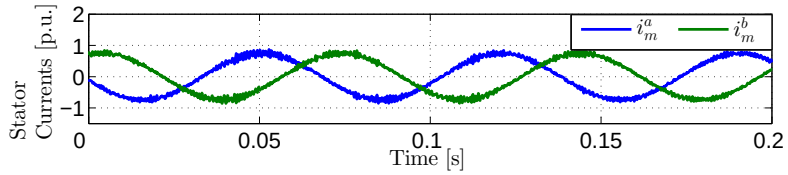

(c) Emulator refreshing rate of 250kHz.

Fig. 9.5: FPGA S-HiL verification of the emulator refreshing rate effect: generator stator current with the same ECU setting but different emulator refreshing rates.

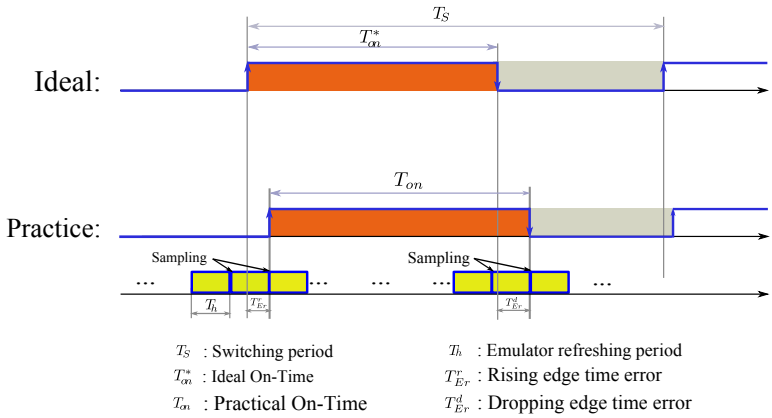

Fig. 9.6: Analysis of the refreshing rate effects.

respectively). Those time errors make the real on-time *(T_{on} in Fig. 9.6) turn out to be*

$$T_{on} = T_{\text{on}}^* - T_{Er}^r + T_{Er}^d, \in [T_{on}^* - T_h, T_{on}^* + T_h]. \tag{9.1}$$

In other words, the existence of the emulator refreshing-period *of T_h is like an extra chattering component added to the fundamental voltages of the converter output, whose amplitude is related to the value of T_h. Clearly, the results shown in Fig. 9.5 confirm this analysis (See Fig. 9.5: as the refreshing rate increases, i.e. when T_h decreases, the amplitudes of harmonic ripples go consequently down).*

Besides the refreshing rate of the emulator, the model accuracy and certain hardware limitations (e.g., conversion rate and resolutions of the hardware analog-to-digital and

digital-to-analog cards) will also effect the fidelity of the results, which remains to be further investigated in this dissertation.

9.3 LVRT and its FPGA based S-HiL evaluation

Distributed energy generations (DEGs) (such as wind, solar and biomass energy generations) are drawing increasingly much attention and are expected to take an even larger portion in the future grid driven by the limitations of conventional energy resources and increasingly severe environmental issues [3, 17, 22, 184–186].

As the capacity of DEG continues to increase globally, more stricter requirements regarding grid connection of DEG are introduced by system operators to ensure the stability of the general grid. Particularly for variable speed wind energy generations[3], for which the energy fed to the grid is not smooth in general and the capacity is getting more and more bigger. To protect the grid (and also the DEG unit) from running into instability, grid codes (which defines the requirements at the point of common coupling (PCC)) for connection between DEGs and grid were developed by transmission system operators. Low voltage ride through (LVRT) [187, 188] ability is one of the requirements for grid-tied wind energy generations, which describes the desired behaviors of the specific wind generation unit to behave during the period of grid voltage dips. Mostly a specific staying-connected time depending on the voltage dip levels is required. Meanwhile, to support the grid recovery, specific amount of reactive power output is desired (often defined as reactive current of the grid fundamental positive sequence). These requirements differ from region to region.

Fig. 9.7 shows the LVRT requirements in Germany, China, Spain and the USA. The wind turbine should remain connected (on-line) to the grid up to 150 [ms] during the voltage dips even if the voltage drops to 0% of the nominal value for Germany (See Fig. 9.7a). When the grid voltage dip occurs, above limit line 1, three-phase short circuit and faulted symmetrical voltage dip must not lead to instability or disconnection from the grid. Between lines 1 and 2, a brief disconnection is allowed in certain cases and under specified conditions. While for China, it is required to stay connected for up to 625 [ms] even when the grid voltage is dipping to 20% of the nominal value (See Fig. 9.7b). (c) and (d) of Fig. 9.7 show the different grid code requirements in Spain and USA, respectively. So, the requirements differ from region to region but all require a specific connection time during the grid dips.

In order to support the local grid voltage recovery, a specific amount of reactive power/current is required to be injected into the grid. The quantity of reactive power/current to be injected into the grid depends on the percentage of grid voltage reduction during the dip, the system rated current, and the reactive current given to the grid before the dip appearance. An example of the voltage/reactive power (current) control requirement is given in Fig. 9.8. The voltage/reactive power (current) control must be activated once a

[3]No requirements from general grids for LVRT of wind turbine generator systems existed before 2003. E.ON-Netz (Germany) was the first to put such need into their grid code [187]

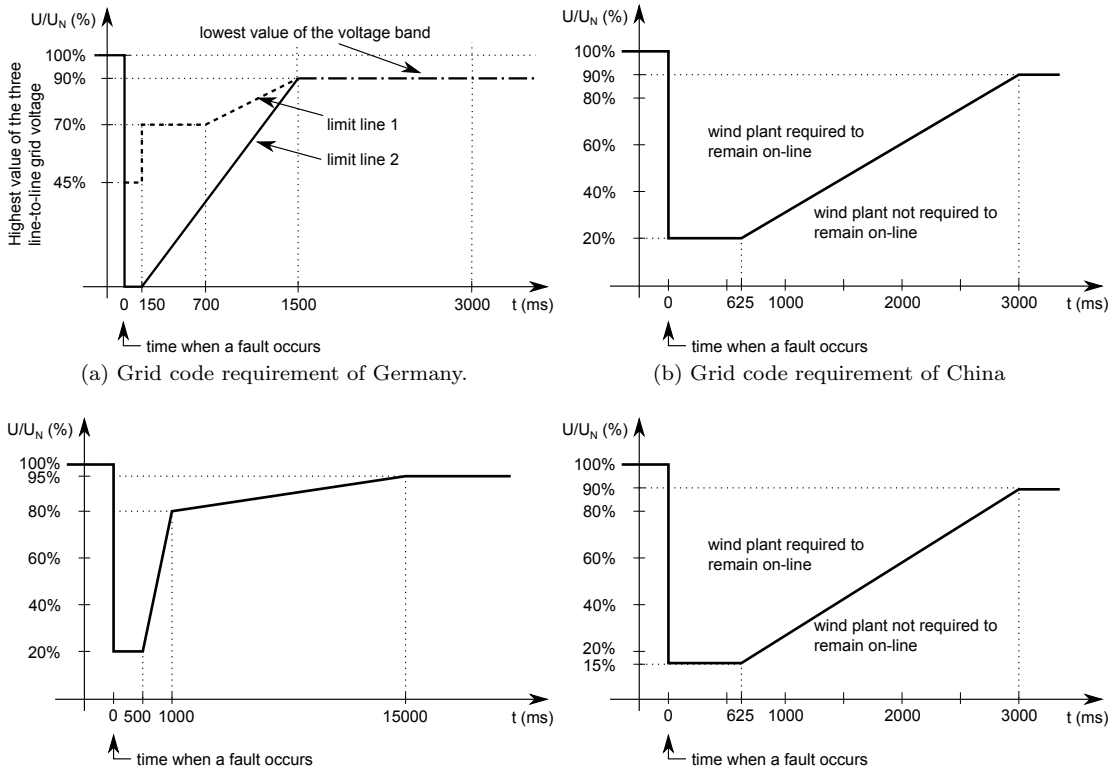

(a) Grid code requirement of Germany.

(b) Grid code requirement of China

(c) Grid code requirement of Spain.

(d) Grid code requirement of USA

Fig. 9.7: Grid code requirement of Germany, China, Spain and the USA.

voltage dip of more than 10% of the nominal value within 20 [ms] after fault recognition by providing a reactive current on the grid side [15, 145, 189].

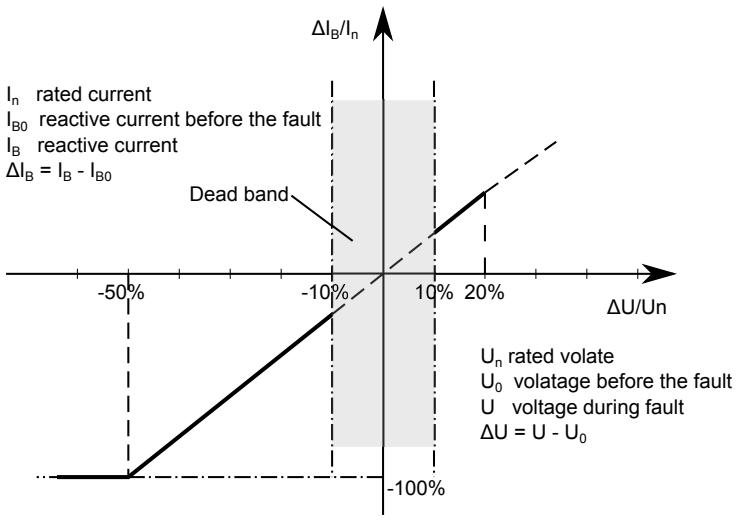

Fig. 9.8: Reactive output current during voltage dip according to the E. ON code [4].

All of these requirements described above make sufficient LVRT control strategy necessary. In the literature many solutions have been proposed (see e.g., [23, 130, 131, 190–192]) which

include: i) blade pitch angle control based solution, ii) DC-Link capacitor sizing based solutions, iii) crowbar circuit based solution, iv) extra DC-link energy storage based solution, and v) rotor inertia kinetic energy storage based solution, etc. The merits and demerits of these solutions are discussed in Sec. 9.3.1 of this work. In Sec. 9.3.2 a solution which combines *rotor inertia kinetic energy storage* and *active crowbar circuit* based techniques is presented and incorporated into the direct model predictive control frame of a grid-tied back-to-back PMSG based wind turbine system.

Verification of LVRT control strategies for a grid-tied wind turbine system is often through off-line (non-real-time software based) simulations or power-in-the-loop solutions. However, for off-line simulation based solutions, besides inevitably much longer simulation time, the real-time (hardware) controller verification is still required before finally deploying the controller into practice. While for power-in-the-loop experimental verification based solutions, although processes of the real-time (hardware) controller verification are already included, costly power sources (to emulate a fault grid) are required and the testing procedures are of great risks but less flexibility. Therefore, the FPGA S-HiL solution introduced in Sec. 9.2 is a nice alternative and is used in this work to verify the proposed LVRT control scheme.

9.3.1 State-of-the-art LVRT control techniques

Enhancing the operation of wind turbines in front of grid faults (especially grid voltage dips) is an important target for any grid-tied wind farms. Principally, during grid voltage dips, the power to feed into the grid is reduced instantaneously due to the grid voltage drop. However, the power extracted through the turbine and generator cannot be reduced without proper control, which generates a power (and energy) mismatch between the generator and grid sides. To fulfill the LVRT requirement, this power (or energy) mismatch is supposed to be governed properly through sufficient regulation techniques. Otherwise both the generator and the power converters will be damaged by over-current. In this section the state-of-the-art LVRT techniques shown in Fig. 9.9 are revisited and their merits and demerits are summarized.

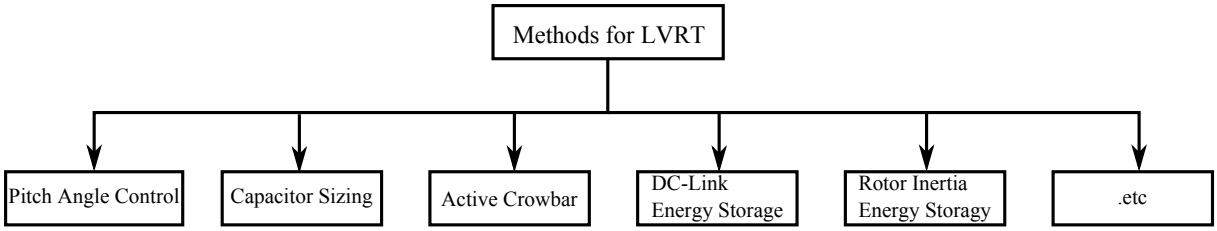

Fig. 9.9: State-of-the-art LVRT techniques for grid-tied wind turbine systems.

9.3.1.1 Blade pitch angle control based solution

Active pitch control is one of the (partial) solutions for variable speed wind turbines *with controllable pitch angle* (i.e., case-II introduced in Chp. 2) to realize LVRT control. The

mechanical power extracted by the wind turbine (the superscript of $(\cdot)^{II}$ in Eq. (9.2) represents the format of power coefficient with pitch control capability as introduced in Chp. 2) from the wind in discrete format is

$$\forall\, k \geq 0\colon\ P_t(k) = 0.5\rho A C_p^{II}\big(\lambda(k), \beta(k)\big)\Big(\frac{R_t}{\lambda(k)}\Big)^3 \times \omega_m^3(k) \geq 0, \tag{9.2}$$

where C_p^{II} is the power coefficient and its relationship with regarding to the pitch angle β (and tip-speed ratio λ) is shown in Fig. 9.10 (more details have been given in Chp. 2). Clearly, through increasing the pitch angle β, one can reduce the power coefficient thereby

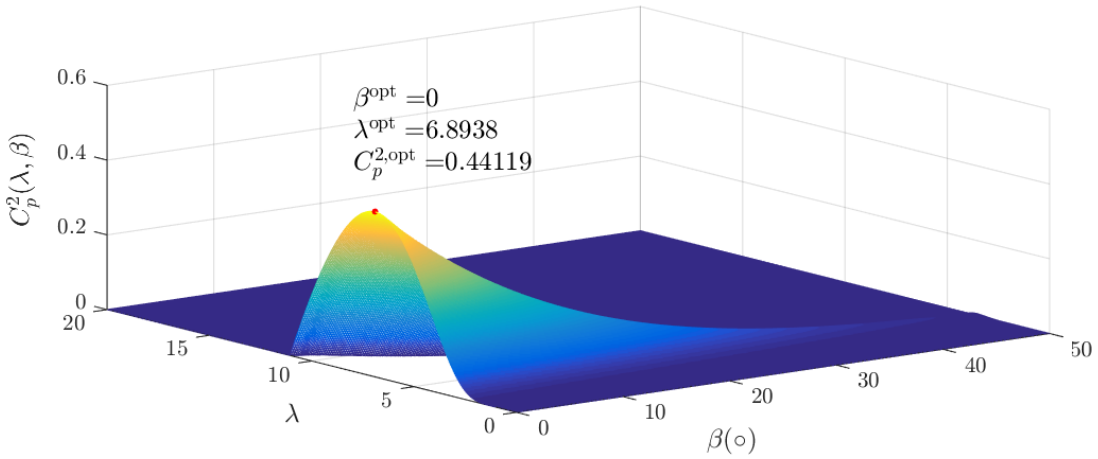

Fig. 9.10: Relationship between C_p^2, β and λ.

reducing the power of P_t, which is what LVRT control is supposed to achieve during grid voltage dip.

However, due to mechanical delay (time constant), the requested pitch angle change can not be delivered immediately. Therefore, significant response limitations are expected in practice. As a result, the DC link voltage rising problem is reduced but not satisfactorily eliminated with this solution. Typically active crowbar circuit based techniques (See Sec. 9.3.1.3) are combined with pitch control technique to realize LVRT control [187]: the captured wind power can be reduced at first with increasing the pitch angle (so to reduce the primary input wind power), and then if the power surplus is still seen in the DC-link, the crowbar circuit will be activated to eliminate the energy imbalance.

9.3.1.2 DC-Link capacitor sizing based solution [187] [193] [194]

DC-link capacitor sizing is another way to deal with the power (energy) mismatch during the grid voltage dip period [194] [187]. The theoretical background is given as follows:

Assuming the voltage dip happens from t_0 to t_1, then the energy which can be stored in capacitor can be expressed as [190] [187]

$$\int_{t_o}^{t_1} P_d(t)dt = \frac{1}{2}C \cdot (V_{d|t_1}^2 - V_{d|t_0}^2) = E_{m|(t_1-t_0)} - E_{n|(t_1-t_0)} = \delta_E(t_1) \tag{9.3}$$

where $P_d(t)$ is the power flow at the DC-link, $\delta_E(t_1)$ is the total mismatch energy during the voltage dip period (i.e., $t_1 - t_0$), $E_{m|(t_1-t_0)}$ and $E_{n|(t_1-t_0)}$ are the energy produced from the generator side and the energy delivered to the grid from the grid side converter, respectively. $V_{d|t_1}$ and $V_{d|t_0}$ are the DC-link voltages at time t_1 and t_0, respectively. Note that, $V_{d|t_1}$ is supposed not to increase beyond the permitted limit $V_d^{\max}$ of the DC-link capacitor for safety concerns. Therefore the required capacitor size (minimum) is

$$C^{\min} = \frac{2\delta_E(t_1)}{(V_d^{\max})^2 - V_{d|t_0}^2} \tag{9.4}$$

In practice, especially for large power rating wind mills, the mismatch energy $\delta_E(t_1)$ during the voltage dip period can be huge. Therefore, huge capacitor (expensive and with short life span) is expected to absorb this energy mismatch hence to maintain the DC-link voltage not to exceed the limitation, which may make it expensively impractical [187].

9.3.1.3 Active crowbar circuit (ACb) based solution

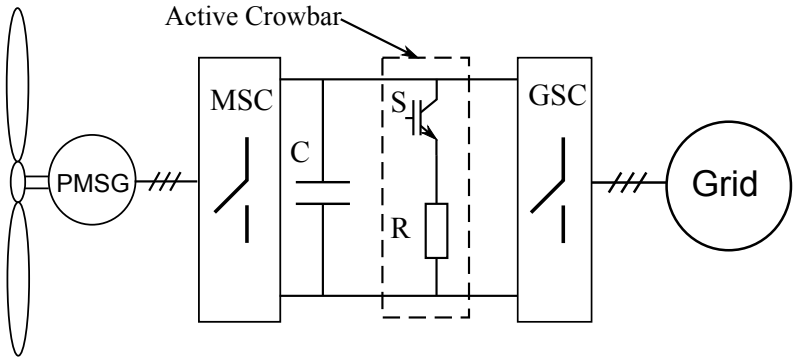

Fig. 9.11: Active crowbar technique.

An energy dissipating resistor can be inserted into the DC-link to dissipate the excess energy caused by the energy mismatch during grid voltage dips. This technique is mostly used in doubly-fed induction generator based configuration [191]. While for PMSG based configuration the crowbar circuit is suggested to be connected at the generator side [187]. The resistor is usually controlled using a power switch such as GTO or IGBT as shown in Fig. 9.11, where R is braking resistor and S is the switch. Through this circuit, simple bang-bang (or hysteresis) controller can be employed: compare $V_d(t)$ with the reference value of $V_d^*(t)$, if $V_d(t)$ is greater than $V_d^*(t)$, the switch is switched to on-mode, otherwise the switch is off.

Shortcoming is that the mismatched energy is dissipated (wasted) in terms of undesired heat energy.

9.3.1.4 DC-Link energy storage system based solution

A wind turbine system with DC-Link energy storage system (ESS) is shown in Fig. 9.12. Compared with active crowbar circuit based solution, this solution improves the LVRT

capacity, which stores the surplus energy in the ESS instead of dissipating the energy through a resistor during the grid faults. The ESS smooths the voltage/power fluctuations and can maximize the reliability of power to the loads. Moreover, the energy utilization can also be improved since the mismatch energy in this case is (afterward voltage recovery) fed to the grid.

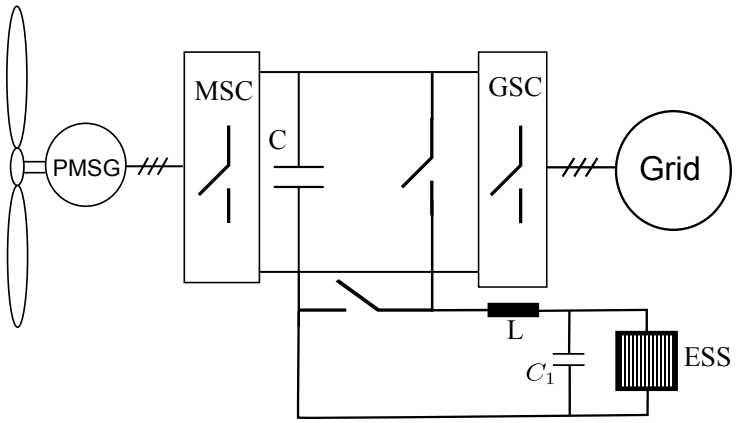

Fig. 9.12: DC-Link Energy Storage System.

However, an additional bi-directional DC/DC converter and big energy storage device are required for this solution. Batteries such as lead-acid battery (LAB) and vanadium redox flow battery (VRB) are usually used as ESS because of their high scalability, long life span, low material price and relatively fast response. However, due to the fact that battery absorbs and dissipates energy by transforming between chemical energy and electrical energy, if the energy to be stored is too much, a longer response time is expected to finish this energy transferring procedure. Therefore similar problem as in the pitch angle control based method introduced in Sec. 9.3.1.1 will be seen. Looking to the future, the superconducting magnetic energy storage (SMES) [187] [130], which has a large superconducting coil capability for storing electric energy in the magnetic field generated by DC current flowing through it, can be used to replace the battery based ESS.

9.3.1.5 SVG and STATCOM based solutions

Solutions using reactive power/current compensation devices can also be used during LVRT process to stabilize the (PCC) grid side voltage to certain level. Static VAR compensator (SVC) [195] [192] is one of the shunt connected reactive power compensators. It usually consists of a thyristor to control capacitors *or* reactors. Using phase angle modulation control of the thyristor, the capacitors or reactors can provide/absorb reactive power to/from the electrical network.

Static synchronous compensator (STATCOM) [192] is new generation of the shunt compensation. It is based on a voltage source converter with a resistor and an inductor. The most common use of STATCOM is to compensate reactive power and to keep voltage stability. Because the voltage source STATCOM usually uses IGBTs, the response time of a STATCOM is shorter than SVC and provides better reactive power support at voltage

dips, and is therefore attractive. However, since for back-to-back full power rating based PMSG wind turbine systems, active and reactive power can be directly controlled by the grid side converter [8, 10]. Thus, STATCOM is just an enhancement for LVRT ability, but is not required to operate solely.

9.3.1.6 LVRT solution with kinetic energy storage through total inertia

Almost all the techniques discussed above require additional devices to support LVRT. However, considering the (huge) total rotor inertia for big wind mills, small rotating speed increase will lead to huge kinetic energy storage. Therefore, in [193] [129] [131] a LVRT technique storing kinetic energy through the total rotor inertia Θ during grid voltage dips was proposed. The technical essence and operation process is: when a grid voltage dip occurs, the d-axis current reference $i_{\mathrm{g}}^{\mathrm{d}*}$ (equivalent as active power, assuming the grid side voltage vector is aligned with d-axis) and q-axis current reference $i_{\mathrm{g}}^{\mathrm{q}*}$ (equivalent as reactive power) shall be commanded by the LVRT strategy to fulfill the requirement as shown in Fig. 9.8, i.e., $i_{\mathrm{g}}^{\mathrm{d}*}$ (used to control the DC-link voltage in normal mode as introduced in Chp. 3) will be reduced essentially, and $i_{\mathrm{g}}^{\mathrm{q}*}$ will be set to certain values according to the voltage dip depth.

The generator continues providing active power during the voltage dip. As a result, if the DC-link voltage is still controlled by the grid side power converter, the capacitor voltage may increase fast to a damaging level. Therefore, the DC-link voltage shall be controlled by the generator side, i.e., the DC-link controller output shall now be the reference value for the active power/torque relevant quantities, e.g., $i_{\mathrm{m}}^{\mathrm{q}*}$ or T_{e}^{*} (See Fig. 9.13), which is used to force the generator to reduce its output active power/torque. The mechanical power will not change in short. Hence, the turbine will speed up due to the mismatch of mechanical and electrical torques. Therefore, the surplus energy will be stored in the rotor inertia. This utilizes the big-inertia character of a big turbine system, and does not require extra devises. However, it can only apply when the voltage dip lasts not long otherwise the wind turbine may run to a damaging speed level.

9.3.2 Proposed LVRT within DMPC scheme

Clearly from the analysis in Sec. 9.3.1, the most economical solution is 9.3.1.6, i.e., *LVRT solution with kinetic energy storage through total rotor inertia*. However, a backup or enhancement shall be considered due to the operation limitation of presented in Sec. 9.3.1.6. The solution presented in Sec 9.3.1.3, i.e., active crowbar circuit (ACb) based solution, is simple to install and control.

Therefore, this work utilizes a LVRT technique which combines both method presented in Sec. 9.3.1.3 and Sec. 9.3.1.6 based on a DMPC scheme. Main idea is: for a short period of grid voltage dip, the generated mismatch energy, which is not much due to short fault time, is regulated to store in the total rotor inertia by speeding the rotor up within its limitation. While when the voltage dip is lasting for a relatively long period or the wind speed is outside the nominal range (stage-III) (See Chp. 2 for details), the active crowbar

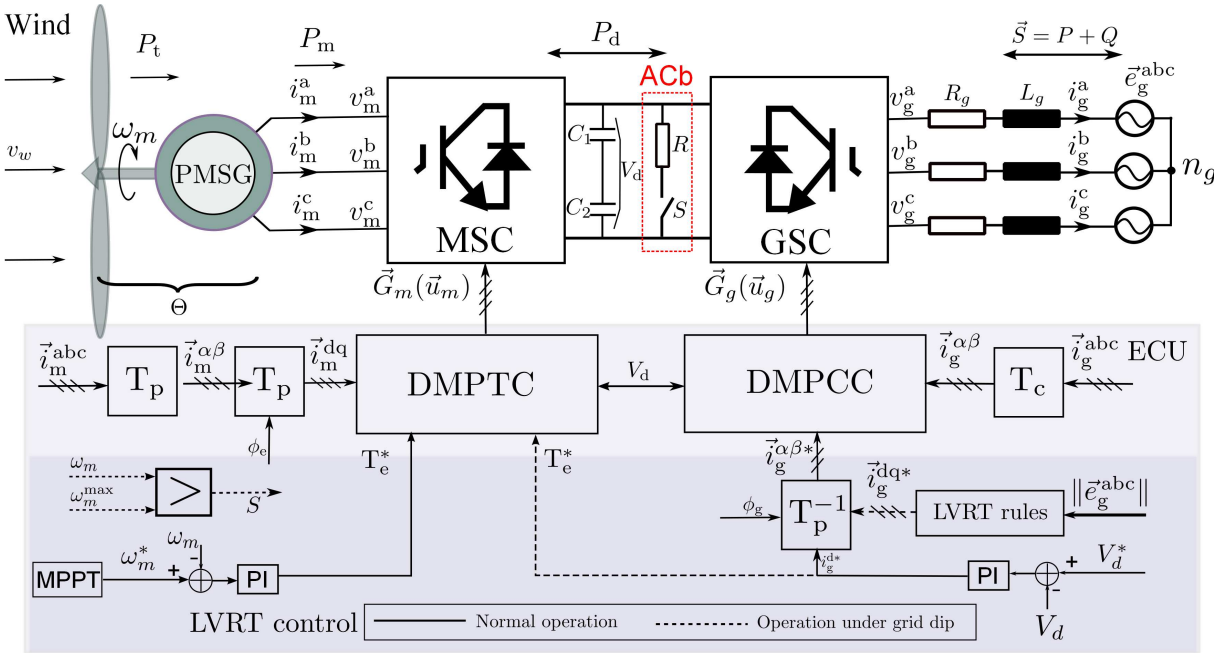

Fig. 9.13: Proposed LVRT method with DMPC control scheme.

circuit will be activated to enhance the LVRT ability.

For the generator and grid sides predictive torque and current control schemes are used. The cost functions which describe the generator and grid side control objectives are designed by (4.7a) and (4.9), respectively as introduced in Chp. 4. An overview of the proposed method is shown in Fig. 9.13.

9.3.3 LVRT evaluations with FPGA S-HiL solution

FPGA realization processes for both the controller and emulator are similar as introduced in Sec. 9.2.1, except that the emulator was modeled and implemented in the same chassis (cRIO-9082) of the ECU in engineering unit to ease the compilation and also future power level evaluations. Due to the limited scope and the available FPGA resources, the relevant PLL part was not implemented in the FPGA. The grid voltage vector angle is assumed to be known to substitute the PLL function.

9.3.3.1 Results of the proposed LVRT control strategy

The grid voltage drops at {0.51, 1.4, 2.4} [s] to 0.4 [p.u.] for around 100 [ms] respectively in the experiment. Fig. 9.14 illustrates the overall control performances. While Fig. 9.15a and Fig. 9.15b depict the zoomed experimental results for the first dip period. As can be seen from Fig. 9.14, the whole system has the same expected response during these three dips. A close look into Fig. 9.15a and Fig. 9.15b yields the following: after the voltage dip occurs, i_g^q changes from 0 to -0.443 [p.u.] to compensate the required reactive

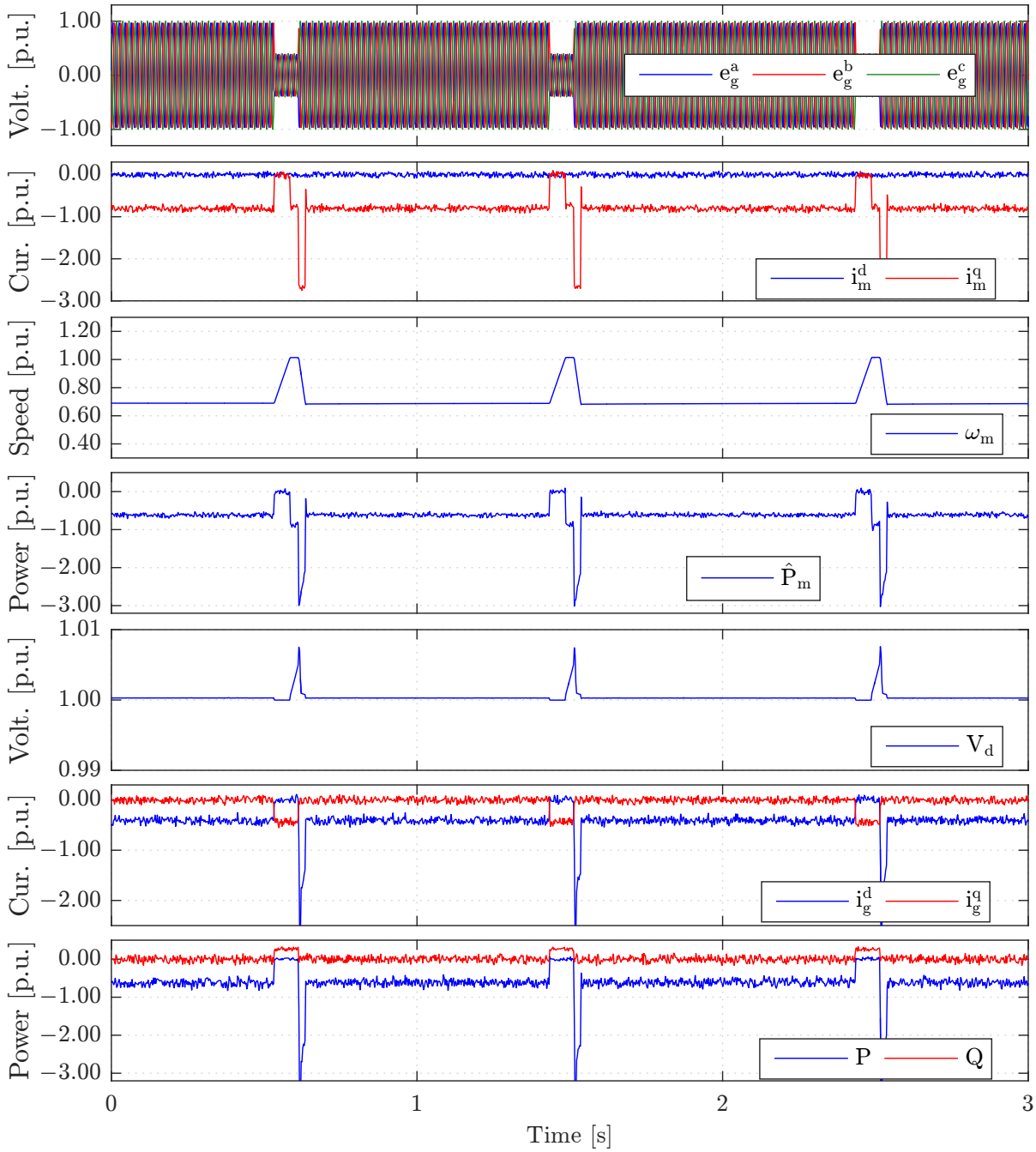

Fig. 9.14: [FPGA HiL simulation results]: Overall performances of the proposed low-voltage-ride-through control with FPGA S-HiL simulation solution. From up to down are the grid side voltages, generator stator current, generator speed, estimated generator output power, DC-link voltage, grid side current and grid side power, respectively.

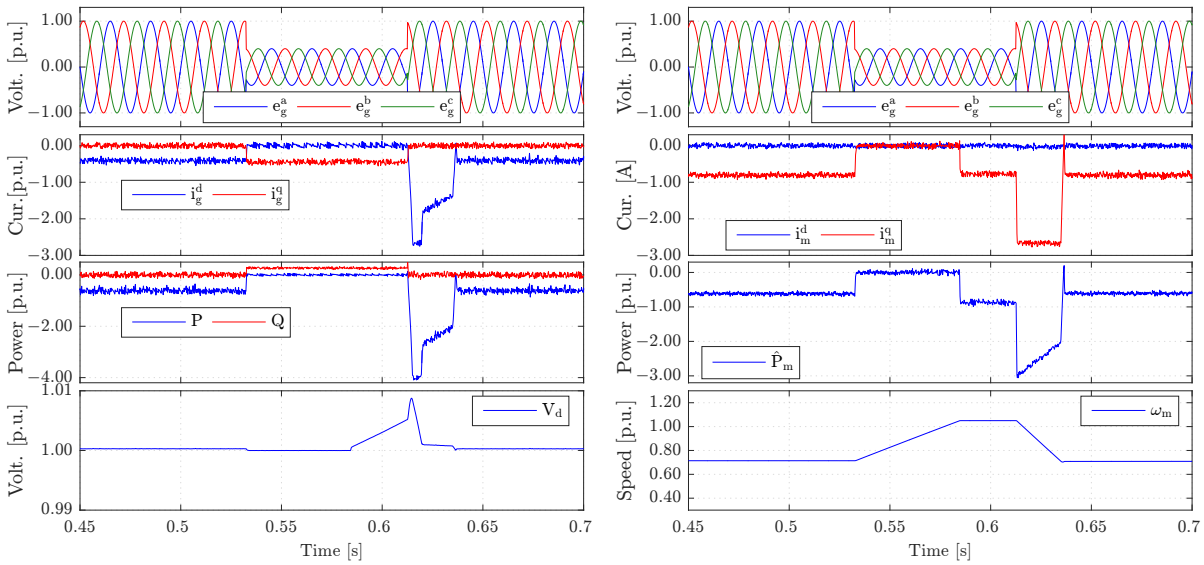

(a) Zoomed performances for GSC and DC-link.

(b) Zoomed performances for MSC.

Fig. 9.15: Zoomed control performances of (a) the grid side, DC-link and (b) machine side control performances.

current/power; while the active power fed into the grid reduces from 0.667 [p.u.] to 0 [p.u.] due to this deep voltage dip. The DC-link voltage started to be governed by the generator side which produces reduced torque references and makes the rotor speed increase during the dip as shown in Fig. 9.15b. For safety reasons, the crowbar circuit begins to work to dissipate the surplus energy coming from wind turbine when the generator speed reaches its operation limit (1 [p.u.]). Therefore, the PMSG rotor speed remains at such value till grid voltage recovers to a nominal value. After the voltage recovers, the optimal speed of the generator is assumed to be the same as the previous one, therefore, $i_{\mathrm{m}}^{\mathrm{q}}$ increases to reduce the rotor speed to its previous value. As a result, the active power produced by the generator is larger than its previous value (See $\hat{P}_m$ in Fig. 9.15b)[4]. The DC-link voltage experiences three main processes accordingly, namely, i) keeps as a "constant" value due to input energy reduction through speeding up the generator, ii) slightly increases, when the craw bar is activated and rotor speed reaches its limit, iii) (fast) recovery after the grid voltage recovers and DC-link control is re-governed by the grid side converter control. Note that, in our experiments, a low power level PMSG with small inertia is used. Therefore, the rotor speed increases significantly within a very short time (40 ms). However, it can be expected that the speed increment is rather small with high power level (MW) PMSG with higher inertia in practice.

Concluding from the experimental results: the proposed scheme works (nicely) as expected and the FPGA HiL method greatly eases the verification process.

[4] A physical explanation which may ease the understanding is that: after the voltage recovery, rotor speed returns to its previous reference value, thus the energy stored in the inertia and extracted from wind will both be delivered into the grid. It is the same reason why $i_{\mathrm{m}}^{\mathrm{q}}$ is larger than its previous value before voltage dip. Similarly, since more energy is delivered to the grid, the $i_{\mathrm{g}}^{\mathrm{d}}$ raises in order to balance energy flow in both side.

9.4 Summary

This chapter has presented the FPGA based HiL simulation solution for the electrical control unit (ECU) verification. The effects of the emulator refreshing rate to the HiL simulation results has been illustrated and theoretically interpreted with real-time evaluation results. Afterward, the general requirement for low voltage ride through (LVRT) has been introduced and the state-of-the-art LVRT techniques for grid-tied wind turbine systems have been reviewed and summarized. A LVRT method combining *rotor inertia kinetic energy storage* and *active crowbar circuit* based solution incorporated into the direct model predictive control frame have been presented. The presented LVRT method has been verified using the fully FPGA based S-HiL solution, with great flexibility, lower cost and risks.

Chapter 10

Conclusions and future prospects

In this work, both classical and modern (model based) control techniques for grid-tied two- and three-level neutral-point-clamped back-to-back power converters and permanent magnet synchronous generator (PMSG) wind turbine systems have been closely investigated. The as-investigated control techniques can be classified into: (i) "framework" level control techniques with the "general control objectives" e.g., to achieve *generator side torque* (*current*), *DC-link voltage* and *grid side power* (*current*) control targets, and (ii) dedicated control techniques to achieve *encoderless control* for the generator side, *advanced DC-link control* for the DC-link control part, *voltage sensorless control* for the grid connected converter part and *low-voltage ride through control* for grid fault situations, etc. The "framework" level control techniques investigated in this dissertation include cascaded control schemes with modulators, i.e., field and voltage oriented control (FOC-VOC) with modulator, direct torque and power control with switching table (ST-DTC-DPC), direct torque and power control with modulator (DTC-DPC with modulator) and predictive controller for both the grid and machine sides. Emphasized efforts have been put into the predictive control class, in particular, the direct model predictive control group, due to its good properties (e.g., straight-forward concept and fast control dynamics, etc.) and promising potentials. More specifically:

In Chp. 2, the mathematical basics with regard to power electronics and drives, in particular, the two- and three-level neutral-point-clamped power back-to-back power converters and permanent magnet synchronous generator wind turbine systems, etc., have been introduced. The underlying back-to-back power converter systems have been explicitly modeled in both continuous and discrete formats to ease the system analysis and controller design process presented in the chapters after. The self-designed test benches for experimentally verifying the control algorithms have been described as well.

In Chp. 3, the classical control methods, including the FOC-VOC, DTC-DPC with switching table/modulators and deadbeat control, are systemically classified and formulated. Their physical/mathematical fundamentals, control principles and realization steps have been clearly discussed and explicitly presented. Their control performances were evaluated using the test-benches presented in Chp. 2, all with an FPGA based solution. These classical control schemes (which are the dominating techniques in the industry applications),

although not the main focus of this dissertation, may serve as a profound survey and assessment for the field of grid-tied back-to-back power converter systems.

The presented experimental results and the realization steps may suggest that the deadbeat control outperforms the other solutions presented in this chapter, in terms of both the required realization efforts and control performances. Its drawbacks of the steady state tracking errors (mainly caused by the model uncertainty) shall be dealt with by certain parameter robust techniques, which can be an interesting research direction.

In Chp. 4, the newly emerged model predictive control techniques for both the grid and machine side control have been comprehensively investigated. In particular, the applications of direct model predictive *current*, *power* and *torque* control methods for the grid-tied two- and three-level neutral-point-clamped back-to-back power converter PMSG wind turbine systems have been formulated and experimentally assessed using an FPGA based digital controller.

In comparison with the classical control techniques presented in Chp. 3, model predictive control has provided a more proper solution when considering system with *multiple control objectives* and *constraints*. Its straight-forward concept and very fast control dynamics are favorable. However, in comparison with the conventional modulator based solutions (e.g., FOC-VOC, DTC-DPC with modulator, deadbeat control, etc.), relatively big steady state control variable ripples (at a similar sampling interval), unfixed switching frequency, etc., are some of its drawbacks. High computational cost is also one of the major concerns for such control technique, particularly for multi-level/multi-phase power converter systems.

In Chp. 5, two major drawbacks of the classical direct model predictive control methods have been formulated, namely *high computational burden* for multilevel power converters (due to the great amount of the available switching vectors) and *big control variable ripples* for two-level power converters (because of the very few freedoms caused by the fixed and very limited switching vectors).

To conquer the heavy computational efforts, required by the classical direct model predictive control concept for multilevel power converter systems, two computationally efficient solutions based on an offline section of the switching sequence groups, for the three-level neutral-point-clamped power back-to-back power converter PMSG wind turbine systems, have been developed and evaluated on an FPGA, in a real-time manner. Realization steps and results have validated that the computational time was reduced evidently with the proposed solutions.

To conquer the drawback of its big control variable ripples of the conventional direct model predictive control solution, multiple switching-vector direct model predictive control concepts have been developed and applied for both the grid and machine side control of the back-to-back power converter PMSG wind turbine systems. Their control performance improvements have been validated via both simulation and experimental data. The results confirm that with the proposed solutions (considerably) enhanced steady state control performances have been achieved, at even reduced sampling frequency. However, the achievements are at the sacrifice of a higher computational burden. The reduced sampling frequency (or increased allowable calculation time) will compensate this drawback easily.

Considering the power rating of power converter systems, for very big power rating (>MW) electrical drives or renewable energy systems, a very desired property is to operate the system at (very) low switching frequency with an acceptable current/power/torque distortions. To achieve this, multilevel ($\geq$ 3 levels) power converter topologies, using predictive control with long prediction horizons (allowing for longer optimization scopes of the control problems) are viable solutions, for which, computationally efficient predictive control techniques are an important research direction to guarantee a viable real-time implementation. While for the low power rating electrical drive systems (some kWs level), for which switching at 5 to 10 kHz (even higher) is permissible, control techniques achieving good steady state control performances (as the conventional modulator base solutions), meanwhile, very good control dynamics (as the direct model predictive control techniques), are interesting research directions. Due to the limited total hardware cost, the increase in the sampling frequency (which imposes higher hardware cost) is undesired. Hence, the proposed multiple switching vector direct model predictive control technique (which reduces control variable ripples, and maintains good control dynamics, but does not rely on a higher sampling frequency) will be a good alternative. Moreover, when considering the future trend in the revolution of the power electronic devices, higher switching frequency, even for high power rating applications, is not a problem any longer, using the already available wide band-gap devices (e.g., the SiC and GaN material based devices). Therefore, the proposed multiple switching vector direct model predictive control solution might also be an interesting alternative for very high power applications.

However, for both the high and low power rating categories, to further booster the system performances hence to ease the hardware requirement (e.g., filter design), *optimal pulse pattern* design with *online fire-angle optimizations* can be a very attractive research direction.

In Chp. 6, the DC-link control issues for back-to-back power converter driven systems have been deeply investigated. Based on a so-called "dynamic reference generation" concept, quasi-centralized direct model predictive control methods for back-to-back power converter systems have been introduced and experimentally evaluated for both back-to-back power systems with RL load and PMSG. The performance improvements and also the potential drawbacks have been illustrated via comparison with the conventional proportional integration controller based methods.

The results and realization steps suggest the proposed quasi-centralized direct model predictive control method might be a good alternative to the conventional proportional integration controller based method, because of its good properties in the reduced tuning efforts, improved controllable control dynamics and also the existing *non-minimum phase* feature of the underlying system (when the current flows from the grid to the load side). The proposed methods have, in essence, taken the *reference design/generation* into the controller, which greatly eases the tuning process. To further enhance performances of the proposed method, disturbance estimation techniques, with good accuracy and fast estimation dynamics, will be a good research direction, which can be helpful to realize a purely "centralized model predictive control" solution for back-to-back power converter systems, without invoking cascaded structures.

In Chp. 7, voltage sensorless control techniques using the virtual flux concept have been investigated. The problems with the conventional solutions have been formulated. Also, a newly proposed method using a time-domain *initial bias compensation* concept has been proposed and experimentally validated. The proposed method achieves accurate estimations at both transient and steady states, requiring very few implementable efforts. Noticeably, the proposed method achieved a *one sampling interval* estimation dynamic, which is theoretically the physical limit of any *digital control* and *online estimation* system.

Different from the classical *filter* based virtual-flux voltage sensorless control solutions, which are mostly in the *frequency domain*, the proposed method is purely in the *time domain* and does not rely on the *harmonic theory*. It is therefore fast in estimation and easy to realize. However, the proposed method greatly relies on these two factors, (i) a (relatively) *fixed* fundamental frequency (which holds true for the grid side system); (ii) in steady state, the "areas" in the positive semi-period and the negative semi-period of the signal to be estimated (e.g., the grid side voltage) shall be equal.

Incorporating certain sequence decoupling methods (i.e., the methods to decouple the unbalanced grid voltages into positive, negative and zero sequences), the proposed *initial bias compensation* based virtual flux voltage sensorless control solution is expected to be capable of dealing with grid-connected systems under grid unbalances. Due to the inherent "integration" relationship between the *virtual flux* and the grid side *voltage*, potentially, *predictive (virtual) flux control* can be a very nice alternative to *predictive current* or *power control* of grid connected systems, when facing distorted or harmonic polluted grid, which, therefore, can be a very interesting research direction.

In Chp. 8 the encoderless control techniques for the generator side control have been studied. Encoderless control, i.e., to operate a motor or generator without a rotational position encoder, is an interesting technique to reduce the hardware cost, system complexity and to improve the system robustness against certain hardware (e.g., encoder and cable) failures. Particularly for big wind turbine systems, the improvement in terms of system robustness against hardware failures is very attractive also very important to reduce the total operation cost of the system. Acoustic pollution and energy losses, coming with the signal injection based solutions, are undesirable. Meanwhile, to start the system from the stand-still is not a key requirement for wind turbine systems. Therefore, in this work the fundamental model based solutions, which are injection power loss-less and do not produce extra acoustic pollution, have been the research focus. More specifically, two dominating observer based techniques, namely, *extended Kalman filter* and *sliding mode observer* based methods have been closely investigated and assessed. A time-varying gain based sliding mode observer solution, achieving good estimation and easy position compensation, was proposed and the extended Kalman filter based method was used to estimate both the load and rotor speed/position. The latter was realized on an FPGA with very little calculation time. In general with these two methods, good estimation accuracy at the middle and high speed ranges can be achieved. The entire capabilities of these methods were not fully explored and certain performance further-enhanced features, such as, encoderless control with parameter online estimation/correction with the Kalman filter based method, chattering-free encoderless control using higher order sliding mode observers, can be interesting research directions.

In Chp. 9, the FPGA based signal level *hardware-in-the-loop* technique has been studied and the emulator refreshing rate effects have been experimentally assessed and theoretically interpreted. In this same chapter, after reviewing the actual *low voltage ride through* (LVRT) control techniques, an LVRT method, via both the *inertia* energy storage solution and *active crow-bar* circuit, has been combined into the direct model predictive control framework. Its effectiveness has been validated via the aforementioned FPGA based signal level *hardware-in-the-loop* technique. In the power electronics and drive fields, solutions to test the"unit-under-test" (e.g., electric control unit for signal level test, or power sources/drives for power level test) in a real-time manner, with good *safety*, *efficiency* and *fidelity*, are very desirable. The FPGA based signal level hardware-in-the-loop techniques have provided a viable solution. In this field, the high-fidelity system models of the plant (to describe the properties of the system more precisely), fast and real-time design structures (to have a very high refreshing rate of an emulator) and the flexibility for certain add-on functionality (to be more efficient and flexible in the testing process), in my eyes, are very interesting research directions. Such techniques might be more widely applied to the electrical drives (e.g., E-mobility), renewable energy generation system (e.g., wind or solar energy systems), electrical energy transmission systems (e.g., high-voltage DC/AC transmissions), etc.

In this work, all the experimental assessments are done with FPGA based digital realizations. The FPGA digital realization solution via the Labview-FPGA technique for power electronics and drive control has been extensively investigated and comprehensively applied, which provided good flexibility and efficiency. Looking into the near future, fast switching devices, even for high power rating system, are going to be used more widely. The allowed high switching frequency of the power switches will, on one hand, help to reduce the variable ripple magnitudes and total distortions, on the other hand, impose much higher computational power requirements upon the *central control unit* (to assure that the control variables, or control output can be refreshed fast enough). To meet this high computational power requirement, hence to better utilize the advantages of these fast switching devices, FPGAs, working as the underlying central control unit, might be more widely employed, thanks to its parallel computational capability.

Apart from the afore-summarized techniques, some other investigation outputs during my Ph.D. research period, e.g., control techniques for induction asynchronous machines, control techniques for dual-fly capacitor active-neutral-point-clamped five-level power converters (DFC-ANPC-5L), disturbance estimation based predictive control solutions (dedicated to improve the outer control speed and DC-link loop performances), long prediction horizon predictive control, robust predictive control solutions for power electronics and drives, etc., have not been presented in this thesis due to the limited scopes. Long prediction predictive control techniques via both the classical direct model predictive control concept and the branch-and-bound techniques (e.g., modified sphere decoding method) for multi-level converters (for both the machine and grid sides) were carried out via simulation. Its real-time realization via FPGA was not done due to that the available resource volume in the FPGA is too small for a back-to-back converter system. Therefore, this research was not presented either. Real-time, experimental verification of the long horizon predictive control techniques (particularly for multilevel power converter

systems), however, will be an interesting and necessary step. Many other interesting control techniques, including continuous model predictive control with constraint optimizations, fixed-switching frequency direct model predictive control techniques, low sampling frequency high performance direct model predictive control with online pulse pattern design, predictive (virtual) flux control of grid side power converters, voltage sensorless control at unsymmetrical grids, full speed range encoderless control within the direct model predictive control framework, etc., will be some of my research focuses in the near future.

Appendices

Appendix A

Symbols and abbreviations

$\mathbb{N}, \mathbb{R}, \mathbb{C}$: natural, real, and complex numbers. $\mathbb{N}_0 := \mathbb{N} \cup 0$: natural number with zero. $\vec{x} \in \mathbb{R}^n$: column vector, $n \in \mathbb{N}$. $\mathbf{A} \in \mathbb{R}^{n \times m}$: matrix with n-row, m-columns. $\mathbf{A}^{-1,\top}$: inverse and transpose of $\mathbf{A}$. $\text{diag}\{a_1, \cdots, a_n\}$: diagonal matrix in $\mathbb{R}^{n \times n}$ with entries $a_1, \cdots, a_n \in \mathbb{R}$. $\mathbf{I}_n \in \mathbb{R}^{n \times n} := \text{diag}\{1, \cdots, 1\}$: identity matrix. General electrical variables and abbreviations are given in Table A.1 and Table A.2. Abbreviations

$i_{\text{m,g}}^{\text{a,b,c}}$	Phase currents of machine side m, and grid side g.
$i_{\text{m,g}}^{\alpha,\beta}$	Phase currents in stationary reference frame
$i_{\text{m,g}}^{\text{d,q}}$	Phase currents in synchronous reference frame
Θ	Moment of inertia of the mechanical shaft
N_{p}	Pair of poles
$\vec{u}_{\text{m,g}}^{\text{a,b,c}}, \vec{v}_{\text{m,g}}$	Switching states and voltage vectors of machine/grid side converters
$T_{\text{e,l}}$	Electromagnetic and Load torque
$v_{\text{m,g}}^{\alpha,\beta}$	Converter voltage in stationary ($\alpha\beta$) reference frame
$v_{\text{m,g}}^{\text{d,q}}$	Converter voltage in rotational (dq) reference frame
$V_{\text{d}}, I_{\text{d}}$	DC link voltage, current
$\vec{S}, P, Q$	Apparent, active, and reactive powers;
$\vec{u}_{\text{m,g}}, \vec{G}_{\text{m,g}}$	Machine and grid side switching states and gate signal vectors;
$\vec{\psi}_{s,r}^{\alpha\beta}$	Stator flux vector in stator reference frame
$\vec{\psi}_{s,r}^{dq}$	Rotorr flux vector in dq reference frame
$\omega_{e,m}$	Electrical and Mechanical rotor speed
$\phi_{e,g}$	Electrical position of voltage or flux vectors
$R_{\text{s}}, R_{\text{g}}, L_{\text{s}}, L_{\text{g}}$	Generator stator and grid side filter resistor and inductance
ψ_{pm}	Flux magnitude of rotor permanent magnet

Table A.1: General electrical variables

AC	Alternating current
AFE	Active front end power converter
C-DMPC	Classical direct model predictive control
DC	Direct current
DTC	Direct torque control
DPC	Direct power control
DBC	Deadbeat control
DMPC	Direct model predictive control
DMPTC	Direct model predictive torque control
DMPCC	Direct model predictive current control
DMPPC	Direct model predictive power control
EKF	Extended Kalman filter
FCS-PTC	Finite control state-predictive torque control
FOC	Field oriented control
FPGA	Field programmable gate array
GPC	Generalized predictive control
GSC	Grid side converter
HiL	Hardware-in-the-loop
IPMSM	Interior permanent magnet synchronous machine
MSC	Machine side converter
MPC	Model predictive control
MRAS	Model reference adaptive system
MTPA	Maximum torque per ampere
NP/NPC	Neutral point/Neutral point clamped
PCC	Predictive current control
PI	Proportional-integral
PMSM	Permanent-magnet synchronous motor
PMSG	Permanent-magnet synchronous generator
PWM	Pulse width modulation
RPM	Revolution per minute
SMO	Sliding mode observer
SVM	Space vector modulation
THD	Total harmonic distortion
VOC	Voltage oriented control
V2,3-DMPC	Two- and three-vector based direct model predictive control
V2,3-DMPPC	Two- and three vector based direct model predictive power control
V2,3-DMPTC	Two- and three-vector based direct model predictive torque control

Table A.2: Abbreviations

Appendix B

Switching matrix

Note that, all the symbols used in the following part are of the same representations as introduced in Chp. 2, and therefore are not repetitively defined.

B.1 Switching matrix for two level power converter

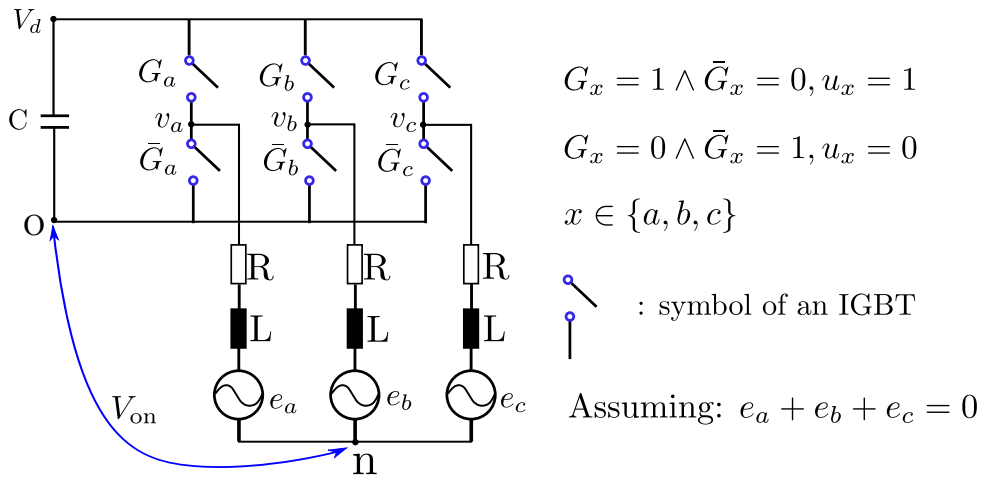

Fig. B.1: Simplified two level voltage source power converter.

A close investigation on Fig. B.1 will yield the following conclusion

$$v_{\text{xo}} = V_d \cdot u_x; \tag{B.1}$$

$$v_{\text{xo}} + v_{\text{on}} = v_{\text{xn}}; \tag{B.2}$$

$$v_{\text{an}} + v_{\text{bn}} + v_{\text{cn}} = 0; \tag{B.3}$$

and,

$$v_{\text{ao}} + v_{\text{bo}} + v_{\text{co}} + 3v_{\text{on}} = v_{\text{an}} + v_{\text{bn}} + v_{\text{cn}} = 0; \tag{B.4}$$

i.e., $v_{\text{on}} = -\frac{1}{3}V_{\text{d}}(u_a + u_b + u_c)$[1]; where u_x, as is indicated in Fig. B.1, is the switching state;

[1] The common mode voltge in this case tuns to be $v_{\text{cm}} = v_{\text{on}} - \frac{V_{\text{d}}}{2}$.

$x \in \{a, b, c\}$ is the phase symbol.

Therefore, the phase-to-neutral voltage vector

$$[v_{an}, v_{bn}, v_{cn}]^\top = \underbrace{\frac{V_d}{3}\begin{bmatrix} 2 & -1 & -1 \\ -1 & 2 & -1 \\ -1 & -1 & 2 \end{bmatrix}}_{=:\boldsymbol{T}_{\mathrm{SW}}} \vec{u}_{\mathrm{abc}}.$$

Note that, for simplicity, in this thesis, phase voltage (vector) is simplified as $[v_{an}, v_{bn}, v_{cn}]^\top = [v_a, v_b, v_c]^\top$.

The line-to-line voltages are therefore:

$$\vec{v}^{\mathrm{ltl}}_{[\mathrm{k}]}(\vec{u}_x) := \begin{bmatrix} v_a - v_b \\ v_b - v_c \\ v_c - v_a \end{bmatrix} = V_d \begin{bmatrix} 1 & -1 & 0 \\ 0 & 1 & -1 \\ -1 & 0 & 1 \end{bmatrix} \vec{u}_{\mathrm{abc}}. \tag{B.5}$$

B.2 Switching matrix for three level power converter

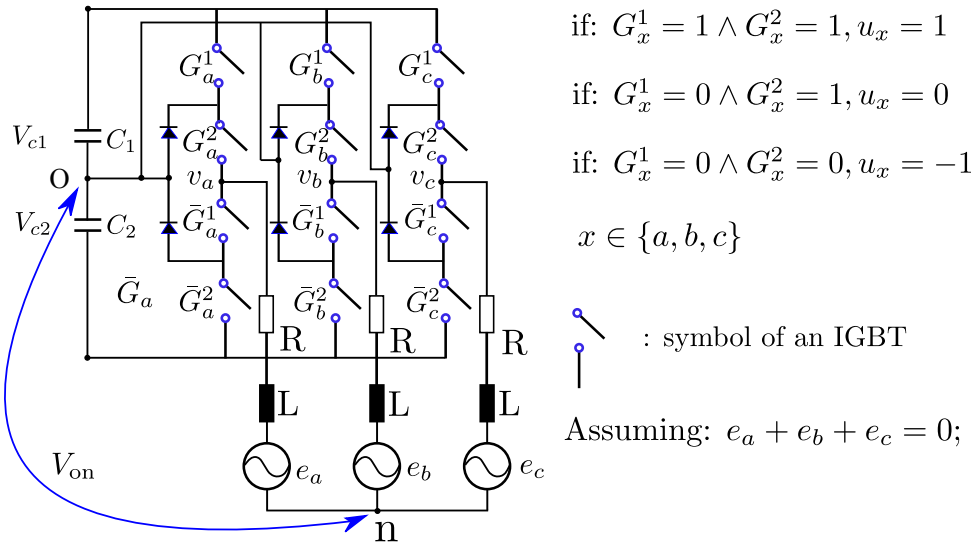

Fig. B.2: Simplified three level NPC power converter.

From the circuit shown in Fig. B.2, it is easy to find:

$$v_{\mathrm{xo}} = \frac{1}{2}(V_{c1} + V_{c2}) \cdot u_x + \frac{1}{2}(V_{c1} - V_{c2}) \cdot |u_x|; \tag{B.6}$$

$$v_{\mathrm{xo}} + v_{\mathrm{on}} = v_{\mathrm{xn}}; \tag{B.7}$$

$$v_{\mathrm{an}} + v_{\mathrm{bn}} + v_{\mathrm{cn}} = 0; \tag{B.8}$$

Therefore[2], $v_{\text{on}} = -\frac{1}{3}\frac{(V_{c1}+V_{c2})}{2}(u_a+u_b+u_c) - \frac{1}{3}\frac{(V_{c1}-V_{c2})}{2}(|u_a|+|u_b|+|u_c|)$. Therefore,

$$\begin{bmatrix} v_{an} \\ v_{bn} \\ v_{cn} \end{bmatrix} = \underbrace{\frac{1}{2}\cdot\frac{(V_{c1}+V_{c2})}{3}\begin{bmatrix} 2 & -1 & -1 \\ -1 & 2 & -1 \\ -1 & -1 & 2 \end{bmatrix}}_{:=\boldsymbol{T}_{\text{SW}}} \vec{u}_{\text{abc}} + \underbrace{\frac{1}{2}\cdot\frac{(V_{c1}-V_{c2})}{3}\begin{bmatrix} 2 & -1 & -1 \\ -1 & 2 & -1 \\ -1 & -1 & 2 \end{bmatrix}}_{:=\boldsymbol{T}_{\text{SW}}} |\vec{u}_{\text{abc}}| \tag{B.9}$$

where $\vec{u}_{\text{abc}} = [u_a, u_b, u_c]^\top$ and $|\vec{u}_{\text{abc}}| = \Big[|u_a|, |u_b|, |u_c|\Big]^\top$.

The line-to-line voltages are therefore:

$$\begin{aligned} &\vec{v}^{\text{ltl}}_{[\text{k}]}(\vec{u}_x) := \\ &\begin{bmatrix} v_a - v_b \\ v_b - v_c \\ v_c - v_a \end{bmatrix} = \frac{1}{2}\cdot(V_{c1}+V_{c2})\begin{bmatrix} 1 & -1 & 0 \\ 0 & 1 & -1 \\ -1 & 0 & 1 \end{bmatrix}\vec{u}_{\text{abc}} + \frac{1}{2}\cdot(V_{c1}-V_{c2})\begin{bmatrix} 1 & -1 & 0 \\ 0 & 1 & -1 \\ -1 & 0 & 1 \end{bmatrix}|\vec{u}_{\text{abc}}| \\ &\qquad = V_{c1}\begin{bmatrix} 1 & -1 & 0 \\ 0 & 1 & -1 \\ -1 & 0 & 1 \end{bmatrix}\frac{|\vec{u}_{\text{abc[k]}}|+\vec{u}_{\text{abc[k]}}}{2} - V_{c2}\begin{bmatrix} 1 & -1 & 0 \\ 0 & 1 & -1 \\ -1 & 0 & 1 \end{bmatrix}\frac{|\vec{u}_{\text{abc[k]}}|-\vec{u}_{\text{abc[k]}}}{2} \end{aligned} \tag{B.10}$$

Remark 22 *It can also be drawn that, for any neutral-point-clamped* n*-level ($n \geq 3$) power converter, assuming the switches are ideal and DC-link capacitor voltages are balanced, then its phase voltage vector can be modeled in the following:*

$$\begin{bmatrix} v_{an} \\ v_{bn} \\ v_{cn} \end{bmatrix} = \underbrace{\frac{1}{n-1}\cdot\frac{V_d}{3}\begin{bmatrix} 2 & -1 & -1 \\ -1 & 2 & -1 \\ -1 & -1 & 2 \end{bmatrix}}_{:=\boldsymbol{T}_{\text{SW}}} \vec{u}_{\text{abc}}. \tag{B.11}$$

Remark 23 *Another more direct modeling solution is to take the gate signal as the input, then the x phase to o point voltage, $v_{\text{xo}} = V_{\text{c1}}G_x^1 - V_{\text{c2}}(G_x^2 - 1)$, where $G_x^{1,2} \in [0,1]$ can be* switching signal *or the* duty ratio*. This concept in modeling will ease the design process for using continuous model predictive control of power converters.*

[2] v_{on} is also the common mode voltage, i.e., $v_{\text{cm}} = v_{\text{on}}$

Appendix C

System per-unit model

Note that, x' represents the per-unit of quantity x; except this, all the symbols used in the following part are of the same representations as introduced in Chp. 2, and therefore are not repetitively defined.

System per-unit (P.U.) modeling can be realized with three steps: (i) fundamental base value determination; (ii) induced based value calculation; (iii) transferring engineering unit (E.U.) models into P.U.

The fundamental base values for such a system include: nominal power of the grid and machine sides $P_{\mathrm{g}}^{\mathrm{n}}, P_{\mathrm{n}}^{\mathrm{n}}$, i.e. $P_{\mathrm{g}}^{\mathrm{B}} = P_{\mathrm{g}}^{\mathrm{n}}, P_{\mathrm{m}}^{\mathrm{B}} = P_{\mathrm{m}}^{\mathrm{n}}$; rated machine speed and grid voltage frequency, i.e. $\Omega_{\mathrm{m}}^{\mathrm{B}} = \Omega_{\mathrm{m}}^{\mathrm{n}}$ (in RPM) and $\omega_{\mathrm{g}}^{\mathrm{B}} = \omega_{\mathrm{g}}^{\mathrm{n}}$; machine and grid side rated voltage (RMS phase value), i.e. $v_{\mathrm{m}}^{\mathrm{B}} = v_{\mathrm{m}}^{\mathrm{n}}$ and $v_{\mathrm{g}}^{\mathrm{B}} = v_{g}^{\mathrm{n}}$. The DC-link voltage base value in this work is chosen as $V_{\mathrm{d}}^{\mathrm{B}} = K_{\mathrm{sc}} \cdot \sqrt{6} v_{\mathrm{g}}^{\mathrm{B}}$ (which is the natural rectified DC-link voltage value[1]). The induced base values, i.e., for step (ii), include, machine and grid side current $i_{\mathrm{m}}^{\mathrm{B}}$, $i_{\mathrm{g}}^{\mathrm{B}}$; resisters $R_{\mathrm{m}}^{\mathrm{B}}$, $R_{\mathrm{g}}^{\mathrm{B}}$; inductance $L_{\mathrm{s}}^{\mathrm{B}}$, $L_{\mathrm{g}}^{\mathrm{B}}$; machine side mechanical and electrical speed $\omega_{\mathrm{m}}^{\mathrm{B}}$ and $\omega_{\mathrm{e}}^{\mathrm{B}}$ ([rad/s]), flux $\psi_{\mathrm{m}}^{\mathrm{B}}$, initial J^{B}, torque T^{B}, and friction B^{B}, which are calculated by [46]

$$i_{\mathrm{m}}^{\mathrm{B}} = \frac{P_{\mathrm{m}}^{\mathrm{B}}}{3 v_{\mathrm{m}}^{\mathrm{B}}},\ i_{\mathrm{g}}^{\mathrm{B}} = \frac{P_{\mathrm{g}}^{\mathrm{B}}}{3 v_{\mathrm{g}}^{\mathrm{B}}},\ R_{\mathrm{m}}^{\mathrm{B}} = \frac{v_{\mathrm{m}}^{\mathrm{B}}}{i_{\mathrm{m}}^{\mathrm{B}}},\ R_{\mathrm{g}}^{\mathrm{B}} = \frac{v_{\mathrm{g}}^{\mathrm{B}}}{i_{\mathrm{g}}^{\mathrm{B}}},\ \omega_{\mathrm{m}}^{\mathrm{B}} = \frac{\Omega_{\mathrm{m}}^{\mathrm{B}}}{30}\pi,\ \omega_{\mathrm{e}}^{\mathrm{B}} = \frac{\Omega_{\mathrm{m}}^{\mathrm{B}}}{30}\pi N_{\mathrm{p}}, \tag{C.1a}$$

$$L_{\mathrm{s}}^{\mathrm{B}} = \frac{R_{\mathrm{m}}^{\mathrm{B}}}{\omega_{\mathrm{e}}^{\mathrm{B}}},\ L_{\mathrm{g}}^{\mathrm{B}} = \frac{R_{\mathrm{g}}^{\mathrm{B}}}{\omega_{\mathrm{g}}^{\mathrm{B}}},\ \psi_{\mathrm{m}}^{\mathrm{B}} = \frac{v_{\mathrm{m}}^{\mathrm{B}}}{\omega_{\mathrm{e}}^{\mathrm{B}}},\ J^{\mathrm{B}} = J\frac{(\omega_{\mathrm{m}}^{\mathrm{B}})^2}{P_{\mathrm{m}}^{\mathrm{B}}},\ T^{B} = \frac{P_{\mathrm{m}}^{\mathrm{B}}}{\omega_{\mathrm{m}}^{\mathrm{B}}},\ B^{B} = \frac{\omega_{\mathrm{m}}^{\mathrm{B}}}{T^{B}}. \tag{C.1b}$$

The principle for performing step (iii) is the equation $x' = \frac{x}{x^{B}}$, where x, x', x^{B} are the E.U., P.U., and base value representations of x, respectively. Invoking the E.U. models developed in Chapter 2, yields the P.U. form of the system model:

$$v_{\mathrm{m}}^{\mathrm{d}'}(t) = R'_{\mathrm{s}} i_{\mathrm{m}}^{\mathrm{d}'}(t) + \frac{L_{\mathrm{s}}^{\mathrm{d}'}}{\omega_{\mathrm{e}}^{\mathrm{B}}}\frac{d i_{\mathrm{m}}^{\mathrm{d}'}(t)}{dt} - \omega_{\mathrm{e}}^{'}(t) L_{\mathrm{s}}^{\mathrm{q}'} i_{\mathrm{m}}^{\mathrm{q}'}(t), \tag{C.2a}$$

$$v_{\mathrm{m}}^{\mathrm{q}'}(t) = R'_{\mathrm{s}} i_{\mathrm{m}}^{\mathrm{q}'}(t) + \frac{L_{\mathrm{s}}^{\mathrm{q}'}}{\omega_{\mathrm{e}}^{\mathrm{B}}}\frac{d i_{\mathrm{m}}^{\mathrm{q}'}(t)}{dt} + \omega_{\mathrm{e}}^{'}(t) L_{\mathrm{s}}^{\mathrm{d}'} i_{\mathrm{m}}^{\mathrm{d}'}(t) + \omega_{\mathrm{e}}^{'}(t)\psi'_{\mathrm{M}}, \tag{C.2b}$$

$$T'_{\mathrm{e}}(t) = \psi'_{\mathrm{M}} i_{\mathrm{m}}^{\mathrm{q}'}(t) + (L_{\mathrm{s}}^{\mathrm{q}'} - L_{\mathrm{s}}^{\mathrm{q}'}) i_{\mathrm{m}}^{\mathrm{q}'}(t) i_{\mathrm{m}}^{\mathrm{d}'}(t); \tag{C.2c}$$

[1] A scaling of $K_{\mathrm{sc}} = 1.2$ is used for the DC-link voltage reference to have more freedom to the grid side control.

$$\frac{d\omega_{\mathrm{m}}^{'}(t)}{dt} = \frac{1}{J^B}\Big[T_m'(t) - T_e'(t) + B' \cdot \omega_{\mathrm{m}}(t)'\Big], \tag{C.3a}$$

$$\frac{d\theta_m(t)}{dt} = \omega_{\mathrm{m}}^{'}(t)\omega_{\mathrm{m}}^{\mathrm{B}}(t), \tag{C.3b}$$

$$v_{\mathrm{g}}^{\alpha'}(t) = R_{\mathrm{g}}' i_{\mathrm{g}}^{\alpha'}(t) + \frac{L_{\mathrm{g}}'}{\omega_{\mathrm{g}}^{\mathrm{B}}}\frac{di_{\mathrm{g}}^{\alpha'}(t)}{dt} - e_{\mathrm{g}}^{\alpha'}(t), \tag{C.3c}$$

$$v_{\mathrm{g}}^{\beta'}(t) = R_{\mathrm{g}}' i_{\mathrm{g}}^{\beta'}(t) + \frac{L_{\mathrm{g}}'}{\omega_{\mathrm{g}}^{\mathrm{B}}}\frac{di_{\mathrm{g}}^{\beta'}(t)}{dt} - e_{\mathrm{g}}^{\beta'}(t). \tag{C.3d}$$

$$\vec{v}_{\mathrm{m}}^{\mathrm{abc}'} = \frac{1}{v_{\mathrm{m}}^{\mathrm{B}}} \cdot \mathbf{T}_{\mathrm{SW}} \cdot \vec{u}_{\mathrm{m}}^{\mathrm{abc}}, \tag{C.3e}$$

$$\vec{v}_{\mathrm{g}}^{\mathrm{abc}'} = \frac{1}{v_{\mathrm{g}}^{\mathrm{B}}} \cdot \mathbf{T}_{\mathrm{SW}} \cdot \vec{u}_{\mathrm{g}}^{\mathrm{abc}}, \tag{C.3f}$$

After transferring into discrete format invoking the Euler forward equation taking T_{r} as the time-step (emulator refreshing interval), yields the discrete equations as[2]

$$i_{\mathrm{m[k+1]}}^{\mathrm{d}'} = \frac{\omega_{\mathrm{e}}^{\mathrm{B}} T_{\mathrm{r}}}{L_{\mathrm{s}}^{\mathrm{d}'}} v_{\mathrm{m[k]}}^{\mathrm{d}'} + \Big(1 - \frac{R'_{\mathrm{s}}\omega_{\mathrm{e}}^{\mathrm{B}} T_{\mathrm{r}}}{L_{\mathrm{s}}^{\mathrm{d}'}}\Big) i_{\mathrm{m[k]}}^{\mathrm{d}'} + \frac{\omega_{\mathrm{e}}^{\mathrm{B}} L_{\mathrm{s}}^{\mathrm{q}'} T_{\mathrm{r}}}{L_{\mathrm{s}}^{\mathrm{d}'}} i_{\mathrm{m[k]}}^{\mathrm{q}'} \omega_{\mathrm{e[k]}}^{'}, \tag{C.4a}$$

$$i_{\mathrm{m[k+1]}}^{\mathrm{q}'} = \frac{\omega_{\mathrm{e}}^{\mathrm{B}} T_{\mathrm{r}}}{L_{\mathrm{s}}^{\mathrm{q}'}} v_{\mathrm{m[k]}}^{\mathrm{q}'} + \Big(1 - \frac{R'_{\mathrm{s}}\omega_{\mathrm{e}}^{\mathrm{B}} T_{\mathrm{r}}}{L_{\mathrm{s}}^{\mathrm{q}'}}\Big) i_{\mathrm{m[k]}}^{\mathrm{q}'} - \frac{\omega_{\mathrm{e}}^{\mathrm{B}} L_{\mathrm{s}}^{\mathrm{d}'} T_{\mathrm{r}}}{L_{\mathrm{s}}^{\mathrm{q}'}} \omega_{\mathrm{e[k]}}^{'} i_{\mathrm{m[k]}}^{\mathrm{d}'} - \frac{\omega_{\mathrm{e}}^{\mathrm{B}} T_{\mathrm{r}} \psi'_{\mathrm{M}}}{L_{\mathrm{s}}^{\mathrm{q}'}} \omega_{\mathrm{e[k]}}^{'}, \tag{C.4b}$$

$$T'_{\mathrm{e[k+1]}} = \psi'_{\mathrm{M}} i_{\mathrm{m[k+1]}}^{\mathrm{q}'} + \Big(L_{\mathrm{s}}^{\mathrm{q}'} - L_{\mathrm{s}}^{\mathrm{d}'}\Big) i_{\mathrm{m[k+1]}}^{\mathrm{q}'} i_{\mathrm{m[k+1]}}^{\mathrm{d}'}, \tag{C.4c}$$

$$\omega_{\mathrm{m[k+1]}}^{'} = \frac{T_{\mathrm{r}}}{J^B}\Big(T'_{\mathrm{e[k]}} - T'_{\mathrm{m[k]}} - B'\omega_{\mathrm{m[k]}}^{'}\Big) + \omega_{\mathrm{m[k]}}^{'}, \tag{C.4d}$$

$$\theta_{\mathrm{m[k+1]}} = \omega_{\mathrm{m[k]}}^{'} \omega_{\mathrm{m}}^{\mathrm{B}} T_{\mathrm{r}} + \theta_{\mathrm{m[k]}}, \tag{C.4e}$$

$$i_{\mathrm{g[k+1]}}^{\alpha'} = \frac{T_{\mathrm{r}}\omega'_{\mathrm{g}}}{L'_{\mathrm{g}}}(e_{\mathrm{g[k]}}^{\alpha'} - v_{\mathrm{g[k]}}^{\alpha'}) + \Big(1 - \frac{T_{\mathrm{r}} R'_{\mathrm{g}} \omega'_{\mathrm{g}}}{L'_{\mathrm{g}}}\Big) i_{\mathrm{g[k]}}^{\alpha'}, \tag{C.4f}$$

$$i_{\mathrm{g[k+1]}}^{\beta'} = \frac{T_{\mathrm{r}}\omega'_{\mathrm{g}}}{L'_{\mathrm{g}}}\Big(e_{\mathrm{g[k]}}^{\beta'} - v_{\mathrm{g[k]}}^{\beta'}\Big) + \Big(1 - \frac{T_{\mathrm{r}} R'_{\mathrm{g}} \omega'_{\mathrm{g}}}{L'_{\mathrm{g}}}\Big) i_{\mathrm{g[k]}}^{\beta'}, \tag{C.4g}$$

$$V'_{\mathrm{d[k+1]}} = \frac{T_{\mathrm{r}}}{C V_{\mathrm{d}}^{\mathrm{B}}}\Big(I'_{\mathrm{m[k]}} i_{\mathrm{m}}^{\mathrm{B}} - I'_{\mathrm{g[k]}} i_{\mathrm{g}}^{\mathrm{B}}\Big) + V'_{\mathrm{d[k]}} \tag{C.4h}$$

$$\vec{v}_{\mathrm{m[k]}}^{\mathrm{abc}'} = \frac{1}{v_{\mathrm{m}}^{\mathrm{B}}} \cdot \mathbf{T}_{\mathrm{SW}} \cdot \vec{u}_{\mathrm{m[k]}}^{\mathrm{abc}}, \tag{C.4i}$$

$$\vec{v}_{\mathrm{g[k]}}^{\mathrm{abc}'} = \frac{1}{v_{\mathrm{g}}^{\mathrm{B}}} \cdot \mathbf{T}_{\mathrm{SW}} \cdot \vec{u}_{\mathrm{g[k]}}^{\mathrm{abc}}. \tag{C.4j}$$

Note all symbols are of the same meaning as defined in the former chapters.

[2]Note that, the harmonics of the current and toque are neglected in these equations, which also suggests the emulator we developed is only capable for a system level evaluation of the controller.

Appendix D

Switching table for three-level NPC power converter

D.1 Vector definition

Fig. D.1 depicts the vector definitions and numbering of a three-level NPC power converter switching vectors. The switching tables bellow are following these definitions and vector numbering. Note that, all the "V" is eliminated for the simplicity in the table expression (e.g., $V1$ is marked simply as 1, and $V7'$ is simply as $7'$ in the tables).

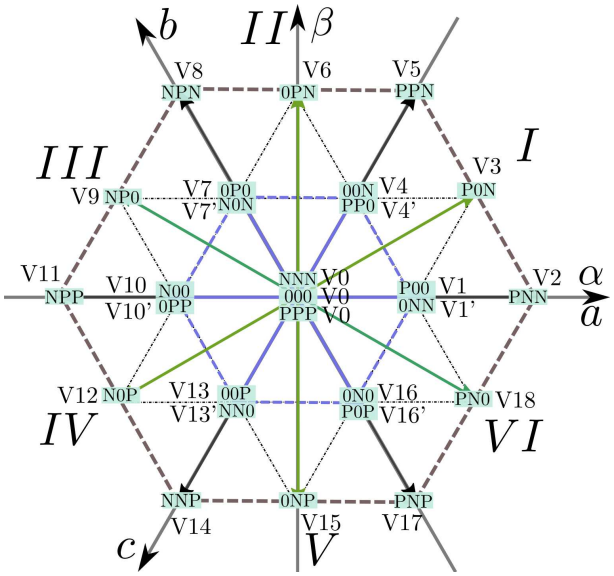

Fig. D.1: Vector definition and numbering of a three level NPC power converter.

D.2 Switching table for 3L NPC power converter using direct torque control

$H_{\vec{\psi}_s}$	H_{T_e}	H_{V_o}	Sector											
			1	2	3	4	5	6	7	8	9	10	11	12
+1	+2	-1	3	5	6	8	9	11	12	14	15	17	18	2
		1	3	5	6	8	9	11	12	14	15	17	18	2
	+1	-1	3	4’	6	7’	9	10’	12	13’	15	16’	18	1’
		1	3	4	6	7	9	10	12	13	15	16	18	1
	0	-1	zero vector											
		1												
	-1	-1	18	1’	3	4’	6	7’	9	10’	12	13’	15	16’
		1	18	1	3	4	6	7	9	10	12	13	15	16
	-2	-1	18	2	3	5	6	8	9	11	12	14	15	17
		1	18	2	3	5	6	8	9	11	12	14	15	17
-1	+2	-1	8	9	11	12	14	15	17	18	2	3	5	6
		1	8	9	11	12	14	15	17	18	2	3	5	6
	+1	-1	7’	9	10’	12	13’	15	16’	18	1’	3	4’	6
		1	7	9	10	12	13	15	16	18	1	3	4	6
	0	-1	zero vector											
		1												
	-1	-1	13’	15	16’	18	1’	3	4’	6	7’	9	10’	12
		1	13	15	16	18	1	3	4	6	7	9	10	12
	-2	-1	14	15	17	18	2	3	5	6	8	9	11	12
		1	14	15	17	18	2	3	5	6	8	9	11	12
0	+2	-1	6	20	9	11	12	14	15	17	18	2	3	5
		1	6	20	9	11	12	14	15	17	18	2	3	5
	+1	-1	6	7’	9	10’	12	13’	15	16’	18	1’	3	4’
		1	6	7	9	10	12	13	15	16	18	1	3	4
	0	-1	zero vector											
		1												
	-1	-1	15	16’	18	1’	3	4’	6	7’	9	10’	12	13’
		1	15	16	18	1	3	4	6	7	9	10	12	13
	-2	-1	15	17	18	2	3	5	6	8	9	11	12	14
		1	15	17	18	2	3	5	6	8	9	11	12	14

Table D.1: Switching table for three-level DTC

D.3 Switching table for 3L NPC power converter using direct power control

H_P	H_Q	H_{V_o}	Sector											
			1	2	3	4	5	6	7	8	9	10	11	12
1	2	-1	7’	9	10’	12	13’	15	16’	18	1’	3	4’	6
		1	7	9	10	12	13	15	16	18	1	3	4	6
	1	-1	10’	10’	13’	13’	16’	16’	1’	1’	4’	4’	7’	7’
		1	10	10	13	13	16	16	1	1	4	4	7	7
	-1	-1	13’	16’	16’	1’	1’	4’	4’	7’	7’	10’	10’	13’
		1	13	16	16	1	1	4	4	7	7	10	10	13
	-2	-1	14	17	17	2	2	5	5	8	8	11	11	14
		1	14	17	17	2	2	5	5	8	8	11	11	14
0	2	-1	6	8	9	11	12	14	15	17	18	2	3	5
		1	6	8	9	11	12	14	15	17	18	2	3	5
	1	-1	4’	4’	7’	7’	10’	10’	13’	13’	16’	16’	1’	1’
		1	4	4	7	7	10	10	13	13	16	16	1	1
	-1	-1	1’	1’	4’	4’	7’	7’	10’	10’	13’	13’	16’	16’
		1	1	1	4	4	7	7	10	10	13	13	16	16
	-2	-1	17	17	2	2	5	5	8	8	11	11	14	14
		1	17	17	2	2	5	5	8	8	11	11	14	14
-1	2	-1	3	5	6	8	9	11	12	14	15	17	18	2
		1	3	5	6	8	9	11	12	14	15	17	18	2
	1	-1	3	5	6	8	9	11	12	14	15	17	18	2
		1	3	5	6	8	9	11	12	14	15	17	18	2
	-1	-1	2	3	5	6	8	9	11	12	14	15	17	18
		1	2	3	5	6	8	9	11	12	14	15	17	18
	-2	-1	2	3	5	6	8	9	11	12	14	15	17	18
		1	2	3	5	6	8	9	11	12	14	15	17	18

Table D.2: Proposed switching table for three-level DPC

Appendix E

List of publications

E.1 Journals

(1) **Zhenbin Zhang**, H. Xu, M. Xu, Z. Chen, T. Sun, R. Kennel, C. Hackl, "Predictive Control with Novel Virtual Flux Estimation for Back-to-Back Converters", *IEEE transactions on Industrial Electronics*, 2015. (published)

(2) **Zhenbin Zhang**, F. Wang, T. Sun, José Rodríguez, R. Kennel, "FPGA Based Experimental Investigation of a Quasi-Centralized Model Predictive Control for Back-to-Back Converters", *IEEE transactions on Power Electronics*, 2016. (published)

(3) **Zhenbin Zhang**, T. Sun, F. Wang, José Rodríguez, R. Kennel, "A Computationally-Efficient Quasi-Centralized DMPC for Back-to-Back Converter PMSG Wind Turbine Systems Without DC-link Tracking Errors", *IEEE transactions on Industrial Electronics*, 2016. (published)

(4) **Zhenbin Zhang**, C. Hackl, R. Kennel, "Computationally Efficient DMPC for Three-level NPC Back-to-Back Converters in Wind Turbine Systems with PMSG", *IEEE transactions on Power Electronics*, 2015. (revision)

(5) **Zhenbin Zhang**, J. Rodríguez, R. Kennel "Multi-vector model predictive power control for grid-tied wind turbine systems with enhanced steady state control performances ", *IEEE transactions on Industrial Electronics* 2016, (revision)

(6) **Zhenbin Zhang**, F. Wang, J. Rodríguez, R. Kennel "Two Nonlinear Direct Control Methods for Grid-Tied 3L-NPC Back-to-Back Power Converter PMSG Wind Turbine Systems", *IEEE Transactions on Industrial Informatics*, 2016 (revision)

(7) F. Wang, **Zhenbin Zhang***, A. Davari, R. Fotouhi, D. Khaburi, J. Rodriguez, R. Kennel, "Encoderless Predictive Torque Control by Using a Revised Prediction Model and EFOSMO", *IEEE transactions on Industrial Electronics, 2014.* (published)

(8) F. Hui, **Zhenbin Zhang***, Xiaoyun Feng, R. Kennel, "Two-Vector-Based Ripple-Reduced MPDPC for Active Front End Power Converters with Extended Switching Vectors and Time-Optimized Control", *IET Journal of Power Electronics, 2015.* (published)

(9) X. Cai, **Zhenbin Zhang***, R. Kennel "Optimum Control for Power Electronics and Drives", *IEEE transactions on Industrial Electronics*, 2016 (revision)

(10) Z. Chen, F. Wang, G. Luo, **Zhenbin Zhang***, R. Kennel, "Sensorless Control for Concentrated Winding SPMSM Using Secondary Saliency Tracking", *IEEE transactions on Industrial Informatics*, 2015. (published)

(11) F. Wang, Z. Chen, **Zhenbin Zhang**, R. Kennel, J. Rodreguez, "Finite Control Set Model Predictive Torque Control of Induction Machine with a Robust Adaptive Observer", *IEEE transactions on Industrial Electronics*, 2015 (published).

(12) F. Wang, **Zhenbin Zhang**, A. Davari, R. Kennel, "An Experimental Assessment of PTC for Electrical Drives by Considering Different Online-Optimization Methods", *Control Engineering Practice, 2014.* (published)

(13) F. Wang, **Zhenbin Zhang**, R. Kennel, J. Rodriguez, "Model Predictive Torque Control with an Extended Prediction Horizon for Electrical Drive Systems" , International Journal of Control, 2014. (**Invited paper**, published)

(14) Z. Chen, J. Gao, F. Wang, Z. Ma, **Zhenbin Zhang**, R. Kennel, "Sensorless Control of Centralized Winding PMSM with Multi-signal Injection", *IEEE transactions on Industrial Electronics*, 2014 (published).

E.2 Conferences

(1) **Zhenbin Zhang**, C. Hackl, F. Wang, Z. Chen, R. Kennel, "Encoderless model predictive control of back-to-back converter direct drive permanent magnet synchronous generator wind turbine systems", *15th European conference on EPE, 2013* (published).

(2) **Zhenbin Zhang**, F. Wang, M. Acikgoz, X. Cai, R. Kennel, "FPGA Based HiL Simulation of Back-to-Back PMSG Wind Turbine Systems", *ICPE 2015-ECCE Asia Conference, 2015.*

(3) X. Cai, **Zhenbin Zhang***, R. Kennel, "Current Balancing Control of High Power Parallel-Connected AFE with Small Current Ripples", *ICPE 2015-ECCE Asia Conference, 2015* (published).

(4) **Zhenbin Zhang**, M. Acikgoz, R. Kennel, "FPGA Based Hardware-in-the-Loop Simulation of MWs Wind Turbine Systems", **Invited Presentation**, *NI-Week, Austin, US, 2014.*

(5) **Zhenbin Zhang**, R. Kennel, "Direct Model Predictive Control of Three-level NPC Back-to-Back Power Converter PMSG Wind Turbine Systems Under Unbalanced Grid", *PRECED 2015, Valpariso, Chile, 2015.* (published)

(6) **Zhenbin Zhang**, R. Kennel, "Fully FPGA Based Performance Enhanced DMPC for Grid-Tied AFE With Multiple Predictions and Reduced Computational Efforts", *IECON 2015, Japan, 2015.* (published)

(7) **Zhenbin Zhang**, R. Kennel, "Fully FPGA Based Direct Model Predictive Power Control for Grid-Tied AFEs with Improved Performances", *IECON 2015, Japan, 2015.* (published)

(8) Z. Chen, **Zhenbin Zhang**, R. Kennel, "Hybrid Sensorless Control for SPMSM With Multiple Saliencies", *IECON 2015, Japan, 2015.* (published)

(9) **Zhenbin Zhang**, R. Kennel, "FPGA Based Direct Model Predictive Power and Current Control of 3L NPC Active Front Ends", *PCIM-2016, Nuernburg, Germany, 2016.* (accepted)

(10) **Zhenbin Zhang**, C. Hackl, R. Kennel, "FPGA Based Direct Model Predictive Current Control of PMSM Drives with 3L NPC Power Converter", *PCIM-2016, Nurnburg, Germany, 2016.* (published)

(11) **Zhenbin Zhang**, C. Hackl, A, Mohamed, R. Kennel, " Voltage Sensorless Direct Model Predictive Control of 3L NPC Back-to-Back Power Converter PMSG Wind Turbine Systems With Fast Dynamics", *PESS-2016, Aachen, Germany, 2016.* **Best Paper Award**, (published)

(12) **Zhenbin Zhang**, R. Kennel, "Predictive Control for 3L-NPC Back-to-Back Converter PMSG Wind Turbine System with Reduced Computational Burden", *SPEEDAM-2016, Capri, Italy, 2016.* (published)

(13) **Zhenbin Zhang**, X. Cai, F. Wang, R. Kennel, "Model Predictive Current Control of 3L NPC Back-to-Back Power Converter PMSG Wind Turbine Systems: FPGA Based Experimental Evaluations", *2016 IEEE 8th International Power Electronics and Motion Control Conference (IPEMC 2016-ECCE Asia). Hefei, China, 2016.* (published)

(14) **Zhenbin Zhang**, C. Hackl, R. Kennel, "Two Direct Torque and Power Control Methods for Back-to-Back Power Converter PMSG Wind Turbine Systems", *2016 IEEE 8th International Power Electronics and Motion Control Conference (IPEMC 2016-ECCE Asia). Hefei, China, 2016.* (published)

(15) X. Cai, **Zhenbin Zhang***, R. Kennel, "Direct Torque-Flux and Deadbeat Control of 3L-NPC Driven Induction Machine: A Comparative Evaluation", *2016 IEEE 8th International Power Electronics and Motion Control Conference (IPEMC 2016-ECCE Asia). Hefei, China, 2016.* (published)

(16) **Zhenbin Zhang**, X. Cai, R. Kennel, "Fully FPGA Based Predictive Control of Back-to-Back Power Converter PMSG Wind Turbine Systems with Space Vector Modulator", *2016 IEEE 8th International Power Electronics and Motion Control Conference (IPEMC 2016-ECCE Asia). Hefei, China, 2016.* (published)

(17) **Zhenbin Zhang**, R. Kennel, "Performance-Enhanced Direct Multiple-Vector Model Predictive Power Control for Grid-Tied AFEs", *2016 IEEE 8th International Power Electronics and Motion Control Conference (IPEMC 2016-ECCE Asia). Hefei, China, 2016.* (published)

(18) X. Cai, **Zhenbin Zhang***, R. Kennel, "DC-bus Voltage Balancing for Three-level NPC Inverter Using Deadbeat Controller", *2016 IEEE 8th International Power Electronics and Motion Control Conference (IPEMC 2016-ECCE Asia). Hefei, China, 2016.* (published)

(19) **Zhenbin Zhang**, F. Wang, G, Si, R. Kennel, "FPGA Based Encoderless Predictive Control of Back-to-Back Power Converter PMSG Wind Turbine Systems with Extended Kalman Filter". *IEEE-SPEC16, Auckland, New Zealand, 2016.* **(Accepted)**

Bibliography

[1] W. E. K. Sudipta Chakraborty Marcelo G. Simoes, *Power Electronics for Renewable and Distributed Energy Systems*, 2013.

[2] F. Blaabjerg, "Future on Power Electronics for Wind Turbine Systems," *IEEE Journal of Emerging and Selected Topics in Power Electronics*, vol. 1, no. 3, pp. 139–152, 2013.

[3] M. Lange and U. Focken, "New developments in wind energy forecasting," in *Power Energy Soc. Gen. Meet. - Convers. Deliv. Electr. Energy 21st Century, 2008 IEEE*, 2008, pp. 1–8.

[4] A. M. Update, "Global wind report annual market 2013: Navigating the global wind power market," 2013.

[5] T. Burton, N. Jenkins, D. Sharpe, and E. Bossanyi, *Wind Energy Handbook*. Wiley, 2011.

[6] R. Ottersten, "On Control of Back-to-Back Converters and Sensorless Induction Machine Drives Department of Electric Power Engineering," *Flux*, 2003.

[7] Z. Chen, J. M. Guerrero, F. Blaabjerg, J. M. Guerrero, F. Blaabjerg, and J. M. Guerrero, "A review of the state of the art of power electronics for wind turbines," *IEEE Trans. Power Electron.*, vol. 24, no. 8, pp. 1859–1875, 2009.

[8] Z. Zhang and R. Kennel, "Direct Model Predictive Control of Three-Level NPC Back-to-Back Power Converter PMSG Wind Turbine Systems Under Unbalanced Grid," Tech. Rep., 2015.

[9] J. L. Li, S. J. Hu, M. Li, Y. Zhu, D. G. Kong, and H. H. Xu, "Research on the application of parallel back-to-back PWM converter on direct-drive wind power system," in *3rd International Conference on Deregulation and Restructuring and Power Technologies, DRPT 2008*, 2008, pp. 2504–2508.

[10] Z. Zhang, F. Wang, T. Sun, J. Rodriguez, and R. Kennel, "FPGA Based Experimental Investigation of a Quasi-Centralized Model Predictive Control for Back-to-Back Converters," *IEEE Transactions on Power Electronics*, vol. 31, no. 1, pp. 662–672, 2016.

[11] J. A. Suul, A. Luna, P. Rodriguez, and T. Undeland, "Virtual-flux-based voltage-sensor-less power control for unbalanced grid conditions," *IEEE Transactions on Power Electronics*, vol. 27, no. 9, pp. 4071–4087, 2012.

[12] L. H. Hansen, P. H. Madsen, F. Blaabjerg, H. C. Christensen, U. Lindhard, and K. Eskildsen, "Generators and power electronics technology for wind turbines," in *I27th Annual Conference of the IEEE Industrial Electronics Society*, vol. 3, 2001, pp. 2000–2005.

[13] I. D. Margaris and N. D. Hatziargyriou, "Direct drive synchronous generator wind turbine models for power system studies," in *Power Gener. Transm. Distrib. Energy Convers. (MedPower 2010), 7th Mediterr. Conf. Exhib.*, 2010, pp. 1–7.

[14] Z. Zhang, C. Hackl, F. Wang, Z. Chen, and R. Kennel, "Encoderless model predictive control of back-to-back converter direct-drive permanent-magnet synchronous generator wind turbine systems," in *Power Electronics and Applications (EPE), 2013 15th European Conference on*, Sept 2013, pp. 1–10.

[15] M. Liserre, R. Cardenas, M. Molinas, and J. Rodriguez, "Overview of Multi-MW Wind Turbines and Wind Parks," *IEEE Transactions on Industrial Electronics*, vol. 58, no. 4, pp. 1081–1095, 2011.

[16] P. Li, Y.-d. Song, D.-y. Li, W.-c. Cai, and K. Zhang, "Control and Monitoring for Grid-friendly Wind Turbines: Research Overview and Suggested Approach," *IEEE Transactions on Power Electronics*, vol. 30, no. 4, pp. 1979–1986, 2015.

[17] Y. Zhang, W. Xie, Z. Li, and Y. Zhang, "Model Predictive Direct Power Control of a PWM Rectifier With Duty Cycle Optimization," *IEEE Transactions on Power Electronics*, vol. 28, no. 11, pp. 5343–5351, 2013.

[18] J. H. Laks, L. Y. Pao, and A. D. Wright, "Control of wind turbines: Past, present, and future," in *2009 American Control Conference*, 2009, pp. 2096–2103.

[19] K.-H. Kim, Y.-C. Jeung, D.-C. Lee, and H.-G. Kim, "LVRT Scheme of PMSG Wind Power Systems Based on Feedback Linearization," *IEEE Transactions on Power Electronics*, vol. 27, no. 5, pp. 2376–2384, 2012.

[20] D. H. Nguyen and M. Negnevitsky, "A review of fault ride through strategies for different wind turbine systems," in *Univ. Power Eng. Conf. (AUPEC), 2010 20th Australas.*, 2010, pp. 1–5.

[21] S. Kouro, M. A. Perez, J. Rodriguez, A. M. Llor, and H. A. Young, "Model predictive control: Mpc's role in the evolution of power electronics," *IEEE Industrial Electronics Magazine*, vol. 9, no. 4, pp. 8–21, Dec 2015.

[22] J. H. Laks, L. Y. Pao, and A. D. Wright, "Control of wind turbines: Past, present, and future," in *Inproceedings of the 2009 American Control Conference*, 2009, pp. 2096–2103.

[23] S. Alepuz, A. Calle, S. Busquets-Monge, J. Nicolas-Apruzzese, and J. Bordonau, "Predictive current control of a back-to-back NPC wind energy conversion system to meet low voltage ride-through requirements," in *Ind. Electron. Soc. IECON 2013 - 39th Annu. Conf. IEEE*, 2013, pp. 5306–5311.

[24] Z. Zhang and R. Kennel, "Direct Model Predictive Control of Three-Level NPC Back-to-Back Power Converter PMSG Wind Turbine Systems Under Unbalanced Grid," in *Predictive Control of Electrical Drives and Power Electronics (PRECEDE 2015), Valparaiso, Chile.*, 2015.

[25] M. Kazmierkowski, L. Franquelo, J. Rodriguez, M. Perez, and J. Leon, "High-performance motor drives," *Industrial Electronics Magazine, IEEE*, vol. 5, no. 3, pp. 6–26, Sept 2011.

[26] W. Leonhard, "Field-orientation for controlling ac machines-principle and application," in *Power Electronics and Variable-Speed Drives, Third International Conference on*, Jul 1988, pp. 277–282.

[27] M. Malinowski, "Sensorless Control Strategies for Three - Phase PWM Rectifiers," pp. 127–127, 2001.

[28] S. Li, T. a. Haskew, and L. Xu, "Conventional and novel control designs for direct driven PMSG wind turbines," *Electric Power Systems Research*, vol. 80, no. 3, pp. 328–338, 2010.

[29] H. Li and Z. Chen, "Overview of different wind generator systems and their comparisons," *IET Renewable Power Generation*, vol. 2, no. 2, pp. 123–138, 2008.

[30] I. Takahashi and T. Noguchi, "A New Quick-Response and High-Efficiency Control Strategy of an Induction Motor," *Industry Applications, IEEE Transactions on*, vol. IA-22, no. 5, pp. 820–827, 1986.

[31] M. Depenbrock, "Direct self-control (DSC) of inverter-fed induction machine," *IEEE Transactions on Power Electronics*, vol. 3, no. 4, pp. 420–429, 1988.

[32] T. Noguchi, H. Tomiki, S. Kondo, and I. Takahashi, "Direct power control of PWM converter without power source voltage sensors," in *IAS Annual Meeting, San Dego, CA,*, vol. 2, 1996, pp. 941–946 vol.2.

[33] X. Dai, G. Liu, and R. Gretsch, "Generalized theory of instantaneous reactive quantity for multiphase power system," *IEEE Transactions on Power Delivery*, vol. 19, no. 3, pp. 965–972, 2004.

[34] H. Akagi, Y. Kanazawa, and A. Nabae, "Instantaneous Reactive Power Compensators Comprising Switching Devices without Energy Storage Components," *IEEE Transactions on Industry Applications*, vol. IA-20, no. 3, pp. 625–630, 1984.

[35] M. Żelechowski, "Space vector modulated–direct torque controlled (dtc–svm) inverter–fed induction motor drive," *Rozprawa Doktorska, Warszawa*, 2005.

[36] M. Malinowski, M. Jasin, and M. P. Kazmierkowski, "Simple Direct Power Control of Three-Phase PWM Rectifier Using Space-Vector," *IEEE Transactions on Industrial Electronics*, vol. 51, no. 2, pp. 447–454, 2004.

[37] R. Kennel and a. Linder, "Predictive control of inverter supplied electrical drives," in *2000 IEEE 31st Annual Power Electronics Specialists Conference. Conference Proceedings (Cat. No.00CH37018)*, vol. 2, 2000, pp. 761–766.

[38] R. Kennel and A. Linder, "Predictive control of inverter supplied electrical drives," in *Power Electron. Spec. Conf. 2000. PESC 00. 2000 IEEE 31st Annu.*, vol. 2, 2000, pp. 761–766 vol.2.

[39] P. Cortes, M. Kazmierkowski, R. Kennel, D. Quevedo, and J. Rodriguez, "Predictive Control in Power Electronics and Drives," *IEEE Transactions on Industrial Electronics*, vol. 55, no. 12, pp. 4312–4324, 2008.

[40] R. Kennel, A. Linder, and M. Linke, "Generalized predictive control (GPC)-ready for use in drive applications?" in *Power Electron. Spec. Conf. 2001. PESC. 2001 IEEE 32nd Annu.*, vol. 4, 2001, pp. 1839–1844 vol. 4.

[41] T. Geyer, N. Oikonomou, and F. D. Kieferndorf, "Direct Model Predictive Control: A Review of Strategies That Achieve Long Prediction Intervals for Power Electronics," *Industrial Electronics Magazine, IEEE*, vol. 8, no. March, pp. 32–43, 2014.

[42] Z. Zhang, F. Wang, T. Sun, J. Rodriguez, and R. Kennel, "Fpga-based experimental investigation of a quasi-centralized model predictive control for back-to-back converters," *Power Electronics, IEEE Transactions on*, vol. 31, no. 1, pp. 662–674, Jan 2016.

[43] P. Cortes, J. Rodriguez, D. Quevedo, and C. Silva, "Predictive current control strategy with imposed load current spectrum," *EPE-PEMC 2006: 12th International Power Electronics and Motion Control Conference, Proceedings*, vol. 23, no. 2, pp. 252–257, 2007.

[44] C. Dirscherl, C. M. Hackl, and K. Schechner, "Explicit model predictive control with disturbance observer for grid-connected voltage source power converters," in *2015 IEEE International Conference on Industrial Technology (ICIT)*, March 2015, pp. 999–1006.

[45] Z. Zhang, H. Xu, M. Xue, Z. Chen, T. Sun, R. Kennel, and C. Hackl, "Predictive control with novel virtual-flux estimation for back-to-back power converters," *Industrial Electronics, IEEE Transactions on*, vol. 62, no. 5, pp. 2823–2834, May 2015.

[46] Z. Zhang, F. Wang, M. Acikgoz, X. Cai, and R. Kennel, "Fpga hil simulation of back-to-back converter pmsg wind turbine systems," in *Power Electronics and ECCE Asia (ICPE-ECCE Asia), 2015 9th International Conference on*, June 2015, pp. 99–106.

[47] Z. Zhang, C. Hackl, and R. Kennel, "Performance-enhanced direct multiple-vector model predictive power control for grid-tied afes," in *IPEMC 2016-ECCE Asia. Hefei, China, 2016*, May 2016.

[48] M. Haque, M. Negnevitsky, and K. Muttaqi, "A Novel Control Strategy for a Variable-Speed Wind Turbine With a Permanent-Magnet Synchronous Generator," *IEEE Transactions on Industry Applications*, vol. 46, no. 1, pp. 331–339, 2010.

[49] L. Y. Pao and K. Johnson, "Control of wind turbines," *IEEE Control Systems*, vol. 31, no. 2, pp. 44–62, 2 2011.

[50] L. Y. Pao and K. E. Johnson, "A tutorial on the dynamics and control of wind turbines and wind farms," *2009 American Control Conference*, pp. 2076–2089, 2009.

[51] K. E. Johnson, "Adaptive Torque Control of Variable Speed Wind Turbines," Ph.D. dissertation, 2004.

[52] S. S. a. S. C. Bunlung Neammanee, "Control Strategies for Variable-speed Fixed-pitch Wind Turbines," in *Wind Power*, 2010, pp. 209–230.

[53] J. Mullen and J. B. Hoagg, "Wind Turbine Torque Control for Unsteady Wind Speeds Using Approximate-Angular-Acceleration Feedback," in *Inproceedings of the 52nd IEEE Conference on Decision and Control*. Florence, Italy: IEEE, Dec. 2013, pp. 397–402.

[54] Z. Zhang and R. Kennel, "Novel Ripple Reduced Direct Model Predictive Control of Three-level NPC Active Front End With Reduced Computational Effort," in *Predictive Control of Electrical Drives and Power Electronics (PRECEDE 2015), Valparaiso, Chile.*, 2015.

[55] Z. Zhang, F. Wang, T. Sun, J. Rodriguez, and R. Kennel, "A computationally-efficient quasi-centralized dmpc for back-to-back converter pmsg wind turbine systems without dc-link tracking errors," *Industrial Electronics, IEEE Transactions on*, Accepted, to appear 2016.

[56] Z. Zhang and R. Kennel, "Direct control methods for 2l back-to-back converter wind turbine systems with pmsg: an experimenal evaluations using fpga," *Sustainable energy system, IEEE Transactions on*, Under preparation, 2016.

[57] ——, "Model predictive current control of three-level npc back-to-back power converter pmsg wind turbine systems," in *IPEMC 2016-ECCE Asia. Hefei, China, 2016*, May 2016.

[58] ——, "Fully fpga based vector control methods with modulator for back-to-back converter wind turbine systems with pmsg," *Energy Conversion, IEEE Transactions on*, Under preparation, 2016.

[59] J. C. H. Guan-Chyun Hsieh, "Phase-locked loop techniques-A survey.pdf," *IEEE Transactions on Industrial Electronics*, vol. 43, no. 6, pp. 609–615, 1996.

[60] Z. Zhang and R. Kennel, "Fully fpga based predictive control of back-to-back power converter pmsg wind turbine systems with space vector modulator," in *IPEMC 2016-ECCE Asia. Hefei, China, 2016*, May 2016.

[61] M. Malinowski, M. P. Kazmierkowski, S. Hansen, F. Blaabjerg, and G. D. Marques, "Virtual-flux-based direct power control of three-phase PWM rectifiers," *Industry Applications, IEEE Transactions on*, vol. 37, no. 4, pp. 1019–1027, 2001.

[62] M. Malinowski, S. Stynski, W. Kolomyjski, and M. Kazmierkowski, "Control of Three-Level PWM Converter Applied to Variable-Speed-Type Turbines," *IEEE Transactions on Industrial Electronics*, vol. 56, no. 1, pp. 69–77, 2009.

[63] Z. Zhang, C. Hackl, and R. Kennel, "Two direct torque and power control methods for back-to-back power converter pmsg wind turbine systems," in *IPEMC 2016-ECCE Asia. Hefei, China, 2016*, May 2016.

[64] L. Zhong, M. F. Rahman, W. Y. Hu, K. W. Lim, and M. A. Rahman, "A direct torque controller for permanent magnet synchronous motor drives," *IEEE Transactions on Energy Conversion*, vol. 14, no. 3, pp. 637–642, Sep 1999.

[65] L. Zhong, M. F. Rahman, W. Y. Hu, and K. W. Lim, "Analysis of direct torque control in permanent magnet synchronous motor drives," *IEEE Transactions on Power Electronics*, vol. 12, no. 3, pp. 528–536, May 1997.

[66] T. Orlowska-Kowalska, F. Blaabjerg, and J. Rodrguez, *Advanced and Intelligent Control in Power Electronics and Drives*. Springer Publishing Company, Incorporated, 2014.

[67] E. J. Fuentes, J. Rodriguez, C. Silva, S. Diaz, and D. E. Quevedo, "Speed control of a permanent magnet synchronous motor using predictive current control," in *Power Electron. Motion Control Conf. 2009. IPEMC '09. IEEE 6th Int.*, 2009, pp. 390–395.

[68] W. Leonhard, "Control of electrical drives," Ph.D. dissertation, 2001. [Online]. Available:

[69] E. Tremblay, S. Atayde, and A. Chandra, "Comparative study of control strategies for the doubly fed induction generator in wind energy conversion systems: a dsp-based implementation approach," Ph.D. dissertation, 2011.

[70] Z. Zhang, C. Hackl, T. Sun, and R. Kennel, "Computationally efficient dmpc for three-level npc back-to-back converters in wind turbine systems with pmsg," *Power Electronics, IEEE Transactions on*, Under revision, 2015.

[71] T. Atalik, M. Deniz, E. Koc, C. O. Gercek, B. Gultekin, M. Ermis, and I. Cadirci, "Multi-DSP and -FPGA-Based Fully Digital Control System for Cascaded Multilevel Converters Used in FACTS Applications," *Industrial Informatics, IEEE Transactions on*, vol. 8, no. 3, pp. 511–527, 2012.

[72] E. Monmasson and M. N. Cirstea, "FPGA Design Methodology for Industrial Control Systems-A Review," *Industrial Electronics, IEEE Transactions on*, vol. 54, no. 4, pp. 1824–1842, 2007.

[73] Z. Zhang, C. Hackl, and R. Kennel, "Fpga based direct model predictive current control of pmsm drives with 3l npc power converter," in *PCIM - 2016, Nurnburg*, May 2016.

[74] Z. Zhang and R. Kennel, "Fpga based direct model predictive power and current control of 3l npc active front ends," in *PCIM - 2016, Nurnburg*, May 2016.

[75] Z. Zhang, J. Rodriguez, and R. Kennel, "Dmpcc, dmpfc and dmpfc for three-level npc power converter driven pmsm: Theoretical discussion and experimental evaluations," *Power Electronics, IEEE Transactions on*, Under preparation 2016.

[76] F. Borrelli, *Constrained optimal control of linear and hybrid systems*. Springer, 2003, vol. 290.

[77] A. Linder and R. Kennel, "Model Predictive Control for Electrical Drives," in *Power Electron. Spec. Conf. 2005. PESC '05. IEEE 36th*, 2005, pp. 1793–1799.

[78] ——, "Direct model predictive control - a new direct predictive control strategy for electrical drives," in *Power Electron. Appl. 2005 Eur. Conf.*, 2005, pp. 10 pp.–P.10.

[79] E. Solano, a. Llor, G. Gateau, T. Meynard, and M. Fadel, "Control strategy with variable commutation instants for MPC based on two flying capacitors connected in parallel," in *2013 15th European Conference on Power Electronics and Applications, EPE 2013*, 2013, pp. 1–9.

[80] T. Geyer, "Low Complexity Model Predictive Control in Power Electronics and Power Systems," Ph.D. dissertation, 2005.

[81] T. Geyer, G. Papafotiou, and M. Morari, "Model Predictive Direct Torque Control-Part I: Concept, Algorithm, and Analysis," *Industrial Electronics, IEEE Transactions on*, vol. 56, no. 6, pp. 1894–1905, 2009.

[82] S. Kouro, M. A. Perez, J. Rodriguez, A. M. Llor, and H. A. Young, "Model predictive control: Mpc's role in the evolution of power electronics," *IEEE Industrial Electronics Magazine*, vol. 9, no. 4, pp. 8–21, Dec 2015.

[83] P. Karamanakos, T. Geyer, S. Member, R. Kennel, and S. Member, "Reformulation of the Long-Horizon Direct Model Predictive Control Problem to Reduce the Computational Effort," pp. 3512–3519, 2014.

[84] H. Abu-Rub, J. Guzinki, J. Rodriguez, R. Kennel, and P. Cortés, "Predictive current controller for sensorless induction motor drive," in *Industrial Technology (ICIT), 2010 IEEE International Conference on*, March 2010, pp. 1845–1850.

[85] T. Geyer and D. E. Quevedo, "Performance of Multistep Finite Control Set Model Predictive Control for Power Electronics," *IEEE Transactions on Power Electronics*, vol. 30, no. 3, pp. 1633–1644, 2015.

[86] J. Rodriguez Perez and P. C. Estay, *Predictive control of power converters and electrical drives*. Chichester West Sussex UK: Wiley-IEEE Press, 2012.

[87] A. Linder, R. Kanchan, R. Kennel, and P. Stolze, *Model-Based Predictive Control of Electric Drives*, 2010.

[88] R. Kennel and D. Schöder, "A predictive control strategy for converters," in *IFAC Control in Power Electronics and Electrical Drives*, 1983, pp. 415–422.

[89] V. Fachbereich, "Programming and Industrial Control Model-Based Predictive Control of 3-Level Inverters," pp. 1–176, 2012.

[90] T. Geyer and D. E. Quevedo, "Multistep direct model predictive control for power electronics- Part 2: Analysis," *Energy Conversion Congress and Exposition (ECCE), 2013 IEEE*, pp. 1162–1169, 2013.

[91] A. Linder, "Model-Based Predictive Contro of Electric Drives," Ph.D. dissertation, 2005.

[92] P. Stolze, P. Landsmann, R. Kennel, and T. Mouton, "Finite-Set Model Predictive Control With Heuristic Voltage," in *EPE-2012*, 2012.

[93] P. Cortes, J. Rodriguez, P. Antoniewicz, and M. Kazmierkowski, "Direct Power Control of an AFE Using Predictive Control," *Power Electron. IEEE Trans.*, vol. 23, no. 5, pp. 2516–2523, 2008.

[94] R. P. Aguilera and D. E. Quevedo, "Predictive Control Formulation for Achieving a Reduced Finite Control Set in Flying Capacitor Converters," in *Proc. Eur. Control Conf. 2009, Budapest, Hungary*, 2009, pp. 3955–3960.

[95] ——, "Predictive Control of Power Converters : Designs With Guaranteed Performance," *IEEE Trans. Ind. Informatics*, vol. 11, no. 1, pp. 53–63, 2015.

[96] M. A. Perez, E. Fuentes, and J. Rodriguez, "Predictive current control of ac-ac modular multilevel converters," in *Industrial Technology (ICIT), 2010 IEEE International Conference on*, March 2010, pp. 1289–1294.

[97] J. Rodriguez, J. Pontt, C. Silva, M. Salgado, S. Rees, U. Ammann, P. Lezana, R. Huerta, and P. Cortes, "Predictive control of three-phase inverter," *Electronics Letters*, vol. 40, no. 9, pp. 561–561, 2004.

[98] J. Rodriguez, J. Pontt, C. A. Silva, P. Correa, P. Lezana, P. Cortes, and U. Ammann, "Predictive current control of a voltage source inverter," *Industrial Electronics, IEEE Transactions on*, vol. 54, no. 1, pp. 495–503, 2007.

[99] P. C. Jose Rodriguez, *Predictive Control of Power Converters and Electrical Drives*, 2012.

[100] P. Cortes, J. Rodriguez, S. Alepuz, S. Busquets-Monge, and J. Bordonau, "Finite-states model predictive control of a four-level diode-clamped inverter," in *Power Electron. Spec. Conf. 2008. PESC 2008. IEEE*, 2008, pp. 2203–2208.

[101] V. Yaramasu, B. Wu, M. Rivera, J. Rodriguez, and S. Member, "A New Power Conversion System for Megawatt PMSG Wind Turbines Using Four-Level Converters and a Simple Control Scheme Based on Two-Step Model Predictive Strategy– Part I : Modeling and

Theoretical Analysis," *IEEE Journal of Emerging and Selected Topics in Power Electronics*, vol. 2, no. 1, pp. 3–13, Mar. 2014.

[102] C. A. Rojas, J. I. Yuz, C. A. Silva, and J. Rodriguez, "Comments on predictive torque control of induction machines based on state-space models;," *IEEE Transactions on Industrial Electronics*, vol. 61, no. 3, pp. 1635–1638, March 2014.

[103] R. P. Aguilera and D. E. Quevedo, "On stability and performance of finite control set MPC for power converters," in *Predict. Control Electr. Drives Power Electron. (PRECEDE), 2011 Work.*, 2011, pp. 55–62.

[104] D. E. Quevedo, R. P. Aguilera, M. A. Perez, P. Cortes, and R. Lizana, "Model Predictive Control of an AFE Rectifier With Dynamic References," *IEEE Transactions on Power Electronics*, vol. 27, no. 7, pp. 3128–3136, 2012.

[105] R. P. Aguilera, P. Lezana, D. E. Quevedo, and S. Member, "Switched Model Predictive Control for Improved Transient and Steady-State Performance," *IEEE Transactions on Industrial Electronics*, vol. 11, no. 4, pp. 968–977, 2015.

[106] T. Geyer and D. E. Quevedo, "Multistep Finite Control Set Model Predictive Control for Power Electronics," *IEEE Transactions on Power Electronics*, vol. 29, no. 12, pp. 6836–6846, 2014.

[107] Z. Zhang, J. Rodriguez, and R. Kennel, "Cost-function and switching table based direct torque and power control of a 3l npc back-to-back power converter pmsg wind turbine systems: an experimental assessment with fpga," *Industrial Electronics, IEEE Transactions on*, Under Preparation 2015.

[108] T. Geyer, "Model predictive direct torque control: Derivation and analysis of the state-feedback control law," *IEEE Transactions on Industry Applications*, vol. 49, no. 5, pp. 2146–2157, Sept 2013.

[109] F. Villarroel, J. Espinoza, C. Rojas, J. Rodriguez, M. Rivera, and D. Sbarbaro, "Multi-objective switching state selector for finite-states model predictive control based on fuzzy decision making in a matrix converter," *Industrial Electronics, IEEE Transactions on*, vol. 60, no. 2, pp. 589–599, Feb 2013.

[110] Z. Chen, J. Gao, F. Wang, Z. Ma, Z. Zhang, and R. Kennel, "Sensorless control for spmsm with concentrated windings using multisignal injection method," *IEEE Transactions on Industrial Electronics*, vol. 61, no. 12, pp. 6624–6634, Dec 2014.

[111] E. J. Bueno, A. Hernandez, F. J. Rodriguez, C. Giron, R. Mateos, and S. Cobreces, "A dsp- and fpga-based industrial control with high-speed communication interfaces for grid converters applied to distributed power generation systems," *IEEE Transactions on Industrial Electronics*, vol. 56, no. 3, pp. 654–669, March 2009.

[112] Z. Zhang, X. Cai, R. Kennel, and F. Wang, "Model predictive current control of three-level npc back-to-back power converter pmsg wind turbine systems," in *2016 IEEE 8th International Power Electronics and Motion Control Conference (IPEMC-ECCE Asia)*, May 2016, pp. 1462–1467.

[113] T. Geyer, S. Member, P. Karamanakos, R. Kennel, and S. Member, "On the Benefit of Long-Horizon Direct Model Predictive Control for Drives with LC Filters," pp. 3520–3527, 2014.

[114] C. Xia, T. Liu, T. Shi, and Z. Song, "A Simplified Finite-Control-Set Model-Predictive Control for Power Converters," *Industrial Informatics, IEEE Transactions on*, vol. 10, no. 2, pp. 991–1002, May 2014.

[115] Z. Zhang, Z. Chen, F. Wang, and R. Kennel, "Fully fpga based performance-enhanced dmpc for grid-tied afes with multiple predictions," in *Industrial Electronics Society, IECON 2015 - 41th Annual Conference of the IEEE*, Nov 2015.

[116] S. Kouro, P. Cortes, R. Vargas, U. Ammann, and J. Rodriguez, "Model Predictive Control: A Simple and Powerful Method to Control Power Converters," *Industrial Electronics, IEEE Transactions on*, vol. 56, no. 6, pp. 1826–1838, 2009.

[117] P. Cortes, S. Kouro, B. La Rocca, R. Vargas, J. Rodriguez, J. I. Leon, S. Vazquez, L. G. Franquelo, P. Cortés, J. Rodríguez, J. I. León, and L. G. Franquello, "Guidelines for Weighting Factors Design in Model Predictive Control of Power Converters and Drives," in *Proceedings of IEEE International Conference on Industrial Technology*, Feb. 2009, pp. 1–7.

[118] "Ieee standard definitions for the measurement of electric power quantities under sinusoidal, nonsinusoidal, balanced, or unbalanced conditions," *IEEE Std 1459-2010 (Revision of IEEE Std 1459-2000)*, pp. 1–50, March 2010.

[119] T. M. Blooming and D. J. Carnovale, "Application of IEEE STD 519-1992 Harmonic limits," in *IEEE IAS Pulp and Paper Industry Conference in Appleton*, 2006.

[120] P. J. Stolze, "Advanced finite-set model predictive control for power electronics and electrical drives," PhD Dissertation, 2014.

[121] S. A. Davari, D. A. Khaburi, and R. Kennel, "An improved fcs-mpc algorithm for an induction motor with an imposed optimized weighting factor," *IEEE Transactions on Power Electronics*, vol. 27, no. 3, pp. 1540–1551, March 2012.

[122] Z. Zhang, H. Fang, and R. Kennel, "Fully fpga based direct model predictive power control for grid-tied afes with improved performance," in *Industrial Electronics Society, IECON 2015 - 41th Annual Conference of the IEEE*, Nov 2015.

[123] P. Landsmann, P. Stolze, and R. Kennel, "Optimal switching time calculation in predictive torque control," in *8th International Conference on Power Electronics - ECCE Asia*, May 2011, pp. 923–930.

[124] Z. Zhang, H. Xu, M. Xue, Z. Chen, T. Sun, R. Kennel, S. Member, and C. M. Hackl, "Predictive Control With Novel Virtual-Flux Estimation for Back-to-Back Power Converters," *IEEE Transactions on Industrial Electronics*, vol. 62, no. 5, pp. 2823–2834, 2015.

[125] P. Antoniewicz, M. P. Kazmierkowski, and M. Jasinski, "Comparative study of two Direct Power Control algorithms for AC/DC converters," in *Comput. Technol. Electr. Electron. Eng. 2008. Sib. 2008. IEEE Reg. 8 Int. Conf.*, 2008, pp. 159–163.

[126] Z. Zhang, Z. Chen, F. Wang, C. Wu, and R. Kennel, "Fully fpga based performance-enhanced dmpc for grid-tied afes with multiple predictions," Tech. Rep., Nov 2015.

[127] G. Giglia, M. Pucci, M. Ieee, C. Serporta, and G. Vitale, "Experimental Comparison of Three-Phase Distributed Generation Systems Based on VOC and DPC Control Techniques Keywords VOC and DPC Techniques," in *Power Electronics and Applications, 2007 European Conference on*, 2007, pp. 1–12.

[128] P. Cortes, J. Rodriguez, C. Silva, and A. Flores, "Delay compensation in model predictive current control of a three-phase inverter," *IEEE Transactions on Industrial Electronics*, vol. 59, no. 2, pp. 1323–1325, Feb 2012.

[129] S. Alepuz, A. Calle, S. Busquets-Monge, S. Kouro, and B. Wu, "Use of stored energy in pmsg rotor inertia for low-voltage ride-through in back-to-back npc converter-based wind power systems," *Industrial Electronics, IEEE Transactions on*, vol. 60, no. 5, pp. 1787–1796, 2013.

[130] ——, "Use of Stored Energy in PMSG Rotor Inertia for Low-Voltage Ride-Through in Back-to-Back NPC Converter-Based Wind Power Systems," *IEEE Transactions on Industrial Electronics*, vol. 60, no. 5, pp. 1787–1796, 2013.

[131] A. Calle-Prado, S. Alepuz, J. Bordonau, J. Nicolas-Apruzzese, P. Cortes, and J. Rodriguez, "Model Predictive Current Control of Grid-Connected Neutral-Point-Clamped Converters

to Meet Low-Voltage Ride-Through Requirements," in *IEEE Transactions on Industrial Electronics*, vol. 62, 2015, pp. 1503–1514.

[132] Y. Suh and T. Lipo, "Modeling and analysis of instantaneous active and reactive power for pwm ac/dc converter under generalized unbalanced network," *Power Delivery, IEEE Transactions on*, vol. 21, no. 3, pp. 1530–1540, July 2006.

[133] Y. Zhang and C. Qu, "Direct power control of a pulse width modulation rectifier using space vector modulation under unbalanced grid voltages," *IEEE Transactions on Power Electronics*, vol. 30, no. 10, pp. 5892–5901, Oct 2015.

[134] T. Noguchi, H. Tomiki, S. Kondo, and I. Takahashi, "Direct power control of PWM converter without power-source voltage sensors," in *Industry Applications, IEEE Transactions on*, vol. 34, 1998, pp. 473–479.

[135] J. Jung, S. Lim, and K. Nam, "A feedback linearizing control scheme for a PWM converter-inverter having a very small DC-link capacitor," *Industry Applications, IEEE Transactions on*, vol. 35, no. 5, pp. 1124–1131, Sep. 1999.

[136] T.-S. Lee, "Input-output linearization and zero-dynamics control of three-phase AC/DC voltage-source converters," *Power Electronics, IEEE Transactions on*, vol. 18, no. 1, pp. 11–22, Jan. 2003.

[137] R. P. Burgos, E. P. Wiechmann, and J. Holtz, "Complex state-space modeling and nonlinear control of active front-end converters," *Industrial Electronics, IEEE Transactions on*, vol. 52, no. 2, pp. 363–377, 2005.

[138] J. Rodriguez, J. Pontt, P. Cortes, and R. Vargas, "Predictive Control of a Three-Phase Neutral Point Clamped Inverter," in *Power Electron. Spec. Conf. 2005. PESC '05. IEEE 36th*, 2005, pp. 1364–1369.

[139] M. Vasiladiotis and A. Rufer, "Dynamic analysis and state feedback voltage control of single-phase active rectifiers with dc-link resonant filters," *Power Electronics, IEEE Transactions on*, vol. 29, no. 10, pp. 5620–5633, Oct 2014.

[140] J. Alcala, V. Cardenas, a. RamÃrez, and J. Gudino, "Study of the bidirectional power flow in Back - to - Back converters by using linear and nonlinear control strategies," *2011 IEEE Energy Conversion Congress and Exposition*, pp. 806–813, 2011.

[141] R. Vargas, U. Ammann, J. Rodriguez, and J. Pontt, "Predictive strategy to reduce common-mode voltages on power converters," in *2008 IEEE Power Electronics Specialists Conference*, June 2008, pp. 3401–3406.

[142] C. Yang and K. Smedley, "Three-Phase Boost-Type Grid-Connected Inverter," *Power Electron. IEEE Trans.*, vol. 23, no. 5, pp. 2301–2309, 2008.

[143] L. Shang, D. Sun, and J. Hu, "Sliding-mode-based direct power control of grid-connected voltage-sourced inverters under unbalanced network conditions," *IET Power Electronics*, vol. 4, no. 5, pp. 570–570, 2011.

[144] A. Bouafia, J.-P. Gaubert, and F. Krim, "Predictive Direct Power Control of Three-Phase Pulsewidth Modulation (PWM) Rectifier Using Space-Vector Modulation (SVM)," *IEEE Transactions on Power Electronics*, vol. 25, no. 1, pp. 228–236, 2010.

[145] Z. Song, C. Xia, and T. Liu, "Predictive current control of three-phase grid-connected converters with constant switching frequency for wind energy systems," *IEEE Transactions on Industrial Electronics*, vol. 60, no. 6, pp. 2451–2464, June 2013.

[146] M. Preindl and S. Bolognani, "Model Predictive Direct Speed Control with Finite Control Set of PMSM Drive Systems," *IEEE Transactions on Power Electronics*, vol. 28, no. 2, pp. 1007–1015, 2013.

[147] S. Mariethoz, A. Fuchs, and M. Morari, "A VSC-HVDC Decentralized Model Predictive Control Scheme for Fast Power Tracking," *IEEE Transactions on Power Delivery*, vol. 29, no. 1, pp. 462–471, 2014.

[148] J. Rodriguez, M. P. Kazmierkowski, J. R. Espinoza, P. Zanchetta, H. Abu-Rub, H. A. Young, and C. A. Rojas, "State of the Art of Finite Control Set Model Predictive Control in Power Electronics," *IEEE Transactions on Industrial Informatics*, vol. 9, no. 2, pp. 1003–1016, 2013.

[149] J. Guzinski and H. Abu-Rub, "Speed Sensorless Induction Motor Drive With Predictive Current Controller," *Industrial Electronics, IEEE Transactions on*, vol. 60, no. 2, pp. 699–709, 2013.

[150] T. Noguchi, H. Tomiki, S. Kondo, and I. Takahashi, "Direct power control of PWM converter without power-source voltage sensors," *IEEE Transactions on Industrial Applications*, vol. 34, no. 3, pp. 473–479, 1998.

[151] S. Hansen, M. Malinowski, F. Blaabjerg, and M. P. Kazmierkowski, "Sensorless control strategies for PWM rectifier," in *Appl. Power Electron. Conf. Expo. 2000. APEC 2000. Fifteenth Annu. IEEE*, vol. 2, 2000, pp. 832–838 vol.2.

[152] J. Gonzalez Norniella, J. M. Cano, G. A. Orcajo, C. H. Rojas, J. F. Pedrayes, M. F. Cabanas, and M. G. Melero, "Improving the Dynamics of Virtual-Flux-Based Control of Three-Phase Active Rectifiers," *IEEE Transactions on Industrial Electronics*, vol. 61, no. 1, pp. 177–187, 2014.

[153] B. Han, H. Lee, and D. Yoon, "Hardware simulator development for PMSG wind power system," in *Power Energy Soc. Gen. Meet. 2009. PES '09. IEEE*, 2009, pp. 1–6.

[154] J. L. Duarte, A. Van Zwam, C. Wijnands, and A. Vandenput, "Reference frames fit for controlling PWM rectifiers," *Ind. Electron. IEEE Trans.*, vol. 46, no. 3, pp. 628–630, 1999.

[155] S. Bhattacharya, A. Veltman, D. M. Divan, and R. D. Lorenz, "Flux-based active filter controller," *Industry Applications, IEEE Transactions on*, vol. 32, no. 3, pp. 491–502, 1996.

[156] J. Hu, J. Zhu, D. G. Dorrell, and J. M. Guerrero, "Virtual Flux Droop Method: A New Control Strategy of Inverters in Microgrids," *IEEE Transactions on Power Electronics*, vol. PP, no. 99, p. 1, 2013.

[157] U.-C. Kwak, Sangshin Moon and J.-C. Park, "Predictive-Control-Based Direct Power Control with an Adaptive Parameter Identification Technique for Improved AFE Performance," *IEEE Transactions on Power Electronics*, vol. 29, no. 11, pp. 6178–6187, 2014.

[158] E. Monmasson and M. Cirstea, "FPGA Design Methodology for Industrial Control Systems - A Review," *IEEE Transactions on Industrial Electronics*, vol. 54, no. 4, pp. 1824–1842, 2007.

[159] Z. Zhang, C. Hackl, and R. Kennel, "Voltage sensorless direct model predictive control of 3l npc back-to-back power converter pmsg wind turbine systems with fast dynamics," in *PESS-2016, Aachen, Germany, 2016*, May 2016.

[160] J. Ribrant and L. M. Bertling, "Survey of Failures in Wind Power Systems With Focus on Swedish Wind Power Plants During 1997–2005," *IEEE Transactions on Energy Conversion*, vol. 22, no. 1, pp. 167–173, 2007.

[161] Z. Chen, F. Wang, G. Luo, Z. Zhang, and R. Kennel, "Secondary saliency tracking based sensorless control for concentrated winding spmsm," *Industrial Informatics, IEEE Transactions on*, vol. PP, no. 99, pp. 1–1, 2015.

[162] P. Landsmann, D. Paulus, P. Stolze, and R. Kennel, "Saliency based encoderless Predictive Torque Control without signal injection for a reluctance synchronous machine," in *Proceedings of the 9th IEEE International Power and Energy Conference (IPEC)*, 2010, pp. S1–10—-S1–17.

[163] P. Landsmann, R. Kennel, H. W. de Kock, and M. J. Kamper, "Fundamental Saliency based Encoderless Control for Reluctance Synchronous Machines," in *Proceedings of the XIX International Conference on Electrical Machines (ICEM)*, 2010, pp. 1–7.

[164] P. Landsmann, D. Paulus, P. Stolze, and R. Kennel, "Reducing the parameter dependency of Encoderless Predictive Torque Control for reluctance machines," in *Proceedings of the IEEE International Symposium on Sensorless Control for Electrical Drives (SLED)*, 2010, pp. 93–99.

[165] S. Bolognani, R. Oboe, and M. Zigliotto, "Sensorless full-digital pmsm drive with ekf estimation of speed and rotor position," *Industrial Electronics, IEEE Transactions on*, vol. 46, no. 1, pp. 184–191, Feb 1999.

[166] S. Bolognani, L. Tubiana, and M. Zigliotto, "Extended kalman filter tuning in sensorless pmsm drives," in *Power Conversion Conference, 2002. PCC-Osaka 2002. Proceedings of the*, vol. 1, 2002, pp. 276–281 vol.1.

[167] S. Bolognani, M. Zigliotto, and K. Unterkofler, "On-line parameter commissioning in sensorless pmsm drives," in *Industrial Electronics, 1997. ISIE '97., Proceedings of the IEEE International Symposium on*, vol. 2, Jul 1997, pp. 480–484 vol.2.

[168] V. Utkin, "Variable structure systems with sliding modes," *Automatic Control, IEEE Transactions on*, vol. 22, no. 2, pp. 212–222, Apr 1977.

[169] K.-L. Kang, J.-M. Kim, K.-B. Hwang, and K.-H. Kim, "Sensorless control of {PMSM} in high speed range with iterative sliding mode observer," in *Proceedings of the 19th Annual IEEE Applied Power Electronics Conference and Exposition*, vol. 2, 2004, pp. 1111–1116.

[170] R. E. Kalman, "A new approach to linear filtering and prediction problems," *ASME Journal of Basic Engineering*, 1960.

[171] ——, "Mathematical description of linear dynamical systems," *SIAM Journal on Control*, vol. 1, no. 2, pp. 152–192, 1963.

[172] ——, "Contributions to the Theory of Optimal Control," *Boletin de la Sociedad Matematica Mexicana*, vol. 5, pp. 102–119, 1960.

[173] S. Bolognani, L. Tubiana, and M. Zigliotto, "Ekf-based sensorless ipm synchronous motor drive for flux-weakening applications," *Industry Applications, IEEE Transactions on*, vol. 39, no. 3, pp. 768–775, May 2003.

[174] K.-L. Kang, J.-M. Kim, K.-B. Hwang, and K.-H. Kim, "Sensorless control of PMSM in high speed range with iterative sliding mode observer," in *Proceedings of the 19th Annual IEEE Applied Power Electronics Conference and Exposition*, vol. 2, 2004, pp. 1111–1116.

[175] H. Kim, J. Son, and J. Lee, "A High-Speed Sliding-Mode Observer for the Sensorless Speed Control of a PMSM," *IEEE Transactions on Industrial Electronics*, vol. 58, no. 9, pp. 4069–4077, 2011.

[176] E. Ryan and C. Sangwin, "Controlled functional differential equations and adaptive tracking," *Systems & Control Letters*, vol. 47, no. 5, pp. 365 – 374, 2002.

[177] V. Utkin, "Variable structure systems with sliding modes," *IEEE Transactions on Automatic Control*, vol. 22, no. 2, pp. 212–222, Apr 1977.

[178] Z. Yan and V. Utkin, "Sliding mode observers for electric machines-an overview," in *IECON 02,IEEE 2002 28th Annual Conference of the Industrial Electronics Society*, vol. 3, Nov 2002, pp. 1842–1847 vol.3.

[179] F. Lehfuss, G. Lauss, P. Kotsampopoulos, N. Hatziargyriou, P. Crolla, and A. Roscoe, "Comparison of multiple power amplification types for power Hardware-in-the-Loop applications," in *2012 IEEE Work. Complex. Eng. COMPENG 2012 - Proc.*, 2012, pp. 95–100.

[180] D. Ocnasu, S. Bacha, I. Munteanu, C. Dufour, and D. Roye, "Real-time power-hardware-in-the-loop facility for shunt and serial power electronics benchmarking," *2009 13th Eur. Conf. Power Electron. Appl.*, 2009.

[181] M. Steurer, C. S. Edrington, M. Sloderbeck, W. Ren, and J. Langston, "A megawatt-scale power hardware-in-the-loop simulation setup for motor drives," vol. 57, pp. 1254–1260.

[182] Y. Han, G. Tan, H. Li, and X. Wu, "Study of multi-level rectifier in high power system based on a novel virtual flux observer," in *Power Electron. Drive Syst. 2009. PEDS 2009. Int. Conf.*, 2009, pp. 989–992.

[183] H. Keyuan, Z. Ying, H. Shoudao, L. Jining, G. Jian, and C. Luoqiang, "Some Practical Consideration of a 2mw Direct-Drive Permanent-Magnet Wind-Power Generation System," in *Energy Environ. Technol. 2009. ICEET '09. Int. Conf.*, vol. 1, 2009, pp. 824–828.

[184] L. Weiliang, C. Lei, O. Jing, and C. Shukang, "Simulation of PMSG wind turbine system with sensor-less control technology based on model reference adaptive system," in *Electr. Mach. Syst. (ICEMS), 2011 Int. Conf.*, 2011, pp. 1–3.

[185] A. A. Daoud, S. S. Dessouky, and A. A. Salem, "Control scheme of PMSG based wind turbine for utility network connection," in *Environ. Electr. Eng. (EEEIC), 2011 10th Int. Conf.*, 2011, pp. 1–5.

[186] Y. Chou and H. Nian, "Sensorless control of PMSG based on dual two-level inverter open winding configuration for wind turbines," pp. 1–6, 2012.

[187] R. A. Ibrahim, M. S. Hamad, Y. G. Dessouky, and B. W. Williams, "A review on recent low voltage ride-through solutions for pmsg wind turbine," in *Power Electronics, Electrical Drives, Automation and Motion (SPEEDAM), 2012 International Symposium on*, June 2012, pp. 265–270.

[188] V. Yaramasu and B. Wu, "Predictive Control of a Three-Level Boost Converter and an NPC Inverter for High-Power PMSG-Based Medium Voltage Wind Energy Conversion Systems," *IEEE Transactions on Power Electronics*, vol. 29, no. 10, pp. 5308–5322, 2014.

[189] A. A. Daoud, S. S. Dessouky, and A. A. Salem, "Control scheme of PMSG based wind turbine for utility network connection," in *Environ. Electr. Eng. (EEEIC), 2011 10th Int. Conf.*, 2011, pp. 1–5.

[190] D. Fujin and C. Zhe, "Low-voltage ride-through of variable speed wind turbines with permanent magnet synchronous generator," in *Industrial Electronics, 2009. IECON '09. 35th Annual Conference of IEEE*, 2009, pp. 621–626.

[191] M. Ezzat, M. Benbouzid, S. M. Muyeen, and L. Harnefors, "Low-voltage ride-through techniques for DFIG-based wind turbines: State-of-the-art review and future trends," *IECON Proceedings (Industrial Electronics Conference)*, pp. 7681–7686, 2013.

[192] M. Molinas, J. Suul, and T. Undeland, "Low voltage ride through of wind farms with cage generators: Statcom versus svc," *Power Electronics, IEEE Transactions on*, vol. 23, no. 3, pp. 1104–1117, May 2008.

[193] M. Rizo, A. Rodriguez, E. Bueno, F. Rodriguez, and C. Giron, "Low voltage ride-through of wind turbine based on interior permanent magnet synchronous generators sensorless vector controlled," in *Energy Conversion Congress and Exposition (ECCE), 2010 IEEE*, Sept 2010, pp. 2507–2514.

[194] S. Alepuz, A. Calle, S. Busquets-Monge, S. Kouro, and B. Wu, "Use of stored energy in pmsg rotor inertia for low-voltage ride-through in back-to-back npc converter-based wind power systems," pp. 1787–1796, May 2013.

[195] A. Yousef, A. Nasiri, and O. Abdelbaqi, "Wind turbine level energy storage for low voltage ride through (lvrt) support," in *Power Electronics and Machines for Wind and Water Applications (PEMWA), 2014 IEEE Symposium*, July 2014, pp. 1–6.